2011

Optically and infrared stimulated luminescence investigations of the Middle and Later Stone Age in East Africa

Luke A. Gliganic
University of Wollongong, lg527@uowmail.edu.au

Optically and infrared stimulated luminescence investigations of the Middle and Later Stone Age in East Africa

A thesis submitted in fulfilment of the requirements for the award of the degree

Doctor of Philosophy

from

University of Wollongong

by

Luke A. Gliganic

B.A. Stony Brook University

Centre for Archaeological Science

School of Earth and Environmental Sciences

2011

Certification

I, Luke A. Gliganic, declare that this thesis, submitted in fulfilment of the requirements for the award of Doctor of Philosophy, in the School of Earth and Environmental Sciences, University of Wollongong, is wholly my own work unless otherwise referenced or acknowledged. The document has not been submitted for qualifications at any other academic institution.

Luke A. Gliganic

31 March 2011

Abstract

The Late Pleistocene was a period during which the behaviour and technology of Middle Stone Age (MSA) and Later Stone Age (LSA) modern humans in East Africa changed considerably. The East African climate shifted between periods of humidity and aridity, and populations of modern humans expanded, contracted and dispersed within, and out of, Africa. During this time, symbolic behaviours proliferated, technological change occurred at a rapid rate and innovative tool types, such as backed microliths, became prevalent. The timing and reasons for these changes in behaviour and technologies remain largely unresolved, however, due to the difficulty of obtaining reliable age estimates for the East African MSA and LSA cultures. Constraining the timing of behavioural and technological changes in the archaeological record can allow an interpretation of *why* these changes occurred, through comparisons with palaeoclimatic and genetic records. To this end, the main aim of this thesis is to resolve *when* various changes in behaviour and technology occurred during the East African MSA and LSA. Two sites were chosen to address this issue: Mumba rockshelter in Tanzania and Moche Borago rockshelter in Ethiopia. Sediment samples for optically stimulated luminescence (OSL) and infrared stimulated luminescence (IRSL) dating were collected to construct improved, numerical-age chronologies for the archaeological deposits at both of these sites. OSL dating is a technique that has been used to estimate accurate and precise depositional ages for Late Pleistocene sediments in other geographic regions and archaeological contexts and, thus, has the potential to construct reliable chronologies for the MSA and LSA in East Africa.

OSL investigations were conducted on individual sand-sized grains of quartz using the single-aliquot regenerative-dose (SAR) procedure. Substantial grain-to-grain variability in OSL signal behaviour was observed and characterised. Dose recovery tests were used to determine the measurement conditions and data analysis procedures most appropriate for objectively isolating grains dominated by the most light-sensitive component of quartz OSL, for which the SAR procedure can be used to obtain reliable estimates of the equivalent dose (D_e). D_e values were estimated for individual grains and the distributions of these values were analysed using well-established statistical models. For samples affected by beta dose rate heterogeneity and post-depositional

mixing, corrections were applied and the D_e populations that best represented the burial ages of the sediments and associated artefacts were used to obtain OSL ages for samples from Mumba rockshelter. Potassium (K) feldspars were also investigated at Mumba to extend the luminescence chronology to the older deposits at this site. Quartz grains from the latter deposits yielded only minimum ages, because the OSL signal was in saturation. The IRSL signal was found to be associated with a high-temperature TL peak at 430°C and the IRSL signal intensity and decay curve shape were largely dependent on stimulation temperature. The IRSL signal measured at an elevated temperature (225°C) after an initial low-temperature (50°C) IR bleach (the 'post-IR IRSL' signal) was shown to be bleachable by sunlight, suitable for D_e estimation using the SAR procedure and suffer only minimally from the malign phenomenon of anomalous fading. Using this signal, D_e values and fading rates were measured, and the fading-corrected IRSL ages were consistent with the single-grain OSL ages for the younger deposits at Mumba, where both techniques could be applied.

Finally, volcanic sediments from Moche Borago were investigated. Quartz was absent or rare and had a poorly-behaved OSL signal that was unsuitable for the SAR procedure. K-feldspars were also investigated and were shown to have substantially different TL and IRSL properties than those from Mumba. Although the IRSL signal passed the standard tests of SAR suitability, the combination of high fading rates, weak luminescence signals and few grains prevented the determination of reliable IRSL ages for the Moche Borago samples.

The OSL and post-IR IRSL ages obtained for the archaeological sequence at Mumba rockshelter are in correct stratigraphic order and provide temporal constraints on the significant behavioural and technological changes recorded at the site. First, the revised chronology constrains the timing of the point-based Kisele Industry (~74–63 ka), the backed piece-based Mumba Industry (~57–49 ka) and the scraper-based Nasera Industry (~37 ka). Second, the timing of the emergence of ornamental OES beads associated with the Mumba Industries is shown to have occurred ~49 ka ago. Third, ages for deposits that contain obsidian from distant sources provide a minimum estimate of the duration of likely long-distance exchange networks between the occupants of Mumba and southern Kenya. The improved chronology for Mumba allows the archaeological record at this site to be compared with existing archaeological,

palaeoenvironmental, genetic and demographic records for East Africa and the continent more broadly. In doing so, possible reasons for the observed technological and behavioural changes that occurred in the Late Pleistocene can be inferred, and such inferences are discussed in the penultimate chapter of this thesis.

Acknowledgements:

I would like to express my deepest gratitude to my principal supervisor, Professor 'Bert' Roberts, for laying the groundwork of this project, providing me with the opportunity and means to pursue this research, and for his helpful feedback and input in regards to this research. I am especially grateful for the time and effort that he put into reading drafts of my writing, particularly this thesis. Bert's insightful comments have certainly made this thesis better and improved my writing immensely, albeit at the expense of my ego.

I am indebted to my co-supervisor, Zenobia Jacobs, for teaching me most of what I know about OSL dating of quartz. The time and effort that she spent teaching me, and reading and commenting on drafts of my writings cannot be overstated and are greatly appreciated. Zenobia provided me with guidance when I needed it, while giving me the leeway and resources to pursue my own research.

I would like to thank Manuel Domínguez-Rodrigo, Mary Prendergast and Audax Mabulla for their thoughtful answers whenever I had questions about Mumba. I would like to thank Steve Brandt and Erich Fisher for providing information about Moche Borago. I am grateful to Gitte Jensen for her help and support in learning the finer points of feldspar IRSL dating. I would also like to thank José Abrantes for his technical support, assistance and company in the lab over the first two years of my research.

I would like to thank several of the members of the OSL lab at the University of Wollongong, namely Steph Kermode, Nathan Jankowski, Michael Meyer and Jan-Hendrik 'Henne' May, for their camaraderie, ideas and support over the past three and a half years. Our 'OSL and Beer' meetings were always fun, therapeutic and (occasionally) even educational. I would like to thank Anders Hallan for everything from his help in editing my work to teaching me to play the guitar (a welcome distraction), but mostly for his friendship and ability to have both scientific and very unscientific discussions, 'as it were'. I would like to thank Brett Heino and Dennis Mitchell for their friendship, conversations, spots and belays over the past three years.

This work would never have been completed (or begun) if not for the support of Amy Robinson. I am eternally grateful for everything she has helped me with, from her unwavering encouragement and patience to the dinners she prepared for my late nights

at the office. Mostly, she could always remind me that I can ‘move mountains’ whenever I needed to hear it.

I would like to thank my family, Dan, Nancy, Andrew and Kim, for their support, encouragement, distractions and late-night phone calls through all these years. Their optimism and encouragement were continual sources of motivation.

This work is dedicated to Dr. Nancy Penncavage, who broke the trail that I am now following, and who is an inspiration for her indomitable spirit and vitality.

Table of Contents

List of Figures

List of Tables

List of Tables

List of Abbreviations:

AAR – amino acid racemisation
ABOX-SC – acid-base wet oxidation and stepped-combustion
AMS – accelerator mass spectrometry
BIC – Bayes Information Criterion
CAM – central age model
CW-OSL – continuous wave – optically stimulated luminescence
DAP – dual-aliquot regenerative-dose
D_e – equivalent dose
ESA – Early Stone Age
EU – early-uptake model
FMM – finite mixture model
HCl – hydrochloric
HF – hydrofluoric
HOW – hot optical wash
ICP-MS – inductively coupled plasma mass spectrometry
IR – infrared
IRSL – infrared stimulated luminescence
K – potassium
ka – thousand years
LED – light-emitting diode
L_{lik} – maximum log-likelihood
LM-OSL – linearly modulated – optically stimulated luminescence
LP – Lower Palaeolithic
LSA – Later Stone Age
LU – linear-uptake model
Ma – million years
MAM – minimum age model
MEK – methyl ethyl ketone
MIS – marine isotope stage
MP – Middle Palaeolithic
MSA – Middle Stone Age
Na – sodium
OES – ostrich eggshell
OSL – optically stimulated luminescence
PIC – photoionisation cross-section
PMT – photomultiplier tube
R – rubidium
SAAD – single-aliquot additive-dose
SAR – single-aliquot regenerative-dose
SARA – single-aliquot regeneration and added dose
TIMS – thermal ionisation mass spectrometry
Th – thorium
TL – thermoluminescence
U – uranium
UP – Upper Palaeolithic
UV – ultraviolet

Chapter 1: Introduction: A geochronological approach to assessing the timing of behavioural change in the East African Middle and Later Stone Ages

1.1 Aims

The overarching aim of this thesis is to contribute to resolving *when* and *why* various behaviours and technologies emerged in sub-Saharan Africa during the Late Pleistocene. During this period, modern humans populations expanded and dispersed throughout, and out of, Africa (Quintana-Murci et al., 1999; Macaulay et al., 2005; Tishkoff et al., 2007; Atkinson et al., 2008, 2009), symbolic behaviours proliferated (Ambrose, 1998; Henshilwood et al., 2002, 2004; Bouzouggar et al., 2007; Texier et al., 2010), and technologies diversified (McBrearty and Brooks, 2000; Ambrose, 2001, 2002; Wadley, 2007; Soriano et al., 2007; Lombard et al., 2010). To elucidate these issues, the main aim of this thesis is to construct an improved chronology for the Middle Stone Age (MSA) and Later Stone Age (LSA) deposits from two sites in East Africa: Mumba and Moche Borago rockshelters. Both sites have long archaeological sequences that contain changes in technology, including the transition from MSA to LSA toolkits. Two significant changes at Mumba include the transition from point-based to backed piece-based toolkits and the emergence of ornamental ostrich eggshell (OES) beads (Mehlman, 1989; Diez-Martín et al., 2009).

The aims of this thesis will be achieved using optically stimulated luminescence (OSL) dating of quartz and infrared stimulated luminescence (IRSL) dating of potassium (K)-feldspar grains to provide numerical-age chronologies for the archaeological deposits associated with these transitions in technologies and behaviours. By creating a reliable chronology for these two sites, comparisons can be made between the technologies, behaviours, existing palaeoclimate reconstructions and genetic evidence for early human demographics. This multidisciplinary approach can yield new insights into the timing of, and potential reasons for, the emergence and dispersal of microlithic, backed piece-based technologies and symbolic behaviours in sub-Saharan Africa during the Late Pleistocene.

1.2 Anatomical and behavioural origins of modern humans

1.2.1 Anatomical origin of modern humans

Historically, there have been two competing general models to explain the evolution of anatomically modern humans (*Homo sapiens*): the "Multiregional" hypothesis (Wolpoff, 1989; Smith et al., 1989) and the "Out of Africa" hypothesis (Stringer and Andrews, 1988). Most research from the past 20 years has supported the "Out of Africa" hypothesis, which postulates that anatomically modern humans evolved in Africa during the Middle Pleistocene and that all living people are descendents of this founder population. The emergence of modern humans broadly coincides with the proliferation of MSA technologies and the abandonment of Early Stone Age (ESA) technologies. During the Late Pleistocene, groups of anatomically modern humans dispersed from Africa to replace archaic hominids in Europe and Asia and to colonise the remaining continents[1]. Fossil evidence supports the "Out of Africa" model, with the earliest *Homo sapiens* fossils, from Ethiopia, being dated to ~160 ka by multiple techniques (Clark et al., 2003; White et al., 2003) and 195 ± 5 ka (McDougall et al., 2005, 2008). In addition, this model is currently supported by the bulk of the genetic evidence (e.g., Cann et al., 1987; Vigilant et al., 1991; Macaulay et al., 2005; Gonder et al., 2007; Atkinson et al., 2008; Oppenheimer, 2009).

1.2.2 Origins of modern human behaviour

There is no consensus about when or where behavioural modernity emerged and developed (McBrearty and Brooks, 2000). Klein (1995, 2001, 2008) has argued that an advantageous mutation in an African population approximately 50 ka begat the fully modern human brain. He argues that the newly acquired cognitive capabilities allowed the development of behavioural modernity, the emergence of LSA technologies and symbolic behaviour (e.g., ornamentation), and the dispersal of modern humans out of Africa.

Increasingly, however, there is evidence for modern behaviours that precede the so-called MSA/LSA transition. Ochre, a potentially symbolic material, has been found

[1] Recent evidence has suggested that the dispersal of anatomically modern humans throughout the Old World did not result in a complete replacement of archaic hominid species. Genetic studies have demonstrated that there was likely some interbreeding between modern humans, Neanderthals (Green et al., 2010), and a recently discovered hominid from the site of Denisova in southern Siberia (Krause et al. 2010; Reich et al., 2010).

in Middle Pleistocene deposits in Zambia, Sudan, and South Africa (Barham, 1998, 2002b; Van Peer et al., 2003; Marean et al., 2007). Ornamentation, such as beads, conveys socially constructed meanings and permits the storage and display of information, thus, providing an archaeological marker for symbolic behaviours (d'Errico et al., 2005; Kuhn and Stiner, 2007). Beads and ochre have been found in Middle Palaeolithic (MP) assemblages from North Africa (Vanhaeren et al., 2006; Bouzouggar et al., 2007; d'Errico et al., 2009). Beads, engraved ochres, and engraved OES fragments have been found in Still Bay and Howiesons Poort MSA assemblages across southern Africa (Henshilwood et al., 2002, 2004, 2009; d'Errico et al., 2005; Mackay and Welz, 2008; Texier et al., 2010). There is also evidence for symbolic behaviours, in the form of beads, burial of the dead, and symbolic ochre use, from deposits associated with Neanderthals (d'Errico and Soressi, 2002; d'Errico et al., 2003; Conard, 2007; Zilhão et al., 2010). The temporal and geographical disparity in the manifestation of symbolic behaviour and its expression by archaic hominids may suggest that the capacity for such behaviour was present from, or before, the anatomical origins of modern humans.

1.3 Defining the MSA and LSA

The scheme used to describe the African Stone Age was introduced by Goodwin and Van Riet Lowe (1929). Its three stages, the ESA, MSA and LSA, were generally the African equivalents of the European Lower Palaeolithic (LP), Middle Palaeolithic (MP) and Upper Palaeolithic (UP), respectively. The MSA is characterised by prepared core technologies and flake-based assemblages. It is likely that composite tool technologies were routine in the MSA, with many points being deliberately modified to facilitate hafting (McBrearty and Brooks, 2000; Lombard, 2005). MSA assemblages generally lack the heavy duty tools that are typical of the ESA (e.g., Acheulian handaxes), and the microlithic tools typical of the LSA (Clark, 1988; McBrearty and Brooks, 2000). Artefacts that are commonly cited as comprising LSA toolkits include backed, often standardised, microliths (Barut, 1994; McBrearty and Brooks, 2000; Ambrose, 2002) and an abundance of bipolar core technology (Mercader and Brooks, 2001). LSA assemblages are also characterised by a lack of MSA-like points.

In practice, individual assemblages often cannot unambiguously be classified as ESA, MSA or LSA. Assemblages that contain features typical of both MSA and LSA toolkits are sometimes referred to as 'intermediate' assemblages. This terminology has largely been abandoned, however, following the discovery that the 'second intermediate' assemblage from the type-site of Magosi was an amalgamation of artefacts from the multiple occupation layers that were mixed during excavation (McBrearty and Brooks, 2000), although it is still used occasionally in the literature. Two sites in Zambia (Twin Rivers and Kalambo Falls), dating to the Middle Pleistocene, contain typical MSA assemblages, except for their association with several stratigraphically secure macrolithic backed pieces (Barham, 2002a). The Howiesons Poort Industry from southern Africa is an MSA toolkit that is often found over- and underlying typical MSA deposits (Singer and Wymer, 1982; Wurz, 1999; Jacobs et al., 2008a; Lombard, 2008; Villa et al., 2010). The defining feature of the Howiesons Poort Industry, however, is the prevalence of LSA-like standardised geometric backed pieces in the same assemblage as MSA tools, such as flake-blades, denticulates, and unifacial and bifacial points (Singer and Wymer, 1982; Wurz, 1999, 2000; Soriano et al., 2007). The Mumba Industry (discussed in detail in Chapter 2) was described by Mehlman (1989) as transitional between the MSA and LSA based on the presence of both points (MSA) and microlithic backed pieces (LSA). LSA-like bone tools are found in Late Pleistocene MSA assemblages from tropical central Africa (Yellen et al., 1995; Brooks et al., 1995) and southern Africa (Singer and Wymer, 1982; Henshilwood and Sealy, 1997; Henshilwood et al., 2001; d'Errico and Henshilwood, 2007; Blackwell et al., 2008). The prevalence of assemblages with features typical of the MSA and LSA suggests that these terms may be ineffective for describing individual lithic industries. The presence of various tool types and technologies in an industry, therefore, may be more informative than the industry's designation as 'MSA' or 'LSA'.

1.4 Dating the MSA and LSA in East Africa

The need for objects and events in the archaeological record to be temporally constrained is important. Without a reliable chronology, the archaeological sequence of a site cannot be compared with that from other sites (in the same and more distant regions), or evidence from other disciplines, such as palaeoclimatic reconstructions. A

variety of dating methods have been developed that can be used to assess the timing of various 'target' events. Each method can be used to determine the age of particular objects/events, using particular materials, over a limited range of time. Figure 1.1 illustrates the broad age ranges over which particular dating methods are applicable.

High precision methods, such as $^{40}Ar/^{39}Ar$, can be used to constrain the timing of the earliest MSA in Africa. Ages for this period cluster between 300 and 240 ka, with Acheulian (typical ESA) assemblages disappearing in Africa by approximately 200 ka (McBrearty and Brooks, 2000; Tyron and McBrearty, 2002). An early MSA assemblage from Gademotta, Ethiopia has been dated using $^{40}K/^{40}Ar$ to ~235 ka (Wendorf et al., 1994). In the Kapthurin Formation, Kenya, MSA technologies have been dated using $^{40}Ar/^{39}Ar$ to >285 ka (Deino and McBrearty, 2002; Tyron and McBrearty, 2002). This antiquity is supported by similar ages (~230 ka or older) obtained by uranium-series dating of speleothem overlying the early MSA assemblages in Zambia (Barham and Smart, 1996).

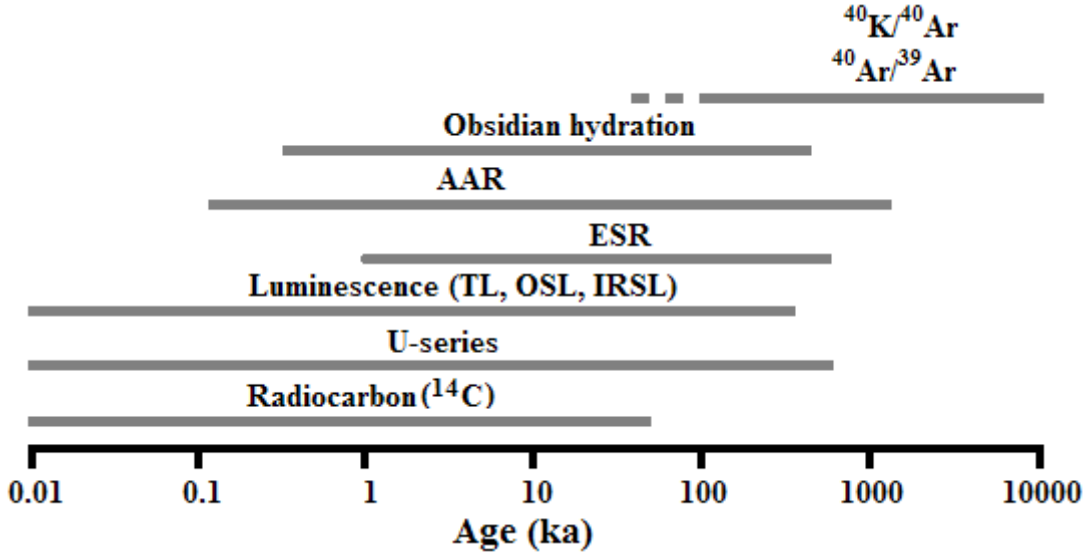

Figure 1.1: Potential age ranges for various dating methods discussed in the text. The limits are only approximations, as they are reliant on factors unique to each method and the nature of the material being dated.

The later MSA and earliest LSA are less well constrained, despite the abundance of MSA, LSA and 'transitional' archaeological sites in East Africa. This is mainly because the time period of interest is difficult to date. It is close to the effective limit of high precision ^{14}C dating (ca. 50 ka) and too young for high precision $^{40}Ar/^{39}Ar$ and

$^{40}K/^{40}Ar$ dating (ca. 100 ka) (Ambrose, 1998; McBrearty and Brooks, 2000; Schwarz, 2002; Roberts and Jacobs, 2008). Thus, over the past 40 years, a series of other dating methods has been applied to estimate ages for MSA and LSA sites in East Africa. However, many of those methods and procedures are now outdated and considered unsuitable for dating, calling into question the reliability of chronologies obtained previously. Most of the methods, such as ^{14}C dating, are still used, though the sample preparation and measurement procedures employed in older studies are no longer considered reliable. A review of the methods used to obtain ages for the East African MSA and LSA, and their pitfalls, will be made in the following sections.

1.4.1 Radiocarbon (^{14}C) dating

Radiocarbon dating is based on the principle that ^{14}C, which is produced in the upper atmosphere and has a half life of 5730 ± 40 yr, is absorbed by the tissues of living organisms and that this uptake ceases after the organism dies (Roberts and Jacobs, 2008). Since the amount of ^{14}C in the organism then decreases by 50% every half life, the amount of ^{14}C that remains can be measured and used to obtain an estimate of when the organism died. Conventional ^{14}C dating involves counting beta particles from a sample to determine the ^{14}C concentration, while AMS radiocarbon dating involves directly measuring the number of ^{14}C atoms in a sample using an accelerator mass spectrometer (AMS). In either case, appropriate pretreatment procedures, which have improved markedly over the last decade (Bird et al., 2003; Bronk Ramsey, 2008), are necessary to isolate the ^{14}C correlated to the target event, and remove any older or younger ^{14}C contamination. Processes such as molecular ultrafiltration of bone collagen (Higham et al., 2006) and acid-base wet oxidation and stepped-combustion (ABOX-SC) pretreatment procedures for charcoal (Bird et al., 1999) have been shown to substantially increase the accuracy of the resulting ^{14}C ages (Bronk Ramsey et al., 2004). Most of the ^{14}C ages available for the East African MSA and early LSA were not obtained using these procedures, which are currently accepted as a prerequisite for accurate ^{14}C age estimation, and are thus considered unreliable.

Radiocarbon ages must also be converted into calendar years, due to fluctuations in the level of ^{14}C in the atmosphere during the past 50 ka (Van der Plicht, 2000; Reimer et al., 2004; Grün, 2006, Roberts and Jacobs, 2008). Dendrochronology was

used to establish calibration curves up to 12 ka ago. Calibrations for the period of time before 12 ka ago have been based on U-series dated corals and speleothems and ^{14}C data from planktonic foraminifera correlated with the GISP2 (Greenland Ice Sheet Project Two) ice core (e.g., Voelker et al., 1998; Bard et al., 1998; Beck et al., 2001). While conventional radiocarbon ages (BP) younger than 24 ka can easily be converted into calibrated ages (cal BP) using calibration curves, calibrated ages older than this threshold, such as many associated with late MSA and early LSA assemblages, are not unambiguous, since considerable differences exist between ^{14}C calibration datasets (Van der Plicht, 2000; Reimer et al., 2004).

There are several datasets that can be used to make the conversion from conventional to calibrated radiocarbon ages (e.g., the IntCal09 curve: Reimer et al., 2009), although ages obtained before these curves were available may need to be calibrated. Unless otherwise stated, all radiocarbon calibrations in this thesis were performed using the IntCal09 curve (Reimer et al., 2009) and will be reported with a 1σ uncertainty.

1.4.2 Uranium-series dating

Uranium (U)-series dating is based on the radioactive decay of two forms of uranium, ^{238}U and ^{235}U, and the in-growth of their 'daughter' nuclides, ^{230}Th and ^{231}Pa, respectively. The $^{230}Th/^{234}U$ ratio has proven useful for dating Late Pleistocene events due to the appropriate half life of ^{230}Th (75,690 ± 230 yr; Grün, 2006). The $^{231}Pa/^{235}U$ ratio can also be used to date the Late Pleistocene (Grün, 2006). While thorium is insoluble in water, uranium is soluble, making the $^{230}Th/^{234}U$ ratio useful for dating when certain materials formed, such as flowstones and speleothems (Roberts and Jacobs, 2008). Speleothems are reliable sources of U-series ages because they exhibit 'closed system' behaviour (i.e., uranium, but not thorium, was present at the time of formation), although the environment of the East African Rift Valley is not ideal for speleothem growth. Mollusc shell and eggshell may be suitable materials for obtaining U-series ages, but only when appropriate procedures are used (Roberts and Jacobs, 2008). Other materials, such as bone and tooth enamel, exhibit 'open system' geochemical behaviour, meaning that the timing and rate of uptake (and loss) of uranium after burial can be variable (Schwarcz, 2002; Grün, 2006; Grün et al., 2010).

Modern U-series techniques may be used to obtain reliable ages using some of these materials (Pike et al., 2002; Grün, 2006; Grün et al., 2010). Recent advances involve generating profiles of uranium and thorium concentrations across sectioned pieces of bone, which are then compared to models of uranium diffusion and absorption (Pike et al., 2002). Reliable ages can only be obtained for bones with certain profiles, however, and this may occur in a minority of cases. Additionally, the original method of obtaining isotope ratios using alpha counting has been superseded by atom counting methods, such as thermal ionisation mass spectrometry (TIMS) and inductively coupled plasma mass spectrometry (ICP-MS), which can be used to obtain ages of up to 500 ka (Grün, 2006; Roberts and Jacobs, 2008).

1.4.3 Obsidian hydration dating

The obsidian hydration method can be used to date when a fresh surface on a piece of obsidian was exposed to the atmosphere. It is based on the observation that ambient water is absorbed by surfaces of obsidian, forming a hydrated layer whose thickness is dependent on time since exposure, the chemical composition of the obsidian, and the ambient temperature (Michels et al., 1983). The thickness of the hydrated layer can be measured using optical microscopy and compared to laboratory-determined layer thicknesses to obtain ages for the exposure of the surface (Michels et al., 1983; Anovitz et al., 1999). However, obsidian hydration ages have proven controversial, inconsistent with independent age estimates, and unreliable over time (Ridings, 1996; Anovitz et al., 1999; but see Hull, 2001, and Rogers, 2007, for response). A study by Anovitz et al. (1999) has suggested that the method's unreliability is due to unsuitable analytical techniques used by most researchers (such as the standard set of equations) and an inappropriate model of the hydration process. In addition, since the hydration rate is temperature dependent, the various palaeoclimatic conditions of the Late Pleistocene will have resulted in inaccurate age estimates, unless they are taken into account. The conclusions of Anovitz et al. (1999) indicate that the obsidian hydration chronologies for several MSA and LSA sites in East Africa (e.g., Prospect Farm and Enkapune Ya Muto, see Section 1.5) may be unreliable and should be viewed with caution.

1.4.4 Amino acid racemisation

Amino acid racemisation (AAR) is a relative dating technique that is based on the observation that amino acids in living organisms are exclusively of a left-handed (L) form, which gradually converts to a balanced ratio of left- and right-handed (D) forms after the death of an organism (Grün, 2006; Roberts and Jacobs, 2008). Obtaining numerical ages with the D/L ratio is not straightforward, however, since the rate of racemisation is dependent not only on time, but also on temperature. In addition, the rate of racemisation (i.e., the D/L ratio) must be calibrated against another dating method (Clarke and Murray-Wallace, 2006; Roberts and Jacobs, 2008). These calibrations entail obtaining the D/L ratios for samples associated with independent age estimates, and using the ratios and independent ages to fit a kinetic model, which is often derived from heating experiments (Grün, 2006). The resulting calibrations are not unambiguous, however, since they are dependent on the chosen model and are applicable only to the shells of a single species (Grün, 2006). In addition, materials that remain chemically 'closed' postmortem, such as mollusc shell and eggshell, can provide reliable age estimates, 'open system' materials, like bone, generally do not (Grün, 2006).

1.4.5 Electron spin resonance dating

The basic principles of electron spin resonance (ESR) dating are the same as for luminescence dating (Section 1.4.6). Electronic charge begins to accumulate in the crystal structure of the mineral hydroxyapatite in the enamel of teeth, following the death of an organism. The rate of charge accumulation is proportional to the flux of ionising radiation within and outside the tooth: the greater the amount of trapped charge, the more radiation the mineral has been exposed to. An ESR age is, thus, based on the measurement of the trapped charge in the tooth enamel and the determined internal and external dose rates (Grün, 2006; Roberts and Jacobs, 2008). The main complication associated with ESR dating is the determination of the appropriate dose rate, which depends critically on the history of uranium uptake by the tooth after burial. Since teeth exhibit 'open system' behaviour, the amount of uranium within a tooth may increase (and perhaps later decrease) during the course of burial, thus increasing (or decreasing) the dose rate (Schwarcz, 2002; Grün, 2006). This uncertainty is addressed

by assuming that the process of uranium-uptake can be approximated by two models: the early-uptake (EU) model and the linear-uptake (LU) model. The EU model assumes that the current uranium concentration was acquired soon after burial, while the LU model assumes that uranium was absorbed steadily throughout the period of burial (Schwarcz, 2002; Grün, 2006; Roberts and Jacobs, 2008). While a minimum age estimate will be obtained using the EU model, the actual age of a sample is usually assumed to lie between the ages obtained using the EU and LU models (Grün, 2006; Roberts and Jacobs, 2008). Combining ESR and $^{230}Th/^{234}U$ dating methods, using techniques such as the "coupled" ESR/U-series dating (Grün et al., 1988) or the closed-system U-series/ESR model (Grün, 2000), can narrow the likely age range of a sample (Roberts and Jacobs, 2008).

1.4.6 Luminescence dating

1.4.6.1 Overview

Luminescence dating is based on the principle that the crystal structure of silicate minerals (e.g., quartz and feldspar) contains defects at which negatively charged electrons or positively charged vacancies ('holes') can become trapped (Aitken, 1985, 1998; Feathers, 1996; Jacobs and Roberts, 2007). Charge becomes trapped in defects following exposure to cosmic rays and ionising radiation from the surrounding environment, the latter resulting from the decay of ^{238}U, ^{235}U, ^{232}Th (and their daughter products), ^{40}K and ^{87}Rb. The rate at which charge is trapped increases with the rate at which ionising radiation is delivered and absorbed. When the mineral is exposed to sufficient sunlight or heated to >300°C, the charge-traps of interest are emptied ('zeroed'). Light (luminescence) is emitted from the mineral as a result of the radiative recombination of electrons and holes at luminescence centres following stimulation with visible light (optically stimulated luminescence [OSL]: Huntley et al., 1985), infrared (IR) stimulation (infra-red stimulated luminescence [IRSL]: Hütt et al., 1988), or heat (thermoluminescence [TL]: Aitken, 1985). Thus, target events that can be dated using TL techniques include the heating of pottery (Aitken, 1985) and lithics (Mercier et al., 1995, 2007) to temperatures greater than 300°C and the last exposure of sediments to sunlight. The target event that OSL and IRSL methods date is the timing

of the previous exposure of a mineral grain to sunlight and its subsequent burial (Figure 1.2). OSL and IRSL methods can also be used to date heated materials.

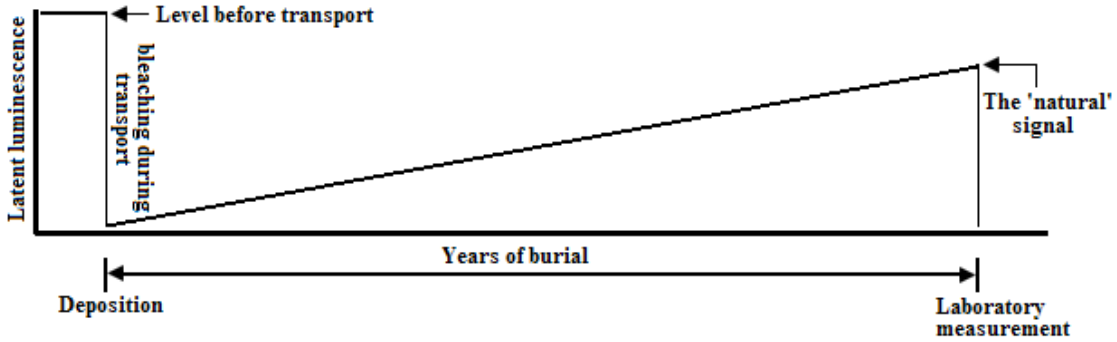

Figure 1.2: Basic principles of luminescence dating of sediment. The latent luminescence signal of a mineral grain is zeroed by sunlight during transport. Following deposition, the signal accumulates due to ionising radiation in the surrounding sediment. The latent luminescence signal that had accrued during burial (i.e., the 'natural' signal) can then be measured in the laboratory. Modified from Aitken (1998).

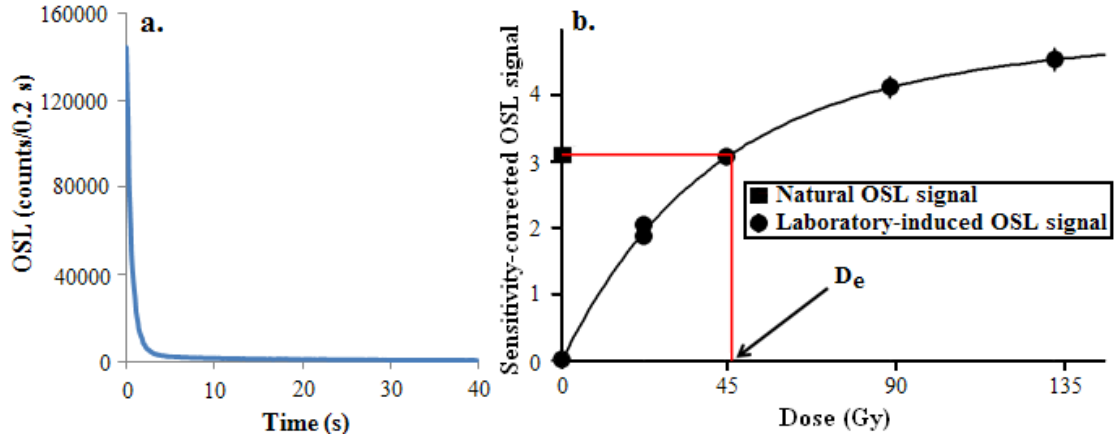

Figure 1.3: Example of an OSL decay curve (a) and a sensitivity-corrected dose-response curve (b).

If a mineral grain is exposed to sunlight, thereby zeroing its OSL or IRSL signal, and is subsequently buried, charge will accumulate in traps at a rate that is proportional to its exposure to ionising radiation. When the grain is stimulated with light or IR in the laboratory, a decay curve (Figure 1.3a) is produced that is proportional to the charge that has accumulated in a mineral grain during burial (the 'natural'). The natural can then be compared to the luminescence signals measured following known laboratory-induced irradiations. The latter signals can be used to construct a dose-response curve (Figure 1.3b), where the sensitivity-corrected natural signal is compared to the sensitivity-corrected laboratory-regenerated signals (see Chapter 3 for more

information). From this curve, an estimate of the equivalent dose (D_e) can be made (Figure 1.3b). This value represents the amount of radiation needed to generate a luminescence signal equal to the natural signal. An OSL age can be obtained using the D_e and an estimate of the environmental dose rate, which is the rate at which ionising radiation in the natural environment is supplied to the sample. The dose rate can be estimated using a series of *in situ* and laboratory methods for measuring the flux of alpha and beta particles and gamma rays from the sediment surrounding the sample. The OSL age (ka) is then obtained by dividing the D_e (Gy) by the environmental dose rate (Gy/ka), and is an estimate of the amount of time since the mineral grain was last exposed to sunlight (or heat), and subsequently buried.

1.4.6.2 Potential problems and pitfalls

There are many challenges to applying OSL and IRSL dating to obtain the depositional age of a sedimentary deposit. It must be ensured that the grains in the sample of interest were fully bleached at the time of deposition; otherwise a residual OSL or IRSL signal will lead to an overestimation of the time of deposition (e.g., Olley et al., 1999, 2004a,b; Arnold et al., 2007). Likewise, it must be ensured that no post-depositional mixing of sediments has occurred. If post-depositional mixing occurred in the deposits of interest, intrusive grains from older or younger deposits may lead to age overestimates or underestimates, respectively (e.g., Roberts et al., 1998a,b, 1999; Feathers, 2003; Feathers et al., 2006; Jacobs et al., 2006b; Bateman et al., 2007). In addition, millimetre-scale spatial heterogeneity in the beta dose rate would result in individual grains in a deposit being exposed to different dose rates and thus, producing different D_e values (e.g., Murray and Roberts, 1997; Olley et al., 1997; Jacobs et al., 2008c). Heterogeneity in the external beta dose rate affects K-feldspar grains less than quartz grains, however, due to the larger internal dose rates of the former (Duller, 1997). These three potential pitfalls can be identified and addressed by measuring single grains of quartz (Jacobs and Roberts, 2007).

In addition to the three problems described in the previous paragraph, the luminescence signals from feldspar grains are affected by anomalous fading, which involves the discharge of electrons out of traps that appear to be thermally stable and, if not addressed, will result in an underestimation of the age (Wintle, 1973; Spooner,

1994b; Huntley and Lamothe, 2001; Huntley and Lian, 2006; Thomsen et al., 2008). While there have been reports of non-fading luminescence signals from various feldspar minerals (e.g., Guérin and Valladas, 1980; Zink and Visocekas, 1997; Gelian et al., 2006; Huntley et al., 2007), fading is ubiquitously present in the IRSL signal of K-feldspars (Spooner, 1994b; Huntley and Lamothe, 2001; Huntley and Lian, 2006). The most common method for addressing anomalous fading has been to measure the fading rate in the laboratory and use it to calculate a fading-corrected age (e.g., Huntley and Lamothe, 2001; Lamothe et al., 2003; Kars et al., 2008). The IRSL signal has been used to obtain fading-corrected ages (using the model of Huntley and Lamothe, 2001) that are in agreement with independent age controls (e.g., Buylaert et al., 2007; Cunha et al., 2008; Martins et al., 2009). In addition, it has been demonstrated that the post-IR IRSL signal from K-feldspar suffers from anomalous fading less than other IRSL signals (Thomsen et al., 2008; Buylaert et al., 2009).

An issue pertaining to the dose rate that must be addressed is the potential for disequilibria in the uranium and thorium decay chains. Disequilibrium is when the parent and daughter nuclides in a decay chain (most commonly the ^{238}U series) are present in unequal activities. Under certain geochemical conditions, various parent and daughter products of a decay chain are likely to migrate. If this happens, the dose rate may change over time, and the measured (i.e., modern) dose rate may need to be corrected (Olley et al., 1996, 1997). To minimise the potential impacts of disequilibria, the nuclides lower down the decay chain, which are the main sources of beta and gamma dose rates, can be measured and used to estimate the environmental dose rate (Jacobs and Roberts, 2007). Another source of dose rate variability that should be considered is the change in potassium concentration in the sediment by leaching or anthropogenic sources (Readhead et al., 1988; Feathers, 1996).

Quartz and feldspar grains from certain geographical regions and geological provenances have proven to have malign characteristics that hinder burial dose estimation. These include areas of mountain building (e.g., Himalayas, European Alps, Andes, and the New Zealand Alps: Richards, 2000; Duller, 2006; Klasen et al., 2006; Preusser et al. 2006, 2007; Steffen et al., 2009) and volcanic activity (e.g., Indonesia, Greece, Japan, the East African Rift Valley: Bonde et al., 2001; Fattahi and Stokes, 2003a; Tsukamoto et al., 2003, 2007; Choi et al., 2006a; Westaway and Roberts, 2006;

Westaway, 2006, 2009). Characterisation studies and new measurement and analysis techniques may be used to overcome the malign properties associated with minerals from these regions (e.g., the dual-aliquot regenerative-dose [DAP] protocol: Westaway and Roberts, 2006). In contrast, quartz and feldspars of metamorphic and sedimentary origins generally have better behaved luminescence characteristics (Preusser et al., 2009).

1.4.7 Summary

It is clear that all of the methods discussed in this section have limitations and pitfalls, many of which were unknown when the chronologies for most MSA and LSA sites were first obtained. The following section will provide a review of sites in East Africa that contain MSA and LSA assemblages and an assessment of their associated chronologies.

1.5 The East African MSA and LSA archaeological record

Before reviewing the current literature regarding the MSA and LSA in East Africa, the implications of the final paragraph in the Section 1.3 should be emphasised. Given the presence of typical MSA and LSA features in many intermediate assemblages in East Africa, these terms may be ineffective for defining individual lithic industries from the Late Pleistocene. In addition, the assignment of many assemblages has changed following more modern excavation and analysis techniques. However, this is the parlance of the literature that has been used by archaeologists for the past eight decades. Thus, the following sections will summarise assemblages from various sites that have been classified in the literature as MSA, MSA/LSA transitional, early LSA and LSA. Figure 1.4 is a map showing locations of sites in East Africa that contain MSA and/or LSA lithic assemblages that are discussed in this chapter. Table 1.1 presents archaeological and chronological information for the sites discussed in this section.

1.5.1 Olduvai Gorge, Tanzania

At Olduvai Gorge, the Ndutu Beds contain a lithic assemblage that has been described as MSA, based on a relatively large abundance of Levallois technology

(Leakey et al., 1972). The overlying Naisiusiu Beds, however, contain a lithic assemblage that has been characterised as LSA (referred to as "Upper Palaeolithic" by Leakey et al., 1972). The assemblage from the Naisiusiu Beds is primarily comprised of blades (42%) and geometric backed microliths (30%). In addition, different raw materials were preferentially utilised for different tool types (Leakey et al., 1972). Obsidian from the Naisiusiu Beds has been sourced to the southern Kenyan site of Sonanchi (Merrick and Brown, 1984; Mehlman, 1989), suggesting that the makers of the LSA assemblage of the Naisiusiu Beds were involved in long distance exchange.

The MSA assemblage of the Ndutu Beds is associated with an infinite ^{14}C age from shell of >29 ka BP (>33.4 cal ka BP) (Leakey et al., 1972). Leakey et al. (1972) reported uncalibrated radiocarbon ages of ~17 ka BP (~21 cal ka BP) and 17.6 ± 1.0 ka

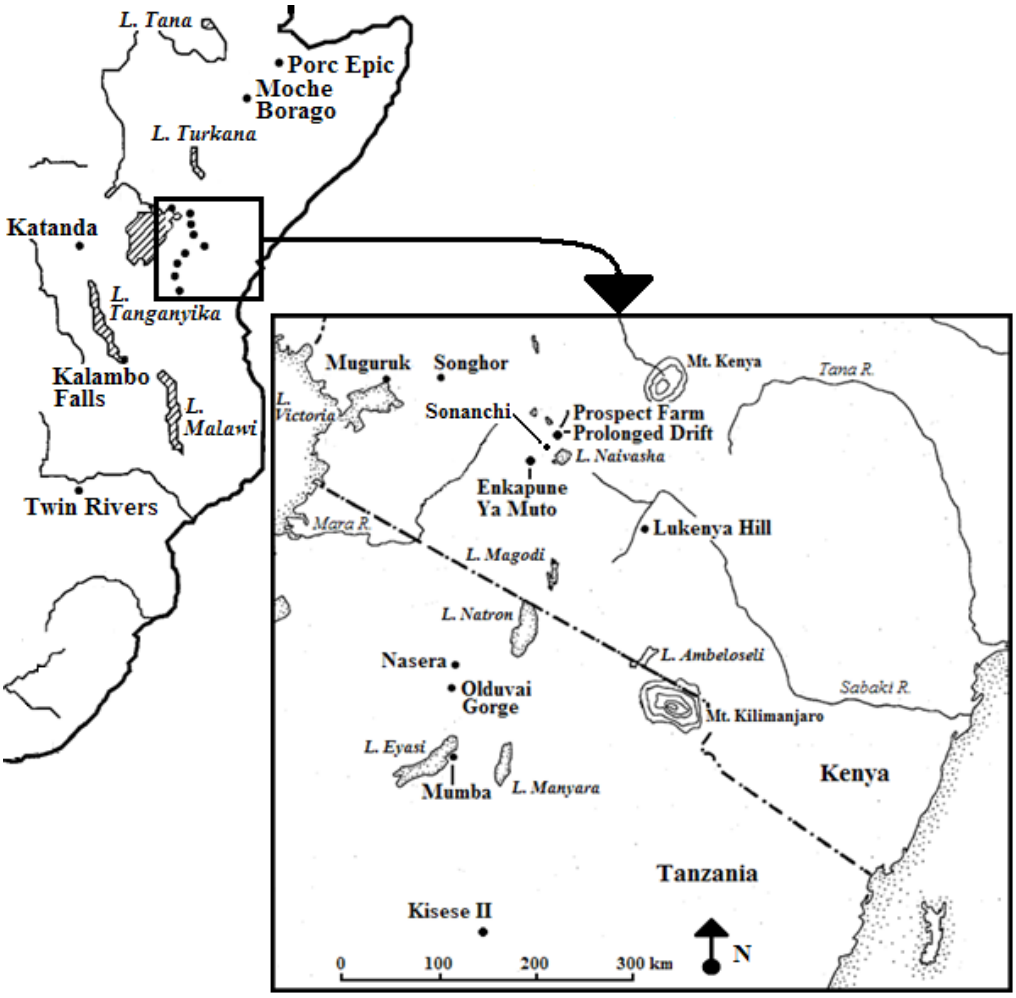

Figure 1.4: Map of East Africa showing the locations of MSA and LSA sites discussed in this chapter. Modified from Merrick and Brown (1984) and McBrearty and Brooks (2000).

Table 1.1: Description of the lithic industries, defining archaeological characteristics and age estimates from the East African MSA and LSA archaeological sites discussed in the text. For each site, the lithic industries are listed in stratigraphic order from top to bottom.

Site/reference	Lithic industry	Defining archaeological characteristics	Age estimate	Methods
Olduvai Gorge, Tanzania Leakey et al. (1972)	Naisiusiu Beds	LSA: Blades and backed pieces, distant obsidian	59 ± 5 ka (EU) 62 ± 5 ka (LU)	ESR (3 teeth)
Skinner et al. (2003)	Ndutu Beds	MSA: Levallois technology	>33.4 cal ka BP	^{14}C (shell)
Nasera, Tanzania Mehlman (1989)	Nasera Industry	Bipolar cores, scrapers, points, distant obsidian	22.2 ± 1.1, 27.1 ± 0.5, 20.3 ± 0.1 cal ka BP	^{14}C (bone)
			$25.6\ ^{+0.6}/_{-0.4}$ ka	U-series (bone)
			~26 ka	AAR (bone)
	"Serengeti Mumba"	Bipolar cores, backed pieces, points	-	
	Kisele Industry (MSA)	MSA: point-based	$56.0\ ^{+2.7}/_{-2.3}$ ka	U-series (tooth)
Enkapune Ya Muto, Kenya Ambrose (1998)	Sakutiek Industry	LSA: Scrapers, knives, OES beads, few backed pieces	40.7 ± 1.3, 41.5 ± 2.0, 43.9 ± 2.3 cal ka BP	^{14}C (charcoal and shell)
			35.3 ± 2.2 ka	Obsidian hydration
	Nasampolai Industry	LSA: Backed piece-dominated	46.4 ± 2.8 ka	Obsidian hydration
	Endingi Industry	MSA: Points, scrapers, few backed pieces	45.0 ± 1.0 cal ka BP	^{14}C (charcoal)
			32.5 ± 1.2 ka	Obsidian hydration
Prospect Farm, Kenya Michels et al. (1983)	Second Intermediate	Early LSA	21.8 to 32.5 ka	Obsidian Hydration
	Prospect Industry, Phase 4	Transitional, scrapers, knives, distant obsidian	53.6 ± 0.3 to 45.7 ± 0.2 ka	Obsidian Hydration
	Prospect Industry, Phase 3	MSA: Distant obsidian	53.1 ± 4.1 to 46.5 ± 1.7 ka	Obsidian Hydration
	Prospect Industry, Phase 3	MSA	119.6 ± 1.7, 106.3 ± 3.2 ka	Obsidian Hydration
Lukenya Hill, Kenya Kusimba (2001)	LSA	Scrapers, few microliths, distant obsidian	4.6 ± 0.2 to 24.9 ± 1.4 cal ka BP	^{14}C (bone apatite and collagen)
Kisese II, Tanzania Inskeep (1962)	"Second Intermediate"	Scrapers, backed microliths, OES beads	35.6 cal ka BP	^{14}C (OES)

Table 1.1 (continued)

Site/reference	Archaeological context	Defining archaeological characteristics	Age estimate	Methods
Twin Rivers, Zambia Barham (2002) Barham and Smart (1996)	Lupemban	Backed pieces	$230\ ^{+35}/_{-28}$ ka	U-series (speleothem overlying deposits)
Katanda, DRC Brooks et al. (1995) Yellen et al. (1995)	Lupemban	Barbed bone points	$89\ ^{+22}/_{-15}$ ka	TL, U-series, ESR
Songhor, Kenya McBrearty (1981)	Sangoan-Lupemban	Distant obsidian	-	
Muguruk, Kenya McBrearty (1988)	Sangoan-Lupemban	Distant obsidian	-	
Prolonged Drift, Kenya Merrick et al. (1994)	MSA	Distant obsidian	-	

BP (21.0 ± 1.2 cal ka BP) associated with the Naisiusiu Beds. In contrast, Manega (1993) obtained infinite AMS ^{14}C ages of >42 ka BP (>45.3 cal ka BP) and ^{40}Ar/^{39}Ar ages from biotite grains of between 42 ± 10 and 90 ± 30 ka. Most recently, Skinner et al. (2003) used three equid teeth recovered during a recent re-excavation of the site to obtain ESR ages of 59 ± 5 ka using an EU model and 62 ± 5 ka using a LU model (see Section 1.4.5 for assumptions of both models). The EU model provides a minimum age estimate, and the actual age is likely to fall between the estimates obtained using the EU and LU models (Grün, 2006; Roberts and Jacobs, 2008). The ESR ages support the infinite AMS ^{14}C age of >42 ka BP and are likely the most reliable estimates for the Naisiusiu Beds assemblage.

1.5.2 Nasera rockshelter, Tanzania

Nasera rockshelter is located approximately 30 km north of Olduvai Gorge and 60 km southwest of Lake Natron, overlooking the 4 km wide valley (Angata Kiti) that connects the Serengeti Plains and the Salei Plains (Mehlman, 1989). Mehlman (1989) suggests that the site was probably used as a seasonal hunting and scavenging base for Late Pleistocene humans, owing to its strategic position on a bottleneck along wildlife migration routes between eastern and western plains, and the lack of nearby permanent freshwater and wildlife in the dry season. The MSA assemblages from the base of the sequence (Level 25) to Level 12 were assigned to the Kisele Industry, which is also present in Bed VIA at Mumba (see Section 2.4.1). Levels 11 to 8/9 contain a very low density of artefacts, which Mehlman (1989) tentatively described as the Serengeti Plains counterpart to the Mumba Industry of Mumba Bed V-lower (see Section 2.4.2), based on the prevalence of bipolar cores and a similar frequency of points and backed pieces in the assemblage. Levels 6 and 7 contain a dense deposit of artefacts from an assemblage assigned to the Nasera Industry (see Section 2.4.3). It is dominated by bipolar core reduction and scrapers, with high proportions of points and low proportions of microlithic backed pieces. An LSA Lemuta Industry assemblage is found in Levels 4 and 5. This assemblage has a conspicuous blade component and is dominated by bipolar cores and scrapers. Backed tools and burins are present in moderate proportions, as are small frequencies of *outils écaillés*. While most artefacts are made from locally available quartz, obsidian and chert are also present; the latter material is

most likely from Olduvai Gorge or Lake Natron. The obsidian artefacts from the Kisele and Nasera Industry layers have been traced to source outcrops approximately 250 km away in southern Kenya (Mehlman, 1989).

A U-series age of 56.0 $^{+2.7}/_{-2.3}$ ka was obtained from a tooth associated with the Kisele Industry of Level 17. Mehlman (1989) reported multiple ages obtained using bone from the Nasera Industry of Levels 6 and 7, including a U-series age of 25.6 $^{+0.6}/_{-0.4}$ ka, an AAR age of ~26 ka, and three ^{14}C ages of 18.5 ± 0.9 ka BP (22.2 ± 1.1 cal ka BP), 22.4 ± 0.4 ka BP (27.1 ± 0.5 cal ka BP) and 17.1 ± 0.1 ka BP (20.3 ± 0.1 cal ka BP). The Lemuta Industry of Levels 4 and 5 produced three ^{14}C ages from bone of 22.5 ± 0.5 ka BP (27.2 ± 0.6 cal ka BP), 18.3 ± 0.6 ka BP (21.8 ± 0.8 cal ka BP), and 21.7 ± 0.6 ka BP (26.0 ± 0.8 cal ka BP) and an AAR age of ~20 ka. Since all ages reported for the MSA and LSA levels were obtained using ^{14}C, U-series, or AAR dating of bone or teeth, materials that have since proven unreliable in these contexts, the chronology for Nasera rockshelter remains ambiguous.

1.5.3 Enkapune Ya Muto rockshelter, Kenya

At Enkapune Ya Muto rockshelter in southern Kenya, the deepest archaeological layer contains the Endingi Industry. It is described as transitional between MSA and LSA by Ambrose (2002), based on the presence of several microlithic backed pieces in an otherwise typical MSA assemblage. It contains an abundance of flakes with faceted platforms from radial cores, points and scrapers, very few blades, and only three backed microliths (Ambrose, 1998). The overlying LSA Nasampolai Industry is present in low artefact densities and represents a long period of ephemeral occupation. The LSA assignment is based on the dominance of large backed blades and geometric microliths in the assemblage, several of which exhibit ochre staining on the modified edge, indicative of hafting (Ambrose, 1998). The second LSA industry, overlying the Nasampolai, is the Sakutiek Industry. The assemblage from these layers is dominated by scrapers and *outils écaillés*, with low frequencies of backed microliths. Typical MSA types, including part-bifacially flaked knives, also occur in low frequencies. The Sakutiek Industry contained abundant OES beads (n = 13), bead preforms (n = 12) and fragments (n = 593).

The chronology reported for Enkapune Ya Muto by Ambrose (1998) consists of obsidian hydration ages and uncalibrated ^{14}C ages, the latter obtained from charcoal and OES. The ^{14}C chronology will be discussed first. The deepest deposits, containing the MSA Endingi Industry, produced an uncalibrated ^{14}C age from charcoal of 41.4 ± 0.7 ka BP (45.0 ± 1.0 cal ka BP). No ^{14}C ages were obtained for the Nasampolai Industry, but four ages on charcoal and OES were obtained for the Sakutiek Industry: 29.3 ± 0.8 ka BP (33.8 ± 0.9 cal ka BP), 35.8 ± 0.6 ka BP (40.7 ± 1.3 cal ka BP), 37.0 ± 1.1 ka BP (41.5 ± 2.0 cal ka BP) and 39.9 ± 1.6 ka BP (43.9 ± 2.3 cal ka BP). Ambrose (1998) suggests that the youngest age (~29.3 ka BP) is unreliable, however, because of the low carbon content of the sample used to obtain it. The calibrated ^{14}C ages are in correct stratigraphic order, ranging from ~45 cal ka BP to ~44 – 41 cal ka BP. However, as discussed in Section 1.4.1, ages that are this old are not straightforward to calibrate. In addition, Ambrose (1998) concluded that the ^{14}C age obtained for the Endingi Industry (~45 cal ka BP) is likely an underestimate of the actual age, since it was obtained from material collected ~1.2 m below the Sakutiek Industry samples and the intervening sediment consisted of wind-deflated gravels, which would likely require longer than 1 ka to accumulate. The agreement of three radiocarbon ages from the deposits containing the Sakutiek Industry, however, adds confidence that ~44 to ~41 cal ka BP is an appropriate age-range for this toolkit.

The obsidian hydration ages were calculated using an effective hydration temperature 5°C cooler than modern temperatures to account for lower temperatures during the last glacial (Ambrose, 1998). An age of 32.5 ± 1.2 ka was obtained for obsidian from the Endingi Industry. The overlying Nasampolai Industry produced an obsidian hydration age of 46.4 ± 2.8 ka. Ambrose (1998) then used this obsidian hydration age, in conjunction with an uncalibrated radiocarbon age from the Sakutiek levels, to estimate sedimentation rates from which he extrapolated an age-range of 55 to 45 ka for the beginning of the Nasampolai deposits. The LSA Sakutiek Industry, which overlies the Nasampolai Industry, produced an age of 35.3 ± 2.2 ka. The ages obtained from obsidian hydration are not in correct stratigraphic order and those for the Endingi (~33 ka) and Sakutiek (~35 ka) Industries are systematically younger than those obtained from ^{14}C dating. Given the questionable reliability of the dating technique

(Ridings, 1996; Anovitz et al., 1998) and the internal inconsistencies, it is likely that the obsidian hydration chronology for Enkapune Ya Muto is unreliable.

1.5.4 Prospect Farm and Prolonged Drift, Kenya

Prospect Farm in the Kenyan Rift Valley, a MSA site for which relatively little has been published, was excavated and described by Anthony (1978). The site had four main episodes of occupation, one of which contained an MSA assemblage. The overlying layers contained a Second Intermediate, or early LSA, assemblage (Michels et al., 1983). The uppermost MSA horizon (Phase 4 of the Prospect Industry) was described as transitional between the local MSA and Second Intermediate technologies, based on the disappearance of points and Levallois technologies and the appearance of small discoidal knives and scrapers (Michels et al., 1983). Most artefacts from the site are made from obsidian. Patterns in raw material source distance indicate that the proportion of local obsidian (sourced from <15 km) decreased from the oldest MSA to the youngest MSA, while the proportion of obsidian sourced from distant sites (>30 km) increased (Merrick et al., 1994).

In regards to the chronology, most available ages were obtained using obsidian hydration dating. Obsidian from Phase 3 of the Prospect Industry from Stratum 9 yielded four ages of between 119.6 ± 1.7 and 106.3 ± 3.2 ka. The overlying Phase 3 assemblages from Stratum 8 resulted in eight ages of between 53.1 ± 4.1 and 46.5 ± 1.7 ka (Michels et al., 1983). Obsidian from the overlying transitional Phase 4 (Strata 5 – 7) resulted in seven ages of between 53.6 ± 0.3 and 45.7 ± 0.2 ka (Michels et al., 1983). Ambrose (2002) suggests that cooler temperatures prior to 12 ka would have reduced hydration rates, implying that these obsidian hydration ages are likely minimum estimates.

Prolonged Drift is another MSA site, located close to Prospect Farm. As at Prospect Farm, despite the proximity of nearby obsidian sources, a large proportion of the artefacts at Prolonged Drift were made of obsidian from a distant source. Nearly 90% of obsidian was imported from 40 – 45 km away (Merrick et al., 1994).

1.5.5 Lukenya Hill, Kenya

At the Kenyan site of Lukenya Hill, obsidian comprises relatively little of the MSA assemblage raw material. In the earlier MSA levels, a relatively small proportion (31%) of the obsidian comes from distant (105 – 135 km) sources of Lake Naivasha and the Kedong Escarpment (Merrick and Brown, 1984; Kusimba, 2001). The proportion of obsidian from a distant source increased to 62% in the later MSA levels. The early LSA assemblages at Lukenya Hill are characterised by a high frequency of scrapers (~60%) and few microliths (~12%), prompting Mehlman (1989) to suggest that they may be related to the Nasera Industry. This contrasts with the youngest LSA assemblage, which includes a larger proportion of microliths that are more standardised, including crescents and a multitude of backed types (Kusimba, 2001). Radiocarbon ages on bone apatite and collagen of between 4.1 ± 0.2 ka BP (4.6 ± 0.2 cal ka BP) and 20.8 ± 1.1 ka BP (24.9 ± 1.4 cal ka BP) were obtained for the LSA layers. Kusimba (2001), however, indicates that these ages are likely substantial underestimates due to bone contamination with modern carbon from carbonates and humic acids (Brooks and Robertshaw, 1990).

1.5.6 Other sites

Other occurrences of MSA toolkits in East Africa include Sangoan-Lupemban and MSA assemblages from Muguruk and Songhor near Lake Victoria. Both of these MSA assemblages contain obsidian sourced from more than 100 km away in southern Kenya (McBrearty, 1981, 1988; Mehlman, 1989). An early Magosian level is present at Kisese II rockshelter in central Tanzania (Inskeep, 1962). Mehlman (1989: 365) states that "the Mumba Industry is almost certainly present below level XI at the Kisese II rockshelter… associated with OES beads. The Nasera Industry is also likely present." The industry Mehlman (1989) refers to is a 'second intermediate' assemblage, dominated by scrapers and *outils écaillés* with low frequencies of microlithic backed forms (Inskeep, 1962). At Twin Rivers in Zambia, the deposits containing a MSA Lupemban Industry are overlain by flowstone, which has been dated to 230 $^{+35}/_{-28}$ ka using on U-series (Barham and Smart, 1996). Macrolithic, unstandardised backed pieces comprise a minor, though technologically significant, component of this assemblage and a similar one from the Zambian site of Kalambo Falls (Barham, 2002a). Large quantities of ochre are also present in these assemblages, leading Barham (1998,

2002b) to infer that pigment was being systematically used in the MSA Lupemban Industry. In the Democratic Republic of Congo, at the site of Katanda in the Semliki Valley, MSA Lupemban Industries have been found to contain a formal tool industry containing barbed and unbarbed bone points, which have been dated to greater than 89 $^{+22}/_{-15}$ ka by combining TL, $^{230}Th/^{234}U$ and ESR ages (Brooks et al., 1995; Yellen et al., 1995). The antiquity of the layers in which these objects were found has been supported by OSL investigations, which demonstrated that partial bleaching of these fluvial sediments was not a concern (Feathers and Migliorini, 2001).

1.5.7 Summary

The archaeological and chronological information from each site discussed in this section is summarised in Table 1.1. Figure 1.5 is a timeline showing the age-ranges for various lithic industries at East African MSA and LSA sites and the method used to obtain them. There are a substantial number of sites described in the literature of East African archaeology that contain MSA and LSA industries. The MSA assemblages from many of these sites contain evidence for modern behaviours, including exotic raw material use (presumably procured through exchange networks, see Section 10.3.1), transitions to LSA toolkits, elaborately crafted bone tool industries, ornaments and evidence for the systematic use of pigments. However, there are significant discrepancies in between the timing of MSA and LSA toolkits at different sites in the region. It is likely that this is, at least in part, due to the unreliable dating methods used to obtain many of the chronologies. The chronologies for most of these sites are lacking consistency and estimates of uncertainty, precluding a proper inter-site comparison of technologies and behaviours. The next section will discuss the importance of constraining the archaeology with a reliable chronology.

1.6 The importance of robust chronologies: resolving technological and behavioural change

It is clear that all of the methods used to constrain MSA and LSA archaeological sites have many caveats and pitfalls, most of which may not have been addressed when the chronologies were obtained. Consequently, the timing of, and reasons for, changes in the behaviour of modern humans, manifested as transitions in technologies and the

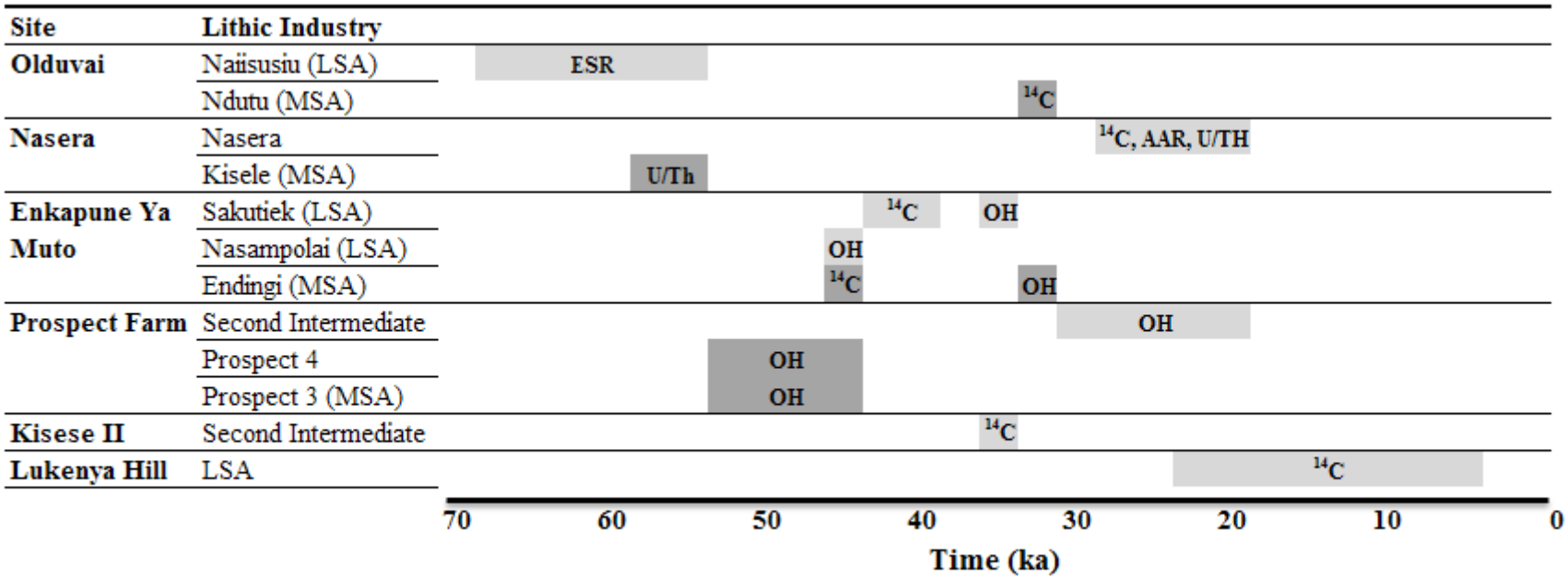

Figure 1.5: Timeline showing methods used to obtain ages and age-ranges for various lithic industries from East African MSA and LSA sites. The lighter shaded ranges indicate LSA or 'second intermediate' lithic assemblages and the darker shaded ranges indicate MSA lithic assemblages.

emergence of symbolic artefacts, during the Late Pleistocene in East Africa remain unresolved.

Two potential factors that have been cited as possible instigators for changing behaviours and technologies are environmental and demographic variations. Environmental differences would likely lead to different behaviours and technologies as a means of efficient survival (Henshilwood and Marean, 2003; McBrearty, 2007). Changes in the availability of various resources, and the associated resource intensification that results from absolute decreases in resources or increased competition for the same resources, are likely to instigate changes in the behaviour and technology of modern humans. Alternatively, the development of social and exchange networks, to mitigate risk in marginal environments or as a function of increased population interaction in a growing population, could result in increased symbolic expression (Deacon and Deacon, 1999; McBrearty and Brooks, 2000; Ambrose, 2002, 2010; Henshilwood and Marean, 2003; Kuhn and Stiner, 2007). Many recent studies have modelled the effects of population size on technological and social complexity (e.g., Shennan, 2001; Henrich, 2004; Powell et al., 2009), the results of which have been supported by archaeological and ethnographic studies (e.g., Kuhn and Stiner, 2007; Riede, 2009; Nowell, 2010; Kline and Boyd, 2010). These studies concluded that larger, more concentrated populations are more likely to be socially and technologically innovative than smaller, more isolated populations (see Section 10.2.1).

Changes in behaviours are, thus, likely associated with changes in the environment, changes in population size and structure, or both. In this regard, a multidisciplinary approach to answering questions regarding behavioural change is essential. Palaeoclimatic reconstructions for the Late Pleistocene can provide a framework within which technological change (identified in the archaeological record) and changes in population size and structure (identified through genetic studies) can be interpreted. Likewise, given that population size affects technological and social complexity, behavioural changes can be interpreted in the framework of genetically-identified demographic changes.

The link that allows data from these three disciplines to be compared and interpreted is chronology. If the archaeological record is temporally constrained, the timing of *when* technologies and behaviours change can be related to the timing of

population changes and past environmental conditions to provide insights into *why* and *how* these changes came about. Without a reliable chronology, however, any interpretation of the archaeological record is conjecture. Archaeological evidence for changes in behaviour and technology must be temporally constrained to allow appropriate comparisons with genetic and palaeoclimatic evidence, provided the chronology of the palaeoclimate record is reliable and the genetic evidence is sound. Geochronology is, thus, the hub of any reliable interpretation of the archaeological record within an environmental and demographic context.

As an example, developments of new measurement procedures, instrumentation and sample preparation and analysis techniques over the previous decade, coupled with the systematic application of dating studies, have greatly improved the chronology of the southern African MSA. Recently, the timing of the Still Bay and Howiesons Poort Industries have been constrained more precisely (Jacobs et al., 2008a), which has allowed the archaeology to be compared with a range of contextual evidence (e.g., Jacobs et al., 2008a; Jacobs and Roberts, 2009; Thackeray, 2009; Villa et al., 2010; Chase, 2010). Jacobs and Roberts (2009) suggest that the technologically and socially innovative Still Bay and Howiesons Poort Industries developed as a result of population increases (as reconstructed from genetic studies; Atkinson et al., 2009) and the resultant increase in information exchange. Chase (2010) suggests that this population increase, in turn, resulted from an ameliorated climate associated with increased precipitation in the southern African Winter Rainfall Zone during MIS 4.

1.7 Objectives

The timing of the latest MSA and earliest LSA in East Africa has proven difficult to resolve due to the limitations of the various dating methods available. The archaeological record of the region needs to be temporally constrained using new and more reliable dating techniques, taking into consideration progress made over the past decade. Ages must be accompanied by appropriate estimates of uncertainty, and they must be obtained from studies that are described so that their validity can be assessed. OSL is a method that has often been used to obtain accurate and precise ages for sedimentary deposits dating to the Late Pleistocene. Few studies, however, have applied this technique in East Africa. Of those that have, most were problematic due to

the challenging nature of the OSL behaviour of quartz from parts of this region (e.g., Choi et al., 2006a). However, accurate ages may be able to be obtained if sites with appropriate sediments (e.g., sediments of metamorphic origin) are investigated, the luminescence behaviours of quartz and feldspar are systematically characterised to determine the appropriate measurement conditions, and the various sources of uncertainty and variability (e.g., post-depositional mixing of sediments, spatial heterogeneity in the dose rate, and high rates of anomalous fading) are assessed and addressed.

There is, thus, enormous potential for OSL dating studies to construct reliable chronologies for MSA and early LSA archaeological deposits in East Africa. To investigate this, OSL samples were collected from two rockshelters in East Africa: Mumba rockshelter in northern Tanzania and Moche Borago rockshelter in the southwest Ethiopian highlands. Both sites have long archaeological sequences that contain a transition from MSA to LSA toolkits and one (Mumba) has evidence for ancient symbolic ornaments.

While the majority of this chapter has provided background information to illustrate the significance of the aims discussed in Section 1.1, this section will detail the specific objectives established to address the aims of this study:

- Obtain measurements of the external dose rate for samples (in the field and laboratory).
- Assess the availability of quartz and feldspar from samples in the laboratory. When ample quartz is available, characterise the luminescence properties of multi- and single-grain aliquots to investigate the suitability of OSL dating for obtaining ages for these samples. Investigate the luminescence properties of quartz, so that any variability in the OSL signal can be identified and addressed accordingly. Use this information to determine the appropriate measurement and data analysis procedures that can be used to obtain a known dose under controlled laboratory conditions, as a prerequisite to measuring the unknown doses (D_e values) in the archaeological samples.
- Use the empirically derived measurement and data analysis procedures to obtain D_e distributions for single grains of quartz. These can be used to investigate potential sources of external variability affecting the dataset, including post-

depositional mixing and beta microdosimetry. If the distributions are consistent with these sources of external variability, appropriate corrections can be made, and the population of D_e values that best represents the burial dose can be used to calculate OSL ages for these samples.

- For samples that do not contain quartz, or for which quartz OSL ages could not be obtained, characterise the luminescence signal from K-feldspar separates. Investigate the luminescence properties to assess the suitability of IRSL dating of K-feldspars. Determine the appropriate measurement and analysis procedures (e.g., the post-IR IRSL procedure) for obtaining a known laboratory-dose and limiting the extent of anomalous fading.
- Use appropriate measurement and analysis procedures to measure the D_e values and fading rates for multi-grain aliquots of K-feldspar grains. Use a previously-developed and well-established technique for correcting anomalous fading (i.e., Huntley and Lamothe, 2001) to obtain fading-corrected ages for the samples. Obtain ages for several key samples using the post-IR IRSL signal from K-feldspar and the OSL signal from quartz to provide a basis for comparison. This will serve as a semi-independent check of the suitability of the two methods and the accuracy of resulting ages.
- Use the OSL and post-IR IRSL chronologies of the MSA and LSA deposits from these sites, in conjunction with existing palaeoclimatic, genetic and regional archaeological records, to gain insights into the timing and potential reasons for the emergence of, and changes in, technologies and symbolic behaviours.

1.8 Scope/Outline of Thesis

The ways that I have gone about achieving the objectives of this thesis are detailed in the following chapters:

Chapter 2: The location, excavation history, setting, stratigraphy, previous chronologies and archaeological context for Mumba and Moche Borago rockshelters will be discussed in this chapter.

Chapter 3: This chapter details the OSL dating methodology used throughout this thesis, focusing on the quartz OSL signal. Included in this chapter are sections detailing a background of the method, the methods of sample collection and preparation, the measurement instrumentation, procedures for measuring D_e values, statistical models for analysing D_e distributions, the various aspects of the OSL signal and the challenges of applying OSL to quartz from various regions of the world.

Chapter 4: The methods for determining dose rates for quartz and K-feldspar grains are discussed in this chapter. The various contributions to the internal and environmental dose rates are detailed, as well as methods for measuring, quantifying and correcting the latter.

Chapter 5: This chapter details the characterisation of the OSL signal of quartz from Mumba. First, the linearly modulated (LM)-OSL signal from multi-grain aliquots is investigated and the effects of adding a hot optical wash (HOW) to the single-aliquot regenerative-dose (SAR) procedure are assessed. Next, the OSL signal from single grains of quartz is characterised and several grain-types, each with different OSL behaviours, are described. The applicability of using the pulsed-irradiation technique with a modified SAR procedure is then assessed with dose recovery experiments. These experiments are then used to assess the measurement and analysis technique most appropriate for objectively rejecting grains with poorly behaved OSL signals, while isolating grains with well-behaved OSL signals for D_e estimation. Finally, dose recovery experiments are performed using multi-grain aliquots, the results of which are compared to the results from single-grain dose recovery experiments.

Chapter 6: First, the total environmental dose rates for samples from Mumba rockshelter are discussed. The remainder of this chapter details the measurement and analysis of D_e values, obtained using the empirically derived procedures determined in Chapter 5, from single grains of quartz from Mumba. The resulting D_e distributions are then characterised and analysed using the appropriate statistical models, to identify any external sources of variability, such as post-depositional mixing and beta dose rate heterogeneity. The D_e populations that best represent the burial dose are identified and

used to obtain ages. Finally, problematic samples for which ages could not be obtained are discussed.

Chapter 7: In this chapter, the characteristics of the luminescence signals of K-feldspar separates from Mumba are detailed. A background to the mineralogy and luminescence characteristics of feldspars is discussed, as well as procedures for measuring and calculating the rate of anomalous fading. The blue emission is chosen as most appropriate for the remaining experiments. The TL signal is characterised and the relationship between TL peaks and the IRSL signal is investigated. The IRSL and post-IR IRSL signals are then characterised as a function of stimulation duration and stimulation temperature, and the sensitivity of the post-IR IRSL signal to sunlight is assessed. Dose recovery and anomalous fading experiments are then described and used to identify the IRSL signal that could best recover a known dose and exhibit the least anomalous fading.

Chapter 8: This chapter details the use of the post-IR IRSL signal to measure D_e values and fading rates that are used to calculate fading-corrected ages for multi-grain aliquots of K-feldspar from Mumba. These fading-corrected ages are then compared to the single-grain quartz-OSL ages described in Chapter 7 to assess the reliability of the K-feldspar post-IR IRSL procedure for age estimation.

Chapter 9: This chapter details the luminescence investigations of quartz and feldspar from Moche Borago. The characteristics of the OSL and LM-OSL signals of quartz will be discussed. Next, the luminescence signal from K-feldspar separates is characterised using TL, pulsed anneal, and IRSL experiments, and the dependence of the IRSL and post-IR IRSL signals on stimulation temperature is investigated. The effects of anomalous fading on the TL signal and various IRSL signals are then characterised. Finally, natural IRSL signal and dose rate measurements are discussed.

Chapter 10: In this chapter, the revised chronology for the MSA and LSA at Mumba rockshelter is assessed in the context of the existing East African archaeological record and existing palaeoclimatic and genetic reconstructions for the region. The chapter

begins with a review of the palaeoclimatic and genetic evidence, as well as studies linking demographic changes to changes in technologies and behaviours. A discussion of the significance of the new chronology for the MSA/LSA archaeology at Mumba and how it relates to the regional archaeological record is followed by a hypothesis that synthesises the available records to assess a potential scenario for the development of various technologies and behaviours in East Africa.

Chapter 11: This chapter presents a summary of results and the contributions of this work towards an improved understanding of the MSA and LSA in East Africa. The suitability of OSL as a reliable chronometric tool for constraining this period of time in East Africa is discussed, followed by recommendations for future research into the timing of this critical period in human evolution.

Chapter 2: Description of study sites: Mumba rockshelter, Tanzania and Moche Borago rockshelter, Ethiopia

Mumba rockshelter, Tanzania

There are relatively few sites in East Africa with archaeological sequences that contain both MSA and LSA assemblages. Mumba rockshelter is a notable exception, containing one of the richest and most continuous MSA to Iron Age archaeological sequences in East Africa. Its MSA and LSA assemblages, in particular, have become the type sequences for these cultural phases in East Africa. The best known archaeological features from Mumba are the presence of geometric microlithic stone artefacts and OES beads found in assemblages throughout the sequence, but most notably in the Bed V Mumba Industry. Microlithic technologies and the manufacture of personal ornaments play a central role in deliberations about the origins of modern human behaviour, the dispersals of modern humans within and out of Africa, and their responses to factors such as climate change (e.g., Ambrose, 1998; Wurz, 1999; McBrearty and Brooks, 2000; Mellars, 2006; Clarkson et al., 2009; Jacobs and Roberts, 2009; Petraglia et al., 2009). The abundant occurrence of microliths, especially geometric backed pieces, and personal ornaments in the archaeological record, is often used to differentiate between the MSA and LSA in Africa (Ambrose, 1998, McBrearty and Brooks, 2000). Although they are the hallmark of the LSA, it is well known that backed tools also occur in some MSA contexts, such as the Howiesons Poort in southern Africa (Wurz, 1999; Soriano et al., 2007; Lombard et al., 2008) and the Lupenbam of Zambia (Barham, 2002a), thereby obscuring the clear distinction between MSA and LSA toolkits, and the timing of the transition between the two.

2.1 Site setting

Mumba rockshelter (3º17'47"E, 3º32'26"S) is located ~1050 m above sea level in the Lake Eyasi Basin in northern Tanzania, ~62 km south of Olduvai Gorge (Figure 2.1). The Lake Eyasi Basin is situated near the southwestern terminus of the Crater Highlands volcanic area, but volcanic debris is found only in the northernmost portion of the lake and does not reach the rockshelter. The basin is of Pleistocene age and is now mostly filled with sediment. As a result, it has very little topography, making it very sensitive to rises and falls in lake level. When dry, the lakebed is subject to severe

aeolian deflation by strong northerly winds. In contrast, the lake level has also been high enough at times to submerge the rockshelter (Mehlman, 1989; Prendergast et al., 2007). Today, the modern lake is approximately 2 to 4 km away from the site depending on the lake level, which continues to fluctuate considerably. The rockshelter is situated at the base of a massive outcrop of diorite and gneiss (Figure 2.2). Like most outcrops in the region, the Mumba outcrop is composed of metamorphic rock of the Mozambique belt.

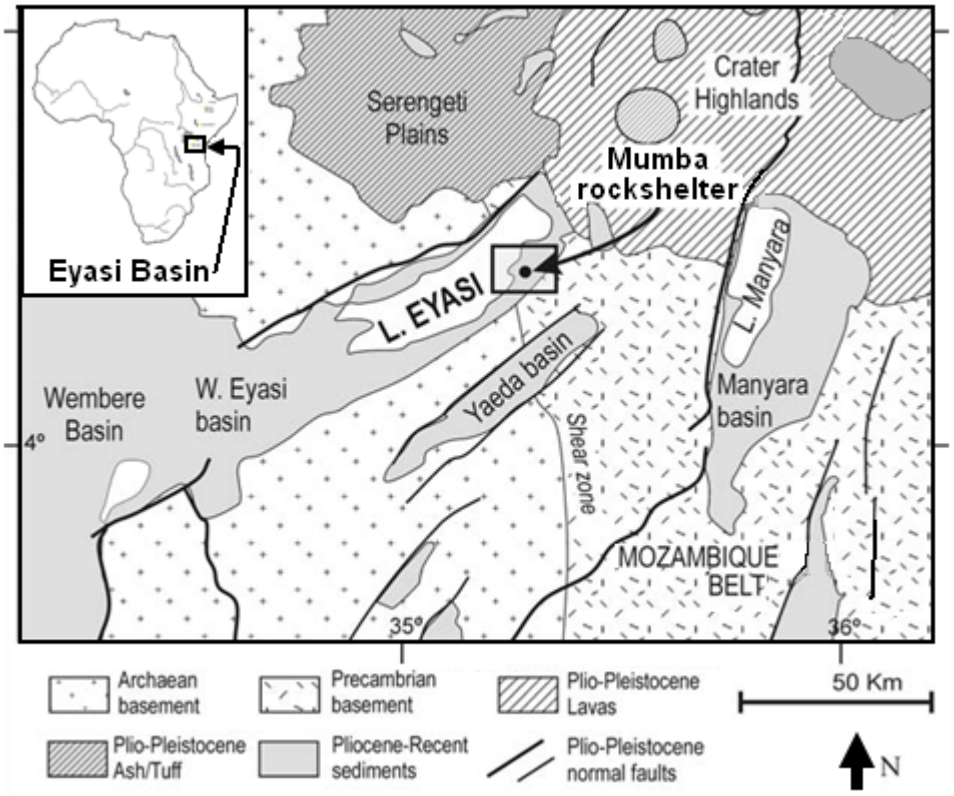

Figure 2.1: The location of the Lake Eyasi Basin and Mumba rockshelter in northern Tanzania as well as the geological features of the surrounding area. Map is modified from Prendergast et al. (2007) and Ebinger et al. (1997).

2.2 History of excavations at Mumba

Mumba rockshelter was first documented by M. and L. Köhl-Larsen (Köhl-Larsen, 1943), who excavated the vast majority of the archaeological deposit (9 x 12.5 x 10.75 m). They excavated a 'test trench' (8 x 4 m) between 1934 and 1936. Over eight months of excavation in 1938, M. Köhl-Larsen expanded the trench to 9 m across the shelter by 12.5 m from the wall of the shelter towards the dripline (Prendergast et al., 2007; see Figure 2.5a). While excavating in 20 to 40 cm thick spits, M. Köhl-Larsen

identified six geological beds in more than 10 m depth of deposit, naming them Beds I to VI (Köhl-Larsen, 1943; Mehlman, 1989). Due to the large volume of sediment moved in such a brief period of time, the excavations were imprecise by today's standards. The Köhl-Larsen collection is now known to be heavily biased in favour of large cores and flakes of exotic raw materials such as obsidian and chert. They discarded many important artefacts, such as microliths and blades made from quartz. These artefacts, along with other retouched artefacts and bone, are well represented in the enormous dump where the Köhl-Larsens deposited their rejected materials (Prendergast et al., 2007). This spoil heap is located outside the shelter, on the western side of the excavation. Quantitative analyses of the Köhl-Larsen lithic collection, stored in Tübingen, Germany, were performed by Mehlman (1989) who confirmed that they were heavily biased. This outcome suggests that further re-studies of this collection (e.g., Conard and Marks, 2006) may be limited in terms of their reliability and meaning.

Figure 2.2: View of Mumba rockshelter from the northwest. Note the two people at the foot of the outcrop for scale. (Photo: R.G. Roberts)

Further investigations of Mumba were performed by M. Mehlman, and are described in his Ph.D. dissertation (Mehlman, 1989). He excavated four 'witness' sections in 1979 and 1981, with the aim of refining the stratigraphy of the site and

obtaining samples for the purposes of dating. A third aim of his excavations was to collect a comprehensive, unbiased sample of the lithics for analysis. Unfortunately, M. Mehlman was unable to return to Tanzania to analyse the samples that he had collected. Prendergast et al. (2007) studied the materials collected by M. Mehlman, which had been in storage at Olduvai Gorge, and found that many lithics from Bed V and almost all fauna were unaccounted for. In the end, Mehlman performed most of his work on the Köhl-Larsen collection, retaining their geological bed nomenclature during his analysis of their lithic assemblage. In doing so, he defined the archaeological sequence for the site (Mehlman, 1989).

In 2005, the site was re-excavated by a team led by M. Domínguez-Rodrigo and A. Mabulla. They opened up a further four trenches along the perimeter of the area excavated by the Köhl-Larsens, naming them Trenches 5 to 8 (Figure 2.5). An unbiased lithic sample was collected from Bed V and analysed by Diez-Martín et al. (2009). Samples were collected for OSL dating by R.G. Roberts and Z. Jacobs in conjunction with these excavations in July, 2007.

2.3 Stratigraphy

As briefly mentioned in the previous section, the Köhl-Larsens identified six geological beds in the Mumba deposits, naming them Beds I to VI (Köhl-Larsen, 1943). Mehlman (1989) retained this six-bed division and provided several further subdivisions (Figure 2.3). He subdivided the lowermost geological unit, Bed VI, into two units: the basal Bed VIB, which he attributed to higher lake levels, and the overlying Bed VIA, which he attributed to falling lake levels and the associated deflation of the desiccated lacustrine floodplain. Mehlman (1989) described Bed V as being comprised of fine-grained aeolian sediments. Bed IV was interpreted as being deposited during a period of high lake levels (~26 m above the modern level) that may have submerged the base of the rockshelter. Bed III was composed of fine-grained sediments of aeolian origin, with carbonates, gravels, LSA stone tools and ceramics (in the upper-most part) located throughout. Mehlman described Bed II as sandy, silty, and containing ceramics, and Bed I as a shallow, grey ashy sandy and silt layer. By correlating the deposits of the rockshelter with those of the lake (using test pits), he established that the Mumba

deposits were younger than the lake deposits and that sedimentation in the rockshelter was the result of lowering lake levels and the associated aeolian deflation.

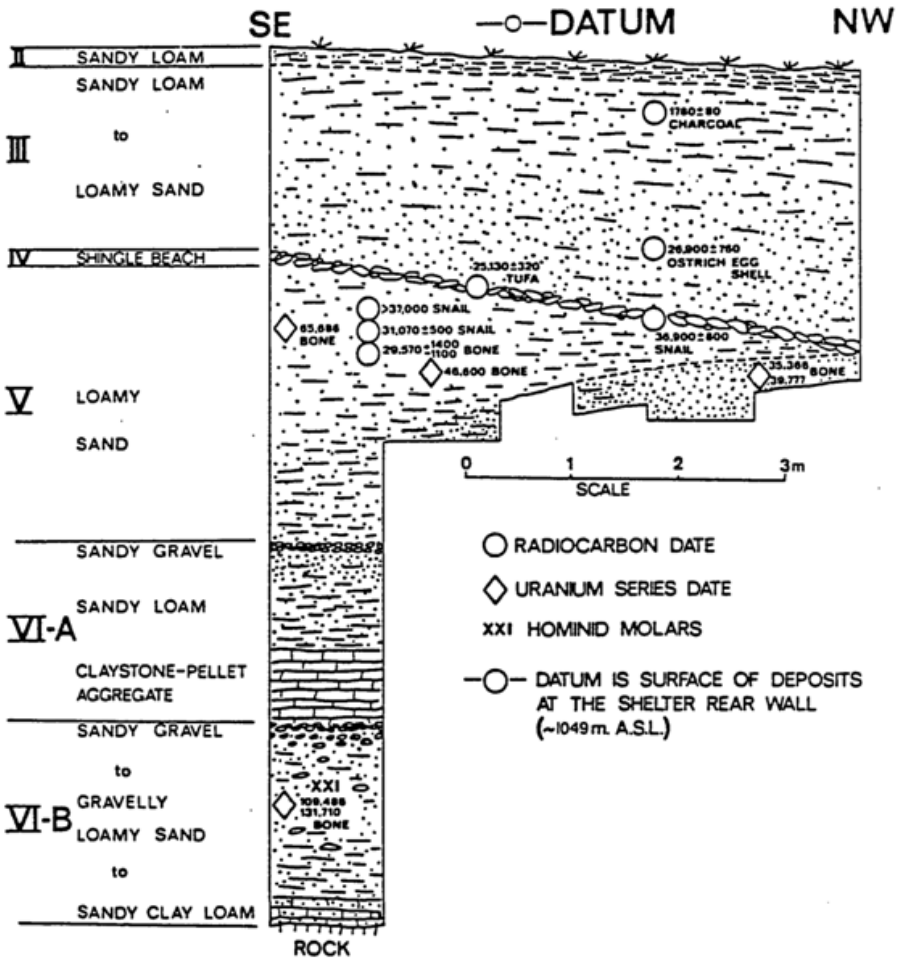

Figure 2.3: The geological beds identified by M. Mehlman, and the locations from where samples for dating were collected and for which radiometric ages were reported. (From Mehlman, 1989: Figure 4.5)

To reassess the overall stratigraphy and history of formation of the site, Prendergast et al. (2007) examined section profiles of the four new trenches as well as cleaned exposures of the original Köhl-Larsen and Mehlman excavations. They subdivided the deposit into a sequence of eight geological units, naming them Units A (at the top) to H (at the base). The units are primarily distinguished by the relative abundance of stone blocks (boulders and cobbles), alternating between units composed of fine-grained aeolian sediments (silts and sands) and units containing rocks (≥ 10 cm) embedded in a silty-sandy matrix. A number of archaeologically sterile units were also identified by Prendergast et al. (2007). The aeolian silts and sands were likely derived

from deflation of the exposed lakebed during drier periods. Alternatively, the boulders and cobbles were transported by gravity from a fracture on the eastern side of the rockshelter during wetter periods (i.e., when weathering was more intense). The different units are most readily differentiated in the east and north of the site and less conspicuous further west, where the gravity-deposited rocks are fewer and smaller (Figure 2.5b). As a result of this lateral variation, the contact between units is rarely horizontal and each unit is of variable thickness across the exposure (Prendergast et al., 2007). Figure 2.4 is a schematic section showing the relation between the eight geological units of Prendergast et al. (2007) and the six geological beds of Mehlman (1989), together with the lithic industries as defined by Mehlman (1989) and Diez-Martín et al. (2009). See Section 2.4 for a detailed discussion of the archaeology of each Bed.

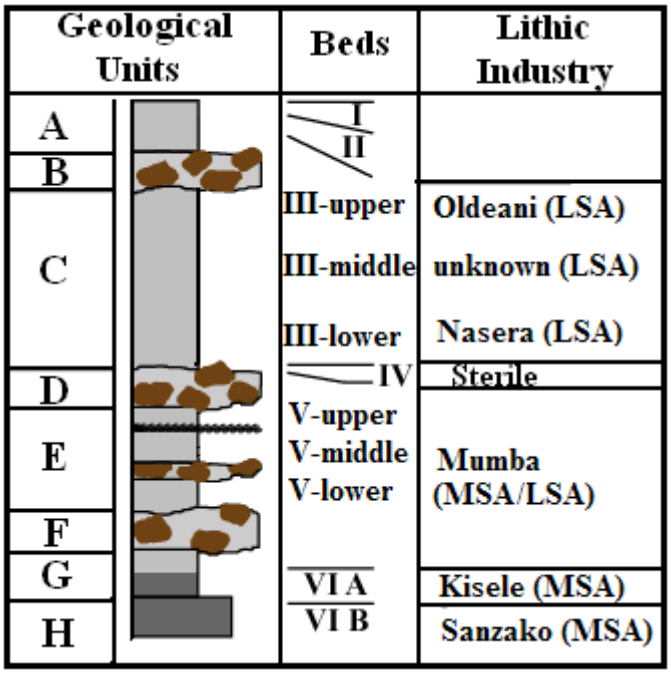

Figure 2.4: Schematic cross-section showing the relationships between the geological units of Prendergast et al. (2007), the beds of Mehlman (1989), and the associated lithic industries following Mehlman (1989) and Diez-Martín et al. (2009).

Each geological unit is described in detail in Prendergast et al. (2007), and will briefly be summarised here:

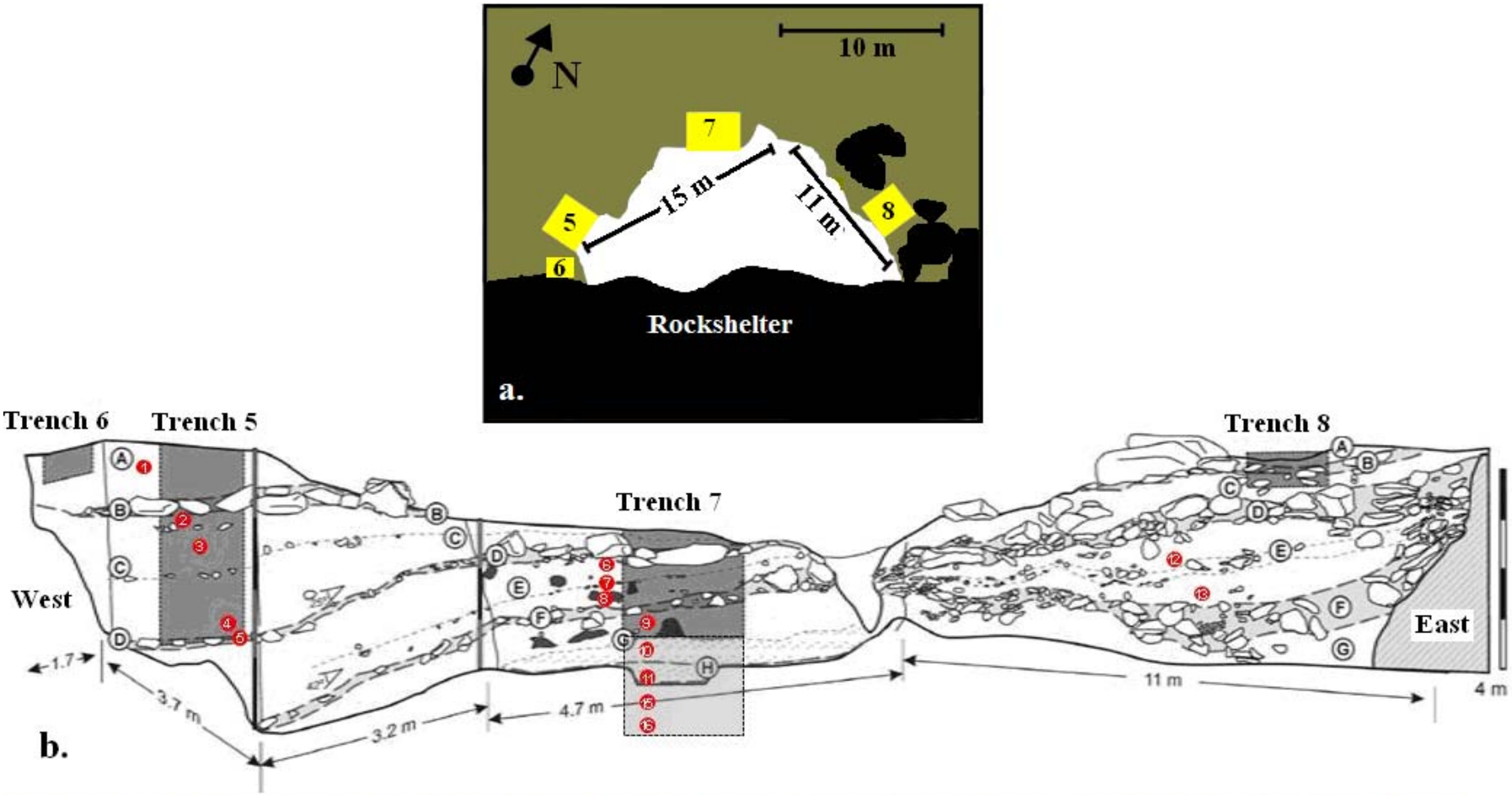

Figure 2.5: a, Planview of the excavated area of Mumba rockshelter. The white shading shows the area excavated by the Köhl-Larsens. Also shown are the trenches excavated in 2005 (yellow boxes). b, View of the cleaned exposures of the profile. The stratigraphy is shown with the geological units of Prendergast et al. (2007) (letters) and the approximate poitions of the collected OSL samples (numbers) overlain.

- Unit H. The sediments that compose this unit are poorly sorted sands, ranging in size from fine to coarse-grained, with a silty-clay matrix. Prendergast et al. (2007) posit that this unit may have an alluvial origin.
- Unit G. This unit was divided into two sub-units. The basal ~0.4 m sub-unit is comprised of fine to moderately fine-grained sediments. The matrix is patchy at the base and more clayish at the top. The upper ~0.25 m sub-unit is composed of very fine-grained loamy sediments, including sands, silts, and infrequent small pebbles. Prendergast et al. (2007) suggest that the basal sub-unit is the result of channel infilling in a fluvial system, and that the change between the basal and upper sub-units was caused by aeolian processes.
- Unit F. This unit is composed mainly of large stone blocks and fragments. These blocks were not transported fluvially, instead being gravity deposits that originated from a fracture on the eastern side of the rockshelter. Consequently, the thickness of this unit varies considerably, from 0.8 m in the east to 0.15 m in the west. There is a clear sloping of the unit downwards towards the west.
- Unit E. The thickness of this unit is variable. It is ~1.1 m thick in the west, ~0.9 m thick along the main section, and ~1.5 m thick near the shelter wall on the east side of the excavation. This unit is thickest in the middle portion of the section and slopes downwards (~30°) towards the west. The basal ~0.2 m portion of this unit is composed of sandy, silty, and loamy sediments, interspersed with several stone blocks. This is overlain by a thin level of stone slabs, *Achatina* snail shells, lithics, and bones. The upper portion of this unit is comprised of sands and fine-grained sands and silts that are moderately cemented by carbonates.
- Unit D. This unit, like Unit F, is composed mainly of stone blocks, the size of which generally decreases from east to west. The unit has an average thickness of ~0.7 m, although it is thicker in the east and slopes downwards towards the west (Figure 2.5b). The blocks that comprise this level are overlain by a level of small rock fragments. The matrix that contains the blocks is composed of loamy sands, which are cemented by carbonates towards the base of the unit and more lightly cemented towards the top of the unit.

- Unit C. The thickness of this unit varies considerably, from 0.6 m in the east to 1.6 m in the west (Figure 2.5b). At the base of this unit is a layer of very fine-grained loamy sands interspersed with rock fragments and bones. This layer is cemented by carbonates (likely of algal origin) to the top of the underlying unit (Unit D), indicative of the presence of permanent fresh water (Prendergast et al., 2007). Above this, two levels of rock fragments and bones are cemented by algal carbonates (~0.3 m thick) and make up the middle of this unit. The top of this unit (~0.3 m) is composed of fine loamy sediments, *Achatina* shell fragments, and bones.
- Unit B. This unit varies in thickness from 0.05 to 0.4 m (Figure 2.5b). It is composed of stone blocks, with a sedimentary matrix of fine loamy sandy silt with abundant rock and *Achatina* shell fragments.
- Unit A. This unit is the top of the deposit, reaching up to 0.35 m in thickness. At the base, this unit is composed of very fine-grained sediments with interspersed small rock fragments from the underlying unit. These sediments contain fragments of *Achatina* shell and bone, and abundant insect nests. At the top of the deposit is a layer of loose, fine loamy sands. Prendergast et al. (2007) report that this upper level shows evidence of anthropogenic disturbance and bioturbation by modern insects.

2.4 Archaeological context

The first description of the lithic assemblages from Mumba is presented in Roller (1954). He based his analysis on the Köhl-Larsen collection and the contemporary literature, suggesting the cultural sequence for Mumba presented in Table 2.1. The validity of the presence of multiple lithic industries in the Bed V deposits was questioned by Mehlman (1979) after a self-described cursory analysis of lithics collected during his 1977 excavation. Later, Mehlman (1989) produced the archaeological sequence for Mumba that is now most commonly cited. He based the archaeological sequence principally on a thorough typological assessment of the collection of lithics collected by the Köhl-Larsens. However, Mehlman (1989) makes regular comparisons to his cursory analysis of the lithics collected during the 1977/81 excavations. Given the biased nature of the Köhl-Larsen collection, it is likely that

valuable information was missing from the assessment made by M. Mehlman, a point that he acknowledges repeatedly throughout his dissertation (e.g., Mehlman, 1989: 313). Later, in 2005, an unbiased sample of lithics was collected from Mumba using modern excavation techniques (Prendergast et al., 2007; Diez-Martín et al., 2009). The results of a recent re-analysis of the unbiased Bed V assemblage were published by Diez-Martín et al. (2009), who did not re-examine any of the other archaeological layers. Consequently, the general validity of the rest of Mehlman's scheme has yet to be examined using unbiased lithic assemblages, such as that collected in 2005. His description of the remaining archaeological layers may thus be subject to revision.

Table 2.1: Cultural sequence for Mumba as determined by Roller (1954). Note that the term 'Stillbay' was used to describe many MSA assemblages in the 1950s, most of which did not conform to definition for the southern African MSA industry as described by Goodwin and Van Riet Lowe (1929) (Wadley, 2007).

Stratigraphic level	Archaeolgical Industry
Beds I, II, and III (upper and middle)	LSA with Pottery
Bed III (lower)	LSA
Bed V (upper)	Magosian
Bed V (middle)	Stillbay
Bed V (lower) and VI (upper)	Proto-Stillbay
BedVI (lower)	Upper Levalloisian

The following sections will describe the lithic assemblages present in the deposits at Mumba. They will be presented in order from the basal to the uppermost units. The descriptions are mainly based on Mehlman (1989) for assemblages in Beds VI, III and II. In regards to the lithic assemblage of Bed V, two descriptions will be presented: that of Mehlman (1989) and that of Diez-Martín et al. (2009).

2.4.1 Bed VI deposits

The archaeological context of all lithics from Bed VI (i.e., VIA and VIB) can be described as MSA on the basis of both typology and technology (Mehlman, 1979, 1987, 1989). The artefacts contained in the basal deposits of the excavated sequence (Unit H, Bed VIB) were designated by Mehlman as the Sanzako Industry. This industry is characterised by high frequencies of scrapers (side and notched) and bifacially modified pieces, which co-occur with heavy-duty tools such as small bifaces and choppers.

Additionally, Levallois technology and retouched points are uncommon (Mehlman, 1989; Mabulla, 2007). The dominant raw material of Sanzako Industry artefacts is quartz (~95%; Mehlman, 1989). There are two further points of interest in regards to the archaeology of this layer. First, three molars from a single *Homo sapiens* were recovered from Bed VIB (Bräuer and Mehlman, 1988), suggesting that the associated MSA artefacts were used by the same species. It seems likely, therefore, that the artefacts from the overlying (i.e., younger) layers were also associated with *Homo sapiens*. The second point of interest is the presence of more than a dozen obsidian artefacts collected during Mehlman's 1977 excavation. Microprobe analyses were used to assess the chemical content of three of these pieces. Results indicated that the obsidian was chemically similar to outcrops in the Njorowa Gorge, located 320 km NNE of Lake Eyasi on the southern side of Lake Naivasha in southern Kenya (Merrick and Brown, 1984; Mehlman, 1989; see maps in Figure 1.4 and Figure 10.2). The implications of the presence of raw material from such a distant source will be discussed in Section 10.3.1. Mehlman (1989: 270) states that "the closest parallels to the Sanzako Industry are MSA assemblages at Songhor (McBrearty, 1981) and those overlying the Sangoan at Muguruk (McBrearty, 1988)", both of which also contain distant obsidian (McBrearty and Brooks, 2000).

The overlying deposits (Unit G, Bed VIA) contained stone artefacts that were assigned to the Kisele Industry. Like the Sanzako Industry, the majority of tools were produced using quartz as raw material. The artefacts are, however, generally smaller than those found in the underlying deposits. Retouched points occur in relatively high frequency (>10% of tools), whereas heavy-duty tools, backed tools and burins were rare. The most distinctive tool types are bifacial and unifacial points (>10% of retouched tools) and scrapers. Technologically, the assemblage is characterised by high frequencies of disc and part-peripheral cores, with a low frequency of Levallois cores (Mehlman, 1989). The 2005 assemblage also contained large-sized artefacts, such as Levallois cores and large scrapers, and lacked any microliths (Diez-Martín et al., 2009). Similarly to Bed VIB, eleven pieces of obsidian were associated with the Kisele Industry. These pieces were analysed and traced to the same sources as their Sanzako counterparts, 320 km from Mumba, near Lake Naivasha in Kenya (Mehlman, 1989). Mehlman (1989) identified an MSA Kisele Industry assemblage below level 12 at

Nasera rockshelter, which is ~60 km to the north of Mumba. Distant raw material use is prevalent in the archaeological record at Nasera, with obsidian being sourced to southern Kenya and chert being sourced to either Olduvai Gorge (~30 km south) or Lake Natron (60 km NNE). Mehlman (1989) has also suggests that the MSA aggregates from Lukenya Hill are similar to the Kisele Industry.

The two industries defined by Mehlman (1989) for Bed VI deposits (i.e., the Sanzako and Kisele Industries) are typical MSA. Their similarities include the presence of both retouched points and radial-disc-Levallois technology. Both assemblages are dominated by quartz artefacts and generally lack core and heavy-duty tools. In addition, both industries include obsidian pieces collected at least 320 km from the site. However, several features of the two industries set them apart from one another. The Kisele assemblage generally contains more points and a lower frequency of scrapers (side and notched), bifacially modified pieces, and heavy-duty tools. In addition, the general size of the artefacts is smaller in the Kisele Industry. Technologically, the range (distinguished by core types) of the Sanzako and Kisele Industries is similar. However, the frequency of various core types varies between the two. The frequency of amorphous cores decreases, and the Levallois technique becomes more prevalent (though still rare) in the Kisele assemblage. When examined together, Mehlman (1989: 183) surmised that the MSA lithic assemblage of the Sanzako is more "primitive" and less diverse than that of the Kisele.

2.4.2 Bed V deposits

Overlying Bed VI deposits is Mehlman's Bed V, which corresponds to the upper part of Unit G, all of Units F and E, and the lower part of Unit D in the geological system of Prendergast et al. (2007). To distinguish their assemblage from that examined by Mehlman (1989), Prendergast et al. (2007) refer to the artefacts that were collected from the Bed V deposits in 2005 as the 'Level V' assemblage. However, Diez-Martín et al. (2009) refer to this same assemblage as 'Bed V'. Since Diez-Martín et al. (2009) describe the assemblage collected in 2005, their nomenclature (i.e., Upper, Middle, and Lower Bed V) will be retained in this thesis. The descriptions of the Bed V lithic assemblage by Mehlman (1989) and Diez-Martín et al. (2009) will be discussed separately, and then compared, in this section.

2.4.2.1 Interpretation of Mehlman (1989)

The name commonly given to the lithic assemblage from Bed V at Mumba, the Mumba Industry, was coined by Mehlman (1989). He concluded that the Mumba Industry was intermediate between the MSA and LSA, representing a transitional lithic assemblage. This conclusion was based on the occurrence of large backed pieces (typical LSA) and retouched points (typical MSA) in the same assemblage. The presence of these two lithic types was not an artefact of examining the biased and hastily collected (i.e., in 20 to 40 cm thick spits) Köhl-Larsen collection, since Mehlman confirmed their co-occurrence in the same 10 cm spits during his excavations. In spite of this, Mehlman (1989) makes clear that the Bed V assemblage of the Köhl-Larsen collection is heavily biased in favour of exotic raw materials and against smaller tool and core types that are characteristically LSA, such as backed microliths and small bipolar cores. Consequently, although Mehlman principally based his description of the lithics from Bed V on the Köhl-Larsen collection, he continually compares it to the results of a cursory analysis of his own unbiased assemblage collected during the 1977/81 excavations.

Mehlman divided the Bed V artefact assemblage into three sub-levels: Bed V-lower, V-middle, and V-upper. In the Bed V-lower assemblage of the Köhl-Larsen collection, points are the most frequently occurring type (~17%), followed by side scrapers (~13%), then backed pieces (~8%), which range from macrolithic to microlithic. The large majority of cores are part-peripheral (39%) or radial/disc (16%), with low frequencies of bipolar types (8%). In contrast, the assemblage collected from Bed V-lower during the 1977/81 excavations is substantially different, although that may be attributed to the low number of artefacts collected. In this assemblage, sundry side scrapers and ends were the most common types. Only one backed piece and one unifacial point were found; this is likely a result of the small number of total flaked tools collected (n = 26). A more significant difference between the Mehlman collection and the Köhl-Larsen collection is the difference in the frequencies of core types. In Mehlman's collection, the frequencies of bipolar and peripherally worked cores are reversed: the majority of cores (56%, n = 20) are bipolar, while peripherally worked cores account for a mere 11% (n = 4). Three pieces of obsidian were collected, though none were analysed for trace elements (Mehlman, 1989).

The middle and upper levels of Bed V contained more LSA-like assemblages. In the Köhl-Larsen collection, points comprise only 5% of tools, while backed pieces (microlithic and macrolithic) comprise 9%. The most common core types are single and multiple platform (~22%), while 15% were bipolar. The Köhl-Larsens also recovered several OES artefacts, but they interpreted them as being intrusive. As in Bed V-lower, the 1977/81 assemblage looks substantially more LSA-like than that collected by the Köhl-Larsens. Backed pieces, the majority of which are microlithic, were the most frequent tool type (14%), while only four points (2%) were found. Technologically, the assemblage is dominated by bipolar cores (75%), while peripherally worked and platform types both accounted for 10%. As in the lower levels, most tools were still made on quartz (95%) with small contributions from fine-grained quartzite and chert. Twelve pieces of obsidian were recovered from Bed V-upper, four of which were traced to distant Kenyan sources: three from Sonanchi and one from the Njorowa Gorge area. Mehlman also recovered multiple OES artefacts (seven beads, one shaped blank, and four drilled fragments) from as deep as 50-60 cm into Bed V. He concluded that they were *in situ* on the basis of AAR investigations, by A. Brooks, of these OES artefacts and several from Bed III.

To summarise, Mehlman's interpretation of the Bed V assemblages was based on a thorough analysis of the biased Köhl-Larsen assemblage and a cursory analysis of the unbiased sample collected during his 1977/81 excavations. He described the assemblage from Bed V as being transitional between the MSA and LSA on the basis of changing frequencies of tool and core types throughout the sequence. While he described no new or different types of artefacts in successive Bed V sub-levels, it was clear that the frequencies of various types changed substantially between the lower and upper parts of the deposit (e.g., points and backed pieces). The two characteristic features of the Mumba Industry, namely large backed pieces and retouched points, are present in equivalent numbers in the Bed V-lower assemblages. In the Bed V-upper and V-middle assemblages, backed pieces (micro and macrolithic) increase in frequency and points become more intermittent. Technologically, radial, platform and bipolar core types are all present throughout the assemblage. Radially flaked cores become less common, while platform and bipolar cores become more common in Bed V-upper, suggesting a shift towards more LSA-like core technologies (Mehlman, 1989). In

addition to the clear presence of symbolic materials, in the form of OES beads, in Bed V-upper and the increase in microlithic backed pieces, this suggests that a shift occurred throughout Bed V, with the Bed V-upper assemblage being more LSA-like than the Bed V-lower assemblage.

2.4.2.2 Interpretation of Diez-Martín et al. (2009)

Diez-Martín et al. (2009) divided the Bed V archaeological collection into three assemblages based on their own stratigraphic observations: Lower, Middle, and Upper Bed V (Figure 2.6). This tripartite division corresponds well with the original Bed V-Upper/Middle/Lower scheme of Mehlman (1989). Additionally, it reflected the observation that the artefacts in Middle Bed V appeared to be separated from those below by a conspicuous layer of medium-sized rocks in Unit E, and from those above by a ≤9 cm-thick layer of sterile sand (Figure 2.6) (Prendergast et al., 2007; Diez-Martín et al., 2009). The subdivisions of Bed V, however, do not represent discrete occupational events, given the lack of clear archaeological layers or discrete depositional units (Prendergast et al., 2007; Diez-Martín et al., 2009).

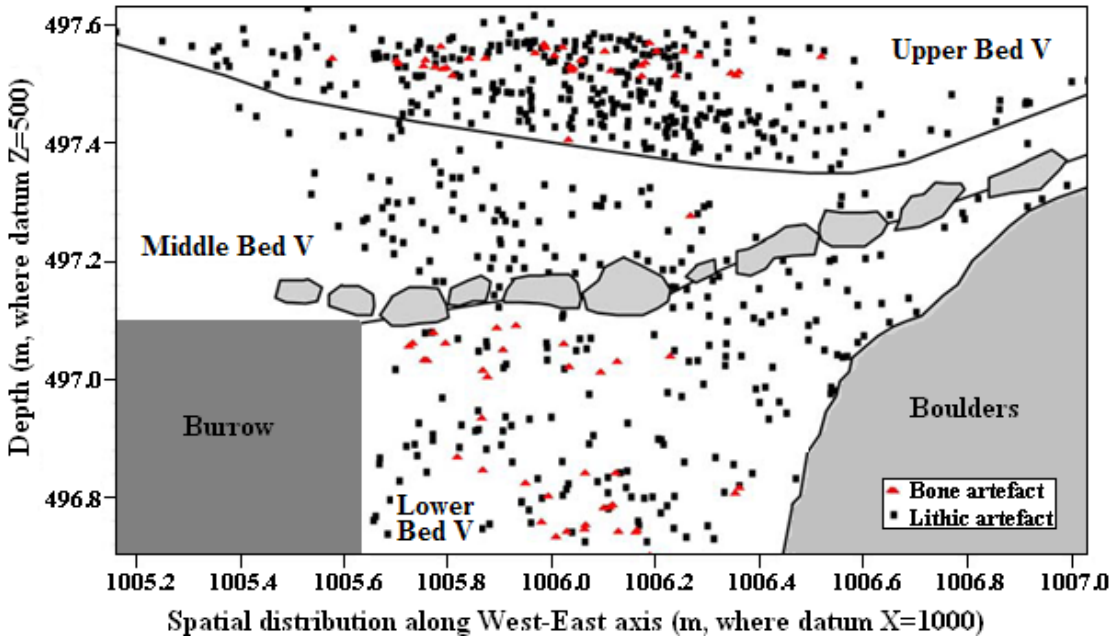

Figure 2.6: Spatial distribution of all artefacts recovered from Trench 7 during the 2005 excavations (modified from Diez-Martín et al., 2009). The black line between Upper and Middle Bed V represents a layer of sterile sands (Prendergast et al., 2007).

The approach used by Diez-Martín et al. (2009) to assess the lithic assemblage from Bed V can be described as typo-technological, as opposed to the purely typological approach of Mehlman (1989). The typological classification scheme of Mehlman (1989: 127-138) was retained, with few modifications (e.g., the inclusion of a type for 'bipolar backed pieces'). Diez-Martín et al. (2009) noted substantial typological differences between the Lower Bed V and Upper Bed V assemblages. In Lower Bed V, 48% of tools (n = 10) were scrapers and 42% (n = 9) were backed pieces. Upper Bed V, in contrast, is dominated by backed pieces (63%, n = 27). In addition, whereas geometric microliths were all but absent from the Lower Bed V assemblage, they constituted a substantial component of the Upper Bed V assemblage. Six (22%) of the Upper Bed V geometric microliths are crescents, a hallmark of the LSA (McBrearty and Brooks, 2000; Ambrose, 2002). In addition, three OES beads and nine ochre fragments were recovered from Upper Bed V. They were located at different depths throughout the sequence and were not associated with the Bed IV/V interface (Diez-Martín et al., 2009). This corroborates the claim of Mehlman (1989) that OES beads are associated with the Mumba Industry and are not derived from the downward migration and, thus, intrusion of Bed III materials. A notable type that was nearly absent from the 2005 assemblage was blades and blade fragments. None were recovered in Lower Bed V and only a few were recovered from Upper Bed V, the latter likely as a result of the larger sample size.

The two main knapping techniques represented in Bed V at Mumba are the bipolar and freehand techniques. The latter corresponds to peripherally worked and platform cores, as defined by Mehlman (1989). The two knapping techniques were by no means independently utilised by the inhabitants of Mumba. Freehand retouch was observed on multiple bipolar flakes. Diez-Martín et al. (2009) confirmed Mehlman's observations of the 1977/81 collection (i.e., in contrast to his observations of the Köhl-Larsen collection), that most cores in the Bed V deposit are bipolar. This reduction technique is typical of LSA technologies in the western Rift Valley (Brooks and Mercader, 2001). Bipolar cores represented the majority of cores collected from Lower, Middle and Upper Bed V assemblages. Diez-Martín et al. (2009) did not identify significant differences in core morphology across levels, observing similar dimensional and technical characteristics. This suggests that similar technological approaches were

used throughout Bed V. This was confirmed by an analysis of the flakes in the assemblage, ~50% of which were produced using the bipolar technique. This reduction technique is most abundant in Upper Bed V, while the freehand technique is more common in Middle and Lower Bed V. No significant differences were observed between Bed V assemblages in the size and shape of bipolar flakes, but a slight trend towards size reduction (<1 cm) in freehand flakes from Lower to Upper Bed V was reported. Diez-Martín et al. (2009) thus concluded, based on the dimensional and technological variables of flakes and cores, that no significant separation can be made between the assemblages of Lower, Middle, and Upper Bed V. They attributed the differences in type frequencies to the differing sample sizes of the three Bed V assemblages.

Interesting patterns were observed, however, when freehand and bipolar reduction techniques were compared. Most of the bipolar cores (~83%) retain cortex on at least one platform, whereas 54% of freehand cores retain no cortex and 23% retain only a very small amount of cortex on their lower surfaces. Very few freehand flakes collected could be assigned to the initial phase of the reduction process, with only 4% of flakes having cortex on their dorsal surface. In addition, the collected freehand cores were consistently small in size, whereas bipolar core size was more variable. When all of these factors are taken into account, it is clear that various stages of the *chain opératoire* for freehand reduction are not uniformly represented in the deposit, with most specimens being attributed to the latest stages of the knapping sequence. The earlier phases of the reduction sequence were likely performed elsewhere. Supporting this conclusion is the very low core-to-flake ratio, which indicates that the core nuclei were also mostly discarded elsewhere. Notably, the reduction technique used tends to correlate with the raw material being exploited. The bipolar technique was preferentially used to exploit lower quality raw materials, with ~85% of bipolar objects being made on orthogneiss, polycrystalline quartz and smoky quartz. In contrast, higher quality raw materials (e.g., hyaline quartz, metarhyolite, nephelinite and chert) were almost exclusively reduced using freehand techniques. While the upper assemblage contained a higher frequency of better quality raw materials (e.g., hyaline quartz) and a lower frequency of low quality raw materials (e.g., orthogneiss and smoky quartz),

Diez-Martín et al. (2009) suggested that the discrepancy is probably due to the small sample size.

While the implications of these patterns of raw material use are not discussed by Diez-Martín et al. (2009), they are interesting. The data from Diez-Martín et al. (2009) indicate that most of the LSA-like features of the assemblages in Bed V (i.e., microlithic backed pieces and blade or blade-fragments) were produced on higher quality raw materials. In Figures 15 and 16 of Diez-Martín et al. (2009), all blades, blade fragments, retouched blade fragments, crescents and sundry backed microliths are made on high quality raw materials (i.e., hyaline quartz, chert, or nephelinite). These higher quality raw materials were likely transported to the site as prepared cores, while the early stages of the reduction sequence were performed elsewhere. They were then preferentially reduced using freehand knapping techniques to produce the more LSA-like features of the toolkit. Any cores not completely exhausted were transported away, probably for further reduction, until exhaustion and subsequent disposal. This pattern may suggest that the higher quality raw materials were more highly valued and harder to come by than the lower quality raw materials. The lower quality raw materials on the other hand, were preferentially reduced using the bipolar technique. These raw materials were likely more accessible, given that the earlier stages of bipolar core reduction are present in the assemblage, bipolar cores retain more cortex, and bipolar cores of variable sizes were discarded. These lines of evidence suggest that lower quality raw material was brought to the rockshelter, reduced from the early states of the reduction sequence using the bipolar technique, and discarded prior to core exhaustion. This implies that lower quality and more available raw materials were regarded as less valuable than higher quality and less available raw material.

2.4.2.3 Summary and discussion of the Mumba Industry

To summarise, Diez-Martín et al. (2009) found that the overall properties of the Bed V assemblages could be classified as LSA. They reported a distinct shift towards bipolar reduction and the use of scrapers and backed tools in Lower Bed V, noting that the artefacts obtained from the immediately underlying MSA deposits in Bed VI did not have these characteristics. No unambiguous technological changes were documented in the Bed V sequence, with bipolar and freehand techniques being equally represented

and the size of flakes remaining fairly consistent across assemblages. The only differences between Bed V levels reported by Diez-Martín et al. (2009) are typological. In Lower Bed V, scrapers and backed pieces were represented in equal frequencies, whereas backed pieces dominated the Upper Bed V assemblage. Importantly, geometric microliths, including crescents, were abundant in the Upper Bed V backed piece assemblage. Symbolic objects (i.e., three OES beads) and potentially symbolic objects (i.e., nine ochre fragments) were also present in this assemblage. However, given the technological consistency, Diez-Martín et al. (2009) considered the typological differences insufficient to signify significant change in the toolkit across the Bed V sequence. They suggested that the typological differences were, instead, an artefact of the relatively small size of their sample. Based on both the technology and typology, Diez-Martín et al. (2009) considered the assemblages in Bed V to be more appropriately defined as LSA.

The revised description of the Mumba Industry by Diez-Martín et al. (2009) supersedes the 'MSA/LSA-transitional' description by Mehlman (1989), given the lack of evidence when an unbiased sample is investigated using modern methods of stone tool analysis. Mehlman (1989) proposed that Bed V contained a transitional industry with typological components that can be described as MSA (e.g., retouched points) and LSA (e.g., geometric microliths and large backed pieces). In contrast, the unbiased Bed V assemblage collected in 2005 did not contain any retouched points or large backed pieces (Diez-Martín et al., 2009). This discrepancy complicates a straightforward comparison with the Mehlman record. It does, however, raise the possibility that the co-occurrence of these elements in the Bed V assemblages described by Mehlman (1989) is an artefact of excavating in thick, horizontal spits (Prendergast et al., 2007; Diez-Martín et al., 2009). Diez-Martín et al. (2009) argue that the co-occurrence of points and large backed pieces in the same assemblage can no longer be unambiguously accepted: given the sloping topography of the deposit, there is considerable potential for mixing of sediments and artefacts from multiple beds when excavated in horizontal spits.

2.4.3 Beds IV and III deposits

The basal few centimetres of Unit C of Prendergast et al. (2007) correspond to Mehlman's Bed IV and are culturally sterile (Figure 2.4). The remainder of Unit C, the overlying Unit B, and the basal part of Unit A are collectively equivalent to Mehlman's Bed III, and contain evidence for LSA occupation (Figure 2.5). Mehlman (1989) divided Bed III into lower, middle and upper sections to define the archaeological industries (Figure 2.4). Bed III-lower is associated with the Nasera Industry, an early LSA tradition that is also present at Nasera rockshelter. The assemblage from Mumba is dominated by scrapers and contains relatively low frequencies of points and microlithic backed pieces (Mehlman, 1989). Blades are very rare and bipolar core reduction is very common. One obsidian artefact was present in the Köhl-Larsen collection. The Bed III-lower assemblage studied by Mehlman (1989) also contained large quantities of OES beads and fragments, and several bored stone balls. The OES bead tally in Bed III-lower includes 243 beads, 25 shaped blanks, nine drilled pieces, and 51 unfinished beads from the Köhl-Larsen assemblage and 78 finished beads, 26 shaped blanks, eight drilled pieces, and 23 unfinished beads from the 1977/81 assemblage. The abundance of OES beads and bored stone balls is unambiguous evidence for symbolic behaviour in the Nasera Industry from Mumba rockshelter. An assemblage from Nasera rockshelter has also been assigned to the Nasera Industry on the basis of similar proportions of backed pieces and points and an abundance of scrapers. Mehlman (1989) also suggests that a Nasera Industry assemblage is present at Kisese II rockshelter. A third assemblage, namely the Sakutiek Industry from Enkapune Ya Muto, shares substantial typological similarities with the Nasera Industry. Like the assemblage of Bed III-lower, it contains very few backed tools, though overlies an assemblage that contains abundant backed pieces. Both assemblages also contain several typical MSA types, are dominated by scrapers, and are associated with an abundance of OES beads.

Mehlman (1989) recognised an aceramic LSA assemblage in the middle section of Bed III, but the small sample size precluded industrial assignment. He noted that this assemblage was deficient in geometric microliths but had a high frequency of curve-backed pieces and large scrapers. In spite of the small sample size, OES beads were found in Bed III-middle as well as a notched bone fragment and a bone point. A

ceramic LSA, known as the Oldeani Industry, appears in upper Bed III, along with a profusion of backed microliths. The ceramics include Kansyore ware, an LSA ware traditionally associated with hunter-gatherers, as well as Narosura and Lelesu wares, which were produced by pastoral Neolithic and Iron Age people, respectively. While these wares have previously been found together in secure stratigraphic contexts, it remains to be demonstrated if this also holds true at Mumba. Beds II and I represent more recent Iron Age deposits (Mehlman, 1989; Prendergast et al., 2007) and are beyond the scope of this study.

2.4.4 Summary

Mumba rockshelter is one of the few sites in East Africa that contains both MSA and LSA assemblages in its archaeological sequence. The contents of each assemblage and the changes of the contents of each assemblage may be indicative of changes in toolkits, subsistence strategies, behaviours and ideas over time. The presence of distant obsidians in Beds VIA, VIB, V and III-lower may be evidence for interactions between distant groups of people. The transition from the MSA, point-based Kisele Industry of Bed VIA to the backed piece-based Mumba Industry of Bed V may reflect a change in subsistence strategies or population dynamics. Likewise, the emergence of ornaments in Upper Bed V and their proliferation in Bed III-lower may reflect changing environmental conditions, population dynamics, behaviours, or a combination of the three. Robust chronologies for each archaeological layer, and thus *when* technologies and ornaments were being used and *when* they changed, will allow comparisons to be made over a wider geographical and temporal region with other sites in eastern and southern Africa. The temporally constrained regional archaeological record can then be interpreted in the context of existing palaeoclimate and genetic reconstructions to infer *why* technologies and behaviours changed through time.

2.5 Geochronology at Mumba

2.5.1 Previous chronologies

As mentioned in Section 2.2, a principal objective of M. Mehlman's 1977/81 excavations at Mumba was to obtain samples for dating, which could be used to construct a chronology for the archaeological sequence. The sample material collected

for radiocarbon and U-series dating included charcoal, bone collagen, bone apatite, OES, *Achatina* shell and tufa. Sixteen ages were obtained in the 1980s and are presented in Mehlman (1989: 103). Since then, several authors have reported additional ages for various levels at Mumba. Table 2.2 presents a compilation of all known age estimates (except two) for Beds III to VI at Mumba. The two ages omitted from the table are ^{14}C ages on charcoal (4860 ± 100 BP) and bone collagen (4890 ± 70 BP) for the human burial in Bed III reported by Mehlman (1989). Given that the human remains were likely interred long after the time of formation of Bed III, they are not relevant to the current discussion.

Three features of the dataset presented in Table 2.2 are of note. First, the ages are stratigraphically inconsistent. The four $^{230}Th/^{234}U$ ages reported by Mehlman (1989) using bone apatite from Bed V illustrate this point. One age was obtained for the Bed V-upper, two from V-middle, and one from V-lower. The two ages obtained for the middle section are significantly different from one another and are inverted with respect to their stratigraphic positions. The sample that yielded the age of ~65.7 ka was collected above the sample that yielded the age of ~46.6 ka in the section (Figure 2.3). In addition, both ages from the middle of Bed V are significantly older than that obtained for the sample from the underlying V-lower (~35.3 ka). Likewise, the ^{14}C ages obtained using bone apatite and *Achatina* shell from Bed V are inverted (Figure 2.3). More broadly, the ^{14}C age obtained using *Achatina* shell from Bed IV is older than several other ^{14}C ages obtained from Bed V-middle, V-lower, and VI.

The second noteworthy feature of Table 2.2 is that most of the ages were obtained using either, sample materials that are now considered unsuitable for dating, or sample preparation and measurement procedures no longer considered reliable (see Section 1.4). These two factors indicate that the existing chronology for Mumba is largely inadequate by modern standards. It is highly likely that these shortcomings are responsible (wholly, or in part) for the inversions and inconsistencies in the reported ages. The two dating methods that were used to obtain the majority of ages at Mumba, namely U-series and radiocarbon dating, were discussed in Section 1.4. They will briefly be considered again to highlight the limitations and deficiencies of their use at Mumba.

All U-series ages reported for Mumba were obtained using bone apatite. Obtaining U-series ages using this material is complicated by the variable timing and rate of uptake of uranium after burial, due to the 'open system' behaviour of bone (Grün, 2006; Grün et al., 2010). A minimum $^{230}Th/^{234}U$ age can be determined if it is

Table 2.2: All ages reported in the literature for Beds III to VI. The two AMS ^{14}C ages for Bed III-upper were calibrated using the IntCal 04 curve (Reimer et al., 2004). All remaining ^{14}C ages were reported as uncalibrated ages and have been calibrated using the IntCal 09 curve (Reimer et al., 2009). The calibrated ^{14}C age range (2σ) is presented in bold under the reported uncalibrated age.

Bed	Material	Method	Age (ka)	Lab No.	Reference
III-upper	charcoal	AMS ^{14}C	0.84 ± 0.08	OS-61329	Prendergast et al. (2007)
III-upper	charcoal	AMS ^{14}C	1.77 ± 0.15	AA69911	Prendergast et al. (2007)
III-upper	charcoal	^{14}C	1.78 ± 0.08 **(1.53 - 1.88)**	ISGS-565	Mehlman (1989: 103)
III-lower	OES	^{14}C	27.0 ± 0.8 **(30.2 - 33.4)**	ISGS-566	Mehlman (1989: 103)
III-lower	OES	AMS ^{14}C	29 - 33	unknown	Conard (2005)
IV	tufa	^{14}C	25.1 ± 0.3 **(29.4 - 30.5)**	USGS-1505	Mehlman (1989: 103)
IV	*Achatina* shell	^{14}C	36.9 ± 0.8 **(40.4 - 43.0)**	ISGS-499	Mehlman (1989: 103)
V-upper	OES	AAR	45 - 65	unknown	McBrearty and Brooks (2000)
V-upper	OES	AAR	52	unknown	McBrearty and Brooks (2000)
V-upper	bone apatite	$^{230}Th/^{234}U$	$23.7\ ^{+1.1}/_{-0.9}$	USGS-83-10	Mehlman (1989: 103)
V-upper		$^{321}Pa/^{235}U$	$23.8\ ^{+2.5}/_{-1.4}$	USGS-83-10	Mehlman (1989: 103)
V-middle	*Achatina* shell	^{14}C	>37.0 **(>41.1)**	GX-6620A	Mehlman (1989: 103)
V-middle	*Achatina* shell	^{14}C	31.1 ± 0.5 **(34.8 - 36.5)**	ISGS-498	Mehlman (1989: 103)
V-middle	bone apatite	^{14}C	$29.6\ ^{+1.4}/_{-1.1}$ **(31.5 - 36.5)**	GX-6621A	Mehlman (1989: 103)
V-middle	bone apatite	$^{230}Th/^{234}U$	$65.7\ ^{+6.0}/_{-5.4}$	USGS-82-22	Mehlman (1989: 103)
V-middle	bone apatite	$^{230}Th/^{234}U$	$46.6\ ^{+2.1}/_{-1.7}$	USGS-82-33	Mehlman (1989: 103)
V-lower	bone apatite	^{14}C	21.0 ± 0.7 **(23.3 - 27.0)**	GX-6622A	Mehlman (1989: 103)
V-lower	bone apatite	$^{230}Th/^{234}U$	$35.3\ ^{+0.7}/_{-0.5}$	USGS-82-20	Mehlman (1989: 103)
V-lower	bone apatite	$^{321}Pa/^{235}U$	$39.8\ ^{+4.2}/_{-3.8}$	USGS-82-20	Mehlman (1989: 103)
VI-B	bone apatite	^{14}C	19.8 ± 0.8 **(21.6 - 25.6)**	GX-6623A	Mehlman (1989: 103)
VI-B	bone apatite	$^{230}Th/^{234}U$	$131.7\ ^{+6.9}/_{-6.0}$	USGS-82-19	Mehlman (1989: 103)
VI-B	bone apatite	$^{321}Pa/^{235}U$	$109.5\ ^{+44.4}/_{-23.0}$	USGS-82-19	Mehlman (1989: 103)
unknown	OES	^{14}C	33.5 ± 0.9	AA3299	Brooks et al. (1990)

assumed that the bone absorbed all of its uranium soon after deposition and none was subsequently lost. The actual age of the bone will be older if uranium-uptake occurred substantially later. It is possible to put some constraints on the history of uranium migration in bone by taking into account the different radioactive half-lives of ^{230}Th in the ^{238}U series and ^{231}Pa in the ^{235}U series (e.g., Cheng et al., 1998): if the ages obtained using ^{230}Th/^{234}U and ^{231}Pa/^{235}U are statistically consistent, then it can be surmised that the bone behaved as a 'closed system' after the uptake of uranium. The paired ^{230}Th/^{234}U and ^{231}Pa/^{235}U ages for three samples reported by Mehlman (1989) for Mumba (two from Bed V and one from Bed VI) are statistically consistent (Table 2.2), but both ages may be underestimated by similar amounts if uranium-uptake occurred long after burial. Conversely, if uranium was lost after burial, the obtained ages will be overestimated by similar amounts. Until the accuracy of these age estimates are verified using modern U-series techniques, such as those discussed in Section 1.4.2, the U-series chronology for Mumba should be viewed as unreliable.

The current ^{14}C chronology for Mumba is at least as deficient as the U-series chronology. Most of the six materials used by Mehlman to obtain ^{14}C ages at Mumba (i.e., charcoal, shells of the land snail *Achatina*, OES, bone collagen, bone apatite and tufa) have since proven problematic. Appropriate pretreatment procedures are necessary in order to isolate the ^{14}C that is correlated to the target event from any older or younger ^{14}C. Given the materials and methods used to obtain ^{14}C ages for Beds IV, V and VI in the 1980s, there are three principal issues with the chronology. First, bone apatite and shells often produce erroneous ages, as a result of the exchange of carbon with the carbonate in the apatite and shell structure during diagenesis (Taylor, 1987; Stafford et al., 1991; Hedges and Van Klinken, 1992; Surovell, 2000; Bronk Ramsey, 2008). Given the evidence for post-depositional formation of carbonates at Mumba (e.g., carbonate nodules and carbonate concretions), the environmental conditions at the site were likely conducive to carbon exchange in such materials. Second, in modern ^{14}C dating of shells, the exteriors are generally removed so that unaltered aragonite crystals can be isolated for analysis. Since *Achatina* shells are thin-walled, it is likely that this precaution was not taken. Third, the preparation procedures for materials such as bone, eggshell and snail shells have improved substantially in the last decade (Bird et al., 2003; Bronk Ramsey, 2008). Processes such as molecular ultrafiltration of bone

collagen have been shown to substantially increase the accuracy of the resulting ^{14}C ages (Bronk Ramsey et al., 2004; Higham et al., 2006). It is likely that most of the ^{14}C ages from Mumba are unreliable since they not were obtained using these procedures, which are currently accepted as a prerequisite for accurate ^{14}C age estimation.

The final notable feature of the existing chronology for Mumba is the recent proliferation of ages that can be found in the literature. Unfortunately, none of these ages has been published with associated estimates of uncertainty or supporting information, both of which are necessary to justify their reliability. These ages include an age range of 29 – 33 ka BP obtained from AMS ^{14}C dating of OES (Conard, 2007) and AAR ages of 52 ka and 45 – 65 ka, also on OES (McBrearty and Brooks, 2000). A ^{14}C age of 33.5 ± 0.9 ka BP was reported for Mumba by Brooks et al. (1990) without a description of its provenance. An OSL study had previously been undertaken using samples from the site (Feathers, personal communication), although no ages have been reported from this work. Without estimates of precision and adequate contextual and methodological information to support the reported age estimates, the reliability of these age estimates cannot be assessed in an informed, scientific manner.

The inadequacy of the current chronology at Mumba is similar to the rest of the East African MSA archaeological record. Its usefulness is extremely limited in regards to placing the significant archaeological features from Mumba in context within the sub-Saharan African archaeological record. Appropriate comparisons cannot be made with existing palaeoenvironmental and genetic evidence to make appropriate inferences about the timing of and reasons for changes in technology and behaviour. Despite the deficient state of the current Mumba chronology, however, several ages have been selectively used in the literature to support individual arguments.

In order to overcome problems associated with the limited chronology, and to chronologically constrain the significant features of Mumba's archaeology, OSL samples were collected for dating. Quartz and feldspar grains from volcanic provinces are known to pose a variety of problems for luminescence dating (Fattahi and Stokes, 2003; Tsukamoto et al., 2003; Westaway and Roberts, 2006). In the East African Rift Valley, some samples of quartz have proven challenging for dating because of their undesirable OSL properties (e.g., Choi et al., 2006a), whereas other samples of quartz, and mineral mixtures dominated by the luminescence emissions from feldspars, have

been used to investigate the soil erosion history and pastoral Neolithic settlement of Tanzania and Kenya (Erikkson et al., 2000; Wright et al., 2007). The Mumba deposits are predominantly derived from metamorphic and not volcanic sources, so it was likely that the mineral grains from these deposits would not exhibit the volcanic-associated poor luminescence behaviours.

2.5.2 OSL sample collection

In June 2007, 16 sediment samples were collected to assess the suitability of the quartz and feldspar grains for OSL dating. Table 2.3 lists the geological units from which all samples were collected and their archaeological contexts. Photographs of the approximate locations of nine of OSL samples are shown in Figure 2.7a and b. The approximate positions of 15 of these samples are shown as filled circles on a section drawing of the stratigraphy of the site (Figure 2.5b); one sample was also collected from the Köhl-Larsen spoil heap to the west of the rockshelter (MR14). Two of the OSL samples (MR12 and MR13) were collected from the northern section wall, but the majority of samples were collected from Trench 5 (MR1, MR2, MR3, MR4, MR5) and Trench 7 (MR6, MR7, MR8), which were originally excavated in 2005. Both trenches were 2 x 2 m in plan area with maximum depths of 2.63 m and 0.92 m, respectively. Trench 5 spans Units A – C of Prendergast et al. (2007), equivalent to Beds I to III of Mehlman (1989), and ends at the boundary of Beds III and IV. Trench 7 includes the base of Unit C and all of Units D – G, which correspond to Mehlman's Beds IV and V. Five samples were collected from below Trench 7 (MR9, MR10, MR11, MR15, MR16), to obtain samples from Bed VI. Since the 2005 investigation did not excavate this deep, the stratigraphic and archaeological associations of the samples are unclear. Mehlman stated that Bed VIA extended 2 m below Bed V. If this is the case, then MR15 and MR16 are from Bed VIB. However, given the sloping topography of the deposits, this cannot be unequivocally known.

All samples were collected at night using dim, red-filtered torchlight (filtered using several layers of Lee 106 "primary red" filter paper: Lamothe, 1995) for illumination. The exposed faces of the excavation were cut back to uncover sediment that had not been exposed during excavation and to ensure that loose material was not sampled. Due to the presence of large rocks in the deposit and the cemented nature of

some of the sediments, it was not practical to obtain samples by hammering plastic or metal tubes into the cleaned section faces. Instead, narrow slots and small-diameter holes were made in the deposit using trowels and an auger, and the excavated sediment was collected in plastic bags that were immediately wrapped in black plastic for protect-

Table 2.3: List of OSL samples collected from Mumba rockshelter, their locations in the excavation, and their corresponding stratigraphic and archaeological associations.

Sample	Trench number	Depth below surface (cm)	Geological unit*	Bed**	Archaeological context
MR1	5	15	A	II	Iron Age
MR2	5	40	C	III-upper	LSA
MR3	5	75	C	III-middle	LSA
MR4	5	155	C	III-lower	LSA
MR5	5	180	D	VI	sterile
MR6	7	248	E	V-upper	Mumba Ind.
MR7	7	288	E	V-middle	Mumba Ind.
MR8	7	316	E	V-lower	Mumba Ind.
MR9	7	350	G	VIA	Kisele Ind.
MR10	7	405	G	VIA	Kisele Ind.
MR11	7	465	H	VIA	Kisele Ind.
MR12	8	298	E	V	Mumba Ind.
MR13	8	345	E	V	Mumba Ind.
MR14	-	spoil heap	-	-	mixed
MR15	7	527	H	VIB?	Sanzako?
MR16	7	589	H	VIB?	Sanzako?

*** Following Prendergast et al. (2007)**

**** Following Mehlman (1989)**

Figure 2.7: Photographs showing the approximate positions of nine of the OSL samples collected from Trench 5 and 7 at Mumba rockshelter.

ion from light and for transport to the laboratory. The resulting slots and holes were large enough to permit *in situ* gamma spectrometry measurements at each sample location. Subsequent to collecting sample material for OSL measurement, sediment was collected for dosimetry and water content determination. These samples were collected from inside the hole in the face of the excavation after OSL sediment sample removal, placed in a plastic bag, sealed with duct tape, and labelled.

Moche Borago Rockshelter, Ethiopia

Moche Borago Rockshelter is currently under investigation by the Sodo Wolayta Archaeology Project (SWAP) team co-directed by S. Brandt (University of Florida, USA) and E. Hildebrand (Stony Brook University, USA). One of the principal goals of the current investigations is to obtain independent ages for the archaeological sequence using a variety of methods. Samples for conventional, ABOX-SC, and pyrolysis radiocarbon dating were collected in addition to samples for ESR and OSL dating. As a consequence of the desire for truly independent ages, the SWAP team directors made very little information about the site available to the participating geochronologists. This lack of information, along with the lack of publications on the site, meant that there was little information available to assist with questions of sample context. The only information offered in regards to Moche Borago has come from a heavily edited copy of the field report on the 2007 excavations (Brandt et al., 2007), the 2009 East African Quaternary Research Association (EAQUA) workshop presentation given by E. Fisher (Fisher et al., 2009), personal communications with E. Fisher in regards to the lithics, and the field notes taken by R.G. Roberts during OSL sample collection.

2.6 Site setting

Moche Borago (37º45'17.8"E, 6º53'49.7"N) is a large rockshelter located near Sodo, Wolayta, in the southwest Ethiopian Highlands (Figure 2.8). It is positioned at ~2300 m above mean sea level, on the western flank of Mt. Damota (2800 m; Figure 2.8b), a dormant volcano to the north of Lake Abaya. The morphology of the cave has been interpreted as a basalt (i.e., lava) flow overlain by a lahar, which was, in turn,

overlain by another basalt flow (Brandt et al., 2007). The rockshelter itself has formed within an erosional cavity in the ancient lahar features.

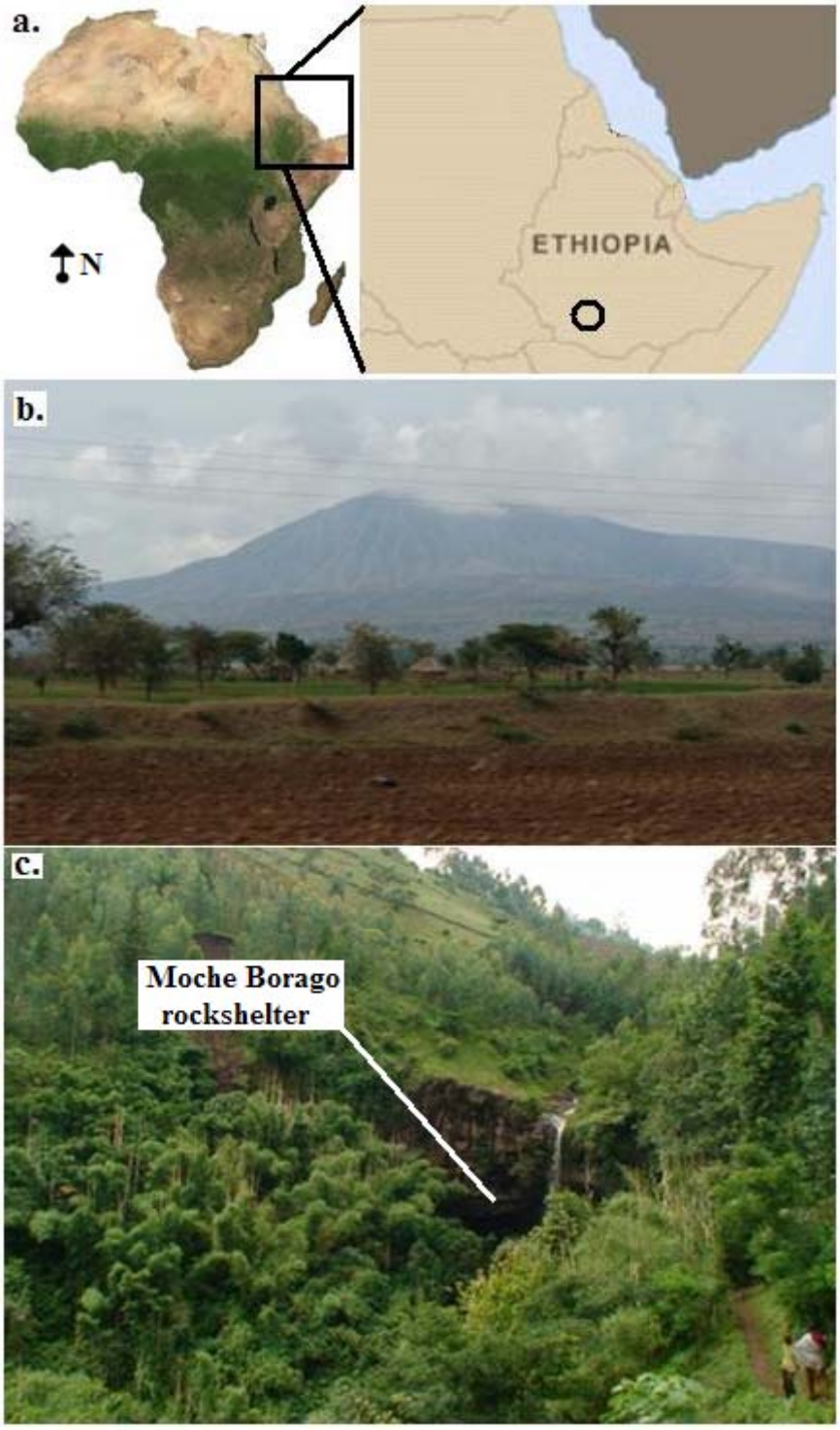

Figure 2.8: Moche Borago Rockshelter. a, Geographic location of Moche Borago in southwest Ethiopia. b, Mount Damota. c, Photograph of Moche Borago Rockshelter.

2.7 Stratigraphic and archaeological context

The rockshelter was originally excavated by a French team, directed by X. Guterez (University of Montpelier) in 1998. Additional field seasons were conducted in 2000, 2001 and 2002. They excavated a 1.5 x 1 m test pit (H10 and half of G10 in Figure 2.9b) down to ~2 m below the surface. The upper 80 cm contained a Holocene sequence of silts, sands and volcanic tephra that contained flaked stone artefacts, grindstones, pottery, pits, hearths and other LSA, Neolithic and Iron Age features.

Underlying these deposits was a thick tephra (named BWT by SWAP in 2006), under which was a metre of silts, sands, and tephra containing LSA and MSA artefacts. The French team proceeded to excavate a 20 m^2 area in the northwest portion of the rockshelter (Figure 2.9), focusing on the Holocene deposits to elucidate the origins of food production in the Horn of Africa. This main area of French excavations was later designated as the Block Excavation Area (BXA) by SWAP, and is denoted by light shading in Figure 2.9b. In addition, they excavated a 1 x 1 m test unit (TU2 in Figure 2.9b) near the centre of the rockshelter.

The SWAP team has been conducting ongoing excavations at the site since 2006. In their pilot field season they completed their official goals of: 1) defining the areas excavated by the French team, 2) constructing a GIS database for the site, 3) recording the profiles excavated by the French for integration into the GIS database, 4) extending excavations, 5) obtaining samples for dating, and 6) assessing changes in stone tool technology throughout the sequence. The subsequent field seasons expanded on each of these issues, with a detailed stratigraphic interpretation and a summary of the investigation of the lithics (conducted by E. Fisher) made available. The SWAP team has mainly focussed their archaeological investigations on the BXA. A brief outline of the stratigraphic sequence (Brandt et al., 2007) and the associated lithics (Fisher, personal communication) from this area is described below and is illustrated in Figure 2.10.

PKT: The base of the 2007 excavations was an archaeologically sterile layer of dense ash or lahar.

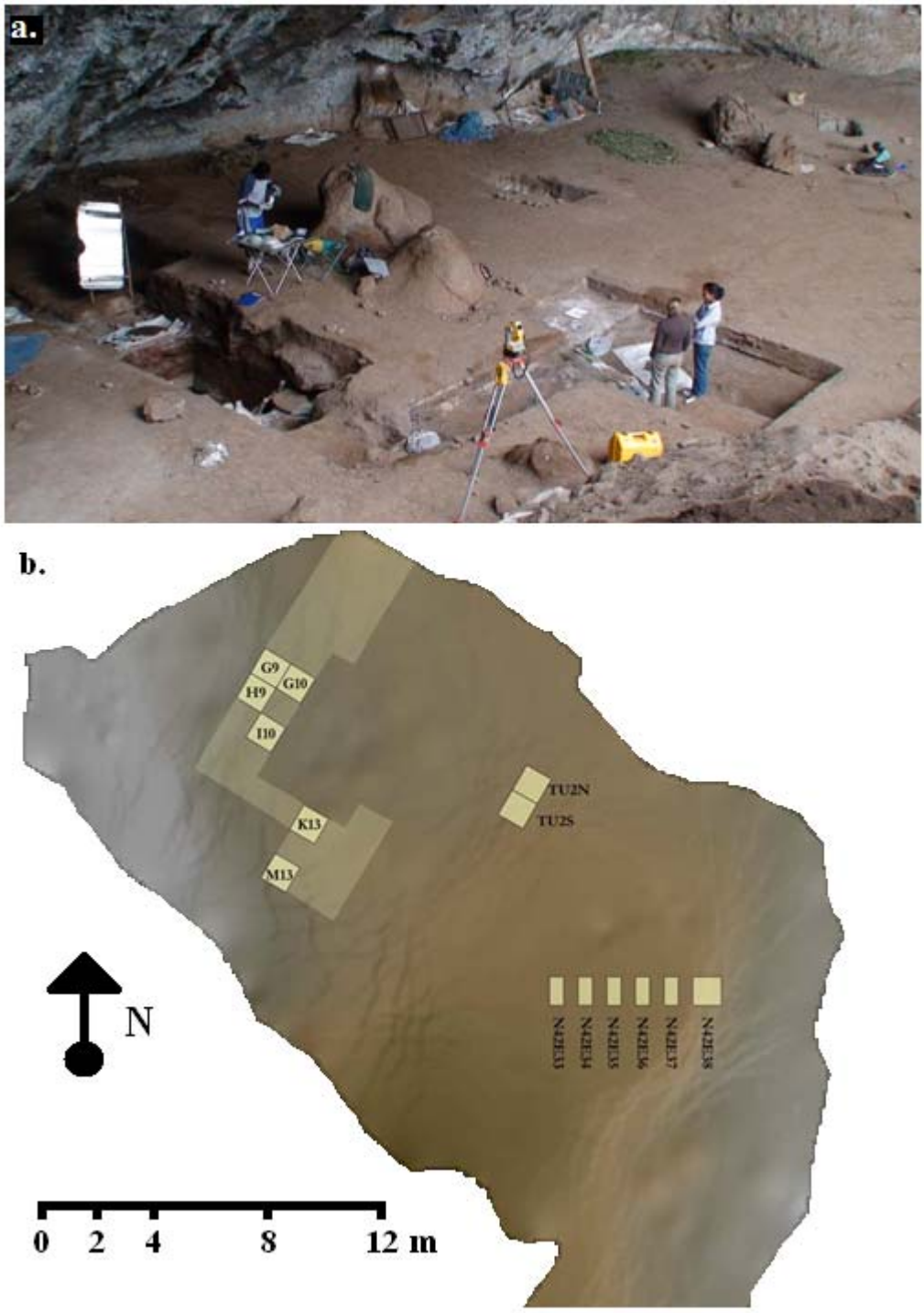

Figure 2.9: Moche Borago Rockshelter. a, Photograph taken from the west of the rockshelter showing the BXA, spanning from left to right in the foreground. b, Planview of the excavations at Moche Borago Rockshelter. The light shading indicates the BXA. Modified from a graphic by E. Fisher in Brandt et al. (2007).

T* Group Deposits: Four stratigraphic units (VHG, CTT, MHD, and DCC) comprise the T* Group, which represents periods of dense human occupation. The lowermost unit, VHG, is a layer of abundant gravels in a clay matrix. The

overlying MHD is a series of stratified hearth deposits, indicating a sustained human presence. Between VHG and MHD in square G10 is a localised ash lens surrounded by clay, named CTT. Above MHD is a thick layer with a high clay component. In the T* Group deposits, Mode 3 Levallois points are found in association with small foliate points made from end-struck flakes and blades with dorsal trimming. The foliate points, of which those from lower in these deposits show affinities with Mode 3 Levallois technology, exhibit features that suggest that they were hafted (e.g., shallow bi-lateral notching or non-uniform lateral edge retouch).

YBT: Overlying the T* Group is a tephra that is composed of ash intermixed with sandy-silt deposits. While this tephra represents an occupational hiatus, artefacts are still present in very low densities, suggesting sporadic occupation during periods of volcanic activity (Brandt et al., 2007).

S* Group Deposits: Four stratigraphic units (OBMB, LVDBS, LMGV, and VDBS) comprise the S* Group. The lowermost unit, OBMB, is a silty-clay that is broadly distributed in the test pit, but has been incised or removed subsequently in some areas. Above this lies LVDBS, a loose, dark brown silt that represents a channel fill deposits, which accumulated during a period of increased humidity. The overlying VDBS appears to cap the channel fill, and is composed of dark silts with an abundance of lithic artefacts. In the S* Group deposits, in spite of the presence of small Levallois cores, no Mode 3 technology projectile points were present. The projectile points in these deposits begin to show a more elongate foliate shape, likely the result of being shaped from blade blanks. They are uniformly small, unifacial or part-bifacial, and exhibit edge retouch and dorsal trimming, as well as features that suggest that they were hafted. In addition, small backed bladelets and a single crescent were recovered from within these deposits.

YBS: Deposits from a second volcanic event overlie the S* Group Deposits. YBS is an archaeologically sterile unit composed of a series of ash layers, interstratified with thin dark lenses. The absence of any cultural materials suggests that the volcanic event forced the rockshelter to be abandoned.

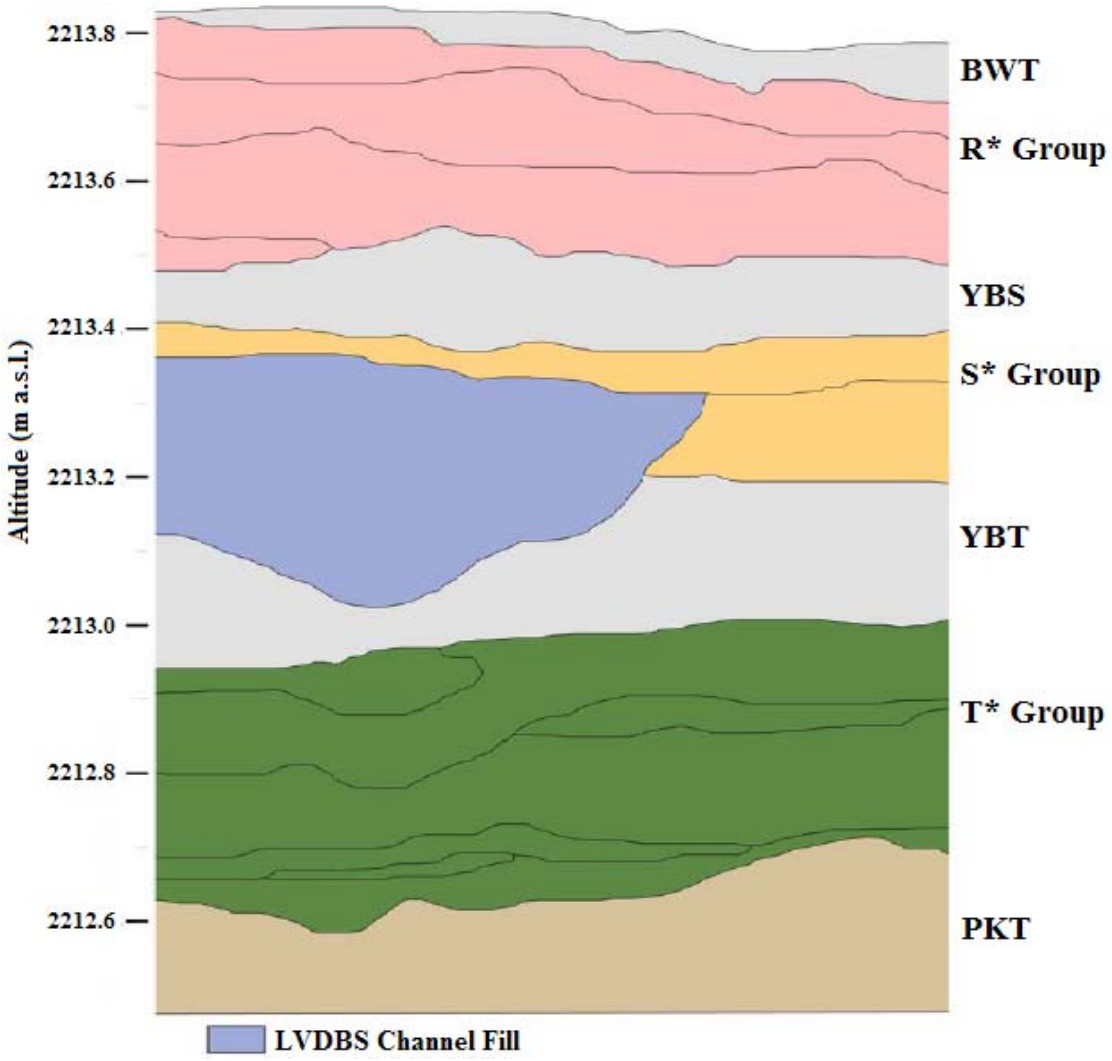

Figure 2.10: Pleistocene deposits of the North profile of square G10 and associated stratigraphic layers. Modified from Fisher et al. (2009).

R* Group Deposits: Three stratigraphic units (RGCB, RCGA, and RCA) compose the R* Group, which overlies the YBS tephra. The sediments that comprise these deposits are red to reddish-brown clays and silty clays, with round to semi-round inclusions and abundant obsidian flakes. The red colour was posited to indicate a change in oxidation of the iron within the deposits due to sub-aerial exposure as a palaeosol. In the R* Group deposits, the projectile points show a more elongate foliate shape.

BWT: This layer is a 20 cm thick, archaeologically sterile tephra. It is layer is a dense, homogeneous white ash lens, which is a clear marker tephra throughout the site.

The general technological trend throughout the assemblage from BXA suggests a convoluted transition from Mode 3 to Mode 4/5 lithic technologies (Fisher, personal communication). Instead of the former technology being replaced by the latter as one moves up the archaeological sequence, the frequency of Mode 3 artefacts (e.g., Levallois points and cores) is reduced, though ever present, while the frequency of Mode 4/5 artefacts (e.g., blade cores, microliths, foliate projectile points) increases through time. In addition, there is a high frequency and diversity in the projectile points, which are present throughout the entire sequence below BWT. The diversity of sizes and shapes of projectile points throughout the sequence suggests that multiple hafted projectile technologies were being used simultaneously at the site. This is supported by the contemporaneous diversity of core types present throughout the sequence.

2.8 Archaeological significance and OSL sample collection

Given the size of the rockshelter (>100 m^2) and its layout, conditions were likely favourable for human habitation, sediment deposition, and preservation of archaeological materials. Correspondingly, the current excavations have revealed a long sequence of archaeological material punctuated by occasional volcanic deposits and episodes of fluvial activity. The duration and richness of the archaeological materials in the sequence is unparalleled for the region and will allow reconstructions of technological and behavioural change over periods of the Late Pleistocene. Constraining the timing of these changes could elucidate the potential migrations of humans within and out of Africa. The richness of the archaeological sequence is probably, at least in part, due to the rockshelter's location in the southwest highlands of Ethiopia. Due to their position relative to the regional atmospheric circulation patterns, the southwest highlands are one of the wettest regions in northeast Africa and could have served as a refugium for humans during periods of increased aridity (Brandt et al., 2007). Additionally, the varied topography means that a range of alititudinally determined environments would have existed, resulting in regional stability as an area of human occupation (Brandt et al., 2007).

In order to try to constrain the archaeological sequence at Moche Borago, OSL samples were collected by R.G. Roberts in June 2007. All samples are listed in Table

2.4 along with their stratigraphic context and depth below the current surface of the rockshelter. Most of the samples that are associated with MSA and LSA assemblages were collected from the East face of the excavation square G10. Only two samples (MB11 and MB12) were collected from the West face of excavation square G9. Samples MB13 to MB17 were collected from the Holocene section, in the West face of square F9. All samples were collected at night using red-filtered head torches for illumination. Samples were collected by creating narrow slots and small-diameter holes in the face using trowels and collecting the excavated sediment in plastic bags, which were immediately wrapped in black plastic for protection from light and for transport to the laboratory. The resulting slots and holes were used for *in situ* gamma spectrometry measurements at each sample location. Additional bags of sediment were collected from inside each OSL sampling hole for laboratory measurements of the environmental dose rate and sediment moisture content.

Table 2.4: List of OSL samples collected from Moche Borago rockshelter, their locations in the excavation, and their corresponding stratigraphic associations.

Sample	Excavation square-Face	Depth below surface (cm)	Stratigraphic Unit
MB1	G10-E	21	RGCA
MB2	G10-E	30.5	RGCB
MB3	G10-E	38	YBS
MB4	G10-E	45.5	VDBS
MB5	G10-E	58	OBMB
MB6	G10-E	75.5	YBT
MB7	G10-E	88.5	DCC
MB8	G10-E	94	PDCC
MB9	G10-E	103.5	MHD
MB10	G10-E	193	VHG
MB11	G9-W	79	BWT
MB12	G9-W	88.5	RCA
MB13	F9-W	7	DBC
MB14	F9-W	24.5	DBCX
MB15	F9-W	36.5	PGT
MB16	F9-W	43	OKBR
MB17	F9-W	68.5	PS
MB18	GeoPit-N	99.5	UPFC
MB19	GeoPit-N	115	MPFC
MB20	TU2-S	55	RGX
MB21	J14-N	surface	DBC

As discussed in Chapter 1, quartz and feldspar grains of volcanic origin have proven to commonly have malign luminescence characteristics (e.g., Fattahi and Stokes, 2003; Tsukamoto et al., 2003, 2007; Choi et al., 2006a; Westaway and Roberts, 2006; Westaway, 2009). Since the Moche Borago deposits are predominantly derived from volcanic sources, including lahars, ashes and tephras, samples were not expected to have straightforward OSL properties. Still, the volcanic origin of these samples and the metamorphic origin of samples from Mumba would provide an interesting comparison between the luminescence properties of the quartz and feldspars from the two different provenances.

Summary

Mumba and Moche Borago rockshelters both have long, continuous records of MSA and LSA occupation. Like most East African sites discussed in Section 1.5, neither of these sites has a robust chronology. Temporally unconstrained transitions in technologies are features of the archaeological sequences at both sites, and severely limit archaeologists' ability to make appropriate interpretations. Obtaining a chronology for the archaeological sequence from Moche Borago will constrain changes in technologies and behaviours. Given the site's strategic position in the Ethiopian Highlands, this information may elucidate Late Pleistocene human migrations within and out of Africa. At Mumba, the timing of the emergence of the backed piece-based Mumba Industry can yield insights into the development of regional LSA technologies. The timing of the appearance and proliferation of OES bead ornaments at Mumba in Bed V-upper and Bed III-lower (respectively) can help elucidate the emergence and development of symbolic behaviours in East Africa. A chronology for Bed VIB, VIA, V and III at Mumba will reveal the span of time over which distant raw materials came to the site, likely via social interaction and exchange networks. It was, thus, the objective of this research to construct robust chronologies for the MSA and LSA archaeological sequences of these two sites. The following two chapters will review the methodological aspects of obtaining and OSL age.

Chapter 3: Methodology: Optically Stimulated Luminescence (OSL)

In this chapter, the characteristics of the OSL signal are introduced and discussed, along with the laboratory instrumentation and procedures used to measure the luminescence emissions and estimate an equivalent dose (D_e). As discussed in Section 1.4.6, the OSL age (ka) is an estimate of the amount of time since a mineral grain was last exposed to sunlight and subsequently buried, and is calculated as:

$$Age\,(ka) = \frac{Equivalent\ dose\,(Gy)}{Dose\ rate\,(Gy/ka)} \qquad \text{Equation 3.1}$$

This chapter, thus, discusses the numerator in the luminescence equation (Equation 3.1). The denominator in this equation is the dose rate and will be discussed in the next chapter (Chapter 4). While both quartz and potassium (K)-feldspars are used as dosimeters and discussed in this thesis, the focus of this chapter is quartz. The luminescence produced by feldspars will be discussed in detail in Chapter 7.

3.1 OSL background

The motivation for the initial development of OSL was to establish a method for dating sediments that was better than thermoluminescence (TL) (Aitken, 1985, 1998). TL utilises heat, whereas OSL utilises light, to stimulate the emission of photons (luminescence) from mineral grains. The photons are then detected using a sensitive photomultiplier tube (PMT) in the laboratory (Aitken, 1998). The TL signal is easily bleached when a material is heated, but it is much more difficult to bleach by sunlight in unheated materials (Aitken, 1985). Thus, the TL signal is well suited to determining the age of heated materials, such as pottery. Parts of the natural TL signal of unheated sediments, however, often contain a residual signal that was accrued prior to deposition and which the bleaching at deposition had been inadequate to remove (Aitken, 1998). The ability to use visible light to stimulate luminescence from unheated sediments to satisfactorily estimate the age of deposition was first demonstrated by Huntley et al. (1985). This was achieved by stimulating quartz grains with green light from a laser. Hütt et al. (1988) later showed that infrared (IR) light could be used to stimulate luminescence (i.e., IRSL) from feldspar grains.

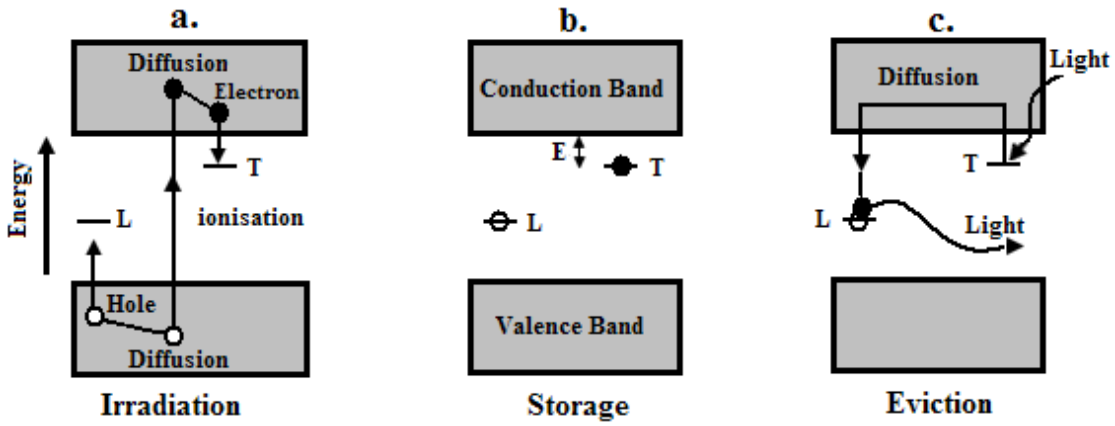

Figure 3.1: Schematic representation of the energy band model of OSL production (modified from Aitken, 1998). a, During irradiation, natural radiation ionises electrons and holes to become trapped at defects, known at traps (T) and luminescence centres (L), in the crystal lattice of quartz. b, During storage, electrons and holes remain trapped in defects, which have a specific depth (E) below the conduction band. c, After being stimulated with light, electrons are evicted from their traps into the conduction band. From there, they may reach a luminescence centre where they recombine and emit light.

The most widely accepted model of the mechanics of luminescence production in quartz is the 'energy band' model (Aitken, 1985, 1998; Preusser et al., 2009). A schematic representation of the energy band model is presented in Figure 3.1. Trapped charge within the crystal lattice of a mineral grain is the agent of luminescence production. Electrons are ionised into defects in the crystal structure of a grain where they become trapped (Figure 3.1a), with the population of trapped electrons accumulating over time. The lack of an electron in the valence band results in a local negative charge deficit referred to as a 'hole', which may also become trapped at defects (Preusser et al., 2009). When a hole gets trapped in the forbidden zone (the region between the valence and conduction bands), it can act as a 'recombination centre'. When an electron is evicted from its trap (due to stimulation by heat or light) it can combine with a hole at a recombination centre, and release energy in the process (Aitken, 1985; Preusser et al., 2009).

There are several types of recombination centres depending on the defect type in which a hole is trapped. 'Luminescence centres' release energy in the form of a photon (the wavelength of which is dependent on the defect that has formed the luminescence centre) when they combine with an electron (Figure 3.1c; Aitken, 1998; Preusser et al., 2009). Other types of recombination centres release heat. While only one or two electrons can be stored in a single trap, many can accumulate in a single 'type' of trap until all individual traps of that type are filled, reaching a state known as 'saturation'

(Aitken, 1998). The different trap types (hereafter referred to as 'traps') can be defined as having different depths (E, described in terms of the unit electron-volts [eV]) below the conduction band (Figure 3.1b). Different traps are responsible for the different luminescence signals that are observed; i.e., the various TL peaks (on a luminescence vs. temperature plot) and components of the OSL signal. The luminescence of a mineral grain resulting from optical stimulation delivered at a constant power (sometimes referred to as continuous wave [CW]-OSL) takes the form of a decay curve (Figure 3.2) and would be expected to decay exponentially if a single trap type were involved (Smith and Rhodes, 1994). Consequent to the fact that the OSL signal in quartz is derived from multiple traps, CW-OSL decay curves have been shown to be best fitted by a number of exponential decay functions (e.g., Smith and Rhodes, 1994; Bailey et al., 1997).

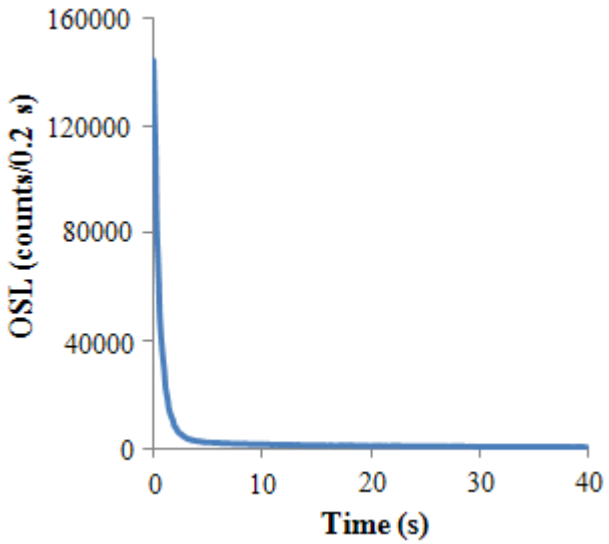

Figure 3.2: Example of an OSL decay curve from a multi-grain aliquot of quartz from Mumba.

Bailey et al. (1997) identified the existence of three different components in the CW-OSL decay curves, namely a 'fast', 'medium' and 'slow' component. The fast component of the OSL signal is of most interest in dating applications, since the most commonly used procedure (the single-aliquot regenerative-dose [SAR] procedure of Murray and Wintle, 2000; see Section 3.3) has been designed to deal with this component only. This component has been shown to be related to the 325°C TL peak (Smith et al., 1986; Smith and Rhodes, 1994; Spooner, 1994a), suggesting a common source trap for the two luminescence signals. The components that make up the

luminescence signal of a single or multi-grain aliquot of quartz can be isolated by fitting the CW-OSL decay curve with multiple exponential functions (e.g., Bailey et al., 1997). The components can be visualised more easily by linearly increasing the intensity of optical stimulation (referred to as linearly modulated [LM]-OSL; Bulur et al., 1996). The various components and the LM-OSL technique will be discussed in Section 3.5.

3.2 Sample preparation and instrumentation

3.2.1 Preparation

Sediment samples were prepared in the laboratory using standard methods (Aitken, 1985; Wintle, 1997). The aim of sample preparation was to recover pure, coarse sand-sized fractions of quartz and K-feldspar without depleting the natural luminescence signal in the process. To this end, all laboratory work was performed in red-light conditions in which all lights were fitted with multiple layers of Lee 106 "primary red" filter paper (Lamothe, 1995). The light sources used in the laboratory included fluorescent tubes fixed in the ceiling and head-torch light-emitting diodes (LEDs). The latter were used in proximity (tens of centimetres) to OSL samples, particularly when mounting material on to discs for measurement.

All samples were unpacked and soaked in 10% hydrochloric (HCl) acid, which reacts with and dissolves carbonates. When no more reaction was observed, samples were rinsed with tap water and then distilled water. Samples were then soaked in 10% hydrogen peroxide (H_2O_2), which reacts with and digests any organic matter. When no more reaction was observed, samples were rinsed and soaked in 50% H_2O_2 overnight. After rinsing with tap water and distilled water, samples were dried in a 50°C oven before being dry-sieved using an electric sieve shaker. All mineral grains >212 μm and <180 μm in diameter were packed into light-tight plastic bags and stored.

Using the 180-212 μm diameter grain-size fraction, heavy minerals (>2.70 g/cm^3) were separated from quartz and feldspar grains using a sodium polytungstate solution with a density of 2.70 g/cm^3. Quartz grains (density of 2.62–2.70 g/cm^3) were then separated from feldspar grains using a solution with a density of 2.62 g/cm^3. K-feldspar grains (density of 2.53 – 2.58 g/cm^3) were separated from sodium (Na)-feldspar using a solution with a density of 2.58 g/cm^3. Finally, for K-feldspar separates from Moche Borago, a fourth separation was performed at a density of 2.52 g/cm^3 to remove

most of the large quantities of pumice present in the sediments. The isolated quartz grains were then soaked in 48% hydrofluoric (HF) acid for 40 minutes to dissolve any remaining feldspar grains that were not removed by density separation. A second reason for the HF acid treatment was to etch the outer rind of each grain that was exposed to external alpha radiation (Wintle, 1997; Aitken, 1998). This is desired in order to simplify dosimetric calculations. The K-feldspar fraction was also soaked in HF acid (10% for 10 minutes) to etch the outer, alpha particle-exposed rind of each grain. The quartz and K-feldspar separates were then soaked in concentrated HCl acid for 40 minutes to remove any precipitated fluorides. After rinsing and drying, the mineral separates were then sieved again to retain the 180-212 μm grain-size fraction. These preparation steps were performed to isolate and prepare the desired mineral (quartz or feldspar) for the measurement of the luminescence signal.

Following sample preparation, mineral grains were mounted on to discs, which were then loaded into the luminescence measurement instruments (Section 3.2.2). Multi-grain aliquots of each sample were mounted on stainless steel discs with a diameter of 10 mm. A silicone oil adhesive (Silkospray) was sprayed on to the clean discs through a mask of the desired diameter. Grains were then mounted on to the disc, sticking to the area of Silkospray as a monolayer. The mask-size diameters used in this study were 1, 3, 5 and 7 mm, which correspond to ~10–20, ~100–200, ~300–500 and ~500–1000 grains per aliquot, respectively (see Appendix 1). Single grains were mounted onto 10 mm in diameter, gold-coated aluminium discs. These discs have 100 holes, each with a diameter of 300 μm, laid out in a 10 x 10 grid. Individual grains were placed into the holes by brushing sample material across the top of the disc. Given the sizes of the grains and holes, it was assumed that one grain was deposited in each hole. This was checked by observing each disc under a microscope to ensure that only one grain occupied each hole.

3.2.1.1 Contamination of stainless steel discs

A potential source of contamination of the luminescence signal that has not been discussed in the literature is the cleanliness of the stainless steel discs on to which grains of sample material are mounted. During multi-grain aliquot measurements of the UV emissions from K-feldspar separates of MB3 in September 2009, a large TL peak at

110°C was measured. Since K-feldspars do not have a 110°C TL peak, this suggested one of two scenarios: 1) that there was quartz contamination in the K-feldspar separates from Moche Borago, or 2) that the discs on to which the sample materials were mounted were contaminated with quartz. The latter was shown to be the case when experiments, in which empty stainless steel discs were irradiated, heated, and optically stimulated using the blue LEDs, resulted in the measurement of 110°C TL peaks and OSL decay curves (Figure 3.3). After visual and microscopic examination showed no grains on the surfaces of the measured discs or the carousel on to which the discs are mounted, it was concluded that the surface of the discs or carousel was contaminated with microscopic quartz residue. This was confirmed when the empty stainless steel discs were removed from the carousel and the empty positions were irradiated with 59 Gy, heated to 300°C, and stimulated with blue LEDs for 40 s at 125°C. No TL peaks or OSL decay curves were measured (inset in Figure 3.4), indicating that the measured TL peaks and OSL decay curves were not caused by contamination of the carousel.

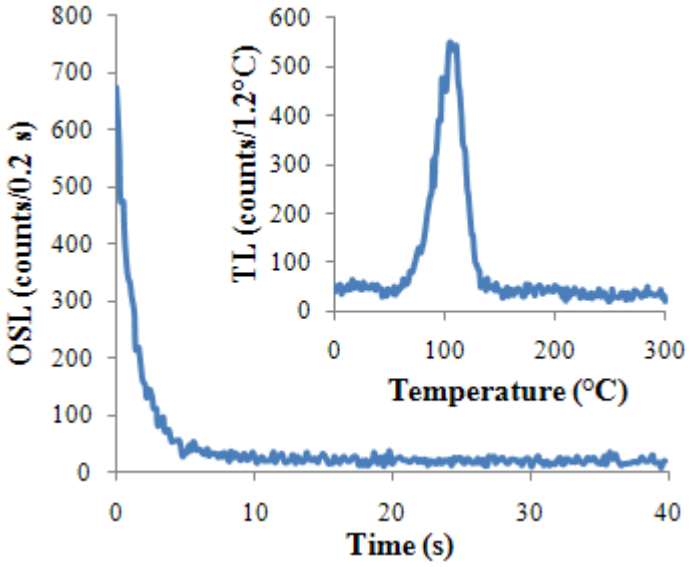

Figure 3.3: Several empty stainless steel discs were irradiated, heated to 300°C, and optically stimulated. The OSL decay curve and the TL curve with the 110°C TL peak (presented in the inset) indicate that there was a quartz residue contamination on the otherwise blank discs.

Upon isolating the stainless steel discs as the source of contamination, a series of experiments were performed to establish a cleaning procedure that would ensure the cleanliness of the discs. Results are presented in Figure 3.4. First, the contaminated discs were wiped down on both sides with a sterile cloth. A 110°C TL peak and an

OSL decay curve were subsequently measured for both discs, with the intensities of both signals being approximately half of those prior to cleaning. This suggested that the contamination was on the surface of the discs and could potentially be abraded off. In the second test, discs were next rinsed in distilled water and soaked in methyl ethyl ketone (MEK) for 30 minutes to dislodge any contaminants on the surface. The discs were again rinsed in distilled water, and then in acetone prior to being measured. Following this treatment, both discs produced a 110°C TL peak and an OSL decay curve, which were of the same intensity as that following the previous cleaning treatment. In the final experiment, the discs were rinsed in water and then abraded with 1200 grit sandpaper for approximately 10 s to remove any residual material from the surface. Discs were then rinsed in acetone, then MEK, then water and placed in an ultrasonic bath for several minutes before being rinsed with distilled water and dried. After performing this procedure, neither disc produced a 110°C TL peak or OSL decay curve. Consequently, this cleaning procedure was performed on all stainless steel discs prior to aliquot preparation for luminescence investigations.

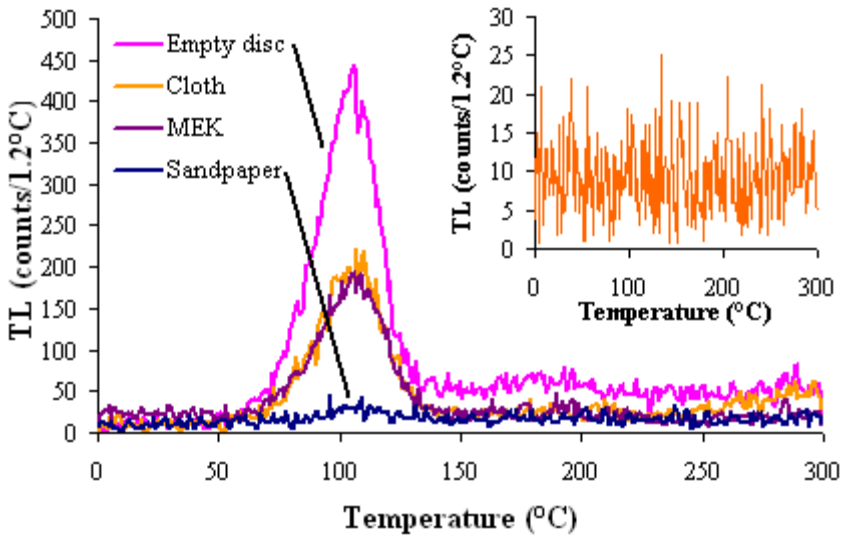

Figure 3.4: TL curves measured for the same blank stainless steel disc after various cleaning methods. "Empty disc" is the TL curve measured for the disc after standard cleaning. The disc was then wiped with a sterile cloth and measured ("Cloth"). The disc was then soaked in methyl ethyl ketone and measured ("MEK"). The disc was then abraded with 1200 grit sandpaper, rinsed in water and acetone, and measured ("Sandpaper"), a treatment that resulted in the removal of the 110°C TL peak. The inset shows the TL curve measured when no stainless steel disc was measured. The lack of any TL peaks indicates the source of quartz contamination is the stainless steel discs and not the carousel.

3.2.1.2 Implications for other multi-grain aliquot investigations

It is believed that disc contamination was not a problem for any other multi-grain aliquot investigations discussed in this thesis. Most measurements using multi-grain aliquots of quartz (Chapter 5) were performed between November 2007 and June 2008. LM-OSL experiments performed on multi-grain aliquots were among the last experiments to be performed in this period of time. Eight blank stainless steel discs, chosen at random, were used for the measurement of instrumental background (Section 3.5.2.1). Empty discs were irradiated, heated to 260°C and optically stimulated in a linearly modulated fashion. None of the discs produced an LM-OSL signal typical of quartz, only producing signals typical of background measurement (e.g., Choi et al., 2006b). Additionally, none of the discs produced a 110°C TL peak. It can thus be assumed that the batch of discs used during and prior to LM-OSL experiments in June 2008 were free from quartz residue. All discs used for multi-grain aliquot measurements made after September 2009 were cleaned using the procedure described above prior to mounting sample material.

3.2.2 Instrumentation

All measurements performed during this study were made using three Risø automated TL/OSL readers housed in the OSL laboratory at the University of Wollongong. The designation and model of the three Risø readers and the samples measured with them are presented in Table 3.1. Risø 2 and Risø 3 have single-grain attachments, and Risø 4 was used for all LM-OSL and K-feldspar measurements presented in this thesis. All readers used in this study are computer-controlled by *Mini-Sys* units that are described by Markey et al. (1997).

3.2.2.1 Irradiation sources

All laboratory radiation sources are $^{90}Sr/^{90}Y$ beta irradiators installed in each Risø reader. Each source is mounted in a stainless steel, vertically oriented wheel positioned above the carousel containing the sample discs. When the source faces upwards, the samples are not irradiated. When the wheel is rotated 180°, the source faces the sample, thereby irradiating it (Markey et al., 1997). Risø 2 and Risø 3 were calibrated by H. Yoshida in October 2001 and March 2005, respectively and Risø 4 was

calibrated by Z. Jacobs. The dose rate of each beta source is recalculated daily to adjust for the natural decay of the source (half-life 28.79 years; Chu et al., 1999). The dose rate received by grains loaded on to aluminium discs differs from that of stainless-steel discs by a factor of 0.9595 (Risø 2) and 0.9413 (Risø 3). In addition, the beta source on Risø 3 does not deliver a spatially uniform dose to all single grains on an aluminium disc (e.g., Thomsen et al., 2005), and this has been considered.

Table 3.1: Information about the three Risø TL/OSL readers, housed at the University of Wollongong, that were used to measure luminescence from mineral separates in this thesis.

UoW Instrument	Model	Luminescence measurements	Site
Risø 2	TL/OSL-DA-15	Single quartz grains	Mumba
		Multi-grain quartz aliquots	Mumba
Risø 3	TL/OSL-DA-15	Single quartz grains	Mumba
Risø 4	TL/OSL-DA-20	Multi-grain quartz aliquots	Mumba, Moche Borago
		Multi-grain feldspar aliquots	Mumba, Moche Borago

3.2.2.2 Stimulation sources

Risø 2 and Risø 3 have four clusters of seven blue LEDs (~470 ± 30 nm) that can deliver a total power of ~40 mW/cm^2. Risø 4 is equipped with clusters of 42 blue LEDs (470 nm) that can deliver a power of 50mW/cm^2. In order to minimise the amount of directly scattered light that reaches the PMT cathode, a green, long-pass filter (GG-420) is placed in front of each cluster of blue LEDs. All readers are also fitted with an IR stimulation source. Risø 2 and Risø 3 have three clusters of seven IR LEDs (875 nm) that deliver ~135 mW/cm^2 to the sample (Bøtter-Jensen et al., 2003). Risø 4 is fitted with a 1 W IR laser diode (830 nm) that can deliver a power density of 300 mW/cm^2.

Risø 2 and Risø 3 are also equipped with a single-grain laser system attachment that allows the stimulation of individual grains (Bøtter-Jensen et al., 2003). This system contains a 10 mW 532 nm Nd:YVO_4 solid-state diode-pumped laser for green-light stimulation. Risø 3 also contains a 150 mW 830 nm IR laser for single-grain IR stimulation. The maximum power density of the green and IR lasers is ~50 and ~500 W/cm^2 respectively (Bøtter-Jensen et al., 2003).

3.2.2.3 Signal detection

Every Risø reader used in this study was mounted with a blue-sensitive bi-alkali Electron Tubes Ltd. 9235QA photomultiplier tube (PMT). Individual photons (e.g., the luminescence emitted by an optically stimulated grain) are counted by the PMT when they interact with a photosensitive cathode mounted inside a vacuum tube within the PMT. The range of wavelengths of photons that is desired can be isolated by mounting coloured glass filters in front of the PMT. For quartz measurements, the ultraviolet (UV) emissions (270-370 nm) were detected after passing through two 3 mm-thick Hoya U-340 filters. Several of the emissions from K-feldspar samples were tested to deduce optimal measurement conditions. This is discussed in detail in Section 7.2.1, where the various filter combinations used to measure these emissions are presented (Table 7.1).

3.3 Equivalent dose estimation: The single-aliquot regenerative-dose (SAR) procedure

Many methods for estimating the D_e value have been used in the past for TL and OSL dating studies. OSL methods that employed multiple aliquots to estimate D_e values were initially developed (e.g., Huntley et al., 1985, 1993; Prescott et al., 1993). However, normalisation techniques were required to account for variation in the luminescence behaviours of each individual aliquot (Aitken, 1998). Methods that involve the repeated measurement of a single-aliquot (single- or multi-grain) to estimate the D_e, such as the single-aliquot additive-dose (SAAD) technique (Duller, 1991; Murray et al., 1997), the single-aliquots regeneration and added dose (SARA) technique (Mejdahl and Bøtter-Jensen, 1994, 1997), and the single-aliquot regenerative-dose (SAR) technique (Murray and Roberts, 1998; Galbraith et al., 1999; Murray and Mejdahl, 1999; Murray and Wintle, 2000, 2003) avoid the need for inter-aliquot normalisation. The problem with single-aliquot procedures is that repeated cycles of irradiation, heating, and optical stimulation instigate sensitivity changes in the aliquot (e.g., Zimmerman, 1971; Stoneham and Stokes, 1991; Roberts et al., 1993; Stokes, 1994a; Junger and Bøtter-Jensen, 1994). The SAR procedure was designed to incorporate a method that will monitor and correct for this sensitivity change using the 110°C TL peak (Murray and Roberts, 1998). It was later modified to use the OSL

response from a small radiation dose (a 'test dose'), administered immediately after OSL measurement of the natural and regenerated doses, to correct for sensitivity changes (Roberts et al., 1998a, 1999; Galbraith et al., 1999; Murray and Mejdahl, 1999; Murray and Wintle, 2000, 2003; Wintle and Murray, 2006). The SAR procedure allows for the repeated irradiation, heating and optical stimulation of individual aliquots to produce regenerated luminescence curves while regularly correcting each measurement for any sensitivity changes. Using this procedure, individual D_e values can be estimated from individual aliquots, allowing for the generation of many D_e estimates for each sample.

The SAR procedure that provided the general framework for luminescence investigations in this thesis is that described by Murray and Wintle (2000, 2003), and is outlined, step-by-step, in Table 3.2. It consists of the measurement of the OSL from the natural dose (L_N) and from a series of 'regenerative doses' (L_x). The measurement of L_N and each L_x is followed by the measurement of the OSL from a small, standardised test dose (T_N and T_x, respectively). Murray and Roberts (1998) and Wintle and Murray (2000) recommend that optical stimulation be carried out for 40 s at a temperature of 125°C to avoid re-trapping of optically evicted charge into the thermally unstable trap responsible for the 110°C TL peak. Each L_x is then divided by its subsequent T_x (L_x/T_x) to create a series of sensitivity-corrected regenerative-dose points. These values are used to construct a sensitivity-corrected dose-response curve on to which the sensitivity-corrected natural (L_N/T_N) is projected and interpolated on to the dose axis to obtain the D_e (Figure 3.5). The series of regenerated doses should be chosen to bracket the expected D_e value, with at least one regenerative dose lower than and larger than the D_e. Every time the SAR procedure was used in this study, between 3 and 5 different regenerative doses were used.

Prior to the measurement of OSL (i.e., L_N, T_N, L_x, and T_x), a high temperature preheat or cutheat is applied to the aliquot. Preheats are commonly held for either 5 or 10 s at a temperature between 160°C and 300°C. A cutheat is a preheat that is held for 0 s. The main purpose of preheating a sample prior to OSL measurement is to remove charge from traps that are filled by laboratory irradiations but are empty when the natural signal is measured. These traps (e.g., those associated with TL peaks at 110°C, 160°C and 280°C) are of variable thermal stability and optical sensitivity (Roberts et al.,

Table 3.2: Step-by-step outline of the SAR procedure (Murray and Wintle, 2000, 2003). Steps 1 to 5 are used to obtain the sensitivity-corrected natural (L_N/T_N). Steps 7 through 13 are used to obtain the sensitivity-corrected regenerative-dose points, which are used to construct a sensitivity-corrected dose-response curve. Step 6 is an elevated temperature blue-light bleach (hot optical wash [HOW]; see text for details).

Step	Treatment	Name
1	Preheat: 160 to 300°C	
2	Optical stimulation: 40 s at 125°C	L_N
3	Test dose	
4	Cutheat: 160°C to <preheat	
5	Optical stimulation: 40 s at 125°C	T_N
6	Optical stimulation: 40 s at 280°C	HOW
7	Regenerative dose	
8	Preheat (identical to step 1)	
9	Optical stimulation: 40 s at 125°C	L_x
10	Test dose	
11	Cutheat (identical to step 4)	
12	Optical stimulation: 40 s at 125°C	T_x
13	Repeat steps 6 to 13	

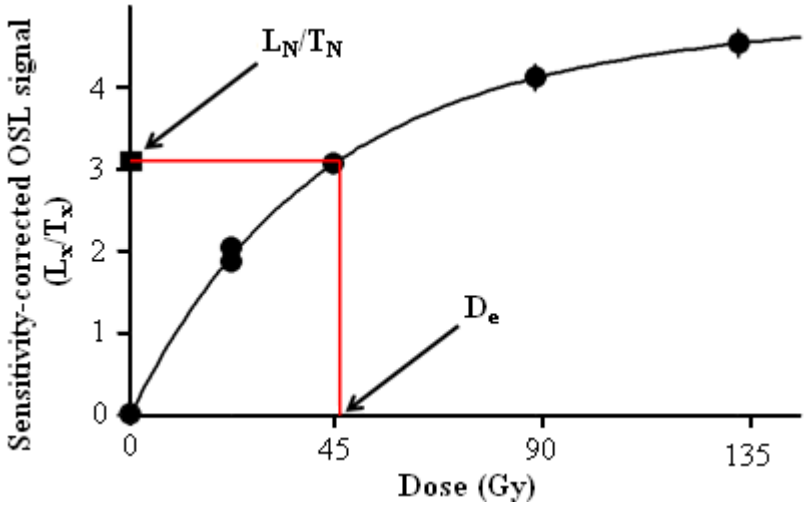

Figure 3.5: Example of a sensitivity-corrected dose-response curve from a single grain of quartz from sample MR3.

1993; Godfrey-Smith, 1994; Wintle and Murray, 1999). In the conventional SAR procedure, the preheat (160°C to 300°C) is held for 10 s prior to measurement of L_N and L_x and a cutheat (160°C to a temperature less than that of the preheat) is made prior to measurement of T_N and T_x (Figure 3.5) (Murray and Wintle, 2003). The reason for the

less stringent preheat prior to the measurement of the test dose is to minimise additional sensitivity change during the test dose cycle, while still removing the thermally unstable components that may interfere with the main OSL signal. High temperature regenerative and test dose preheats (e.g., 260°C and 220°C) have been shown to reduce the effects of unwanted components in the OSL signal (e.g., Jain et al., 2003; Singarayer and Bailey, 2003; Choi et al., 2003; Jacobs et al., 2006a). Based on these studies all applications of the SAR procedure using quartz described in this thesis include a natural and regenerative dose preheat of 260°C for 10 s and a test dose preheat of 220°C for 5 s, unless otherwise stated.

Another thermal treatment that is often added to the SAR procedure is an elevated temperature (280°C) blue-light bleach at the end of every L_x/T_x cycle, directly after measurement of the test dose (Murray and Wintle, 2003). Hereafter, this bleach will be referred to as a 'hot optical wash' (HOW). The HOW, suggested by Murray and Wintle (2003) and tested by Jacobs et al. (2006a), serves two purposes. First, it reduces the effects of charge transfer, which involves the accumulation of charge in light-insensitive traps following the measurement of the test dose. The phenomenon of re-trapping of charge during laboratory heating is known as thermal transfer (Smith and Rhodes, 1994; Rhodes, 2000). During the subsequent preheat following the regenerative dose, which is more severe than the preheat following the test dose, this accumulated charge may be thermally transferred into optically-sensitive traps, resulting in an aberrant OSL signal (Murray and Wintle, 2003). Charge transfer is also referred to as 'recuperation' by some authors (e.g., Aitken and Smith, 1988). Any charge transfer that may occur during the SAR procedure is monitored using the 'recuperation test' as described in Section 3.3.2.1. A second, related, purpose of a HOW is to reduce the build of up the S3 component of Jain et al. (2003) (see Section 3.5), which is thought to be related to the geologically unstable trap associated with the TL peak at 280°C (Singarayer, 2002; Singarayer and Bailey, 2003; Arnold et al., 2008). The build up of the S3 component throughout the SAR sequence of measurements could lead to D_e, and thus age, underestimation (Jacobs et al., 2006a). Based on these studies, a HOW was administered following the measurement of the test dose (T_x) for all applications of the SAR procedure using quartz described in this thesis, unless otherwise stated

3.3.1 The sensitivity-corrected dose-response curve

The sensitivity-corrected dose-response curve, on to which the sensitivity-corrected natural is projected to obtain the D_e, is the foundation of the SAR procedure. All OSL analyses in this study were conducted using the Luminescence Analyst program (Version 3.22b), written by G.A.T. Duller (Duller, 2007). This section details the calculation of the sensitivity-corrected values and the construction of the dose-response curve.

3.3.1.1 Calculation of L_x/T_x

To build a sensitivity-corrected dose-response curve, the value of L_x/T_x must be calculated for each regenerative-dose cycle. This value is calculated using the background-subtracted signal of the OSL decay curve following a regenerative dose (L_x) and its subsequent test dose (T_x), which then expressed as a ratio (L_x/T_x). The value of L_N/T_N is calculated in the same way. The background-subtracted OSL signal is calculated by summing the initial portion of the decay curve (*x* channels) and subtracting a mean 'late light' background signal. The background signal is calculated as the sum of the last *m* channels divided by *m*/*x*. The purpose of performing the 'late light' background subtraction is to remove any instrumental noise and remaining signal from slower OSL components from the initial signal, ensuring that only the fast component is sampled (Murray and Wintle, 2000).

Four different initial and background signal combinations were used in this thesis. For quartz from Mumba, multi-grain aliquots were stimulated with the blue LEDs at 70% power for 40 s. Unless otherwise noted, the OSL signal used for all calculations was the sum of the first 0.45 s of stimulation with the last 8.0 s of signal used to calculate a background (i.e., the 'late-background' approach). An 'early-background' approach (Cunningham and Wallinga, 2010) was also tested for multi-grain aliquots of quartz from Mumba (Section 5.4.3). This approach entailed using the sum of the first 0.45 s of signal minus a background calculated from the subsequent 1.31 s of signal. For all feldspar measurements, multi-grain aliquots were stimulated with the IR diodes at 90% power for 100 s. The IRSL signal used for all calculations was the sum of the first 2.0 s of stimulation with the last 10.2 s used to calculate the background. For all quartz measurements of single grains, the green laser was used at 90% power for 2.0

s. The default OSL signal used was the sum of the first 0.2 s of stimulation with the last 0.3 s used to calculate the background. Due to variability in the shape of single-grain decay curves, the initial signal was occasionally varied from as low as 0.1 s to as high as 0.3 s of stimulation in order to integrate only the decaying portion of the OSL signal.

3.3.1.2 Error calculation for L_x/T_x

The uncertainty associated with each L_N, T_N, L_x and T_x value is derived from two sources (Duller, 2007):

1. A random uncertainty associated with photon-counting statistics of each OSL measurement (e.g., L_x and T_x). This is calculated for each OSL measurement using Equation 3 of Galbraith (2002).
2. An uncertainty associated with instrumental error. This is determined for each reader using instrumental reproducibility tests (e.g., Jacobs et al., 2006b) and is expressed as a percentage value. Instrumental errors of 1% and 2% were used for all multi-grain aliquot and single-grain aliquot measurements in this study, respectively. These values are based on measurements made for each Risø TL/OSL reader and are consistent with values presented in the literature (e.g., Armitage et al., 2000; Thomsen et al., 2005; Jacobs et al., 2006b; Duller, 2007).

These two error terms are added in quadrature to produce the uncertainty on L_N/T_N and L_x/T_x measurements (Duller, 2007).

3.3.1.3 Constructing the sensitivity-corrected dose-response curve

The sensitivity-corrected dose-response curve was constructed using regenerative-dose points (L_x/T_x) obtained for multiple irradiation doses. In the majority of cases, the regenerative dose points were fitted using a saturating-exponential-plus-linear function described as:

$$V = V_0 + V_{\max}(1 - e^{-D/D_0}) + KD \qquad \text{Equation 3.2}$$

where V is the sensitivity-corrected luminescence intensity, V_0 represents the initial offset of the signal from zero, $V_{\max}$ represents the upper limit of the intensity of the

luminescence signal at saturation, D is the regenerated laboratory dose, and D_0 and K are constants. D_0 describes the onset of signal saturation and K is the additional linear term added to the exponential function to account for continued growth at high doses.

Occasionally, fitting a single saturating exponential function is more appropriate than Equation 3.2. This is defined as:

$$V = V_0 + V_{\max}(1 - e^{-D/D_0}) \qquad \text{Equation 3.3}$$

There are several circumstances in which Equation 3.3 is preferable to Equation 3.2. First, given the large diversity in the shapes of dose-response curves produced by different grains of the same sample (e.g., Roberts et al., 1999; Yoshida et al., 2000; Jacobs et al., 2003b, 2006b, 2008c), a single saturating exponential function may produce a better fit for an individual grain or aliquot than a saturating-exponential-plus-linear function. In addition, although the dose-response curves of many samples are best fitted by a saturating-exponential-plus-linear function (e.g., Roberts and Duller, 2004; Murray et al., 2008; Pawley et al., 2008), the mechanism that gives rise to the additional linear component is unclear (Bøtter-Jensen et al., 2003; Lowick et al., 2010; Lowick and Preusser, 2011). Second, Equation 3.3 can be used to determine the saturation characteristics of a grain's dose-response curve using the D_0 value. The D_0 value is a fitted parameter of a single saturating exponential function that equates to the dose at which the OSL intensity reaches 63% of the saturation intensity. In this study, the D_0 value was used to identify grains that produced dose-response curves that saturated at low doses (Section 5.3.3.1).

3.3.1.4 Error calculation for D_e estimates

The uncertainty on each D_e estimate is comprised of random and systematic errors. The random uncertainty is comprised of the two sources described in Section 3.3.1.2, added in quadrature to a third source: a dose-response curve-fitting error (Duller, 2007), which expresses the average deviation of the measured data points from the fitted dose-response curve. The deviation between the measured value and that predicated by the fit is the 'fitting residual'. This uncertainty is calculated as the square root of the averaged sum of the squared fitting residuals. The combined error is then transformed into the 1σ limits on the D_e estimate (Gy) by interpolating the upper and

lower limits of L_N/T_N on to the dose-response curve (Duller, 2007). A 2% systematic error, which accounts for uncertainty in the calibration of the beta source in the Risø TL/OSL reader, is added in quadrature to the random error to obtain the uncertainty on the D_e.

3.3.2 Assessing the suitability of the SAR procedure

There are several tests that can be used to ensure that the luminescence signal from a sample behaves appropriately for dose estimation using the SAR procedure. This includes internal checks to ensure that any sensitivity changes are being sufficiently corrected for, no unwanted charge transfer is occurring, and that feldspar contamination is absent from the quartz separates being measured. In addition, it is essential to ensure that a known dose can be obtained using the SAR procedure.

3.3.2.1 Assessing the effects of charge transfer: the 'recuperation' test

In order to monitor for the effects of charge transfer that cannot be observed directly, measurement of a 0 Gy regenerative dose point is undertaken. If charge transfer has taken place during the preceding test dose cycle, then the subsequent regenerative dose preheat will thermally stimulate some of this aberrant charge into optically sensitive traps. This results in additional, unwanted signal in the following OSL measurement. The zero-dose point can monitor for the thermal transfer: if charge transfer occurs, it will result in a measurable zero-dose signal. In the SAR procedure, the sensitivity-corrected 0 Gy regenerative-dose point is divided by the sensitivity-corrected natural (i.e., $[L_0/T_x]/[L_N/T_N]$) as a means of assessing the extent of charge transfer. If this value (referred to in this thesis as the 'recuperation value') is substantially large (i.e., $\geq$0.05), recuperation may significantly affect the calculated D_e (Murray and Olley, 2002; Murray and Wintle, 2003). Unless otherwise noted, any aliquots (single- or multi-grain) measured and described in this thesis that had recuperation values greater than 0.05 were rejected as unsuitable (Murray and Olley, 2002; Jacobs et al., 2006b).

3.3.2.2 Assessing the effectiveness of sensitivity correction: the 'recycling ratio' test

It must be ensured that the test dose correction is reliably monitoring sensitivity change throughout the entirety of the measurement sequence that is used to construct the sensitivity-corrected dose-response curve. To this end, two identical regenerative doses were measured (Roberts et al., 1998, 1999; Galbraith et al., 1999; Murray and Wintle, 2000). One usually followed the measurement of the natural signal and the other followed the measurement of the 0 Gy regenerative-dose signal (i.e., one at the beginning of, and the other towards the end of, the SAR measurement sequence). If the ratio of the repeat sensitivity-corrected dose point to the initial sensitivity-corrected dose point deviates more than 2σ from unity, the test dose is not adequately corrected for sensitivity change and the aliquot (single- or multi-grain) should be rejected as unsuitable.

3.3.2.3 Assessing feldspar contamination in quartz separates

Despite the effectiveness of density separation followed by an HF acid etch for isolating quartz separates (Wintle, 1997), the technique is imperfect (e.g., Godfrey-Smith and Cada, 1996). Due to the considerable differences in the luminescence behaviours of quartz and feldspars, it is important to ensure that the mineral of interest is being measured without contamination from the other. In order to identify feldspar contamination in single-grain quartz samples, the OSL-IR depletion ratio test of Duller (2003) was used. It involves adding a third repeat regenerative-dose point to the end of the SAR measurement sequence. After the regenerative dose is delivered, the aliquot (single- or multi-grain) is stimulated with an IR bleach for 40 s at 50°C. The aliquot is then preheated and the luminescence is measured (L_x). This is followed by a standard test dose cycle. Since IRSL at room temperature is strong in feldspars (Hütt et al., 1988; Spooner, 1994b) but weak or nonexistent in quartz (Spooner, 1994a), the IR bleach will empty the IR-sensitive traps in any feldspar grains or inclusions, while leaving the optically-sensitive traps in quartz grains unaffected. The subsequent OSL measurements can then be compared with those of the preceding regenerative dose-point for the same dose (i.e., the second repeat dose used to obtain the 'recycling ratio'). If the OSL-IR depletion ratio is more than 2σ below unity, then it is likely that there is some feldspar contamination and the grain or multi-grain aliquot should be rejected.

3.3.2.4 Dose recovery test

The 'dose recovery' test is a useful experiment that can be used to assess whether the experimental procedures of the SAR procedure (e.g., preheat temperatures, stimulation temperatures, application of a HOW) are appropriate for the sample being tested. This test, first used and described by Roberts et al. (1998, 1999) and Galbraith et al. (1999), involves exposing individual grains or multi-grain aliquots of a sample to natural sunlight at ambient temperature to empty the traps associated with the OSL signal without causing substantial sensitivity change. The bleached aliquots or grains are then given a known dose in the laboratory (the 'given' dose) that acts as a surrogate natural and is treated as an unknown quantity. The SAR procedure can then be used to estimate the dose. This can be repeated for many different aliquots or grains using different experimental procedures (i.e., varying the preheat and stimulation temperature) of the SAR procedure to assess those that best estimate the given dose. The ratio of the measured and given doses (the 'measured/given dose ratio') should be consistent with unity at 2σ for a successful dose recovery test.

A successful dose recovery experiment does not necessarily reveal that the tested SAR procedure will accurately estimate the natural dose. Instead, it indicates whether a sample is unsuitable for the SAR procedure (Galbraith et al., 1999; Murray and Olley, 2002). This is because the given dose does not exactly mimic the natural dose due to time-dependent effects that cannot be replicated in the laboratory (e.g., differences in dose rate) (Murray et. al., 2002). Nevertheless, it is unlikely that the SAR procedure can be used to accurately estimate the natural dose if it cannot accurately estimate a laboratory dose. Therefore, successful results in a dose recovery test for a sample should be a minimum standard before attempting to estimate a D_e value using the tested SAR procedure (Wintle and Murray, 2006).

For this study, unless otherwise stated, all aliquots (single and multi-grain) were bleached for at least 3 days in direct natural sunlight. Despite the results of multiple studies that indicate that two optical stimulations using blue-light LEDS for 1000 s with a 10,000 s pause at room temperature are sufficient to bleach the OSL signal in an aliquot (e.g., Murray and Wintle, 2003; Choi et al., 2003), natural sunlight was chosen because it has been shown to not cause sensitivity changes to the quartz OSL signal (Choi et al., 2009) and because it more closely mimics the conditions under which the

sample was bleached in nature. In this study, a successful result in the dose recovery test was a minimum requirement prior to attempting to estimate the D_e using the SAR procedure. Various experimental conditions in the SAR procedure (e.g., dose-delivery technique, preheat and stimulation temperature, stimulation duration and pre-stimulation bleaches) were also tested using dose recovery experiments to assess whether they were appropriate for the sample being investigated. Consequently, for both quartz and feldspar, dose recovery tests were performed on at least one sample from each site.

3.3.2.5 Summary

The tests described in the previous sections can be used to identify grains and multi-grain aliquots that possess characteristics that would likely lead to inaccurate D_e estimates. The recuperation test can be used to ensure that no unwanted charge transfer is taking place during the steps of the SAR measurement procedure. The recycling ratio test can be used to ensure that the test dose cycle is appropriately monitoring and correcting for any changes in the sensitivity of the OSL signal. The OSL-IR depletion ratio test monitors for the presence of feldspar contamination in the quartz separates comprising each aliquot (single- or multi-grain). Finally, the dose recovery test can be used to ensure that the SAR procedure can be used to accurately obtain a dose estimate. Success in these tests, thus, suggests that the OSL signal is suitable for accurately estimating the D_e value for a sample.

3.4 Overview of D_e distribution analysis: graphical displays and age models

Using automated instrumentation, such as the Risø TL/OSL readers, and the SAR procedure, many accurate D_e estimates can be obtained from individual grains or aliquots of each sample (Bøtter-Jensen et al., 2003; Wintle and Murray, 2006). The increased resolution at the single-grain level allows the generation of D_e distributions from which insights can be gained into the pre-depositional, depositional and post-depositional processes that may have affected the given sample (Duller, 2008).

Individual grains from the same sample can have different post-depositional mixing histories (Roberts et al., 1998a,b, 1999; Feathers et al., 2006; Jacobs et al 2006b; Olley et al., 2006; Bateman et al., 2007; David et al., 2007), different bleaching histories

(Olley et al., 1999, 2004a,b; Arnold et al., 2007; Page et al., 2007), differences in microdosimetry resulting from inhomogeneity in the beta dose rate (Murray and Roberts, 1997; Olley et al., 1997; Nathan et al., 2003; Mayya et al., 2006; Jacobs et al., 2008c) and variable behaviour in response to OSL measurements (Roberts et al., 1999; Duller et al., 2000; Yoshida et al., 2000; Jacobs et al., 2003b, 2006b, 2008c). This grain-scale variety in the luminescence behaviour and history of individual grains means that, when a multi-grain aliquot is measured, the resulting OSL signal is an 'average' of the signal from many individual grains. This averaging-out effect has been observed by many studies (Roberts et al., 1998a; Bateman et al., 2003; Forest et al., 2003; Adamiec, 2005; David et al., 2007). In sedimentary deposits that are believed to have been mixed, the spread in the D_e distribution increases as the size of the aliquot is decreased, down to a single grain. A good example of this effect is when the D_e distributions of young fluvial samples are examined (e.g., Olley et al., 1998, 1999, 2004a; Arnold et al., 2007, 2008, 2009). These studies have shown that as the number of grains that comprise an aliquot is decreased, the distribution of D_e values from those aliquots gets more spread. This is because, as the size of an aliquot increases, the resulting D_e is the average of D_e values from increasing numbers of single grains, resulting in a more uniform D_e distribution (Olley et al., 1999; Duller, 2008). Even in cases where the sediment is homogeneous and all grains are thought to be well-bleached, such as some aeolian dune sands, multi-grain aliquots may be insufficient to account for bioturbation (Lomax et al., 2007; Carr et al., 2007).

In archaeological contexts, sediment may often be mixed, contain unbleached roofspall, suffer from beta microdosimetry, be partially bleached and bioturbated (e.g., Smith et al., 1997; Roberts et al., 1998a, 1999; Jacobs et al., 2003b, 2006b, 2008c; Feathers et al., 2006; Olley et al., 2006; David et al., 2007) so that single-grain analysis is preferable. Given the variety of processes that are likely to have affected the D_e distributions of samples from archaeological sites, in order to accurately estimate an age using OSL it is essential to: 1) identify the processes that have resulted in the D_e distribution for a given sample, and 2) select a suitable age model to obtain a representative estimate of the burial dose. This section will discuss how D_e values were graphically displayed in order to assist in identifying the processes that resulted in the measured distribution. Visual assessment of the data helped enable the identification of

the age model that was most appropriate for obtaining an accurate burial dose. The ages models that were used in this study, the central age model (CAM), the finite mixture model (FMM) and the minimum age model (MAM) (Galbraith et al., 1999) will also be discussed in this section.

3.4.1 Graphical display of D_e distributions

Radial plots, described by Galbraith (1988) and Galbraith et al. (1999), were first used for fission-track dating and are an informative means of displaying the measured dose along with its measurement error. They have been widely been used to display single and multi-grain aliquot D_e distributions in optical dating studies (e.g., Roberts et al., 1998, 1999; Yoshida et al., 2000; Jacobs et al., 2003b, 2006b, 2008c; Duller, 2006). Radial plots, unlike histograms, plot individual D_e values according to the magnitude of the dose as well as the precision of the dose estimate. In this way, radial plots present useful visual representations of datasets composed of D_e values with uncertainties of varying precision (Galbraith et al., 1999; Lian and Roberts, 2006) and can be used to identify a single or multiple populations of D_e values (Duller, 2008). In this thesis, all dose and D_e distributions are presented as radial plots.

An example of a radial plot is presented in Figure 3.6. Each D_e value is represented by a dot. The magnitude is plotted in an arc on the right-hand side of the plot. The magnitude of each individual D_e is read by drawing a straight line from the '0' on the left hand axis (Standardised Estimate), through the dot that represents the D_e, on to the arced right-hand axis. The precision and relative error of each D_e value is plotted on the x-axis, where the D_e values that are further to the left of the graph have the lowest precisions, and those plotted towards the right have the highest precision. Because of the way in which the radial plot is constructed, a 95% confidence interval (2σ) can be drawn to encompass values that are statistically consistent with a common dose. If 95% of the data points lie within any single band projecting from the standardised estimate axis, then they are consistent with a common dose at two standard deviations. In Figure 3.6, the grey band captures ~91% of the data; the extra spread amounts to an overdispersion of 15 ± 4%. Radial plots thus allow the identification of D_e distributions that are spread more widely than measurement uncertainties alone can account for. Such distributions would be expected if samples exhibit heterogeneous

bleaching, post-depositional mixing, or small-scale spatial inhomogeneity in the dose rate.

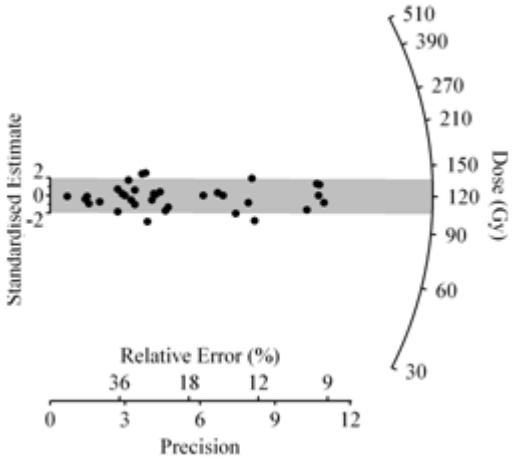

Figure 3.6: Example of a radial plot of data collected during a single-grain dose recovery experiment using sample MR 6. The distribution is centred on 116 Gy and has an overdispersion of 15 ± 4%.

3.4.2 Age models

3.4.2.1 Central age model (CAM) and overdispersion

In a setting in which all grains are well bleached prior to deposition and there has been no post-depositional mixing or other field-related complications, the distribution of D_e values can be expected to exhibit lognormal statistical properties (Galbraith et al., 1999). This means that the D_e distribution is expected to be symmetrical on a log scale where all values are centred on the mean. Galbraith et al. (1999) proposed that the CAM may be appropriate to derive a representative burial dose in such circumstances. When the CAM is applied, it is assumed that each D_e estimate is not necessarily statistically consistent with a single dose, but is instead a random sample drawn from a lognormal distribution that has a mean (μ) and a standard deviation, or 'overdispersion' (σ). These two unknown parameters are solved for by maximum likelihood. The overdispersion value (reported as a percentage) denotes the amount of variation in D_e values that cannot be accounted for by measured uncertainties on the individual dose estimates (i.e., the uncertainties associated with instrumental reproducibility, counting statistics and dose-response curve-fitting errors). This extra

variation results from natural or experimental variation between aliquots or grains being measured (e.g., Galbraith et al., 2005).

The overdispersion values, as calculated in the CAM, are often used as an estimate of the spread of D_e values for a sample. It has also been used as a tool to indicate whether a dose distribution represents a sample that is well bleached and undisturbed following deposition (e.g., Olley et al., 2004a; Jacobs et al., 2006b; Bateman et al., 2007). Several authors have suggested that an overdispersion value of 20% can be used as a threshold value to establish if a dose distribution represents a single dose population for which the CAM can be used to estimate a burial dose (Olley et al., 2004a, 2004b; Galbraith et al., 2005; Jacobs et al., 2006a; Anderson et al., 2006). In studies investigating single grains from well bleached samples (where the expected overdispersion value is theoretically zero), overdispersion values in the range of 0 to 40% have been reported (e.g., Murray and Roberts, 1997; Roberts et al., 1998a; Jacobs et al., 2003b, 2006a; Olley et al., 2004a, 2004b; Anderson et al., 2006; Arnold et al., 2007; Carr et al., 2007; Arnold and Roberts, 2009). While these additional sources of scatter that lead to a non-zero overdispersion value can sometimes be identified (e.g., Thomsen et al., 2005; Galbraith et al., 2005), they are usually not fully known (Thomsen et al., 2005; Jacobs et al., 2006b, 2008c; Lian and Roberts, 2006). This emphasises the need to characterise samples from every site to assess the normal range of variability in overdispersion values specific to that site and to determine an overdispersion value representative of well bleached samples. The minimum overdispersion value that can be expected for a single component from a given sample can be estimated from the overdispersion obtained during dose recovery experiments (Roberts et al., 2000; Jacobs et al., 2008c).

3.4.2.2 Finite mixture model (FMM)

In some cases, the spread in D_e values is larger than expected. Post-depositional mixing, which involves the movement of grains through the profile following deposition, is one such case (Roberts et al., 1998a, 2000; Bateman et al., 2003; Jacobs et al., 2006b). Another such case is where there is spatial inhomogeneity in the beta dose rate, due to the presence of material with higher or lower radioactivity (Olley et al., 1997; Mayya et al., 2006; Jacobs et al., 2008c). The measurement of single grains can

potentially expose these post-depositional processes, both of which can be manifested as multi-modal dose distributions that have distinct populations with differing D_e values (Roberts et al., 2000; Jacobs et al., 2008b). When such dose distributions are encountered, a sound understanding of the depositional environment is required to correctly obtain the burial dose using statistical models. A statistical model that can be used to distinguish multiple, discrete components in single-grain D_e distributions is the FMM, described by Roberts et al. (2000) and Galbraith (2005). This model is applicable only for single-grain, and not multi-grain aliquot, D_e distributions (Arnold and Roberts, 2009). By assuming that every log D_e value belongs to a mixture of (log)normally distributed component populations, the FMM can be used to provide information on the number of discrete D_e populations (k) of grains in a distribution, each component's mean (μ) and standard deviation, and the proportion of grains that falls into each population (π) (Roberts et al., 2000). The FMM has been successfully used in single-grain OSL studies of synthetic populations of laboratory-irradiated grains (e.g., Roberts et al., 2000; Jacobs et al., 2006c; Arnold and Roberts, 2009) and archaeological sites (e.g., Jacobs et al., 2006a, 2008b,c; David et al., 2007).

To use the FMM, two parameters are assumed to be known. These are k and the standard deviation (σ) of each population component (i.e., the overdispersion value, which is assumed to be the same for each component). A systematic approach is used to find the optimal combination of σ and k, as described by Galbraith (2005), David et al. (2007), and Jacobs et al. (2008b). The Bayes Information Criterion (BIC) (Schwartz, 1978) was used to assess the suitability of the fit of the FMM to the dataset to decide which combination of σ and k best described the dataset. The BIC is calculated as:

$$BIC = -2L_{lik} + (2k_{n-1})\ln(n) \qquad \text{Equation 3.4}$$

where L_{lik} is the maximum log-likelihood estimate for each FMM fit and n is the number of values (D_e values in this case) in the dataset. The BIC and L_{lik} values were calculated for each combination of σ and k (i.e., k = 2, 3, 4...; σ = 16, 18, 20%). As an extra population component is added and the L_{lik} value increases, the BIC value will decrease only if the component improves the fit to the data. The BIC value will increase if further components are fitted and do not improve the L_{lik} value significantly.

Therefore, the optimal combination of k and σ for a dataset is that with the highest L_{lik} and, in particular, the lowest BIC values. A worked example is presented in Table 3.3. Whenever this age model was used in this thesis, it was fitted using the S-PLUS statistical package using the FMM program written by R. Galbraith. For samples from Mumba, a value of ~15% was used as a 'minimum' σ value to account for the unexplained scatter usually observed in well-beached sediments (Galbraith et al., 2005) and because this was the smallest overdispersion value obtained for laboratory-bleached and irradiated grains during dose recovery experiments.

Table 3.3: Worked example of the application of the finite mixture model (FMM) for single-grain data from MR7. See text for details of procedure. The optimal fit of the model to the data is estimated by varying the overdispersion value and number of components (k). The combination of these two variables that produces the largest maximum log likelihood (L_{lik}) and, in particular, the smallest Bayes Information Criterion (BIC) provides the best fit. The largest L_{lik} and the smallest BIC are produced with the combination of 20% overdispersion and k = 2.

Overdispersion (%)	k	Component number	D_e (Gy)	Proportion	L_{lik}	BIC
16	2	1	145.3 ± 7.7	0.81 ± 0.08	-30	71.6
		2	59.3 ± 7.0	0.19 ± 0.08		
	3	1	164.2 ± 28.2	0.44 ± 0.47	-29.5	78.3
		2	119.7 ± 30.2	0.41 ± 0.45		
		3	56.0 ± 8.7	0.16 ± 0.09		
18	2	1	144.3 ± 8.1	0.81 ± 0.08	-29.8	71.1
		2	59.2 ± 7.7	0.19 ± 0.08		
	3	1	156.8 ± 32.8	0.52 ± 0.77	-29.6	78.5
		2	119.7 ± 48.3	0.33 ± 0.75		
		3	56.7 ± 9.5	0.16 ± 0.09		
20	**2**	**1**	**143.3 ± 8.5**	**0.82 ± 0.08**	**-29.7**	**70.9**
		2	**59.0 ± 8.5**	**0.18 ± 0.08**		
22	2	1	142.2 ± 9.0	0.83 ± 0.08	-29.7	71.1
		2	58.8 ± 9.3	0.17 ± 0.08		

3.4.2.3 Minimum age model (MAM)

The MAM, described by Galbraith et al. (1999), can be used to analyse dose distributions to obtain an appropriate burial dose for samples that are likely to have been partially bleached at deposition (e.g., Roberts et al., 1998, 1999; Olley et al., 2004a; Anderson et al., 2006; Eriksson et al., 2006; Page et al., 2007; Arnold et al., 2007, 2008). In a deposit where partial bleaching may be expected (e.g., fluvial or glacial deposits), the D_e distribution would be expected to be positively skewed; the long 'tail'

extending toward the upper end of the distribution is the result of grains with substantial residual doses, while the lowest doses most closely approximate the burial dose (Olley et al.,1998, 1999, 2004a; Bailey and Arnold, 2006; Arnold et al., 2007). Given that all of the grains investigated in this thesis are thought to have been deposited by aeolian processes, partial bleaching was not considered to be a major cause for concern. The MAM, however, can also be used to assess whether various post-depositional processes and scenarios, such as spatial heterogeneity in the beta dose rate, are consistent with the measured D_e distribution (see Jacobs et al., 2008c and Section 4.4.2.1 of this thesis). Given the large quantities of carbonate and shell noted during excavations at Mumba, small scale differences in the beta dose rate, in the form of radioactive 'cold' spots, were expected.

In this study, the MAM was fitted using the MAM-4 and MAM-3 programs written by R. Galbraith. An additional overdispersion value of 15% was added, in quadrature, to the measured uncertainty of each D_e (Galbraith et al., 2005; Arnold et al., 2009; Arnold and Roberts, 2009) to account for the scatter in D_e values expected for a well-bleached sample of grains from Mumba. An overdispersion of 15% was used because it was the lowest overdispersion value obtained during dose recovery experiments on the Mumba samples.

3.5 Linearly-Modulated OSL (LM-OSL)

3.5.1 Overview

It has been demonstrated that the OSL decay curve obtained when grains of quartz are stimulated with green or blue light and measured in the UV is the sum of more than one exponential decay functions (e.g., Bailey et al., 1997; Jain et al., 2003; Singarayer and Bailey, 2003). Bailey et al. (1997) used CW-OSL to identify three components (named the 'fast', 'medium' and 'slow' components) based on their relative decay rates. Bulur (2000) described the CW-OSL decay curve as the sum of multiple exponential functions using Equation 3.5:

$$L(t) = n_0 b \exp(-bt) \qquad \text{Equation 3.5}$$

where n_0 is the initial number of trapped electrons, t is time, and b is the detrapping probability. The value of b can be described in terms of the photoionisation cross-section (PIC) and the maximum light intensity (L_0), such that b = PIC*L_0. The b and PIC values of an OSL component are indicative of the type of trap associated with that component (Bulur, 2000).

For an alternative picture of the number and types of components that make up the OSL signal, LM-OSL measurements can be made. This technique for measuring the OSL signal was first proposed by Bulur (1996), and involves linearly increasing the power of the stimulation source from zero to a preset value. By increasing the power of the stimulating light, each component is manifested in the LM-OSL vs. stimulation time curve as a peak. The resulting LM-OSL curve is thus the sum of multiple peaks, each related to an individual component (e.g., Figure 3.7). The measured LM-OSL curve can be de-convoluted into its constituent components using Equation 4.2 from Bulur et al. (2002):

$$L(t) = n_0 \frac{b}{P} t \exp\left(-\frac{bt^2}{2P}\right) \qquad \text{Equation 3.6}$$

where P represents the total stimulation time of the LM-OSL measurement.

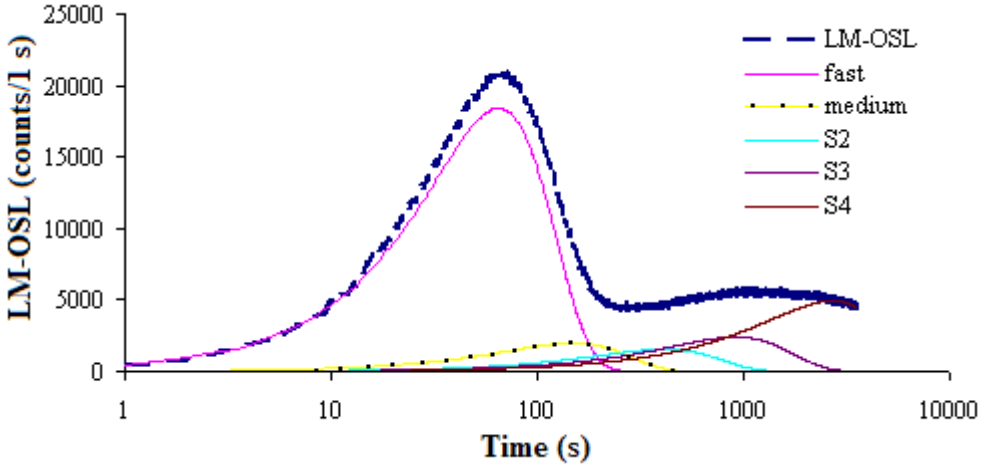

Figure 3.7: An example of a LM-OSL curve from a laboratory-irradiated aliquot of MR7. The de-convoluted components, identified using the nomenclature and relative PIC values of Jain et al. (2003), are presented along with the measured LM-OSL.

Two early studies into the LM-OSL characteristics of quartz (Jain et al., 2003; Singarayer and Bailey, 2003) reported on the presence of at least seven different components, as well as their absolute and relative PIC values (Table 3.4). Jain et al. (2003) de-convoluted LM-OSL curves from nine different quartz samples from four continents. They reported the presence of seven different components, which they termed the ultrafast, fast, medium, slow 1, slow 2, slow 3 and slow 4 components. Singarayer and Bailey (2003), using the same techniques on samples from a variety of locations, reported the identification of five discrete components: fast, medium, slow 1, slow 2 and slow 3. The two studies, along with others (e.g., Choi et al., 2006a), have corroborated one another by independently reporting similar absolute and relative PIC values for each component.

These two studies identified different numbers of slow components, resulting in two different naming systems (Wintle and Murray, 2006). The two naming systems and their respective absolute and relative PIC values are presented in Table 3.4 along with the values from Choi et al. (2006a). All absolute PIC values are similar, having slight differences but being of the same order of magnitude for each component in each study. The relative PIC values, on the other hand, are the same for Singarayer and Bailey (2003) and Jain et al. (2003) and only slightly different, but of the same order of magnitude, in Choi et al. (2006a). This means that upon identifying the presence of a fast component, the relative PIC values (or the relative *b* values) can be used to identify the remaining components. Unless otherwise stated, all component nomenclature used in this thesis is based on that presented by Jain et al. (2003).

Table 3.4: Various components published by three studies and their associated nomenclature. Unless otherwise noted, all component nomenclature used in this thesis is based on Jain et al. (2003).

Singarayer and Bailey (2003)			Jain et al. (2003)			Choi et al. (2006a)		
Component	**PIC (cm^2)**	**Relative PIC**	**Component**	**PIC (cm^2)**	**Relative PIC**	**Component**	**PIC (cm^2)**	**Relative PIC**
Ultrafast	7.0×10^{-16}	28	Ultrafast	2.9×10^{-16}	13	-	-	-
Fast	2.5×10^{-17}	1	Fast	2.3×10^{-17}	1	Fast	2.0×10^{-17}	1
Medium	5.9×10^{-18}	0.2	Medium	5.6×10^{-18}	0.2	Medium	3.9×10^{-18}	0.2
-	-	-	Slow 1	1.3×10^{-18}	0.06	-	-	-
Slow 1	2.1×10^{-19}	0.01	Slow 2	2.1×10^{-19}	0.01	Slow 1	4.8×10^{-19}	0.02
Slow 2	1.2×10^{-20}	0.001	Slow 3	2.1×10^{-20}	0.001	Slow 2	5.7×10^{-20}	0.003
Slow 3	1.9×10^{-21}	0.0001	Slow 4	2.8×10^{-21}	0.0001	Slow 3	4.6×10^{-21}	0.0002

While several studies have reported components with PIC and *b* values similar to those presented in Table 3.4 (e.g., Li and Li, 2006b; Arnold et al., 2008), many others have observed a great deal of variability in the identification of OSL components. Several studies have encountered difficulties in identifying specific components, especially in the later part of the LM-OSL curve (e.g., Tsukamoto et al., 2003; Li and Li, 2006b) while others have identified different OSL components (e.g., Tsukamoto et al., 2007).

It is clear from the studies noted above that the OSL signal from different samples is commonly composed of different constituent components (Jain et al., 2003; Singarayer and Bailey, 2003; Choi et al., 2006a,b). Additionally, many studies indicate that different aliquots of the same sample can contain different constituent components or different proportions of components (Choi et al., 2006a; Arnold et al., 2008). Variability in OSL components has even been observed between individual quartz grains from the same sample (e.g., Bulur et al., 2002; Yoshida et al., 2003). This inter- and intra-sample variability in LM-OSL composition is not surprising given the variety of OSL behaviours regularly observed for individual grains of a given sample (e.g., Roberts et al., 1999; Duller et al., 2000; Yoshida et al., 2000, 2003; Jacobs et al., 2003b, 2006b, 2008c). Adamiec (2005) has found that, when the OSL properties of individual grains on an aliquot are inhomogeneous, the components observed using LM-OSL of multi-grain aliquots may not accurately represent the trap structure of the quartz; instead they represent a manifestation of the variety of luminescence properties of the individual grains. This suggests that grain-scale heterogeneity in OSL properties may result in erroneous conclusions when using multi-grain aliquots for LM-OSL measurements.

Different OSL components have different sensitisation characteristics, thermal stabilities, degrees of recuperation, dose-response curve shapes and bleaching characteristics (Jain et al., 2003; Singarayer and Bailey, 2003, 2004). In regards to thermal stability, Singarayer and Bailey (2003) found that all components, with the exception of the ultrafast and the S3 components (the latter corresponds to their S2 component), were stable up to 270°C and have thermal lifetimes greater than 300 Ma. The ultrafast component can be removed using higher temperature preheats (e.g., 260°C; Jain et al., 2003; Choi et al., 2003; Jacobs et al., 2006a). The S3 component,

which has been linked to the thermally unstable 280°C TL peak (Singarayer, 2002), can be depleted by 50% when preheated to 260°C (Jain et al., 2003). Singarayer and Bailey (2003) confirmed this for their S2 component (equivalent to the S3 component of Jain et al., 2003) by showing that it could be depleted by heating up to 220°C and had a thermal lifetime of ~1 ka at 20°C. If this thermally unstable OSL component is substantially large in a sample of interest, then the use of the SAR procedure may result in an underestimate of the D_e (Jacobs et al., 2006a). Due to its short thermal lifetime, this component will be present in the laboratory regenerated OSL signals but not in the natural signal. Jacobs et al. (2006a) found that by increasing the test dose preheat to 220°C and including a HOW in the SAR procedure, the unwanted effects of the S3 component were substantially reduced. In addition to these components, Choi et al. (2003), Li and Li (2006a) and Pawley et al. (2010) identified a thermally unstable medium component that led to systematic age underestimations. Pawley et al. (2010) also identified a thermally unstable S2 component and calculated the thermal lifetimes of this and the medium component to be <1 ka at 20°C.

The SAR procedure was designed for the use of the fast component to estimate D_e values (Galbraith et al., 1999; Murray and Wintle, 2000; Wintle and Murray, 2006). Consequently, many samples that have OSL signals dominated by a fast component have been successfully dated using the SAR procedure. The results of many other studies have shown that, for some samples, the fast component is either not dominant or not present (e.g., Tsukamoto et al., 2003, 2007; Choi et al., 2006a,b; Westaway, 2006, 2009; Steffen et al., 2009). Choi et al. (2006a) were unable to identify a fast component in quartz from the volcanic region of the Kenyan Rift Valley. Tsukamoto et al. (2007) could not identify a fast component in quartz derived from Japanese tephras. They concluded that the OSL signal from volcanic quartz was composed of a suite of different components than is present in sedimentary quartz, and was unsuitable for age estimation. During luminescence investigations of samples from Peru, Steffen et al. (2009) found that ages obtained using the OSL signal from quartz underestimated feldspar IRSL ages due to the presence of a very weak fast component and a thermally unstable medium component.

The studies described above highlight the limitations and the usefulness of LM-OSL measurement and de-convolution as a tool to assess the constituent components

that make up the OSL signal from a sample of quartz. The identification of a fast component is necessary to allow for reliable age estimation using the SAR procedure. Additionally, the identification of aberrant OSL components, such as the ultrafast and the S3 components, can alert the researcher to the need for potential modifications of the SAR procedure (such as an elevated preheat temperature or the application of a HOW) to aid in reliable D_e estimation. However, given the results of Adamiec (2005), caution should be used when interpreting LM-OSL data measured using multi-grain aliquots.

3.5.2 Measurement and de-convolution of LM-OSL curves

Multi-grain aliquots consisting of several hundred grains of sample material were used for the LM-OSL experiments described in this thesis. LM-OSL measurements, all of which were performed on Risø 4, were made by increasing the stimulation power from 0 to 90% power (0 to ~45 mW/cm^2) over 3600 s, with data collection every 1 s. Samples were held at a constant temperature of 125°C for the entire 3600 s. After measurement, the LM-OSL curves were de-convoluted into their respective peaks in order to discern the components that made up the luminescence signal from quartz. The de-convolution procedure used in this study is the same as that described by Choi et al. (2006b) and was implemented using the commercially available SigmaPlot^{TM} (ver. 9.0) software that employs the Marquardt-Levenberg algorithm for linear and non-linear fitting.

3.5.2.1 Estimating background

Prior to fitting LM-OSL curves, the background OSL signal resulting from steadily increasing the stimulation power over 3600 s must be taken into consideration (Choi et al., 2006b). Choi et al. (2006b) observed an increase in background count rate with stimulation power, inferring that stimulation light was penetrating the detection filter (Hoya U-340s for both Choi et al., 2006b and this study). In this study, the background count rate was calculated using eight blank stainless steel discs that were coated with a layer of Silkospray, administered using a 3 mm in diameter mask (the same mask size used for the LM-OSL measurements of aliquots of MR7 described in Chapter 5). The eight blank discs were irradiated, preheated at 260°C, and then held at

125°C while being stimulated with the blue LEDs, with the power increased from 0 to 90% while the photon counts were measured. Results for background measurements are presented in Figure 3.8 and are in good agreement with those of Choi et al. (2006b). The background count increases with stimulation light intensity for all discs, such that a channel-by-channel average of the eight discs was best fitted using a quadratic function ($y = 0.000005x^2 + 0.0093x + 45.789$), which gave an R^2 value of 0.9637. The observation that the background does not increase linearly was also observed by Choi et al. (2006b), who suggested that a slight change in the wavelength of the stimulation light emission as the power was increased allowed more photons to pass through the filters. The quadratic function depicted in Figure 3.8 was taken as the background for measurements made on Risø 4 and was subtracted from all subsequent LM-OSL measurements prior to de-convolution.

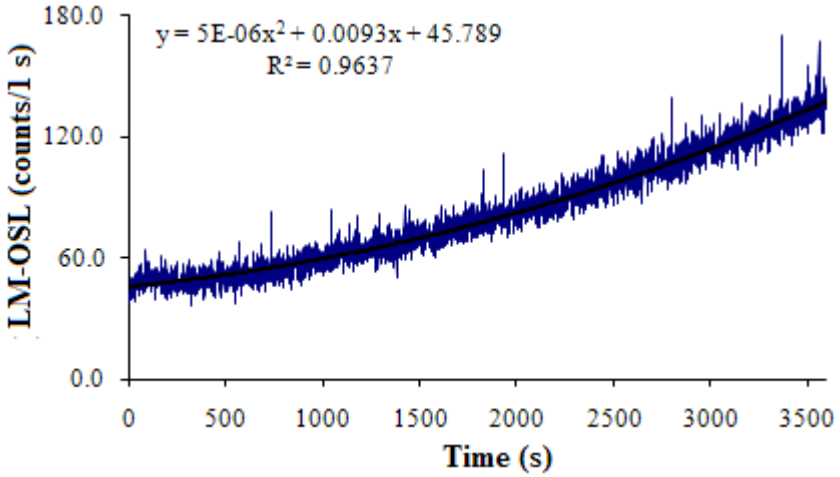

Figure 3.8: A channel-by-channel average of LM-OSL measurements on eight blank stainless steel discs. The data was best fitted by a quadratic function (R^2 of 0.9637). This function was then used to calculate the background to subtract from all LM-OSL measurements made on Risø 4.

3.5.2.2 De-convolution of LM-OSL curve

After measurement of the LM-OSL from an aliquot, the ramping time and background-subtracted LM-OSL photon count datasets were transferred into the SigmaPlot™ software for curve fitting. Equation 3.7 was the basis for the equation entered into the software's fitting program (*Regression Wizard*), following Equation 2 from Choi et al. (2006b):

$$f = n_1 b_1 \frac{t}{P} \exp\left(-\frac{b_1 t^2}{2P}\right) + n_2 b_2 \frac{t}{P} \exp\left(-\frac{b_2 t^2}{2P}\right) + ... + n_N b_N \frac{t}{P} \exp\left(-\frac{b_N t^2}{2P}\right)$$

Equation 3.7

where the total stimulation time (P) was fixed at 3593 s and values of n_N (the number of trapped electrons) and b_N (the detrapping probability) are the variables obtained through mathematical fitting. The variable N (the number of components being fit for) was fixed prior to fitting. The value of P was set at 3593 s, because the first seven channels of every 3600 s measurement (i.e., up to 0.45% power) produced zero or negative background-subtracted LM-OSL counts. A potential reason for this could be that below ~0.5% the power is too low to switch on the blue LEDs, resulting in instrumental noise for those first few channels. The value of b (s^{-1}) was used for identification of specific components in lieu of the PIC (cm^2) value, because it is equally suitable and more convenient to work with in the software program (Choi et al., 2006b). The initial values entered for n_N were set at 100,000 and the initial values for b_N were based on those given in Choi et al. (2006b). The value of P was fixed at 3593 s, the maximum number of iterations was 10^5 with a step size of 100, and the tolerance was set to 10^{-500} (Choi et al., 2006b). In situations where a fit could not be obtained, values of n were varied between 100 and 100,000.

To determine the model that best fit the background-subtracted LM-OSL data, each curve was fitted for a varying numbers of components (i.e., 2, 3, 4, 5 and 6 components represented by N = 2, 3, 4, 5 and 6 in Equation 3.7). The model (i.e., value of N) that provided the best fit to the data was identified from the sum of the squared residuals, with the best-fit being that with the smallest sum. In situations where multiple LM-OSL curves were measured, de-convoluted, and compared for the same aliquot (such as in the LM-OSL SAR experiments described in Chapter 5), the de-convolution model used for each LM-OSL curve was chosen using *Method 2* described in Appendix 2. This method involves de-convoluting the LM-OSL measurements for each test dose for a given experiment (≤6 regenerative-dose cycles) for the largest value of N that could be fit. This always resulted in a range of b values for the fast component of ≤0.10 s^{-1}. The de-convolution model for each regenerative dose was then chosen based on the N value that resulted in a fast component with a b value in the range

produced by the test doses. This method ensured that the *b* values of the fast component for all regenerative and test doses fell within a narrow (0.10 s^{-1}) range. This approach agrees with the recommendation of Li and Li (2006b) that fixing the peak position (analogous to the *b* value) results in improved reproducibility when comparing different LM-OSL measurements for the same aliquot.

3.6 Summary

In this chapter, the general properties of the OSL signal emitted from quartz were described, in addition to the procedures used for determining the numerator in the luminescence age equation (i.e., the equivalent dose, D_e). Procedures for collecting and preparing samples for D_e determination were discussed, along with the requisite instrumentation. The main procedure for estimating D_e values used in this thesis, namely the SAR procedure, was then described, as well as tests for assessing the suitability of applying the SAR procedure to samples, including checks for recuperation, adequate sensitivity correction, and recovery of known (given) doses. The age models (CAM, FMM and MAM) used to analyse D_e distributions were also introduced and discussed. Finally, the measurement technique used to assess the constituent components of the OSL signal, namely LM-OSL, was then described, along with the measurement and analytical procedures used to obtain and de-convolute the curves. The next chapter will discuss the second half of OSL dating, namely the measurement and calculation of the denominator in the age equation (i.e., the environmental dose rate).

Chapter 4: Methodology: Dose rate evaluation

The mechanism that causes the redistribution and accumulation of electrons in traps and defects in the crystal lattice of quartz and feldspar grains is naturally occurring ionising radiation. The rate at which electrons accumulate in traps within a grain, is proportional to the rate at which the grain absorbs energy from the flux of radiation to which it is exposed (i.e., the 'dose rate'; Aitken, 1998). The dose that a sample receives is defined in terms of absorbed energy per kilogram and is expressed using the measurement unit *Gray* (Gy); 1 Gy = 1 J/kg[1] (Aitken, 1998). The ionising radiation is primarily derived from potassium (^{40}K), the decay of uranium (^{238}U and ^{235}U) and thorium (^{232}Th) and their daughter products, as well as cosmic rays. Owing to the fact that the half lives of these parental nuclides are sufficiently long so that their abundance is effectively unchanged over the timescales at which OSL is operative, past dose rates can be estimated by measuring the present radiation flux, provided the main decay chains of interest (^{238}U and ^{232}Th) are in secular equilibrium. The ionising radiation from the decay of radionuclides in the sediment comes in three forms; alpha and beta particles and gamma rays (Aitken, 1985).

The total dose rate that a grain is exposed to can be separated into two parts: the internal and the external dose rates. The internal dose rate comes from alpha and beta particles, emitted during the radioactive decay of U and Th in quartz, with an additional contribution from ^{40}K and rubidium (^{87}Rb) in K-feldspars. The external dose rate comes from alpha, beta and gamma radiation from K, U and Th in the environment surrounding the mineral grain, as well as cosmic rays (Aitken, 1985). The focus of this chapter is the estimation the internal and external dose rates that combine to make up the total dose rate, and thus the denominator in the age equation (Equation 3.1). The components of the dose rate will be discussed, along with the instrumentation (laboratory and field) and procedures used to measure them. Finally, potential problems, such as disequilibrium in the uranium decay series and small scale inhomogeneity in the beta dose rate, are discussed.

4.1 Internal contributions to the dose rate

The internal contribution to the dose rate depends on the abundance of radionuclides (^{40}K, ^{87}Rb, U and Th, and the decay products of the latter pair of parents)

within the mineral grain of interest. Since these abundances vary significantly between mineral grains, the internal component of the total dose rate needs to be calculated separately for quartz and K-feldspar separates.

4.1.1 Quartz

The presence of trace amounts of U and Th within typical quartz grains means that a portion of the dose rate comes from the decay of these nuclides within each grain. Due to the small amounts of these nuclides usually found in grains of quartz, the internal dose rate is typically very small and inconsequential relative to the external contribution (Aitken, 1998; Zhao and Li, 2005). Therefore, an internal dose rate value of 0.03 ± 0.01 Gy/ka was assumed in this thesis as the dose rate for quartz from all sites. This value is based on measured values from Feathers and Migliorini (2001), Bowler et al. (2003) and Jacobs et al. (2006c).

4.1.2 K-feldspar

K-feldspars have an internal beta dose rate that originates from ^{40}K and ^{87}Rb and ^{238}U, ^{235}U and ^{232}Th and their decay products, as well as an internal alpha dose rate from U and Th. Concentrations of K, Rb, U and Th were not measured directly for any samples in this study and were instead assumed, based on previously published and widely used values in the literature. Since the contribution to the internal dose rate from each nuclide is dependent on the size fraction of the grains being measured, the dose rate value was calculated from the assumed radionuclide concentrations given in the literature, as described below.

Mejdahl (1987) proposed that, when using alkali feldspars as a dosimeter, the contribution to the dose rate from internal U, Th, ^{87}Rb and ^{40}K must be taken into consideration. He measured the internal U concentration for several samples using a delayed neutron counting technique and reported that the majority of K-feldspar samples had internal U contents below 0.3 ppm with a modal range of 0.0 to 0.15 ppm. Two samples (~2%) had U contents in the range of 1.35 to 1.65 ppm (Mejdahl, 1987). Due to the difficulty in measuring the internal Th content directly, Mejdahl (1987) also made measurements that indicated that the Th:U ratio in K-feldspars is typically 2.36:1. Balescu et al. (1997), measuring four sedimentary K-feldspar samples, obtained internal

U and Th contents that ranged from 0.4 to 0.6 ppm and 0.4 to 1.5 ppm, respectively. Zhao and Li (2005) measured multi-grain aliquots of HF acid etched K-feldspar grains from two sedimentary and three granitic samples using ICP-MS. The measured internal Th and U concentrations for the five different samples ranged from 0.47 to 2.92 ppm and 0.43 to 0.72 ppm, respectively. In this thesis, the assumed internal U and Th contents of all K-feldspar samples are 0.3 ± 0.15 ppm and 0.7 ± 0.35 ppm, respectively. These values are based primarily on the results of Mejdahl (1987). The associated 50% uncertainties on the U and Th contents accommodates for variation observed in most other studies. The internal ^{40}K content is assumed to be 12.5 ± 0.5% based on the measurements of Huntley and Baril (1997). The internal ^{87}Rb content is assumed to be 400 ± 100 ppm, based on a similar study by Huntley and Hancock (2001).

The grain size fraction used in this study is 180-212 µm. The internal alpha and beta dose rate contribution from U and Th and the internal beta dose rate contribution from ^{40}K were calculated using the concentrations cited above and the conversion factors of Adamiec and Aitken (1998). An assumed alpha efficiency value of 0.07 ± 0.03 was used, on the basis of previously published values for feldspar and polymineral fine grains (Rees-Jones, 1995; Lang and Wagner, 1997; Banerjee et al., 2001; Lang et al., 2003). Beta absorption coefficients of 0.146, 0.206 and 0.0702 were applied to the U, Th and ^{40}K contents, respectively (Mejdahl, 1979). The internal beta dose rate contribution from ^{87}Rb was calculated using the conversion factors from Readhead (2002). The internal dose rate data assumed for K-feldspar separates from Mumba are presented in Table 4.1.

Table 4.1: Internal dose rates for ~180-212 µm diameter K-feldspar grains calculated on the basis of previously published studies.

Radionuclide	Content	Internal beta dose rate (Gy/ka)	Internal alpha dose rate (Gy/ka)	Total internal dose rate (Gy/ka)
U	0.3 ± 0.15 ppm	0.006 ± 0.003	0.06 ± 0.03	
Th	0.7 ± 0.35 ppm	0.004 ± 0.002	0.04 ± 0.02	
^{40}K	12.5 ± 0.5%	0.69 ± 0.03		
^{87}Rb	400 ± 100 ppm	0.10 ± 0.02		
Total		0.80 ± 0.03	0.10 ± 0.03	0.90 ± 0.05

4.2 External contributions to the dose rate

The external contribution to the dose rate depends on the abundance of potassium, uranium and thorium in the soil matrix surrounding the grain, as well as the effects of cosmic radiation. Since the rate at which energy is absorbed is assumed to be equal to the rate at which it is emitted, it is possible to calculate the dose rate to buried sediments. This can be done by determining the concentrations of radionuclides in the deposits or by directly measuring the emissions of alpha and beta particles and gamma rays within the sediment (Aitken, 1998). The latter approach was used in this study and is outlined in this section, which deals with estimating the four components of the external dose rate: alpha, beta and gamma emissions and cosmic rays. Since this component of the total dose rate is derived from sources external to the mineral grains used as dosimeters, it is the same for both quartz and feldspar grains.

4.2.1 Alpha contribution

Alpha particles, although highly ionising, only have a penetrating range of ~0.025 mm from the emitting nucleus (Aitken, 1998). Therefore, when sand-sized grains are considered, the external alpha contribution does not penetrate the internal core of a grain, instead only affecting the outer rind. This results in inherent uncertainties in determining the external alpha dose rate because different regions of the same grain will have received different alpha contributions (Aitken, 1998). To circumvent this problem of partial penetration and inhomogeneous alpha irradiation, the external alpha contribution has been reduced to negligible levels by removing the outer ~9 μm of each grain by HF acid etching (see Section 3.2.1) all samples during preparation (Aitken, 1998). Subsequent to HF acid etching, the external alpha contribution to the quartz and K-feldspar grains is assumed to have been removed and is not considered further.

4.2.2 Cosmic-ray contribution

Despite the fact that cosmic rays typically make up only a small fraction of the environmental dose rate, estimates of their contributions to the total dose rate should be included (Prescott and Hutton, 1988). Cosmic rays are a lightly ionising form of radiation with two components. The 'soft' component is absorbed in the top ~50 cm of

sediment. The 'hard' component is composed of muons capable of penetrating to considerable depths, although with decreasing intensity as the depth of overlying sediment or rock increases (Aitken, 1998). The cosmic-ray contribution to the dose rate of a sample, thus, decreases as the thickness of overlying sediments and rocks increases.

In this study, the contribution of cosmic rays to the environmental dose rate was estimated using the procedures described by Prescott and Hutton (1994). This approach takes into account the latitude, longitude and altitude of the study sites. The effect on the cosmic-ray dose rate of the thickness of sediment overburden, which was assumed to be 2.0 g/cm^3, and the cos^2 ø-zenith angular distribution of cosmic rays to account for rock shielding (Smith et al., 1997) were also taken into account. A systematic error of 10% was used to account for the uncertainty associated with the primary cosmic-ray flux (Prescott and Hutton, 1994). The cosmic-ray contribution to the total environmental dose rates for samples from Mumba is low (3-4% of the total dose rate for most samples).

4.2.3 Beta and gamma contributions

The majority of the environmental dose rate for both quartz and feldspar separates in this study is derived from beta particles and gamma rays. These components of the dose rate result from ^{40}K and the decay of ^{238}U, ^{235}U, ^{232}Th and their daughter products in the surrounding sediment.

Beta particles and gamma rays have penetration ranges of up to 3 mm and 30 cm, respectively (Aitken, 1998). The short penetration range of beta particles means that an adequate representation of the bulk natural beta dose rate can often be obtained from a small sediment sample in the laboratory. This is in contrast to the dose rate resulting from gamma rays. Laboratory measurements of a small sediment sample may not be representative of the natural surroundings of the sample, unless the 30 cm-radius gamma sphere is homogeneous in composition (e.g., sand dune deposits). In this study, all samples were collected from archaeological sites that consist of complex and heterogeneous sedimentary deposits. Archaeological sites typically contain large numbers of artefacts, shell, bone, carbonate nodules and possible ashy lenses, each of which has different concentrations of radioactive materials. It is for this reason that, whenever possible, the gamma-ray contribution to the dose rate was measured *in situ*

using a field gamma spectrometer. The sedimentary heterogeneity also has consequences for the beta dose rate. This will be discussed later in this chapter (Section 4.4.2).

In Section 4.2.3.1, the method for measuring the gamma-ray contribution to the total dose rate using a field gamma spectrometer is discussed. Section 4.2.3.2 details the method for measuring the beta component of the environmental dose rate using GM-25-5 beta counting.

4.2.3.1 In situ gamma spectrometry

Field gamma spectrometry measurements were made for most of the OSL samples at Mumba and Moche Borago rockshelters by R.G. Roberts at the time of sample collection (June and July 2007). Measurements were made using a gamma spectrometer with a 2 inch in diameter NaI(Tl) crystal. The field gamma spectrometer was calibrated by Z. Jacobs using the 'Oxford Blocks' (Rhodes and Schwenninger, 2007) at the Research Laboratory for Archaeology and the History of Art, University of Oxford. The total gamma dose rate from U, Th and K in the sediment was determined using the 'threshold' technique (Mercier and Falguéres, 2007). The concentrations of K, U and Th are ascertained by locating specific high-energy gamma peaks within the spectra that correspond to ^{40}K and the daughter radionuclides of ^{238}U and ^{232}Th: ^{214}Bi and ^{208}Tl, respectively. For ^{40}K, the peak emits at 1460 KeV, for uranium the ^{214}Bi peak is 1760 KeV, and for thorium the ^{208}Tl peak is at 2620 KeV (Jacobs, 2004; Mercier and Falguéres, 2007). The peak used for derivation of the Th concentration is the only peak in the gamma-ray spectrum that is not significantly interfered with by other peaks, despite the large number of gamma emitters in the ^{232}Th decay series. The ^{40}K peak is also reasonably interference-free (Jacobs, 2004). Each spectrum in this study was obtained by inserting the field gamma spectrometer into a 30 cm deep and ~6 cm wide horizontal hole in the archaeological section, created by taking OSL samples, and measuring the counts for 60 min. A relative error of 2.5% was used.

4.2.3.2 Beta counting

The bulk beta contribution to the environmental dose rate was estimated from beta counting measurements made using a low-level Risø beta counter (GM-25-5),

which is described in Bøtter-Jensen and Mejdahl (1985, 1988). The instrument is comprised of a gas flow counter (using a gas composed of 99% argon and 1% isobutane), five individual Geiger-Müller cylindrical detectors, and a common guard counter. The detectors are mounted in a row with their mylar windows facing downwards to record pulses derived from the sample material loaded into five cylindrical containers ('pots') with a diameter of 25 mm. These containers are loaded on to a sliding vessel to ensure that their locations underneath the detectors are precise and reproducible. The whole instrument is encased inside 10 cm of lead brick shielding to reduce the background signal from cosmic rays.

Sub-samples to be measured in the beta counter were dried and ground to a fine powder. The loose powder was dispersed into the pots and enclosed using a plastic film (i.e., 'Glad Wrap'). The pots containing the sample material were then loaded into three of the five positions in the instrument, with the other two positions reserved for pots containing material used to measure the background signal and a calibration standard. The material used for background measurements was a sample of magnesium oxide (MgO) that has an average count rate of 0.17 counts/min. The calibration standard was a dried sample of Nussloch Loess ('Nussi'), which has a known beta dose rate calculated using high resolution gamma spectrometry (Kalchgruber, 2002), and an average count rate of ~5 counts/min. The beta dose rate of Nussi, when calculated using the conversion factors of Adamiec and Aitken (1998), is 1.49 Gy/ka (Kalchgruber, 2002; Bauer, 2007). Measurements of the five positions were made simultaneously for 24 cycles, each one hour (i.e., 24 hours of measurement time).

To calculate the beta dose rate for the sample being measured, the total number of counts for each position from all 24 cycles was summed. The total counts from the MgO pot were then subtracted from the total counts from each sample position and the Nussi calibration standard. The background-corrected total for each sample was then divided by the background-corrected total for the calibration standard, and multiplied by the known beta dose rate for Nussi. The calculated beta dose rates for the three replicates were then averaged to obtain a final, bulk beta dose rate for the sample.

It was assumed that the three sub-samples measured in the beta counter were three independent measurements of the beta dose rate of the sample. Following this, the uncertainty associated with the bulk beta dose rate for each sample was obtained by

calculating the standard deviation of the three background-corrected sub-sample measurements. This was divided by the background-corrected sub-sample mean beta dose rate to obtain the relative error, which was then added, in quadrature, to the relative error on the Nussi standard to obtain the uncertainty on the bulk beta dose rate. The error on Nussi was calculated as 3% by combining, in quadrature, the U, Th and K concentration uncertainties (Kalchgruber, 2002).

4.3 Correction factors: beta attenuation and water content

Before the total environmental dose rate could be calculated for each sample, several corrections needed to be made to the measured external contributions to the dose rate. First, the beta dose rate needs to be corrected for beta attenuation caused by the relatively small ionising range of beta particles. Second, each external dose rate component needs to be corrected for the presence of water, which attenuates the ionising radiation from beta particles and gamma and cosmic rays.

Beta attenuation occurs within each grain. The extent of attenuation of beta particles varies for U, Th and K and is dependent on the grain size being examined. In this study, the grain-size fraction used for all samples was 180–212 μm. Consequently, the beta attenuation factors used are those from Mejdahl (1979) for grains of 200 μm in diameter. These are 0.930, 0.854 and 0.794 for K, U and Th, respectively. A fractional error of 3% arising from uncertainties associated with the derivation of the beta-attenuation factors was added in quadrature to the uncertainty on the beta dose rate.

The environmental dose rate of sediment containing moisture will be smaller than for the same sediment if were dry, due to the fact that water in the sediment absorbs radiation at a higher rate than the grains themselves (Aitken, 1998). The various radiation emissions (beta particles and gamma and cosmic rays) are attenuated to different degrees by water. If water content is ignored, the resulting OSL age may be considerably underestimated (Aitken, 1998). The water content of the sample when collected (the 'measured water content') is expressed as a percentage of the dry mass of the sample and is calculated by dividing the mass of water in the sample by the mass of the dry sample. The measured water content may not be representative of the long-term average water content over the course of the sample's burial ('historical water content'),

and so this must be estimated. The correction to the dose rate for water content can be expressed as:

$$D_{water-corrected} = \frac{D_{dry}}{1 + HWF} \qquad \text{Equation 4.1}$$

where $D_{water\text{-}corrected}$ is the water content-corrected dose rate, D_{dry} is the measured dose rate for a particular emission, WF is the historical water content, and H is the dose rate attenuation factor for the emission (Aitken, 1998). H values of 1.25, 1.14 and 1.176 were used for beta particles, gamma rays and cosmic rays, respectively (Aitken 1985; Readhead, 1987).

It must be noted that the measured *in situ* gamma dose rate ($D_{in\text{-}situ\ gamma}$) is already attenuated by the measured water content ($W_{in\text{-}situ}$). This field measurement must be first converted to a 'dry' gamma dose rate ($D_{dry\ gamma}$) as follows:

$$D_{dry\ gamma} = \frac{D_{in-situ\ gamma}}{1 + HW_{in-situ}} \qquad \text{Equation 4.2}$$

The dry gamma dose rate is then used in Equation 4.1 to calculate the water corrected gamma dose rate for the historical water content.

4.4 Potential environmental dose rate problems

4.4.1 Radioactive disequilibrium

A radioactive decay chain is in secular equilibrium if each member of the chain decays to the succeeding member at the same rate as it is produced from the preceding member. At secular equilibrium, therefore, the activities of daughter and parent nuclides are equal. Alternatively, if a decay chain is in disequilibrium, the activities of the daughter and parent nuclides will be unequal (Olley et al., 1996). Disequilibrium results when a process preferentially moves parent or daughter nuclides into, or out of, an open system at a significant rate relative to the half-life of the daughter product (Olley et al., 1996). The three main mechanisms that cause disequilibria in sediments

are: 1) precipitation and solution reactions, 2) diffusion of the gaseous radon isotopes, and 3) alpha particle recoil (Olley et al., 1996).

Since it is not always possible to accurately assess past episodes of disequilibrium, assumptions must be made about the radioactive history of a sample. The two main assumptions made in luminescence dating are: 1) the radioactive decay chains have always been in secular equilibrium, or 2) that the modern dose rate is representative of the dose rate that has prevailed during burial, which does not imply secular equilibrium (Olley et al., 1996). Dose rate evaluation techniques that measure the activity of parent nuclides (e.g., neutron activation analysis, atomic absorption spectrometry, and ICP-MS) rely on the first assumption. Alternatively, dose rate evaluation techniques that count emissions (e.g., beta counting, *in situ* gamma spectrometry and thick source alpha counting) rely on the second assumption (Olley et al., 1996). While emission counting techniques measure the activity of all nuclides in the U and Th decay chains, the majority of the measured dose rate is contributed by the radionuclides in the lower half of the decay chains (Olley et al., 1996).

Olley et al. (1996, 1997) showed that, when the modern dose rate is assumed to have prevailed during burial and the dose rate is estimated from the activities of the shorter-lived daughter nuclides, the presence of disequilibrium in the ^{238}U decay chain caused a small disparity (<3%) between the calculated and true dose rates. Alternatively, when secular equilibrium was assumed and the concentrations of the parent nuclides were measured to determine the dose rate, the disparity between calculated and true dose rates was greater (~8%) (Olley et al., 1996, 1997). Consequently, all dose rate evaluations in this thesis were made using emission-counting techniques (i.e., beta counting and *in situ* gamma spectrometry) that do not assume secular equilibrium.

4.4.2 Beta microdosimetry

Many archaeological sites, including Mumba and Moche Borago rockshelters, have complex sedimentary deposits that are heterogeneous in composition. Aside from sediment grains, they contain large concentrations of shell, bone, stone artefacts, ash lenses and carbonate nodules, each of which has different radioactive properties. Millimetre-scale spatial inhomogeneity in deposits can lead to heterogeneity in the beta

dose rate due to the presence of material that is high in radioactivity (i.e., 'hotspots') or low in radioactivity (i.e., 'cold spots') (Olley et al., 1997; Nathan et al., 2003; Mayya et al., 2006). Mayya et al. (2006) suggested that microscopic fluctuations in the distribution of highly radioactive beta-emitting ^{40}K in the sediment could cause a heterogeneous dose rate (and, hence, D_e) distribution. Alternatively, the presence of 'cold spot' materials, such as carbonate fragments, gypsum, opal, calcite and carbonaceous materials such as shell fragments, can also lead to spatial inhomogeneity in the dose rate (Murray and Roberts, 1997; Olley et al., 1997; Nathan et al., 2003; Mercier et al., 2007; David et al., 2007; Jacobs et al., 2008c)

Differences in the dose rate derived from sediment heterogeneity have little effect on D_e distributions when aliquots consisting of many grains are measured. This is because the effects of sediment (and, thus, dose rate) heterogeneity are averaged out among grains when the total environmental dose rate is used in the age equation with a D_e estimated using a summed luminescence signal from multi-grain aliquots (Olley et al., 1997; Nathan et al., 2003). As the size of the aliquots measured decreases to the single-grain level, the differences in beta dose rate resulting from sediment heterogeneity become progressively more significant, potentially resulting in D_e distributions with large scatter (Olley et al., 1997; Mayya et al., 2006). Beta dose rate heterogeneity has been used in many previous studies as one explanation for the large spread in single grain D_e distributions (e.g., Murray and Roberts, 1997; Olley et al., 1997; Roberts et al., 1999; Feathers, 2003; Lomax et al., 2007; Jacobs et al., 2008b,c).

A method was developed by Jacobs et al. (2008b,c) to attempt to resolve the ambiguities associated with the beta dose rate to individual grains. It involves analysing single-grain D_e distributions with the FMM and using the discrete components, along with the bulk beta dose rate, to model and correct for beta microdosimetry variations. This correction procedure will be discussed in the next two sections.

4.4.2.1 Beta microdosimetry identification

An analytical test that must be undertaken in order to verify the possible presence of beta microdosimetry variations is based on Jacobs et al. (2008c). It involves modelling the effects of grains that were completely surrounded by 'cold spot' material, thus receiving no beta dose. The MAM is used to analyse each single-grain

dataset to obtain the statistically smallest D_e value, which is divided by the bulk dose rate with the beta contribution set to 0 Gy/ka (i.e., internal alpha, external gamma and cosmic-ray contributions only). The resulting age applies to those hypothetical grains that have been encased in 'cold spot' material throughout their burial history, thereby reducing their beta dose rates to zero.

There are three possible outcomes of this analysis. First, if this age is smaller than that calculated using the major D_e component (identified using the FMM) and the total bulk dose rate (i.e., including the measured, average beta dose rate), then beta microdosimetry can be ruled out as the sole or principal source of the observed scatter in D_e values. This result indicates that the MAM component is composed of grains with burial doses that are too small to be the result solely of them having received no beta dose throughout their burial history. If the latter were a sufficient explanation by itself, then they would have produced larger D_e estimates. Second, if the age obtained using MAM and the dose rate minus the beta contribution is greater than the age obtained using the major D_e component and the total bulk dose rate, then beta microdosimetry is a possible explanation for the observed overdispersion. In this case, the MAM component consists of grains that received a beta dose rate less than the average measured beta dose rate received by the bulk sample. Finally, if the two ages are statistically consistent, then beta microdosimetry variations are a possible explanation. In this scenario, the MAM component is comprised of grains that were completely surrounded by material with low radioactivity, receiving a beta dose rate of 0 Gy/ka for most of their burial history. While this analysis does not definitively confirm that beta dose rate heterogeneity is the process that has resulted in the observed D_e distributions, it can establish whether the observed distributions cannot be explained as a function of differences in beta dose rate among grains.

4.4.2.2 Beta dose rate correction

The method that was used to correct for heterogeneity in the beta dose rate in this study was tested and used by Jacobs et al. (2008c) on samples from archaeological deposits in South Africa. It uses the relative proportion of grains in each population (π) fitted using the FMM and the measured beta dose rate to estimate the beta dose rate received by the majority of grains. The measured bulk beta dose rate represents a

combination of above-average beta dose material and below-average beta dose (i.e., 'cold spot') material. In the laboratory, these materials were combined into a homogeneous powder and measured, thus producing an average beta dose rate for the sample. If results from the analysis described in Section 4.4.2.1 indicate that beta microdosimetry may be present, it could be assumed that the grains that comprise the minor component in the D_e distributions (as indicated by the FMM) were surrounded by material with low radioactivity, and that these grains experienced a below-average beta dose rate. This means that the grains in the main D_e component must have received a beta dose rate higher than the measured, average beta dose rate. The grains in the minor component received some beta dose rate between zero (in the case of a grain completely surrounded by 'cold spot' material) and a value less than the bulk beta dose rate.

A step-by-step worked example of the beta microdosimetry correction is presented in Table 4.2 for sample MR7 from Mumba. It is based on the principal that the bulk beta dose rate for a sample is equal to the sum of the fractional beta dose rate for the minor and major D_e components. It was assumed that the beta dose rate received by the grains in the minor D_e component was equal to half the bulk beta dose rate (Table 4.2, B), which was multiplied by the proportion of grains assigned to the this component by the FMM to estimate the fraction of the bulk beta dose rate associated with these grains (Table 4.2, C). This value could then be subtracted from the bulk beta dose rate to obtain the fraction of the bulk beta dose rate that pertains to the grains in the main D_e component (Table 4.2, D). The fraction of the bulk beta dose rate that is associated with the main component was divided by the proportion of grains in the main D_e component to obtain the beta dose rate applicable to these grains (Table 4.2, E).

The beta microdosimetry correction can also be expressed as follows:

$$\beta DR_{\text{main}} = \frac{\beta DR_{\text{average}} - (\beta DR_{\text{minor}} \times \pi_{\text{minor}})}{\pi_{\text{main}}} \qquad \text{Equation 4.3}$$

where βDR_{main} is the beta dose rate for the main D_e component, $\beta DR_{\text{average}}$ is the bulk beta dose rate, βDR_{minor} is the beta dose rate that the minor D_e component received, π_{minor} is the proportion of grains that fall into the minor component, and π_{main} is the proportion of grains that comprise the main component.

Table 4.2: Worked example of beta microdosimetry dose rate correction for MR7 using component proportions from the FMM (see Table 6.3 and Table 6.5). See text for details of the procedure. Using the proportions of the components determined by the FMM, the measured bulk (average) beta dose rate, and an assumed beta dose rate of half the bulk beta dose rate for the minor component, the beta dose rate of the main component can be estimated

Beta microdosimetry correction				
		Described procedure	Formula	Example (Gy/ka)
		Adjusted beta dose rate		
A.	$\beta DR_{average}$	(Average beta dose rate)		1.58
B.	βDR_{minor}	(Minor component beta dose rate)	(A)/(2)	0.79
C.	π_{minor}	(Fractional contribution, minor component)	(B)*(0.18)	0.14
D.	π_{minor}	(Fractional contribution, main component)	(A)-(C)	1.44
E.	βDR_{main}	(Beta dose rate, main component)	(D)/(0.82)	**1.76**
		Uncertainty		
F.	1σ		(B)/(2)	0.40
G.	n		(48)*(0.82)	39.36
H.	Standard error		(F)/(√G)	**0.06**

The uncertainty on the adjusted beta dose rate was obtained by assuming that all beta dose rates experienced by grains in the minor component (i.e., surrounded by 'cold spot' materials) are effectively captured at 2σ (95% confidence interval) on either side of half of the average beta dose rate value. The uncertainty at 1σ (68% confidence interval) for the minor component (i.e., [midpoint value]/2: Table 4.2, F) is then divided by ($\sqrt{n}$) (Table 4.2, H), where n is the number of D_e values in the main component (Table 4.2, G). This value represents the standard error on the mean for the main D_e component. This error is then added in quadrature to the bulk beta dose rate measurement error to estimate the uncertainty on the adjusted beta dose rate for the grains in the main D_e component.

4.5 Summary

In this chapter, the denominator of the age equation, namely the dose rate, was introduced and the different components of the dose rate described. Details of the instrumentation and procedures used in this study to measure the different dose rate components were provided as were the methods used to correct for water content and beta dose attenuation. Finally, two problems associated with estimating the environmental dose rate were discussed, along with how they were addressed in this

thesis. The effects of potential disequilibrium in the U and Th decay series were kept to a minimum by using emission counting methods, which measure short-lived daughter nuclides down the decay chain and do not assume secular equilibrium, for all dose rate measurements. Heterogeneity in the beta dose rate is a likely cause of large spreads in D_e distributions from archaeological sites. A technique that had published previously (Jacobs et al., 2008c) for modelling and correcting for small-scale beta dose rate heterogeneity was discussed, and a worked example was given in Table 4.2.

Chapter 5: Characterising the OSL signal of quartz from Mumba rockshelter using single grains and multi-grain aliquots

In this chapter, investigations of the OSL signal from multi-grain and single-grain aliquots of quartz from Mumba are described. The samples that were used to characterise the OSL signal of quartz from Mumba are both from the Bed V archaeological unit, which contains the Mumba Industry. Multi-grain aliquots of quartz from MR7 were investigated. This sample was not used for single-grain studies, however, due to the relatively small quantity of MR7 material remaining. Consequently, OSL investigations of single grains were performed on quartz from MR6. Since both samples are from the same geological unit (Unit E; Table 2.4), their origins and luminescence behaviours were expected to be the same.

The main aim of these studies was to identify an OSL signal that could be used to obtain reliable D_e estimates for samples from Mumba using the SAR procedure. Several objectives were established to meet this aim. First, LM-OSL measurements were used to verify the presence of a fast component in the OSL signal of natural and laboratory irradiated aliquots. A dominant fast component is necessary for reliable D_e determination using the SAR procedure (Galbraith et al., 1999; Murray and Wintle, 2000). Second, the OSL signal from single grains of quartz was characterised, and modified SAR procedures were tested. Third, dose recovery experiments were performed to assess the suitability of the modified SAR procedure for obtaining accurate dose estimates. These experiments were used to develop rejection criteria that could be used to isolate grains with well-behaved OSL signals. Finally, the effects of intra-sample OSL variability on the OSL signal from multi-grain aliquots were investigated.

5.1 LM-OSL investigations of quartz from Mumba

5.1.1 Establishing the presence of a fast component

As discussed in Chapter 3, the SAR procedure was designed as a technique to obtain D_e values using the fast component of the OSL signal from quartz (Galbraith et al., 1999; Murray and Wintle, 2000; Wintle and Murray, 2006). On this basis, LM-OSL investigations were undertaken with the primary aim of identifying the presence of a

fast component in the natural signal of quartz from Mumba. A second aim was to identify the optically less-sensitive slower components present in quartz from Mumba.

To achieve these aims, the natural LM-OSL signals from eight multi-grain aliquots of MR7, each consisting of ~500 quartz grains, were measured. Samples were preheated to 260°C for 10 s prior to LM-OSL measurements, which were made and analysed as described in Section 3.5. The stimulation power was linearly increased from 0 to 90% power (0 to ~45 mW/cm^2) over 3600 s while the temperature was kept constant at 125°C. The number of components that provides the optimal fit to the measured LM-OSL curve was determined by minimising the sum of the squared residuals. The individual components could then be distinguished based on their PIC, absolute *b*, and relative *b* values, which were compared to published values (e.g., Table 3.4).

The LM-OSL curves measured on the eight aliquots of MR7 were subsequently de-convoluted and the data is presented in Table 5.1. LM-OSL curves from four of these aliquots are also shown in Figure 5.1 along with their fitted components. The number of components (*N*) that best fit the data varied for each aliquot. Most aliquots (75%, n = 6) were best fitted using five or more components. Each component that was fitted for each aliquot was allocated into a column (A–F) according to its *b* value (Table 5.1). At the bottom of the table, the average *b*-values, relative *b* (relative to the first component), and PIC for each column are presented. There are two components present in all aliquots measured, namely those presented in columns A and F in Table 5.1. These represent the fastest and slowest components, respectively. The components represented by columns B and E were also present in all aliquots, except aliquot 7, which could only be de-convoluted using an equation where $N = 2$.

Although the component represented in column B was present in most aliquots, it has a large range of *b* values (~0.3–0.7 s^{-1}) and appears to be more closely related to the components represented by column C. This can be inferred by scrutinising the aliquots that were de-convoluted for five or more components. When five components were fitted, only one (column B) was present and when six components were fitted, components corresponding to both columns B and C were present. Li and Li (2006b) made similar observations. They noted that the fastest component had a similar peak position (related to the *b* value) for different aliquots, but that the slower components

were difficult to separate clearly, making it difficult to determine the size and number of components in the later part of the LM-OSL curve. There seems to be a spectrum of *b* values for components presented in columns B and C, from 0.13 to 0.71 s^{-1}. There is no intuitive separation between the two, making it difficult to discern between them. This may suggest that the components represented by columns B and C may actually be a single component with a continuum of *b* values.

Table 5.1: De-convolution data for the natural LM-OSL signal measured for eight aliquots of MR7. Each LM-OSL curve was de-convoluted using the sum of the squared residuals to determine how many components optimally fit the data. Each component was then grouped by its *b* value into columns.

		b values (s^{-1})					
Aliquot	***N***	**A**	**B**	**C**	**D**	**E**	**F**
1	4	0.90	0.33			0.009	0.0005
2	6	1.19	0.64	0.20	0.04	0.007	0.0004
3	6	1.17	0.61	0.17	0.03	0.006	0.0004
4	6	0.90	0.48	0.13	0.03	0.006	0.0004
5	5	0.80	0.29		0.03	0.005	0.0004
6	5	0.97	0.45		0.07	0.006	0.0005
7	2	1.04					0.0007
8	6	1.22	0.71	0.18	0.03	0.008	0.0005
Average *b* value (s^{-1})		**1.02**	**0.5**	**0.17**	**0.04**	**0.007**	**0.0005**
Average relative *b* value		**1**	**0.48**	**0.15**	**0.04**	**0.007**	**0.0006**
Average PIC (cm^2)		**1E-17**	**5E-18**	**2E-18**	**4E-19**	**6E-20**	**4E-21**

Despite the difficulty in identifying discrete slower components, three components were consistently identified in all aliquots, namely those presented in columns A, E and F. If only these three components are considered, they can be associated with the fast, S2 and S3 components of Choi et al. (2006a) (roughly equal to the fast, S3 and S4 components of Jain et al., 2003). If this is so, then components B and C may represent a medium component, and component D may represent the S1 component of Choi et al. (2006a) (the S2 component of Jain et al., 2003). Additionally, the size of the component represented by column B, relative to the component represented by column A, is variable for each aliquot (Figure 5.1).

It is peculiar that the S3 component (S2 component of Singarayer and Bailey, 2003) was identified in the natural signal, given that this component has previously been described as thermally unstable (Singarayer and Bailey, 2003). However, atypical

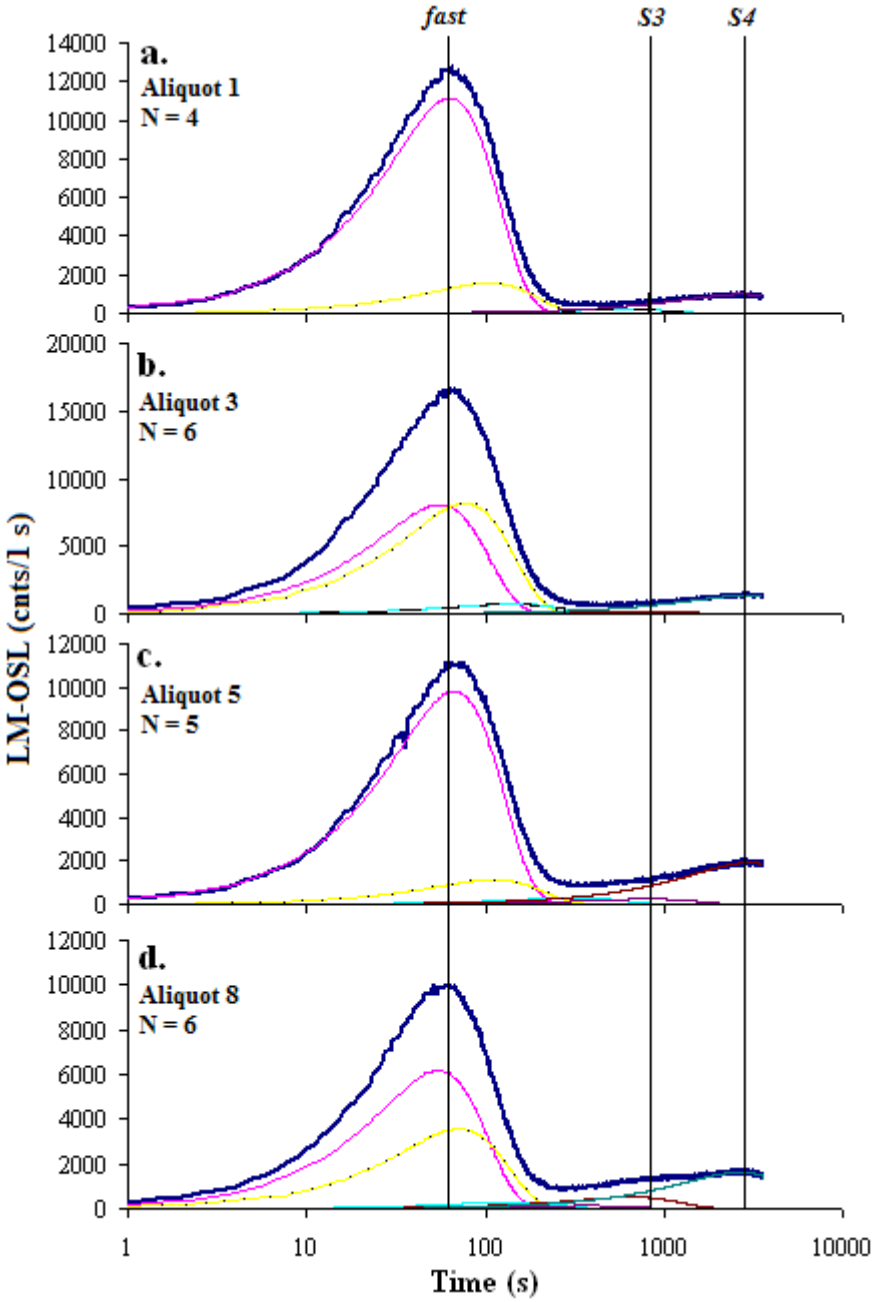

Figure 5.1: LM-OSL curves of the natural signal from four multi-grain aliquots of MR7 plotted on a linear-logarithmic scale. The background-subtracted LM-OSL is shown (in bold) with the fitted components underlying it. The approximate positions of the peak of the three components that were consistently identified in MR7 (fast, S3 and S4) are also presented.

results, such as the identification of an S3 component and the continuum of *b*-values identified for several components, may be the result of measuring the combined LM-OSL signal from hundreds of grains. Adamiec (2005) found that, in the case of an inhomogeneous sample (where homogeneity is defined as all grains having the same OSL properties, such as decay form and thermal sensitisations), components observed

in LM-OSL curves of multi-grain aliquots may not accurately represent the trap structure of the quartz. Instead, they may represent a manifestation of heterogeneous luminescence properties, which could lead to erroneous conclusions. Variability in the luminescence signal of individual grains of quartz from the same samples is well established (e.g., Roberts et al., 1999; Duller et al., 2000; Adamiec, 2000; Yoshida et al., 2000, 2003; Bulur et al., 2002; Jacobs et al., 2003b, 2006b, 2008c).

5.1.2 Assessing the behaviour of the LM-OSL signal over multiple SAR measurement cycles

With the composition of the natural OSL signal generally known and the presence of a fast component confirmed, experiments were undertaken to assess the composition of the laboratory-irradiated OSL signal. To do this, four aliquots, consisting of ~500 grains of MR7, were bleached in natural sunlight for one week. They were then given a beta dose of 116 Gy, followed by a preheat of 260°C for 10 s, and then stimulated by linearly ramping the blue LEDs from 0 to 90% over 3600 s. Subsequent to the LM-OSL measurement, a test dose cycle was performed that consisted of a test dose of 11 Gy, a preheat of 220°C for 5 s, and a LM-OSL measurement for 3600 s. The first two aliquots (Aliquots 1 and 2) were not given a HOW and the other two aliquots (Aliquots 3 and 4) were given a HOW. This was repeated for a total of five measurement cycles, keeping the regenerative dose constant.

There were two main purposes in performing this experiment, which are addressed in the next two subsections. First, the constituent components that make up the OSL signal following a laboratory irradiation could be ascertained and compared to those that constitute the natural signal. This would identify the presence of any potentially thermally unstable components that may not be present in the natural signal due to trap instability over geological timescales, but that may be present in the laboratory-irradiated OSL signal (Jain et al., 2003; Singarayer and Bailey, 2003; Li and Li, 2006a; Jacobs et al., 2006a; Pawley et al., 2010). The aberrant effects of these thermally unstable components have been shown to be reduced by certain laboratory treatments (e.g., using a 220°C test dose cutheat and applying a HOW; Jacobs et al., 2006a). Second, this experiment would provide information regarding the effect of a HOW on the accumulation of signal over multiple SAR measurement cycles. This

could be achieved by comparing the shapes of LM-OSL curves from the same aliquots over multiple cycles of irradiation, preheating and optical stimulation. The results from the two aliquots for which a HOW was used could then be compared to those that did not include this additional step.

5.1.2.1 Assessing the constituent components of a laboratory-irradiated OSL signal

The first LM-OSL curves measured after sun-bleach, irradiation and preheat were analysed for each of the four aliquots (Figure 5.2). These LM-OSL curves were de-convoluted as described in Section 3.5. Results are presented in Table 5.2. Three of the four aliquots (Aliquot 1, 2 and 3) were best fitted with four components. The fourth aliquot (Aliquot 4) was best fitted with six components. All aliquots have four components in common, namely those represented by column A, C, D and F. A comparison of these components' PIC and *b* values with those in Table 3.3 indicates that these four components are likely the fast, medium, S2 and S4 (using the nomenclature of Jain et al., 2003). For Aliquot 4, the component represented by column B has not been reported in the literature, though it is generally similar to the component present in the natural signal represented by column B in Table 5.2. The component represented by column E for Aliquot 4 can be identified by its PIC and *b* values: they indicate that this component is a S3 component, which was also identified in the natural signal (column E in Table 5.2).

Table 5.2: De-convolution data for the laboratory-irradiated LM-OSL signals obtained for four aliquots of MR7. The components represented in the columns by letters are equivalent to those in Table 5.1.

		b values					
Aliquot	***N***	**A**	**B**	**C**	**D**	**E**	**F**
1	4	1.12		0.18	0.01		0.0005
2	4	1.20		0.12	0.01		0.0005
3	4	1.29		0.23	0.02		0.0006
4	6	1.39	0.81	0.21	0.04	0.007	0.0005
Average *b* (s^{-1})		**1.25**	**0.81**	**0.18**	**0.02**	**0.007**	**0.0005**
Average relative *b*		**1.00**	**0.59**	**0.15**	**0.02**	**0.005**	**0.0004**
Average PIC (cm^2)		**1E-17**	**8E-18**	**2E-18**	**2E-19**	**6E-20**	**5E-21**

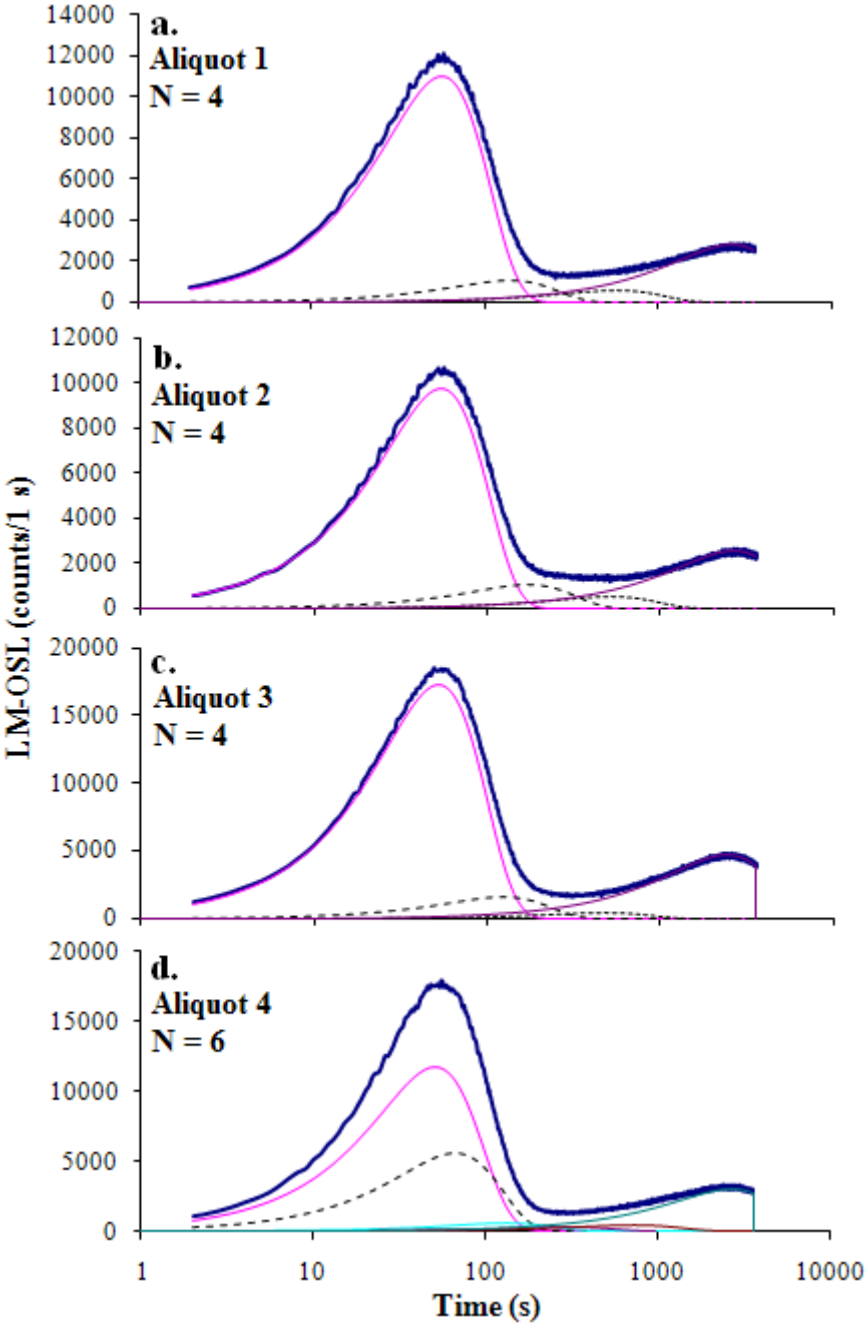

Figure 5.2: LM-OSL curves for four aliquots of MR7 following laboratory irradiation plotted on a linear-logarithmic scale. The background-subtracted LM-OSL is shown (in bold) with the fitted components underlying it.

5.1.2.2 Assessing the effect a of HOW on the LM-OSL signal

The second objective of this experiment was to assess the effect that a HOW had on the accumulation of OSL signal over the course of repeated cycles of irradiation, heating, and optical stimulation. To this end, all of the background-subtracted LM-OSL curves for each aliquot were normalised to their peak intensity and plotted together on a

linear-logarithmic scale (Figure 5.3a,c). In this way, any accumulation of OSL signal or changes in sensitivity in different components, indicated by changes in the shape of the LM-OSL curve with repeated SAR measurement cycles, could be examined. These changes could be compared between those aliquots whose SAR measurement procedure included a HOW (Figure 5.3c) and those aliquots whose measurement procedure did not (Figure 5.3a). When the HOW is included, the main LM-OSL peak (i.e., that of the fast component) consistently stays in the same position (with respect to measurement time) over repeated measurement cycles. Conversely, when no HOW is administered, the highest point of the main peak migrates to the right by as much at 12 s. This migration of the main peak suggests that when no HOW is administered, a slower component may accumulate under the fast component, thereby shifting the position of the main peak. A potential candidate for this slower component, underlying the main peak of the LM-OSL curve, is represented by column B in Table 5.2. In Figure 5.2d, this component can be seen underlying the later portion (i.e., the right side) of the main LM-OSL peak. If this component accumulates or sensitises proportionally more than the fast component, then the position of the main peak would shift towards the right.

The later portions of the LM-OSL curves show that slower components are accumulating over the course of each SAR measurement cycle. Moreover, due to the normalised nature of Figure 5.3 (a and c), it is apparent that the slower components are accumulating more than the fast component that comprises the main LM-OSL peak. Figure 5.3 (b and d) show point-by-point subtractions of the first regenerated LM-OSL curve and the final (fifth) regenerated LM-OSL curve (R_5 - R_1) from Figure 5.3 (a and c), respectively. These curves show that, although signal is accumulating in the later region of the LM-OSL curve when a HOW is employed, more signal accumulates when a HOW is not used. By calculating the area under each curve, the difference in signal accumulation can be gauged. There is approximately twice as much signal that accumulates in the later region of the LM-OSL curve over five measurement cycles when a HOW is not applied compared to when a HOW is used. The curves in Figure 5.3 (b and d) were then de-convoluted using the same procedure outlined in Section 3.5 with the aim of discerning the components in the LM-OSL signal that were accumulating. Figure 5.3b was best fitted using four components ($R^2 = 0.979$), namely

the S1, S2, S3 and S4. Figure 5.3d was best fitted using three components ($R^2 = 0.956$), namely the S2, S3 and S4.

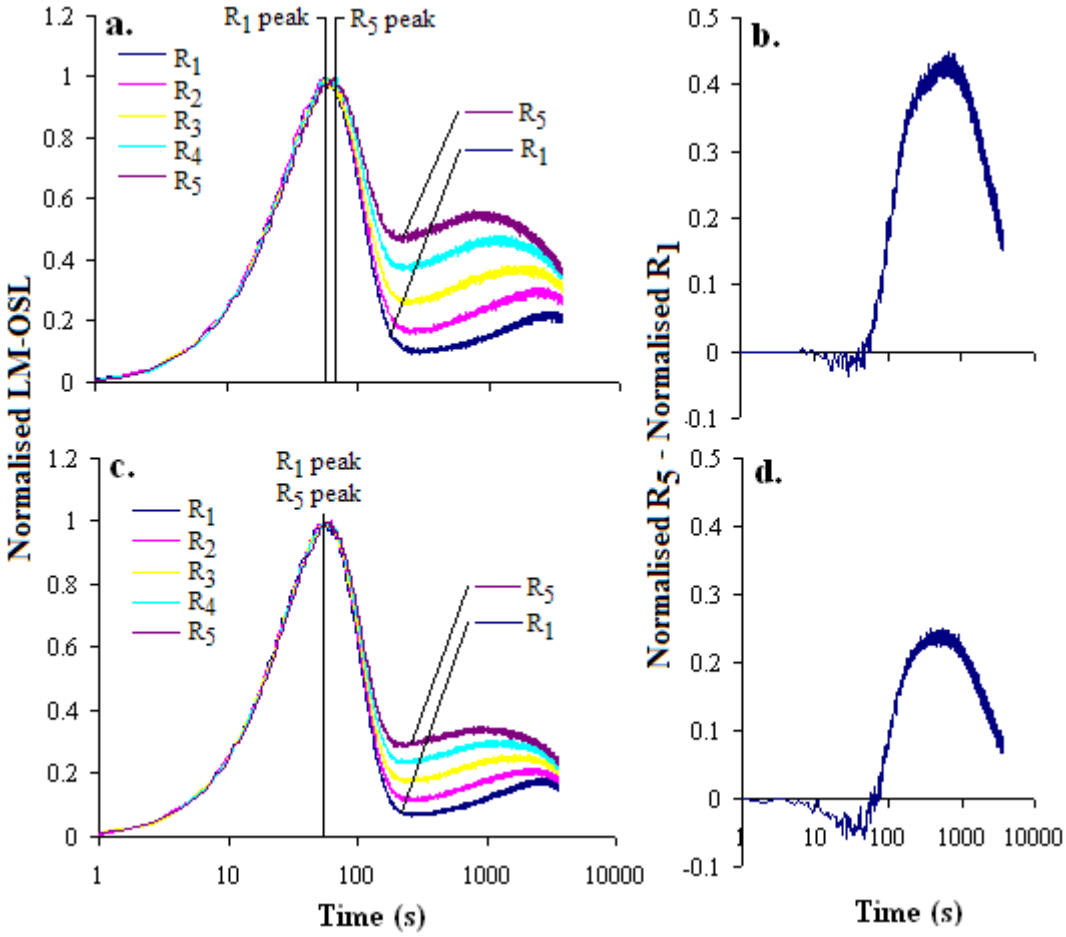

Figure 5.3: Background-subtracted LM-OSL measurements for an individual aliquot whose SAR procedure did not include a HOW (a) and an individual aliquot whose SAR procedure did include a HOW (c). Each curve (from progressive SAR measurement cycles with a regenerative dose of 116 Gy) is normalised to its peak intensity. (b) and (d) show the accumulation of LM-OSL signal over five SAR measurement cycles. The first normalised background-subtracted LM-OSL curves in (a) and (b) were subtracted (point-by-point) from the final curves (i.e., R_5 - R_1).

Results from these analyses suggest that the inclusion of a HOW in the regenerative-dose procedure for samples from Mumba is beneficial. The use of a HOW reduced the accumulation of signal in the slower components that make up the later region of the LM-OSL curve and completely eliminated the contribution from S1. The components that made up these accumulated signals included the S3 component, which has been reported to be thermally unstable (Singarayer and Bailey, 2003; Jain et al., 2003; Jacobs et al., 2006a). Over five regenerative cycles, these slow components accumulated twice as much in the aliquots whose measurement procedure did not

include a HOW. The HOW also reduced the extent of accumulation of signal in a slower component that underlies the main LM-OSL peak, closest to the fast component. This prevented migration of the main peak position over the course of multiple SAR measurement cycles. When a HOW was not included, the accumulation of signal under the main LM-OSL peak was observed as a shift of the peak towards the right, suggesting that the early portion of the CW-OSL curve may be affected as well.

5.1.2.3 Summary

This LM-OSL experiment provided important information regarding the composition and behaviour of the constituent components of the OSL signal of quartz from Mumba. First, it verified the presence of a fast component in the laboratory-irradiated OSL signal. This confirmed that the fast component was present in both the natural and laboratory-irradiated OSL signals, a feature that is necessary to successfully obtain a reliable D_e value using the SAR procedure (Murray and Wintle, 2000, 2003; Preusser et al., 2009). Second, this test showed that there is an accumulation of signal in the slower component region of the LM-OSL curve over the course of multiple SAR measurement cycles. This accumulating signal is best fitted with a S1, a S2, a thermally unstable S3 and a S4 component. Third, this test confirmed the usefulness of the addition of a HOW in the SAR procedure. The accumulation of signal in the S2, S3 and S4 components over the course of five measurement cycles was reduced by half and no S1 component accumulated when a HOW was included, compared to when it was not. Additionally, the position of the main LM-OSL peak stayed constant through all five measurement cycles when a HOW was administered, compared to the rightward shift in peak position observed when it was not applied. This indicates that, when a HOW is not included, a slower component may underlie and obscure the fast component.

The presence of multiple slow components, including a potentially thermally unstable component, suggests that a high temperature preheat combination (e.g., 260°C/220°C) is appropriate for quartz samples from Mumba (Murray and Wintle, 2003; Jain et al., 2003; Singarayer and Bailey, 2003; Jacobs et al., 2006a). In addition, the accumulation of slow components in the later portion of the LM-OSL signal, a feature that could complicate the measurement of the fast component during CW-OSL investigations, was substantially reduced when a HOW was included in the SAR

measurement cycle. This confirms the utility of this treatment in the SAR procedure for measuring quartz samples from Mumba.

Following the results summarised above, it was necessary to assess whether the SAR procedure was suitable for dose estimation using the OSL signal of quartz from Mumba. Therefore, a dose recovery test was performed, using only the de-convoluted LM-OSL fast component, to assess whether a known dose could be accurately measured in the laboratory with this procedure.

5.1.3 Dose recovery experiment using the fast component, isolated from the LM-OSL signal

Previous research has demonstrated that the fast component, isolated from LM-OSL measurements, can be used to obtain D_e estimates that are in agreement with those obtained using CW-OSL (Li and Li, 2006b). Li and Li (2006b) stated that the results from such LM-OSL SAR experiments can be checked using the same tests of SAR suitability as are used for CW-OSL SAR experiments, namely a recycling ratio test and a dose recovery test. Pawley et al. (2010) used curve fitting to isolate the fast component from an OSL signal that included a thermally unstable medium and S2 components to obtain ages that were in agreement with expected ages of up to ~450 ka.

To ensure that the fast component of quartz from Mumba was reliable as a chronometer, a dose recovery test was performed. Five aliquots of MR7, each consisting of ~500 grains, were bleached for at least three days in natural sunlight. Each aliquot was then given a laboratory irradiation of 122 Gy that was treated as a surrogate natural dose. A preheat of 260°C for 10 s was administered, followed by an LM-OSL measurement for 3600 s at 125°C. This was followed by a test dose cycle consisting of a 12 Gy irradiation, a preheat of 220°C for 5 s, and a LM-OSL measurement for 3600 s at 125°C, followed by a HOW. This procedure was repeated for regenerative doses of 61, 122, 183, 244 and a repeated dose of 61 Gy, which were used to build a dose-response curve. A 0 Gy regenerative dose was not included in this experiment. Each regenerative and test dose LM-OSL curve was de-convoluted as described in Section 3.5. *Method 2* of Appendix 2 was used to determine the number of components fitted to each curve. This ensured that the *b* value of the component being

compared would remain consistent for a given aliquot throughout the entire SAR procedure.

Following the de-convolution of each LM-OSL curve, the isolated fast components were used to obtain values of L_x/T_x for each SAR measurement cycle. The uncertainties estimated for both L_x and T_x values included a systematic error, a fitting error and an error related to counting statistics. A systematic error of 1% was used (see Section 3.3.1.2). A fitting error was produced for all components during the fitting procedure using the Sigmaplot software. The uncertainty related to counting statistics was estimated based on a modification of Equation 3 from Galbraith (2002). Galbraith (2002) addresses the quantification of statistical uncertainties for CW-OSL decay curves. This involves signals and backgrounds that are measured in fundamentally different ways than for LM-OSL curves. For the purposes of this LM-OSL study, the statistical uncertainties were calculated as:

$$rse(\hat{\mu}_s) = \frac{\sqrt{Y_0 + \overline{Y}}}{Y_0 - \overline{Y}} \qquad \text{Equation 5.1}$$

where $rse(\hat{\mu}_s)$ is the relative standard error for the counting statistics, Y_0 is the cumulative LM-OSL signal measured and $\overline{Y}$ is the sum of the estimated background count. This counting statistics uncertainty was added, in quadrature, to the systematic and fitting uncertainties to estimate the uncertainty on both the values of L_x and T_x. Dose-response curves were then built, on to which the values of L_x/T_x for the surrogate natural could be projected and interpolated on to the dose axis. Since a 0 Gy regenerative dose was not used, each dose-response curve was fitted with an additional L_x/T_x value of 0, which forced the curve through the origin.

Dose-response curves are presented in Figure 5.4 for the four aliquots for which dose-response curves could be constructed. One of the five aliquots was rejected due to instrumental malfunction during measurement of the LM-OSL signals. Results are somewhat ambiguous. The four remaining aliquots successfully recycled a duplicate regenerative dose, with a weighted mean recycling ratio of 0.99 ± 0.01. This suggests that, when the fast component is isolated, the test dose can successfully correct for any sensitivity changes that occurred over the course of multiple SAR measurement cycles.

However, the given dose (122 Gy) was underestimated for three aliquots and overestimated for one. In spite of this, the weighted mean dose estimate for the four aliquots, obtained using the CAM, is 111.4 ± 11.0 Gy with an overdispersion of 18 ± 7%. This corresponds to a weighted mean measured/given dose ratio of 0.92 ± 0.09, which is consistent with unity at 1σ.

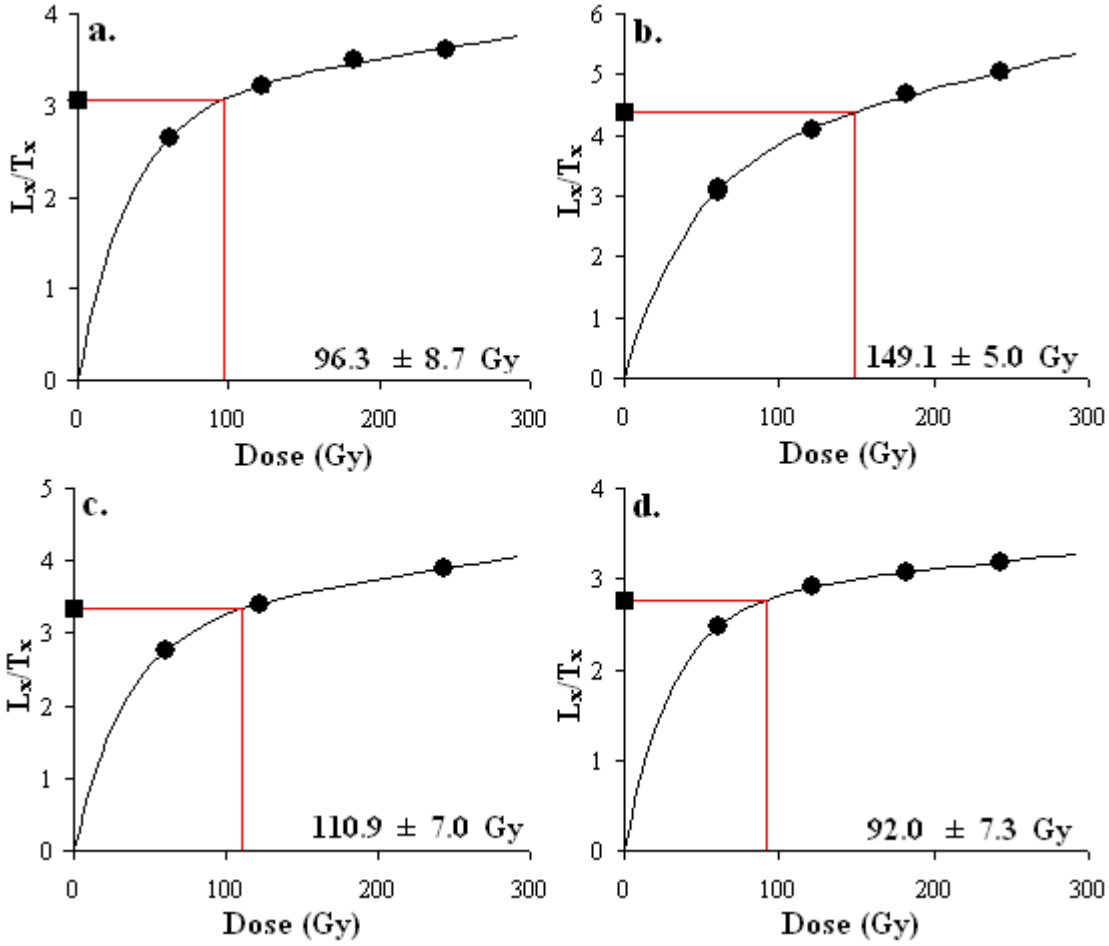

Figure 5.4: Dose-response curves built using the fast component, isolated using de-convoluted LM-OSL measurements. Curves are shown for the four aliquots for which curves could be constructed, along with the measured dose. Each curve was forced through the origin. The given dose was 122 Gy.

While the given dose was, on average, recovered successfully, a larger sample size would have made these results substantially more robust. It is a protracted process to measure and de-convolute LM-OSL curves and isolate the fast component from each natural, regenerative and test dose signal. In addition, there are several fundamental statistical limitations of such approaches (Adamiec, 2005; Bluszcz and Adamiec, 2006). Adamiec (2005) found that, in the case of an inhomogeneous sample (where

homogeneity is defined as all grains having the same OSL properties, such as decay form and thermal sensitisations), components observed in LM-OSL curves of multi-grain aliquots may not accurately represent the trap structure of the quartz, but may, instead, represent a manifestation of heterogeneous luminescence properties, which could lead to erroneous conclusions.

It is highly likely, given the large intra-sample variability in luminescence properties reported for single grains of quartz (e.g., Roberts et al., 1999; Duller et al., 2000; Adamiec, 2000; Yoshida et al., 2000, 2003; Bulur et al., 2002; Jacobs et al., 2003b, 2006b, 2008c), that multi-grain aliquots of quartz from Mumba are also inhomogeneous in their OSL behaviour on a single-grain level. This heterogeneity has been confirmed by the measurement and analysis of individual grains of quartz (see Section 5.2). Consequently, further multi-grain aliquots were not measured, and single grain investigations were undertaken.

The following section details the characterisation of the OSL behaviour of individual grains of quartz from Mumba. Large intra-sample variability in the OSL signal is demonstrated, suggesting that the identification of individual slower components in the LM-OSL signal from multi-grain aliquots of MR7 quartz does not necessarily reflect a physical property of the quartz.

5.2 Characterisation of the OSL signal of single grains of quartz

A major benefit of using single grains of quartz for OSL dating is that large numbers of grains can be investigated, providing the opportunity to assess and characterise the luminescence characteristics of many individual grains from the same sample (Roberts et al., 1999; Jacobs et al., 2003b, 2006b, 2008c). This allows for the identification and subsequent rejection of grains that do not possess the qualities needed to obtain a reliable D_e estimate using the SAR procedure. This latter point means that grains that may have led to relatively poor performances in multi-grain aliquot experiments can be identified and rejected from single grain datasets (Jacobs et al., 2006b).

Following the results of LM-OSL investigations presented in Section 5.1, the SAR procedure used to investigate single grains of quartz from Mumba included a regenerative/test dose preheat combination of 260/220°C and a HOW.

5.2.1 Characterising the types of quartz grains

In order to assess the variability in the OSL signal, individual quartz grains from sample MR6 were bleached in sunlight for at least 3 days, given a surrogate natural dose (120 Gy), preheated at 260°C for 10 s, and stimulated with the green laser for 2 s at 125°C. They were then given a test dose of 10 Gy, a test dose preheat of 220°C for 5 s, and stimulated with the green laser for 2 s at 125°C. Each test dose measurement was followed by the application of a HOW (40 s of blue LED stimulation at 280°C). Regenerative doses of 60, 120, 180, 240, 0 and a second 120 Gy dose were used to construct dose-response curves. An OSL-IR depletion ratio test (Duller, 2003) was also performed for each grain to check for feldspar contamination.

Individual grains of quartz from Mumba exhibited a wide range of different behaviours when put through the SAR measurement procedure. The array of various behaviours could generally be classified into five broad grain-types based on differences in their OSL decay curve shapes (Figure 5.5), extent of sensitisation of the OSL signal over multiple measurement cycles (insets to Figure 5.5), and dose-response curve shapes (Figure 5.6). Dose-response curves constructed by representative grains of the five types are presented in Figure 5.6. Decay curves from the same individual grains shown in Figure 5.6 are presented in Figure 5.5. The decay curves are those measured following the test dose, recorded during the first and final regenerative-dose cycles. The insets to Figure 5.5 show the test dose OSL signals (T_x) normalised to the first test dose measurement (T_N) as a function of SAR measurement cycle. These T_x/T_N plots show the change in OSL signal sensitivity as a function of measurement cycle. Although all three of the features discussed were used, the shape of the dose-response curve was the principal characteristic that was used to classify grain-types. In this section, the five general classes of grain-types that are prevalent at Mumba will be described, compared, and discussed. It is important to recognise the differences in behaviour of the various grain-types, so that reliable D_e values can be obtained for age calculation.

The first grain-type is the ideal type for D_e estimation using the SAR procedure. Figure 5.5a and Figure 5.6a show the OSL decay curves and the dose-response curve from a representative grain of this type. The OSL signal decays rapidly, reaching inst-

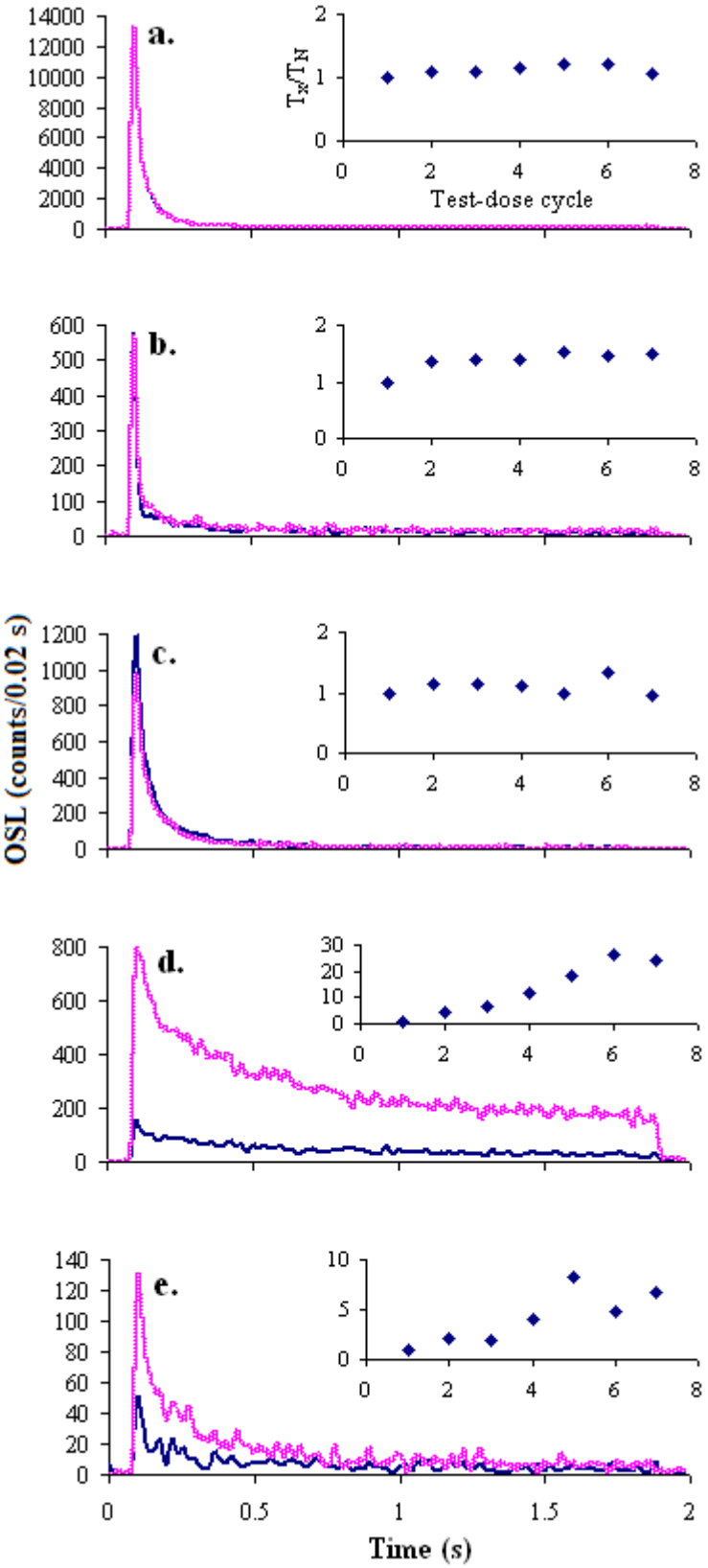

Figure 5.5: OSL decay curves for grains that are representative of the five general grain-types. The two decay curves were measured during the test dose cycle of the first (blue) and final (pink) regenerative-dose cycles. The inset plots show the ratio of test dose responses (T_x/T_N) as a function of measurement cycle for each grain to illustrate changes in sensitivity.

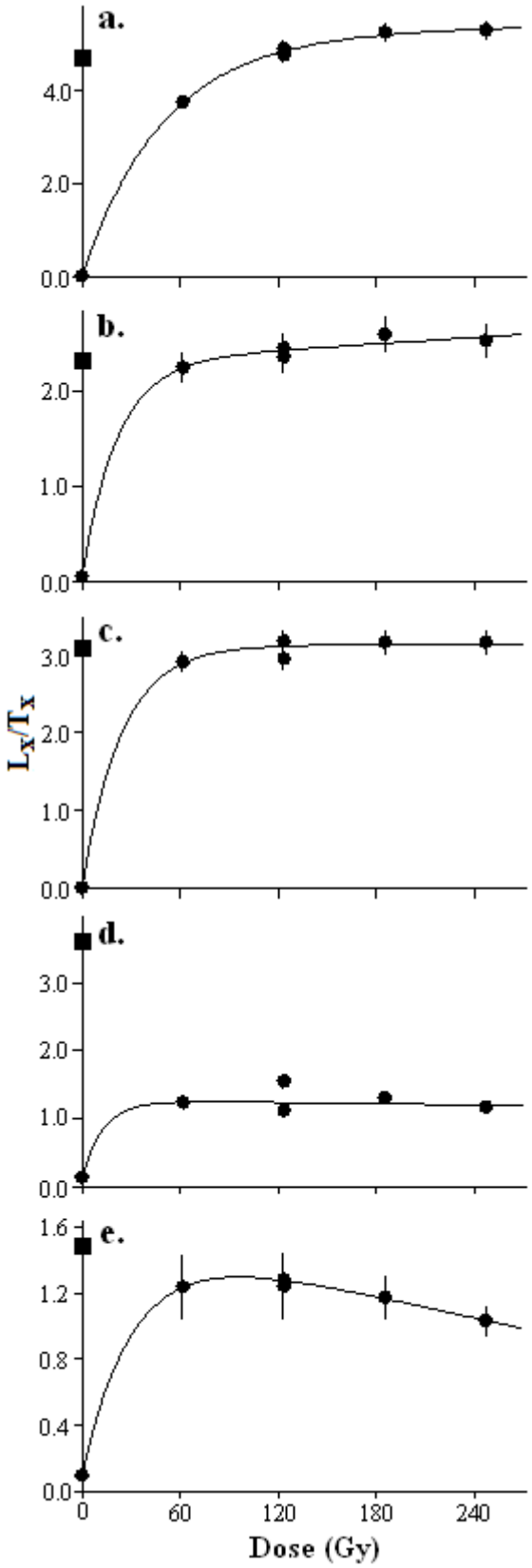

Figure 5.6: Dose-response curves from grains that are representative of the five general grain-types. These grains correspond to those presented in Figure 5.5.

rumental background within the first ~0.2 s of green laser stimulation, indicating that it is dominated by the fast component. The shape of the OSL decay curve does not change over the course of multiple SAR measurement cycles (Figure 5.5a), indicating that that fast component remains dominant and that slower components are not accumulating. Additionally, any sensitivity changes in the OSL signal are negligible, as seen by the T_x/T_N plot for which all ratios are close to unity (inset to Figure 5.5a). Any sensitivity changes that do occur are corrected for using the test-dose cycle, resulting in recycling ratios that are consistent with unity. The dose-response curves that are built for these grains can be fitted with a single saturating exponential function (Figure 5.6a), on to which the sensitivity-corrected natural signal (L_N/T_N) can be projected and interpolated onto the dose axis to obtain a D_e estimate. Ideally, the D_e estimate should be no more than twice the size of the D_0 value (Wintle and Murray, 2006). As discussed in Section 3.3.1.3, the D_0 value is a fitted parameter of a saturating exponential function that equates to the dose at which the OSL intensity reaches 63% of the saturation intensity.

The second type of grain has OSL decay curves and dose-response curves like those presented in Figure 5.5b and Figure 5.6b. A main feature of these grains that separates them from the first grain-type is that their OSL signals saturate at relatively low doses despite their dose-response curves requiring an additional linear term to describe the continual, low rate of growth in sensitivity-corrected OSL signal at higher doses (Figure 5.6b). This low-dose saturation can be quantified by the relatively low D_0 values (<25 Gy) when the dose-response curves resulting from grains of this type are fitted with a single saturating exponential function. Grains that have dose-response curves with these characteristics generally show changes in OSL sensitivity that are more substantial than those seen in the first grain-type (inset to Figure 5.5b). Although these grains experience changes in OSL sensitivity, they are generally able to successfully recycle a duplicate regenerative dose. However, since the OSL signal of grains of this type saturates at early doses, the duplicate regenerative dose is not a genuine test of reproducibility, since all regenerative dose points (e.g., 60, 120, 180 and 240 Gy in Figure 5.6b) are statistically consistent with one another. In these grains, therefore, the effectiveness of the sensitivity-correction is not being monitored using the recycling ratio test. In addition, many of these grains have OSL signals that decay more

slowly in response to optical stimulation than grains of the first type. This suggests that the OSL signal from these grains, while still mainly composed of a fast component, may be comprised of additional components to a larger extent than grains of the first type.

The third grain-type constitutes grains that have OSL signals that are fully saturated at relatively low doses, as evidenced by their very low D_0 values. The dose-response curves built using these grains have sensitivity-corrected regenerative-dose points that are equivalent to one another at higher doses (e.g., ~100 Gy in Figure 5.6c). Due to the early onset of signal saturation in these grains, finite D_e values usually cannot be obtained because the sensitivity-corrected natural signals (L_N/T_N) project on to the saturated region of the dose-response curve. Any projection of L_N/T_N on to this kind of dose-response curve can only result in a minimum D_e estimate. Grains of this type usually have OSL signals that are dominated by the fast component and are subject to some changes in sensitivity (inset to Figure 5.5c). The shape and rate of decay curves do not change over multiple measurement cycles (Figure 5.5c), suggesting that the slower components are not accumulating and interfering with the fast component. Like the second grain-type, the OSL signals from grains of this type are in saturation at very early doses. The recycling ratio test, thus, does not appropriately monitor the effectiveness of the sensitivity correction, even though these grains may be able to successfully recycle a duplicate regenerative dose.

The fourth grain-type has been referred to previously as 'Class 3' grains by Yoshida et al. (2000). The defining characteristic of this type of grain is that the L_N/T_N value is significantly greater than any of the sensitivity-corrected regenerative-dose points that were used to construct the dose-response curve, even at high doses (Figure 5.6d). Quartz grains of this type, which occur in high abundance at Mumba, have been shown to be prevalent in southern Africa (Jacobs et al., 2003b, 2006b, 2008a,c) and Australia (Yoshida et al., 2000). The majority of these Class 3-type grains at Mumba showed four further characteristics. First, the dose-response curves from these grains often do not grow, being either saturated at an early dose (Figure 5.6d) or are hyperbolic in shape. Second, the OSL decay curves produced by a grain of this type generally change shape considerably over the course of multiple SAR cycles (Figure 5.5d). Slow components appear to accumulate in the OSL signal, a feature that is manifested as a

slowing of the decay rate and a progressive increase in the later portions of the decay curve with successive measurement cycles (Figure 5.5d). Third, these grains often exhibit considerable changes in OSL sensitivity (inset to Figure 5.5d). The grain in Figure 5.5d (inset) showed a 26-fold (2600%) increase in test dose signal intensity over six measurement cycles. This is in contrast to changes in sensitivity over six measurement cycles of 20%, 50% and 30% for the grains presented in Figure 5.5a, b and c, respectively. Fourth, the substantial changes in sensitivity frequently are not appropriately corrected for by the test-dose cycle, as evidenced by the recycling ratios that are inconsistent with unity (Figure 5.6d). Nevertheless, a small proportion of these grains are able to recycle a duplicate regenerative dose within 2σ of the original value, although they generally have OSL signals that exhibit smaller changes in shape and sensitivity over the course of multiple measurement cycles. The poor recycling ratios and the inability of L_N/T_N values to intercept with the dose-response curves precludes the estimation of D_e values from these grains using the SAR procedure. Although the cause of Class 3-type grains is unknown, the presence of these grains has limited consequences for D_e estimation from single-grain measurements. However, the presence of bright Class 3-type grains in a multi-grain aliquot may compromise the reliability of the resulting D_e estimate (Yoshida et al., 2000).

Grains of the fifth type showed a decrease in both absolute and sensitivity-corrected OSL intensity with increasing radiation doses, resulting in dose-response curves that exhibit a hyperbolic shape. This anomalous behaviour has previously been reported elsewhere in the literature for quartz grains from Australia (e.g., Roberts et al., 1999) and South Africa (e.g., Jacobs et al., 2008c). Dose-response curves from grains that are representative of this type are presented in Figure 5.6e and Figure 5.7. For Mumba, the defining feature of grains of this type was the paradoxical condition of higher regenerative-dose points having sensitivity-corrected OSL values lower than those obtained using smaller regenerative doses. The dose-response curves constructed from grains of this type, however, turned hyperbolic at varying doses. This is illustrated in Figure 5.7, which presents the dose-response curves and associated decay curves of three different grains of this type. The low-dose portion of the dose-response curves from these grains often grew before turning hyperbolic (Figure 5.7d and f). For other grains, the lowest regenerative dose (60 Gy) resulted in the largest sensitivity-corrected

OSL signal, and each successive regenerative dose resulted in progressively smaller sensitivity-corrected OSL signals. This resulted in a dose-response curve that appeared to decrease with increasing dose (Figure 5.7b).

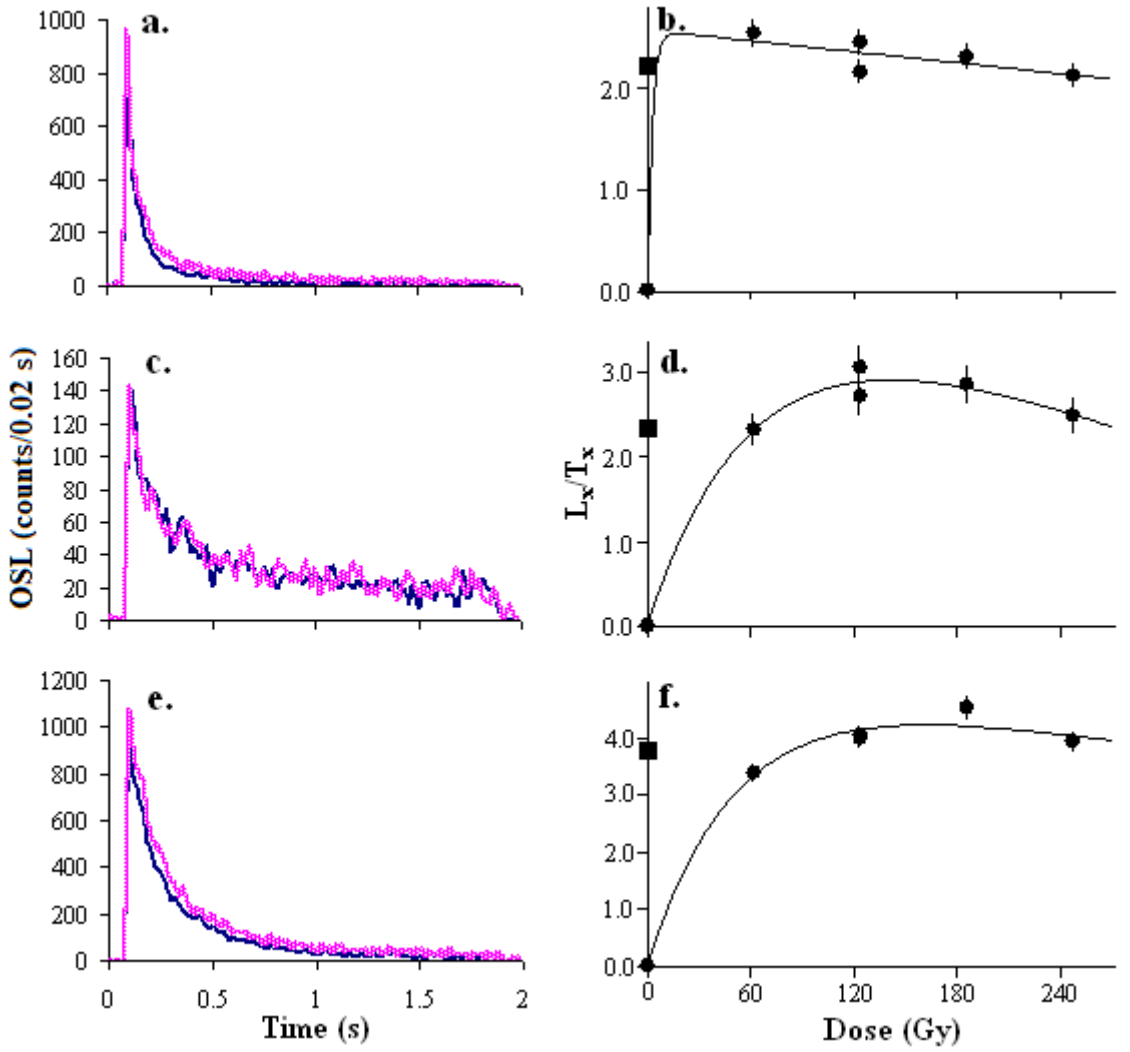

Figure 5.7: OSL decay curves (left column) and dose-response curves (right column) from three individual grains of the fifth grain-type. The two decay curves in each plot in the left column were measured during the test dose cycle of the first and final regenerative-dose cycles. Each plot in the right-hand column corresponds to its adjacent plot in the left-hand column. These grains show dose-response curves that turn hyperbolic at varying regenerative doses.

Generally, the OSL signal from grains of this type decayed slowly during stimulation with the green laser (Figure 5.5e and Figure 5.7c and e). This suggests that there is a substantial contribution to the total OSL signal from one or more slower components. In addition, the shapes of the decay curves generally remained unchanged over the course of multiple measurement cycles, despite the substantial sensitivity

changes that were often observed. These changes in sensitivity often commenced with increases on the order of 100% between the natural and first regenerative dose cycles (e.g., inset to Figure 5.5e), followed by further increases or decreases in sensitivity. The effectiveness of the sensitivity-correction cannot be appropriately assessed in these grains, however, since their OSL signal does not respond to dose in a predictable way. The sensitivity-corrected OSL signals for the duplicate regenerative dose is statistically consistent with those of the preceding and succeeding regenerative doses for the grains presented in Figure 5.6d and Figure 5.7b and 5.7d. The recycling ratio test, therefore, is not an appropriate check for reproducibility in grains of this type.

5.2.2 Discussion

As mentioned in the introduction to this section, it is imperative that the differences in behaviour of different types of grains are recognised so that reliable D_e estimates can be obtained and used for age calculation. Fortunately, many grains that posses aberrant OSL characteristics can be identified and removed from the datasets by applying a standard range of objective rejection criteria (Jacobs et al. 2003b, 2006a). Several of these criteria were introduced in Section 3.3.2, namely the recycling ratio test, the recuperation check and the OSL-IR depletion ratio test. Additionally, grains that have weak test dose OSL signals (i.e., the initial intensity of a grain's T_N signal is less than three times its background intensity) were eliminated in this study. This removes grains that produce no or very dim luminescence from the dataset. Grains were also rejected if their L_N/T_N values did not intercept with the fitted dose-response curve; an estimate of the D_e cannot be made for such grains. This final standard rejection criterion precludes all Class 3-type grains (fourth grain-type) and many saturated grains (third grain-type) from being included in the dataset. As a result of these rejection criteria, grains that are unsuitable for the D_e estimation using the SAR procedure and Class 3-type grains, regardless of their prevalence in a sample, should not have an effect on the sample's D_e distribution. It is important to emphasise that grains are rejected due to their aberrant physical properties, not on their estimates of D_e. The latter cannot be obtained with confidence from grains that exhibit the malign behaviours that are screened for using these criteria (Jacobs et al., 2006a). However, two features are not monitored for using standard rejection criteria: namely, the onset of signal

saturation and the presence of grains of the fifth type. The former feature will be briefly discussed in the following paragraph and further explored in Section 5.3.3. The latter feature will be discussed in the remainder of this section.

The dose at which an OSL signal, dominated by the fast component, saturates is a major limitation of OSL dating. This is because the fast component commonly saturates at relatively low doses (Wintle and Murray, 2006). Given the relatively high environmental dose rates for samples from Mumba (~2–3 Gy/ka, see Table 6.1, natural doses in excess of 100 Gy will accrue after just ~30–50 ka of burial. This is uncomfortably close to the saturation limit observed for the first two grain-types and above the saturation limit of the third. When these first three grain-types are compared, it is clear that they share marked similarities. All three have OSL signals that are mainly dominated by the fast component and have relatively small changes in sensitivity when regenerated. The major difference is the dose at which their OSL signals begin to saturate. Grains of the third-type will normally be rejected outright, due to the inability of their sensitivity-corrected natural signals to intersect the non-saturated portion of the dose-response curve, preventing D_e estimation. A point to emphasise is that all three of these grain-types are characterised as having relatively well behaved OSL behaviours, with varying levels of saturation. Consequently, the D_0 value could be used as a means of quantifying grains that saturate at low doses, so as to remove them from the D_e dataset for a sample. Reasons to support such a rejection criterion for grains from Mumba will be discussed further in Section 5.3.3.

Unlike the first three grain-types, grains of the fifth-type, which were particularly common in samples from Mumba when higher doses were investigated (see Section 5.3.2), exhibit a suite of aberrant OSL behaviours. The hyperbolic shape of their dose-response curves was often caused by a decrease in the absolute OSL signal at higher doses relative to lower doses. Put another way, the decrease in regenerative dose points (L_x/T_x) at higher doses was often the result of a decrease in L_x and not an increase in T_x. The effectiveness of the test dose cycle to appropriately correct for sensitivity changes also cannot be assessed, even though grains of this type often produce recycling ratios that are consistent with unity. Although the origin of this aberrant behaviour is unknown, it is an unwanted property of the dose-response curve that sheds doubt on the reliability of D_e values obtained from these grains. Bailey

(2004) suggested that erroneous dose-response curves may be generated in the laboratory because of difference in the rate at which OSL traps are filled in nature compared to in the laboratory. As a result, he recommended delivering laboratory irradiations as multiple small doses (e.g., as 10 Gy pulses), separated by heat treatments (e.g., cutheat of 240°C), to more closely mimic the natural dose rate. This 'pulsed-irradiation' technique will be discussed further in the following section as a possible means of reducing the proportion of grains with hyperbolic dose-response curves.

5.2.3 Overview of the pulsed-irradiation technique

5.2.3.1 The case for pulsed-irradiation

Bailey (2004) and Bailey et al. (2005) suggested, modelled and tested the method of pulsed-irradiation as a technique for overcoming dose-rate effects in quartz. These dose-rate effects arise from the disparity between the environmental dose rate (on the order of ~3 Gy/ka, or ~9 x 10^{-11} Gy/s, for samples from Mumba) and the rate at which laboratory irradiations are given (~0.08 Gy/s). In nature, the low dose rate ensures that the concentration of thermally unstable charge-trapping centres remains consistently low. By contrast, the high dose rate used in the laboratory keeps these thermally unstable traps filled. The occupancy of these thermally unstable centres following laboratory irradiation alters the natural distribution of thermally stable and unstable traps, resulting in increased competition among those traps responsible for OSL (Bailey, 2004). Consequently, the OSL output following a high laboratory irradiation will be lower than the OSL output following an environmental irradiation of the same magnitude. This causes the sensitivity-corrected OSL signal to be lower at high laboratory doses, which can result in the measured D_e being an overestimate of the true burial dose (Bailey, 2004). Several previous studies have concluded that dose-rate effects in quartz are negligible. Wallinga et al. (2002) experimentally concluded that dose-rate (shallow trapping) effects are not significant in quartz. Alternatively, the theoretical approach used by Banerjee et al. (2002), using the model of Bailey (2001), concluded that there is no significant effect on quartz luminescence when the dose rate is varied over two orders of magnitude (0.001–0.1 Gy/s). However, as noted by Bailey (2004), the difference in dose rates modelled by Banerjee et al. (2002) is too small to

predict effects arising from the actual difference between laboratory and environmental dose rates (i.e., nine orders of magnitude).

Bailey (2004) modelled the OSL response arising from irradiations at rates of ~1 Gy/s (simulated laboratory dose rate) and ~1 Gy/ka (~3 x 10^{-11} Gy/s; simulated natural dose rate). He reported that the laboratory dose response was lower than the simulated environmental dose response, resulting in an overestimate of the D_e. These effects are magnified for larger doses. The cause for this dose-rate effect was surmised to be an increase in competition for electrons during laboratory irradiations. Increased competition resulted from an increased concentration of holes at the R_1 centre, a thermally unstable recombination centre (E = 1.43 eV compared to E = 1.7–2.6 eV for the main OSL trap) that is effectively empty at environmental dose rates due to the slow flux of holes into the centre being equal to the slow thermal de-trapping rate (Bailey, 2004; Bailey et al., 2005). In contrast, during laboratory irradiations, the flux of holes is ~10 orders of magnitude greater than in nature, resulting in a higher concentration of holes trapped in the R_1 centre, which in turn results in stronger competition for free electrons (Bailey, 2004). It is this increased competition from the R_1 centre that reduces the number of free electrons that can access OSL traps, resulting in a smaller luminescence output per unit dose. It is impractical to administer laboratory doses at environmental dose rates to avoid these dose-rate effects. Alternatively, by administering laboratory irradiations in 10 Gy pulses (low enough to not saturate the R_1 centre) separated by cutheats of 240°C (to reduce the concentration of the R_1 centre), the thermally unstable centres are kept at a low concentration and the effects of competition are reduced, thus allowing a more natural distribution of free electrons (Bailey, 2004; Bailey et al., 2005). As an aside, successive cutheats of 240°C were shown to produce no extra thermal erosion of the OSL signal beyond that of the administered preheat of 260°C for 10 s (Bailey et al., 2005).

Simulations (Bailey, 2004) and experiments on samples from a wide geographic range (Bailey et al., 2005) showed that when individual aliquots were used to measure the natural signal and build multiple dose-response curves (first using single-irradiation, then using pulsed-irradiation), the resulting curves using a single-irradiation procedure were consistently lower than those resulting from a pulsed-irradiation procedure for doses above ~40 Gy (e.g., Figure 5.8). The D_e values estimated using the pulsed-

irradiation dose-response curves were consistently lower and less scattered than those estimated using the single-irradiation curves. This feature has implications for a major prediction of the model of Bailey (2004), namely the existence of Class 3-type behaviour (though he does not use this term to refer to the behaviour). When a single-irradiation SAR procedure was used, this behaviour was observed for both simulations (Bailey, 2004) and experiments (Bailey, 2004; Bailey et al., 2005). For one aliquot in the experiment described above (Liwa/pit/10), the sensitivity-corrected natural signal exhibited Class-3 type behaviour for the dose-response curve constructed using a single-irradiation procedure, but intersected the curve when pulsed-irradiation was employed to construct the dose-response curve (Figure 12 in Bailey et al., 2005).

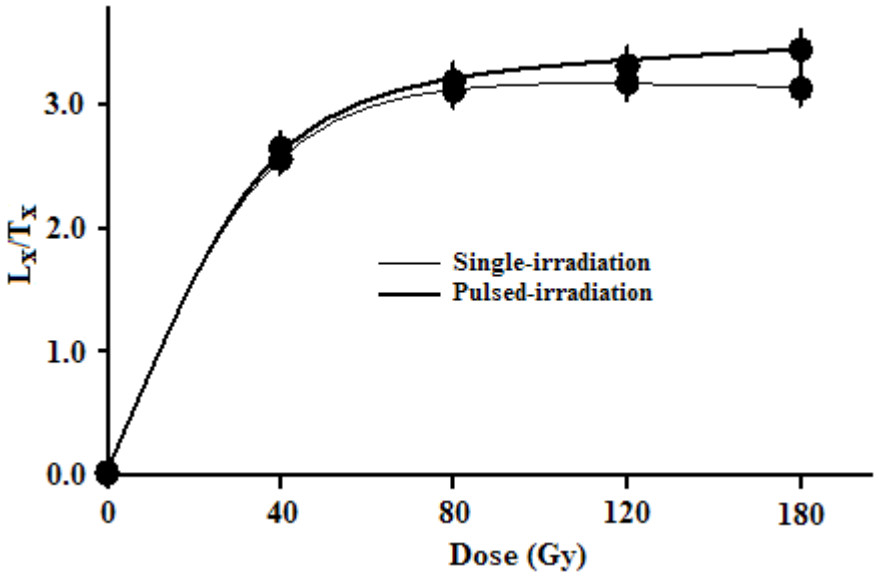

Figure 5.8: Dose-response curves constructed for the same grain of MR6 that was bleached in sunlight. The grain was measured using two back-to-back SAR procedures that were identical except for the mode of dose delivery. In the first the regenerative doses were administered using a single-irradiation technique and in the second the regenerative doses were administered using a pulsed-irradiation technique. Regenerative and test dose preheats of 260°C for 10 s and 220°C for 5 s were used, in addition to the application of a HOW.

5.2.3.2 Pulsed-irradiation application

The ability of the pulsed-irradiation technique to lift the higher dose region of the dose-response curve (relative to dose-response curves built using single-irradiation) could potentially reduce the effects of low-dose saturation and hyperbolic dose-response

curve shape: aberrant properties that were frequently observed during investigations of single grains of quartz from Mumba. Consequently, dose recovery experiments were performed to compare single-irradiation results with pulsed-irradiation results (Section 5.3). The pulsed-irradiation technique, as applied to single grains of quartz from Mumba, involved delivering regenerative doses in alternating cycles of 10 Gy pulses and 240°C cutheats (Table 5.3).

Table 5.3: Step-by-step outline of the modified SAR procedure (see Table 3.2) using pulsed-irradiation to administer the laboratory doses (Bailey, 2004). All laboratory doses were applied in 10 Gy pulses (step 7) followed by a cutheat of 240ºC (step 8). This was repeated *d* times so that the intended regenerative dose was administered (e.g., if the intended regenerative dose is 120 Gy, *d* = (120/10) - 1 = 11). A HOW was applied subsequent to the measurement of each test dose.

Step	Treatment	Name
1	Preheat: 160 to 300°C	
2	Optical stimulation: 40 s at 125°C	L_N
3	Test dose	
4	Cutheat: 160°C to <preheat	
5	Optical stimulation: 40 s at 125°C	T_N
6	Optical stimulation: 40 s at 280°C	HOW
7	10 Gy laboratory dose	
8	Cutheat: 240°C	
9	repeat steps 7 and 8 *d* times	
10	Preheat (identical to step 1)	
11	Optical stimulation: 40 s at 125°C	L_x
12	Test dose	
13	Cutheat (identical to step 4)	
14	Optical stimulation: 40 s at 125°C	T_x
15	Repeat steps 6 to 15	

d = (intended regenerative dose/10) - 1

5.3 Single-grain dose recovery experiments

One way of investigating the effects of various OSL characteristics, such as dose saturation, on the determination of D_e values is to perform dose recovery tests (Galbraith et al., 1999; Wintle and Murray, 2006). These experiments can also be used to test and refine modifications to the conditions used in the SAR procedure and methods of data analysis most appropriate for an individual sample. This will enable improved reliability in D_e estimation. If the chosen experimental conditions and methods of data analysis are appropriate for the sample being investigated, then the

measured/given dose ratio should be consistent with unity. In this study, dose recovery tests were the principal means used to assess the suitability of various modifications to the experimental conditions of the SAR procedure.

Four dose recovery experiments, using four subsets of sun-bleached quartz grains of MR6 (Table 5.4), are described in this section. After grains of quartz were bleached in natural sunlight for at least three days, a surrogate natural dose of either 40 or 120 Gy was given in the laboratory using the $^{90}Sr/^{90}Y$ beta source built into the Risø TL/OSL reader. The larger dose is analogous to D_e values that were expected for many of the Mumba samples. However, this dose lies close to the saturation limit of many grains from Mumba, which may adversely influence the accurate recovery of the given dose. Thus, the smaller dose was used so that the appropriateness of the measurement conditions could be established in the absence of any complications resulting from the early onset of signal saturation. Subsets of grains for each surrogate natural dose were then measured using the SAR procedure. For one subset, the surrogate natural and regenerative doses were delivered in uninterrupted, single applications – that is, in the conventional manner (subsets 1 and 3 in Table 5.4). For the other subset, the surrogate natural and regenerative doses were delivered using the pulsed-irradiation technique (subsets 2 and 4 in Table 5.4). Results were then compared.

Table 5.4: Description of four subsets of sun-bleached quartz grains from MR6 that were used for the four dose recovery experiments described in Section 5.3. Note that the surrogate natural and regenerative doses were delivered using the prescribed irradiation technique.

	Subset			
	1	2	3	4
Surrogate natural dose (Gy)	40	40	120	120
Irradiation technique	single	pulsed	single	pulsed
Number of grains meausred	500	500	700	700

Several objectives could be met by performing these dose recovery experiments in this way. First, the appropriateness of using both single-irradiation and pulsed-irradiation techniques in the SAR procedure to obtain a known dose was assessed (Section 5.3.1). Second, the ability of the pulsed-irradiation technique to overcome the malign properties of quartz from Mumba was investigated. These properties included the low doses at which the OSL signal saturates, the presence of Class 3-type grains,

and the presence of grains that produce hyperbolic dose-response curves. Third, these tests were used to refine the criteria used to analyse single-grain data, enabling the identification and rejection of grains that would be incapable of obtaining reliable D_e values (Section 5.3.3).

5.3.1 Assessing the suitability of single- and pulsed-irradiation techniques at lower doses during the SAR procedure

To assess the suitability of the SAR procedure using the conventional irradiation technique and without complications caused by the early onset of saturation, a dose recovery test was performed using a lower dose. A set of 500 grains was bleached in natural sunlight and given a surrogate natural dose of 40 Gy. Grains were then preheated to 260°C for 10 s and stimulated with the green laser for 2 s at 125°C. A test dose cycle was then performed consisting of a 10 Gy irradiation, a 220°C preheat for 5 s, and an optical stimulation for 2 s at 125°C using the green laser. The measurement of each test dose was followed by the application of a HOW. The sensitivity-corrected OSL responses to regenerative doses of 40, 10, 60, 80 and 0 Gy and a duplicate 40 Gy dose were used to construct dose-response curves. An OSL-IR depletion ratio test was also performed.

Seventy-two grains out of the 500 measured (14.4%) passed all tests of SAR suitability (see Section 3.3.2 for a description of tests) and produced dose estimates. Of these 72 grains, four (5.6%) were of the fifth grain-type (i.e., had an OSL signal that decayed slowly and a hyperbolic dose-response curve shape). Additionally, 16 grains (3.2%) passed all tests of SAR suitability, but exhibited Class 3-type behaviour, preventing dose estimation. Despite the malign dose-response curve shapes of ~5% of the grains for which doses could be estimated, the weighted mean measured dose from the 72 dose estimates was 42.7 ± 1.6 Gy, recovering the given dose within 2σ. This corresponds to a measured/given dose ratio of 1.07 ± 0.04. However, the spread in the 72 individual dose estimates is larger than expected, given the size of their measurement errors. The distribution of dose estimates is presented in Figure 5.9a. The overdispersion value for the distribution, calculated using the CAM, is 27 ± 3%. This value is larger than many others reported in the literature for quartz samples under controlled laboratory conditions (e.g., Roberts et al., 2000; Thomsen et al., 2005;

Galbraith et al., 2005; Jacobs et al., 2006b; Arnold and Roberts, 2009). The large spread in the dose distribution suggests that the given dose was unable to be recovered using some of the grains, despite the grains passing the standard rejection criteria.

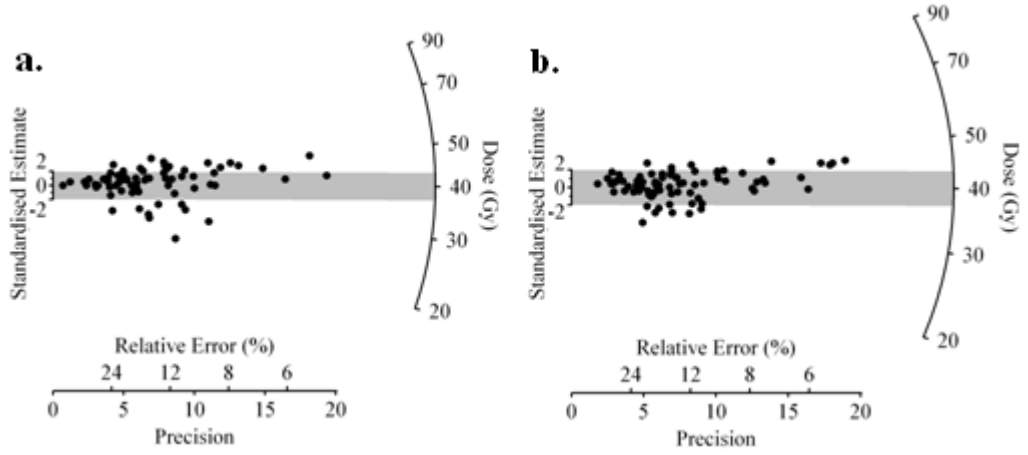

Figure 5.9: Dose distributions from dose recovery tests on single grains of quartz of MR6 displayed in radial plots, which are centred on the surrogate natural dose (40 Gy). a, Dose recovery in which laboratory doses were delivered in the conventional single-irradiation fashion. The measured/given dose ratio was 1.07 ± 0.04 with an overdispersion of 27 ± 3%. b, Dose recovery in which laboratory doses were delivered using the pulsed-irradiation technique. The measured/given dose ratio was 1.04 ± 0.02 with an overdispersion of 14 ± 2%.

To investigate the appropriateness of the SAR procedure when laboratory doses were delivered using the pulsed-irradiation technique, a second dose recovery experiment was performed. A group of 500 grains of MR6 were bleached in natural sunlight for at least three days. The surrogate natural dose of 40 Gy was then delivered in a pulsed fashion; that is, in four successive pulses of 10 Gy irradiations alternated with 240°C cutheats. The low surrogate natural dose would not only limit the effects of the early onset signal-saturation, it would also reduce any dose-rate effects resulting from increased competition from the R_1 centre. This allowed the SAR measurement procedures to be tested without complications related to these two features. Grains were then preheated at 260°C for 10 s and stimulated with the green laser for 2 s at 125°C. This was followed by the application of a 10 Gy test dose, a 220°C preheat for 5 s, and an optical stimulation of 2 s at 125°C using the green laser. Each test dose cycle was immediately followed with the application of a HOW. All regenerative doses (40, 10, 60, 80, 0 and a duplicate 40 Gy dose) were administered using the pulsed-irradiation technique. The experimental conditions for this dose recovery test were identical to

those described at the beginning of this section, with the sole exception of the method of delivering laboratory doses to the grains.

Results from this experiment are similar to the results for the corresponding single-irradiation counterpart. Four grains of the 500 measured (0.8%) passed all tests of SAR suitability but exhibited Class 3-type behaviour, preventing dose estimation. Seventy-eight grains (15.6%) proved suitable for the SAR procedure by passing all rejection criteria and producing dose estimates. Of these, four (5.1%) grains were of the fifth grain-type (i.e., had a hyperbolic dose-response curve shape). The weighted mean measured dose from the 78 grains, which recovered the given dose within 2σ, was 41.2 ± 0.9 Gy with an overdispersion of 14 ± 2%. This corresponds to a measured/given dose ratio of 1.04 ± 0.02. Although both the proportion of accepted grains and the measured/given dose ratios were similar to those obtained for the single-irradiation dataset, the spread in the dose estimates in this 'pulsed' dataset was substantially less. Additionally, the estimated overdispersion value was similar to other values reported in the literature for a single population of well bleached quartz grains (e.g., Roberts et al., 2000; Thomsen et al., 2005; Galbraith et al., 2005; Jacobs et al., 2006b; Arnold and Roberts, 2009).

These results indicate that a SAR procedure using the pulsed-irradiation technique can recover a low laboratory dose (40 Gy) at least as well as a SAR procedure using conventional single-irradiation. The low proportion of the fifth grain-type in both the 'pulsed' and 'non-pulsed' dose recovery experiments also suggests that hyperbolic dose-response curves may be associated with higher doses and an early onset of OSL signal saturation. Consequent to the satisfactory results from these dose recovery tests, a second set of experiments were performed using a higher surrogate natural dose and higher regenerative doses. The following section will assess the effects of the two irradiation techniques on the prevalence and behaviour of grains with low saturation levels and hyperbolic dose-response curves.

5.3.2 Assessing the suitability of single- and pulsed-irradiation techniques at higher doses during the SAR procedure

The dose recovery experiment described in the previous section showed that single grains of quartz from Mumba were suitable for the application of the SAR

procedure to accurately obtain a 40 Gy radiation dose. Consequently, a second set of dose recovery experiments was conducted to assess the ability of single grains to accurately measure a higher given dose, namely one that is nearer to the expected burial doses for many samples from Mumba. The first dose recovery test was performed on 700 single grains of MR6. The grains were bleached for at least three days in natural sunlight before being given a surrogate natural dose of 120 Gy as a single, uninterrupted, irradiation. The grains were then preheated to 260°C for 10 s and stimulated with the green laser for 2 s at 125°C. This was followed by a test dose cycle that included a 10 Gy irradiation, a preheat of 220°C for 5 s, and an optical stimulation for 2 s at 125°C with the green laser. The measurement of each test dose was immediately followed by the application of a HOW. The dose-response curves were constructed using the sensitivity-corrected OSL signals following regenerative doses of 120, 60, 180, 240, 0 Gy and a duplicate 120 Gy dose, which were delivered in the single-irradiation fashion. An OSL-IR depletion ratio test was also performed.

Many of the measured grains were saturated, with only 3.7% (n = 26) passing standard rejection criteria and resulting in finite dose estimates. The dose distribution of the 26 grains for which dose estimates were obtained is presented in Figure 5.10a. The dose estimates are overdispersed by 30 ± 6%, and produced a weighted mean dose estimate of 89.8 ± 6.6 Gy. This corresponds to a measured/given dose ratio of 0.75 ± 0.06, which is significantly different from unity and underestimates the given dose by ~25%.

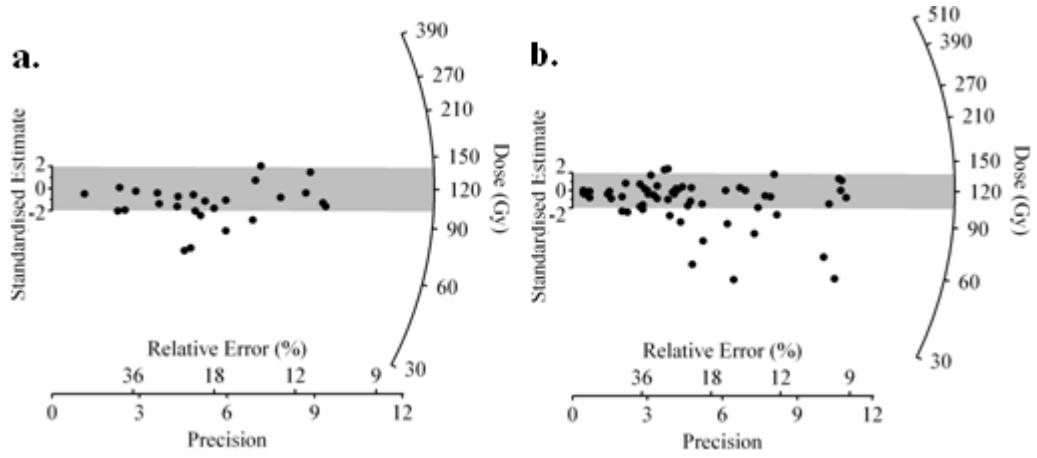

Figure 5.10: Dose distributions from dose recovery tests on single quartz grains of MR6 using standard rejection criteria. The data is displayed in radial plots that are centred on the given dose (120 Gy). a, Single-irradiation. b, Pulsed-irradiation.

A conspicuous characteristic of the dataset is that ~77% of grains that produced dose estimates (n = 20) were of the third or fifth grain-type; that is, they had completely saturated or hyperbolic dose-response curves. These grains produced dose estimates because their L_N/T_N values intercepted the dose-response curves in the low-dose region. Additionally, of the grains that successfully passed the standard rejection criteria (n = 36), dose estimates could not be obtained for 28% (n = 10) of the grains because they exhibited Class 3-type behaviour. Only six of the grains that passed standard rejection criteria and produced dose estimates (23%) were of the first grain-type; that is, their dose-response curves continued to grow at higher regenerative doses. When only these six grains are considered, the given dose is successfully recovered with a weighted mean of 123.3 ± 11.4 Gy (12 ± 11% overdispersion), corresponding to a measured/given dose ratio of 1.03 ± 0.09. This result was encouraging, although several factors detracted from its apparent success. First, the large uncertainty in the measured/given dose ratio is the result of the large spread in estimated doses, which, ranged from 80 to 161 Gy. Second, the very low rate of recovery (0.8% of all grains measured) means that accepting only grains that produced dose-response curve that consistently grow at higher regenerative doses would require a large amount of instrument time.

A second dose recovery test was performed to assess the effects of using the pulsed-irradiation technique on the behaviour of grains at higher doses. An aim of this investigation was to discern whether this technique could be used to offset the effects of early signal saturation and hyperbolic dose-response curve shape. A group of 700 grains of MR6 were bleached in sunlight for at least three days before being given a surrogate natural dose of 120 Gy, delivered in a pulsed fashion (i.e., 10 Gy pulses interspersed with 240°C cutheats). Grains were then given a 260°C preheat for 10 s before being stimulated with the green laser for 2 s at 125°C. The subsequent test dose cycle was comprised of a 10 Gy irradiation, a 220°C preheat for 5 s, and an optical stimulation for 2 s at 125°C with the green laser. This was immediately followed by the application of a HOW. The sensitivity-corrected OSL signal following regenerative doses of 120, 60, 180, 240 and 0 Gy and a duplicate 120 Gy dose, delivered using the

pulsed-irradiation technique, were used to construct dose-response curves. An OSL-IR depletion ratio test was also administered.

Fifty-eight grains (8.3%) were deemed suitable for dose determination, producing a weighted mean of 91.7 ± 6.5 Gy, with an overdispersion of 45 ± 6%. The dose distribution is presented in Figure 5.10b. This corresponds to a measured/given dose ratio of 0.77 ± 0.05. These results are similar to those of the corresponding single-irradiation dose recovery experiment, in that the given dose is underestimated and the overdispersion is high. Despite these similarities, several features of the 'pulsed' dose distribution are improved. The proportion of grains of the third and fifth grain-type (i.e., grains with saturated or hyperbolic dose-response curves) was substantially decreased when laboratory irradiations were delivered in a pulsed fashion. Only 43% of grains that passed all standard rejection criteria (n = 25) exhibited these malign features, compared to ~77% (n = 20) for the single-irradiation dataset.

Notwithstanding the inability to recover the given dose, the smaller proportion of grains of the third and fifth grain-type suggests that the pulsed-irradiation technique helps to correct for these abnormal behaviours to some extent, and may aid in reducing the effects of saturation at low doses. However, the inability to recover a known dose and, more importantly, the presence of grains of the fourth grain-type in both dose recovery experiments described in this section indicates that these malign features were not the result of dose-rate effects. In contrast to the results of Bailey (2004) and Bailey et al. (2005), the number of grains that exhibited Class 3-type behaviour did not decrease when the results following pulsed-irradiation were compared to the corresponding dose recovery results using conventional single-irradiation techniques. In the pulsed-irradiation dose recovery, ~37% (n = 34) of all grains that passed standard rejection criteria (n = 92) exhibited Class 3-type behaviour, similar to the proportion of Class 3-type grains in the single-irradiation dataset (~28%). It is unknown at the present time why pulsed-irradiation lowers the proportion of grains that exhibit hyperbolic dose-response curve behaviour (fifth grain-type) but does not affect the proportion of grains that exhibit Class 3-type behaviour (fourth grain-type) for single grains of quartz from Mumba, but it is evident that the causes of the two grain-types are not related.

It is interesting to note that in the cases of both single- and pulsed-irradiation dose recovery tests described in this section, the higher surrogate natural dose was underestimated and a relatively high proportion of the grains that passed standard rejection criteria and produced finite dose estimates (77% and 43% for single- and pulsed-irradiation, respectively) were of the third or fifth grain-type. In contrast, in both dose recovery experiments described in Section 5.3.1, the lower given dose was recovered when all grains that passed standard rejection criteria were used. Additionally, fewer grains that passed standard rejection criteria and produced finite dose estimates (~5% for both single- and pulsed-irradiation) were of the third or fifth grain-type. These results suggest that many individual quartz grains from Mumba have the malign property of a relatively early onset of signal saturation. This property would not affect the estimation of lower doses (e.g., 40 Gy), but would hinder the estimation of higher doses (e.g., 120 Gy). Given the archaeological context and relatively high dose rates for samples from Mumba (~3 Gy/ka), D_e values for samples from Bed V and VI were expected to be on the order of ≥100 Gy. This indicates that the early onset of OSL signal saturation in quartz from Mumba may be a problem. Consequently, the data from these dose recovery experiments were scrutinised further to seek additional objective criteria to identify and remove grains that underestimated the given dose due to features associated with the early onset of signal saturation.

5.3.3 Examining dose distributions to refine rejection criteria

When the dose distributions from the dose recovery experiments described in Section 5.3.2 are examined, it becomes clear that the majority of dose estimates are consistent with the given dose. When the distributions are plotted in radial plots, ~80% of the grains (21 of 26 in Figure 5.10a, and 46 of 58 in Figure 5.10b) fall within the shaded 2σ band. This means that ~80% of the grains have measured doses that are statistically consistent with the given dose, suggesting that the measurement procedures are appropriate for the majority of grains. However, the remaining 20% of grains yielded dose estimates that were significantly smaller than the given dose. Additionally, many of these low dose estimates have relative errors of less than 20%. The inclusion of these small, relatively precise dose estimates in the calculation of the weighted mean accounts for the disparity of the measured/given dose ratios from unity.

When these low-dose grains are examined, it is clear that they have one of two specific characteristics that will be discussed in the following sections: 1) they have aberrant dose-response curve shapes and saturate at low doses (i.e., they are of the third or fifth grain-type), or 2) the pattern of sensitivity change is distinctly different from that exhibited by grains that produced dose estimates that were consistent with the given dose.

5.3.3.1 Investigating saturation and hyperbolic dose-response curve shape

To investigate early dose saturation in individual quartz grains from Mumba, the D_0 value, as defined in Equation 3.3, of each grain was characterised. The D_0 value is one of the fitted parameters of a single saturating exponential function, and is a measure of the onset of signal saturation. It is equivalent to the dose at which the OSL intensity reaches 63% of the saturation intensity. Previous studies on single grains have reported that D_0 values from quartz grains vary widely, ranging from 16 to 600 Gy (e.g., Roberts et al., 1999; Duller et al., 2000; Yoshida et al., 2000; Jacobs et al., 2003b). Figure 5.11 shows the distribution of D_0 values for all of the grains that produced dose estimates in the pulsed-irradiation dose recovery test plotted in Figure 5.10 and described in Section 5.3.2. There is considerable variability in the onset of saturation for individual grains. Most D_0 values fall between 15 and 45 Gy with a mean and median of 39 Gy and 33 Gy, respectively. Three outliers have values of 96, 100 and 189 Gy.

The main objective of computing the D_0 value of each individual grain was to quantify the shape of each dose-response curve. Grains of the third or fifth grain-type saturate at low doses, producing dose-response curves that are either horizontal or hyperbolic in shape. These grains will have lower D_0 values than grains of the first or second grain-type, which have dose-response curves that continue to grow with increasing dose. This can be observed when the 25 grains of the third or fifth grain-type were investigated. These grains are represented in Figure 5.11 with light shading. Every grain that has a D_0 value of 25 Gy or lower has a horizontal (i.e., third grain-type; Figure 5.6c) or hyperbolic (i.e., fifth grain-type; Figure 5.6e) dose-response curve shape. Of the 25 grains of the third or fifth grain-type, 80% (n = 20) fall into this category. The remaining 20% of these grains (i.e., those with D_0 values above 25 Gy) produced dose-response curves that continue to grow above the point at which the

L_N/T_N is projected on to the dose-response curve, only turning hyperbolic after 180 Gy. These results suggest that grains from Mumba that have a D_0 value of 25 Gy or below are likely to be of the third or fifth grain-type and suffer from early signal saturation.

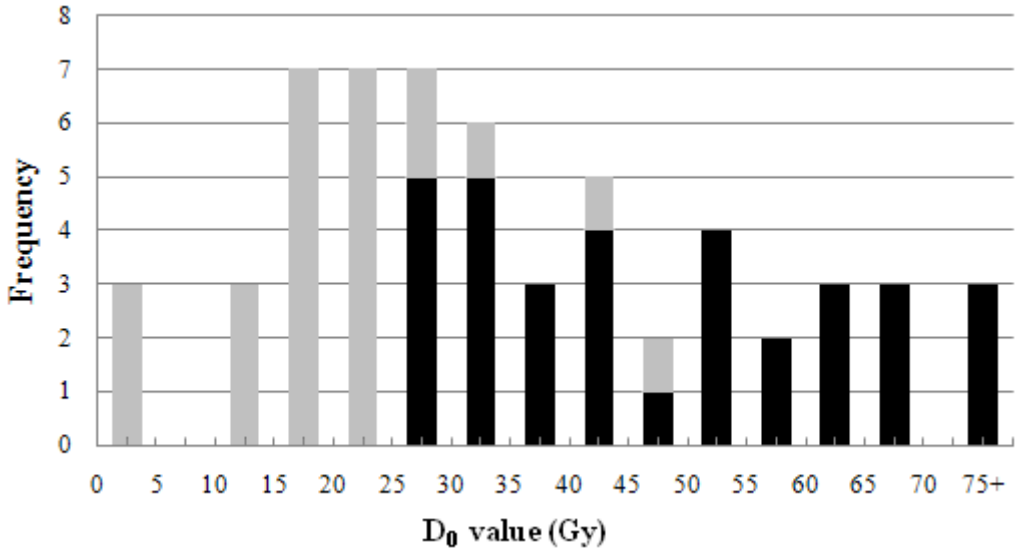

Figure 5.11: D_0 distributions for all grains of MR6 that passed standard rejection criteria tests from the single grain dose recovery experiment using pulsed irradiation described in Section 5.3.2. Grains whose signal saturated at an early dose, as distinguished by their dose-response curve shape being horizontal or hyperbolic, are represented by the lighter shading.

A feature of the distribution shown in Figure 5.11 is the large number of grains that have low (<45 Gy) D_0 values. Murray and Wintle (2000) advised against using samples with a low saturation dose, cautioning that samples with D_e values that were larger than two times their D_0 values could prove problematic. Unfortunately, the number of grains from Mumba that pass standard rejection criteria and produce dose estimates is low for this sample (~8%). Of these, the number of grains that fall below the aforementioned threshold of Murray and Wintle (2000) is very low, and only 16 grains would be accepted (~2% of all grains measured). Therefore, to obtain a significant number of dose estimates, the D_e/D_0 ratio was not used as a rejection criterion in this study. Demuro (2009) also accepted grains with D_e/D_0 ratios that fell above the threshold of Murray and Wintle (2000). She was able to accurately estimate ages for known-age samples, indicating that the inclusion of these grains was not detrimental to accurate age estimation.

To remove grains that saturate at an early dose, while retaining a significant number of grains to produce robust dose distributions, a new rejection criterion was

applied. Based on the pattern observed in Figure 5.11, this new criterion involved rejecting grains that had D_0 values equal to or lower than 25 Gy. This value was chosen as the rejection threshold because all grains that had D_0 values under this threshold also had abnormally shaped dose-response curves. This resulted in the rejection of 20 grains from the pulsed-irradiation dataset. The dose estimates from the remaining 38 grains were overdispersed by 30 ± 5% and had a weighted mean of 108.5 ± 6.7 Gy, corresponding to a measured/given dose ratio of 0.87 ± 0.06. The distribution of dose estimates from these grains is shown in Figure 5.12b. While the measured/given dose ratio is substantially closer to unity when these early-saturation grains are rejected, the given dose is still significantly underestimated. The reason for the continued underestimation of the given dose is apparent when the radial plot is again examined. While most of the low-dose grains have been removed, two doses measured with high precision (shown in the circle in Figure 5.12b) continue to form a low-dose component. The inclusion of these two grains in the dose distribution causes the underestimation of the given dose and the high overdispersion.

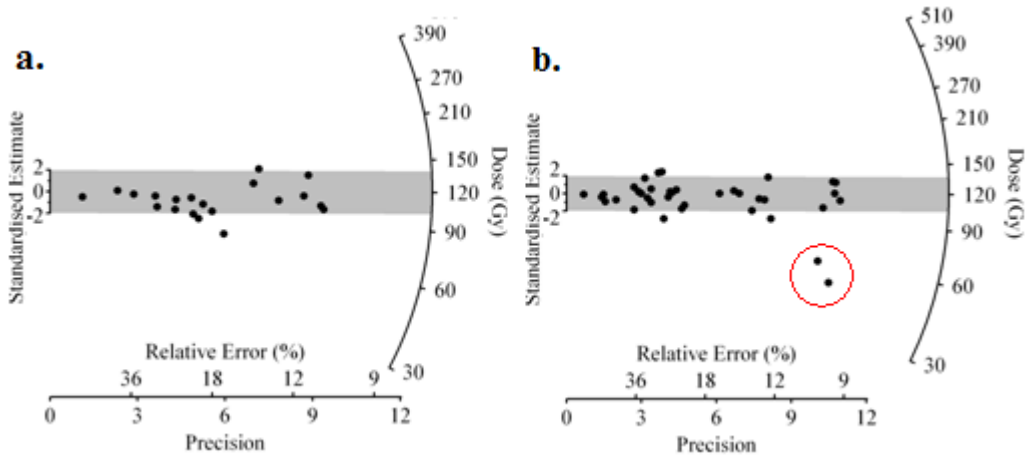

Figure 5.12: Dose distribution from dose recovery tests on single quartz grains of MR6 described in Section 5.3.2. The data is shown in radial plots centred on the given dose (120 Gy). After the application of standard rejection criteria (Figure 5.10), grains that produced low D_0 values (≤25 Gy) were also rejected. a, Single-irradiation. b, Pulsed-irradiation.

5.3.3.2 Identifying aberrant sensitivity change

All 38 grains that were not rejected were further characterised. The two grains that form the low-dose component were among four grains that exhibited a unique

pattern of sensitivity change, as identified by their distinctive T_x/T_N curves. Two T_x/T_N plots are presented in Figure 5.13. The curves of the two low-dose grains have T_x/T_N curves that decrease linearly to a ratio of <0.70 after eight regenerative-dose cycles (Figure 5.13a), a behaviour that is shared by two other grains. This pattern is unique amongst this population of grains, as illustrated by a sample of T_x/T_N plots from the other 34 grains (Figure 5.13b).

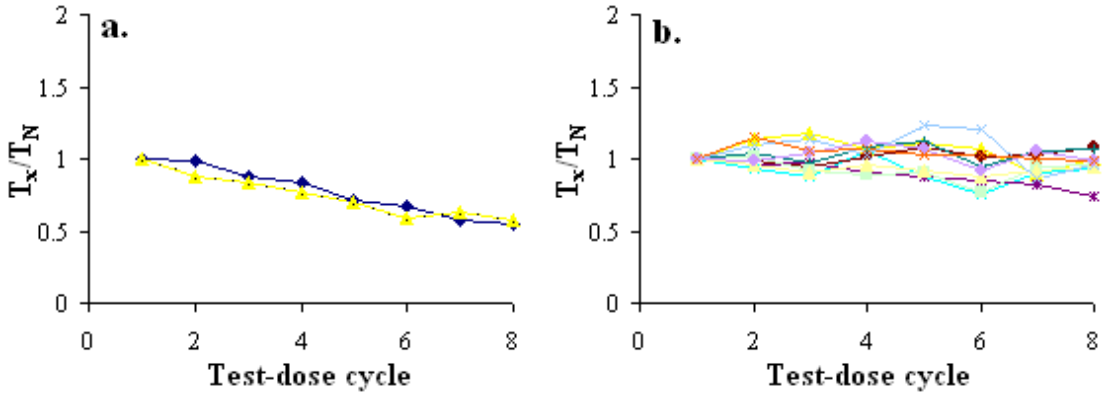

Figure 5.13: T_x/T_N plots for quartz grains of MR6 from the dose recovery test involving pulsed-irradiation described in Section 5.3.2. a, The 2 grains that form the low-dose component circled in Figure 5.12b, as well as 2 other grains, show a unique pattern of sensitivity change. Their T_x/T_N plots that linearly decrease to a ratio of <0.70. b, T_x/T_N plots showing the patterns of sensitivity change of a sample of the remaining 34 grains.

While the cause of this feature is unknown, the fact that it is shared by grains that significantly underestimate the given dose suggests that it can be used to identify grains that would produce unreliable D_e estimates. Consequently, these four grains were rejected based on their atypical T_x/T_N plots, resulting in the dose distribution presented in Figure 5.14. The dose estimates from the remaining 34 grains recovered the given dose given dose within 1σ, with a weighted mean recovered dose of 116.0 ± 5.1 Gy, corresponding to a measured/given dose ratio of 0.96 ± 0.04. Additionally, the overdispersion decreased to 15 ± 4%. This value agrees with other values reported in the literature for a single population of well bleached quartz grains (e.g., Roberts et al., 2000; Thomsen et al., 2005; Galbraith et al., 2005; Jacobs et al., 2006b; Arnold and Roberts, 2009).

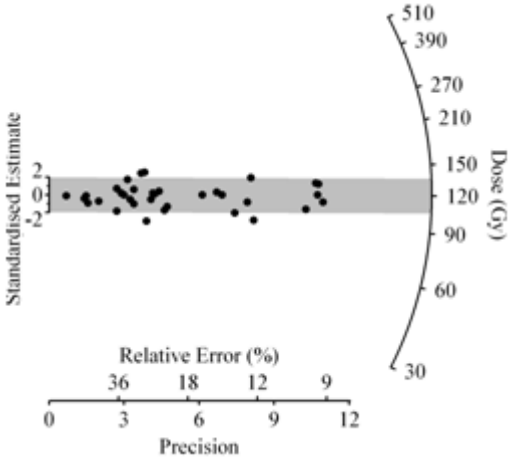

Figure 5.14: Dose distribution from the pulsed-irradiation dose recovery test using single quartz grains of MR6 described in Section 5.3.2. After rejecting grains on the basis of standard criteria and on the basis of the criterion described in Section 5.3.3.1, grains that exhibited aberrant sensitivity change (i.e., decreased linearly to a ratio of 0.70) were rejected. The data is shown in a radial plot centred on the given dose (120 Gy).

5.3.3.3 Application of new rejection criteria to single-irradiation dataset

These new rejection criteria were then applied to the single-irradiation dose recovery dataset described in Section 5.3.2 and plotted in Figure 5.10a. Six grains were rejected on the basis of low D_0 values, but no grains exhibited the deleterious T_x/T_N behaviour. While the resulting dose distribution is improved (Figure 5.12a), the given dose is still significantly underestimated. The weighted mean of the remaining 20 dose estimates was 102.7 ± 6.0 Gy (overdispersion of 18 ± 6%), corresponding to a measured/given dose ratio of 0.86 ± 0.05. This result is worse than that obtained for the pulsed-irradiation dose recovery experiment.

5.3.3.4 Application of new rejection criteria to 40 Gy dose recovery experiment dataset

These new rejection criteria were then applied to the datasets from the dose recovery experiment with a given dose of 40 Gy described in Section 5.3.1 and plotted in Figure 5.9. When the two rejection criteria were applied to the single-irradiation dataset, 38 additional grains were rejected, all on the basis of low D_0 values. The remaining 34 grains produce a weighted mean dose estimate of 48.4 ± 1.3 Gy with an overdispersion of 9 ± 3%. This is a significant overestimation of the given dose, corresponding to a measured/given dose ratio of 1.22 ± 0.03. When these criteria are applied to the pulsed-irradiation dataset, 41 grains are rejected: 37 on the basis of low

D_0 values and 4 on the basis of aberrant sensitivity change. The remaining 37 grains produced a weighted mean dose estimate of 44.3 ± 0.8 Gy (overdispersion of 4 ± 3%). This, also, significantly overestimates the given dose, corresponding to a measured/given dose ratio of 1.11 ± 0.02.

For both 40 Gy dose recovery datasets, the application of the two new rejection criteria resulted in poorer results than the standard rejection criteria. In both datasets, most grains were rejected on the basis of having D_0 values below 25 Gy. This rejection criterion was developed to overcome the low doses at which the OSL signals of many grains of quartz saturate (Section 5.3.3.1). However, the given and regenerative doses in this experiment (e.g., ~40 Gy) are low enough that the dose-response curve was less-affected by low-dose saturation. The proportions of grains of the third and fifth grain-types in these datasets support this. In the pulsed-irradiation 120 Gy dose recovery experiment, ~43% of grains had saturated or hyperbolic dose-response curves (Section 5.3.2). In contrast, only ~5% of grains had those features in the pulsed-irradiation 40 Gy dose recovery experiment (Section 5.3.1). The application of the new rejection criteria to the pulsed-irradiation 40 Gy dose recovery dataset resulted in the removal of ~47% of grains, a substantial proportion of which (~42%) had well-behaved OSL signals, and the given dose was significantly overestimated. In contrast, the use of standard rejection criteria allowed the given dose to be recovered. This suggests that low-dose saturation and hyperbolic dose-response curve shape do not adversely affect the ability of the SAR procedure to accurately estimate known doses up to 40 Gy using the OSL signal of quartz grains from Mumba. Consequently, the new rejection criteria were considered inappropriate for estimation of low doses.

5.3.4 Summary of single-grain dose recovery experiments

The dose recovery experiments described in this section have highlighted the usefulness of this test as a means of refining an OSL methodology tailored to the particular behaviours of a sample that exhibits several malign luminescence characteristics. In this study, the dose recovery experiment was used as the main tool to discern the optimal experimental conditions used to measure doses and to refine the rejection criteria to overcome problems specific to these samples.

Characterising the signal from various types of individual grains (Section 5.2) indicated that the OSL signal of quartz from Mumba saturated at relatively low doses. To test the suitability of the SAR procedure to single grains of quartz without the complications arising from low-dose saturation, a 40 Gy dose recovery experiment was performed (Section 5.3.1). Two SAR procedures with different experimental conditions were tested: one in which laboratory doses were delivered in a conventional, single-irradiation fashion and the other in which laboratory doses were delivered using the pulsed-irradiation technique. In both cases, the given dose was recovered (measured/given dose ratios in agreement with unity at 2σ) when standard rejection criteria were used. In addition, neither set of experimental conditions produced a high proportion of grains that exhibited third or fifth grain-type behaviour (i.e., saturated or hyperbolic dose-response curves).

Following the verification that the SAR procedure, using either dose delivery technique, could be used to determine a known dose in the region well below saturation intensity of the dose-response curve, a 120 Gy dose recovery experiment was performed to assess the suitability of the SAR procedure at a high dose (closer to saturation). Based on the relatively high dose rate (~3 Gy/ka) and archaeological/ lithic context of the layers of interest at Mumba, burial doses for many of the samples were expected to be on the order of ≥100 Gy. Given this, as well as the aberrant behaviours of the OSL signal at high doses observed for several grain-types, it was considered necessary to test a higher surrogate natural dose (Section 5.3.2). Again, the two sets of experimental conditions were compared. Applying the regenerative doses in a pulsed fashion resulted in a greater number of dose estimates and a smaller proportion of grains of the fifth grain-type, relative to single-irradiation application. This suggests that the pulsed-irradiation technique reduced the number of grains with hyperbolic dose-response curves.

In both 120 Gy dose recovery tests, following the application of standard rejection criteria, the dose estimates from the majority of grains were consistent with the given dose. However, the weighted mean dose estimate was significantly smaller due to the presence of a substantial low-dose component measured with high precision. These low-dose grains were characterised and found to have one of two specific OSL characteristics: 1) they saturated at very low doses, as indicated by their D_0 values of

less than 25 Gy, or 2) they exhibited a distinctly different pattern of sensitivity change over the course of the entire SAR procedure. Consequently, new rejection criteria were introduced to remove these grains based on the OSL properties of: 1) having a D_0 value below 25 Gy, or 2) decreasing in sensitivity by more than 30% over the course of the SAR procedure (manifested in T_x/T_N plots that decrease linearly to a ratio smaller than 0.70). After the application of these new rejection criteria, the SAR procedure using the pulsed-irradiation technique recovered the given dose within 1σ. The SAR procedure using conventional single-irradiation failed to do so, continuing to significantly underestimate the surrogate natural dose. In addition, these new rejection criteria were shown to be inappropriate for the 40 Gy dose recovery experiment. It is important to emphasise that grains were rejected based on their aberrant physical characteristics and not on their measured doses per se. The new rejection criteria were developed based on patterns of irregular OSL characteristics, and are applied to attempt to limit dose determination to the first grain-type (Figure 5.5a and Figure 5.6a).

These results indicate that the SAR procedure is capable of accurately recovering a low radiation dose (~40 Gy) when the regenerative doses are delivered in a pulsed fashion and standard rejection criteria are used. They also indicate that higher doses can reliably be obtained using the pulsed-irradiation SAR procedure, provided the data are analysed utilising the newly developed rejection criteria described above. These new rejection criteria effectively reduce the effects of grains with OSL signals that saturate at early doses and have atypical patterns of sensitivity change. The next section will detail dose recovery experiments using multi-grain aliquots of quartz from Mumba to assess the effects of using the summed OSL signals from multiple grain-types for SAR measurements.

5.4 Dose recovery experiments using multi-grain aliquots of quartz

In Section 5.2, large intra-sample variability in the OSL signal from individual grains of quartz from Mumba was demonstrated. By characterising the OSL signal from individual quartz grains during dose recovery experiments, appropriate rejection criteria were developed that allowed the appropriate use of the SAR procedure to obtain accurate estimates of known, laboratory doses (Section 5.3). However, if only multi-grain aliquots had been investigated, the OSL behaviours of individual grains would not

have been characterised, and standard SAR procedures may have been employed to investigate quartz from Mumba. This section will examine the effects of using the sum of the OSL signals from many individual quartz grains when multi-grain aliquots are measured using the SAR procedure.

Six aliquots of MR 7, each consisting of ~50 grains, were bleached in sunlight for at least three days and given a laboratory dose of 83 Gy. Aliquots were then preheated to 260°C for 10 s before being stimulated with the blue LEDs for 40 s at 125°C while the OSL was measured. This was followed by a test dose cycle that included a 1.3 Gy irradiation, a 220°C preheat for 10 s, and an OSL measurement for 40 s at 125°C. For three of the aliquots, a HOW was administered following the measurement of each test dose (T_x). This measurement cycle was repeated for regenerative doses of 42, 83, 125 and 0 Gy to construct dose-response curves. A repeat (42 Gy) dose cycle was also measured to assess each aliquot's ability to recycle a duplicate regenerative dose.

The results of these dose recovery experiments will be described in the next three sections. First, the results of the dose recovery experiment using a standard SAR procedure without a HOW will be described (Section 5.4.1). In Section 5.4.2, the results of the dose recovery experiment using a modified SAR procedure included a HOW are discussed. Finally, Section 5.4.3 assesses whether the use of an 'early-background' approach (Cunningham and Wallinga, 2010) to OSL signal analysis improves the results of both dose recovery experiments presented in the preceding sections.

5.4.1 Standard SAR procedure

The shape of the OSL decay curves changes substantially between each SAR measurement cycle when a HOW is not administered. Figure 5.15 shows the normalised test dose OSL decay curves for each SAR measurement cycle for one of the aliquots that was not given a HOW. The OSL signal decays more slowly and to a higher background with each progressive regenerative dose cycle. Compared to the initial portion of the decay curve (i.e., the first ~0.45 s) the later portion of the decay curve (i.e., the final 8 s) increased by >100% over the course of six SAR measurement cycles. This suggests that there is a portion of the OSL signal that is not being fully

bleached by the 40 s optical stimulation. The decay curve of the test dose following the surrogate natural (Figure 5.15) decays rapidly over the first ~2 s of optical stimulation, which is consistent with the depletion of the fast component. However, the increasingly shallow shape of the decay curve with each progressive measurement cycle suggests that a slower component, or series of slower components, may be accumulating at different rates. The accumulation of signal in these CW-OSL curves is reminiscent of the accumulation of signal in LM-OSL curves (Figure 5.3). In addition, the accumulation of signal in the region of the CW-OSL signal corresponding to the fast component (i.e., before ~3 s of stimulation: Bailey et al., 1997; Arnold et al., 2008; Pawley et al., 2010) may be related to the component represented by column B or C in Table 5.1 and Table 5.2, both of which underlie the fast component.

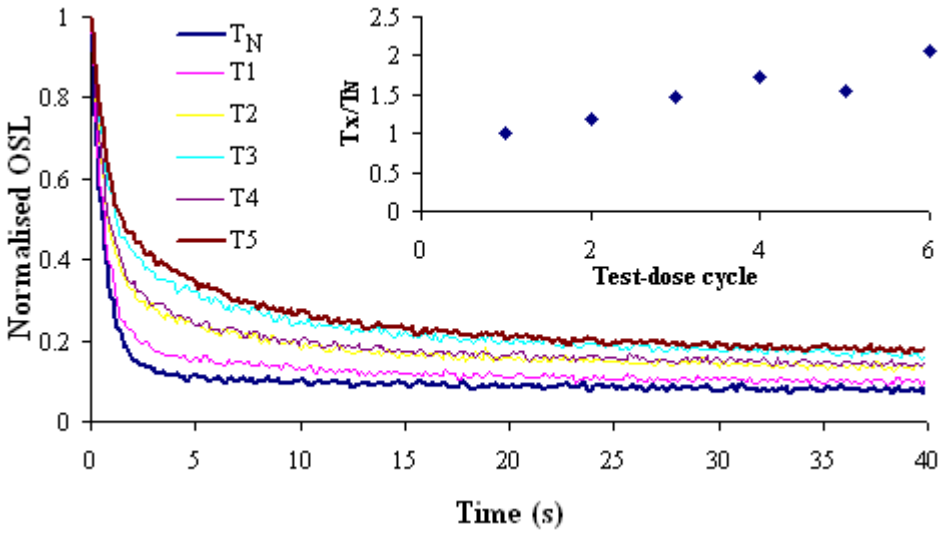

Figure 5.15: Normalised test dose OSL decay curves for the one aliquot whose SAR procedure did not include a HOW. Results are representative. The inset plots show the test dose signals (T_x) normalised to the first test dose measurement (T_N), as a function of the test dose cycle for the same aliquot. These data were integrated using the standard intervals (i.e., sum of the first 0.45 s minus a background calculated from the final 8 s).

Several other observations support this conclusion. First, the background (calculated from the last 8.0 s of stimulation)-subtracted sum of the initial 0.45 s of test dose signal increases with each progressive SAR measurement cycle. The inset to Figure 5.15 shows the test dose signals (T_x) normalised to the first test dose measurement (T_N), as a function of the SAR measurement cycle for the same aliquot (T_x/T_N plots). The OSL response following the test dose increases with each progressive SAR measurement cycle, changing in sensitivity by ~200% for all aliquots.

Second, the unbleached components of the OSL signal are accumulating with each regenerative and test dose, suggesting that each progressive OSL measurement has a residual signal from the previous OSL measurement underlying it. This can be directly observed by looking at the OSL decay curve following the 0 Gy regenerative dose (Figure 5.16b). A sample that has an OSL signal that is dominated by the fast component will not produce a measurable OSL signal following the 0 Gy regenerative dose because the fast component is bleachable within 5 s of optical stimulation (Bailey et al., 1997). For samples from Mumba, a clear and bright decay curve is produced (Figure 5.16b), confirming the presence of a residual unbleached signal underlying each OSL measurement.

A representative dose-response curve, constructed for an aliquot whose SAR procedure did not include a HOW, is presented in Figure 5.16a. Results indicated that the SAR procedure is unsuitable when applied to all aliquots. Although all aliquots produced satisfactory recuperation values (weighted mean of 3 ± 1%), the ratio of the two repeat points (the recycling ratio) is not consistent with unity for any of the aliquots (weighted mean recycling ratio of 0.73 ± 0.04 for the three aliquots). The shapes of the dose-response curves were anomalous as well. The sensitivity-corrected regenerative dose points (L_x/T_x) decreased at higher doses, resulting in dose-response curves with a hyperbolic shape. Additionally, the sensitivity-corrected surrogate natural (L_N/T_N) fell above the dose-response curve for all three aliquots. This behaviour precludes the natural signal from intercepting the dose-response curve, preventing dose (or, in the case of natural aliquots, D_e) estimation. Yoshida et al. (2000) observed this dose-response curve behaviour when investigating the natural signal from single grains of quartz. During OSL investigations of multi-grain aliquots of quartz from southern Africa, Armitage et al. (2000) also noted the presence of aliquots that have a natural signal greater than the saturation intensity of regenerated doses. The two aberrant characteristics of the dose-response curves described above (i.e., hyperbolic shape and Class 3-type behaviour) are similar to the characteristics of grains of the fourth and fifth grain-type (Section 5.2).

It is likely that the changes in sensitivity of multiple OSL components over the course of progressive SAR measurement cycles, and the unbleached OSL signals that accumulate as a result (Figure 5.15 and Figure 5.16b), are the likely causes of the poor

recycling ratios and aberrant dose-response curve behaviours. The presence of several slowly bleaching, thermally unstable slow components may be the cause of the sensitivity changes and signal accumulation (e.g., Murray and Wintle, 2003; Jacobs et al., 2006a). The addition of a HOW to the measurement procedure may overcome problems associated with the accumulation of residual signal from slow components in the OSL signal.

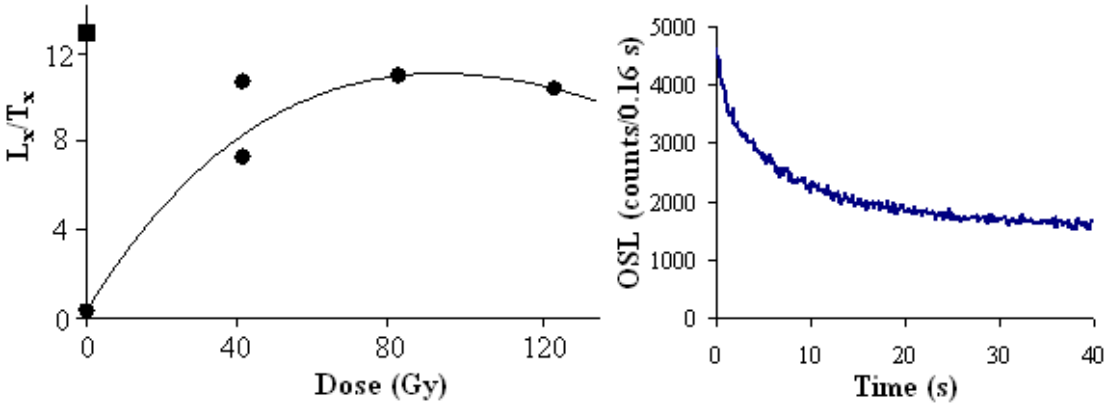

Figure 5.16: Results for one aliquot whose SAR procedure did not include a HOW. a, dose-response curve. b, the OSL produced following the 0 Gy regenerative dose.

5.4.2 Modified SAR procedure: Application of a HOW

The addition of a HOW to the SAR procedure reduced the effects of multiple, unwanted components in the OSL signal. Figure 5.17 presents the normalised test dose OSL decay curves for each measurement cycle for one aliquot whose SAR procedure included a HOW. It is apparent that the signal is still accumulating in the later parts of the decay curve and that the decay curve shape gets shallower with each SAR measurement cycle. Both features are, however, considerably reduced in comparison to those presented in Figure 5.15. Relative to the first 0.45 s of the OSL signal, the final 8.0 s of signal increases by ~30% from the first to the last regenerative dose. This is substantially reduced from the ~100% increase observed when no HOW was administered. The reduction in CW-OSL signal accumulation when a HOW was used is similar to the reduction in LM-OSL signal accumulation (Figure 5.3).

When the T_x/T_N plots for these aliquots (inset to Figure 5.17) are observed, it is clear that the OSL output of the test dose continues to increase with each progressive SAR measurement cycle. However, when a HOW is applied the signal increased by between 50 and 80% from the first to the final regenerative dose cycle, lower than the

increase of ~200% observed when no HOW was applied. A third feature is that the OSL signal measured after the 0 Gy regenerative dose (Figure 5.18b) is considerably smaller than its counterparts when a HOW was not used. Unfortunately, the absolute signal of the 0 Gy decay curve for aliquots that received a HOW cannot be directly compared to the signal measured for those that did not receive this treatment, due to the fact that different aliquots were measured for both experiments and individual aliquots will have different signal intensities. The absolute intensity for the aliquot in Figure 5.18b is, however, significantly less (~30%) than that in Figure 5.16b. This suggests that less signal had accumulated in optically less-sensitive components over the course of SAR measurement cycles when a HOW was administered.

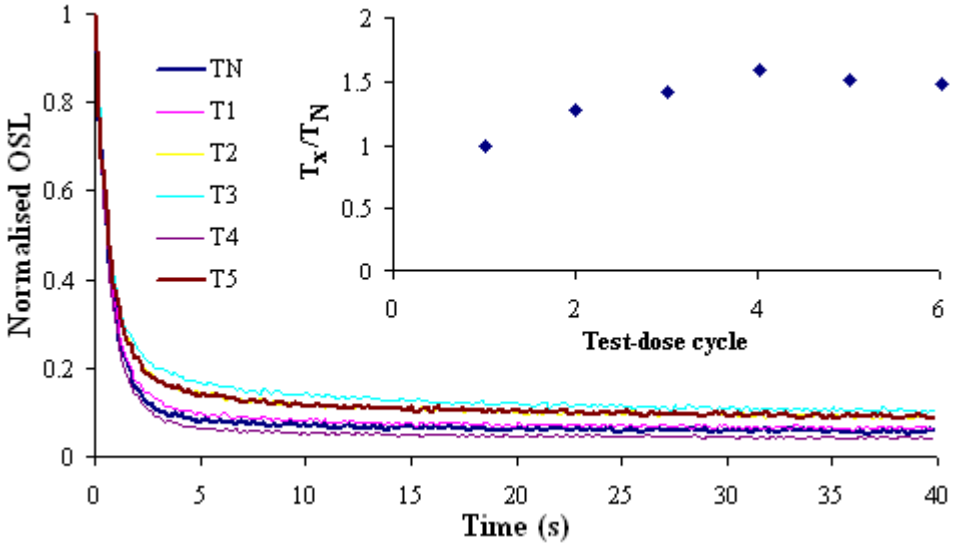

Figure 5.17: Normalised test dose OSL decay curves for the one aliquot whose SAR procedure included a HOW. The inset plots show the test dose signals (T_x) normalised to the first test dose measurement (T_N), as a function of the test dose cycle for the same aliquot. These data were integrated using the standard intervals (i.e., sum of the first 0.45 s minus a background calculated from the final 8 s).

This difference in the absolute intensity of the 0 Gy dose points, and accumulation of the OSL signal from cycle-to-cycle, can be quantified by examining the recuperation values, which was reduced with the addition of the HOW. While the recuperation values passed the rejection criteria when a HOW was not used (weighted mean of 3 ± 1%), they were an order of magnitude smaller when the HOW was added to the measurement procedure (weighted mean of 0.3 ± 0.1%). These results suggest that the addition of a HOW reduced the accumulation of unwanted signal over multiple

measurement cycles, and that the total OSL signal changed composition much less from one measurement cycle to the next.

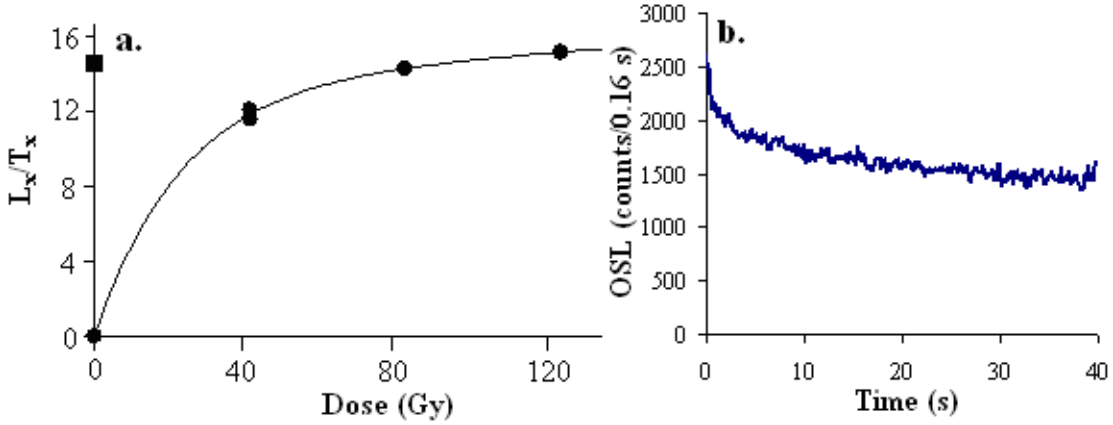

Figure 5.18: Results for one aliquot whose SAR procedure included a HOW. a, dose-response curve. b, the OSL produced following the 0 Gy regenerative dose.

The dominance of the fast component throughout the course of progressive measurement cycles is necessary for reliable dose estimations to be made using the SAR procedure (Wintle and Murray, 2006). By reducing the contribution of the unwanted components to the total OSL signal, the addition of a HOW enabled the fast component can remain dominant. This is the likely reason for the improved results in tests of SAR suitability when a HOW was included in the measurement procedure. Two of the three aliquots successfully recycled a duplicate regenerative dose within 2σ, with a weighted mean recycling ratio of 0.96 ± 0.02. The third aliquot was rejected due to a low recycling ratio value of 0.91 ± 0.03.

A dose-response curve produced by one of the well-behaved aliquots is presented in Figure 5.18a and is representative. The two aberrant dose-response curve features that were present when a HOW was not administered (Figure 5.16a) are markedly reduced. First, the curve in Figure 5.18 does not exhibit Class 3-type behaviour. For all three aliquots, the sensitivity-corrected surrogate natural (L_N/T_N) could be projected on to the dose-response curve and interpolated to obtain a dose estimate. Furthermore, the two aliquots that passed the recycling ratio test successfully obtained dose estimates that were within 1σ of the given dose, with a weighted mean measured/given dose ratio of 1.04 ± 0.07. Second, these dose-response curves do not exhibit a hyperbolic shape, with each higher regenerative dose yielding a larger

sensitivity-corrected regenerative dose point (L_x/T_x). However, despite the consistent growth of the dose-response curves for all three aliquots, they all appear close to saturation. As mentioned in Section 3.3.1.3, one way of monitoring the onset of saturation in a dose-response curve is to use the D_0 value from Equation 3.3. The dose-response curves of these three aliquots saturated at a relatively low dose, with a weighted mean D_0 value of 33 ± 2 Gy. This is consistent with the single-grain investigations presented in Section 5.2 and Section 5.3, which suggested that many grains saturate at low doses.

5.4.3 Analysing dose recovery results using an early-background approach

The integration interval chosen for CW-OSL data analysis will have an effect on the components that contribute to the net OSL count (Cunningham and Wallinga, 2010). It is common practice to use a 'late-background' approach (see Section 3.3.1.1), which entails using the sum of the initial signal (e.g., 0.45 s) minus a background calculated from the later portion of the signal (e.g., the final 8.0 s). In contrast, Cunningham and Wallinga (2010) have suggested that an 'early-background' approach to choosing the integration interval can reduce the proportion of the net OSL signal originates from slow components and increase the proportion of the net OSL signal that originates from the fast component. They summed the OSL signal from the initial 0.4 s of stimulation and subtracted a background calculated using the OSL signal from 0.4 to 1.4 s of stimulation (i.e., 2.5 times the initial integration interval). Their results indicate that the early-background approach reduced thermal transfer and recuperation, and produced tighter D_e distributions. In addition more aliquots produced accurate D_e values with the early-background approach than when the late-background approach was used (Cunningham and Wallinga, 2010).

To see if the results from the dose recovery experiments described in Section 5.4.1 and Section 5.4.2 could be improved, the data were reanalysed using the early-background approach. Dose-response curves, constructed using the sum of the first 0.45 s of OSL signal minus a background calculated using the OSL signal from 0.45 to 1.76 s of stimulation, are presented in Figure 5.19. The dose-response curves in Figure 5.19a and b were constructed using the OSL signal from the same aliquots whose dose-

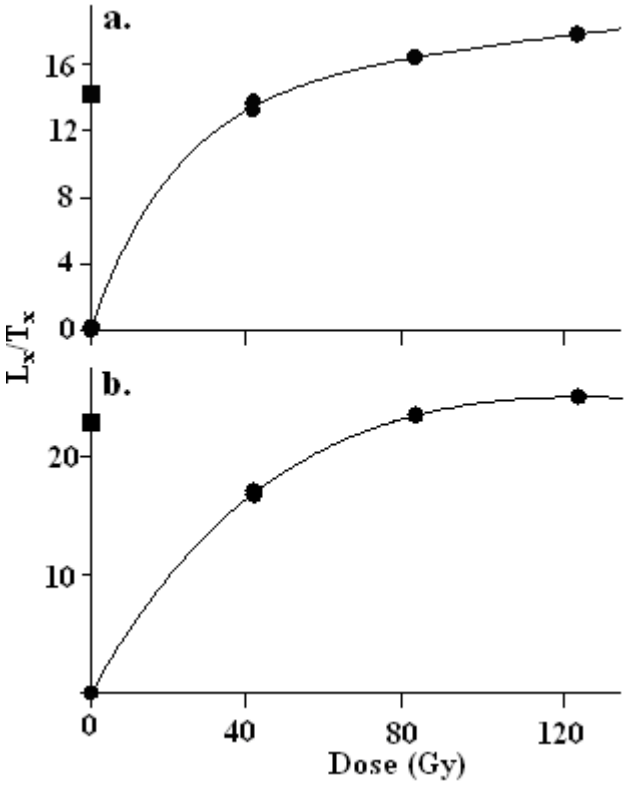

Figure 5.19: Dose-response curves, constructed using the early-background approach (see text for details) to analyse OSL signals from two aliquots. a, Corresponds to the aliquot whose dose-response curve, constructed using the OSL signal obtained during a SAR procedure did not include a HOW, presented in Figure 5.16a. b, Corresponds to the aliquot whose dose-response curve, constructed using the OSL signal obtained during a SAR procedure that included a HOW, presented in Figure 5.18a.

response curves are presented in Figure 5.16a and Figure 5.18a, respectively. Results from tests of SAR suitability, produced when the early-background approach to OSL signal analysis was used, suggested that the standard SAR procedure without a HOW was suitable for multi-grain aliquots of MR7. None of the dose-response curves produced by the OSL signal from the three aliquots had either a hyperbolic shape or Class 3-type behaviour. The OSL signal from all three aliquots successfully recycled a duplicate regenerative dose within 2σ, with a weighted mean recycling ratio of 0.97 ± 0.03. The recuperation value was also reduced (weighted mean of 2.4 ± 0.1%). However, the given dose was significantly underestimated by all three aliquots, which resulted in a weighted mean measured/given dose ratio of 0.62 ± 0.06. This suggests that, while the shape of the dose-response curve improved and the tests of SAR suitability were successfully passed when data were analysed using the early-

background approach, the standard SAR procedure without a HOW was inappropriate for dose estimation.

When the OSL signal data obtained using a SAR procedure that included a HOW were reanalysed using the early-background approach, all three aliquots passed all tests of SAR suitability. All aliquots were able to successfully recycle a duplicate regenerative dose, producing a weighted mean recycling ratio of 1.00 ± 0.02. The recuperation value of each aliquot was also reduced, with a weighted mean value of 0.1 ± 0.01%. However, unlike the results of late-background analysis, two of the three aliquots significantly underestimated the given dose. The weighted mean measured/given dose ratio is 0.85 ± 0.04. This is in contrast to the results for these same aliquots when the OSL signals were analysed using the late-background approach, for which the given dose was recovered within 1σ (see Section 5.4.2).

5.4.4 Summary multi-grain aliquot dose recovery experiments

The dose recovery tests described in the previous sections highlight the usefulness of single-grain analysis over multi-grain analysis. When a HOW was not included in the SAR procedure, optically less-sensitive components were observed to accumulate over the course of several SAR measurement cycles, resulting in a substantial residual signal and a change in OSL sensitivity. The OSL signal of the test dose following the surrogate natural appeared to be dominated by the fast component, decaying rapidly over the initial 2 s of blue-light stimulation. However, the accumulation of unwanted components with repeated cycles of irradiation, preheating, and optical stimulation changed the composition of the total OSL signal, thus reducing the relative contribution of the fast component to the part of the signal that was integrated and used to construct a dose-response curve. The HOW reduced the degree of build-up of unwanted components. In doing so, the composition of the total OSL signal and, in particular, that part that was integrated and used to construct the dose-response curve, changed less over the course of multiple SAR measurement cycles, with less contribution by slower components and a continuance of the dominance of the fast component. This was supported by improvements in all tests of SAR suitability. When a standard late-background approach was used to analyse OSL signals an construct dose-response curves, the SAR procedure that included a HOW provided satisfactory

results, whereas the SAR procedure without a HOW did not. When the HOW was included in the measurement procedure, a duplicate regenerative dose was able to be recycled, the recuperation values were reduced, and the measured/given dose ratios were in agreement with unity.

To assess whether the proportion of the signal dominated by the fast component could improved using analytical techniques, the data from both dose recovery experiments were reanalysed using the early-background approach of Cunningham and Wallinga (2010). Results indicated that both SAR procedures (i.e., with and without a HOW) were suitable for all aliquots; a duplicate regenerative dose could be successfully recycled and the recuperation values were lower when the early-background approach was used. In addition, whereas late-background analysis resulted in dose-response curves that were hyperbolically shaped and exhibited Class 3-type behaviour, the standard SAR procedure produced well-behaved dose-response curves when data were analysed using the early-background approach. These results are in agreement with those of Cunningham and Wallinga (2010), who also observed improvements in tests of SAR suitability when the early-background approach was used. However, in spite of these improvements in dose-response curve shape and behaviour and SAR suitability tests, the early-background approach resulted in the given dose being significantly underestimated in the case of both SAR procedures. This suggests that, when quartz from Mumba was measured using the SAR procedure that included a HOW, the late-background approach was more appropriate for OSL signal analysis than the early-background approach.

5.5 Conclusions

In this chapter, the OSL signal of quartz grains from Mumba was characterised. The main results and conclusions that were established from these investigations are summarised below:

- LM-OSL investigations revealed several important features of the OSL signal of quartz from Mumba:
    - The presence of a fast component was established by de-convoluting the LM-OSL signal of naturally and laboratory irradiated aliquots. When

this component was used in isolation during an LM-OSL dose recovery experiment, it could recycle a duplicate regenerative dose.

- The presence of several slower components was also established by de-convoluting the LM-OSL signal of natural and laboratory irradiated aliquots. These components were shown to accumulate faster than the fast component over multiple cycles of irradiation, preheating and LM-OSL stimulation. This accumulation of slower components, however, was substantially reduced by adding a HOW into the measurement procedure. As a result of the presence of several slow components and the beneficial effects of a HOW, a high temperature preheat combination (260/220°C) and a HOW were considered to be appropriate for the measurement of quartz from Mumba using the SAR procedure.

- Investigations of single grains of quartz demonstrated that there was significant intra-sample variability in the OSL signal. Five general classes of grain-types were established and characterised. The OSL signals from many grains were shown to saturate at low doses, exhibit Class 3-type behaviour and/or produce hyperbolically shaped dose-response curves. The proportion of grains with hyperbolic dose-response curves was reduced by delivering laboratory doses using a pulsed-irradiation technique (Bailey, 2004; Bailey et al., 2005).
- To assess the suitability of the SAR procedure without the complications arising from low-dose saturation, dose recovery experiments were conducted using a low given dose (40 Gy). The SAR procedure was tested using both the single-irradiation and pulsed-irradiation techniques. In both cases, the proportions of grains that exhibited Class 3-type behaviour or had hyperbolic dose-response curves were low, and the given dose could be recovered (within 2σ) using standard rejection criteria.
- To assess the suitability of the SAR procedure at doses closer to those expected for samples from Mumba, a dose recovery experiment was conducted using a higher given dose (120 Gy). Using standard rejection criteria, both the single-irradiation SAR procedure and the pulsed-irradiation SAR procedure significantly underestimated the given dose. By characterising the grains that underestimated the given dose, new rejection criteria were established that

removed grains whose OSL signals saturated at low doses (D_0 value ≤25 Gy) and exhibited aberrant sensitivity changes (T_x/T_N plots that decreased linearly below 0.70). After the application of these two rejection criteria, the given dose was successfully recovered within 1σ using the pulsed-irradiation SAR procedure. The single-irradiation SAR procedure still significantly underestimated the given dose.

- To assess the effects of combining grains with substantially different OSL signals on the same aliquot, the OSL signal from multi-grain aliquots of quartz was investigated.
    - The SAR procedure without a HOW was shown to be unsuitable for quartz from Mumba when the standard late-background approach was used. Duplicate regenerative doses could not be recycled and dose-response curves exhibited Class 3-type behaviour and hyperbolic shapes. The OSL signal was shown to change shape and accumulate signal over multiple measurement cycles. When data were analysed using the early-background approach (Cunningham and Wallinga, 2010), tests of SAR suitability and the dose-response curve behaviour were improved, however, the given dose was significantly underestimated.
    - The SAR procedure that included a HOW was shown to be suitable for quartz from Mumba when the late-background approach was used for data analysis. Two of three aliquots recycled a duplicate regenerative dose and successfully recovered the given dose within 1σ. Over multiple measurement cycles, the amount of signal-accumulation and shape-change in the decay curve was substantially reduced when a HOW was used (relative to when a HOW was not used). When the data were reanalysed using the early-background approach, the OSL signal from all three aliquots could successfully recycle a duplicate regenerative dose and tests of SAR suitability were passed. However, the given dose was significantly underestimated, suggesting that the late-background approach to data analysis was more appropriate for quartz from Mumba.

The results presented in this chapter indicate that, when single grains of quartz are investigated, the pulsed-irradiation SAR procedure including a HOW is capable of accurately recovering low doses (~40 Gy) using standard rejection criteria and higher doses using the new rejection criteria. The SAR procedure including a HOW was shown to be appropriate for recovering a given dose using multi-grain aliquots of quartz. However, given the likelihood of sediment mixing, beta microdosimetry, partial bleaching and bioturbation in archaeological contexts (e.g., Roberts et al., 1998a, 1999; Jacobs et al., 2003b, 2006b, 2008c; Feathers et al., 2006; Olley et al., 2006; David et al., 2007), single-grain analysis is preferable to multi-grain aliquot analysis. The next chapter will describe the measurement of D_e values from single grains of quartz from Mumba using the experimental conditions and methods of data analysis developed in this chapter.

Chapter 6: Single-grain D_e distributions, dose rate determinations and age estimations for quartz from Mumba rockshelter, Tanzania

In the preceding chapter, investigations of the OSL signals of quartz grains from Mumba were discussed. The signal was characterised, and five general classes of grain-type were identified. Grains were classified into types based on the shape and behaviour of their dose-response curves and OSL decay curves, and the way in which they sensitised over multiple SAR measurement cycles (Section 5.2). Many of the grain-types were shown to have malign OSL properties, resulting in many dose-response curves that saturated at low doses and many more that were hyperbolically shaped. The presence of large numbers of grains with these properties in the Mumba samples was the likely cause of aberrant OSL behaviours of multi-grain aliquots of quartz, which were unable to recover a given laboratory dose (Section 5.1 and 5.4).

Single-grain dose recovery experiments demonstrated that delivering regenerative doses using the pulsed-irradiation technique (Bailey, 2004; Bailey et al., 2005) resulted in fewer grains that had hyperbolic dose-response curves. The SAR procedure using pulsed-irradiation was shown to be appropriate for obtaining doses of 40 Gy when standard rejection criteria were used to analyse the dose distributions. Saturation was shown to interfere with the ability to obtain a higher known dose (120 Gy) when this measurement procedure was used. Two new rejection criteria were thus developed to overcome problems of low-dose saturation and abnormal OSL sensitisation (Section 5.3.3). Since these two rejection criteria were inappropriate for estimating the given dose of 40 Gy (Section 5.3.3.4), they are only applicable when the expected dose is relatively large. When these new rejection criteria were applied, the 120 Gy given dose was successfully recovered. This indicated that the SAR procedure using pulsed-irradiation was appropriate for obtaining dose estimates from well-behaved single grains of quartz from Mumba. However, as mentioned in Section 3.3.2.4, while a successful dose recovery experiment can indicate the suitability of a sample for use of the SAR procedure, it does not necessarily reveal that the tested SAR procedure will be able to obtain accurate D_e estimates.

In this chapter, the estimation of ages obtained using single grains of quartz from Mumba will be discussed. The total environmental dose rates for samples from Mumba are presented in Section 6.1. The determination of D_e values is detailed in

Section 6.2, followed by the analysis and characterisation of the D_e distributions (Section 6.3). Section 6.4 presents evidence that the D_e distributions of most Mumba samples are consistent with the effects of beta microdosimetry. An appropriate correction procedure is then described and applied to obtain beta-adjusted age estimates. Finally, samples for which single-grain OSL ages could not be obtained are discussed in Section 6.5.

6.1 Total environmental dose rate for samples from Mumba

The total dose rates calculated in this study used the methods described in Chapter 4 to measure the contributions to the dose rate from the various sources of ionising radiation. These were corrected for beta attenuation and for historical water content (Section 4.3). The environmental dose rates and associated uncertainties are presented in Table 6.1 for samples from Mumba rockshelter, Tanzania.

The measured water contents for samples from Mumba range from 3.3 to 8.2% and are presented in Table 6.1. Due to the palaeoenvironment of the region (see Section 10.1), with periods of higher lake levels that potentially submerged (and thus saturated the sediment in) the rockshelter interspersed with periods of aridity, it is unlikely that the measured water content would be identical to the historical water content. Consequently, a historical water content of 10 ± 2% was assumed for all samples from Mumba. This was based on the high likelihood that the relatively low measured water contents for all samples were due to drying out of the deposits after excavation (e.g., Köhl-Larsen et al., 1943; Mehlman, 1989; Prendergast et al., 2007). Additionally, there is a high likelihood that the environmental conditions were wetter, with higher lake levels, over parts of the Late Pleistocene. It should be noted, however, that the calculated OSL ages are not especially sensitive to the choice of assumed water content. An increase (or decrease) of 1% assumed water content will yield a ~1% increase (or decrease) in the calculated age.

6.2 Single-grain D_e determinations

The modified SAR procedure using pulsed-irradiation was shown to be appropriate for obtaining reliable dose estimates from single grains of quartz when the refined rejection criteria were applied. As a result, natural single quartz grains were me-

Table 6.1: Dose rate data for samples from Mumba rockshelter, Tanzania. All external dose rates have been corrected for water content and beta attenuation. The measured water contents are illustrated in the table, but a historical water content of 10 ± 2% was assumed for all samples in order to calculate the final dose rates. Beta dose rates were corrected for beta attenuation values of Mejdahl (1979) for a grain size of 200 µm. Beta dose rates are based on measurements using a GM-25-5 beta counter. Gamma dose rates are based on *in situ* gamma spectrometry measurements.

	MR2	MR3	MR4	MR6	MR7	MR8	MR9	MR10
Beta dose rate (Gy/ka)	1.50 ± 0.09	1.22 ± 0.08	1.27 ± 0.07	1.35 ± 0.07	1.58 ± 0.08	1.54 ± 0.08	1.67 ± 0.09	1.91 ± 0.10
Gamma dose rate (Gy/ka)	0.98 ± 0.03	0.93 ± 0.02	0.71 ± 0.02	1.04 ± 0.03	0.92 ± 0.02	0.91 ± 0.02	0.93 ± 0.02	1.00 ± 0.03
Cosmic-ray dose rate (Gy/ka)	0.10 ± 0.01	0.09 ± 0.01	0.09 ± 0.01	0.08 ± 0.01	0.08 ± 0.01	0.08 ± 0.01	0.08 ± 0.01	0.08 ± 0.01
Measured water-content*	5.8	5.9	6.1	3.7	4.0	3.3	8.2	7.3
Total Quartz dose rate (Gy/ka)^	2.61 ± 0.12	2.28 ± 0.11	2.11 ± 0.10	2.50 ± 0.11	2.62 ± 0.12	2.57 ± 0.12	2.71 ± 0.13	3.02 ± 0.14
Total K-Feldspar dose rate (Gy/ka)^^		3.15 ± 0.12		3.37 ± 0.12			3.58 ± 0.13	3.89 ± 0.15

*The measured water content is expressed as the % of the dry sample mass.

^Quartz total dose rate includes an internal contribution of 0.03 ± 0.01 Gy/ka.

^^K-feldspar total dose rate includes an internal contribution of 0.90 ± 0.05 Gy/ka (based on Table 4.1).

asured and used to obtain D_e values for samples MR2 to MR10. Grains were preheated to 260°C for 10 s before the natural OSL signal was measured using a green laser stimulation for 2 s at 125°C. Subsequently, a test dose cycle was administered that included a 10 Gy irradiation, a preheat of 220°C for 5 s, and an optical stimulation for 2 s at 125°C using the green laser. The measurement of each test dose was immediately followed by the application of a HOW. Dose-response curves were then constructed using the sensitivity-corrected OSL signals from between four and five different regenerative doses. After the measurement cycle involving the highest regenerative dose was completed, the standard tests of SAR suitability (i.e., those described in Section 3.3.2) were performed. These included the application of a 0 Gy dose point (recuperation test), the measurement of a duplicate regenerative dose (recycling ratio test), and the OSL-IR depletion ratio test to check for feldspar contamination. Individual grains were then either accepted or rejected based on their performance in these tests using the criteria of Jacobs et al. (2003b, 2006b). Grains were rejected if:

- Their OSL signal was too dim for D_e calculation. This was quantified using the test dose signal from each grain. If the initial intensity of the T_N signal was less than three times the corresponding background intensity, the grain was rejected as being too dim.
- They had L_N/T_N values equal to or greater than the saturation intensity of the dose-response curve, thus preventing estimation of a finite D_e estimate. This includes grains of the third grain-type (completely saturated) and four grain-type (Class 3 grains).
- They exhibited high levels of recuperation. Grains were rejected if the L_x/T_x value for the 0 Gy regenerative dose point was more than 5% of the L_N/T_N value.
- The test dose cycle was not appropriately correcting for sensitivity changes, identified using the recycling ratio test. Grains were rejected if the ratio of the L_x/T_x values for duplicate regenerative doses differed from unity by more than 2σ.
- Feldspar contamination was inferred from the OSL-IR depletion ratio test (Duller, 2003). Grains were rejected if there was a significant loss of OSL signal after IR stimulation. If the ratio of the L_x/T_x values for the regenerative

dose cycle that included an IR bleach and the preceding regenerative dose cycle was more than 2σ below unity (see Section 3.3.2.3).

Dose distributions were obtained after the application of the five rejection criteria listed above. If the weighted mean D_e value of a sample was 40 Gy or less, the dose distributions were considered acceptable, on the basis of results from the 40 Gy dose recovery experiment (see Section 5.3.1 and Section 5.3.3.4). If the weighted mean D_e value of a sample was greater than 40 Gy, the two additional rejection criteria, determined experimentally during the 120 Gy dose recovery experiments (see Section 5.3.3), were applied. The application of these criteria removed:

- Grains that had OSL signals that saturated at small doses. Grains were rejected if they had a D_0 value of less than 25 Gy.
- Grains that exhibited the aberrant pattern of sensitivity change determined during dose recovery experiments. Grains were rejected if their sensitivity decreased by more than 30% over the course of an entire SAR measurement sequence, identified by T_x/T_N values of less than 0.7.

Between 400 and 1700 individual grains were measured for each sample. Table 6.2 lists the number of grains measured for each of the Mumba samples, alongside the number of grains rejected for each criterion. For most samples, 70–80% of the measured grains were rejected because their OSL signals were so weak that the initial T_N intensity was indistinguishable from background. A large number of grains were also rejected because they had poor recycling ratios. Between 4 and 6% of all measured grains from samples MR6, MR7, MR8 and MR9 were fully saturated or exhibited Class 3-type behaviour. A further ~5% of grains from these samples were rejected because they had D_0 values less than 25 Gy. For samples MR2 and MR3, feldspar contamination resulted in the rejection of 11% and 20% of the quartz grains, respectively. Feldspar contamination affects these two samples (both from Bed III-upper) considerably more than any other samples.

A feature of Table 6.2 that should be addressed is the omission of MR5. No D_e values could be determined for this sample, due to an apparent lack of a natural OSL signal. For many of the grains, the test doses and all subsequent regenerative doses produced measurable OSL signals from which dose-response curves could be

constructed. However, each grain produced a D_e estimate of zero due to the absence of a natural signal. This peculiar characteristic is unlikely to be a result of a sample preparation mistake or, more specifically, an unfortunate bleaching error during preparation. This is because MR5 was prepared at the same time and in the same space as MR4, MR6, MR7, MR8 and MR9, none of which exhibits this feature. One explanation is the possibility that the sample was accidentally bleached during sample collection. A second possibility is that it is a phenomenological issue unique to MR5. A third scenario is that all of the grains in MR5 are modern, however, this scenario is unlikely, given the measured D_e values for samples overlying and underlying this sample (Table 6.2). MR5 was collected from Bed IV, corresponding to the contact between Geological Units D and C (Table 2.3). This layer shows evidence of being deposited in an environment of fairly permanent freshwater, as opposed to most of the other samples, which appear to have been deposited in an aeolian manner (as deflation from the lake bed). This alternative mode of deposition suggests that the sediment from which MR5 was collected has a different origin, and thus possibly different luminescence properties, to samples from the aeolian layers. Regardless, OSL investigations of this sample were terminated due to the anomalous behaviour of its natural signal.

6.3 Single-grain D_e distributions

In total, between 3 and 9% of all measured grains passed the rejection criteria and produced reliable D_e estimates. The weighted mean D_e values and overdispersion values for each sample, obtained after analysis using the CAM, are presented in Table 6.2. The D_e distributions are plotted as radial plots (Figure 6.1), which are centred on the central D_e value. One feature of the data is the large overdispersion values obtained for all samples, ranging from 29 ± 4% for MR6 to 73 ± 6% for MR2. None of the samples from Mumba has a D_e distribution that is consistent with a single, common dose. Given that the OSL signal has been characterised, and refined rejection criteria limit the distributions to D_e values from grains of the first and second grain-type, internal factors are an unlikely source of spread above the 10–20% commonly reported for well-bleached quartz (e.g., Roberts et al., 2000; Thomsen et al., 2005; Galbraith et al., 2005; Jacobs et al., 2006b; Arnold and Roberts, 2009). It is more likely that the additional overdispersion is the result of external factors. The three possible explanat-

Table 6.2: The number of grains that were rejected for each criterion, the number of accepted grains, and the resultant 'central' D_e value and overdispersion

Sample	MR2	MR3	MR4	MR6	MR7	MR8	MR9	MR10
Bed	III-upper	III-middle	III-lower	V-upper	V-middle	V-lower	VIA	VIA
Total number of grains measured	1200	1200	900	1700	1300	1500	1500	600
Grains rejected for the following reasons								
T_N signal <3 x BG	877	645	633	1315	1008	1083	1139	476
Poor recycling	109	191	145	125	110	130	117	27
OSL-IR depletion ratio	136	241	8	15	4	17	8	34
0 Gy dose > 5% L_N/T_N	0	0	1	7	5	8	13	4
$D_e = 0$	0	3	3	1	2	1	9	1
Class 3-type grains	0	5	21	44	27	32	16	4
Fully saturated grains	0	9	19	33	26	53	46	11
$D_0 < 25$ Gy	N/A	N/A	24	89	64	89	67	23
$T_X/T_N < 0.70$	0	0	0	4	6	6	1	0
Sum of rejected grains	1122	1094	854	1633	1252	1419	1416	580
Acceptable individual D_e-values	78	106	46	67	48	81	84	20
Overdispersion values (%)	73 ± 6	52 ± 4	35 ± 5	29 ± 4	40 ± 6	47 ± 5	59 ± 6	34 ± 9
Central D_e value* (Gy)	8.5 ± 0.6	33 ± 2	72 ± 5	119 ± 6	121 ± 8	123 ± 8	123 ± 9	133 ± 14

T_N is the OSL signal measured in response to the test dose given after measurement of the natural OSL signal

L_N is the natural OSL signal

Recycling ratio is the ratio of the sensitivity-corrected OSL signal measured from two duplicate regenerative doses

OSL-IR depletion ratio is the ratio of the sensitivity-corrected OSL signal from two duplicate doses, one of which included IR stimulation prior to OSL stimulation

*The central D_e values are not used to calculate the burial age of samples. See text for details.

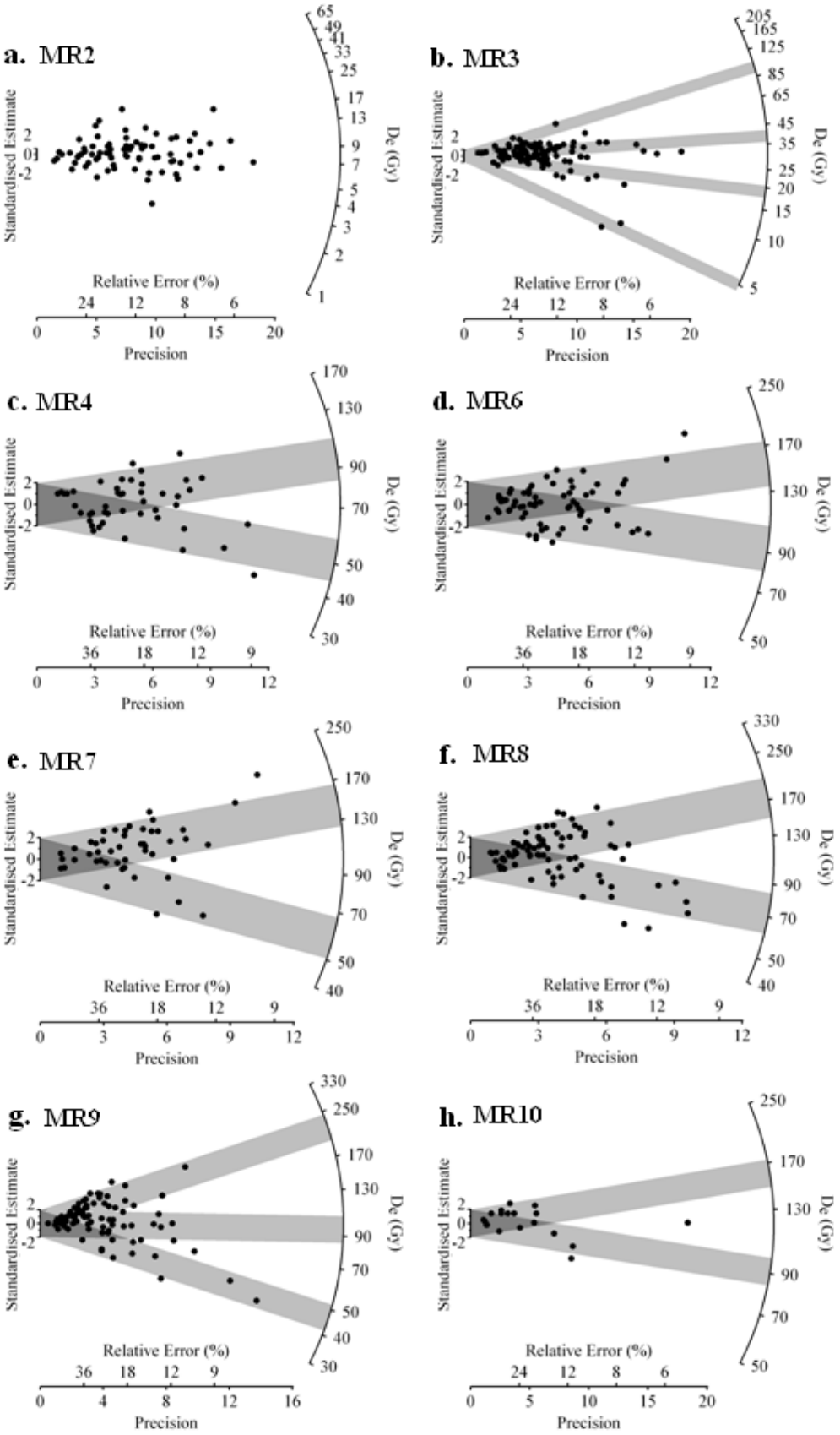

Figure 6.1: Single-grain D_e distributions for samples from Mumba presented as radial plots. The grey bands in each plot are centred on the D_e values identified for discrete dose components by the finite mixture model.

ions for such high overdispersion values include: 1) inhomogeneous bleaching of grains prior to deposition, 2) mixing of grains with significantly different burial doses after deposition, or 3) millimetre-scale differences in the beta dose rate to individual grains deposited at the same time (Jacobs and Roberts, 2007). Incomplete bleaching of the OSL signal is, generally, only a concern for sediments that have been exposed to sunlight only briefly before deposition, such as in fluvial (Olley et al., 1999; Arnold et al., 2007, 2008, 2009) or glacial (Duller, 2006) environments. Given the aeolian deposition of most of the sediments at Mumba, partial bleaching is considered unlikely (Aitken, 1998; Duller, 2008). This suggests that the other two external mechanisms, post-depositional mixing and beta microdosimetry, are the more likely causes of the scatter in D_e values beyond that commonly reported for well-bleached grains of quartz in the absence of complicating extrinsic factors.

Prendergast et al. (2007) reported an assortment of features indicating that the upper layers of the Mumba deposit (i.e., above Bed III-middle, equivalent to Geological the middle of Unit C) suffered from anthropogenic disturbance. Archaeological artefacts that are distinctly LSA, pastoral Neolithic and Iron Age were found occurring together in these layers. This observed post-depositional mixing of artefacts would likely be associated with a post-depositional mixing of sediments, a feature that should be manifested as a large spread in D_e. The high overdispersion values (Table 6.2) obtained for samples from these layers (i.e., MR2 and MR3) support this. This suggests that post-depositional mixing contributed to the observed spread in D_e values for these two samples.

In contrast, no mixing was reported for layers below Bed III-lower/Geological Unit C-lower (MR4 to MR10). Small scale differences in the beta dose rate (as described in Section 4.4.2) are, thus, the most likely cause of scatter in D_e for grains from these layers. An abundance of small carbonate nodules, bones, and shells in these deeper deposits was reported by Prendergast et al. (2007). In addition, all artefacts were heavily concreted (Prendergast et al., 2007; Diez-Martín et al., 2009). These reports were corroborated by the abundance of egg shell, shells and smaller carbonate nodules observed during the collection and preparation of these OSL samples (Figure 6.2). The large amount of this carbonaceous material was verified by relatively volatile chemical reactions with HCl acid and by the accompanying loss of sample mass during laboratory

preparation of these OSL samples. Carbonates commonly have substantially lower radioactivity than the surrounding lithogenic sediments, leading to spatial inhomogeneity in the dose rate (Murray and Roberts, 1997; Olley et al., 1997; Nathan et al., 2003; Jacobs et al., 2008c). Consequently, a grain of quartz that was coated in, or abutted, carbonate-rich materials (e.g., Figure 6.2) would have received a substantially smaller beta dose during burial than a similar grain that was not. Therefore, grains that were deposited at the same time would be expected to have a range of D_e values, due to their exposure to different beta dose rates during burial, leading to a scattered D_e distribution. To distinguish between the most likely causes of the observed spread (i.e., post-depositional mixing or beta microdosimetry) the finite mixture model (FMM; Roberts et al., 2000) was used to analyse D_e distributions from Mumba.

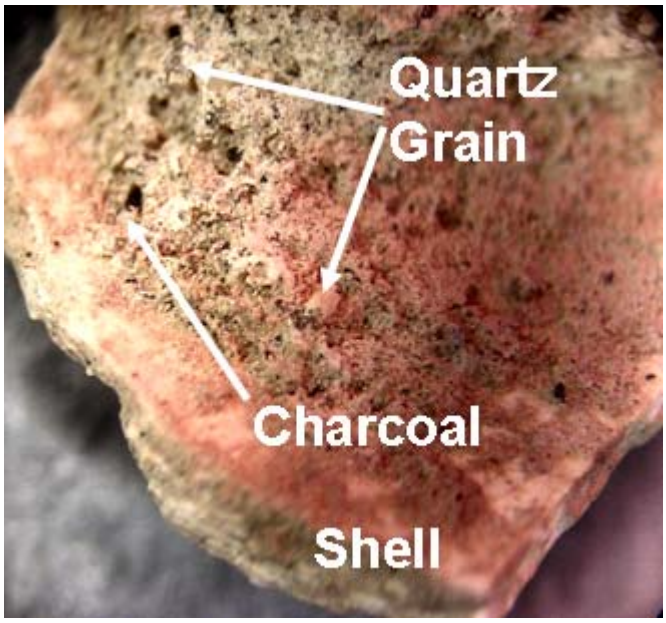

Figure 6.2: Photograph of a shell from Mumba. This shell was contained in the sediment sample (MR7) taken for OSL dating and was found during sample preparation. Note the two quartz grains affixed to the shell. These two quartz grains would likely have received half as much beta dose rate as a grain that was not abutting material with low beta activity.

6.3.1 Analysis of D_e distributions using the FMM

The D_e distributions can be investigated for the presence of human-induced mixing, dosimetry-induced scatter, or a combination of both, and a D_e value that is appropriate for the depositional event of interest can be obtained. The FMM (described in detail in Section 3.4.2) was systematically applied to all single-grain D_e distributions to identify the existence of discrete D_e components. The FMM can be fitted using the

approach described in detail by Galbraith (2005), David et al. (2007), Jacobs et al. (2008b) and in Section 3.4.2. An example of the fitting procedure is also presented in Section 3.4.2. The FMM could be appropriately used to fit two or more discrete D_e components to the D_e distributions from all but one samples from Mumba. The FMM fitting results are presented in Table 6.3. The range of optimal overdispersion values (16–20%) was considered appropriate for these samples, given the overdispersion value obtained for bleached and laboratory irradiated grains during the dose recovery experiment (15 ± 4%; Section 5.3.3.2). Five samples had D_e distributions that could be adequately fitted using two components. These kinds of distributions are referred to as 'scattered', following the terminology of Jacobs et al. (2008b), and will be discussed in Section 6.3.2. Additional components were required to optimally fit the D_e distributions

Table 6.3: Results of FMM analysis of D_e distributions for samples from Mumba. The optimal fit for each distribution was determined as described in Section 3.4.2.2. The main D_e component is denoted in italics. No discrete components could be fitted for sample MR2. Instead, the minimum and maximum D_e values were calculated using the minimum and maximum age models, respectively, for which a 20% standard error, as an estimate of inherent overdispersion, was added in quadrature to the measurement error for each individual D_e value.

Sample	No. of grains in D_e distribution	Overdispersion (%)	No. of fitted components	Component	Proportion (%)	D_e value (Gy)
MR2	78	20	No discrete components	Minimum		2.3 ± 0.3
				Maximum		31.3 ± 4.2
MR3	106	20	4	1	2 ± 1	5.0 ± 0.8
				2	25 ± 8	19.3 ± 1.9
				3	69 ± 8	*39.1 ± 2.2*
				4	5 ± 3	96.7 ± 22.0
MR4	46	16	2	1	44 ± 12	50.9 ± 4.3
				2	56 ± 12	*95.1 ± 7.2*
MR6	67	16	2	1	48 ± 14	92.2 ± 7.9
				2	52 ± 14	*153.3 ± 11.3*
MR7	48	20	2	1	18 ± 8	59.0 ± 8.5
				2	82 ± 8	*143.3 ± 8.5*
MR8	81	20	2	1	38 ± 8	72.3 ± 5.5
				2	62 ± 8	*173.3 ± 11.5*
MR9	84	18	3	1	16 ± 7	47.8 ± 5.6
				2	38 ± 9	95.8 ± 10.3
				3	46 ± 9	*216.9 ± 16.5*
MR10	20	20	2	1	33 ± 35	90.8 ± 24.2
				2	67 ± 35	*160.3 ± 34.9*

of two other samples. The latter kinds of distributions are referred to as 'mixed', following Jacobs et al. (2008b), and will be discussed in Section 6.3.3.

One sample, MR2, had a continuum of D_e values that were highly scattered (overdispersion value of 73 ± 6%) and could not be fitted satisfactorily using the FMM (Figure 6.1a). For this sample, the best fit that could be obtained using the FMM was a three-component model with the overdispersion set to 26%; this is higher than the maximum value of 20% used for the FMM based on the overdispersion values commonly reported for well-bleached quartz samples that are unaffected by complicating external factors (Roberts et al., 2000). This suggests that the three-component model, while it fits the data, does not actually describe discrete populations of D_e values. The majority of the D_e values for MR2 lie within a range of ~3 to ~30 Gy, with a weighted mean of ~9 Gy (Figure 6.1a and Table 6.2). Given the high degree of turbation observed for Bed III-upper (Prendergast et al., 2007), it is unsurprising that the width of the D_e distribution is so large. This sort of distribution is typical of deposits in which sediments from multiple depositional events have undergone prolonged mixing (Feathers et al., 2006; David et al., 2007; Jacobs et al., 2008b,c). It is, thus, impossible to identify any common D_e values that correspond to a particular depositional event. Instead, D_e values can be identified that correspond to grains that have been buried for the longest and shortest durations. In these cases, the range between the maximum D_e values, corresponding to grains that were deposited earliest, and minimum D_e values, corresponding to grains that were deposited most recently, is the best outcome that can be achieved. This can be accomplished using two other statistical models, namely the minimum age model (MAM; Galbraith et al., 1999) and the maximum age model (Olley et al., 2006). The results from the analysis of the D_e distribution of MR2 using these models are presented in Table 6.3.

6.3.2 'Scattered' D_e distributions

The five samples that could be adequately fitted with two components are MR4, MR6, MR7, MR8 and MR10 (Table 6.3 and Figure 6.1). Scattered distributions like these are similar to those presented in Jacobs et al. (2008c, Figure 4), which were explained as being the result of beta microdosimetry. Since no apparent sediment mixing was reported during archaeological investigations of the geological units from

which these samples were collected (Unit C-lower, Unit E and Unit G) (Prendergast et al., 2007), inhomogeneity in the beta dose rate is thought to be the most likely cause of the scattered D_e distributions.

An analytical test must be performed to verify the possibility that all grains were deposited at the same time, but had experienced a range of beta dose rates over the period of burial. This test models the effects on the D_e distribution of D_e values from grains that were completely enveloped by >2 mm of low-radioactivity material, such as carbonate, thus accumulating the smallest dose during burial. This approach is based on Jacobs et al. (2008c) and is described in detail in Section 4.4.2.1; it is described only briefly here. The smallest D_e component in the distribution is obtained using the MAM, and is assumed to represent grains that received no beta dose during the course of burial. The validity of this assumption can be tested by dividing the MAM D_e estimate by an adjusted bulk dose rate that does not include any beta dose contribution (i.e., gamma, alpha, cosmic-ray and internal contributions only). The assumption is considered valid only if this age is equal to, or greater than, the age obtained by dividing the main D_e component, identified using the FMM, by the total environmental dose rate (i.e., including the measured, average beta dose rate). The results of this analysis are presented in Table 6.4. For all five samples that have scattered distributions, the age calculated for the minor D_e population that experienced no beta dose is equal to, or greater than, the age calculated using the main D_e component and the total environmental dose rate. This result indicated that beta microdosimetry could be a likely cause for the observed spread in the scattered D_e distributions of these five samples.

6.3.3 'Mixed' D_e distributions

Three samples from Mumba could not be fitted with the FMM using two components (MR2, MR3 and MR9). One of these samples, MR2, has been discussed in Section 6.3.1. No discrete components could be identified in the D_e distribution of MR2 using the FMM and overdispersion values of 20% or less. This, along with the reported turbation of the layer from which this sample was collected, implies that MR2 consists of a mixture of grains from a great many depositional events, but only the first and last can be distinguished (Figure 6.1a). For samples MR3 and MR9, 4 and 3 discrete D_e

components could be identified using the FMM, respectively (Table 6.3). The presence of multiple dose components in these distributions can be attributed to these samples consisting of grains derived from multiple, discrete depositional events being mixed together afterwards.

When the D_e distribution from MR3 is examined, it is clear that two of the fitted components collectively account for less than 8% of the grains (Table 6.3). These minor D_e components have the largest and the smallest D_e values, while the majority of the grains (~92%) are included in the two middle components. The highest component makes up ~5% of the total distribution and is comprised of grains that have D_e values ~2.5 times that of the main component. The D_e of this component is statistically consistent with D_e values for grains from the underlying sample, MR4. It is, thus, likely that the grains that produced D_e values in the highest component are intrusive grains from these older layers. The smallest D_e component is comprised of 2 grains (Figure 6.1b), making up ~2% of the total number of grains. These two grains have D_e values of ~5 Gy, which cannot be explained solely in terms of reduced beta dose rates; they are considered to be intrusive grains.

The D_e distribution of MR9 is similar to that of MR3. The component with the lowest D_e value comprises approximately 16% of all of the accepted grains. The grains that make up this component have a mean D_e value that is too small to be explained by beta microdosimetry.

The presence of these minor components in the distributions of MR3 and MR9 are likely the result of small-scale mixing. Consequently, the small numbers of intrusive grains that make up these components were removed from the D_e distributions. Once these grains were removed, 92% and 84% of the total number of grains remained for samples MR3 and MR9, respectively. For both samples, the two remaining components have D_e values that differ by an amount consistent with inhomogeneity in the beta dose rates (Table 6.4). The existence of the smaller component could be the result of these grains receiving a smaller-than-average beta dose rate during burial. Thus, after removing the small number of intrusive grains from both samples, MR3 and MR9 were treated as 'scattered' D_e distributions.

Table 6.4: Results for beta microdosimetry-identification test (decribed in Section 4.4.2.1 and Jacobs et al., 2008c). The age obtained for the modelled grains that received an assumed beta dose rate of 0 Gy/ka must be greater than, or equal to, the age obtained for the majority of grains using the D_e of the main component identified by the FMM and the total bulk dose rate.

		Grains with attenuated beta dose rate					
Sample	Total dose rate (Gy/ka)	MAM D_e (Gy)	Adjusted total dose rate, 0 beta dose (Gy/ka)	Age (ka) with adjusted dose rate	FMM, Main component D_e (Gy)	Age (ka) with total dose rate	Possible beta micro-dosimetry?
MR3	2.28 ± 0.11	16.3 ± 1.2	1.06 ± 0.04	15.4 ± 1.3	39.1 ± 2.2	17.2 ± 1.3	yes
MR4	2.11 ± 0.10	49.2 ± 1.1	0.83 ± 0.03	59.0 ± 2.7	95.1 ± 7.2	45.1 ± 4.1	yes
MR6	2.50 ± 0.11	89.3 ± 1.5	1.16 ± 0.04	77.3 ± 3.3	153.3 ± 11.3	61.2 ± 5.5	yes
MR7	2.62 ± 0.12	57.6 ± 1.1	1.04 ± 0.04	55.5 ± 2.4	143.3 ± 8.5	54.7 ± 4.3	yes
MR8	2.57 ± 0.12	68.2 ± 1.2	1.03 ± 0.03	66.4 ± 2.9	173.3 ± 11.5	67.4 ± 5.7	yes
MR9	2.71 ± 0.13	108.5 ± 1.8	1.04 ± 0.03	104.4 ± 4.4	216.9 ± 16.5	80.1 ± 7.3	yes
MR10	3.02 ± 0.14	85.0 ± 1.8	1.11 ± 0.04	76.4 ± 3.3	160.3 ± 34.9	53.0 ± 11.9	yes

6.4 Beta microdosimetry correction and age determinations

6.4.1 Beta microdosimetry correction

The burial ages of all samples were determined using the main D_e component identified using the FMM (shown in italics in Table 6.3). The main D_e component for each sample was defined as that which contained the largest proportion of grains. The environmental dose rate then needed to be adjusted for these grains to take into account the following: if grains that were coated in low dose-rate material, such as carbonates, had experience below-average beta dose rates, then the other grains (i.e., those that comprise the main D_e component) must have received above-average beta dose rates. Both of these materials (i.e., high and low dose rate materials) were pulverised together and used for beta counting to produce the measured beta dose rate (as described in Section 4.2.3.2). This represents an average beta dose rate for the bulk sample, and is not the same as the dose rate received by the grains in the main D_e component during burial. Unfortunately, the beta dose rate for these grains cannot be measured directly. Instead, it was determined using the modelling approach introduced by Jacobs et al. (2008c) and described in Section 4.4.2.2. Results are presented in Table 6.5.

The dose distributions for three of the samples (MR4, MR6 and MR9) are comprised of two D_e components that contain nearly equal proportions of grains. When this is the case, the modelling used to correct the beta dose rate has very little effect on the final age determination. An age calculated using the weighted mean D_e value (obtained using the CAM) and the measured environmental dose rate (including the bulk beta dose rate) will be very similar to the age calculated using the main D_e component identified using the FMM and its corresponding adjusted dose rate. When these two age estimation methods are compared for these three samples (Table 6.5), it is clear that the paired age estimates are statistically indistinguishable.

6.4.2 Estimated uncertainty on age determinations

The uncertainties on the ages are calculated by combining, in quadrature, the uncertainties of the D_e and the dose rate. For the uncertainty on the D_e value, the FMM provided the random error, which was combined in quadrature with the systematic uncertainty of 2% associated with laboratory beta source calibration (see Section 3.3). The total uncertainty on the dose rate was obtained by adding in quadrature all random

Table 6.5: Final D_e values, total dose rates, and ages for single grains of quartz from Mumba. Data for different age models with associated ages are shown for comparison.

	CAM			FMM						
	Measured dose			Adjusted dose			Age	Dose rate		
Sample	D_e (Gy)	rate (Gy/ka)	Age (ka)	D_e (Gy)	rate (Gy/ka)	Age (ka)	model	D_e (Gy)	(Gy/ka)	Age (ka)
MR2							Min	2.3 ± 0.3	2.61 ± 0.12	0.9 ± 0.1
							Max	31.3 ± 4.1	2.61 ± 0.12	12.0 ± 1.7
MR3				39.1 ± 2.2	2.51 ± 0.12	15.6 ± 1.2				
MR4	72.4 ± 4.6	2.11 ± 0.10	34.3 ± 2.8	95.1 ± 7.2	2.58 ± 0.12	36.8 ± 3.4				
MR6	119.3 ± 5.8	2.50 ± 0.11	47.7 ± 3.3	153.3 ± 11.3	3.12 ± 0.14	49.1 ± 4.3				
MR7				143.3 ± 8.5	2.79 ± 0.14	51.3 ± 4.2				
MR8				173.3 ± 11.5	3.04 ± 0.14	56.9 ± 4.8				
MR9	152.5 ± 9.7*	2.71 ± 0.13	56.3 ± 4.6	216.9 ± 16.5	3.42 ± 0.15	63.4 ± 5.7				
MR10				160.3 ± 34.9	3.49 ± 0.16	45.9 ± 10.3**				

*For MR9, the low-dose, intrusive grains (16% of the total) were removed prior to calculation of the CAM D_e.

**For MR10, the calculated age is considered a minimum estimate due to saturation of the natural OSL signal (see text).

errors and the systematic uncertainties related to sample water content and grain-size (see Section 4.3 and Section 6.1). The uncertainty on the final age is given as one standard deviation.

6.4.3 Age determinations and comparisons

The final ages derived from single grains of quartz from Mumba are presented in Table 6.5. Ages or age ranges were calculated for eight samples. For seven samples, the D_e of the main component is presented along with the corresponding beta-adjusted dose rate and age. Since no discrete D_e populations could be identified for MR2 using the FMM (using appropriate overdispersion values), an age range was determined that represents grains deposited earliest (largest D_e values and ages) and most recently (smallest D_e values and ages).

Three samples have D_e distributions that are comprised of two components of equal proportions (i.e., MR4, MR6 and MR9). For these samples, the weighted mean D_e (obtained using the CAM) is also presented, alongside the corresponding bulk sample dose rate and the resultant age. Because the total dose rate depends on the model chosen for age estimation, an appropriate comparison of the two statistical models (i.e., FMM and CAM) can only be made using the ages, and not the D_e values. Additionally, to facilitate a direct comparison of the CAM and the FMM ages for sample MR9, the presumed intrusive grains (16% of the total number) were removed from the distribution, and the CAM D_e was recalculated. For these three samples, there is good agreement between the beta-adjusted FMM age and the weighted mean CAM age. The CAM/FMM age ratios for samples MR4, MR6 and MR9 are 0.93 ± 0.11, 0.97 ± 0.11 and 0.89 ± 0.11, respectively. The internal consistency of the ages obtained using the CAM and FMM methods (Table 6.5) suggests that the adjustment made to the beta dose rate is valid for the Mumba samples. It also indicates that, for samples with suitable D_e distributions, the OSL ages are not dependent on the statistical model chosen for analysis. These conclusions provide confidence in the estimated ages for the quartz samples from Mumba.

The ages obtained using single grains of quartz are in correct stratigraphic order, with the exception of that for the deepest sample (MR10). This discrepancy will be addressed in the next section (Section 6.5). Several of these ages are also in agreement

with independent ages cited in the literature. Specifically, the ages obtained for samples from Bed V (MR6, MR7 and MR8) are in agreement with an age of 52 ka and an age range of 45–65 ka, obtained using AAR (amino acid racemisation) on OES from Bed V deposits, reported by McBrearty and Brooks (2000). The internal consistency of this chronology provides confidence in the single-grain quartz ages for samples from Mumba.

6.5 Problematic samples

Reliable OSL ages were not obtained from quartz for several samples presented in this study: namely, MR2, MR5 and MR10. MR2 comes from a layer where substantial turbation was observed (Prendergast et al., 2007). The best result is an age range identified using the MAM and the maximum age model, which give an age range of between 0.9 ± 0.1 ka and 12.0 ± 1.7 ka (Table 6.5).

Grains of quartz from MR5 produced no natural OSL signal despite producing OSL in response to laboratory irradiations. Since no age could be obtained for sample MR5, the best result that can be achieved is an age range based on the ages of the samples taken directly above and below this sample. Thus, MR5 must have been deposited sometime between 36.8 ± 3.4 ka (MR4) and 49.1 ± 4.3 ka (MR6).

The final sample that requires discussion is MR10. Several factors indicated that estimating D_e values for this sample would be problematic. First, the proportion of grains rejected from this sample's dataset (~97%, Table 6.2) was higher than for any other sample from Mumba. Proportionally, twice as many grains were recovered for the overlying sample (MR9), which is from the same geological unit as MR10: 6% and 3% of all grains measured from MR9 and MR10, respectively, were accepted. Second, many grains from Mumba experienced an early onset of OSL signal saturation. Although many of these grains were rejected using the experimentally determined rejection criterion, saturation was expected to be particularly problematic for MR10 since it was taken from the deepest layer sampled. Accordingly, the natural OSL signals of the quartz grains from this sample were very close to the saturation intensity, resulting in only minimum estimates of D_e. This is supported by a comparison of the D_e distribution for MR10 with that MR9. When the FMM is used to analyse the dataset of MR10, the D_e of the minor component is statistically consistent with the D_e of the minor

component identified for MR9 (~95 Gy). The main component identified for MR9 is centred on ~216 Gy. The main component identified for MR10 is 160.3 ± 34.9 Gy, which is consistent with 216 Gy at 2σ. In addition, 55% (n = 11) of D_e values obtained from grains of MR10 were consistent with 216 Gy at 2σ. Given the higher dose rate measured for MR10 (~0.3 Gy/ka higher than for MR9), and the fact that it was taken from below MR9 (and is, thus, older), it is plausible that the burial dose of MR9 was low enough that it could be obtained from the highest, unsaturated portion of well-behaving dose-response curves. The burial dose of MR10, by contrast, may be high enough that the natural OSL signal that is representative of the main depositional event lies above the saturation dose of the well-behaved grains. It was thus concluded that the OSL signals from many of the quartz grains from sample MR10 were most likely saturated and that the estimated D_e values could only be considered as minimum estimates.

6.6 Summary

In this chapter, the measurement and analysis of D_e distributions for eight samples from Mumba was described. The major results are as follows:

- The D_e distribution of MR2 included grains from too many depositional events to distinguish as discrete entities. It was concluded that these grains were deposited at different times and were subsequently mixed after burial, supporting the observed turbation reported by Prendergast et al. (2007). As a result, an age range of 0.9 ± 0.1 ka to 12.0 ± 1.7 ka was the best outcome that could be achieved.
- The D_e distributions of two samples (MR3 and MR9) showed evidence of post-depositional mixing. Populations of intrusive grains were identified using the FMM. When these grains were subsequently removed from the datasets, the distributions were treated as 'scattered'.
- The 'scattered' D_e distributions of five samples (MR4, MR6, MR7, MR8 and MR10), as well as those of MR3 and MR9 (after the removal of intrusive grains), were consistent with two components. The presence of the minor component was inferred to be the result of beta dose rate heterogeneity.

- Ages were calculated for eight samples (MR3, MR4, MR6, MR7, MR8, MR9 and MR10) using the main population of grains and a beta-adjusted dose rate. The age obtained for MR10 using single grains of quartz should be considered a minimum age due to the small D_e dataset (n = 20) and the fact that many grains had OSL signals that were in saturation. With the exception of MR10, all ages are in correct stratigraphic order. The ages obtained for Mumba using single grains of quartz will be compared with ages obtained from IRSL measurements of feldspars in Chapter 8. The archaeological implications of this revised chronology for Mumba will be discussed in Chapter 10.

The inability to obtain a robust OSL age using quartz from MR10 indicates the limitations of this mineral to estimate burial doses beyond the saturated region of the dose-response curve. Accurate ages for Bed VI are crucial to achieving one of the objectives of this thesis. To identify when the transition from an MSA lithic toolkit to the Mumba Industry occurred, ages need to be obtained for layers containing each of these technologies. All samples collected from Bed V (MR6, MR7 and MR8), which contains the Mumba Industry, could be dated using OSL on single grains of quartz. Only one sample from Bed VIA (MR9) could be dated. More ages for Bed VIA (i.e., sample MR10) were, thus, desirable to identify when an MSA lithic toolkit was being used at Mumba. To circumvent problems associated with the saturation observed in quartz from MR10, the suitability of using feldspar separates to obtain an IRSL age was explored, as feldspars have a much higher saturation limit than quartz. These investigations are the subject of the next chapter.

Chapter 7: Characterisation of the luminescence signal of K-feldspars from Mumba rockshelter, Tanzania

The quartz from Mumba has some malign OSL properties that hinder age estimation for older samples. A major problem is the relatively low doses at which the OSL signal from quartz grains saturates, and the relatively high dose rate of the sediment surrounding the samples. Consequently, ages could be estimated for samples from Bed V and only the uppermost sample from Bed VI.

In this chapter, investigations of the luminescence signal from potassium (K)-feldspar grains from Mumba are described. The main aim of investigating K-feldspars was to obtain ages for samples form Bed VIA. There were four main objectives that were set in order to achieve the aim of this study. First, the luminescence mechanics in feldspars were investigated by comparing the shape and intensity of TL glow curves and infrared stimulated luminescence (IRSL) decay curves. The temperature at which IR stimulation was performed was also investigated. Second, the optimal stimulation conditions for estimating D_e values using improvements to conventional measurement procedures (namely the SAR procedure) were investigated. Third, use the improved measurement procedures to find a signal that suffered from anomalous fading the least. Anomalous fading is the discharge of electrons out of traps that appear to be thermally stable over geologic time, thus resulting in an underestimation of the burial dose and age (see Section 7.1.2; Wintle, 1973; Spooner, 1994b; Thomsen et al., 2008). Fourth, use the outcomes from the first three aims to obtain ages for K-feldspar grains from Mumba.

7.1 Feldspar background

7.1.1 Feldspar mineralogy

Feldspar is a term used to refer to a broad spectrum of alumino-silicate minerals with tetrahedral structures composed of four oxygen atoms and a silicon atom (SiO_4) (Duller, 1997; Krbetschek et al., 1997). When silicon atoms are replaced with aluminium atoms, cations, typically K, sodium (Na), calcium (Ca) and occasionally barium (Ba), may be inserted into the lattice. Feldspars represent a solid-solution series that can be illustrated as a ternary diagram (Figure 7.1). The end-members of this series are made entirely of K (orthoclase or K-feldspars), Na (albite) and Ca (anorthite) with

the intermediate feldspars being composed of varying proportions of these end members in a continuous series (Duller, 1997). Feldspars of potassium and sodium (K+Na) and of sodium and calcium (Na+Ca) composition are known as alkali and plagioclase feldspars, respectively (Krbetschek, et al., 1997). The structural state of a feldspar (that is, the ordering of aluminium and silicon atoms within the lattice) is principally the result of its thermal history. Feldspars are typically disordered if they crystallise at high temperatures (such as feldspars of volcanic origin) and are ordered if they crystallise at low temperatures (Duller, 1997; Krbetschek, et al., 1997). Generally, feldspars of intermediate composition that are crystallised at a high temperature will have a disordered, homogeneous composition. Alternatively, if these feldspars were crystallised at a low temperature, they will have an ordered structure with phase separation (i.e., alkali feldspars will form regions of K-rich and Na-rich composition) (Duller, 1997). Many authors agree that feldspars with a more disordered structure tend to have higher rates of anomalous fading (Spooner, 1994b; Visocekas et al., 1994, 1998; Fattahi and Stokes, 2003a), although Huntley and Lian (2006) presented evidence that the fading rates of volcanic and non-volcanic feldspars do not differ significantly.

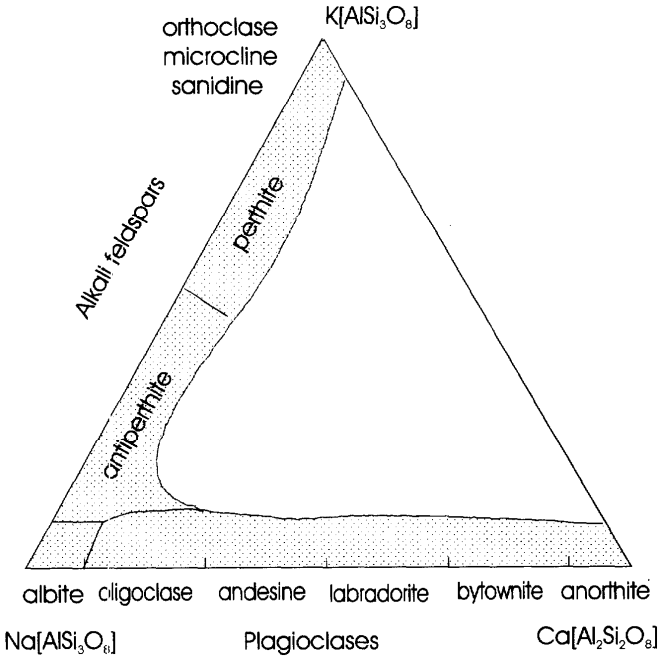

Figure 7.1: Feldspar nomenclature and chemical composition shown as a ternary diagram (from Krbetschek et al., 1997).

7.1.2 Feldspar luminescence

Feldspar has several advantages over quartz as a luminescence dosimeter. First, the luminescence emitted from K-feldspars per unit dose is often 10–50 times brighter than that from quartz (Duller, 1997), which results in better counting statistics, higher precision of measured doses, and smaller doses that can be measured precisely. Second, feldspar luminescence can be stimulated using IR photons, which allows technically easier measurement of a blue/UV emission due to the large difference in wavelength between the stimulating and the measured wavelength (Hütt et al., 1988; Duller, 1997; Aitken, 1998). Third, the feldspar luminescence signal saturates at higher radiation doses than the luminescence signal from quartz. Older samples can, therefore, be dated using feldspars (Huntley and Lamothe, 2001). Fourth, K-feldspars have a relatively high ^{40}K content (12.5 ± 0.5%; Huntley and Baril, 1997) and ^{87}Rb content (400 ± 100 μg/g; Huntley and Hancock, 2001). These internal contributions to the dose rate are unaffected by variations in water content and beta dose rate heterogeneity, thus reducing the overall dose rate uncertainty (Duller, 1997). These final two points are particularly beneficial for luminescence investigations of sediment from Mumba, where beta dose rate heterogeneity and low saturation levels of the luminescence signal from quartz hindered age estimation.

Aside from the positive properties listed above, feldspars have a malign property that has limited their use as chronometers, namely anomalous fading. This phenomenon was first observed by Wintle (1973) in TL studies of lava flows. Spooner (1994b) showed anomalous fading to be virtually ubiquitous in an IRSL study of museum feldspar samples. Several studies have also confirmed the phenomenon's ubiquity in sediment samples (Huntley and Lamothe, 2001; Huntley and Lian, 2006). The physical model used to describe anomalous fading is based on quantum-mechanical tunnelling (Visocekas, 1985), which is summarised by Aitken (1985: Appendix F).

The work of Hütt et al. (1988) showed that luminescence in feldspars is dominated by electron transfer from a single defect type. This single-trap origin for feldspar IRSL has been confirmed by later studies (Krbetschek et al., 2000; Trautmann et al., 2000; Baril and Huntley, 2003a; Thomsen et al., 2008; Murray et al., 2009). The pathways of electrons from the ground state of this single defect type to a recombination centre to create luminescence following IR stimulation are, however, still unclear. The

difference between the main peak of the stimulation spectrum (1.41–1.47 eV: Bailiff and Barnett, 1994; Clark and Sanderson, 1994; Poolton et al., 1995; Duller, 1997) and the depth of the ground state of the IRSL electron trap below the conduction band (~2 eV; Poolton et al., 2002b) in alkali feldspars indicates that there is a ~0.5 eV gap between the excited state and the conduction band (Poolton et al., 2002a). Hütt et al. (1988) posited that electrons are stimulated to the exited state by IR and are then thermally assisted to the conduction band where they are highly mobile and can reach distant recombination centres. This model, partially supported by later studies (Bailiff and Poolton, 1991; Hütt and Jaek, 1993; Clark and Sanderson, 1994), was largely contradicted by the results of others (e.g., Baril and Huntley, 2003b) that showed that the thermal activation energies are too small to thermally excite the excited electrons directly into the conduction band (Thomsen et al., 2008).

Poolton et al. (1995, 2002a,b, 2009) posited that a donor-acceptor recombination process is at the root of IRSL from feldspars. This model, supported by the results of several other studies (e.g., McKeever et al., 1997; Thomsen et al., 2008; Li, 2010), suggests that after electrons are stimulated to the excited state (where their tunnelling range is larger than from the ground state), they can either tunnel directly to a recombination centre without passing through the conduction band (a possibility also suggested by Baril and Huntley, 2003b) or they are transferred into low-mobility band-tail states or the conduction band (with thermal assistance) where they can reach more distant recombination centres. Band-tail states are localised deformations in the conduction band potential that allow electrons to move, although with less mobility than electrons in the conduction band (Poolton et al., 2002b). They are formed by the presence of imperfections (charged impurities or non-standard bond angles) in the crystal structure of feldspars (Poolton et al., 2002b). Regardless of the mechanics of IRSL production in feldspars, electrons that are trapped in defects can tunnel directly from the ground state to the recombination centre if it is close enough (Poolton et al., 2002a). This has been directly observed as tunnelling afterglow following a laboratory irradiation (Spooner, 1994b; Visocekas et al., 1994, 1998; Visocekas, 2002) and is the reason for the observed decrease in luminescence with time, i.e., anomalous fading (Visocekas, 1985, 2002; Aitken, 1985; Poolton et al., 2002a,b; Huntley, 2006).

Much of the research regarding feldspar as a luminescence dosimeter has been focused on addressing this issue of anomalous fading, which can be quantified using the *g*-value (%/decade, where a decade is a factor of 10 in time since irradiation; see Section 7.6.2.2). Several studies have claimed to have found non-fading signals from feldspars using specific TL peak temperatures, emissions, and feldspar mineralogies (Guérin and Valladas, 1980; Zink and Visocekas, 1997; Gelian et al., 2006; Huntley et al., 2007). Others have reported using grain-to-grain and aliquot-to-aliquot variability in fading rates as a method for estimating a correct D_e (Lamothe and Auclair, 1999). All of these methods either require specialised equipment or the correct mineralogy of feldspar to be present. Other methods have not withstood scrutiny. For lack of finding a non-fading feldspar signal, the most common and practical method for addressing anomalous fading has been to measure the fading rate and correct the estimated age for it. Aitken (1985: Appendix F) presents a model based on quantum-mechanical tunnelling and can account for some anomalous fading data. This model is the basis for the most commonly used anomalous fading correction, based on the work of Huntley and Lamothe (2001). This correction, however, has its limitations. Specifically, it becomes unreliable for old samples for which the D_e does not fall on to the linear portion of the dose-response curve. Other fading corrections have been developed (e.g., Lamothe et al., 2003; Kars et al., 2008), but the method presented by Huntley and Lamothe (2001) has proved to be sound for samples with doses up to 200 Gy and is used in many feldspar studies (e.g., Balescu et al., 2003; Buylaert et al., 2009; Martins et al., 2010; Tsukamoto et al., 2010). Martins et al. (2010) infer from their results and the literature that the Huntley and Lamothe (2001) correction for anomalous fading works well up to a dose of at least ~200 Gy.

7.2 Emission characterisation

There are several main emissions that have been used in past studies of feldspar TL and IRSL. A comprehensive summary of these studies on TL and IRSL spectra from feldspars can be found in Krbetschek et al. (1997). The major emissions that are currently being researched as those most applicable for dating purposes are the UV, blue, yellow and red. There are two UV emission bands. One is centred at 275–290 nm (Prescott et al., 1994; Krbetschek and Rieser, 1995; Rendell and Clarke, 1997; Clarke et

al., 1997) and is considered thermally unstable (Wintle and Duller, 1991; Krbetschek et al., 1997). The second is centred at 320–340 nm, is dominant in plagioclase feldspars, and is considered thermally stable owing to its intensity at high temperatures (Krbetschek and Rieser, 1995; Krbetschek et al., 1996).

The blue emission (~390–440 nm) is considered the main IRSL emission from K-feldspars (Clarke and Rendell, 1997; Krbetschek et al., 1997), although it is present in some Na-feldspars (Clarke and Rendell, 1997) and plagioclase feldspars (Krbetschek and Rieser, 1995). Baril and Huntley (2003b) showed a correlation between K content and increased intensity of the ~410 nm emission band.

The yellow emission (~550–570 nm) has been shown to be related with Mn substituting for Ca, making it more likely to be produced by plagioclase feldspars (Krbetschek et al., 1997; Baril and Huntley, 2003b). The yellow emission generally dominates the TL spectra of plagioclase feldspars (Huntley et al., 1988, Prescott et al., 1990), although it has been reported in other feldspar types also (Krbetschek et al., 1996; Clarke and Rendell, 1997). In addition, the yellow TL emission from plagioclase feldspars has been shown to be non-fading in one study (Gelian et al, 2006). Huntley et al. (2007) also suggest that the yellow emission from plagioclase feldspars (with <5% Ca content) may be non-fading.

The red emission (~600–750 nm) has been shown to be present in many feldspar types (Krbetschek et al., 1997), with the far-red emission (~700–710 nm) attributed to Fe^{3+} substituting for Al^{3+} (Zink et al., 1995). Several TL studies have also shown that the red emission fades less than the blue emission and can be used to successfully obtain an age from alkali and plagioclase feldspars (Zink et al., 1995, Zink and Visocekas, 1997; Visocekas and Guérin, 2006). Despite the technical problems associated with stimulating with IR and measuring a red emission (Fattahi and Stokes, 2003b), red IRSL has been suggested to be non-fading by Fattahi and Stokes (2003a). Using the far-red IRSL emission, the SAR procedure was shown to be suitable for application using K-feldspar separates with mixed results (Arnold et al., 2003; Fattahi, 2004). Tests on the potential non-fading red IRSL emission were also inconclusive (Fattahi and Stokes, 2003c; Fattahi, 2004).

Owing to the diversity in feldspar mineralogy, it can be expected that there may be a large diversity in luminescence emissions. To this end, it is worth investigating the

presence of the various emissions in the feldspars from Mumba. It should be noted that, due to instrumental limitations, the technique of measuring the far-red emission was not investigated in this study.

7.2.1 Instrumentation – IRSL measurement and filter combinations

All IRSL measurements on feldspars from Mumba were made using the same Risø TL/OSL reader (Risø 4). The instrument is fitted with a 1 W IR laser diode (830 nm) that can deliver a power density of 300 mW/cm^2. The measurement of all emissions was performed using a blue-sensitive bialkali Electron Tubes Ltd 9235QA PMT. This tube has a high quantum efficiency in the blue portion of the spectrum and is thus not ideal for measurement of yellow emissions (~550 nm).

Table 7.1: Filter combinations used to measure different luminescence emissions from K-feldspar separates.

Emission	Wavelength (nm)	Filters	Thickness (mm)
Ultraviolet	270-390	U-340	7
Blue	350-450	BG39	2
		Kopp 7-59	4
Blue	350-550	BG39	2
		Kopp 5-60	4.3
Yellow	540 - 683	BG39	2
		GG400	3
		OG550	1

Filter combinations used to isolate the desired wavelength are presented in Table 7.1. The UV emissions were measured using two U-340 (3 mm) filters, which have a maximum transmittance at ~330 nm. Blue emissions were measured using two different combinations. The standard blue filter combination included a band-pass BG39 (2 mm) filter and a Kopp 7-59 (4 mm) filter. The second blue filter combination included a band-pass BG39 (2 mm) filter and a Kopp 5-60 (4.3 mm) filter with a maximum transmittance at ~420 nm. The yellow emission was measured using a band-pass BG39 (2 mm) filter, a long-pass GG400 (3 mm) filter and a long-pass OG550 (1 mm) filter with a maximum transmittance at ~559 nm. The BG39 band-pass filter used

to transmit all emissions (except UV) is used to reduce the effect of scattered photons from the IR diodes (Fattahi and Stokes, 2003b).

7.2.2 Comparing TL and IRSL emissions from K-feldspars from Mumba

To compare various emissions from K-feldspar separates from Mumba, the TL and IRSL signals from two aliquots, consisting of ~500 grains of sample MR9, were measured through the four different filter combinations. The aliquots were first heated to 500°C, cooled to room temperature and immediately given a ~117 Gy irradiation, preheated to 260°C for 60 s, and then stimulated with the IR diodes for 100 s at 50°C. The filters were then changed and the procedure was repeated using the same two aliquots, beginning with the 500°C heat treatment. This measurement cycle was performed a total of five times. The first cycle served to sensitise the two aliquots and the luminescence was measured through the standard blue filter combination. The second, third, fourth and fifth cycles were measured through the yellow, second blue filter combination (BG39 and Kopp 5-60), the UV and the standard blue filter combination (BG39 and Kopp 7-59), respectively. By performing the experiment in this way, the shape and intensity of decay curves and TL glow curves could be compared for the same aliquot for different emissions. It also provided an internal reproducibility check; by measuring the first and final cycles through the standard blue filter combination, the shape and intensity of the first and final decay curves could be compared to ensure that no unaccounted for sensitisation had occurred.

Figure 7.2 illustrates the TL glow curves for the 500°C heat treatment following IR stimulation. The TL curves show consistent peak positions regardless of the filter combination used. There are three general peaks present: at ~180°C, at ~350°C and one on the shoulder of the ~350°C TL peak at ~430°C. The only difference between the two blue and UV emissions is the intensity of the glow curve. The TL glow curves measured through the two blue filter combinations were about an order of magnitude brighter than the TL viewed through the UV. The TL viewed through the standard blue filter combination was brighter than that of the second blue combination for temperatures greater than ~200°C. The glow curve measured using the yellow emission has the same general shape as the other glow curves up to ~375°C, although it is about an order of magnitude dimmer than the UV emission glow curve. At temperatures

above ~375°C, the yellow emission glow curve begins increasing through 500°C, showing the opposite behaviour to those observed for the other three filter combinations.

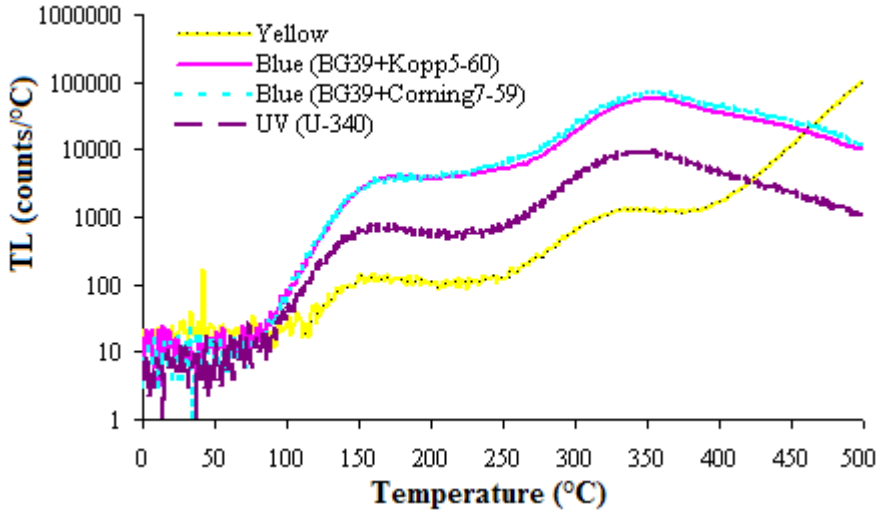

Figure 7.2: TL glow curves for various emissions from one aliquot of MR9. Results are representative of both aliquots measured. The TL peaks remain in the same position regardless of the emission observed; only the intensity of the TL changes.

These results suggest that there are major differences in brightness of the TL signal from various emissions. On the other hand, there are only minor differences in the shapes of TL glow curves from different emissions. The exception is the high-temperature portion of the yellow emission TL curve, which may represent the low-temperature portion of a high-temperature (i.e., >500°C) TL peak

Figure 7.3 presents IRSL decay curves measured using the various filter combinations. These results are from the same aliquot whose TL curves are presented in Figure 7.2. First, it should be noted that the two IRSL decay curves measured using the standard blue filter pack (i.e., in the first and final measurement cycles) are identical and are very similar in intensity (~2.3 million and ~2.4 million counts, where the IRSL signal is calculated as described in Section 3.3.1.1). This indicates that differences in decay curve brightness observed for different filter combinations are the product of changes in observed emissions, not of sensitisation of the aliquot. Similarly to the TL glow curves, the IRSL decay curve shape is consistent when measured in the blue and UV emissions. The UV signal, however, is approximately an order of magnitude dimmer than the blue signal. The IRSL decay curves measured using the two different

blue filter combinations (i.e., standard and second) are approximately equal in brightness, similar to their TL glow curves. The yellow emission produces a very different decay curve. It is substantially dimmer than that of the UV and it decays as an overall slower rate, although the slope looks similar to the other decay curves over the first 1–2 s of stimulation. Instead of decreasing to a background level, it stops decaying after ~10 s of IR stimulation and gradually increases as a function of increasing IR stimulation time.

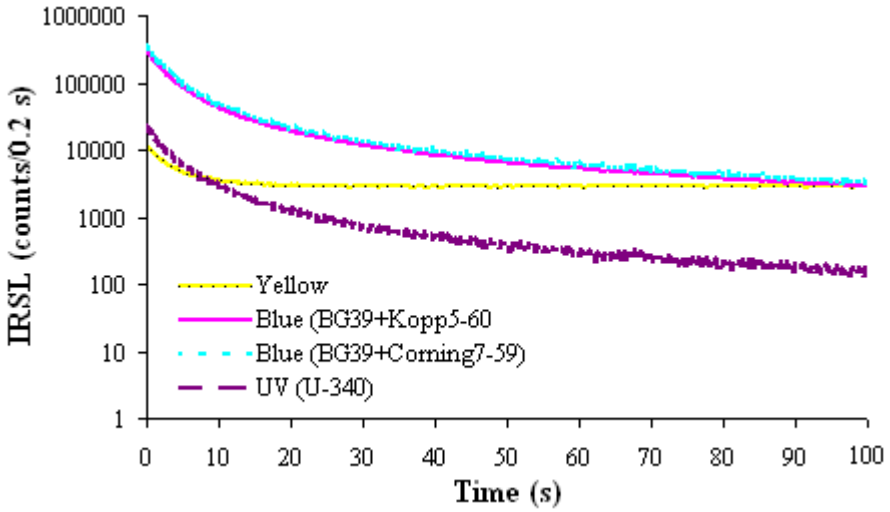

Figure 7.3: IRSL decay curves for various emissions from one aliquot of MR9. Results are representative of both aliquots measured. Note the logarithmic scale for the y-axis.

The results from the above experiment and analyses suggest that the remaining investigations of the IRSL signal from K-feldspars from Mumba should be carried out using a blue filter combination to maximise the IRSL signal intensity that is measured. Due to the abnormal appearance of its decay curve, the yellow emission is not considered practical at this time for dating purposes using standard procedures. While there is no difference in IRSL decay curve or TL curve shape measuring either the blue or UV emissions, the greater signal intensity obtained from the blue emissions will increase counting statistics and result in more precise data. The UV filters transmit both the stable peak between 320 and 340 nm and the unstable peak between 275 and 290 nm (Krbetschek et al., 1997), making this filter combination less suitable for dating than either of the blue filter combinations. In addition, several studies have noted that the UV emission that is IR stimulated from feldspars suffers from anomalous fading more

than the blue emission (e.g., Preusser, 2003; Klasen et al., 2007; Tsukamoto and Duller, 2008; Morthekai et al., 2008). The blue emission is the most commonly measured emission in IRSL studies of feldspars (e.g., Balescu et al., 1997; Huntley and Lamothe, 2001; Preusser, 2003; Auclair et al., 2007). The TL and IRSL signals measured for the two different blue filter combinations were very similar in shape and magnitude. Subsequently, all remaining luminescence measurements described in this chapter were made using the standard blue filter combination (BG39 + Corning 7-59). The choice of this filter combination also ensures that these results can be compared with those of the many other studies that employed the same filter combination (e.g., Wallinga et al., 2000a,b; Auclair et al., 2003; Thomsen et al., 2008).

7.3 Thermoluminescence from K-feldspars

7.3.1 Overview

No TL peaks have been shown to be present in all feldspars, although several peaks have been shown to be common. Many natural K-feldspars often exhibit two TL peaks centred at 250–280°C and 330°C, and laboratory-irradiated feldspars often exhibit a large TL peak at ~150°C (Duller, 1997). Also, unlike quartz where OSL is generally believed to originate from the trap associated with the 325°C TL peak (Smith et al., 1986; Spooner, 1994a), there is no consensus regarding a correlation between a specific TL peak and the source trap for IRSL in feldspars (Duller, 1997). Godfrey-Smith et al. (1988) reasoned that the traps that generate IRSL in feldspars are not important in TL production, based on the contrasting bleaching rates of each, although most other studies (e.g., Li, 1991; Bøtter-Jensen et al., 1991; Duller and Wintle, 1991; Duller, , 1994, 1995; Murray et al., 2009) are not in agreement with this claim. Pulsed-annealing experiments have been used to assess the temperatures at which the charge that produces the IRSL signal is evicted (e.g., Li, 1991; Bøtter-Jensen et al., 1991; Duller, 1994; Murray et al., 2009), and these generally point towards a higher temperature TL peak as the source of the IRSL. The effects of IR stimulation on TL peaks has also been investigated (e.g., Duller and Wintle, 1991; Duller, 1995; Murray et al., 2009). These studies have shown that IR stimulation reduces the intensity of the TL peaks, although not necessarily uniformly. Murray et al. (2009) reported that their TL peak at ~310°C was unaffected by IR stimulation. They also observed that the ~150°C TL peak does

not contribute to IRSL, supporting the earlier conclusion of Duller and Bøtter-Jensen (1993). The outcomes from these studies suggest that IRSL originates from charge associated with higher temperature (>310°C) TL peaks (Duller, 1997). Murray et al. (2009) go so far as to identify the high-temperature TL peak at 410°C as the source trap for IRSL.

The large variety of TL characteristics is likely due to the range of chemical compositions within the feldspar group (Duller, 1997). As a result, a thorough characterisation of the feldspar signal should be performed for every dating study.

7.3.2 Characterising the TL signal of K-feldspars

For three aliquots comprised of ~500 grains of MR9, an additive laboratory dose of 0, 60 or 240 Gy was applied in addition to the natural dose. The aliquots were then heated to 500°C and the TL was measured (Figure 7.4). A blank stainless steel disc was also measured and used to subtract any background TL from the aliquots. There is little difference in the composition of the TL peaks in the higher temperature region (i.e., >300°C) between the aliquot with no added dose and aliquots that had received a laboratory dose. Humps at ~350°C and ~430°C can be observed in the TL curves of all three aliquots. The main difference is that laboratory irradiation results in a large TL peak in the low-temperature region (at ~150°C), and this peak is not present in the natural aliquot. At 150°C, the aliquot that received a 60 Gy additive dose produced a TL signal ~50,000 times greater than the aliquot that received no laboratory dose. Many studies have observed this large, low-temperature TL component and have concluded that it does not contribute to the measured IRSL signal (Bøtter-Jensen et al., 1991; Duller and Bøtter-Jensen, 1993; Murray et al., 2009). However, in order to ensure that the luminescence signals resulting from laboratory and natural irradiations were as similar as is reasonably possible, the low-temperature TL components should be removed for purposes of dating. This could be achieved through the application of a high-temperature preheat. The natural TL signal begins to reach a peak at ~260°C, which is approximately the same temperature that the TL curves for the irradiated aliquots begin to take the same shape as that of the natural aliquot. Based on this, and on results from many recent feldspar IRSL studies taken from the literature (e.g., Huot

and Lamothe, 2003; Cunha et al., 2008; Buylaert et al., 2009), a preheat of 260°C for 60 s was chosen.

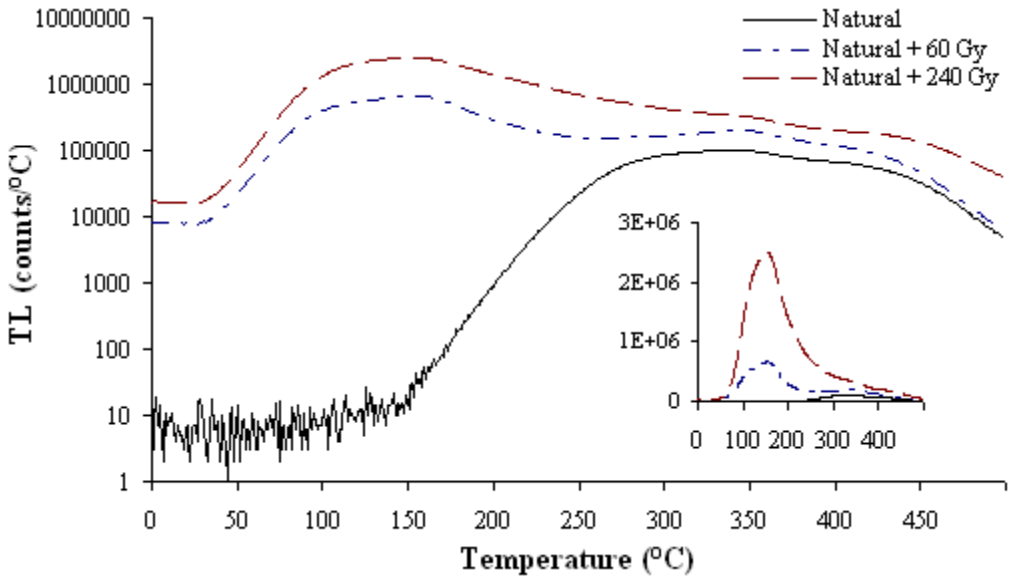

Figure 7.4: TL glow curves from three aliquots of MR9. Each aliquot was given a different laboratory irradiation followed by a 500°C heat treatment. Note that the inset plot shows the same data as the main figure, but with the y-axis on a linear scale.

Further TL experiments were conducted in order to investigate: 1) the relationship between the TL curve and IR stimulation, and 2) how the TL curve changes throughout the steps of one SAR cycle (see Section 3.3). Table 7.2 presents a step-by-step outline of this experiment. Several aliquots of MR9 were heated to 500°C and then had their TL signal recorded (while heating to 500°C) after successive steps of a SAR cycle. First, the TL was recorded following an irradiation of 117 Gy. Then the TL was recorded following an irradiation (117 Gy) and a preheat of 260°C for 60 s. Then the TL was recorded following an irradiation (117 Gy), preheat, and IR stimulation at 50°C for 100 s. Finally, the TL was recorded following an irradiation (117 Gy), preheat, IR stimulation at 50°C, and an IR stimulation at 225°C for 100 s; the latter is referred to as post-IR IR stimulation (Thomsen et al., 2008; Buylaert et al., 2009) and will be discussed in Section 7.5 (Figure 7.5).

Table 7.2: Step-by-step outline of the experiment described in this section. Note that the "TL curve" corresponds to the nomenclature in Figure 7.5.

Labotatory treatment	TL curve
Heat to 500°C	
117 Gy dose	
Heat to 500°C	A. Dose
117 Gy dose	
Heat at 260°C for 60 s	
Heat to 500°C	B. Dose+PH
117 Gy dose	
Heat at 260°C for 60 s	
IR stimulation at 50°C for 100 s	
Heat to 500°C	C. Dose+PH+IR
117 Gy dose	
Heat at 260°C for 60 s	
IR stimulation at 50°C for 100 s	
IR stimulation at 225°C for 100 s	
Heat to 500°C	D. Dose+PH+post-IR IR

The TL following only the irradiation shows the same three peaks observed in Figure 7.4, at ~150, 350 and 430°C. The extent of decrease of the two higher-temperature TL peaks in response to various laboratory treatments is listed in Table 7.3. As expected, the preheat thermally removes the low temperature TL component. The 350°C peak is reduced by ~14% after the preheat, while the 430°C peak remains virtually unaltered (reduction of ~0.6%). The effects of an IR stimulation following a preheat are markedly different from those of only a preheat. The IR stimulation at 50°C induces phototransfer of charge back into the low-temperature TL peaks. This phototransfer is not observed following the post-IR IR stimulation because the stimulation temperature of 225°C keeps the low-temperature TL traps empty. In the TL glow curve following an IR stimulation at 50°C, compared to that after only a preheat, the 350°C peak is reduced by ~19%. In contrast, the 430°C peak is reduced by ~54%. The TL following a post-IR IR stimulation, compared to that after the IR (50°C) stimulation, reduces the 350°C peak and the 430°C peak by a further ~16% and ~33%, respectively. It is interesting to note that with each successive treatment and TL measurement (i.e., 'preheat' compared to 'preheat + IR' compared to 'preheat + IR [50°C] + post-IR IR [225°C]'), the 350°C peak is reduced by roughly the same propor-

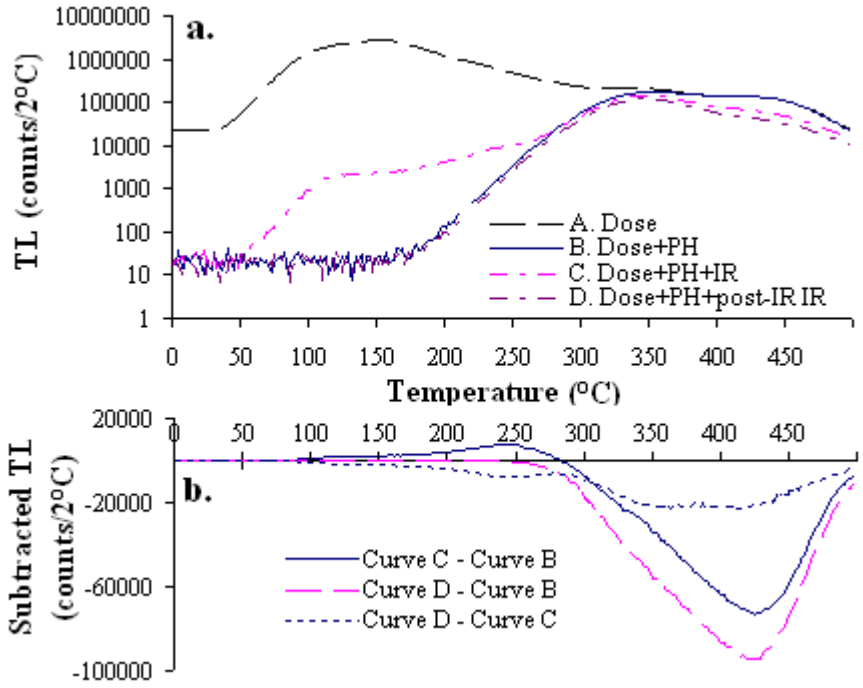

Figure 7.5: a, TL glow curves following various steps of the SAR procedure for aliquots of MR9. The 'Dose' is a 117 Gy laboratory irradiation, 'PH' is a preheat of 260°C for 60 s, 'IR' is an IR stimulation at 50°C for 100 s, and 'post-IR IR' is an IR stimulation at 225°C for 100 s following an IR bleach at 50°C. Note the logarithmic scale of the y-axis. b, The TL curves from Figure 7.5a are shown as difference curves. This illustrates the temperatures at which the TL signal is reduced following various kinds of stimulation.

Table 7.3: The data presented shows how the two major TL peak intensities (i.e., 350°C and 430°C) are reduced following various thermal and IR stimulations. The curve in the top row is divided by the curve in the left column for both TL peaks. Note that the curve nomenclature is taken from Figure 7.5a.

TL peak (°C)		Curve A	Curve B	Curve C	Curve D
350	**Curve A**	1.00	0.86	0.69	0.59
430		1.00	0.99	0.46	0.31
350	**Curve B**		1.00	0.81	0.68
430			1.00	0.46	0.31
350	**Curve C**			1.00	0.84
430				1.00	0.67

tion (16 ± 3%). In contrast, the 430°C is unaltered following the preheat, and is then reduced by 54% by IR (50°C) and a further 33% by post-IR IR (225°C). This suggests that the 350°C peak is affected by both the preheat and IR stimulation, whereas the

430°C peak is only affected by IR stimulation and is unaffected by thermal stimulation of 260°C for 60 s. These results suggest that a large proportion of the charge that produces IRSL is related to the traps that produce the 430°C TL peak. This supports the observations of Murray et al. (2009) that a potential source of the IRSL in K-feldspars is a high-temperature TL trap (~410°C in that study). They also noted that their TL peak at ~310°C was "unbleachable" (Murray et al., 2009). Here, similarly, the ~350°C TL peak observed in MR9 is less bleachable by IR stimulation than is the ~430°C TL peak.

To compare the TL curves and see how the distribution of TL signal changes after various stimulation conditions, the TL curves presented in Figure 7.5a were subtracted from one another (Figure 7.5b). When the TL curve following an IR stimulation (both at 50°C and the post-IR IR at 225°C) is subtracted from that following a preheat, the largest reduction in TL signal occurs at 430°C. The post-IR IR stimulation at 225°C produces a greater reduction of the 430°C peak than IR at 50°C. It is noteworthy that the subtraction trough (where most charge on the TL curve is being emptied) stays constant at 430°C. In the case of IR stimulation at 50°C, charge is supplied to the traps that give rise to the low-temperature peaks (positive values at temperatures below ~280°C indicating phototransfer). When the TL curve following an IR (50°C) stimulation is subtracted from the TL curve following a post-IR IR stimulation, one trough and a shallow trough are observed. The trough is at ~250°C and the shallow trough is between 350°C and 430°C. The 250°C trough is the result of charge transfer following IR stimulation at 50°C into low-temperature traps. This phototransfered charge is thermally removed from these low-temperature traps by the post-IR IR stimulation at 225°C, creating the subtraction trough. The shallow trough indicates that the post-IR IR stimulation at 225°C removes an equal amount of charge from the 350 and 430°C TL peaks, compared to IR stimulation at 50°C.

It is shown in later experiments (Section 7.4.2, Figure 7.10 and Figure 7.11) that the reduction of the 350°C and 430°C TL peaks by the post-IR IR stimulation is not the result of the 100 s of heating at 225°C during elevated-temperature IR stimulation. It follows, then, that the 350°C peak can be reduced by IR stimulation. It is also possible that the observed reduction of the 350°C TL peak following IR stimulation is the result of a reduction of a broad 430°C TL peak that may underlie the 350°C peak. In this case, the 350°C peak is reduced following IR stimulation, not by electron eviction from

traps responsible for this TL peak, but by eviction of electrons from traps responsible for the 430°C peak underlying the 350°C peak. A third possibility for the reduction in the 350°C TL peak following IR stimulation, suggested by Murray et al. (2009), is that the IR stimulation changes the luminescence recombination probability prior to the TL measurement. In this scenario, IR stimulation does not evict electrons from traps associated with TL peaks. Instead, IR stimulation reduces the number of TL recombination centres available for the electrons that are subsequently stimulated by the heat treatment, thus reducing the TL yield (Murray et al., 2009). The effects of IR stimulation on these two TL peaks are further discussed later in this chapter (Section 7.4.2): they lend support to this third possibility and to a relationship between IRSL production and the 430°C TL peak.

7.4 Characterising the IRSL signal from K-feldspars from Mumba

The following sections detail experiments performed to characterise the IRSL signal of K-feldspar separates from Mumba. Following the tests and conclusions from Section 7.2, all measurements were made using the standard blue filter combination (BG39 + Corning 7-59) and a preheat of 260°C for 60 s.

7.4.1 Assessing the dependence of IRSL on stimulation time

A feature of the IRSL decay curve noted in Figure 7.3 is that the signal intensity continued decaying throughout the 100 s period of stimulation and did not reach a constant background. It has been noted in previous studies that a longer stimulation time can make the signal intensity decay to background (Preusser, 2003; Demuro, 2009). Demuro (2009) made all IR stimulations for 500 s to reduce the signal to background levels, after her initial measurements of feldspars indicated that the IRSL signal decayed slowly for all emissions.

A step-by-step outline of the experiment described in this section is presented in Table 7.4. To test the effects of a longer duration IR stimulation on K-feldspar samples from Mumba, two ~50-grain aliquots of MR9 were bleached in sunlight for at least three days. They were then given a laboratory irradiation of 117 Gy, preheated to 260°C for 60 s, then stimulated with IR at 50°C for varying durations. Following each cycle, a test dose cycle consisting of a laboratory irradiation of 12 Gy, a preheat of

260°C for 60 s, and an IR stimulation at 50°C for the same duration as the preceding measurement cycle was performed to monitor for sensitivity changes. Following the test dose, a 0 Gy dose was applied, followed by a preheat of 260°C for 60 s and an IR stimulation at 50°C for the same duration as that used to stimulate the first laboratory dose of the cycle. This was followed by a second test dose cycle. This whole procedure was performed four times for IR stimulation durations of 100, 200, 300 and 500 s. The purpose of the 0 Gy irradiation cycle was to mimic the recuperation test performed during the SAR procedure, to determine whether a longer IR stimulation may reduce the background, the build-up of background, and the recuperation value (see Section 3.3.2.1) as a result.

Table 7.4: Step-by-step outline of the experiment described in this section to investigate the effect of stimulation time on the IRSL signal. IR stimulation durations of 100, 200, 300 and 500 s were tested during the first, second, third, and final cycle, respectively.

Step	Laboratory treatment
1	Beach in sunlight for 3 days
2	117 Gy dose
3	Preheat at 260°C for 60 s
4	IR stimulation at 50°C for specified duration
5	12 Gy dose
6	Preheat at 260°C for 60 s
7	IR stimulation at 50°C (same duration as step 4)
8	0 Gy dose
9	Preheat at 260°C for 60 s
10	IR stimulation at 50°C (same duration as step 4)
11	12 Gy dose
12	Preheat at 260°C for 60 s
13	IR stimulation at 50°C (same duration as step 4)
14	repeat steps 2 through 13 for various IR stimulation durations

Results are presented in Figure 7.6. As expected, the initial intensity of the IRSL decay curve is identical for all decay curves regardless of the stimulation duration. The shape of decay curve for each IR stimulation is also identical (through to the termination of each stimulation). Unlike the results obtained by Demuro (2009), however, after 500 s of IR stimulation the signal is still decreasing. This also holds true for the IRSL decay curves following a 0 Gy dose (Figure 7.6b).

Figure 7.6b shows the IRSL decay curves following a 0 Gy irradiation. For all stimulation durations, except 100 s, the initial signal intensity (i.e., the first 2 s of signal) is very similar (between 36,000 and 38,500 counts). For the 100 s stimulation, the initial signal intensity is ~20% greater. The IRSL signal also decays more rapidly with an increase in stimulation time. This suggests that the IRSL trap continued to be emptied throughout the entire duration, albeit at a slower rate. The result is that there were fewer electrons in IR-sensitive traps when the aliquots were stimulated with IR again following the 0 Gy irradiation. This is consistent the predictions of a donor-acceptor model of feldspar luminescence, as electrons from traps that are farther from recombination centres would take longer to tunnel from their excited state.

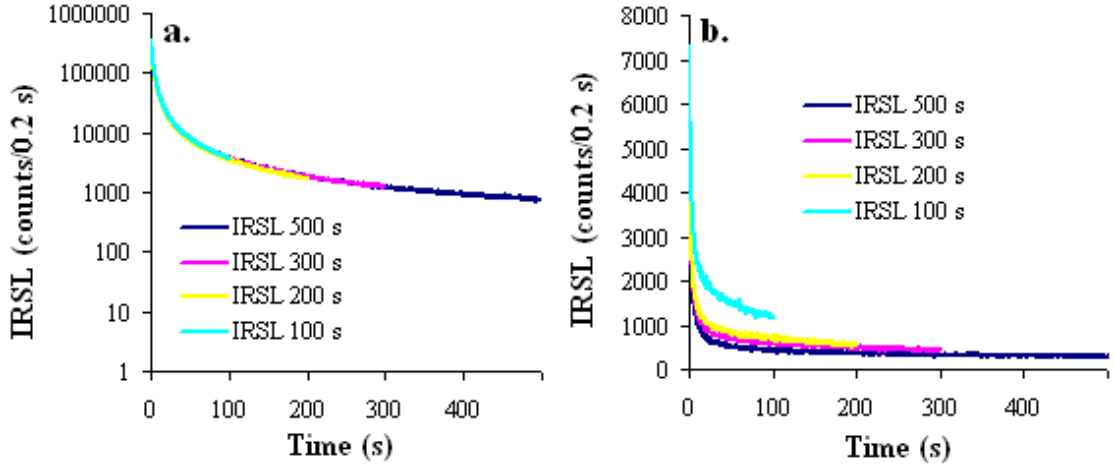

Figure 7.6: IRSL decay curves from aliquots of MR9 after various IR stimulation durations. a, IRSL decay curves following a laboratory irradiation of ~117 Gy. b, IRSL decay curves following a 0 Gy irradiation. Note the logarithmic scale for the y-axis in Figure 7.6a.

To quantify the amount of signal remaining following each cycle, the recuperation value ($[L_0/T_x]/[L_{117}/T_x]$) was calculated (Figure 7.7). The L_0/T_x value was calculated using the background-subtracted signals of the IRSL following the 0 Gy irradiation and its subsequent test dose. The L_{117}/T_x value was calculated using the background-subtracted signals of the IRSL following the 117 Gy irradiation and its subsequent test dose. Each L_0/T_x value was divided by the L_{117}/T_x value calculated from the preceding measurements to obtain the recuperation value. Despite the results in Figure 7.6b, the recuperation values are minimally affected by stimulation time for durations of 200 s and longer. The recuperation value for a stimulation of 100 s (2.02 ± 0.06%) is still well under the 5% value used as the rejection criterion during the SAR

procedure for quartz (see Section 3.3.2.1) and feldspar (e.g., Wallinga et al., 2000b). This suggests that the 100 s stimulation time, despite not reducing the signal to background, reduces it sufficiently to be used for the SAR procedure. There are two other benefits to keeping the stimulation duration relatively short. First, the demand on instrument time for every experiment is reduced. Second, several recent studies investigating the IRSL from K-feldspar utilised a 100 s stimulation time (e.g., Wallinga et al., 2000a; Auclair et al., 2003; Thomsen et al., 2008), so the results obtained here will be more comparable to theirs than if a longer-duration stimulation were used.

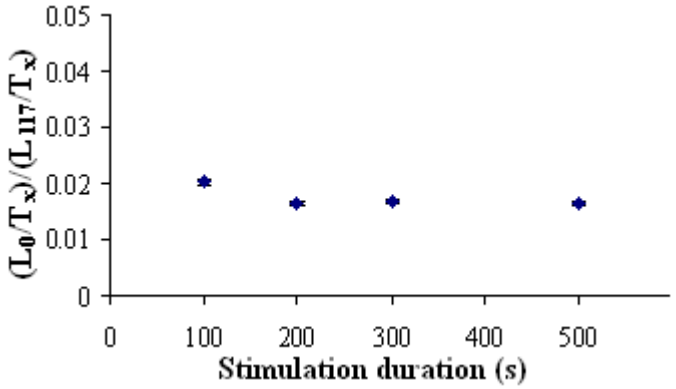

Figure 7.7: Recuperation value plotted as a function of IR stimulation duration (s).

7.4.2 Assessing the dependence of IRSL and TL on stimulation temperature

7.4.2.1 Overview

It has previously been observed that the intensity of the IRSL signal increases with increasing stimulation temperature, from 25°C to 250°C (Duller and Wintle, 1991; Duller, 1997; McKeever et al., 1997; Poolton et al., 2002b; Thomsen et al., 2008). There is, however, no consensus with regards to the dependence of the shape of the IRSL decay curve on stimulation temperature. Duller and Wintle (1991) and McKeever et al. (1997) reported that as the IRSL intensity increased with stimulation temperature, the rate of decay of the IRSL signal increased as well, suggesting a thermally assisted recombination process (McKeever et al., 1997). In contrast, Poolton et al. (2002b) and Thomsen et al. (2008) reported that the rate of decay observed for the IRSL signal stays constant regardless of stimulation temperature. Thomsen et al. (2008) interpreted this as suggesting that the same trap was accessed at increasing stimulation temperatures,

but with an increased number of electrons available for stimulation. As an alternative, they suggested that the elevated temperatures may increase the luminescence efficiency. The interpretations of both sets of studies are in agreement with most other research that suggests that IRSL from feldspars is the result of a donor-acceptor recombination process from a single trap-type (see Section 8.1.2).

In regards to dating applications, some studies recommend avoiding the measurement of IRSL at elevated temperatures (e.g., Rieser et al., 1997; Poolton et al., 2002b), whereas several recent studies have produced results that encourage it (e.g., Thomsen et al., 2008; Murray et al., 2009). A potential benefit recently revealed is that the IRSL signal measured at an elevated temperature may fade less than that measured at lower temperatures (Thomsen et al., 2008; Buylaert et al., 2009; Murray et al., 2009). Before experimenting with fading rates and SAR procedures, it was important to characterise the dependence of the IRSL and TL signals on stimulation temperature.

7.4.2.2 Dependence of the measured IRSL and TL signal of K-feldspars on stimulation temperature

Two aliquots of MR9, each composed of ~50 grains, were bleached in sunlight for at least one week in order to assess the dependence of the IRSL and TL signals on the temperature at which IR stimulation is performed. Table 7.5 is a step-by-step outline of the experiment that is described in this section. The sun-bleached aliquots were given a laboratory irradiation of 117 Gy, a preheat of 260°C for 60 s, and an IR stimulation for 100 s at a specified temperature. A test dose cycle, consisiting of a 30 Gy laboratory dose, a preheat of 260°C for 60 s, and an IR stimulation at 50°C for 100 s, was also performed to monitor, but not correct, for changes in sensitivity. This procedure was repeated for specified IR stimulation temperatures of 50°C, 100°C, 150°C, 200°C, 225°C, 250°C, 300°C, 350°C, 400°C, 450°C, 500°C and 550°C. After all IR stimulation temperatures were measured, the entire procedure was repeated for most stimulation temperatures with a heat treatment of 500°C administered in lieu of a test dose cycle to observe how the TL peaks changed when the IR stimulation temperature was varied.

Table 7.5: Step-by-step outline of the experiment described in this section.

Step	Laboratory treatment
1	Bleach in sunlight for 1 week
2	117 Gy dose
3	Preheat at 260°C for 60 s
4	IR stimulation for 100 s at specified temperature
5	30 Gy dose
6	Preheat at 260°C for 60 s
7	IR stimulation for 100 s at 50°C
8	Repeat steps 2 to 8 for various IR stimulation temperatures
9	Heat to 500°C
10	117 Gy dose
11	Preheat at 260°C for 60 s
12	IR stimulation for 100 s at specified temperature
13	Heat to 500°C
14	Repeat steps 10 to 13 for various IR stimulation temperatures

Decay curves measured during IR stimulations at various temperatures, measured during steps 2 to 8 in Table 7.5, are shown in Figure 7.8a, and the IRSL signal intensity as a function of stimulation temperature is shown as diamonds in Figure 7.8b. The observed change in IRSL signal intensity for stimulation temperatures up to 225°C is in accordance with data provided by the literature (e.g., Bailiff and Poolton, 1989; Duller and Wintle, 1991; McKeever et al., 1997; Thomsen et al., 2008), although it should be noted that most of the cited studies used U-340 filters as opposed to the standard blue filter combination (see Section 7.2.1) used in this study. As the IR stimulation temperatures increases, the IRSL intensity also increases. At 225°C, the IRSL signal is ~6 times greater than that at 50°C, which is similar to the five-fold increase of reported by Thomsen et al. (2008). IRSL intensity increases approximately linear up to a stimulation temperature of 250°C. A significant change occurs at 300°C where the IRSL intensity increases by ~60% from the value observed for a 250°C stimulation temperature. At a stimulation temperature of 350°C, a decrease of ~10% is observed, followed by even greater decreases in signal intensity at 400°C and 450°C (40% and 70%, respectively).

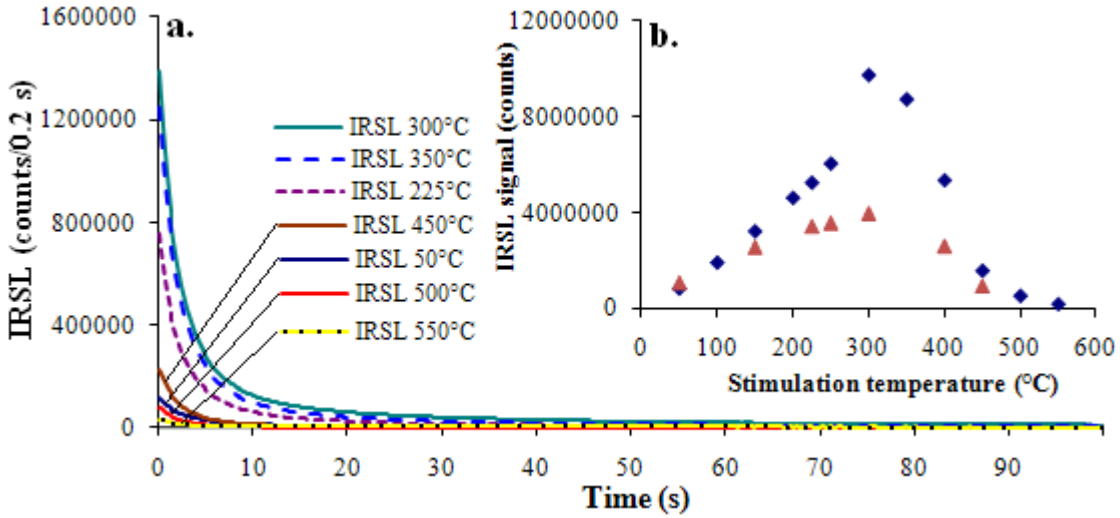

Figure 7.8: Analysis of the change in IRSL with stimulation temperature. a, Decay curves measured for IR stimulation at various temperatures. Note that the legend is arranged by brightness, from the brightest stimulation (IRSL 300ºC) at the top to the dimmest stimulation (IRSL 550ºC) at the bottom. b, IRSL signal intensity as a function of stimulation temperature. The IRSL signal is calculated as the background-subtracted signal. Diamonds were calculated from the IRSL measured during steps 2 to 8 in Table 7.5. Triangles were calculated from the IRSL measured during steps 10 to 14 in Table 7.5.

The IRSL signal intensities measured during steps 10 to 14 in Table 7.5 (triangles in Figure 7.8b) also increase with stimulation temperature up to 300°C, though the increase is substantially less: at 225°C, the IRSL signal is ~3 times greater than that at 50°C. The difference between the two datasets displayed in Figure 7.8b needs to be addressed and sheds further light on the high-temperature source of IRSL from feldspars. The data presented as diamonds Figure 7.8b comes from IRSL measured with a test dose cycle performed after each IR stimulation, whereas the data presented as triangles in Figure 7.8b comes from IRSL measured with a heat treatment of 500°C performed after each IR stimulation. This suggests that the 500°C heat treatment is the source of the difference between the shapes of the two graphs. Murray et al. (2009) reported that their 310°C TL peak was completely optically insensitive. The 350°C TL peak observed for feldspar from Mumba has been shown to be less optically sensitive than the 430°C TL peak (Table 7.3). It is likely that, for the first experiment, which did not include a heat treatment (i.e., steps 2 to 8 in Table 7.5), the 350°C TL peak may have been accumulating signal with each successive cycle, due to its relative optical insensitivity. The large increase in IRSL signal intensity at the IR stimulation temperature of 300°C (diamonds in Figure 7.8b) is, thus, likely to have been the result of thermal erosion of an enlarged 350°C TL peak that had been accumulating

charge over the six previous cycles of irradiation, preheating, IR stimulation, and test dose cycles. In contrast, when a 500°C heat treatment was performed after IR stimulation, the 350°C TL peak was thermally eroded after every cycle of irradiation, preheating and IR stimulation. This would have prevented any accumulation of charge in the traps responsible for the 350°C TL peak, leading to a smaller isothermal TL signal when IR stimulation was performed at 300°C. This can be observed as a smaller increase in IRSL signal intensity at the stimulation temperature of 300°C when the 500°C heat treatment was included (triangles in Figure 7.8b) relative to when no heat treatment was included (diamonds in Figure 7.8b). This conclusion is also supported by results in the next two sections, which investigate the isothermal TL signal underlying the IRSL signal measured at elevated temperatures (Figure 7.12b).

When the decay curves presented in Figure 7.8a are normalised to their first 0.2 s stimulation interval, the change in decay curve shape as a function of stimulation temperature can be assessed (Figure 7.9a and c). The decay rate increases for IRSL at 50°C to 225°C. It is similar at 225°C and 250°C, although the background is large and flat at 250°C. The decay rate then is substantially slower at 300°C. At 350°C, the decay rate returns to approximately the same decay rate as for 225°C. The decay rate then increases and is fastest at 400°C and 450°C. It is inconclusive as to which is faster: the signal measured at 400°C and 450°C decay fastest for both aliquots, but the two aliquots differ (i.e., Disc 33: 450°C is fastest, Disc 34: 400°C is fastest). Finally, for IRSL at 500°C and again at 550°C, the decay curve shape changes markedly. For both stimulation temperatures, the IRSL signal decays rapidly over the first ~10 to 20 s of stimulation to large and flat background (relative to the initial decay). The normalised curves for each elevated-temperature IRSL signal were then divided by the normalised decay curve for IR stimulation at 50°C (Figure 7.9b and d) to show how the rate of decay changes for various IR stimulation temperatures. Figure 7.9b and d demonstrates that the early portion (the first ~5 to 10 s) of the decay curve is the region where the most change occurs in the rate of decay of the IRSL signal. Most decay curves then become flatter for the remainder of the 100 s of IR stimulation.

The increase in IRSL intensity and the accompanying increase in decay rate with stimulation temperature from 50°C to 225°C observed for K-feldspar samples from Mumba supports the results of Duller and Wintle (1991) and McKeever et al. (1997),

but differs from the results of Thomsen et al. (2008) and Poolton et al. (2002a), who did not see any change in decay rate despite the associated increase in IRSL intensity.

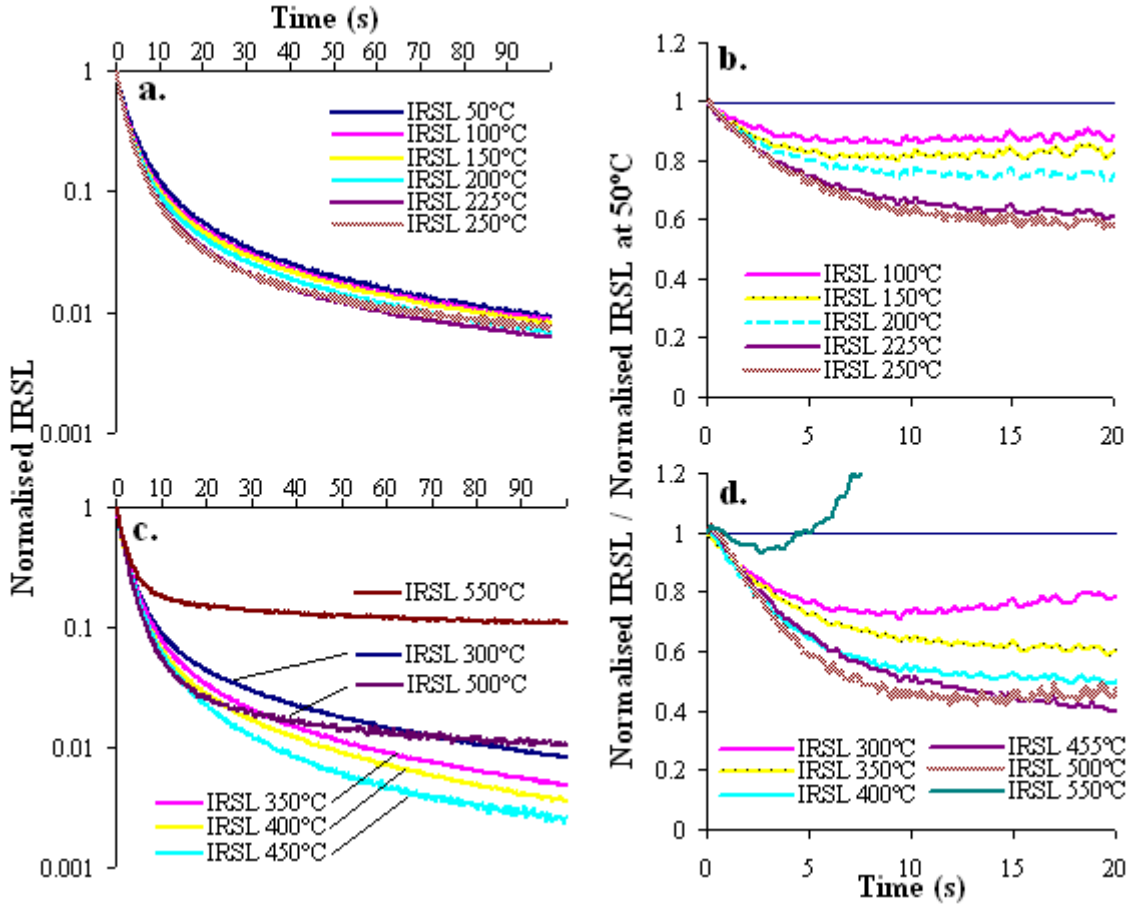

Figure 7.9: a and c, Normalised decay curves for various IR stimulation temperatures. The normalised curves are shown in the two graphs to show the difference in decay curve shape between stimulation temperatures of 50-250°C (a) and from 300-550°C (c). The normalised decay curves (from a and c) were divided by the normalised decay curve for IRSL at 50°C (b and d, respectively) to see how the decay rate at various elevated temperatures changed, relative to IRSL at 50°C, over the first 20 s of IR stimulation. Note that in (d), IRSL at 550°C continues to increase to a ratio of 2.7 by 20 s of IR stimulation.

When TL curves following IR stimulation at elevated temperatures are observed, additional patterns can be established. The IRSL intensities and decay curve shapes for stimulation temperatures of 300°C and above can more readily be interpreted. TL curves following each IR stimulation at the specified temperature are presented in Figure 7.10. All TL curves have a peak at ~350°C (except when it is heated through during IR stimulation at an elevated temperature). Some of the curves have a ~430°C peak. As in Figure 7.5, phototransfer is observed for all stimulation temperatures below 225°C.

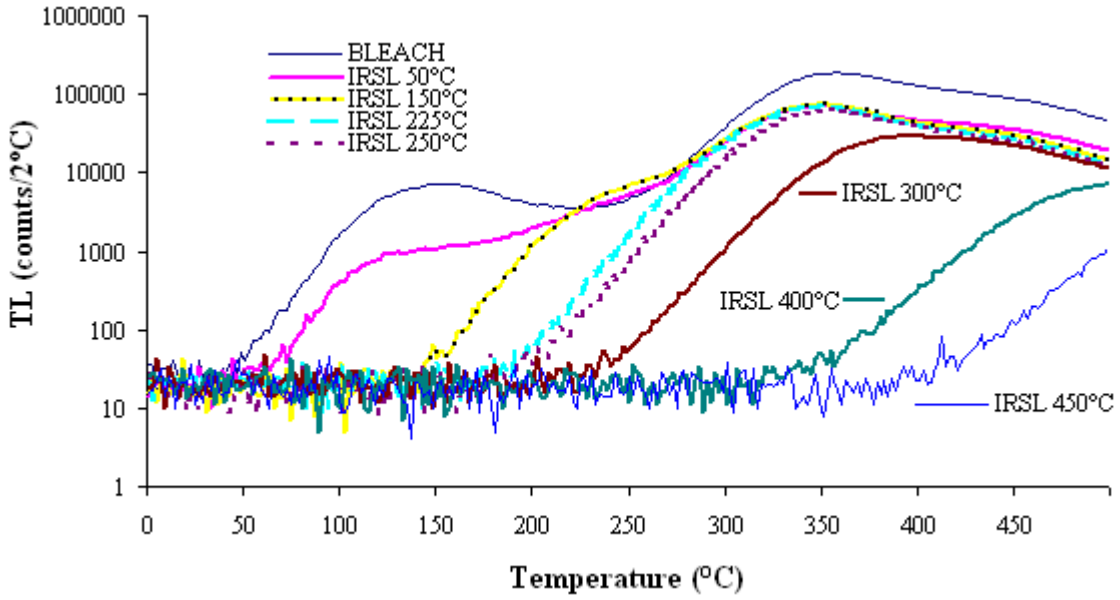

Figure 7.10: TL curves measured following IR stimulation at various temperatures.

As shown in Figure 7.8, the IRSL intensity increases in an apparently systematic way up to a stimulation temperature of 250ºC, followed by a large increase in signal intensity at 300ºC, and then a decrease in signal intensity from 350ºC to 550ºC. It is also between 250°C and 350°C that a change in the shape of the decay curve and rate of decay changes significantly. This change at 300ºC is significant. When the TL glow curves (following IR stimulation at the specified temperatures) are observed, the peak at ~350ºC remains constant up to a stimulation temperature of ~225ºC (Table 7.6). Following IR stimulation at ~250ºC for 100 s, the TL peak at ~350ºC begins to be thermally eroded by the elevated temperature of IR stimulation. After stimulation at 400ºC for 100 s, no 350ºC peak remains and it appears that the TL peak at ~430ºC is almost completely thermally eroded. IR stimulation at 400ºC also coincides with the large reduction in IRSL signal (Figure 7.8b). After stimulation at 450ºC, there is hardly any 430ºC TL peak remaining (Figure 7.10) or IRSL signal (Figure 7.8b).

The results presented in Table 7.6 for stimulation temperatures of 50–225ºC also show that the 350°C TL peak remains relatively unchanged when IR stimulation is performed at 50ºC to 225°C for 100 s. This may suggest that the increase in IRSL intensity associated with an increase in stimulation temperature is not associated with trap charge from the TL peak at 350°C. The 430°C TL peak on the other hand, is reduced by ~10% following each increase in IR stimulation temperature. This reduction cannot be the result of thermal erosion, since the 350°C TL peak would also be reduced

if thermal erosion was the cause of the decrease in the 430ºC TL peak. As the stimulation temperature is increased to 225°C, the IRSL intensity increases and the 430°C TL peak is reduced. This observation lends support to a high-temperature TL peak, 430°C in this case, as a source trap for IRSL in feldspars, supporting the conclusions of Murray et al. (2009) and the results from Section 8.3.

Table 7.6: The data presented shows how the TL peaks at 350ºC and 430ºC are reduced following IR stimulation at a range of elevated temperatures. The TL peak following the IR stimulation temperature noted in the top row is divided by the TL peak following the IR stimulation temperature noted in the left column.

TL peak (°C)		IR (50°C)	IR (150°C)	IR (225°C)	IR (250°C)	IR (300°C)	IR (400°C)	IR (450°C)
350	IR (50°C)	1	1.06	0.99	0.87	0.20	0.00	0.00
430		1	0.88	0.79	0.75	0.65	0.03	0.00
350	IR (150°C)		1	0.94	0.83	0.19	0.00	0.00
430			1	0.90	0.86	0.74	0.04	0.00
350	IR (225°C)			1	0.88	0.20	0.00	0.00
430				1	0.96	0.82	0.04	0.00
350	IR (250°C)				1	0.22	0.00	0.00
430					1	0.86	0.05	0.00
350	IR (300°C)					1	0.00	0.00
430						1	0.05	0.00
350	IR (400°C)						1	0.17
430							1	0.05
350	IR (450°C)							1
430								1

7.4.2.3 Characterising the isothermal TL signal

The results presented in Figure 7.8, Figure 7.9 and Figure 7.10 can be understood more clearly in conjunction with the results of another experiment that was designed to assess the contribution of an isothermal TL signal (the TL that is produced by holding a mineral grain at a constant temperature) to the elevated-temperature IRSL signal. Table 7.7 is a step-by-step outline of the experiment discussed in this section. Two more aliquots of MR9 were prepared and heated to 500°C. After cooling to room temperature, they were given a laboratory irradiation of 117 Gy and a preheat of 260°C for 60 s. They were then brought to an elevated temperature and held there while their TL was recorded for 100 s. Finally, they were heated to 500°C again and their TL glow curves were recorded. This was repeated for various stimulation temperatures of 50, 150, 200, 225, 250, 300, 350, 400, 450 and 500°C. After the completion of this

procedure, the process was repeated with an elevated-temperature IR stimulation in place of the isothermal TL stimulation.

Table 7.7: Step-by-step outline of the experiment described in this section

Step	Laboratory treatment
1	Heat to 500°C
2	117 Gy dose
3	Preheat at 260°C for 60 s
4	Heat at specified temperature for 100 s (isothermal TL measurement)
5	Heat to 500°C
6	Repeat steps 2 to 5 for various temperatures in step 4
7	117 Gy dose
8	Preheat at 260°C for 60 s
9	IR stimulation for 100 s at specified temperature
10	Heat to 500°C
11	Repeat steps 7 to 10 for various temperatures in step 9

Results presented in Figure 7.11a show the isothermal TL curves produced by holding the aliquots at each elevated temperature for 100 s following a 260°C preheat for 60 s. The 250°C stimulation temperature is the first to produce an isothermal TL curve above instrumental background. Maximum isothermal TL is observed for stimulation temperatures at 300°C and 350°C. This suggests that any change in IRSL with stimulation temperature up to, and including, 225°C (e.g., Figure 7.8) is not resultant from an isothermal TL signal underlying the IRSL signal. This is further illustrated in Figure 7.11b in which the signal intensity is calculated for the isothermal TL curves. The signal intensity was calculated by integrating initial 2 s of stimulation and subtracting a background calculated using the final 10.2 s of stimulation (see Section 3.3.1.1). The first increase of the isothermal TL signal occurs at 250°C, followed by large increases at 300 and 350°C. This suggests that, when a 260°C preheat is applied for 60 s prior to IRSL measurement, IR stimulation at temperatures of ≥250°C may thermally empty TL traps in addition to stimulating traps associated with IRSL. This could result in an isothermal TL signal underlying the IRSL signal for IR stimulation temperatures above 250°C. A third set of data supporting this conclusion is presented in Figure 7.11c, which shows that the shape and intensity of all the TL glow curves measured following isothermal TL stimulation up to 225°C are identical.

Following isothermal TL measurements at 250°C, the 350°C TL peak begins to be thermally eroded.

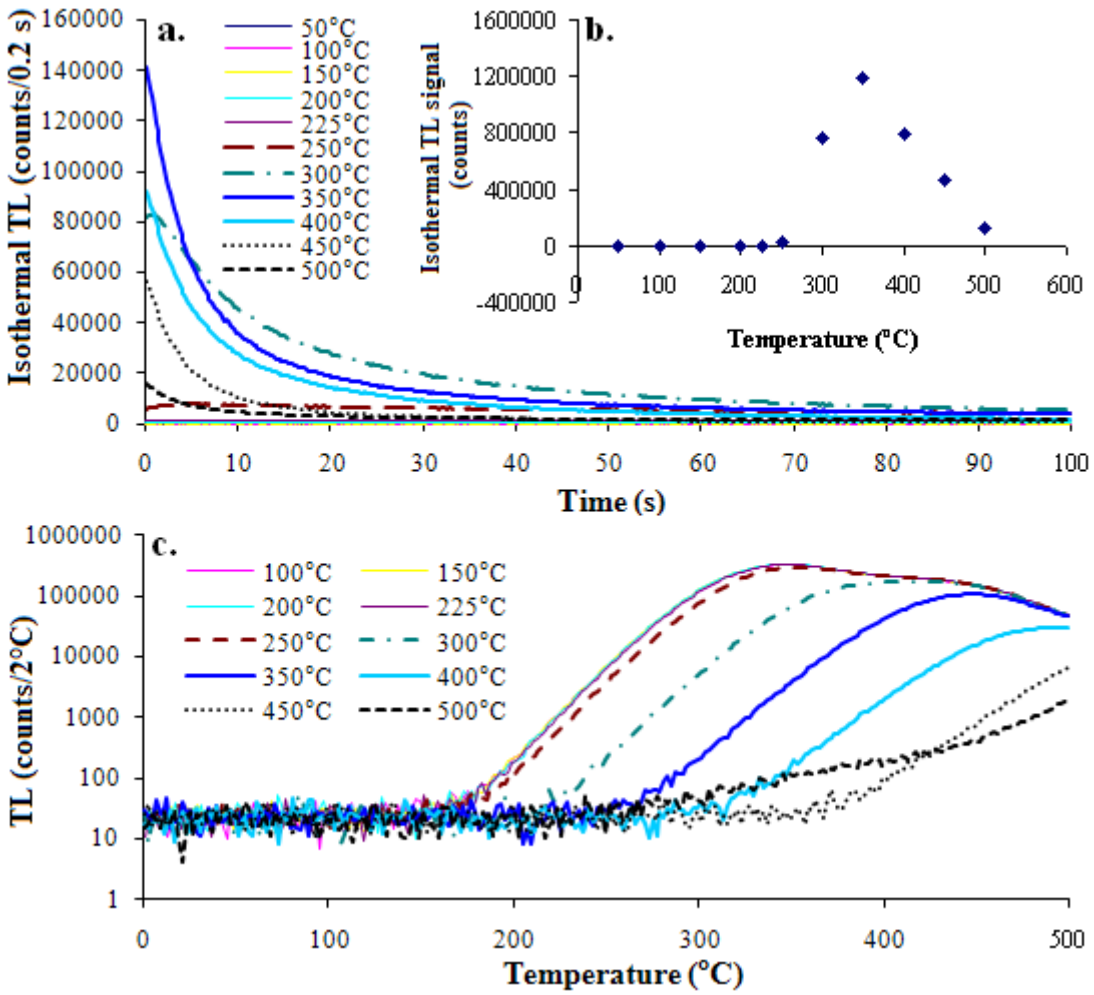

Figure 7.11: a, Isothermal TL curves for various elevated temperatures. b, Isothermal TL signal intensity calculated using the first 2 s of signal minus a background calculated from the final 10.2 s of signal as a function of stimulation temperature. c, TL glow curves recorded after the isothermal TL measurements presented in (a).

7.4.2.4 Interpretation of stimulation temperature tests – the dependence of the isothermal TL-subtracted IRSL signal on stimulation temperature

There are several possible explanations for why IRSL intensity and TL glow curve shapes change the way they do when the stimulation temperature is varied. When the isothermal TL curves are subtracted (channel-by-channel) from the measured IRSL decay curves produced for each elevated temperature (Figure 7.12), it can be seen that IR intensity increases with increasing stimulation temperature up to 300°C, after which

is begins to decrease (Figure 7.12b). This curve represents the response of IR stimulation at elevated temperature without the isothermal TL signal underlying it.

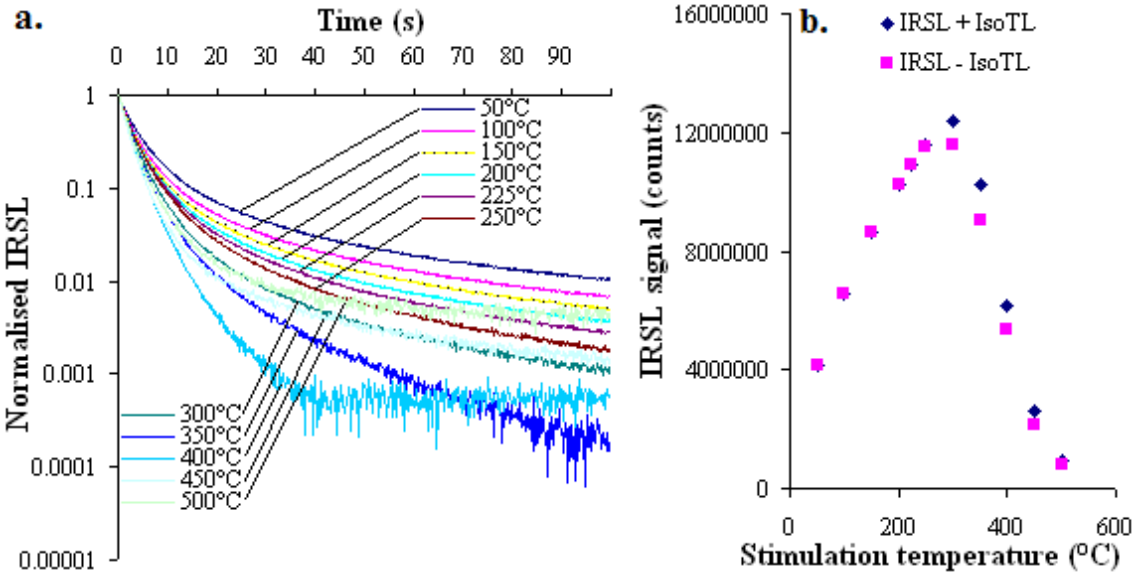

Figure 7.12: a, Normalised IRSL decay curves from which the isothermal TL curves (measured from the same aliquot and presented in Figure 7.11a) were subtracted. b, IRSL signal intensity (calculated as the initial 2 s of stimulation minus a background calculated from the final 10.2 s) plotted as a function of stimulation temperature. 'IRSL + IsoTL' is the signal intensity from the measured IRSL signal. 'IRSL – IsoTL' is the data from 'IRSL + IsoTL' curves with the isothermal TL data from Figure 7.11b subtracted. Both the IRSL and isothermal TL signals were measured using the same aliquot.

The normalised decay curves resulting from IR stimulation at elevated temperatures from which the isothermal TL signal was subtracted are presented in Figure 7.12a. As stimulation temperature is increased up to 400°C, the rate of decay of the IRSL signal increases. Electrons in traps that are farther away from recombination centres may access those recombination centres faster at higher temperatures due to the thermal assistance of the electrons into the conduction band. This adds to the luminescence produced by the tunnelling recombination of close trap-recombination centre pairs, resulting in brighter IRSL signals and a faster rate of IRSL decay. A possible reason for the drop in IRSL brightness above 300°C is the thermal removal of electrons from optically sensitive traps prior to IR stimulation and measurement, thus reducing the number of electrons available to produce IRSL. These results lend support to the observations of McKeever et al. (1997) and suggest that increasing the IR stimulation temperature increases a thermally assisted process of recombination. These results also support the conclusions reached by Li (2010) that a thermally assisted

recombination process (via the conduction band) contributes to the athermal tunnelling recombination process to produce IRSL in feldspars.

7.4.3 Summary

It is important to characterise the TL and IRSL properties of K-feldspar samples prior to attempting to estimate a burial dose or age, owing to the large diversity of K-feldspar mineralogies and luminescence behaviours (Duller, 1997). In the case of the blue emission from K-feldspars from Mumba, the stimulation time has been shown to make little difference in regards to practical application to dating. In regards to the temperature at which IR stimulation is performed, it has been shown that increasing the stimulation temperature up to 300°C results in increased IRSL brightness, even when the isothermal TL component resulting from the high stimulation temperature is removed. This isothermal TL component has been shown not to affect the IRSL signal for stimulation temperatures below 250°C when it is preceded by a preheat of 260°C for 60 s. These results indicate that, for dating applications, the IRSL signal measured at 250°C and above will include an isothermal TL component that would be difficult to account for during D_e measurement procedures. This suggests that an IR stimulation temperature of 225°C is the highest temperature that can be reliably used for IR stimulation of samples from Mumba.

7.5 The post-IR IRSL signal from K-feldspars

7.5.1 Overview

The major drawback of using feldspar as a luminescence dosimeter is anomalous fading, the malign property that is ubiquitous to all K-feldspars thus far described (Wintle, 1973; Spooner, 1994b; Huntley and Lamothe, 2001). Despite descriptions of several non-fading feldspar signals (e.g., Guérin and Valladas, 1980; Zink and Visocekas, 1997; Gelian et al., 2006; Huntley et al., 2007), none have proved universally applicable. The short-comings of fading-correction models based on measured anomalous fading rates (Huntley and Lamothe, 2001), and the absence of a reliable non-fading signal, have prompted research to find a feldspar IRSL signal that fades the least. The post-IR IRSL technique (e.g., Table 7.8), introduced by Jain and Singhvi (2001), expanded upon and tested by Thomsen et al. (2008), and tested here on

the Mumba samples, has the potential to exploit a feldspar signal that exhibits minimal anomalous fading.

Jain and Singhvi (2001) reported that IRSL measured at 50°C and at 220°C probed distributions of two different trap types: Type A traps that are sensitive to both IR at 50°C and blue-green light, and Type B traps that are sensitive only to blue-green light. Their results indicated that IRSL at 50°C probes Type A traps, while IRSL at 220°C probes both Type A and Type B traps. They concluded that measuring IRSL at 220°C could be used to access the deeper, more thermally stable, Type B traps in feldspars that may show less fading (Jain and Singhvi, 2001). Thomsen et al. (2008) showed that the fading rate does, indeed, decrease when IRSL is measured at 225°C for 100 s following a 100 s IR bleach at 50°C. They contended that by using a signal that fades less the correction to the measured age will be smaller and, therefore, less dependent on the age correction model (Thomsen et al., 2008). Their measured fading rate for samples measured using a post-IR IRSL procedure was often on the order of <1 %/decade. For this reason, the post-IR IRSL signal from Mumba was investigated.

Table 7.8: Step-by-step outline of the SAR procedure using the post-IR IRSL signal.

Step	Treatment	Name
1	Preheat at 260°C for 60 s	
2	IR stimulation at 50°C for 100 s	
3	IR stimulation at 225°C for 100 s	L_N
4	Test dose	
5	Preheat at 260°C for 60 s	
6	IR stimulation at 50°C for 100 s	
7	IR stimulation at 225°C for 100 s	T_N
8	Regenerative dose	
9	Preheat at 260°C for 60 s	
10	IR stimulation at 50°C for 100 s	
11	IR stimulation at 225°C for 100 s	L_x
12	Test dose	
13	Preheat at 260°C for 60 s	
14	IR stimulation at 50°C for 100 s	
15	IR stimulation at 225°C for 100 s	T_x
16	Repeat steps 8 to 15	

Unless otherwise noted, all post-IR IRSL procedures described in this chapter consist of an IR bleach at 50°C for 100 s and a post-IR IR stimulation at 225°C for 100 s. The SAR procedure, using the post-IR IRSL signal to measure a dose or D_e, is illustrated in Table 7.8.

7.5.2 Characterising the post-IR IRSL signal from Mumba

Two ~50-grain aliquots of MR9 were bleached in sunlight for at least three days. They were then given a laboratory irradiation of 120 Gy, preheated at 260°C for 60 s, stimulated with IR photons for 100 s at 50°C, then stimulated with IR photons for 100 s at 225°C. Decay curves for the post-IR IRSL signal are presented in Figure 7.13a. The post-IR IRSL signal (calculated using the first 2 s of stimulation minus a background calculated using the final 10.2 s) is ~21% weaker than the IRSL signal measured at 50°C that preceded it. Normalising the two decay curves to their initial 0.2 s interval (inset to Figure 7.13a) allows the decay rate of the two signals to be compared. The post-IR IRSL signal decays more slowly than the IRSL signal measured at 50°C. This is confirmed when the normalised post-IR IRSL signal is plotted as a ratio of the IRSL (50°C) signal (Figure 7.13b). This shows that the post-IR IRSL signal decays more slowly than the IRSL (50°C) signal over the first 10 to 15 s of stimulation, after which their decay rates are very similar. The decrease in the rate of decay for the post-IR IRSL is consistent with similar observations reported by Thomsen et al. (2008).

When the post-IR IR stimulation temperature is varied from 50 to 400°C, the results, presented in Figure 7.13c, are similar to those in Figure 7.9. The IR bleach stimulation temperature was always held constant at 50°C. The rate of decay is slowest for post-IR IR stimulation at 50°C, and starts to increase as the post-IR IR stimulation temperature is increased up to 225°C. The decay curve for post-IR IRSL at 250°C is similar to IRSL at 250°C. Both the IRSL and post-IR IRSL signals measured at 250°C have different decay curve shapes relative to the IRSL and post-IR IRSL signals measured at 225°C, respectively (Figure 7.13d). In addition, both IRSL and post-IR IRSL measured at 250°C result in weaker background-subtracted signals relative to IRSL and post-IR IRSL measured at 225°C, respectively. The decay rate for post-IR IRSL at 300°C is the slowest of all stimulation temperatures above 225°C. The decay

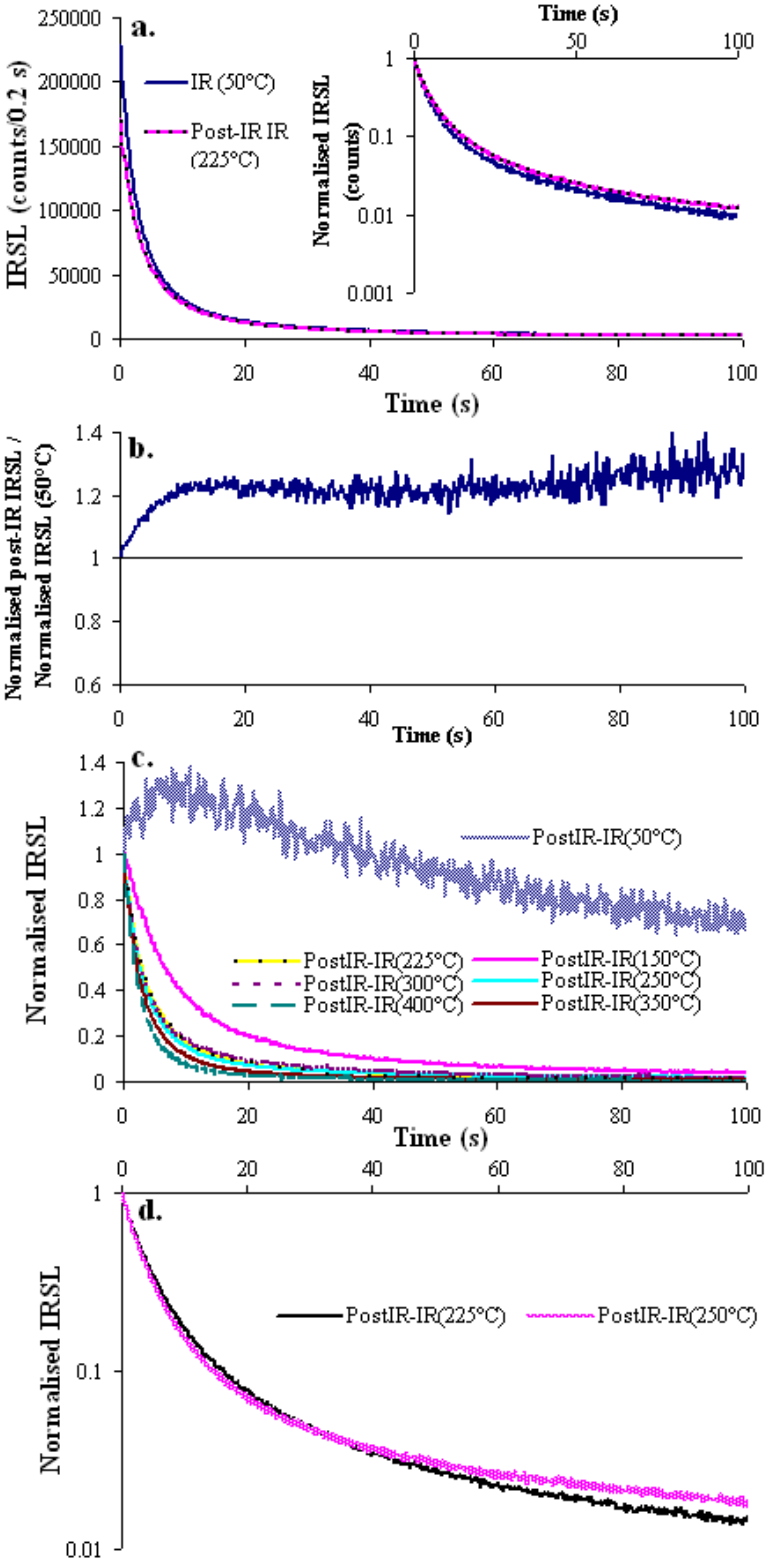

Figure 7.13: Post-IR IRSL decay curves from one aliquot of MR9. a, Decay curves for IR (50°C) bleach and post-IR IRSL (225°C). The inset shows these same two decay curves normalised to their first 0.2 s interval. b, The normalised decay curves from the inset of Figure 8.12a plotted as a ratio of one another (normalised post-IR IRSL curve / normalised IRSL (50°C)). c, Normalised post-IR IRSL decay curves for various post-IR IR stimulation temperatures. d, Normalised post-IR IRSL decay curves for stimulation temperatures of 225°C and 250°C. Note the logarithmic scale for the y-axis.

rate increases for post-IR IR stimulation at 350°C and 400°C. This pattern of a decrease in the decay rate and a change in shape of the decay curve at 300°C is the same as that observed for standard IRSL when the stimulation temperature is 300°C (Figure 7.9). As with standard IRSL, the observed pattern is likely due to the contribution of an isothermal TL signal in post-IR IRSL at temperatures above 225°C, (see Section 7.4.2). It is, therefore, likely that when the isothermal TL component under the IRSL is removed, the decay rate will increase with increasing post-IR IR stimulation temperature up to ~450°C. This suggests that post-IR IR stimulation temperatures above 225°C should not be used during dating applications, when measured after a preheat of 260°C for 60 s. This is because the isothermal TL signal from the elevated IR stimulation temperature would be difficult to account for during D_e measurement procedures.

It can be seen in Figure 7.13c that the post-IR IRSL signal measured at 50°C increases for 10 s of stimulation before beginning to decrease. This is similar to what was observed when 'interrupted' IRSL measurements were made by McKeever et al. (1997) following Poolton et al. (1995). They argued that this observation is indicative of a donor-acceptor recombination process for the origin of IRSL in feldspars.

The donor-acceptor recombination model can also be used to explain the low fading rates for post-IR IRSL signals in feldspar reported by Thomsen et al. (2008) and others. If anomalous fading is the result of close trap-recombination centre pairs for which, over geological time, the electron from the trap tunnels to the recombination centre, then the fading rate is a function of the number of these closely spaced pairs. Over laboratory time scales, this tunnelling does not have sufficient time to take place. Therefore, more IRSL is measured for a laboratory dose, relative to environmental dose of the same magnitude, resulting in an age underestimation. It has been shown in Section 7.4.2 that IR stimulation at 225°C, while stimulating the same closely spaced trap-recombination centre pairs as IRSL at 50°C, can also access traps that are farther from recombination centres, by thermally assisting electrons into the conduction band. By applying an IR bleach at 50°C prior to the measured IRSL at 225°C, the electrons in these close pairs will be elevated to an excited state and will either tunnel or pass through band-tail states to the closest recombination centre. This reduces the population of closely spaced trap-recombination centre pairs, which would have tunnelled over

geological time. The post-IR IR stimulation at 225°C that follows stimulates electrons from traps that are more distant from recombination centres, and were, thus, less likely to tunnel over geological time. These electrons are stimulated into either the conduction band or band-tail states where they are more mobile and can reach more distant recombination centres. This explanation is largely supported by results from Thomsen et al. (2008), Li (2010), and by results from this study presented already and later in this chapter.

7.5.3 Assessing the sensitivity of the post IR-IRSL signal to sunlight

Godfrey-Smith et al. (1988) explicitly measured the bleachability of the TL, OSL and IRSL signals from quartz and feldspar using natural sunlight. Their results showed that the OSL signal from quartz bleached more rapidly than the IRSL signal of feldspar, which reached 1% of its initial brightness after ~9 min of sunlight exposure and was posited to decrease to a negligibly low level given enough time. The purpose of the experiment described in this section was to test the sensitivity of the post-IR IRSL signal to sunlight.

The use of elevated stimulation temperatures for IRSL measurements of K-feldspar has generally been eschewed in previous studies. For a sample with a known D_e of ~1 Gy, Poolton et al. (2002b) noted an increase in measured D_e from ~1 to 6 Gy as they increased the stimulation temperature from 50 to 200°C. They suggested that OSL or IRSL performed at elevated temperatures allows access to traps that were not bleached in nature, leading to an overestimation of the D_e. Later, bleaching experiments by Thomsen et al. (2008) showed only very subtle differences in bleachability between the IRSL signal at 50°C and the IRSL signal at 225°C. In their experiments they used modern beach sands resulted in quartz OSL D_e values of <39 mGy, K-feldspar IRSL (50°C) D_e values of ~0.5 Gy, and K-feldspar IRSL (225°C) D_e values of ~2 Gy (Thomsen et al., 2008). They suggested that this confirmed that feldspars are bleached more slowly than quartz by natural sunlight and that IR stimulation at elevated temperatures accesses less bleachable traps. A similar experiment described by Buylaert et al. (2009) showed no obvious disparity in bleachability between IRSL at 50°C and post-IR IRSL for known-age Holocene samples, although both signals tended to overestimate the quartz OSL age. Both studies suggested that a small residual dose

may be present when using an elevated-temperature IRSL signal; if older sediments are measured, this residual will likely be insignificant.

To measure the extent to which the post-IR IRSL signal is reduced in K-feldspar separates from Mumba, a bleaching test was performed. Twenty-seven ~50-grain aliquots of MR9 were prepared and bleached in natural sunlight for approximately one week. A 59 Gy beta dose was given to each aliquot and they were bleached in direct sunlight for varying durations of time, ranging from 3 to 3600 s (1 hr) in groups of three aliquots. Using a post-IR IRSL SAR procedure (see Table 7.8), each aliquot's dose was measured and compared with the given dose. By comparing the measured/given dose ratios for various bleaching durations, the bleaching rate of the post-IR IRSL signal could be assessed. This bleaching experiment is based on the assumption that the post-IR IRSL signal is capable of recovering a known dose using the SAR procedure. This is shown to be true in Section 7.6.1. Results for the bleaching experiment are presented in Figure 7.14. The residual dose corresponds to ~8% of the given dose (4.3 ± 1.1 Gy) after 360 s (6 min) of sunlight exposure, and ~2% (1.1 ± 0.1 Gy) after 3600 s (1 hr).

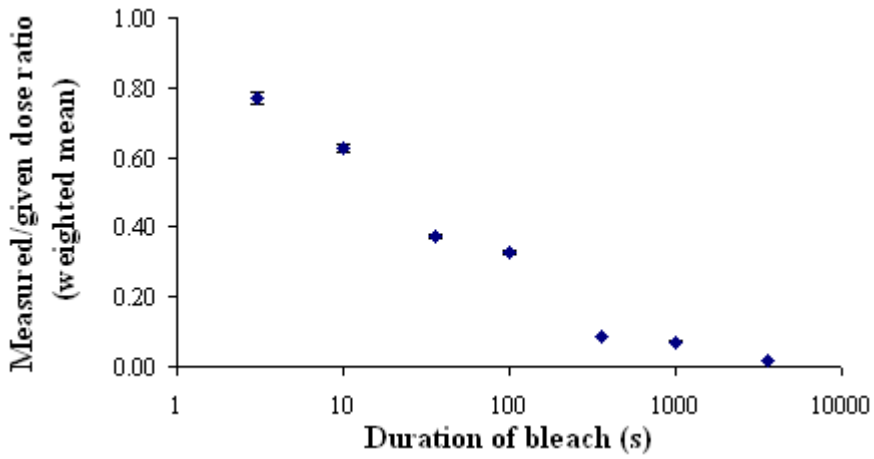

Figure 7.14: Bleaching rate of the post-IR IRSL signal of K-feldspars from Mumba. Each point represents the weighted mean measured/given dose ratio of three aliquots.

As a follow-up experiment to assess whether there was any residual signal remaining from an irradiation that preceded a 1 hr bleach, three ~50-grain aliquots were bleached for more than a week in sunlight, then given a laboratory dose of 59 Gy. The aliquots were then bleached again for 1 hour in direct sunlight, given another 59 Gy laboratory dose, and measured using the SAR procedure to try to recover the given dose. The weighted mean measured/given dose ratio for the three aliquots was 1.01 ±

0.02. These results indicate that, after a laboratory irradiation and one hour of sunlight bleaching, the post IR-IRSL signal is sufficiently reduced that a dose given after the bleach can still be recovered accurately. This implies that, in nature, one hour of direct sunlight exposure is likely to be sufficient to reduce the post IR-IRSL signal to negligible levels, and hence act as an accurate dosimeter for older sediments. This supports the conclusions of Buylaert et al. (2009).

7.6 Assessing the optimal IR stimulation conditions for samples from Mumba

7.6.1 Dose recovery experiments

After characterising the TL and IRSL signals of K-feldspar separates from Mumba, it was important to confirm that the various heat treatments used as part of the SAR procedure will result in accurate D_e determinations. One way of testing it is to perform dose recovery experiments (see Section 3.3.2.4). Wallinga et al. (2000a,b) demonstrated that the SAR procedure could be used as a robust and fast means for D_e determination in feldspars. They used a regenerative dose preheat of 290°C for 10 s, a test dose cutheat of 210°C, and made all measurements using the standard blue filter pack. They demonstrated that D_e values estimated using the SAR procedure were consistent with those obtained using the SAAD procedure (Duller, 1991; Murray et al., 1997), although ages calculated using both procedures underestimated the known ages of the deposits (Wallinga et al., 2000a). Their study also showed that the IRSL signal in K-feldspar samples could accurately recycle a duplicate regenerative dose within 10% and produce recuperation values that were less than 5% the natural IRSL signal. The given doses in dose recovery experiments, however, were consistently underestimated by approximately 27% (Wallinga et al., 2000b). They proposed that the underestimation of the given doses resulted from an increase in the electron trapping probability due to preheating above 200°C. Later, Blair et al. (2005) demonstrated that, in contrast to standard SAR procedures for quartz, regenerative dose preheats and test dose preheats should be identical. In their study, they observed the UV emission from various feldspar types and demonstrated that sensitivity changes can be monitored and corrected for using preheat combinations of between 160 and 300°C. They then used regenerative and test dose preheats of 220°C for 10 s during a SAR procedure and were able to recover a known dose (within 5%).

Nine sets of four ~50-grain aliquots of MR9 were used for dose recovery experiments. All aliquots were bleached in sunlight for at least three days, and were then given a laboratory irradiation of 117 Gy. The sensitivity-corrected IRSL signals resulting from regenerative doses of 58, 117, 176, 234, 0 Gy and a duplicate dose of 58 Gy were used to build dose-response curves. A test dose of 12 Gy was used. Nine different IRSL stimulation conditions were tested. All measurements were made using the standard blue filter combination (see Section 7.2.1). An identical preheat of 260°C for 60 s was used for all regenerative and test doses. The standard tests of SAR suitability were performed (see Section 3.3.4). The various stimulation conditions tested were as follows:

1. IR stimulation for 100 s at 50°C
2. IR stimulation for 100 s at 225°C
3. IR stimulation for 100 s at 300°C
4. IR stimulation for 100 s at 350°C
5. IR stimulation for 100 s at 400°C
6. IR stimulation for 100 s at 450°C
7. Post-IR (100 s at 50°C) IR stimulation for 100 s at 225°C
8. Post-IR (100 s at 100°C) IR stimulation for 100 s at 225°C
9. IR stimulation for 500 s at 50°C; where the signal intensity is calculated using the sum of the first 2 s of stimulation and subtracting a background calculated using the final 10.2 s (i.e., from 489.8 to 500.0 s) of stimulation.

Results are presented in Figure 7.15. It is clear that some of the dose recovery results are better than others. Stimulation conditions with measured/given dose ratio weighted means that recovered the given dose within 2σ include those numbered above as 1 (0.99 ± 0.02), 2 (1.00 ± 0.01), 3 (1.04 ± 0.02), 7 (1.00 ± 0.01), 8 (0.99 ± 0.02) and 9 (0.97 ± 0.02). Aliquots measured using these stimulation conditions also passed all standard tests of SAR suitability, suggesting that the SAR procedure is able to accurately estimate a laboratory dose and may be appropriate for estimation of the burial dose of grains of K-feldspar. The dose recovery tests failed when stimulation temperatures above 300°C were used: all but two aliquots overestimated the given dose.

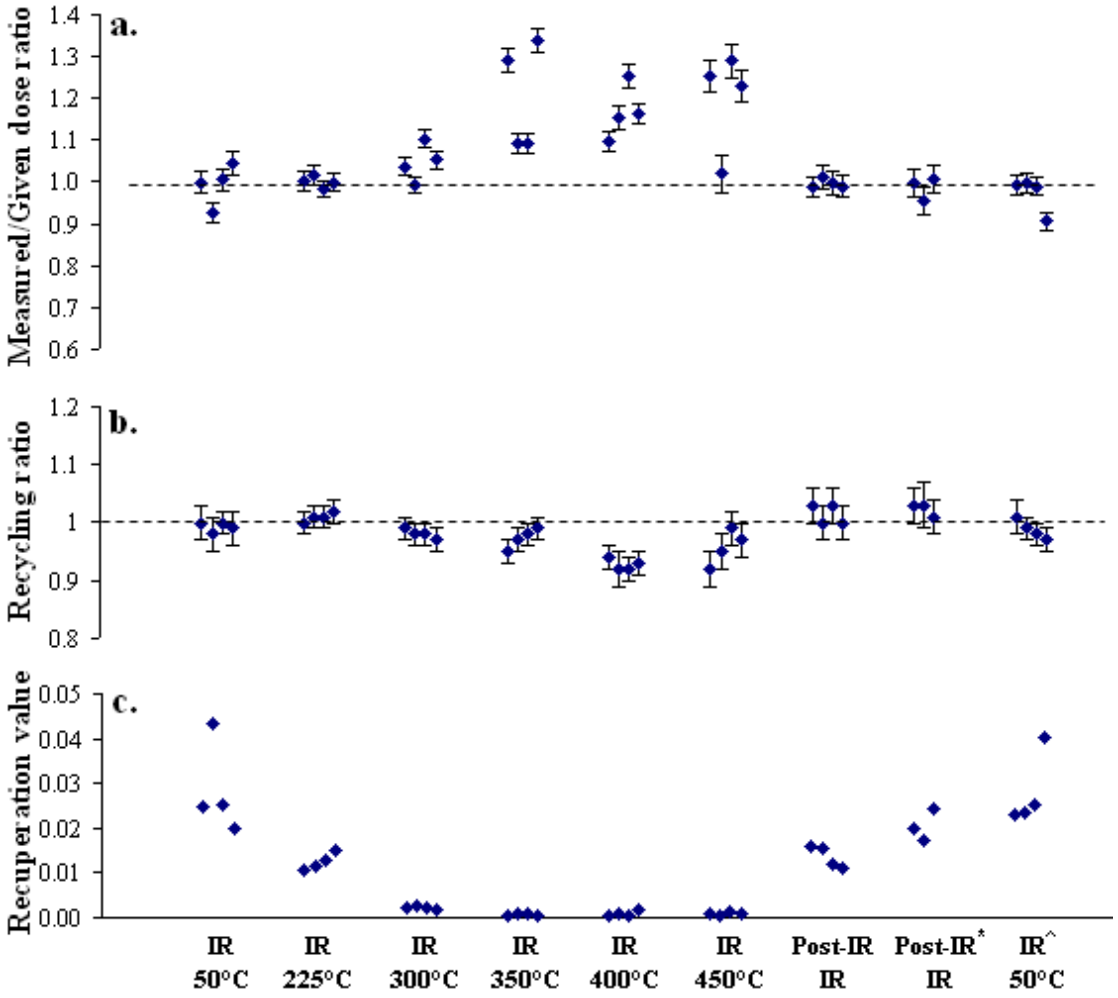

Figure 7.15: Dose recovery results for aliquots of MR9 using various IR stimulation conditions. a, Measured/given dose ratios. b, Recycling ratios. c, Recuperation values (calculated as the sensitivity-corrected IRSL signal from the 0 Gy regenerative dose divided by that of the surrogate natural). Note that 'post-IR IR' includes an IR bleach at 50°C, whereas 'post-IR* IR' includes an IR bleach at 100°C. 'IR^ 50°C' was stimulated for 500 s.

These results support those of Section 7.4, and indicate that stimulation temperatures at or below 225°C are the most suitable for dating applications using the SAR procedure.

7.6.2 Anomalous fading tests

Several of the stimulation conditions tested in Section 7.6.1 proved suitable for dose determination using the SAR procedure. The next step was to determine the extent to which K-feldspar separates from Mumba suffer from anomalous fading. To do this, the same aliquots from the dose recovery experiment were used to perform anomalous fading tests. An individual fading rate was calculated for each aliquot, in view of the

findings of several studies that have shown that there is grain-to-grain (Lamothe and Auclair, 1997) and aliquot-to-aliquot (Huntley, 1997; Huntley and Lian, 2006) variability in the fading rate. Huntley and Lian (2006) state that the fading rates used to correct an age for anomalous fading should be applicable to the aliquots on which each D_e is measured.

7.6.2.1 Measuring the fading rate

Wallinga et al. (2000a) suggested that the SAR procedure could be used as a tool to calculate the rate of anomalous fading in K-feldspars. This was followed by Auclair et al. (2003), who compared various methods of estimating the fading rate, ultimately demonstrating that a fading test based on the SAR procedure is reliable.

The purpose of the fading tests performed here was to compare fading rates for the various stimulation conditions. To this end, several of the sets of aliquots from the dose recovery experiment had their fading rates measured using the same stimulation conditions used in the dose recovery test (i.e., the set of aliquots stimulated with IR at 225°C in the dose recovery test had its fading rate measured using IR stimulation at 225°C). Following Thomsen et al. (2008), the objective was to find the stimulation conditions that yielded a signal that was most stable (i.e., fades least over time). A lower fading rate means the observed age needs a smaller correction, which reduces the dependence of the final age on the age-correction model (Thomsen et al., 2008).

A step-by-step procedure for the measurement of the fading rate is illustrated in Table 7.9. The aliquots from the dose recovery experiment were given a 59 Gy irradiation followed immediately by a preheat (Auclair et al., 2003) of 260°C for 60 s. Aliquots were then stored for various durations, ranging from 0 s to ~24 hr (~86,400 s) before receiving an IR stimulation at a specified temperature for 100 s or a post-IR IR stimulation (L_x). This was followed by a test dose cycle consisting of a 12 Gy dose, a preheat of 260°C for 60 s, followed immediately by an IR stimulation identical to that used to obtain L_x (T_x). This procedure was repeated an average of 23 times using various storage durations.

It should be noted that the storage times used in this experiment were relatively short compared to those of other studies. The purpose of this experiment was not to correct any measured ages, but to compare fading rates for various stimulation

conditions. The storage times were, therefore, relatively inconsequential, so long as they were standard for all stimulation conditions being compared. To this end, 'prompt' measurements (storage time of 0 s) were the first three measurements made. Prompt measurements were also made following each longer storage time. These measurements served to monitor for reproducibility.

Table 7.9: SAR procedure used to measure the fading rate for samples from Mumba. In step 9, *t* is varied for a range of storage durations. When the post-IR IRSL signal is being tested, Step 3 includes an IR bleach at 50°C for 100 s followed by an IR stimulation at 225°C for 100 s. The signal from the latter stimulation is used to calculate L_x and T_x values

Step	Treatment	Name
1	Give 59 Gy	
2	Preheat: 260°C for 60 s	
3	IR stimulation	L_x
4	Give 12 Gy test dose	
5	Preheat: 260°C for 60 s	
6	IR stimulation (same as step 3)	T_x
7	Give 59 Gy	
8	Preheat: 260°C for 60 s	
9	Store at room temperature for time *t*	
10	IR stimulation (same as step 3)	L_x
11	Give 12 Gy test dose	
12	Preheat: 260°C for 60 s	
13	IR stimulation (same as step 3)	T_x
14	Repeat steps 7-13	

7.6.2.2 Calculating the fading rate

Anomalous fading has been explained using a model based on quantum-mechanical tunnelling (Visocekas, 1985; Aitken, 1985). In this model, the luminescence signal decreases linearly with the logarithm of time (Huntley and Lamothe, 2001). The observed luminescence induced by IR stimulation (I) at time t after irradiation can be described as follows:

$$I = I_c\,[1 - \kappa \ln(t/t_c)] \qquad \text{Equation 7.1}$$

where I_c is the luminescence intensity at an arbitrary time (t_c) and κ is a constant, characteristic of the sample, that represents the fractional decrease in luminescence

intensity with time for the time interval t_c to 2.30 t_c. The fading rate is generally described using the *g*-value (Aitken, 1985: Appendix F), which is defined as the percent decrease in luminescence intensity per decade, where a decade is a factor of 10 in time since irradiation (%/decade). The *g*-value can be derived from the κ value using an equation from Huntley and Lamothe (2001), as follows:

$$g = 100\kappa \ln(10) \qquad \text{Equation 7.2}$$

which changes the fading equation to:

$$I = I_c [1 - g/100 \log_{10}(t/t_c)] \qquad \text{Equation 7.3}$$

The choice of t_c weakly influences the κ and *g*-values (Huntley and Lamothe, 2001; Auclair et al., 2003). To enable comparisons between studies, the *g*-value is commonly expressed in the literature for a t_c of 2 days (g_{2days}), following Huntley and Lamothe (2001).

A consideration that must be made is that the 'time since irradiation' must account for the anomalous fading that takes place during the administration of the laboratory dose. As mentioned in the section above, a dose of 59 Gy, which takes approximately 500 s to be delivered to the sample, was used for fading measurements in this study. Equations F9 and F11 from Aitken (1985: Appendix F) account for this by replacing *t* and t_c with t^* and t_c^* respectively:

$$t^* \cong t_1 + (t_2 - t_1)/2 \qquad \text{Equation 7.4}$$

where t_1 is the elapsed time between the end of irradiation and the beginning of luminescence stimulation and t_2 is the elapsed time between the beginning of irradiation and the beginning of luminescence stimulation. Therefore, $(t_2 - t_1)$ is equal to the duration of irradiation (Auclair et al., 2003). Following this, all fading rate calculations made during this study replaced *t* and t_c in Equation 7.1 with t^* values as calculated in Equation 7.4.

The procedure laid out in Table 7.9 was performed as described in Section 7.6.2.1. The L_x/T_x values for the various delay times were then plotted against log delay time and a regression line was fitted to the measurements from which g_{2days}-values were calculated (e.g., Figure 7.16). A g_{2days}-value was thus obtained for each aliquot measured.

7.6.2.3 Fading test results

The six stimulation conditions for which fading rates were measured include: IR stimulation for 100 s at 50°C, 225°C, 300°C and 350°C, IR stimulation for 500 s at 50°C and post-IR IR stimulation as described in Section 7.5 (i.e., IR stimulation at 225°C following an IR stimulation at 50°C). Despite the unsuitability of IR stimulation at 300°C and 350°C for dating applications due to their inability to obtain a known dose, it was of interest to determine the extent of fading at higher temperatures.

Values of L_x/T_x are plotted as a function of delay time for representative aliquots from each stimulation condition in Figure 7.16 and are used to calculate the *g*-value. Fading rates for each measured aliquot are displayed in Figure 7.17. As the IR stimulation temperature is increased to 300°C, the fading rate decreases, supporting the results of Thomsen et al. (2008) who tested temperatures up to 225°C. For stimulation temperatures above 300°C, the fading rate is unchanged. The fading rates measured for the post-IR IR stimulation are considerably lower than the fading rates calculated for any of the other stimulation conditions. The post-IR IRSL fading rate of four aliquots resulted in a weighted mean g_{2days} of 0.9 ± 0.3%/decade. This is ~94% and ~87% lower than the weighted mean fading rates of four aliquots each for IR stimulations at 50°C and 225°C, respectively. The small fading rates measured using the post-IR IRSL signal support the results of Thomsen et al. (2008) and Buylaert et al. (2009), who obtained average fading rates for the initial post-IR IRSL signal of 1.28 ± 0.07 and 1.62 ± 0.06 %/decade, respectively.

The fading rates obtained using an IR stimulation for 500 s at 50°C (Figure 7.16f) deserve mention. It should be noted that two fading rates are not plotted in Figure 7.17 and have g_{2days}-values of 62.0 ± 1.1 and 86.0 ± 1.7 %/decade. These fading rates are remarkably large, especially considering that the only difference between this stimulation condition and the others is the extended duration of IR stimulation. The

fading rates were recalculated using, for background, the part of the decay curve between 89.8 and 100 s (i.e., the same interval used for the 100 s IR stimulations), instead of the interval 489.8 and 500 s. The fading rates changed little, increasing by 3

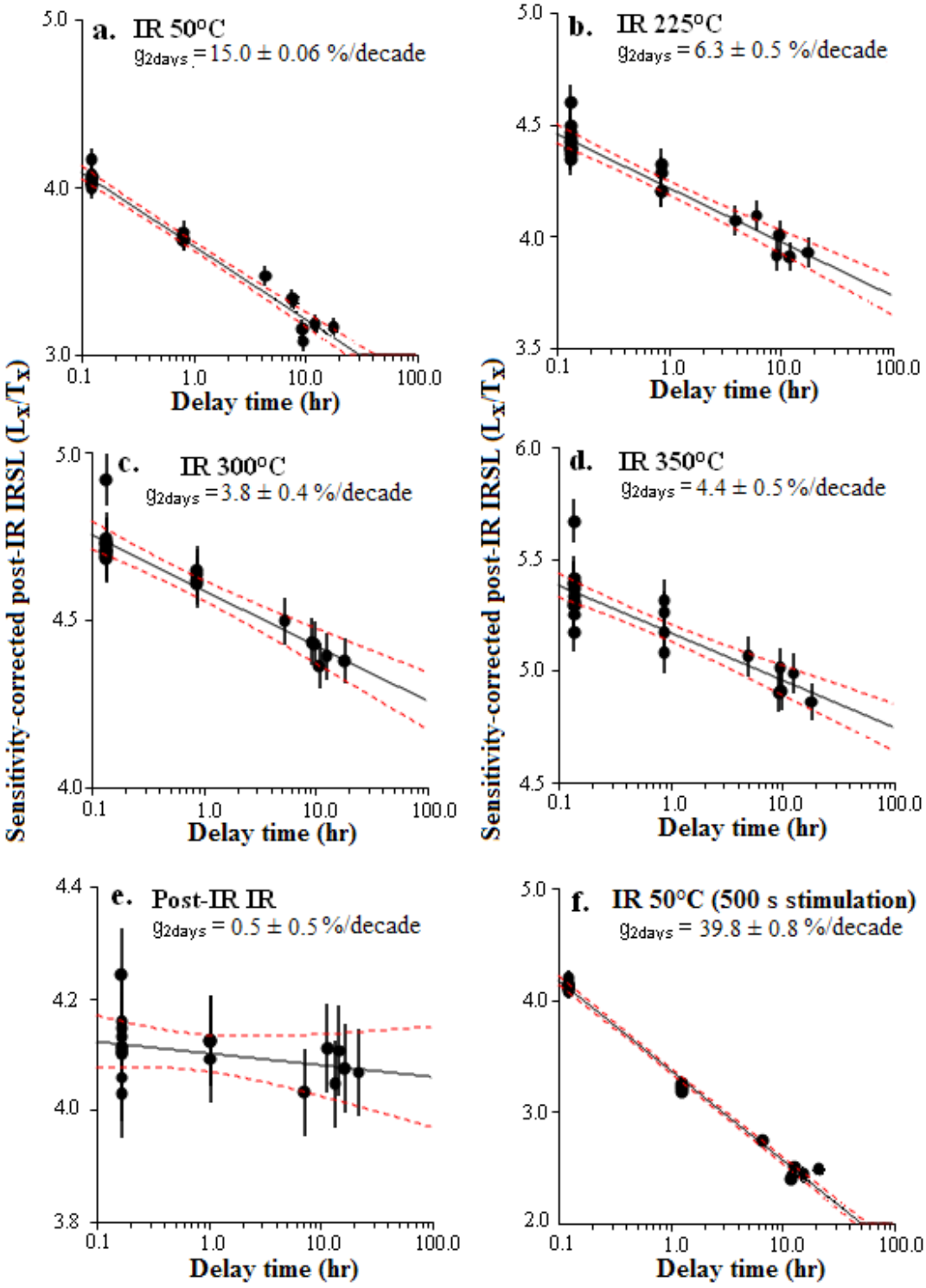

Figure 7.16: Measured fading rates for six representative aliquots (one aliquot for each stimulation condition tested) of MR9. Dashed lines indicate 2σ.

± 2%/decade. Given the purpose of these experiments and analyses was to identify the measurement conditions associated with the lowest fading rates, IR stimulation for 500 s was no longer considered a viable procedure.

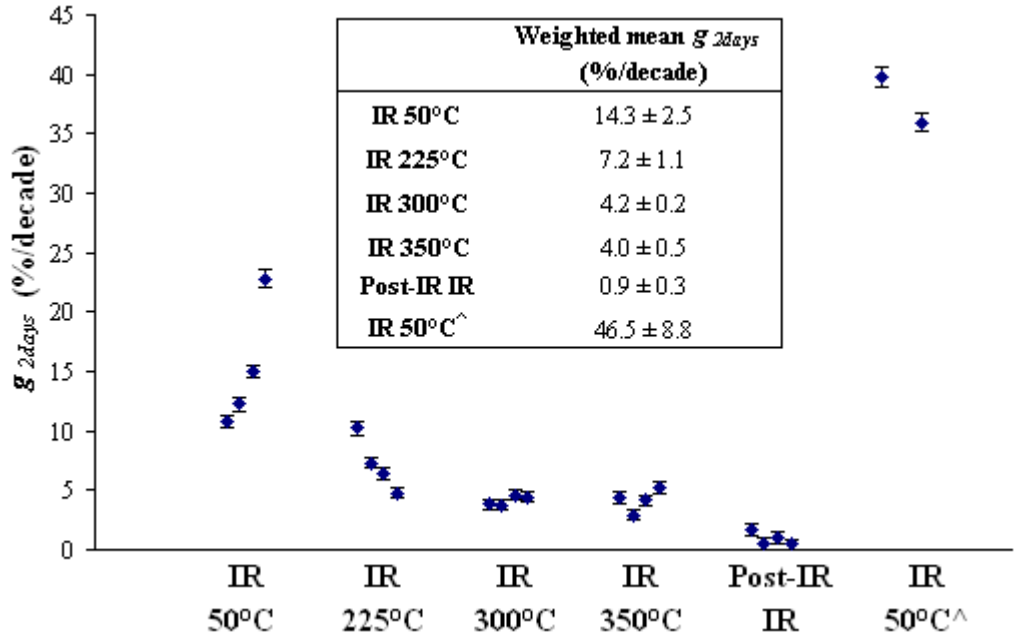

Figure 7.17: Measured fading rates for all aliquots of MR9 under various stimulation conditions. Two data points for the IR stimulation for 500 s lie off the graph (discussed in text). Inset shows the weighted mean fading rate of four aliquots for each stimulation condition. Note that ^ indicates IR stimulation for 500 s.

All of the fading rates in Figure 7.17 were calculated using the same part of the decay curve that has been used in the rest of this study (i.e., integrating the first 2 s of signal and using the final 10.2 s of IR stimulation to calculate the background). Thomsen et al. (2008) and Li (2010) have also reported that when the later parts of the IRSL and post-IR IRSL decay curves are used to obtain a background-subtracted signal, the calculated fading rate is lower. To investigate this, the data used to calculate the fading rates in Figure 7.17 were reanalysed. The signal integration interval was varied in 2 s periods (i.e., 0–2 s, 2–4 s, 4–6 s… 20–22 s.). For each interval, L_x/T_x was recalculated for each delay time and prompt measurement and new values of g_{2days} were calculated. The interval used to calculate the background was kept the same as previously (final 10.2 s stimulation).

Results are presented in Figure 7.18 for IR stimulation at 50°C and 225°C and for post-IR IR stimulation. Each point represents the weighted mean of the four

aliquots measured. As the signal integration interval is moved further down the decay curve, the calculated fading rate decreases markedly for IR stimulation at 50°C and 225°C. It is reduced by ≥50% when the signal is integrated between 4 and 6 s of IR stimulation. This same analysis was performed for IR stimulation at 50°C for 500 s and these data displayed similar results, decreasing to a weighted mean g_{2days} of 5.75 %/decade when the signal integration interval was shifted from 0 – 2 s to 20 – 22 s of IR stimulation. The post-IR IR stimulation fading rates, however, stayed consistent, regardless of which part of the decay curve was integrated. The initial signal integration period used throughout this study (0–2 s) does not seem to fade significantly more or less than any other integration interval analysed for the post-IR IRSL signal. These results support those of Thomsen et al. (2008) in regards to IR stimulation at 50°C and 225°C, but not in regards to the post-IR IR stimulation, as they observed a decrease in fading rate when the later parts of the decay curve were integrated as signal.

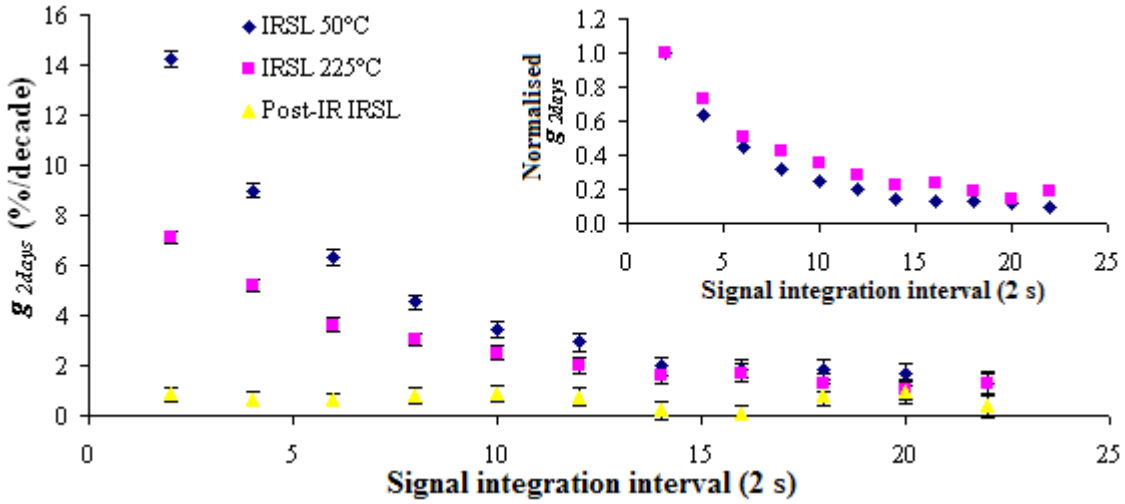

Figure 7.18: Fading rates for various signal integration periods. The initial integration period was varied in two second intervals from 0–2 s through to 20–22 s. The background, calculated from the final 10.2 s of stimulation, remained constant for all calculations. The inset shows normalised fading rate as a function of the integration interval for IRSL at 50°C and 225°C.

Also of interest is that these results, like those of Thomsen et al. (2008) and Li (2010), support the donor-acceptor model of feldspar luminescence. If transport through the conduction band was the pathway for electrons to travel from the excited state to a recombination centre, then the fading rate should stay the same regardless of the integration period; electrons from all traps would have approximately the same chance of accessing distant recombination centres via the high-mobility conduction

band. In the donor-acceptor model, the closest trap-recombination centre pairs are the most likely to fade and would be the first to recombine upon IR stimulation. This suggests that the earlier part of the IRSL decay curve will be dominated by closer, less stable trap-recombination centre pairs that are more likely to tunnel (i.e., fade), while the later parts of the decay curve will be dominated by farther spaced, more stable pairs that would be less likely to tunnel. This is supported by the results in Figure 7.18. The post-IR IRSL fading rate is largely unaffected by the part of the decay curve integrated as signal. This suggests that the close trap-recombination centre pairs that are likely to lead to fading over time do not contribute to the post-IR IRSL signal because they are sufficiently removed by the 50°C IR bleach.

7.6.3 Summary

The purpose of performing the experiments described in this section was to compare various IR stimulation conditions to find those that resulted in an IRSL signal that could best recover a given dose and fade the least, thereby making any calculated ages less dependent on a fading-correction model. After comparing the various stimulation conditions tested in this section, the post-IR IRSL procedure produced the most promising results. The SAR procedure proved suitable for measurement of the post-IR IRSL signal, which passed all tests of suitability, was bleachable by sunlight, recovered a known laboratory dose and faded the least of all stimulation conditions tested.

7.7 Conclusions

In this chapter, the luminescence signal of K-feldspar separates from Mumba was characterised. The main results and conclusions that were established from these investigations are summarised as follows:

- The decision to make luminescence measurements using the blue emission, isolated using the standard blue filter combination (BG39 + Kopp 7-59), was made on the basis of two criteria: 1) luminescence investigations of the various emissions from K-feldspars indicated that the blue emission provided the brightest TL and IRSL signal, and 2) many other studies have used this blue filter combination, making our results directly comparable to theirs.

- The TL glow curves of natural aliquots possessed peaks at ~350°C and ~430°C. Laboratory-irradiated aliquots possessed a third peak, at ~180°C. The following features suggest that the ~430°C TL peak may share the same source trap as the IRSL signal in K-feldspars from Mumba:
  - The TL peak at ~350°C was shown to be less optically sensitive than the TL peak at ~430°C. The ~350°C TL peak was reduced by roughly the same amount by a preheat (260°C for 60 s), as by IR stimulation at 50°C, and by a post-IR IR stimulation. When the IR stimulation temperature was increased from 50°C to 150°C and then to 225°, with the TL glow curves recorded after each stimulation, the ~350°C TL peak was not reduced, despite the increased IRSL output. The ~350°C TL peak was inferred to accumulate charge following repeated irradiations, preheats, and IR stimulations up to 225°C.
  - The ~430°C TL peak was shown to be unchanged following a preheat of 260°C for 60 s, although IR stimulation at 50°C and post-IR IR stimulation both reduced the peak substantially. In addition, when the IR stimulation temperature was increased from 50°C to 150°C and then to 225°C, the IRSL output increased, and the ~430°C TL peak was reduced by ~10% with each step increase in stimulation temperature.
- The IRSL signal intensity and decay curve shape were shown to be largely dependent on stimulation temperature.
  - The IRSL signal intensity increased as IR stimulation temperature was increased from 50°C to 300°C, after which it began to decrease. This finding holds true even when the isothermal TL signal resulting from the elevated temperature is taken into account. Elevated-temperature stimulations at, or below, 225°C were shown not to have a substantial isothermal TL signal when a preheat of 260°C for 60 s preceded it. These results suggested that 225°C was the maximum temperature at which IR or post-IR IR stimulation could reliably be made.
  - When the isothermal TL signal was subtracted from the IRSL signal measured at a variety of temperatures, the decay rate of the IRSL signal

was shown to increase as stimulation temperature was increased from 50°C to 400°C.

- Dose recovery experiments indicated that the SAR procedure would be applicable for measurement of the post-IR IRSL signal and the IRSL signal at a number of different stimulation temperatures (50°C and 225°C). They passed all tests of SAR suitability and recovered a known dose. A modified dose recovery test was also used to show that the post-IR IRSL signal was bleachable to negligible levels in a relatively short period of time by direct sunlight exposure.
- Anomalous fading was shown to be ubiquitous regardless of the IR stimulation conditions (50°C, 225°C, 300°C, 350°C and post-IR IR). The fading rate was shown to decrease as the IR stimulation temperature was increased up to 300°C. The later portions of the IRSL signals measured at 50°C and 225°C were shown to suffer less from anomalous fading than the initial portions of these signals. The post-IR IRSL signal consistently showed the smallest rate of anomalous fading across the entire decay curve.
- The donor-acceptor model of feldspar IRSL production (Poolton et al., 1995, 2002a,b, 2009) was largely supported by the results presented in this chapter.
    - It was shown that the anomalous fading rate of the IRSL signal measured at 50°C and 225°C decreased as the portion of the signal that was integrated was moved later into the decay curve. This suggests that the later parts of the decay curve are increasingly the result of IRSL resulting from distant trap-recombination centre pairs (i.e., those less likely to anomalously fade). The population of close trap-recombination centre pairs (i.e., those more likely to anomalously fade), which recombine through tunnelling from the excited state, is more likely to produce the IRSL in the early part of the decay curve and is, thus, more likely to be exhausted by the later part of the decay curve. As stimulation time increases, IRSL is increasingly produced by distant trap-recombination pairs, resulting in lower fading rates.
    - The observation that the decay rate of the IRSL signal increases as IR stimulation temperature is increased from 50°C to 400°C suggests that

the early portion of the IRSL signal, which is usually produced mainly by close trap-recombination centre pairs, is increasingly contributed to by IRSL produced by distant trap-recombination centre pairs. As the IR stimulation temperature is increased, the thermally assisted process of IRSL production, whereby electrons are thermally assisted into the conduction band and can thus reach distant recombination centres more quickly, adds signal to the tunnelling recombination process that is responsible for the IRSL signal at low temperatures.

- The low fading rate of the post-IR IRSL signal can also be explained using this model. The initial IR stimulation (50°C) bleaches the IRSL signal produced by the close trap-recombination centre pairs that would be more likely to fade in nature, leaving electrons in the traps associated with the more distant pairs. These pairs are accessed with the IR stimulation at an elevated temperature (225°C), resulting in an IRSL signal that suffers much less from anomalous fading. This is further supported by the observation that the fading rate of the post-IR IRSL signal does not change as the signal that is integrated is moved to later portions of the decay curve. This suggests that the same population of traps (i.e., distant trap-recombination pairs) is being accessed throughout the duration of post-IR IR stimulation.

Owing to its ability to recover a known dose, be bleached by sunlight, and suffer from almost negligible levels of anomalous fading, the post-IR IRSL signal was used to estimate D_e values and measure fading rates for multi-grain aliquots of K-feldspar of four strategic samples from Mumba (MR3, MR6, MR9 and MR10). The following chapter describes the measurement of these D_e values and fading rates, as well as the age-correction model used to correct for anomalous fading. The fading-corrected K-feldspar ages will then be compared with the OSL ages obtained from single grains of quartz.

Chapter 8: Comparison of K-feldspar and quartz ages from Mumba rockshelter, Tanzania

In the previous chapter, investigations of the TL and IRSL signals from multi-grain aliquots of K-feldspar separates from Mumba were described. Infrared stimulation was performed at various temperatures and the resultant luminescence signals were characterised. Following these results, which support those reported by Thomsen et al. (2008), a post-IR IR stimulation, performed at 225°C, was investigated for its applicability at Mumba. The post-IR IRSL signal from K-feldspars was shown to be appropriate for the use of the SAR procedure. It could be used to recover a known radiation dose in the laboratory (Section 7.6.1) and the signal was shown to be bleachable by natural sunlight (Section 7.5.3). In addition, the post-IR IRSL signal exhibited the least anomalous fading of the six different stimulation conditions investigated (Section 7.6.2). Following these results, it was concluded that the post-IR IRSL signal could be used to determine D_e values and fading rates for aliquots of K-feldspar from Mumba. These could then be used to calculate fading-corrected ages.

In this chapter, the measurement of D_e values and fading rates from multi-grain aliquots is described, together with the model for correcting anomalous fading. Fading-corrected ages will be presented for K-feldspar separates of four samples from Mumba, and then compared with the OSL ages obtained from single grains of quartz.

8.1 Measurement of D_e values and fading rates

D_e values and anomalous fading measurements were made for four strategic samples from Mumba, namely MR3, MR6, MR9 and MR10. Separates of K-feldspar from the first three of these samples were measured because ages were also obtained using single grains of quartz. The latter provided a semi-independent, internal check of the ages obtained using the post-IR IRSL procedure. A second reason for making measurements on MR9 was because the natural OSL signal from quartz was close to saturation. Separates of K-feldspar from MR10 were measured because a reliable age could not be obtained using quartz, due to the natural OSL signal being in saturation.

Twenty-four aliquots of MR3 and MR6, and twenty-three aliquots of MR9 and MR10, were used to obtain D_e values using the post-IR IRSL procedure (described in detail in Section 7.5). Each aliquot, consisting of ~50 grains, was preheated to 260°C

for 60 s, bleached using the IR diodes at 50°C for 100 s, and stimulated using the IR diodes at 225°C for 100 s while the IRSL was measured (L_N). A test dose cycle was then administered, which consisted of a 12 Gy irradiation, a 260°C preheat for 60 s, an IR bleach at 50°C for 100 s, and an IR stimulation at 225°C for 100 s (T_N). The aliquots were then given a regenerative dose, bleached with the IR diodes at 50°C for 100 s, and the IRSL was measured at 225°C for 100 s (L_x), followed by a test dose cycle (T_x).

Dose-response curves were constructed for MR3 using the sensitivity-corrected IRSL signal following regenerative doses of 60, 120, 180, 240, 0 and a second 60 Gy. Dose-response curves for MR6, MR9, and MR10 were constructed using the sensitivity-corrected IRSL signal following regenerative doses of 60, 30, 90, 120, 180, 240, 360, 0 and a second 60 Gy. The second 60 Gy regenerative dose was measured to determine the recycling ratio, which was used to check that any changes in sensitivity were corrected for. Only one aliquot from sample MR9 failed to recycle this duplicate regenerative dose and was consequently rejected.

The sensitivity corrected natural (L_N/T_N) for each aliquot was projected onto its dose-response curve to obtain a D_e estimate. For each aliquot of samples MR3, MR6 and MR9, the L_N/T_N value was able to intercept the dose-response curve and produce a D_e estimate. All aliquots of MR10 produced dose-response curves that continued to grow at higher doses, but four aliquots had L_N/T_N values that fell above the 360 Gy regenerative-dose point. Consequently, a higher regenerative dose of 480 Gy was included for these four aliquots of MR10. The higher regenerative-dose point meant that the L_N/T_N values of all aliquots could be projected on to the dose-response curves, thus producing D_e estimates. Examples of dose-response curves from representative aliquots of each sample are presented in the left-hand plots in Figure 8.1.

Fading rates were measured for each aliquot as described in Section 7.6.2.1. Following D_e estimation, each aliquot was given repeated regenerative cycles of 60 Gy with test doses of 12 Gy. The delay times were varied between 0.17 hr (10 min) and up to 1765 hr (~74 days). Fading rates (expressed as *g*-values normalised to a delay time of two days) were then calculated as described in Section 7.6.2.2 (right-hand plots in Figure 8.1).

8.2 Calculating fading-corrected ages

The method used to correct K-feldspar ages for fading is based on that of Huntley and Lamothe (2001), which uses the equation:

$$T_f/T = 1 - \kappa[\ln(T/t_c^*)-1] \qquad \text{Equation 8.1}$$

where T is the corrected age that would be calculated if fading was not present, and T_f is the age calculated when using the measured, fading-affected D_e value. The variable t_c^* represents the period between irradiation and stimulation, taking into account the duration of irradiation. The variable κ was determined at time t_c^* using the results from fading tests, as described in Section 7.6.2.

An important caveat to this anomalous fading-correction model was emphasised by Huntley and Lamothe (2001). They stated that the correction model is limited to the linear portion of the dose-response curve, and should not be expected to be appropriate for samples with D_e values in the non-linear portion of the growth curve; this may restrict its use to samples younger than ~20–50 ka. To the contrary, though, several recent studies have shown that the age correction model may be applicable to older samples with larger doses. Martins et al. (2010) pointed out that the dose-response curve is not expected to be truly linear even very close to the origin, and suggest that the fading-correction model may be appropriate for doses as high as ~200 Gy. Buylaert et al. (2007) used the model of Huntley and Lamothe (2001) to correct IRSL-SAR ages from Chinese loess. They concluded that the resultant fading-corrected ages were in good agreement with independent age controls in the range ~70 to ~130 ka. By contrast, the SAR-OSL ages obtained for quartz from the same samples underestimated the independent ages (Buylaert et al., 2007). Later, Buylaert et al. (2008), investigating samples from Northern Russia, compared quartz OSL ages with K-feldspar IRSL ages (also corrected for anomalous fading using the model of Huntley and Lamothe, 2001) and concluded that they were indistinguishable, although both underestimated the expected age. Cunha et al. (2008) and Martins et al. (2009) have also demonstrated that there is good agreement between fading-corrected feldspar IRSL ages and quartz OSL and U-series ages for a number of samples from the Portugal in the rage of ~35 to ~60 ka.

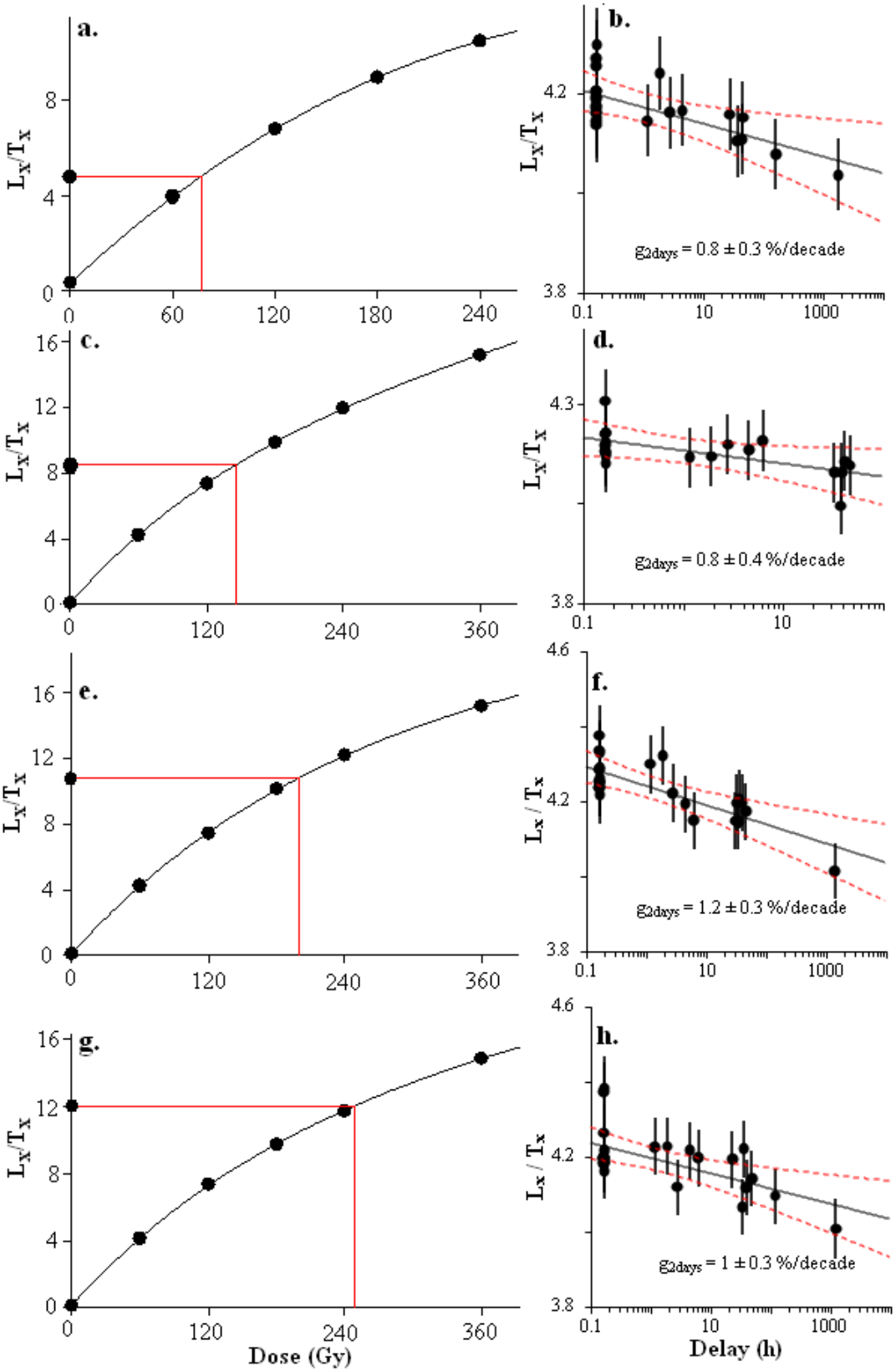

Figure 8.1: Examples of dose-response curves (a, MR3; c, MR6; e, MR9; g, MR10) and fading rates calculated from plots of L_x/T_x vs. delay time (b, MR3; d, MR6; f, MR9; h, MR10) for a representative aliquot of each sample. The fading rates are expressed as g_{2days} values (see Section 7.6.2.2 for details). The dashed lines in (b), (d), (f) and (h) indicate 2σ.

A second caveat for fading-corrected ages is that correction procedure is based on the fading rates measured in the laboratory. Since storage tests can only be performed on laboratory time scales, it is assumed that the measured fading rates are representative of those experienced by the sample over the total duration of burial. To minimise any errors that might arise from this assumption, the IRSL signal of K-feldspars from Mumba that faded the least was identified (Section 7.6) and used to obtain D_e values. Use of the signals with low fading rates minimises the dependence of the fading-corrected ages on the assumptions and limitations of the correction model (Huntley and Lamothe, 2001; Thomsen et al., 2008).

8.3 Assessing the reliability of fading-corrected ages

The D_e distributions obtained for samples MR3, MR6, MR9 and MR10 are presented in Figure 8.2a, c, e and g respectively. The weighted mean D_e value and spread of each distribution (overdispersion) are presented in Table 8.1. The measured D_e and g_{2days} values for each aliquot were used, together with the bulk sample environmental dose rate, to calculate a fading-corrected age for each aliquot as described in Section 8.2. The distributions of the resultant fading-corrected ages for each sample are presented in Figure 8.2 (b, d, f and h). Table 8.1 lists the fading-corrected ages and their spread, obtained using the CAM, for the four samples from Mumba. The dose rates (from Table 6.1), weighted mean D_e values and the uncorrected CAM ages are also presented for comparison.

Three features of the data presented in Table 8.1 confirm the internal consistency and reliability of ages obtained using K-feldspar separates from Mumba. First, all ages, fading-corrected and -uncorrected, are in the correct stratigraphic order, including MR10 for which the quartz OSL age was significantly younger than MR9. This outcome provides confidence in the ages obtained using the post-IR IRSL signal. Second, the agreement between fading-corrected and -uncorrected ages reflects the limited extent to which fading-corrected ages are reliant on the correction and its caveats. The corrected/uncorrected age ratios for the four samples are 1.10 ± 0.16 (MR3), 1.06 ± 0.06 (MR6), 1.11 ± 0.07 (MR9) and 1.11 ± 0.08 (MR10), each of which is statistically consistent with unity. This outcome indicates that the ages obtained using the post-IR IRSL signal from K-feldspar are not critically dependent on the meas-

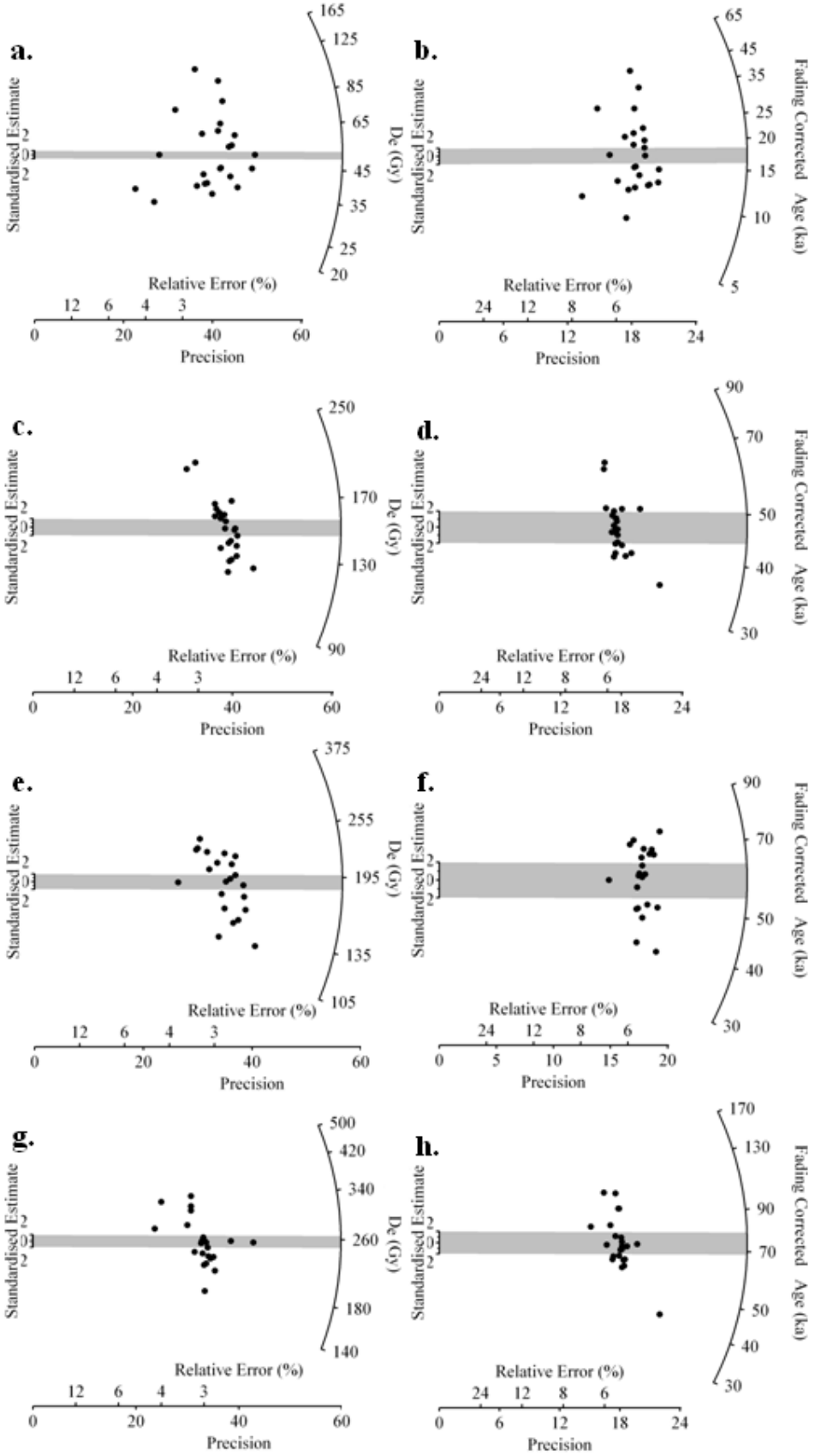

Figure 8.2: Radial plots showing distributions of D_e values (a, MR3; c, MR6; e, MR9; g, MR10) and fading corrected ages (b, MR3; d, MR6; f, MR9; h, MR10) for all samples measured.

Table 8.1: The CAM was used to obtain the weighted mean D_e values (Gy), uncorrected ages (ka), and fading-corrected ages (ka) for each sample. The environmental dose rate, weighted mean g_{2days} values, and the overdispersion of D_e values and fading-corrected ages for each sample are also presented.

Sample	D_e value (Gy)	Overdispersion (%)	Dose rate (Gy/ka)	g_{2days} (%/decade)	Uncorrected age (ka)	Fading-corrected age (ka)	Overdispersion (%)
MR3	51.4 ± 5.3	51 ± 7	3.15 ± 0.12	1.0 ± 0.1	16.3 ± 1.7	17.9 ± 1.9	51 ± 7
MR6	150.9 ± 5.8	19 ± 3	3.37 ± 0.12	0.7 ± 0.1	44.8 ± 1.7	47.6 ± 1.8	18 ± 3
MR9	190.8 ± 9.2	22 ± 3	3.58 ± 0.13	1.1 ± 0.1	53.3 ± 2.6	58.9 ± 2.6	19 ± 3
MR10	258.1 ± 12.5	23 ± 3	3.89 ± 0.15	1.1 ± 0.1	66.3 ± 3.2	73.6 ± 3.8	24 ± 4

ured fading rates, as a result of the low measured fading rates. As a consequence, these ages are also not critically dependent on the model used to correct for fading, or its associated assumptions and limitations (Huntley and Lamothe, 2001). Nonetheless, the age that is corrected for anomalous fading is likely to be more accurate than the uncorrected age. This is because the fading-corrected age at least compensates for the limited extent of fading observed on laboratory timescales. Third, the fading-corrected ages obtained using K-feldspar separates from MR3, MR6 and MR9 are in good agreement with the corresponding OSL ages obtained from single grains of quartz (Table 8.2). The latter act as semi-independent age controls and indicate that the fading-corrected ages obtained using the post-IR IRSL signal from K-feldspars from are at least as accurate as ages obtained using the OSL signal from single grains of quartz, provided the deposit has not been subjected to significant post-depositional disturbance. The single-grain OSL ages are not truly independent from feldspar-IRSL ages because the two share many of the same dose rate terms.

Table 8.2: Ages obtained for samples from Mumba using quartz and K-feldspar grains.

	Age (ka)	
Sample	Quartz	K-feldspar (fading-corrected)
MR3	15.6 ± 1.2	17.9 ± 1.9
MR4	36.8 ± 3.4	
MR6	49.1 ± 4.3	47.6 ± 1.8
MR7	51.3 ± 4.2	
MR8	56.9 ± 4.8	
MR9	63.4 ± 5.7	58.9 ± 2.6
MR10	45.9 ± 10.3*	73.6 ± 3.8

*The MR10 quartz age should be considered a minimum estimate due to saturation of the natural OSL signal

8.4 Age comparisons: K-feldspar and quartz

In Section 6.4.3, the ages obtained from single grains of quartz using the FMM and beta microdosimetry correction were shown to be in correct stratigraphic order (except MR10) and in agreement with the available independent age estimates. In this chapter, the fading-corrected ages obtained using multi-grain aliquots of K-feldspar

separates were described. They were also shown to be in correct stratigraphic order, and not critically reliant on the limitations and assumptions of the age-correction model (Huntley and Lamothe, 2001). Having established the internal consistency of the quartz and feldspar ages independently, they will now be compared in this section. Table 8.2 shows the ages obtained in this study for each sample. The ages shown in the left column were obtained using single grains of quartz, and have been corrected for beta microdosimetry variations. The ages shown in the right column were obtained using the post-IR IRSL signal from multi-grain aliquots of K-feldspar, and have been corrected for anomalous fading. Three of the four samples for which both quartz and K-feldspar ages were obtained (MR3, MR6 and MR9) show good agreement between the two ages. The feldspar/quartz age-ratio for each of these samples is consistent with unity at one standard error: 1.15 ± 0.15 (MR3), 0.97 ± 0.09 (MR6) and 0.93 ± 0.09 (MR9).

8.4.1 Sample MR6

Sample MR6 is the most appropriate sample for assessing the consistency of ages obtained using quartz and K-feldspar. This is because the distribution of single grain quartz D_e values suggested that this sample was not subject to any apparent problems associated with either post-depositional mixing or low-dose saturation (Figure 6.1). For this sample, therefore, the effects of 'summing' the luminescence signals from multiple grains when measuring multi-grain aliquots of K-feldspar should be negligible. For this reason, the feldspar/quartz age-ratio of 0.97 ± 0.09 for MR6 provides further confidence in the procedures used to obtain both ages. That is, the close agreement offers assurance that the fading-correction procedure applied to the K-feldspar ages and the beta-dose correction applied to the single grain quartz ages did not introduce significant bias. In addition, the consistency in the quartz and feldspar ages also provides increased confidence in an age estimate of ~48 ka for the uppermost section of Bed V at Mumba. However, it would be invalid to determine the weighted mean of the ages obtained using quartz and feldspar for this, or any other, sample from Mumba, because they are not truly independent age estimates, as discussed in Section 8.3. As a result, the age obtained using single grains of quartz from MR6 should be considered the more accurate, due to the higher resolution afforded by single-grain analysis and the ability to reject any aberrant or intrusive grains.

8.4.2 Samples MR3 and MR9

The single-grain D_e distributions of samples MR3 and MR9 exhibited a large spread in D_e values (Figure 6.1). Using the FMM, four discrete D_e components were identified for MR3 (Table 6.3). For this sample, the components with the lowest and highest D_e values consisted of just two and five grains, respectively. The central D_e of the lowest component was one-eighth as large as that of the majority of the other grains. The highest component had a central D_e that was 2.5 times as large as the majority of the other grains. Consequently, the populations of grains that gave rise to these D_e components were considered to be intrusive and were, thus, removed from the dataset. The remaining grains could be fitted by two D_e components, which were analytically shown to be compatible with small-scale variations in the beta dose received by individual grains.

There are two reasons why beta microdosimetry variations would not have had a substantial effect on the spread of D_e values for multi-grain aliquots of K-feldspar. First, when multiple grains are amassed on an aliquot, the luminescence measured is a sum of that produced by each individual grain. Thus, the problem of individual grains experiencing different dose rates, and hence different burial doses, is not manifested. Second, K-feldspar grains have a higher internal dose rate than quartz, making them less susceptible to the effects of external beta microdosimetry. The internal dose rate of the mineral of interest is unaffected by the dose rate from the surrounding environment. Thus, if the fractional contribution of the internal dose rate to the total dose rate is large, then the effects of uncertainties associated with the external dose rate will be smaller. Since the internal dose rate to K-feldspar from the decay of ^{40}K, ^{87}Rb, U and Th is 30 times larger than that of quartz (Table 6.1), it constitutes a substantial proportion of the total dose rate (~29% in the case of MR3). This means that differences in the beta dose rates received by individual grains of K-feldspar are less consequential.

In contrast, the mixing of grains that were deposited earlier or later than the majority of grains could have an effect on the K-feldspar age. The presence of these intrusive grains would likely increase the spread in D_e values. The two populations of intrusive grains that were identified during quartz single-grain measurements are the likely reason for the large overdispersion (51 ± 7%) in the K-feldspar D_e distribution of MR3 (Table 8.1). Additionally, intrusive grains may increase or decrease the measured

D_e estimates, and corresponding ages, obtained using multi-grain aliquots. This source of possible bias may account for the slight overestimation of the fading-corrected IRSL age, which resulted in a feldspar/quartz age-ratio of 1.15 ± 0.15. Since the intrusive high-dose component constituted a larger proportion of the total number of grains (5 ± 3%) than the intrusive low-dose component (2 ± 1%) in this sample, it is likely that the former had a greater effect on the 'summed' luminescence signal from multi-grain aliquots. Nonetheless, the feldspar/quartz age-ratio for MR3 is statistically consistent with unity, indicating that any D_e overestimation resulting from the inclusion of intrusive grains in multi-grain aliquots of K-feldspar was insufficient to significantly skew the IRSL age.

The situation for sample MR9 is similar to that of MR3. For this sample, three discrete, single-grain quartz D_e components were identified using the FMM (Figure 6.1 and Table 6.3). The component with the lowest D_e values was comprised of ~11 grains (16 ± 7%), which were interpreted as being intrusive. When this population of grains was removed from the dataset, analytical tests showed that the remaining two components could be explained in terms of small-scale variations in the beta dose rate received by individual grains. Again, beta microdosimetry variations would likely not have had a substantial effect on the D_e and age determinations from multi-grain aliquots of K-feldspar. Alternatively, the inclusion of the intrusive, younger grains on multi-grain aliquots may account for the feldspar/quartz age-ratio of 0.93 ± 0.09 for this sample. In spite of this slight disparity, this ratio is within one standard error of unity, confirming that the K-feldspar and single-grain quartz ages are statistically indistinguishable. As was the case for MR3, this indicates that the presence of a small number of intrusive grains on multi-grain aliquots of K-feldspar was not sufficient to significantly skew the IRSL age.

Although the quartz and K-feldspar ages are in statistical agreement, it would not be valid to determine a final age by taking the weighted mean of the two ages, owing to their correlated dose rate terms. Following the conclusion reached for MR6, the OSL ages obtained using single grains of quartz from MR3 and MR9 are considered more reliable, because intrusive grains were identified in both samples. These grains were subsequently rejected from the OSL datasets prior to age determination, but the same does not apply to the multi-grain aliquots used for IRSL determination.

8.4.3 Sample MR10

This sample, from the lowest stratigraphic unit, exhibited a substantially larger disparity between the ages obtained from quartz and K-feldspar grains. The feldspar/quartz age-ratio for MR10 is 1.60 ± 0.37, and is compatible with unity at the 95% confidence interval. This outcome is misleading, however, as the observed statistical consistency is only due to the large relative error (>20%) on the quartz age. The reasons for the younger age obtained using quartz from MR10, and its large associated uncertainty, were discussed in Section 6.5. Due to the proximity of the natural OSL signals to saturation, the age obtained using single grains of quartz from MR10 should only be taken as a minimum estimate. In addition, the large uncertainty on the age is a result of the correspondingly large uncertainties on the (minimum) D_e estimates, which arise from the projection of the sensitivity-corrected natural OSL signal on to the low slope of the dose-response curve as it approaches saturation.

The inability to obtain a reliable, finite age estimate for MR10 from single grains of quartz was the impetus for investigating K-feldspar as a potential luminescence dosimeter at Mumba. Since the IRSL signal from K-feldspars saturates at considerably higher doses than does the OSL signal from quartz (Figure 8.1g) (Duller, 1997), the age determined using K-feldspars from MR10 is considered more accurate. In addition, the precision of the K-feldspar age is substantially improved.

8.5 Conclusions

A robust OSL age could not be obtained using single grains of quartz from the deepest sample collected at Mumba, MR10. This was because the natural OSL signal from many quartz grains from this sample fell on to the saturated portion of the dose-response curve, precluding the reliable estimation of finite D_e values. To achieve the objectives of this thesis, and identify when the transition from a MSA toolkit to the Mumba Industry occurred at Mumba rockshelter, robust age estimates for the MSA-bearing Bed VI deposits were necessary. To avoid problems associated with dose saturation in quartz, the suitability of using K-feldspar separates to estimate an age for MR10 was, thus, explored.

Although the IRSL signal from K-feldspars saturates at higher doses than the OSL signal from quartz (Duller, 1997), it suffers from the malign phenomenon of

anomalous fading, and the widely-used correction model for fading has several limitations (Huntley and Lamothe, 2001). These can be reduced by using an IRSL signal that fades only slightly. The post-IR IRSL signal (Thomsen et al., 2008) was tested due to its reportedly low fading rates and, thus, lesser dependence on the assumptions of the fading-correction model. In Chapter 7, the post-IR IRSL signal of K-feldspars from Mumba was shown to be able to recover a known dose, be bleached by sunlight, and suffer little from anomalous fading. Consequently, this signal was used to obtain D_e values and measure fading rates for multi-grain aliquots of K-feldspar from four strategic samples (MR3, MR6, MR9 and MR10). The D_e values were then used with the measured rates of fading and the environmental dose rates to obtain fading-corrected ages for all four samples. The consistency between fading-corrected and fading-uncorrected ages (Table 8.1) demonstrates that IRSL ages obtained from K-feldspars from Mumba are not critically dependent on the limitations and assumptions of the fading-correction model. In addition, the fading-corrected ages are consistent with the single-grain quartz OSL ages for the three samples (MR3, MR6 and MR9) for which reliable D_e estimates could be made using both minerals. This agreement increases the confidence in the luminescence chronology for Mumba, as well as providing evidence that post-IR IRSL K-feldspar ages can be as accurate as single-grain quartz OSL ages. The archaeological implications of the luminescence chronology from Mumba will be discussed in Chapter 10.

Chapter 9: Luminescence investigations of quartz and feldspars from Moche Borago, Ethiopia

As discussed in Chapter 2, Moche Borago is a rockshelter located on the western flank of the dormant volcano Mt. Damota in Ethiopia. Sediments of volcanic origin are ubiquitous at the site. Many previous studies have shown that quartz and feldspar of volcanic origin have properties that are unsuitable for standard luminescence dating (e.g., Wintle, 1973; Visocekas, 2002; Fattahi and Stokes, 2003a; Choi et al., 2006b; Westaway and Roberts, 2006; Tsukamoto et al., 2007).

In this chapter, investigations of the luminescence signals from multi-grain aliquots of quartz and K-feldspar from Moche Borago are described. A small amount of quartz was present in only one of the three sediment samples prepared. K-feldspar, while extracted from all samples, was also present only in small amounts. The small quantity of luminescent material was exacerbated by the fact that the luminescence signals (i.e., TL, IRSL and OSL) from both minerals were very dim. All measurements made on samples from Moche Borago and discussed in this chapter were performed on the same Risø TL/OSL reader – Risø 4.

9.1 OSL measurements on multi-grain aliquots of quartz

Of the three samples prepared (MB1, MB2 and MB3), quartz could be extracted from only one: sample MB1. There were sufficient quartz grains to prepare only ten small multi-grain aliquots, each consisting of ~100 grains. Quartz could not be used, therefore, as a dating dosimeter for samples from Moche Borago. However, investigations into the OSL characteristics of quartz from MB1 were undertaken. To use sample material as sparingly as possible, only two aliquots, each consisting of ~100 grains, were prepared and used for the following experiments.

9.1.1 Dose recovery experiments using a standard SAR procedure

To assess whether quartz from Moche Borago possessed luminescence characteristics suitable for the application of the SAR procedure, a set of dose recovery experiments was performed. Two aliquots were bleached at 50°C using blue LEDs for 4000 s in Risø 4, and were then given a laboratory irradiation of 47 Gy. A standard SAR procedure (see Table 3.2) was then applied using regenerative doses of 47, 24, 70,

0 and a duplicate 47 Gy dose. The OSL signal following a test dose of 6 Gy was used to correct for sensitivity changes. The preheats applied following the regenerative doses and test doses were 260°C for 10 s and 220°C for 5 s, respectively.

OSL decay curves produced from one aliquot following the surrogate natural (47 Gy) and the subsequent test dose (6 Gy) are presented in Figure 9.1a. The OSL signal decays relatively slowly in comparison to grains from Mumba (e.g., Figure 5.15 and Figure 5.16). This suggests that a fast component may not be present. The presence of a substantial slow component is further inferred from the OSL measured following the 0 Gy regenerative dose (Figure 9.1b). The OSL signal for L_0 decays over the course of optical stimulation and instrumental background is never reached. It is likely that this is the decay of a slow component that was not fully bleached by optical stimulation for 40 s at 125°C and had accumulated throughout repeated regenerative-dose cycles. Alternatively, the 4000 s blue LED bleach may have been insufficient to completely deplete the source traps of the slower components. Regardless, the presence of a substantial slow component and apparent lack of a fast component have been reported by several studies investigating volcanic quartz (e.g., Choi et al., 2006b; Tsukamoto et al., 2003, 2007) and have often proven to be problematic for D_e estimation.

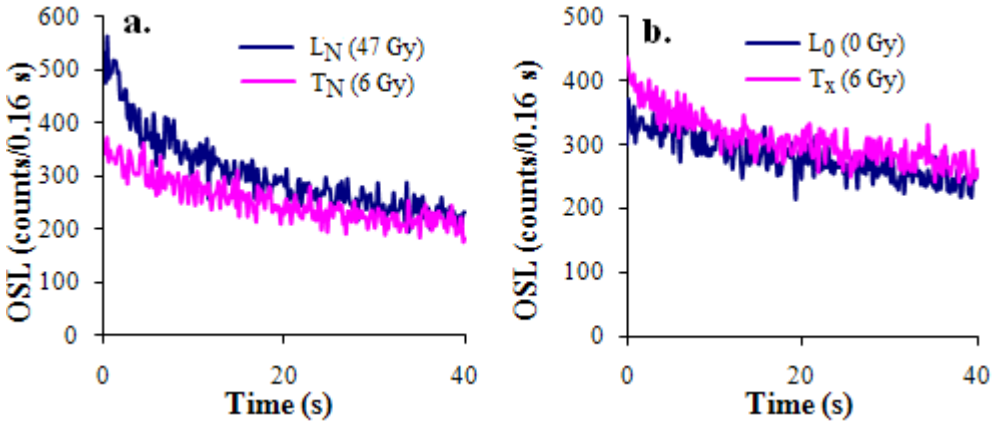

Figure 9.1: OSL decay curves measured for aliquot A. a, Decay curves measured for the surrogate natural (L_N) and the subsequent test dose (T_N). b, Decay curves measured for the 0 Gy regenerative dose (L_0) and its test dose (T_x).

Dose-response curves for both aliquots are presented in Figure 9.2. Poor counting statistics resulted from the very dim OSL signal of quartz from MB1 (Figure 9.1). Both aliquots passed the recycling ratio test, but had relatively high associated uncertainties (0.79 ± 0.15 and 0.89 ± 0.43). One aliquot failed the recuperation test (29

± 7%), while the other produced a recuperation value consistent with 0 (6 ± 10%). The relatively poor performance of these aliquots in the SAR procedure was likely, at least in part, because of the dimness of the sample. The OSL per unit dose produced by the aliquot from Figure 9.2b was approximately one third as bright as that from the aliquot from Figure 9.2a.

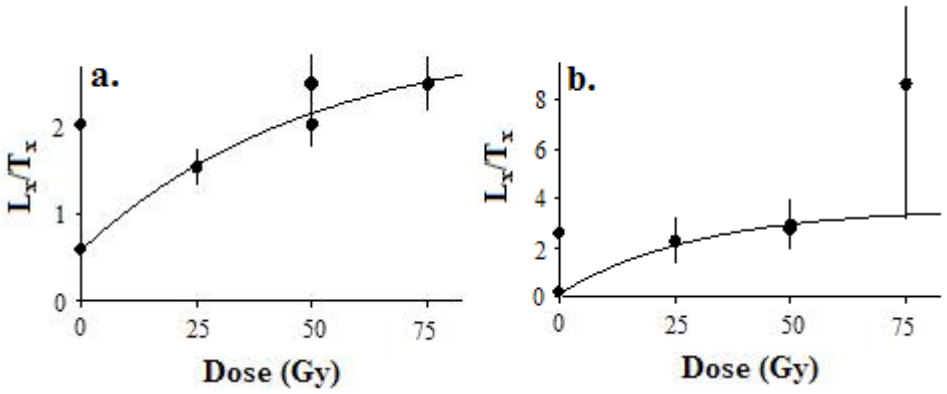

Figure 9.2: Dose-response curves obtained for two aliquots of quartz from MB1. a, Aliquot A. b, Aliquot B.

9.1.2 Assessing the constituent components of quartz from MB1 using LM-OSL

The OSL decay curves measured for quartz samples from MB1 appear to lack a fast component. To assess the components that make up the regenerated OSL signal, LM-OSL curves were measured for the same two aliquots presented in Figure 9.2. The aliquots were given a 120 Gy beta dose and preheated to 260°C for 10 s. LM-OSL curves were then measured and de-convoluted as described in Section 3.5. The sum of squared residuals was used to assess the most appropriate number of components (*N*) needed to fit the data.

The measured LM-OSL curve for one aliquot is presented in Figure 9.3; it is representative of the other aliquot. The data were best fitted using three components, corresponding to S2, S3 and S4 (using the nomenclature of Jain et al., 2003). The *n* (trapped charge concentration), PIC (photoionisation cross-section) and *b* (detrapping probability) values obtained for this fit are presented as an inset in Figure 9.3. No fast component could be identified. Many other studies of volcanic quartz have reported that a fast component was either not present or not dominant in the OSL signal (e.g., Choi et al., 2006b; Tsukamoto et al., 2003, 2007; Westaway, 2009). In many cases,

with the exception of Tsukamoto et al. (2003) and Watanuki et al. (2005), a burial dose cannot be obtained for volcanic quartz using the OSL signal and SAR procedure.

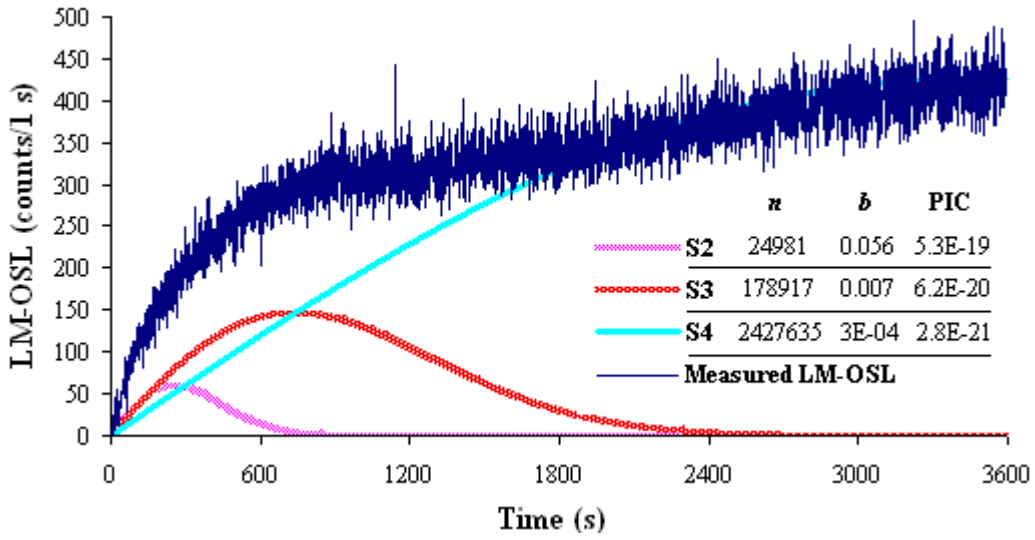

Figure 9.3: Regenerated LM-OSL curve with the fitted components underlying the measured data. The inset table presents the calculated parameters of each fitted component.

9.1.3 Summary of OSL investigations of quartz from Moche Borago

Only a small quantity of quartz could be extracted from a single sample from Moche Borago (MB1). Measurements indicated that the OSL signal from quartz was weakly luminescent and had characteristics that made is unsuitable for burial dose estimation using the SAR procedure. As a result, luminescence investigations of quartz were ceased. The remainder of this chapter will focus on the characteristics of the luminescence signal from K-feldspar separates from Moche Borago, with the aim of finding a signal that could be used for burial dose estimation.

9.2 Problems prior to luminescence investigations of K-feldspars

Before describing the investigations into K-feldspar grains from Moche Borago, several problems that hindered their study will be addressed. These include the contamination of K-feldspar separates with pumice and the small quantities of K-feldspar with weak luminescence emissions obtained from every sample.

9.2.1 Contamination of K-feldspar separates

Following the density separation stage of sample preparation, it was evident that the mineral separates from Moche Borago were contaminated with dark coloured grains, which were presumed to be pumice. Sample MB3 was density separated with sodium polytungstate solution with a specific gravity of 2.62 g/cm^3. The portion of the sample that had a density of <2.62 g/cm^3 was very dark in colour. Density separation at 2.58 g/cm^3 produced little material of >2.58 g/cm^3 (i.e., Na-feldspars). The material with a density of <2.58 g/cm^3 was then etched in HF acid and rinsed in HCl acid and distilled water (as described in section 3.2), second sieved to remove grains with a diameter below 180 μm, and density separated a final time at a specific gravity of 2.53 g/cm^3. Grains with a density between 2.53 and 2.58 g/cm^3 were extracted as K-feldspar separates (Aitken, 1985). An aliquot of ~1000 grains was prepared and visually inspected under the microscope, revealing that only ~15% of the material was crystalline grains K-feldspar (Figure 9.4a). Given the volcanic origin of most of the sediments at Moche Borago (i.e., tuffs, ash falls, etc.), the low-density, dark material is likely to be pumice. However, since density separation is an imperfect method for isolating mineral grains due to the range of densities of particular minerals (Godfrey-Smith and Cada, 1996; Wintle, 1997), it is possible that the Moche Borago K-feldspar separates also contain contaminant Na- and Ca-feldspar grains.

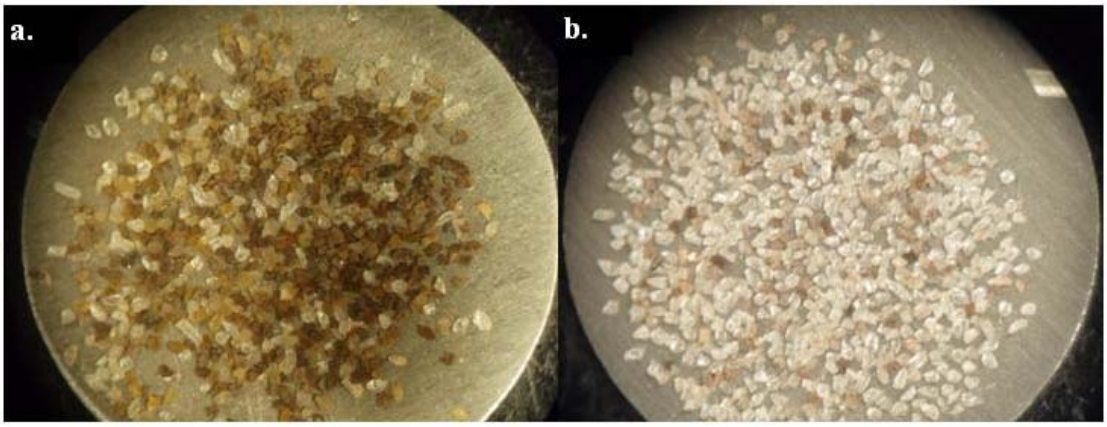

Figure 9.4: Photographs of aliquots of K-feldspar separates from MB3. a, A ~1000-grain aliquot of sample material after density separation (material is between 2.53 and 2.58 g/cm^3), HF acid etching and second sieving. Note the large proportion of dark, non-crystalline contaminant grains (~85% of the grains in this photo). b, A ~1000-grain aliquot of material from the same sample after ultrasonic bath treatment described in the text. Note that the proportion of dark, non-crystalline contaminant grains has decreased markedly (~10% of the grains in this photo).

Given that HF acid etching did not remove the putative pumice grains from the sample, it was unlikely that the grains could be removed with further acid treatment. Instead, the samples were put into beakers filled with distilled water and placed in an ultrasonic bath for ~10 min. After decanting the water, the sample material was dried, and then sieved again at 180 μm, removing a large portion of the contaminant material that had been disaggregated by the ultrasonic bath treatment. A second aliquot of ~1000 grains was prepared and visually inspected under the microscope. While the ultrasonic bath treatment had not removed all of the contaminant grains, ~90% of the grains making up the aliquots were crystalline K-feldspar grains (Figure 9.4b).

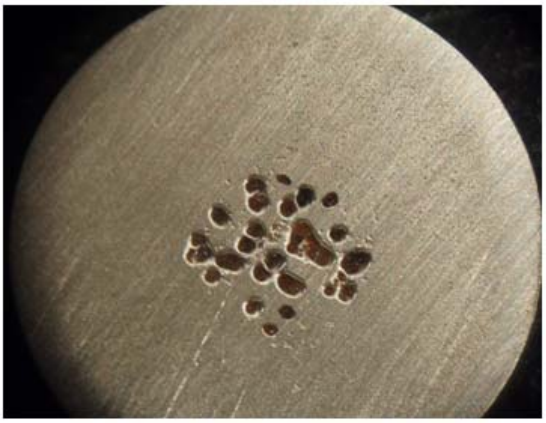

Figure 9.5: Photograph of an aliquot that was prepared to include ~30 grains of the dark, non-crystalline contaminant material.

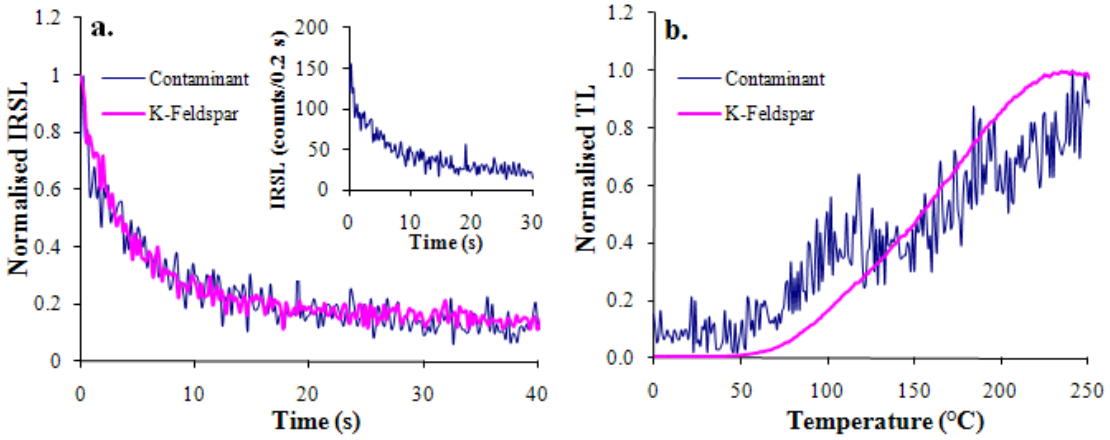

Figure 9.6: Luminescence measured from an aliquot consisting of contaminant grains compared to luminescence measured from an aliquot consisting of K-feldspar grains from the same sample (MB3). a, IRSL curves. b, TL curves. The inset to (a) is the first 30 s of IRSL from the aliquot containing contaminant grains.

To investigate the luminescence properties of the contaminant material, an aliquot consisting of ~30 grains of the contaminant material was prepared (Figure 9.5). This aliquot was given a laboratory irradiation of 235 Gy, preheated to 260°C for 10 s, and stimulated with the IR diodes for 100 s at 50°C. The resulting IRSL decay curve is presented as an inset to Figure 9.6a. While the IRSL signal is dim (~160 counts/0.2 s at its peak), it is present. The IRSL and TL curves were normalised to their brightest interval (counts/0.2 s and counts/°C, respectively) and compared to normalised IRSL and TL curves from an aliquot of K-feldspar grains from MB3. The IRSL decay curves are nearly identical in shape (Figure 9.6a). While the TL curve of the contaminant grains has a hint of a 110°C TL peak, it is similar in shape to the TL curve from K-feldspar grains; they both peak at ~240°C (Figure 9.6b). The similarity in the IRSL and TL signals produced by the contaminant and K-feldspar grains suggests that they likely contain K-feldspar and/or behave in a similar way to K-feldspar. Consequently, contamination of the K-feldspar separates was not considered problematic, although large portions of pumice on an aliquot will have a diluting effect. Care was, thus, taken to make all aliquots of K-feldspar as pristine as possible.

9.2.2 Small quantities of weakly luminescent material

Only small amounts of K-feldspars were present in each of the samples, with MB3 producing the most. All measurements to characterise the luminescence signal of K-feldspars from Moche Borago were, therefore, performed on extracts from MB3.

The problems associated with the relative dearth of quartz and K-feldspar were exacerbated by the weak luminescence signal from K-feldspar separates of MB3. This necessitated the use of large aliquots, each comprised of ~1000 grains, and large test doses (of between 30 and 60 Gy). Owing to the paucity of material, many experiments performed on K-feldspar separates and presented in this chapter required the re-use of aliquots that had previously been used for other experiments. All aliquots that were re-used were given a heat treatment of 500°C prior to experimentation to empty all deep traps that may still contain charge, such as those associated with the IRSL signal and corresponding to the 430°C TL peak (see Chapter 7). It is noted in the descriptions of each experiment throughout this chapter whether the luminescence signals measured

from the aliquots being used were natural, bleached, or annealed prior to experimentation.

9.3 Characterising various TL and IRSL emissions of K-feldspar from Moche Borago

9.3.1 Comparison of TL signals

As discussed in Chapter 7, there are four major emissions from feldspars that have been discussed in the literature: UV, blue, yellow and red/far-red (Duller, 1997; Fattahi and Stokes, 2003a,c). The filter combinations used to investigate various emissions from K-feldspar separates from Moche Borago are presented in Table 7.1. The red and far-red emissions were not measured for feldspars in this study.

To investigate the various emissions from K-feldspar separates for samples from Moche Borago, two aliquots of ~1000 grains of MB3 were prepared and heated to 500°C. The aliquots were then given a laboratory beta dose of 120 Gy, preheated to 260°C for 60 s, and stimulated with IR at 50°C for 100 s. The filters were then changed and the procedure was repeated for both aliquots, beginning with the 500°C heat treatment. The filter combinations were alternated in the same order as in the experiment presented in Section 7.2.2; the standard blue filter combination, yellow, the second blue filter combination, UV, and then the standard blue filter combination again. The first filter combination was repeated at the end of this sequence to ensure reproducibility (using the IRSL signal) and produce a TL glow curve that could be compared with the others. As in the experiment described in Section 7.2.2, the first cycle (heat treatment, irradiation, preheat and IR stimulation) was measured through the standard blue filter combination (BG39 + Kopp 7-59). For analysis purposes, this first cycle was treated as an 'annealing cycle', and the TL and IRSL emissions from the final cycle (measured using the standard blue filter combination again) were compared with the other emissions. In this way, the shape and intensity of IRSL decay and TL glow curves could be compared for different emissions from the same aliquot.

The TL curves are presented in Figure 9.7. There is one main peak at ~340°C for all emissions, which occur consistently in the same position regardless of the emission measured. The TL curves measured through the two different blue filter combinations are almost identical, with that measured through the standard blue filter

combination being slightly brighter. The shape of the UV emission TL curve is similar to the blue emission TL curves, but the former is an order of magnitude weaker. The yellow emission TL curve also has a peak at ~340°C, but it is even weaker than the UV emission. The yellow emission TL curve, however, differs markedly from the other three emissions in the low and high temperature regions of the glow curve. In the low-temperature region, the yellow emission glow curve shows an elevated, but stable signal compared to the other three curves, and only starts to increase at ~270°C. In the high-temperature region, the yellow TL emission shows a significant increases from ~380°C to >500°C. This is in contrast to the blue and UV emission TL curves, which remain at instrumental background until ~150°C, followed by a substantial increase at ~260°C, peaking at 340°C, then decrease after the peak through 500°C.

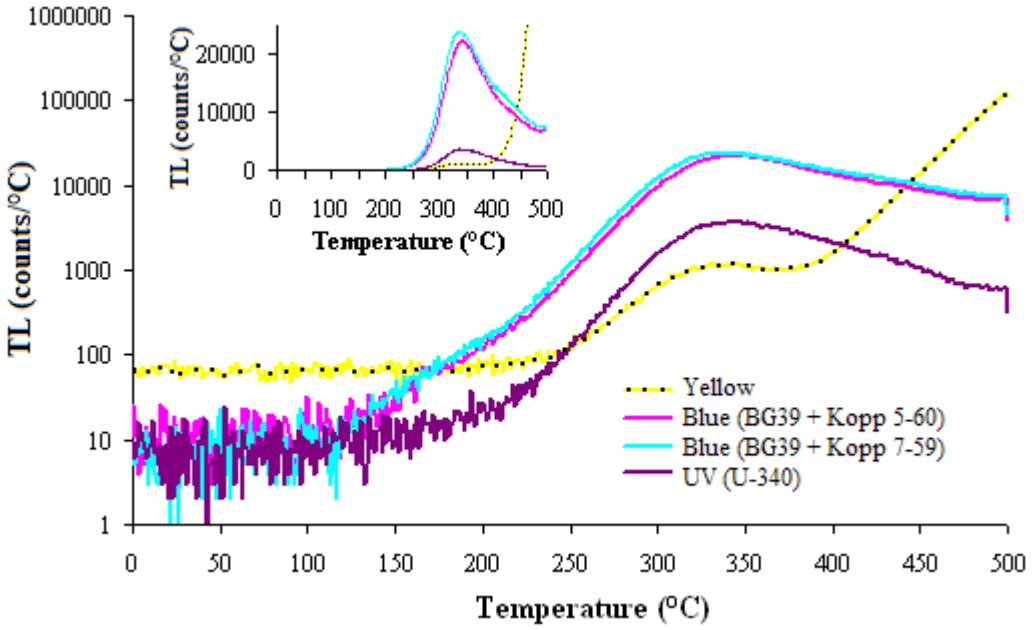

Figure 9.7: TL glow curves measured using various filter combinations (see Table 7.1) from one aliquot of MB3. Results are representative. Note that data in the main plot is plotted on a log-linear y-axis. The inset shows the same data plotted on a linear y-axis.

The difference in the yellow emission TL curve shape from MB3 is similar to that observed for K-feldspar grains of MR9 from Mumba rockshelter (Figure 7.2). Both samples show the large increase in yellow emission TL above ~380°C, but the elevated TL counts from 0 to 250°C observed for MB3 is not present in MR9. This suggests that the elevated count level in the low-temperature region of the yellow emission TL curve from MB3 is unlikely to have an instrumental cause, such as increased background due

to the specific filters. If this were the case, then the yellow emission TL curve from MR9 should presumably also show the same behaviour, since it was measured on the same instrument using the same filter combination. The yellow emission TL curve from MB3 also differs from MR9 in that there is no discernable peak at ~150°C. Differences in TL peak composition between the two samples are explored further in Section 9.4.

These results suggest that the TL peak at ~340°C is present regardless of the emission measured. Furthermore, the only difference between the two blue emissions and the UV emission is the brightness of the glow curve. The yellow emission TL curve, while having a TL peak at ~340°C, is markedly different in the high- and low-temperature regions.

9.3.2 Comparison of IRSL signals

Decay curves measured for the various emissions are presented in Figure 9.8. The IRSL signal intensity is calculated for each decay curve in the standard manner (i.e., the count rate over the final 10.2 s of the IRSL decay curve is used to calculate the background [see Section 3.3.1.1], which is then subtracted from the initial signal, which is calculated using the sum of the first 2 s of IRSL). The decay curves measured using the two blue filter combinations are similar in shape and intensity (both have background-subtracted IRSL signals of ~29,000 counts). The decay curve measured for the UV emission also has a similar shape to those measured using the blue emissions, but it is approximately an order-of-magnitude less bright (background-subtracted IRSL signal of ~1,300 counts). Results for these three filter combinations are similar to those for K-feldspar separates from MR9 (Figure 7.3). The yellow emission IRSL from MB3 does not decay, instead showing a slight increase throughout the 100 s of IR stimulation. This is in contrast to MR9, which had a yellow emission IRSL signal that decayed over the first ~10 s of IR stimulation, before subsequently increasing. From ~20 s into IR stimulation, the IRSL decay curves for both MB3 and MR9 are very similar in shape and intensity.

All IRSL signals from MB3 (except the later portion of the yellow emission IRSL) are significantly dimmer than those from MR9. For example, the blue emission IRSL signal for MB3 is nearly two orders of magnitude dimmer than that from MR9).

These results, like those from Section 7.2.2, suggest that the blue emission is the optimal emission with which to measure luminescence from K-feldspars at Moche Borago. The standard blue filter combination (BG39 + Kopp 7-59) was, therefore, chosen for all subsequent investigations of the IRSL and TL signals of K-feldspar separates from Moche Borago. This emission produced the brightest luminescence and the results can be easily compared with those from Mumba and with other studies that have commonly used this filter combination (e.g., Wallinga et al., 2000a,b; Auclair et al., 2003; Thomsen et al., 2008).

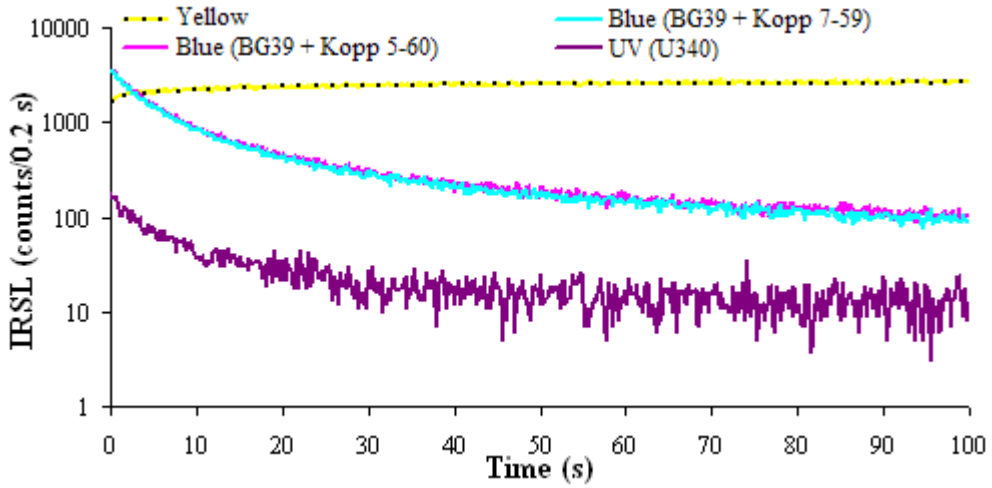

Figure 9.8: IRSL decay curves for various emissions from one aliquot of MB3. Results are representative of both aliquots measured. Note the log-linear scale on the y-axis.

9.4 Characterising K-feldspars from Moche Borago: TL and IRSL

9.4.1 TL from K-feldspar separates

While no TL peaks have been shown to be ubiquitously present in all K-feldspars, several common peaks that have been reported in the literature were identified during TL investigations of K-feldspar separates from Mumba. These peaks include a large, low temperature peak at ~150°C that is present only in laboratory-irradiated samples, a peak at ~350°C and a peak at ~430°C (Chapter 7; Duller, 1997; Murray et al., 2009). Investigations into the luminescence properties of K-feldspars from Mumba suggested that the TL peak at ~430°C was associated with the source trap for IRSL (Chapter 7), in agreement with the conclusions of Murray et al. (2009). Due

to the range of TL properties exhibited by various feldspars reported in the literature, the TL properties of one of Moche Borago samples (MB3) were characterised.

Three aliquots of ~1000 grains of K-feldspar from MB3 were each given a different laboratory dose of 0, 60 or 240 Gy, in addition to the natural dose, and heated to 500°C at a rate of 5°C/s while the TL was measured. A blank stainless steel disc was also heated to 500°C at a rate of 5°C/s, and the resulting photon count was subtracted, point-by-point, from each of the measured TL curves. Results are presented in Figure 9.9. The TL curves are different from those measured for MR9, for which three main TL peaks (i.e., at ~150°C, ~350°C and ~430°C) could be identified (Figure 7.4). The TL curves measured from aliquots of MB3 are also an order of magnitude dimmer than those from MR9. The natural TL curve of MB3 has two broad TL peaks: one centred at ~310°C and the other at ~480°C. The TL signal remains at instrumental background until ~150°C. The aliquots that were given a laboratory beta dose exhibit one broad TL peak that begins to increase in intensity substantially by ~50°C, attain a maximum intensity at ~230°C and decrease in intensity by ~400°C. It also appears that the ~480°C TL peak observed in the natural TL signal is present in the laboratory-irradiated TL signals, in the form of a shoulder on the main TL peak.

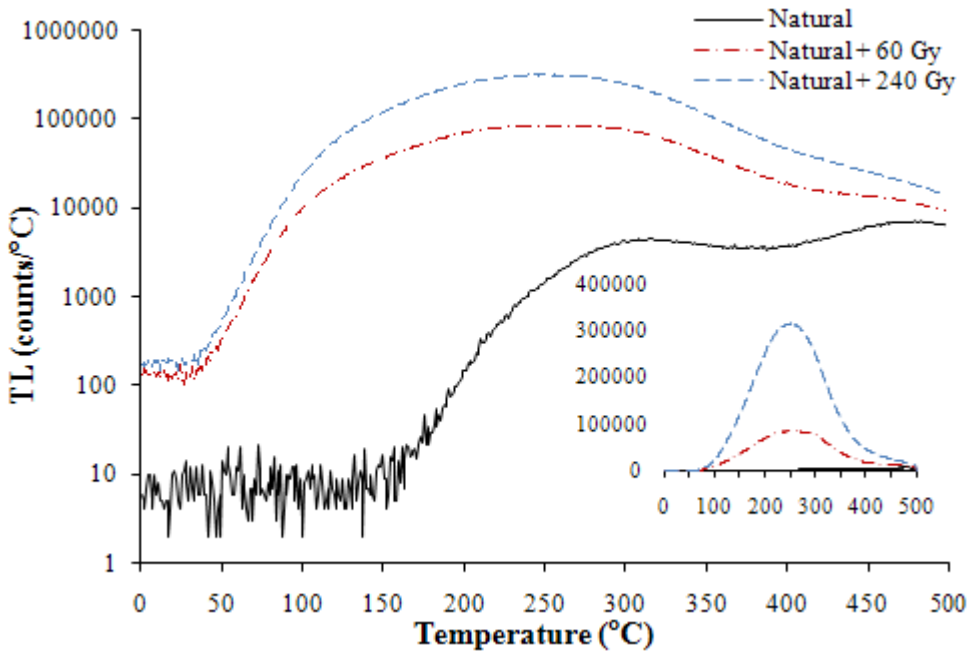

Figure 9.9: TL glow curves plotted on a linear-logarithmic scale for three natural aliquots of MB3. Each aliquot was given a different additive dose, followed by a TL measurement from 0 to 500°C. Note that the inset plot shows the same data as the main figure, but with the y-axis on a linear scale.

There are two possible explanations for the width of the main peak produced by the aliquots that received an additive laboratory dose. First, the peak may represent a single, very broad TL peak centred at ~230°C. Alternatively, the peak may be composed of several peaks that amalgamate to form a single, broad peak. The latter possibility is more likely, given the shape of the natural TL curve. In the TL signals of the laboratory-irradiated aliquots, the two TL peaks identified in the natural are likely to be present, but are obscured by a large, thermally unstable TL component arising from the laboratory irradiation.

Results from this experiment suggest that a preheat of 260°C would be appropriate when comparing natural and laboratory radiation doses. This is because the TL signal of the natural does not increase above background until the sample is heated to a temperature of ~150°C, meaning that any TL produced at or below this temperature, such as that observed for laboratory-irradiated aliquots, is likely to be associated with traps that are thermally unstable over geological timescales. Several studies have concluded that the low-temperature TL component does not contribute to the IRSL signal (e.g., Bøtter-Jensen et al., 1991; Duller and Bøtter-Jensen, 1993; Murray et al., 2009). However, to ensure that the laboratory signal is as similar to the natural as possible, the removal of the low-temperature, thermally unstable TL components prior to IR stimulation, by applying a high-temperature preheat, was considered desirable. Consequently, a preheat of 260°C for 60 s was used throughout the investigations of K-feldspars from Moche Borago.

9.4.2 Dependence of IRSL on preheat temperature: Pulsed anneal experiments

To assess the dependence of IRSL from MB3 on temperature, several pulsed anneal experiments were performed. These are generally conducted measuring either the natural signal or the signal from a laboratory-dosed aliquot that is stimulated with a short, low-intensity pulse of IR (e.g., 0.1 s at 1% power), so that the IRSL signal is not significantly depleted (e.g., Duller, 1994; Murray et al., 2009). The aliquot is then preheated to the lowest temperature desired before another IR pulse is given. This sequence is repeated, increasing the preheat temperature in small (e.g., 10°C) increments until the IRSL signal is completely depleted (e.g., Duller, 1994; Murray et al., 2009). A short-shine pulsed anneal was performed on the natural signal from three

~1000-grain aliquots. Each aliquot was heated to a specified temperature, where it was held for 0 s (i.e., cutheat) and the IRSL produced by a low-intensity pulse of IR stimulation (0.1 s at 1% power) was then measured. The cutheat temperature was increased in 10°C increments from 100°C to 450°C. Unfortunately, however, the IRSL produced by the natural signal from MB3 was too dim for this short-shine technique to provide meaningful results. For all three aliquots, no patterns could be discerned from the results (inset to Figure 9.10). As a result, an alternative approach was used, similar to that described by Demuro (2009).

A step-by-step outline of the pulsed anneal experiment is presented in Table 9.1. An aliquot of ~1000 grains of K-feldspar from MB3 was annealed using repeated heat treatments (heating the sample to 500°C) and IR stimulations. The aliquot was then given a laboratory dose of 120 Gy, preheated at the specified temperature for 60 s, and stimulated using the IR diodes for 100 s at 50°C (L_x). This was followed by a test dose cycle that consisted of a 30 Gy dose, a preheat of 180°C for 60 s, and an IRSL measurement (100 s at 50°C: T_x). This process was then repeated 31 times, increasing the specified preheat temperature in 10°C increments, beginning at 100°C and ending at 400°C. The test dose preheat was kept constant at 180°C.

Table 9.1: Step-by-step outline of the pulsed anneal experiment described in this section, the results of which are presented in Figure 9.10.

Step	Laboratory treatment	Name
1	120 Gy dose	
2	Preheat at specified temperature for 60 s	
3	IR stimulation for 100 s at 50 °C	L_x
4	30 Gy dose	
5	Preheat at 180°C for 60 s	
6	IR stimulation for 100 s at 50 °C	T_x
7	Repeat steps 2 to 6*	

*Repeat, increasing the preheat temperature in step 2 in 10°C increments, beginning at 100°C and ending at 400°C

Results are presented in Figure 9.10 and look substantially different from most other pulsed anneal results in the literature (e.g., Figure 9.11). Pulsed anneal curves

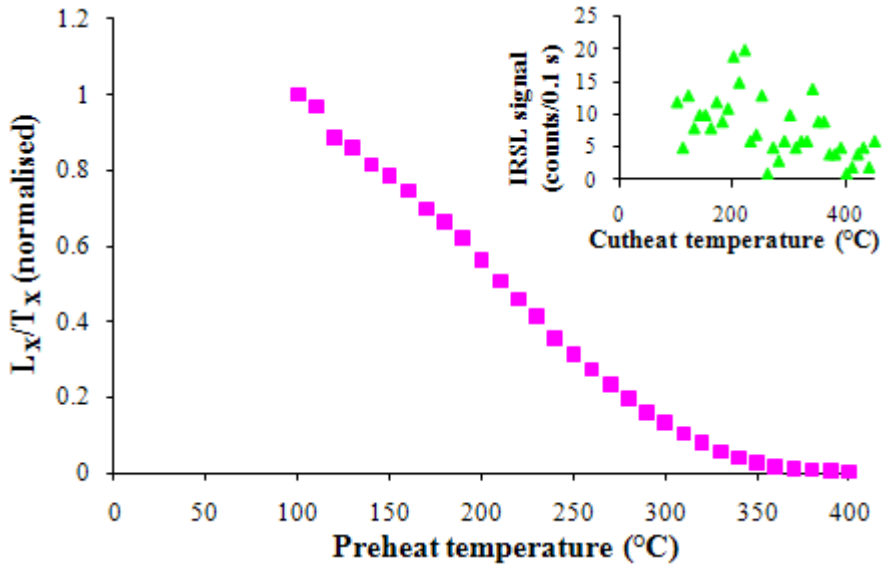

Figure 9.10: Results from a pulsed anneal experiment based on the SAR technique (see text) for a laboratory-irradiated aliquot of MB3. The sensitivity-corrected IRSL signal (L_x/T_x) is shown, and is normalised to the 100°C data point. The inset shows the pulsed anneal data measured using the short-shine technique (as described in the text) applied to a natural aliquot from MB3.

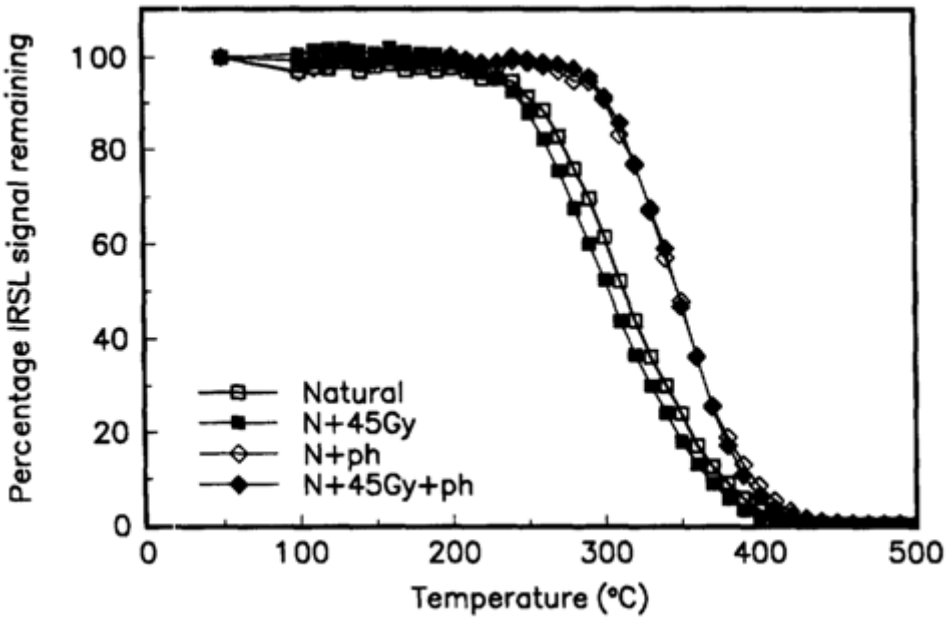

Figure 9.11: Pulsed anneal data from K-feldspar separates from Duller (1994). A short-shine pulsed anneal was performed and the data is plotted as the proportion of the IRSL signal that remains after annealing at the specified temperature. Note that "ph" is a preheat at 220°C for 10 min. Data and Figure are from Duller (1994, 1997).

from K-feldspar generally do not begin to decrease until ~300°C (e.g., Duller, 1994; Murray et al., 2009). In contrast, the sensitivity-corrected IRSL signal (L_x/T_x) begins decreasing from 100°C and continues decreasing throughout. It is reduced to 1% of the initial value (at 100°C) by 380°C. These results are similar to the pulsed anneal results

for K-feldspar separates from sample QGC1 presented in Demuro (2009, Figure 6.8), who performed a pulsed anneal in a similar way.

It is likely that the atypical results from this experiment were due to the atypical experimental design. The duration of the specified preheat (given before the measurement of L_x) may have affected the results of this experiment. It is likely that the preheat duration of 60 s resulted in isothermal decay of the IRSL signal before the IRSL was measured. If these results are meaningful, however, it would suggest that the IRSL resulting from laboratory irradiations of K-feldspar from MB3 originated from a trap associated with a lower temperature TL peak.

A second set of pulsed anneal experiments was performed to improve the reliability of the results. Two natural aliquots, each composed of ~1000 grains, were annealed at 500°C. The aliquots were then given a laboratory dose of 240 Gy, and a short-shine pulsed anneal experiment was performed. The aliquots were heated at a specified cutheat temperature (for 0 s) before the luminescence produced by a short IR pulse (1% power for 0.1 s) was measured. The cutheat temperature was increased in 10°C increments from 100°C to 450°C. Results are presented in Figure 9.12. The laboratory-irradiated aliquot produced a substantially brighter short-shine IRSL signal than did the natural aliquot (i.e., inset to Figure 9.10), although the signal was still relatively dim. Apart from the large initial decrease (~43%) from 100°C to 110°C, the largest decrease in IRSL signal occurred between 200°C and 300°C. During this interval, the IRSL signal decreased from ~70% to ~15% of the signal measured at 110°C, in agreement with the results presented in Figure 9.10. Note that in Figure 9.12, the short-shine IRSL signal is normalised to 110°C, instead of 100°C, due to the large decrease in signal between 100°C and 110°C.

The same aliquots were then heated at 500°C again, and a second pulsed anneal experiment, based on the SAR procedure, was performed. A step-by-step outline of this experiment is presented in Table 9.2. In this experiment, the aliquots were given a laboratory dose of 60 Gy. They were then heated to a specified cutheat temperature and then stimulated with the IR diodes for 100 s at 50°C (L_x). This was followed by a test dose cycle consisting of a 60 Gy irradiation, a cutheat of 100°C, and an IR stimulation for 100 s at 50°C (T_x). This process was repeated for specified cutheat temperatures between 100°C and 450°C. The test dose cutheat was kept constant at 100°C. Several

features of this pulsed anneal experiment (Table 9.2) make it more sound than the one described at the beginning of this section (Table 9.1). First, in this experiment the specified cutheats are held for 0 s instead of specified preheats for 60 s. As a result, the IRSL signal should not isothermally decay in this experiment. Second, the test dose used in this experiment is larger (60 Gy, compared to 30 Gy), resulting in a brighter IRSL signal with improved counting statistics for the sensitivity correction.

Table 9.2: Step-by-step procedure of the pulsed-anneal experiment described in this section, the results of which are presented in Figure 9.12.

Step	Laboratory treatment	Name
1	60 Gy dose	
2	Cutheat at specified temperature	
3	IR stimulation for 100 s at 50 °C	L_x
4	60 Gy dose	
5	Cutheat at 100°C	
6	IR stimulation for 100 s at 50 °C	T_x
7	Repeat steps 2 to 6*	

*Repeat, increasing the cutheat temperature in step 2 in 10°C increments, beginning at 100°C and ending at 450°C

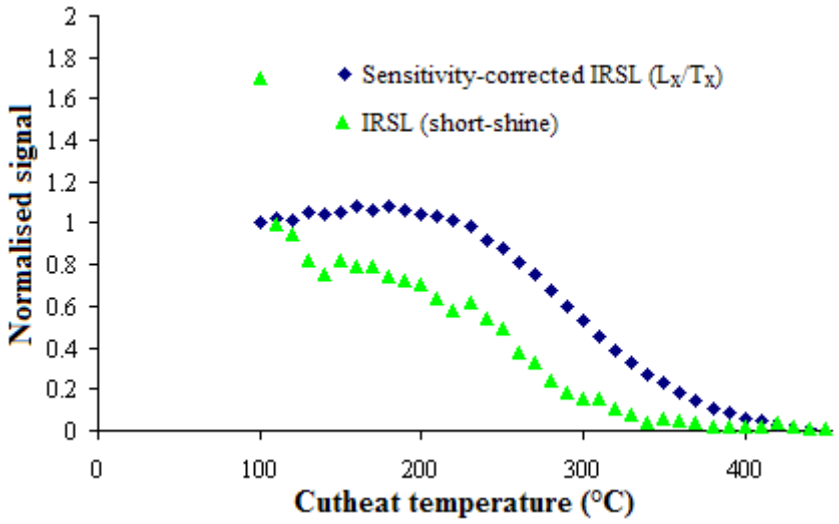

Figure 9.12: Results from the second set of pulsed anneal experiments. These results are from a laboratory-irradiated aliquot of MB3 and are representative of both aliquots measured. The triangles show results for pulsed anneal experiment using the short-shine technique (see text) on grains given a 240 Gy laboratory dose. The data points for this technique are normalised to the value at 110°C. The diamonds represent results from a second pulsed anneal experiment based on the SAR technique (see text). The data points for this technique are normalised to the value at 100°C.

Results are presented in Figure 9.12 and are in closer agreement with other pulsed anneal results in the literature (e.g., Duller, 1994; Murray et al., 2009; Figure 9.11). For the sensitivity-corrected IRSL signal (i.e., L_x/T_x), the signal does not begin decreasing until 220°C. The signal is reduced to 50% at 300°C, ~15% by 360°C and ~5% by 400°C. This suggests that the IRSL signal is not wholly associated with a low-temperature TL peak (i.e., at ~250°C), as was suggested by the results presented in Figure 9.10, but may originate from traps associated with TL peaks in the range of ~220°C to 410°C.

9.4.2.1 Summary of pulsed anneal results

Four different pulsed anneal experiments were conducted on K-feldspar separates from Moche Borago and each produced different results. The natural signal proved too dim to allow measurement of a standard short-shine pulsed anneal curve. A laboratory-irradiated signal, while bright enough to produce IRSL in response to a short IR pulse, was still dim. The latter experiments suggested that the largest decrease in IRSL occurred between ~200°C and ~300°C and that the signal was mostly removed by ~350°C. To overcome the problem associated with weak IRSL signal intensities of K-feldspars from MB3, a pulsed anneal technique based on the SAR procedure was used, and a sensitivity-corrected IRSL signal was obtained for different preheat temperatures. Two of these SAR-based pulsed anneal experiments were performed. The first (Figure 9.10) suggested that the IRSL signal was mostly removed by heat treatments between ~180°C and ~300°C. The second, more sound, pulsed anneal experiment (Figure 9.12) showed that the IRSL signal did not begin to be removed until ~220°C, with substantial signal still present at 300°C, and some signal remaining at 400°C. This suggests that the IRSL signal originates from traps associated with TL peaks in the region of 220°C to 410°C. The pulsed anneal experiments could not conclusively identify the dependence of the IRSL signal on preheat or cutheat temperature, although the results presented in Figure 9.12 are considered more valid than those in Figure 9.10, due to the improved design of the experiment.

9.4.3 Relationship between IRSL and TL

Experiments were performed to assess whether an association could be observed between the IRSL and TL signals of K-feldspars from MB3. A step-by-step outline of the experiment is presented in Table 9.3. A ~1000-grain aliquot of MB3 was annealed at 500°C. It was then given a laboratory beta dose of 240 Gy and heated to 500°C at a rate of 5°C/s while the TL was measured to serve as a first control. It was then given another 240 Gy dose, stimulated with the IR diodes (100 s at 50°C) and the TL was measured. The aliquot was then given a third 240 Gy dose, preheated to 260°C for 60 s, and its TL was measured. Finally, the aliquot was given a fourth 240 Gy dose, preheated, stimulated with the IR diodes, and the TL was measured. This experiment allowed the effects of preheating and IR stimulation on the TL curve to be assessed for a laboratory-irradiated sample.

Table 9.3: Step-by-step outline of the experiment described in this section.

Step	Laboratory treatment	Name
1	240 Gy dose	
2	Measure TL to 500°C	Dose
3	240 Gy dose	
4	IR stimulation for 100 s at 50 °C	
5	Measure TL to 500°C	Dose + IR
6	240 Gy dose	
7	Preheat at 260°C for 60 s	
8	Measure TL to 500°C	Dose + PH
9	240 Gy dose	
10	Preheat at 260°C for 60 s	
11	IR stimulation for 100 s at 50 °C	
12	Measure TL to 500°C	Dose + PH + IR

TL curves are presented in Figure 9.13a. Both TL curves that were not preceded by a preheat (i.e., 'Dose' and 'Dose + IR') overlap each other for temperatures above 150°C, suggesting that IR stimulation has little effect on the high-temperature region of the TL curve. The same is true for the two TL curves that were preceded by a preheat (i.e., 'Dose + PH' and 'Dose + PH + IR'). The only differences are in the lower temperature region of the TL curves. For the TL curve preceded by a preheat and IR stimulation, there is a very small low temperature peak (~150°C) not present in the TL

curve that was preceded only by a preheat. This small peak is most likely the result of phototransfer of charge into low-temperature TL peaks, which had been emptied by the 260°C preheat, following IR stimulation.

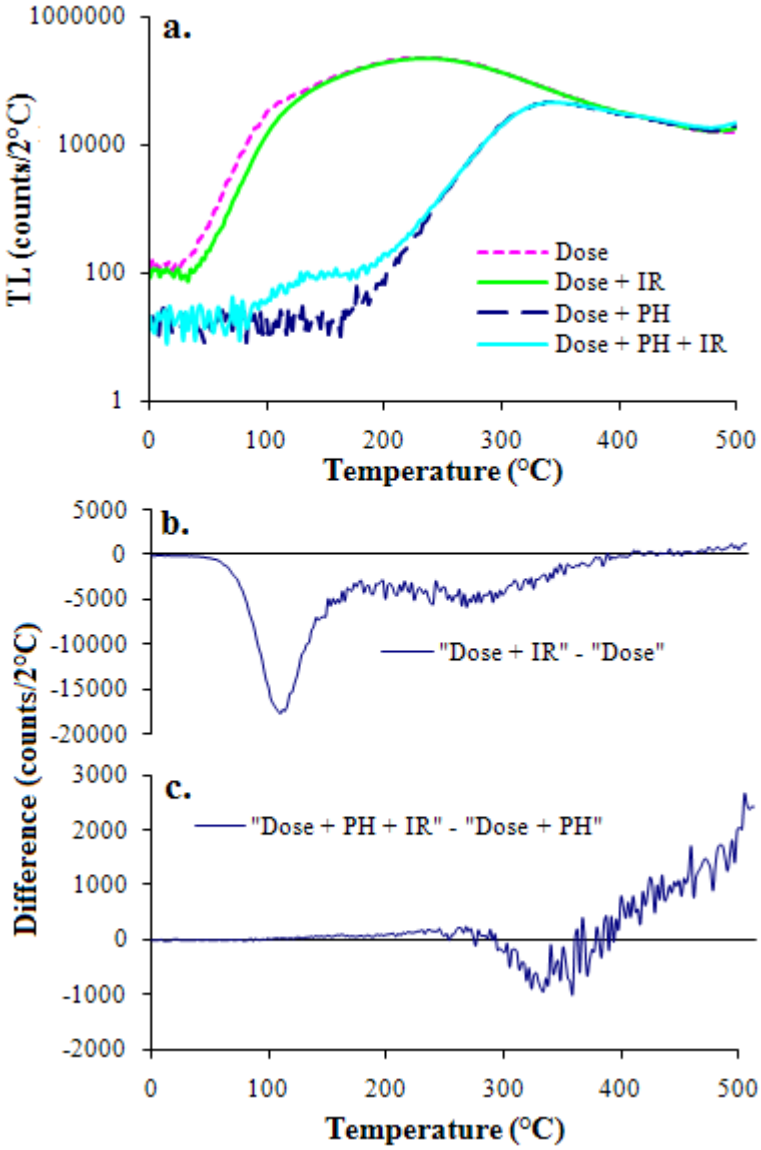

Figure 9.13: a, TL curves for the same aliquot following various laboratory treatments. b, The TL curve following irradiation was subtracted from the TL curve following irradiation and IR stimulation, showing the effect of IR stimulation on the TL curve. c, The TL curve following an irradiation and a preheat was subtracted from the TL curve following an irradiation, preheat, and IR stimulation. Note the log-linear scale on the y-axis of (a) and the linear scale on the y-axis of (b) and (c).

To elucidate the temperature interval over which the TL signal changed following IR stimulation, the TL curves were subtracted from one another. When the TL curve following only an irradiation is subtracted from the TL curve following an

irradiation and IR stimulation, the signal loss due to IR stimulation is greatest in the low temperature region (≤150°C; Figure 9.13b). There is then a region of smaller signal loss that begins to decrease from ~290°C and has disappeared by 370°C. After a brief temperature region where there is no loss of signal due to IR stimulation, the TL curve following IR stimulation becomes larger than its control for temperatures over ~450°C. This same feature is present when the two TL curves measured after irradiation and preheating are examined (Figure 9.13c). A small amount of phototransfer is observed from 100°C to 280°C, followed by a region of TL signal loss (280°C to 370°C) due to IR stimulation, with the greatest loss occurring at ~320°C. Above 380°C, the TL signal measured after IR stimulation is larger than that of the control.

These results are different to those from a similar experiment performed on K-feldspars from Mumba (Section 7.3.2). For MR9, the TL peaks at 350°C and 430°C decreased following IR stimulation, with the decrease for the latter peak being ~3 times greater than the decrease of the former (Figure 7.5). This, along with results from several other experiments (see Chapter 7), was taken to suggest that the 430°C TL peak was associated with the source trap for the IRSL signal in K-feldspar separates from Mumba. As was shown in Section 9.4.1, the discrete TL peaks observed for MR9 are not apparent in MB3. Results from the experiments reported in this section show that a decrease in TL signal following IR stimulation of grains of MB3 occurs from the low-temperature region of the TL curve (~180°C) up to ~370°C (Figure 9.13b, c). These results suggest that IRSL from K-feldspar separates from MB3, when compared to MR9, may be associated with a lower temperature region of the TL glow curve (i.e., below 370°C). The increase in TL signal intensity above ~450°C following IR stimulation is also atypical. The reason for this increase of signal in the high-temperature TL region following IR stimulation is not presently known.

9.5 Characterising the IRSL signal of K-feldspars from Moche Borago

In K-feldspars, the temperature at which IR stimulation is performed has an effect on the resultant luminescence signal intensity and rate of IRSL decay as a function of stimulation time (Duller, 1997). During investigations of K-feldspar from Mumba, the IRSL signal intensity was shown to increase with stimulation temperature up to 300°C (Section 7.4.2). This was in agreement with many other studies that have

reported that the IRSL signal intensity increases with increased stimulation temperatures (e.g., Duller and Wintle, 1991; McKeever et al., 1997; Poolton et al., 2002b; Thomsen et al., 2008). Results from Mumba also showed that the shape of IRSL decay curves changed with stimulation temperature, in accordance with the results reported by Duller and Wintle (1991) and McKeever et al. (1997). When the isothermal TL produced by the elevated stimulation temperatures was taken into account (Figure 7.11) and subtracted (Figure 7.12), the rate of decay of the IRSL signal was shown to increase with increased stimulation temperatures up to 400°C. In addition, it was shown that as the IR stimulation temperature was increased up to at least 225°C, the fading rate of the resulting IRSL signal decreased.

Given the relatively dim luminescence signals of K-feldspars from MB3, an increased IRSL yield from an elevated-temperature IR stimulation would be beneficial for IRSL investigations. Before elevated-temperature IR stimulations could be used for dose estimation or fading measurement, however, the dependence of the measured IRSL signal, the isothermal TL signal, and the isothermal TL-subtracted IRSL signal on stimulation temperature was assessed

9.5.1 IRSL dependence on stimulation temperature

9.5.1.1 Characterising the dependence of the measured IRSL signal on stimulation temperature

Two ~1000-grain aliquots of MB3 were annealed at 500°C. They were then given a laboratory beta dose of 120 Gy, preheated to 260°C for 60 s, and stimulated using the IR diodes for 100 s at a specified temperature. This procedure was performed for IR stimulation temperatures of 50°C, 100°C, 150°C, 200°C, 225°C, 250°C, 300°C, 350°C, 400°C, 450°C and 500°C. The intensity of the IRSL signal, calculated as the sum of the counts in the initial 2 s minus a background derived from the counts in the final 10.2 s of IR stimulation, is presented in Figure 9.14. The IRSL signal intensity increases steadily from 50°C to 250°C. There is then a large increase in sensitivity at 300°C and, again, at 350°C. The signal then starts to decrease from 400°C to 500°C. The increase in IRSL intensity up to a stimulation temperature of 250°C agrees with the results for Mumba described in Section 7.4 and also with other studies (e.g., Bailiff and Poolton, 1989; Duller and Wintle, 1991; McKeever et al., 1997; Thomsen et al., 2008).

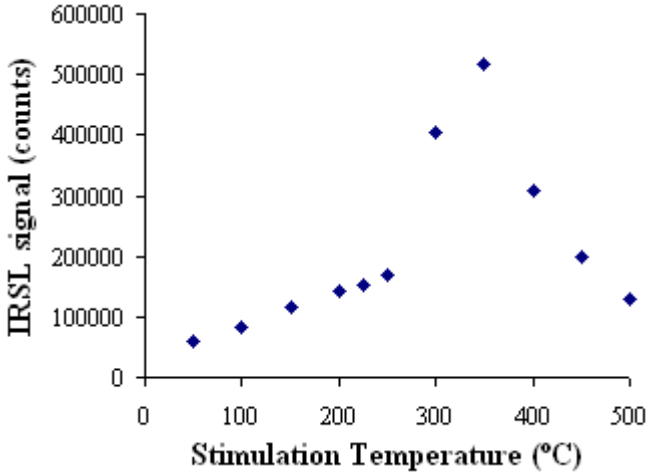

Figure 9.14: IRSL signal (calculated as the background-subtracted sum of the first 2 s of measured IRSL) plotted as a function of stimulation temperature.

The IRSL signals were normalised to the first 0.2 s of stimulation time (i.e., the first data channel) to assess how the shape of the decay curve changed as a function of increased stimulation temperature (Figure 9.15a, c). The normalised decay curves for each stimulation temperature were then divided by the normalised decay curve for IR stimulation at 50°C. This data is plotted in Figure 9.15 (b and d) for the first 20 s of stimulation time to show how the IRSL decay curves differ in shape, relative to IRSL at 50°C, over the early period of stimulation. The shapes of the IRSL decay curves are similar for stimulation temperatures between 50°C and 200°C. They then change at 225°C and 250°C. The rate of decay increases slightly from 50°C to 225°C, before decreasing at 250°C (Figure 9.15b). The rate of decay then increases again at 300°C and 350°C (which has a similar decay curve shape to IR stimulation at 50°C) before decreasing slightly at 400°C. The decay curves for IR stimulation at 450°C (which has a similar shape to IRSL at 250°C) and 500°C then change shape and rate of decay substantially.

These patterns of changes in decay curve shape as a function of IR stimulation temperature are similar, but not identical, to those observed for K-feldspars from Mumba. At Mumba, the changes were inferred to be the result of a substantial isothermal TL signal underlying the IRSL signal at stimulation temperatures above 250°C. When this unwanted isothermal TL signal was characterised and removed, the true response of IRSL to stimulation temperature could be assessed.

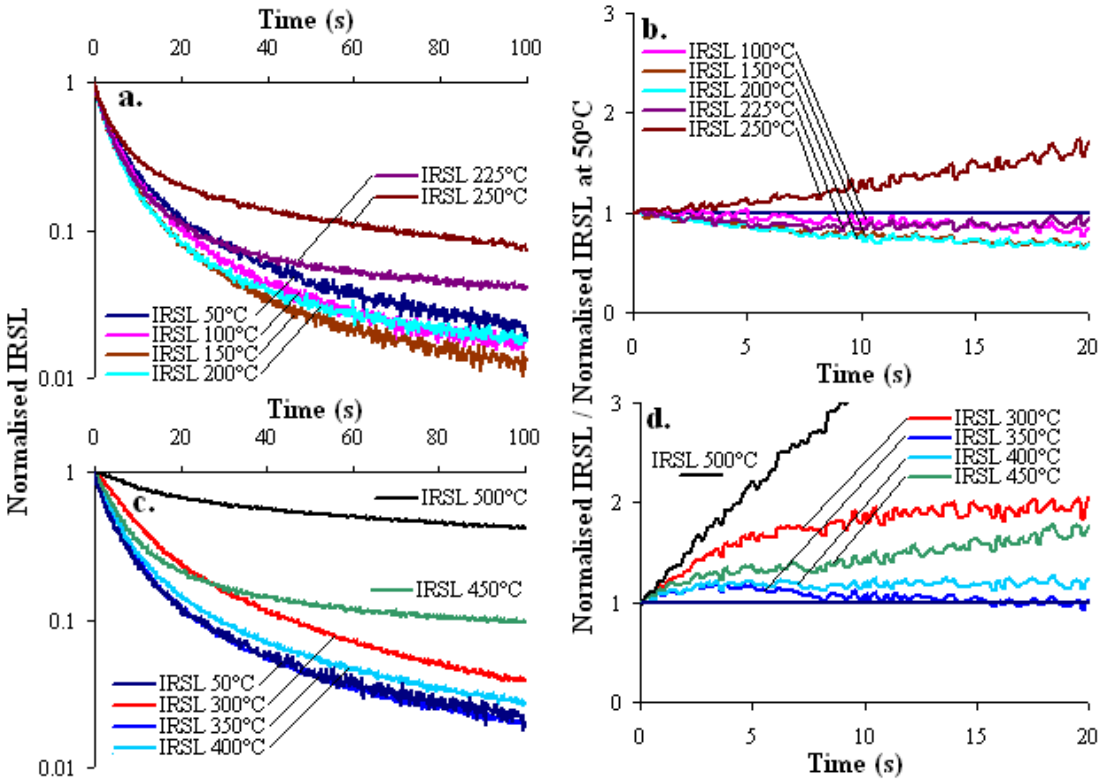

Figure 9.15: a and c, Normalised IRSL decay curves for various stimulation temperatures. The normalised curves are shown in the two graphs to show the difference in decay curve shape for stimulation temperatures of 50-250°C (a) and from 300-550°C (c). IRSL at 50°C is also shown in (c) for comparison. The normalised decay curves (from a and c) were divided by the normalised decay curve for IRSL at 50°C (b and d, respectively) to plot the decay rate at various elevated temperatures relative to the IRSL at 50°C over the first 20 s of IR stimulation. Note that in (d), the IRSL signal measured at 500°C continues to increase to a ratio of 5.7 by 20 s of IR stimulation.

9.5.1.2 Characterising the isothermal TL signal

To characterise the isothermal TL signal for MB3, a second experiment was performed using the same two aliquots from the experiment described in the previous section (Section 9.5.1.1). The aliquots were annealed at 500°C, given a laboratory beta dose of 120 Gy, preheated to 260°C for 60 s, then brought to an elevated temperature and held there while the isothermal TL was recorded for 100 s. This procedure was repeated, and the isothermal TL recorded for elevated temperatures of 50°C, 100°C, 150°C, 200°C, 225°C, 250°C, 300°C, 350°C, 400°C, 450°C and 500°C. Results are presented in Figure 9.16, and are similar to the results of an analogous experiment performed on samples from Mumba (Figure 7.11). The background-subtracted isothermal TL signal intensity (Figure 9.16b) was calculated in the same way as the IRSL signal intensity. The isothermal TL signal is negligible up to a temperature of 200°C, after which it increases slightly at 225°C and 250°C. There is then a substantial

increase in the isothermal TL signal at 300°C, and again at 350°C. From 400°C to 500°C, the isothermal TL signal decreases, although a sizeable signal is still measured. The stimulation temperature of 350°C resulted in the brightest measured IRSL and isothermal TL signal from MB3. The isothermal TL signal intensity for temperatures below 250°C is likely small because the 260°C preheat emptied most of the traps associated with TL at these temperatures.

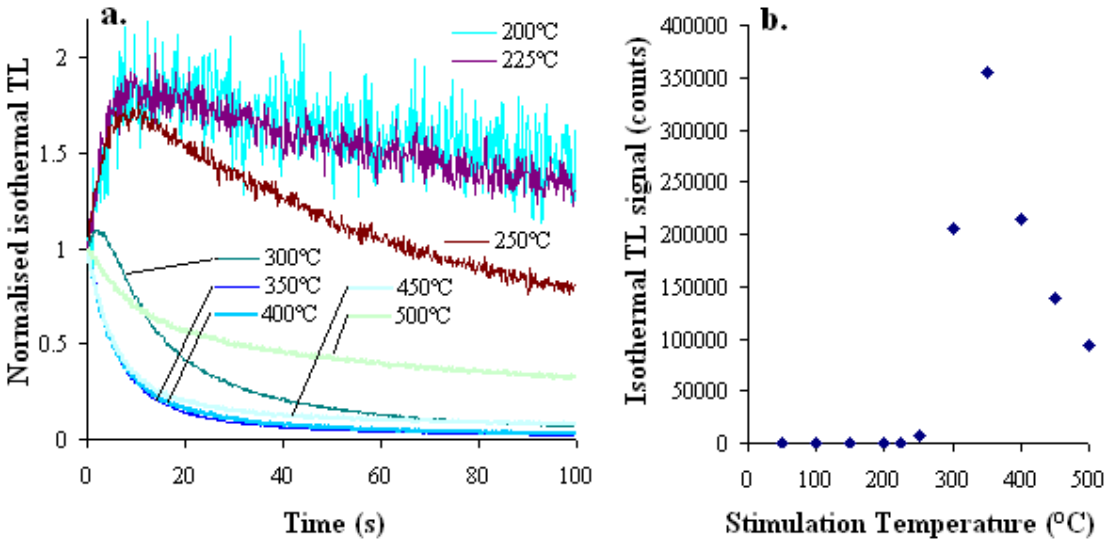

Figure 9.16: a, Isothermal TL curves measured by holding an aliquot at a specified temperature for 100 s. Curves have been normalised to the first 0.2 s of stimulation time to show differences in shape and decay rate. b, The isothermal TL signal (calculated as the background-subtracted sum of counts in the first 2 s of stimulation) plotted as a function of stimulation temperature.

Normalised isothermal TL curves (normalised to their first 0.2 s of stimulation) are presented in Figure 9.16a to show how the shape of the isothermal TL signal changes with stimulation temperature. Isothermal TL curves for temperatures of 50°C, 100°C and 150°C are indistinguishable from background and were not included in the figure for clarity. For IR stimulation temperatures of 200°C, 225°C and 250°C, the isothermal TL signal increases over the first ~10 s of stimulation time before decreasing. The shape of the isothermal TL curves at temperatures of 200°C and 225°C are similar, with the latter being ~8 times brighter than the former. At 250°C, after reaching a peak at ~10 s, the signal decays more quickly than either 200°C or 225°C. The decay rate for the isothermal TL curves then increase at 300°C and again at 350°C and 400°C. The curves for 350°C and 400°C are similar in shape despite the signal intensity of the latter being ~60% that of the former. The decay rate then decreases at

450°C and 500°C, at which point the shape of the isothermal TL curve becomes markedly different, decaying to a substantially higher background, similar to what was observed for the IRSL signal at 500°C (Figure 9.15c).

9.5.1.3 Assessing the dependence of the isothermal TL-subtracted IRSL signal on stimulation temperature

Since all measurements presented in this section were made on the same aliquots, the isothermal TL curves (Figure 9.16) could be subtracted from the measured IRSL curves (Figure 9.15a, c) to show the luminescence response to IR stimulation at elevated temperatures without the underlying isothermal TL signal (Figure 9.17). These results more appropriately show the dependence of IRSL on stimulation temperature. Figure 9.17b shows the dependence of the isothermal TL-subtracted IRSL signal intensity on stimulation temperature. The signal increases in a systematic way up to 250°C. There is then a large increase in signal intensity at 300°C, after which the signal begins decreasing. The largest decrease in signal intensity is between 350°C and 400°C, after which it continues to decrease up to 500°C. These results differ from those for Mumba (Figure 7.12), which, after a systematic increase up to 250°C, exhibited no change up to 300°C and then a slow decrease of signal intensity at higher temperatures.

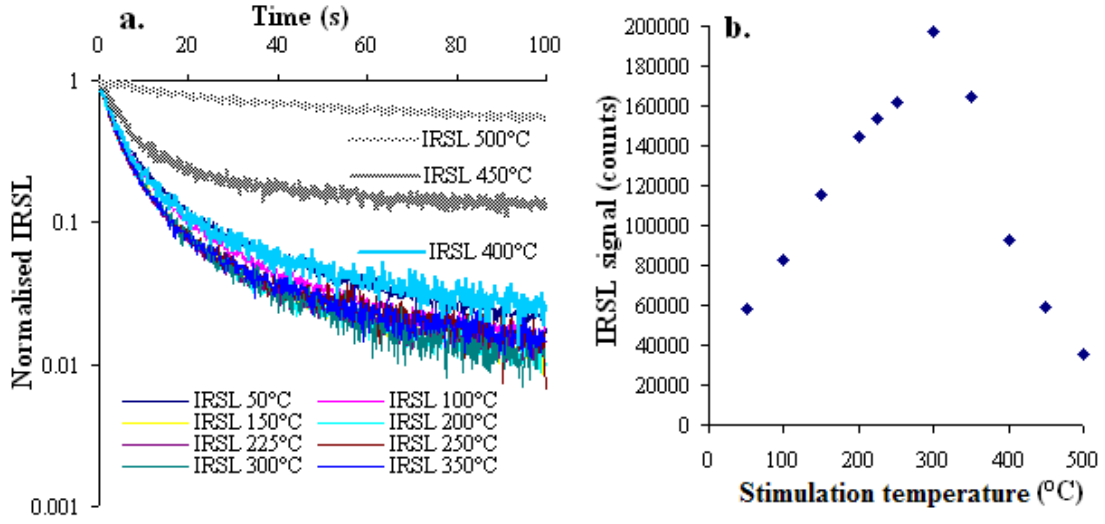

Figure 9.17: a, Normalised isothermal TL-subtracted IRSL decay curves at specified stimulation temperatures. Curves are normalised to show the dependence of the rate of decay and shape of the IRSL signal on stimulation temperature. All curves are normalised to the first 0.2 s of stimulation time. b, The isothermal TL-subtracted IRSL signal (calculated as the background-subtracted sum of the first 2 s of measured IRSL) plotted as a function of stimulation temperature.

Normalised isothermal TL-subtracted IRSL decay curves are displayed in Figure 9.17a to show how the rate of decay of the IRSL signal changes with stimulation temperature. As discussed in Chapter 7, two different patterns have been reported in the literature for the way in which the shape of the IRSL decay curve changes with increases in stimulation temperature up to ~250°C. Duller and Wintle (1991) and McKeever et al. (1997) observed that the decay rate of the IRSL curves increased with increasing stimulation temperature. This behaviour was also observed for K-feldspars from Mumba (Section 7.4.2.4). Alternatively, Poolton et al. (2002a) and Thomsen et al. (2008) reported that the decay curve shape did not change with increasing stimulation temperature for their samples. The results for Moche Borago are more similar to those reported by Poolton et al. (2002a) and Thomsen et al. (2008), and are in contrast to the results from Mumba (Figure 7.12). Figure 9.17a indicates that there is very little change in IRSL decay curve shape for MB3 at stimulation temperatures of between 50°C and 400°C. The rate of IRSL decay then decreases substantially at 450°C and 500°C, and decays to a higher absolute background level.

9.5.1.4 Comparing IRSL from Mumba and Moche Borago

The experiments that have been described in the previous three subsections (Sections 9.5.1.1–9.5.1.3) were similar to those described in Section 7.4.2 for Mumba. A comparison of the results from the two sites suggests that there may be a TL peak in MB3 analogous to the optically insensitive 350°C TL peak in MR9. The isothermal TL signal attains a maximum intensity at 350°C for both MB3 and MR9, indicating that there is a large amount of charge that can be thermally evicted in the TL region around 350°C. This may be associated with the results of the measured IRSL signal intensity (Figure 9.14 and Figure 7.8b), for which there is a large increase at 300°C for both MB3 and MR9. For Mumba, this was explained as being the result of the accumulation of charge in the trap associated with the 350°C TL peak over the previous cycles of irradiation, preheating and IR stimulation. The accumulated charge, which began to be isothermally evicted when the IR stimulation temperature was held at 300°C, suggested that the trap associated with the 350°C TL peak was relatively optically insensitive (Section 7.4.2). This was supported by subsequent experiments in which IR stimulations at elevated temperatures were followed by a 500°C heat treatment (an

experiment that was not performed on MB3). When the latter was included, the increase in IRSL intensity at 300°C was considerably reduced, most likely because the heat treatment thermally removed all charge from the 350°C TL peak after each cycle, preventing the progressive accumulation of charge.

For MB3, the fact that the measured IRSL signal intensity at 350°C is larger than that at 300°C (i.e., in contrast to what was observed for MR9) should be addressed. The increase in signal intensity at 350°C may be a function of the low sensitivity of the IRSL signal compared to the TL signal for MB3. The dim IRSL means that the large isothermal TL signal at 350°C would add proportionally more to the measured IRSL signal at 350°C for MB3 than for MR9. This interpretation is supported by the observation that when the isothermal TL is subtracted from the measured IRSL, the resulting signal intensity at 350°C is lower than that at 300°C (i.e., in contrast to what is observed for the measured IRSL signal, but in agreement with the results from MR9). While not conclusive, these results are consistent with the presence of an optically less-sensitive TL peak in MB3 analogous to the TL peak at ~350°C in MR9.

There are several substantial differences in the response of the IRSL signal to stimulation temperature between K-feldspars from Mumba and Moche Borago. The different behaviours regarding the change in IRSL decay rate with stimulation temperature (Figure 9.17 and Figure 7.12) have the broadest implications. For K-feldspars from both sites, the IRSL signal intensity was shown to increase with stimulation temperature up to at least 300°C, in agreement with the literature (Duller and Wintle, 1991; McKeever et al., 1997; Poolton et al., 2002b; Thomsen et al., 2008). The differences between MB3 and MR9 lie in the rate of decay of the IRSL signal at different stimulation temperatures. For MR9, the rate of decay increases with stimulation temperature up to ~400°C, in agreement with Duller and Wintle (1991) and McKeever et al. (1997). This suggests that increases in the IR stimulation temperature may increase a thermally assisted process of recombination (Section 7.4.2). For MR3, there is no change in IRSL decay rate with stimulation temperature up to ~400°C, in agreement with Poolton et al. (2002b) and Thomsen et al. (2008). Thomsen et al. (2008) conclude that this relationship between IRSL decay rate and stimulation temperature suggests that tunnelling recombination dominates IRSL production at the stimulation temperatures measured, and that thermal assistance is not significant.

9.5.1.5 Summary of results for MB3

The potential benefits of using an elevated-temperature IR stimulation for luminescence investigations of MB3 are substantial. They include the reduction of fading rate reported by several studies (Thomsen et al., 2008; Buylaert et al., 2009) and an increased IRSL yield at elevated temperatures (Duller and Wintle, 1991; McKeever et al., 1997; Poolton et al., 2002b). The latter feature would be particularly beneficial for measurement of the relatively dim IRSL of MB3. The measured IRSL signal from MB3 was shown to increase in intensity with stimulation temperature up to 350°C. The isothermal TL signal was assessed and shown to be present at temperatures greater than 200°C, attaining a maximum intensity at 350°C. The isothermal TL signal was observed not to affect the IRSL signal for stimulation temperatures below ~200°C when a 260°C preheat was applied. These results indicate that an IR stimulation temperature of 200°C is the highest that can be used to avoid the inclusion of any unwanted isothermal TL in the measured IRSL signal from Moche Borago.

9.5.2 The post-IR IRSL signal

The post-IR IR stimulation procedure was described in detail in Section 7.5. Briefly, it involves an IR bleach (100 s at 50°C) following the regenerative and test dose preheats, and prior to the measurement of IRSL at an elevated temperature (e.g., 225°C; Jain and Singhvi, 2001; Thomsen et al., 2008). Several studies have reported that the post-IR IRSL signal is bleachable, can recover a known dose, and has a substantially lower rate of anomalous fading than the IRSL signal measured at 50°C (Thomsen et al., 2008; Buylaert et al., 2009). Results for K-feldspar separates from Mumba (Chapter 7) confirm these features of the post-IR (50°C) IRSL (225°C) signal, showing that the signal is bleachable, can recover a known laboratory dose, and has a lower rate of anomalous fading than the IRSL signals measured at all stimulation temperatures tested for MR9. The post-IR IRSL signal was then used to obtain ages, which were in agreement with those obtained from single grains of quartz (see Chapter 8).

Results from the stimulation temperature tests on K-feldspar separates from MB3 (Section 9.5.1) have implications for the potential use of a post-IR IR stimulation procedure. Thus far, most uses of a post-IR IRSL procedure reported in the literature (e.g., Thomsen et al., 2008; Buylaert et al., 2009) and in this thesis have used an

elevated temperature IR stimulation of 225°C. In Chapter 7, for K-feldspar from Mumba, it was shown that IRSL measured at, or above, 250°C included a substantial isothermal TL signal, suggesting that 225°C was the highest appropriate IR stimulation temperature. In the case of MB3, there is a noticeable isothermal TL signal when IR stimulation is performed at 225°C and above (Figure 9.16). The isothermal TL signal at 225°C is approximately eight times greater than the isothermal TL signal at 200°C. This suggests that the highest stimulation temperature that could be used without any unwanted isothermal TL contribution is 200°C. Therefore, the post-IR IR stimulation of MB3 was performed at 200°C, instead of the oft-used 225°C.

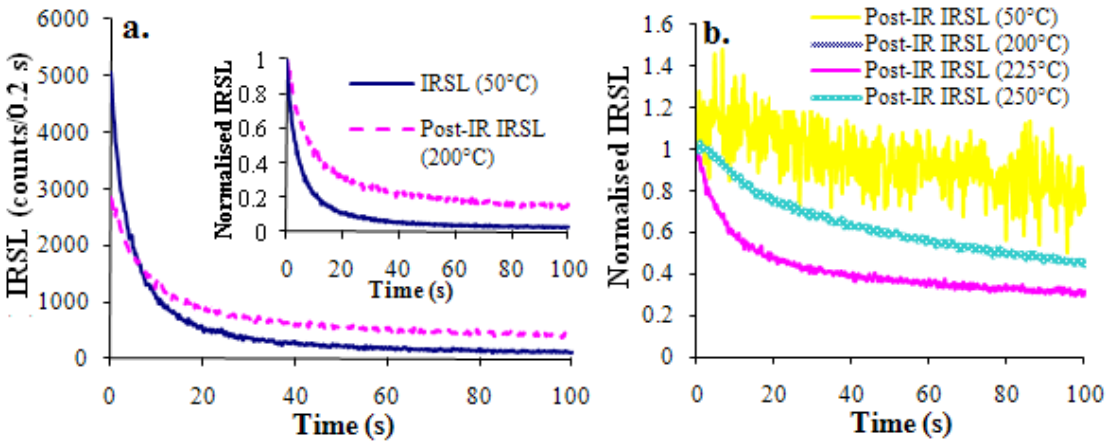

Figure 9.18: IRSL decay curves produced during post-IR IRSL experiments performed on an aliquot of MB3. a, IRSL decay curves shown for an IR bleach (100 s at 50°C) and the post-IR IRSL (100 s at 200°C). The inset shows the same two decay curves normalised to the first 0.2 s of stimulation time to show difference in their decay curve shape. b, Normalised decay curves for post-IR IRSL at various stimulation temperatures. All of these decay curves were measured at the specified temperature following an IR bleach (at 50°C).

Decay curves are presented in Figure 9.18a for an IR bleach (50°C) and a post-IR IR stimulation (200°C) of K-feldspar from MB3. These results are similar to those for Mumba (Figure 7.5.2), although they are different in magnitude. The post-IR IRSL signal is ~54% as bright as the signal induced by the IR stimulation at 50°C that preceded it (Figure 9.18a). In addition, the post-IR IRSL signal decays more slowly than the signal induced by the IR stimulation that preceded it. This decrease in decay rate is consistent with the results from Mumba (Figure 7.13a) and with those reported by Thomsen et al. (2008). When the temperature of the post-IR IR stimulation is varied between 50°C and 250°C (Figure 9.18b), the rate of decay is slowest for IR stimulation at 50°C, which produced very little luminescence. The rate of decay increases from IR

stimulation at 50°C to stimulation at 200°C, at which temperature the signal decays the fastest. The rate of decay then decreases for stimulation at 225°C and 250°C. This pattern of change in the decay rate with increasing stimulation temperature is the same as that observed for standard IRSL (i.e., without a preceding bleach; Figure 9.17). Therefore, similar to the inference made in Section 7.5, the decrease in decay rates for stimulation temperatures above 200°C is thought to be the result of the underlying isothermal TL signal. This corroborates the conclusion drawn in the previous section, that 200°C is the highest stimulation temperature that can be used for standard IR or for post-IR IR stimulation of MB3, to ensure that no unwanted TL signal underlies the IRSL signal.

9.5.3 Assessing the optimal IR stimulation conditions for samples from Moche Borago

In Section 7.6, it was demonstrated that IRSL at elevated stimulation temperatures and the post-IR IRSL signal performed as well as IRSL at 50°C in the SAR procedure, and had lower rates of anomalous fading, for samples from Mumba. To compare how various stimulation conditions performed in the SAR procedure, modified dose recovery experiments were performed on K-feldspar from MB3. If this experiment had been performed in the conventional manner, five sets of three, ~1000-grain aliquots (fifteen in total) would have been prepared and bleached in natural sunlight for at least three days. Each set would then have been given a known laboratory dose, which would be measured using the SAR procedure. There was not enough sample material remaining, however, to prepare 15 aliquots for a single experiment and leave enough grains for the measurement of D_e values. As a result, three aliquots were repeatedly annealed at 500°C. These aliquots were then given a laboratory dose of 120 Gy, which were then measured using SAR procedure (see Table 3.2), consisting of regenerative doses of 60, 120, 180, 0 and 60 Gy, a test dose of 60 Gy, and a regenerative and test dose preheat of 260°C for 60 s. The specified IR stimulation conditions were performed for 100 s. After the given dose was measured using the SAR procedure, the aliquots were heated to 500°C and given a dose of 120 Gy, which was measured using the SAR procedure with a different set of IR stimulation conditions. Five experiments were performed to test IR stimulation temperatures of

50°C, 100°C, 150°C and 200°C and a post-IR (50°C) IRSL (200°C) procedure. It should be noted, however, that since this experiment was conducted using grains that had been annealed at 500°C, the applicability of the following results to natural grains may be limited.

The IRSL intensity increased with stimulation temperature, as was expected following the results presented in Section 9.5.1. The post-IR IRSL procedure resulted in an IRSL intensity that was ~40% of that produced by IRSL at 50°C, making it the weakest signal measured. For this reason, larger uncertainties are associated with values produced by the post-IR IRSL procedure. Results for the tests of SAR suitability (i.e., measured/given dose ratio, the recycling ratio and the recuperation value) are presented in Figure 9.19. While all aliquots for all stimulation conditions were able to recover the given dose within 2σ, the only conditions for which all three aliquots recovered the given dose within 1σ are IRSL at 150°C, IRSL at 200°C and the post-IR IRSL procedure (Figure 9.19a). Furthermore, as stimulation temperature is increased from 50°C to 200°C (including the post-IR IRSL at 200°C), the weighted mean measured/given dose ratio increases from 0.95 ± 0.01 to 0.99 ± 0.02.

Results for the recycling ratios present a different pattern (Figure 9.19b). All three aliquots recycled a duplicated dose within 1σ for all four elevated IR stimulation temperatures. All aliquots stimulated using the post-IR IRSL procedure also produced satisfactory results, although only two of the aliquots recycled the duplicate dose within 1σ. The final SAR suitability test, the recuperation value, showed a different pattern. As the IR stimulation temperature was increased, the recuperation value decreased, from a weighted mean of 11.5 ± 0.3% at 50°C to 5.4 ± 0.2% at 200°C. The post-IR IRSL procedure produced a similar recuperation value to that obtained for IR stimulation at 200°C (weighted mean of 6.1 ± 0.4%). Only IR stimulation at 200°C and the post-IR IRSL procedure produced recuperation values at or below the 5% rejection threshold, and below the value (i.e., 6.3 ± 0.1%) accepted by Buylaert et al. (2008).

These results suggest that, in spite of the relatively high recuperation values, all of the stimulation conditions were capable of recovering a known dose within 2σ. In addition, all aliquots for all stimulation conditions (with the exception of one aliquot from the post-IR IRSL set) recycled a duplicate dose within 1σ. This validates the fading test procedures presented later in this chapter (Section 9.6.2). The fading tests

are effectively duplicate regenerative doses repeated with varying amounts of delay time between the preheat and the measurement of the IRSL. Since all aliquots for all stimulation conditions performed well in the recycling ratio test, it can be inferred that the measurement of fading rates using these stimulation conditions is valid.

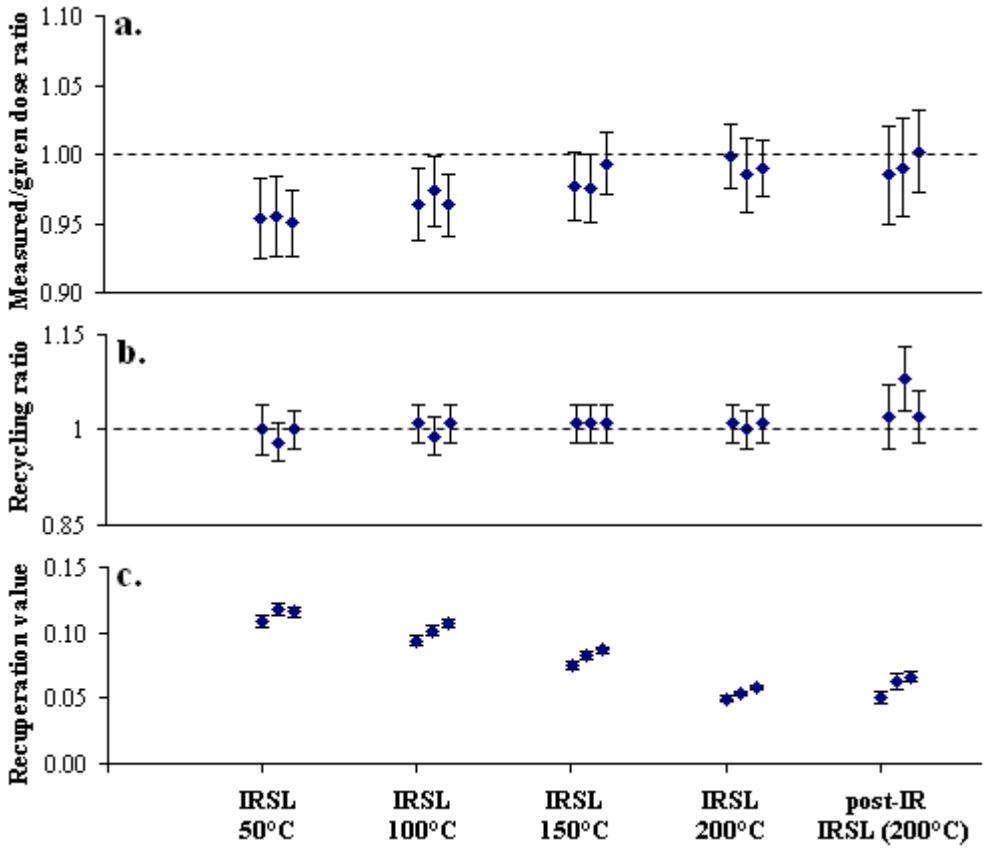

Figure 9.19: Results from experiments described in this section using three annealed aliquots of MB3. The suitability of the SAR procedure was assessed for the various IRSL signals using three standard tests: a, Measured/given dose ratio, b, recycling ratio, and c, recuperation value ($[L_N/T_N]/[L_0/T_x]$, where N is the given dose).

9.6 Characterisation of anomalous fading in MB3

Anomalous fading is an ubiquitous feature of the luminescence signal of K-feldspars (Wintle, 1973; Spooner, 1994b, Huntley and Lamothe, 2001; Huntley and Lian, 2006). Any attempts to use K-feldspar separates as a luminescence dosimeter must either circumvent or correct for this malign phenomenon. By characterising the anomalous fading behaviour of K-feldspar separates from Mumba (Chapter 7), the fading rate was reduced from ~15%/decade for IRSL measured at 50°C to ~1%/decade for the post-IR IRSL signal (Figure 7.17). The lower fading rates meant that IRSL ages

corrected for fading were less reliant on the age-correction model and its associated limitations and uncertainties (e.g., Huntley and Lamothe, 2001), resulting in a more robust chronology. Following the results for Mumba, investigations were undertaken into the fading behaviour of K-feldspar separates from Moche Borago, using sample MB3.

9.6.1 Anomalous fading: TL

To observe how the TL signal of K-feldspar from MB3 was affected by anomalous fading, a storage experiment was performed. Two aliquots consisting of ~1000 grains of K-feldspar from MB3 were heated to 500°C at a rate of 5°C/s, and the TL of the natural signal was recorded (natural in Figure 9.20a). They were then given a laboratory irradiation of 240 Gy and the TL was immediately measured (curve 1 in Figure 9.20a). The aliquots were then given an identical laboratory irradiation and stored for ~15 hours before the TL was measured again (curve 2 in Figure 9.20a). Figure 9.20c presents these data, plotted on a log-linear y-axis. The absolute TL intensity of the natural signal is much smaller than that of either laboratory-irradiation induced TL curve over the entire temperature range up to ~490°C. The TL intensity is also substantially reduced over the entire temperature range after the 15 hour delay. When the two laboratory-irradiated glow curves are compared, the position of the main TL peak shifts slightly. The TL measured immediately after irradiation peaks at ~235°C, while the TL measured after the delay peaks at ~250°C.

In the temperature range from 0 to 100°C, TL curve 2 is between 10 and 100 times less bright than TL curve 1 (Figure 9.20c). Between ~100°C and ~200°C, the amount of signal loss between the two curves is also large. It is likely that the large difference between TL curves 1 and 2 below 200°C is the result of a thermally unstable TL signal, as opposed to the anomalous fading. This can be inferred when the TL of the natural is compared to TL curve 1 and 2 (Figure 9.20c). The natural TL curve does not begin to increase until ~200°C, compared to ~100°C for TL curve 2 and ~50°C for TL curve 1. This progressive loss of signal in the low-temperature (<200°C) region of the glow curve with delay time suggests that the difference between TL curves 1 and 2 over the 100–200°C temperature range is the result of the loss of a short-lived, unstable TL signal, and the difference between the two curves above ~200°C is the result of longer-

term anomalous fading. This lends support to the use of a higher temperature (i.e., >200°C) preheat to remove the unstable, low-temperature component.

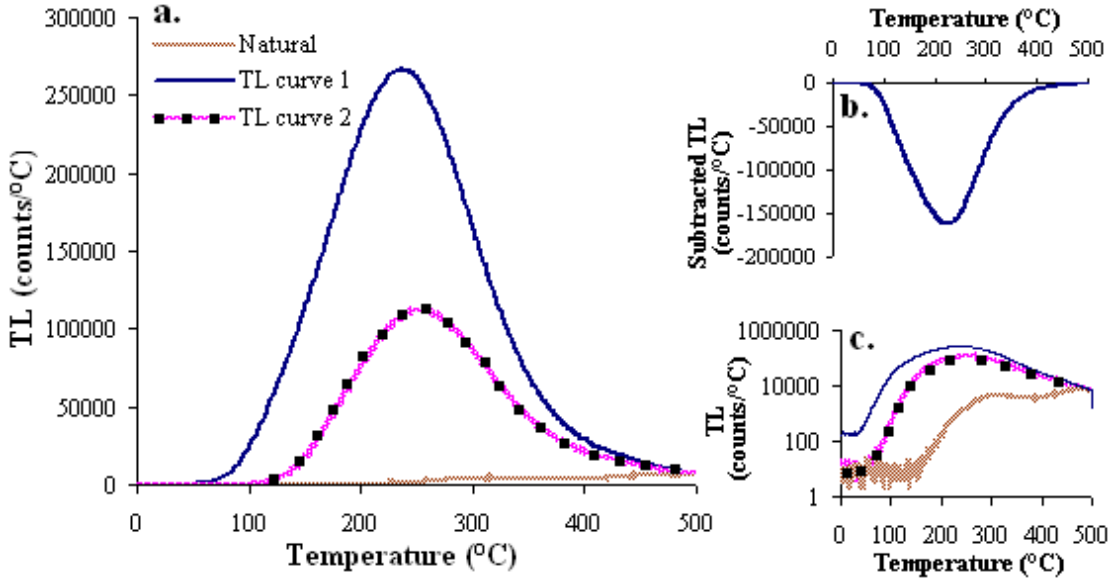

Figure 9.20: The effect of anomalous fading on TL glow curve shape and size. a, Three TL curves measured from the same aliquot. TL curve 1 was measured immediately after a 240 Gy irradiation and TL curve 2 was measured approximately 15 hours after a 240 Gy irradiation. b, To visualise the loss of TL signal with delay time, the two laboratory-irradiated TL curves are subtracted from one another ('TL curve 2' - 'TL curve 1'). c, The same dataset from (a), but plotted on a log-linear y-axis.

The effects of anomalous fading can be visualised further by subtracting TL curve 1 from TL curve 2 (Figure 9.20b). The resulting subtraction-curve is the mirror image of the TL glow curves, indicating that the TL signal is reduced throughout the entire temperature range. The amount of signal loss between the two curves increases between ~100°C and ~200°C, with the greatest loss occurring at ~225°C (Figure 9.20b). After ~225°C, the amount of signal loss begins to decrease until ~400°C. This may suggest that the effects of anomalous fading on the TL glow curve are greatest over the temperature range ~200°C to 400°C. For temperatures above ~400°C, the two curves are similar, suggesting that the effects of anomalous fading on the TL signal may be smaller at higher temperatures (>400°C). The idea that the high-temperature region of the TL curve suffers from less or no anomalous fading has been suggested previously by Guérin and Valladas (1980) who worked with volcanic, plagioclase feldspars. They suggested that the malign effects of anomalous fading could be avoided by measuring the TL signal at approximately 600°C.

A second, similar anomalous fading experiment was performed to elucidate the effects of anomalous fading in the high-temperature region of the glow curve. The same two aliquots were heated to 500°C. They were then given a laboratory dose of 240 Gy, preheated to 260°C for 60 s, and then their TL curves were measured up to 500°C. They were then given the same laboratory dose and preheated again. They were then stored for 2700 s (~46 min) before their TL curves were measured. A second TL curve was measured immediately after irradiation and preheating to check that there were no sensitivity changes. Finally, the aliquots were given the same laboratory irradiation, followed by a preheat, and then stored for 15,300 s (~4.25 hr) before their TL curves were measured. The purpose of this experiment was to eliminate the influences of the low-temperature TL components that may have obscured the effects of anomalous fading in Figure 9.20. By preheating the aliquots to 260°C the low-temperature TL peaks, which are not present in the natural, were removed from the laboratory-irradiated aliquots. This allowed for the investigation of how anomalous fading affected the higher temperature regions of the TL curve.

Results for one representative aliquot are presented in Figure 9.21. The two TL curves that were measured immediately after irradiation and preheating overlap ('240 Gy (1)' and '240 Gy (2)' in Figure 9.21a), indicating that no sensitivity changes occurred during the measurement of the '240 Gy + 2700 s' TL curve. All TL curves, regardless of storage time, have the same shape, with a large TL peak between ~300°C and 480°C, which peaks at 350°C. Above 480°C, the each TL signal begins to increase slightly, suggesting that an unmeasured, higher temperature TL component may exist. When the TL curve measured after no delay is subtracted from the TL curve measured after a delay of 15,300 s (Figure 9.21b), the regions of the TL curve that are most affected by anomalous fading can be identified. After storage, the intensity of the TL signal is reduced between ~250°C and ~490°C. The loss in TL signal is a mirror image of the TL curves, with the trough at ~350°C. Between ~490°C and 500°C, there is very little change in the TL signal before and after storage. This corroborates the results presented in Figure 9.18, which suggested that the higher temperature region of the TL curve may suffer less from anomalous fading than the lower temperature region.

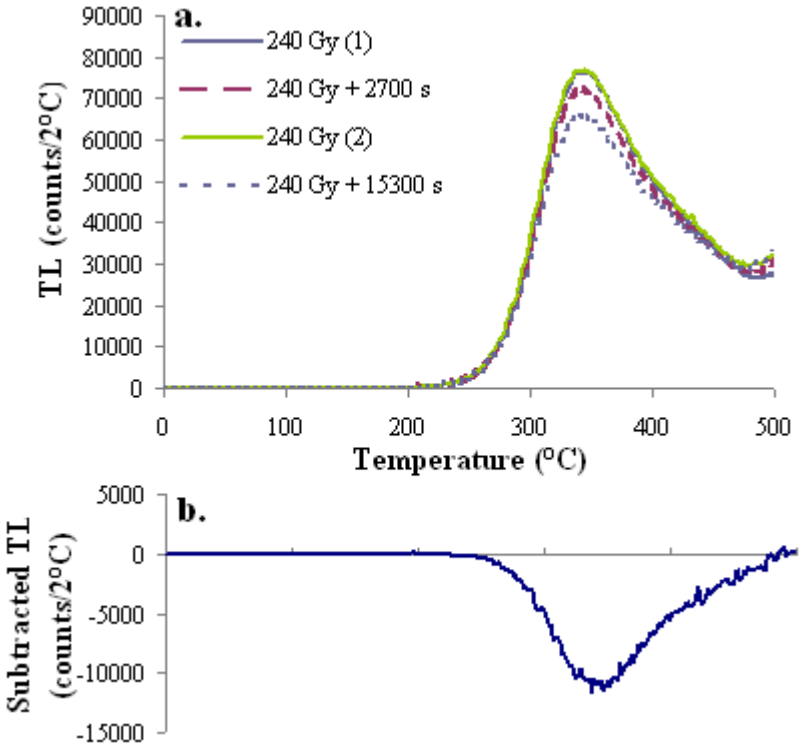

Figure 9.21: Anomalous fading in the TL curves from one aliquot of MB3. a, The two TL curves that were measured immediately after irradiation and preheating overlap. The other two TL curves were measured following different storage times between preheating and TL measurement. b, The difference between the TL curve measured after a 15,300 s storage time and the TL curve measured immediately after the second irradiation and preheat. This shows the TL signal that has been lost due to anomalous fading.

9.6.2 Assessing the rate of anomalous fading of the IRSL signal

The TL tests described in the previous section confirmed that K-feldspar separates of MB3 suffer from anomalous fading. Experiments were undertaken, therefore, to assess both the rate of anomalous fading of the IRSL signal and whether the observed fading showed a dependence on IR stimulation temperature. The latter was shown to be the case for MR9, for which the fading rate decreased as the stimulation temperature was increased. The rate of anomalous fading was measured as described in Section 7.6.2.1. In this experiment, two ~1000-grain aliquots that had been previously subjected to multiple IR stimulations and heat treatments of 500°C were used. They were given a dose of 120 Gy and immediately preheated (Auclair et al., 2003) to 260°C for 60 s. They were then stored for different durations of time that ranged from 695 s (~11.5 min) to 36,824 s (~10.3 hr) before being stimulated with the IR diodes for 100 s at the specified temperature. Following the measurement of the resulting IRSL (L_x), a test dose cycle was performed that consisted of an irradiation of

30 Gy, a 260°C preheat for 60 s, and an IR stimulation for 100 s at the same temperature as the L_x measurement. Stimulation temperatures of 50°C, 100°C, 150°C and 200°C were tested. Each of these IR stimulation temperatures was shown to be capable of recycling a duplicate regenerative dose within 1σ (Section 9.5.3), indicating that the use of the standard fading measurement procedure was sound. The fading rate of the post-IR IRSL signal was not measured, despite its ability to recycle a duplicate regenerative dose.

This procedure was repeated seven times for various storage durations for each aliquot. Similar to the experiment described in Section 7.6.2.1, the storage times used in this experiment were relatively short compared to those used in other studies. The purpose of this experiment was not to correct a measured IRSL age, but to assess the fading rate for K-feldspar separates of MB3 and to compare the fading rates for various stimulation conditions. This meant that the number and duration of different storage times needed only to be consistent for each stimulation condition. After the measurements described above were performed, the rate of anomalous fading (normalised to a *g*-value of 2 days, g_{2days}) was calculated for each aliquots, as described in Section 7.6.2.2.

Representative results for one of the two aliquots of MB3 are presented in Figure 9.22. The graphs show the weighted regressions from which the g_{2days} values were calculated. There is a decrease in the fading rate as the stimulation temperature is increased. For both aliquots, the fading rate when IR stimulation was performed at 200°C was ~57% of that for IR stimulation at 50°C. The observed dependence of fading rate on stimulation temperature agrees with the findings of Thomsen et al. (2008) and with the results obtained for K-feldspar from Mumba (Chapter 7). Despite the similar behaviour in response to stimulation temperature, the fading rates measured for K-feldspars from Moche Borago are significantly larger than any reported by Thomsen et al. (2008) and measured for Mumba (with the exception of IR stimulation at 50°C for 500 s). The mean fading rate for MB3 using IR stimulation at 50°C is approximately four times greater than that from Mumba (mean fading rates of 56 and 14 %/decade for MB3 and MR9, respectively). The difference in mean fading rates at elevated stimulation temperatures (200°C for MB3 and 225°C for MR9) is also about four-fold (mean fading rates of 32 and 7 %/decade for MB3 and MR9, respectively). The

unusually high rates of fading obtained for MB3 indicate that the measured fading rates cannot be representative of fading over geological timescales.

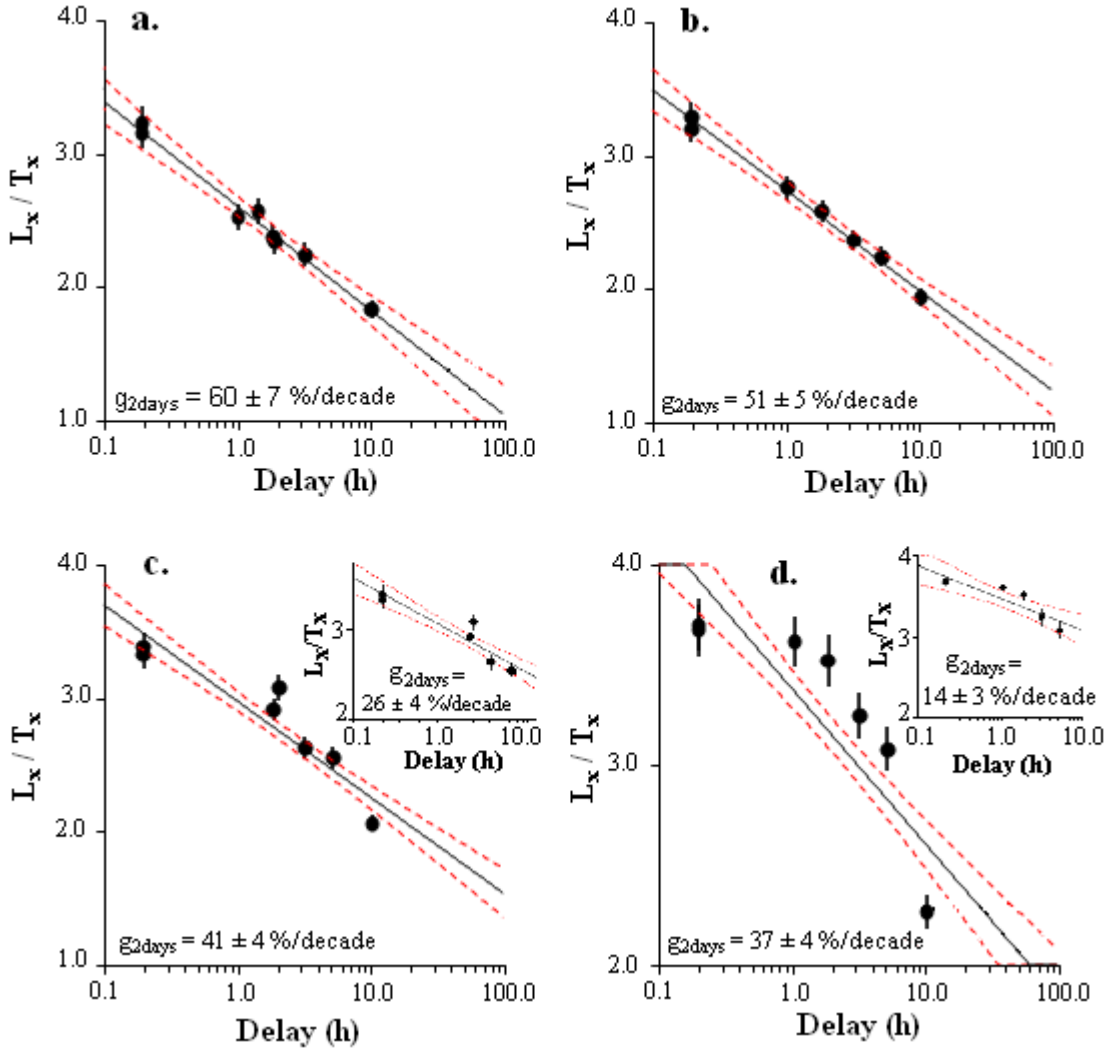

Figure 9.22: Results of anomalous fading tests using an aliquot of K-feldspar from MB3. The graphs show the regression lines used to calculate the g_{2days} values displayed in each graph. The fading rate calculations are for IRSL stimulation temperatures of 50°C (a), 100°C (b), 150°C (c) and 200°C (d). The inset to (d) is the same data, replotted after the datapoint for a delay time of 10 hr was removed. Dashed lines indicate 2σ.

It should be noted that fits produced by the fading data from the IRSL signal at higher temperatures (i.e., 150°C and 200°C, corresponding to Figure 9.22c and d, respectively) are poor. None of the datapoints shown in Figure 9.22d lie within the 2σ band. The poor fits are the result of the datapoints that lies at a delay time of 10 hr. When this datapoint is removed from the IRSL (200°C) dataset, the fit improves considerably (inset to Figure 9.22d), and the g_{2days} value is reduced to ~14 %/decade.

When the datapoint at 10 hr is removed from the dataset plotted in Figure 9.22c, the fit also improves and the g_{2days} value decreases (to ~26 %/decade) (inset to Figure 9.22c). This pattern of improved fit and decreased g_{2days} values does not hold for the lower stimulation temperatures (Figure 9.22a, b). The poor fits in Figure 9.22 (c and d) suggest that the fading rate measured for smaller delay times (<10 hr) may not represent the fading rate measured for longer delay times (>10 hr), implying that laboratory-measured fading rates of the elevated-temperature (150°C and 200°C) IRSL signal of MB3 may not be representative of the fading rate over geological timescales. Given the inconsistent fading behaviour of the elevated-temperature IRSL signal of K-feldspar from MB3, this signal is considered unsuitable for D_e determination.

9.6.3 Discussion

K-feldspar separates from Moche Borago suffer from significantly more anomalous fading than K-feldspars from Mumba. The disparity in fading rates between Moche Borago and Mumba may be a result of the different geological origins of sediments from these sites: sediments from Mumba are of metamorphic origin, whereas sediments from Moche Borago are of volcanic origin. The ordering of aluminium and silicon atoms in the lattice of crystalline feldspars (the structural state) is largely determined by the thermal history of the mineral. Volcanic feldspars, such as those at Moche Borago, typically crystallise at high temperatures and have a disordered structural state (Fattahi and Stokes, 2003a). With the exception of Huntley and Lian (2006), who reported observing no difference between the fading rates of volcanic and sedimentary feldspars, there is general agreement in the literature that volcanic feldspars with a disordered structure tend to suffer from more anomalous fading than low-temperature ordered feldspars (e.g., Spooner 1994b; Visocekas et al., 1994, 1998; Fattahi and Stokes, 2003a). A comparison of the measured fading rates of K-feldspar from Mumba and Moche Borago support this consensus view.

The fading-correction model of Huntley and Lamothe (2001) is not expected to be valid for samples that are sufficiently old (with ages corresponding to D_e values that fall in the non-linear region of the dose-response curve) or that have high fading rates. The IRSL signal from K-feldspar samples from Liang Bua, Indonesia, also had a high measured fading rate and could not reliably be corrected for fading, prompting

Morwood et al. (2004) to conclude that their IRSL ages should be viewed as minimum estimates. Given the atypically high fading rates measured in the laboratory for a sample from Moche Borago, the Huntley and Lamothe (2001) model would be inappropriate for calculating fading-corrected ages. Consequently, any IRSL ages obtained for K-feldspars from Moche Borago should be considered as minimum estimates.

9.7 D_e value, dose rate and minimum age estimates for MB3

To investigate the natural IRSL signal of MB3, two aliquots (each consisting of ~1000 grains) were preheated to 260°C for 60 s, and stimulated with IR at 50°C for 100 s (L_N). This was followed by a test dose cycle consisting of a 30 Gy beta dose, a 260°C preheat for 60 s, and an IR stimulation at 50°C for 100 s (T_N). The aliquots were then given a 60 Gy regenerative dose, preheated to 260°C for 60 s, and stimulated with IR at 50°C for 100 s (L_x), followed by a test dose cycle (T_x). The sensitivity-corrected IRSL signal following subsequent regenerative doses of 30, 90, 120, 180, 240 Gy and a repeat dose of 60 Gy were used to construct dose-response curves, on to which the sensitivity-corrected natural signal (L_N/T_N) was projected to obtain a D_e estimate.

Results suggest that the SAR procedure is suitable for MB3, at least in terms of the recycling ratio and extent of recuperation. The weighted mean recycling ratio for both aliquots was 0.99 ± 0.06 and the weighted mean recuperation value was 5.7 ± 1.0%. Two IRSL decay curves are presented in Figure 9.23a: the natural IRSL signal and the IRSL signal following the first laboratory irradiation of 60 Gy. While the shape and intensity of the two decay curves are similar, the normalised curves (inset to Figure 9.23a) suggest that the laboratory-irradiated signal decays slightly more quickly than the natural. A representative dose-response curve is presented in Figure 9.23b. Both aliquots produced dose-response curves that grew to 240 Gy, but not at a linear rate. The curves were fitted by a saturating exponential function and the D_e values obtained for the two aliquots were 67.4 ± 22.6 Gy and 53.2 ± 3.4 Gy. The weighted mean D_e (53.6 ± 3.4 Gy) and the measured dose rate were then used to calculate an age estimate for MB3 (Table 9.4). No fading measurements were made for these aliquots, so the age presented in Table 9.4 is not corrected for anomalous fading and is, thus, considered as a minimum estimate of the actual depositional age.

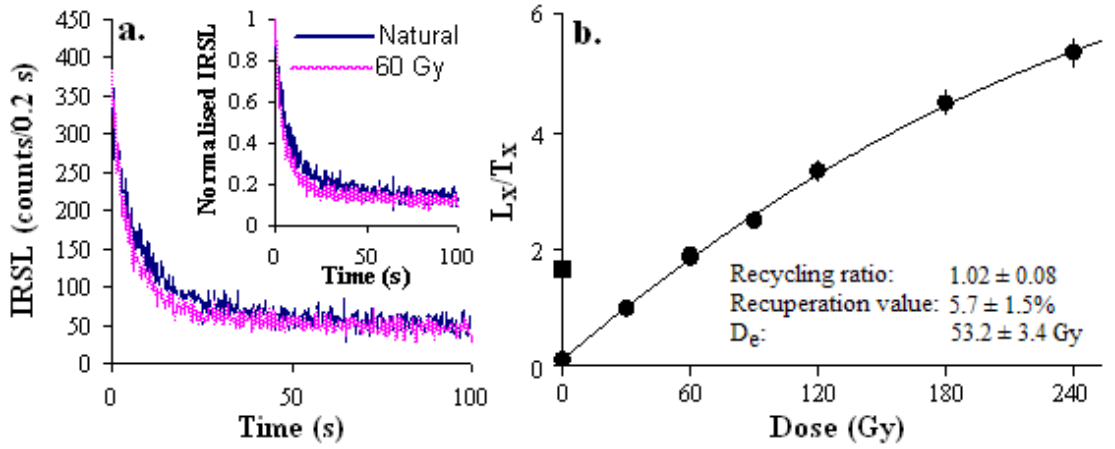

Figure 9.23: Results for a representative aliquot of K-feldspar from MB3. a, The natural IRSL signal and the signal produced following a 60 Gy regenerative dose. The inset shows the same curves normalised to their initial 0.2 s stimulation interval. b, Dose-response curve for the same aliquot, with the sensitivity-corrected natural intensity (L_N/T_N) shown as a solid square on the y-axis.

Table 9.4: Measured dose rate and D_e data used to calculate the fading-uncorrected age estimate for MB3. The beta dose rate was measured using a GM-25-5 beta counter (see Section 4.2.3.2) and was corrected for beta attenuation (see Section 4.3). The gamma dose rate is based on *in situ* gamma spectrometry measurements (see Section 4.2.3.1). The cosmic-ray dose rate was calculated using the procedures described by Prescott and Hutton (1994) (see Section 4.2.2) and the total dose rate was corrected for the measured water content (see Section 4.3).

	MB3
Beta dose rate (Gy/ka)	2.62 ± 0.15
Gamma dose rate (Gy/ka)	0.19 ± 0.01
Cosmic-ray dose rate (Gy/ka)	0.05 ± 0.01
Measured water-content*	19.0
Total K-feldspar dose rate (Gy/ka)^	**3.77 ± 0.18**
Weighted mean D_e (Gy)	**53.6 ± 3.4**
Age (ka)	**14.2 ± 1.2**

*The measured water content is expressed as the % of the dry sample mass.

^K-feldspar total dose rate includes an internal contribution of 0.90 ± 0.05 Gy/ka (based on Table 4.1).

9.7.1 Discussion of fading rate, D_e and age estimates for MB3

Given the presence of a measurable natural IRSL signal, the fading rate measured in the laboratory (average of ~56 %/decade for IRSL at 50°C; Section 9.6.2) cannot be valid over longer time scales. If it were, then a measurable natural signal

would not be expected. Why, then, is the measured fading rate so high? It is possible that K-feldspars from MB3 may have a high proportion of close trap-recombination centre pairs (i.e., those that tunnel and cause anomalous fading) compared to distant trap-recombination centre pairs (i.e., those that do not tunnel). In nature, electrons would progressively accumulate in distant trap-recombination centre pairs, whereas the close trap-recombination centre pairs would remain empty due to tunnelling. During laboratory irradiation, many electrons may become trapped in both close and distant trap-recombination centre pairs. Therefore, the laboratory-induced IRSL signal (L_x) would likely be dominated by the recombination of electrons associated with close trap-recombination centre pairs, whereas the natural IRSL signal (L_N) would likely be dominated by the recombination of electrons associated with distant trap-recombination centre pairs.

Since the origin of the laboratory-irradiated and natural IRSL signals may be different, it would be inappropriate to compare the two signals. As the probability of an electron reaching a recombination centre is higher for close trap-recombination centre pairs (Poolton et al., 1994), then an IRSL signal dominated by close trap-recombination centre pairs would likely decay faster than an IRSL signal dominated by distant pairs, and this is borne out by the faster rate of decay of the regenerative-dose IRSL signal compared to the natural signal (Figure 9.23a). Consequently, the projection of L_N/T_N on to the regenerated dose-response curve, and the resulting D_e estimate, may be invalid.

The age estimate presented in Table 9.4 was calculated using the weighted mean of two D_e values and is considered a minimum estimate. Given, 1) the caveats related to the measured D_e values, 2) that the fading rate was not measured for the IRSL signal from these two aliquots and, thus, no fading correction was made to the age, and 3) the ambiguity of many of the luminescence behaviours described in this chapter, including the unusually high fading rate, the fading-uncorrected age for K-feldspar from MB3 should be regarded with caution.

9.8 Conclusions

The results of luminescence investigations of quartz and K-feldspar separates from Moche Borago, Ethiopia will be summarised in this section.

- The small quantities of quartz that could be extracted from the Moche Borago samples prevented the use of this mineral as a dating dosimeter. Luminescence investigations of quartz from MB1 (the only sample from which quartz could be extracted) indicated that the OSL signal was weakly luminescent and possessed characteristics that made it unsuitable for burial dose estimation using the SAR procedure. LM-OSL investigations showed that no fast component was present and that the OSL signal was dominated by slow components. These results are in general agreement with those of other OSL investigations of volcanic quartz (e.g., Choi et al., 2006b; Tsukamoto et al., 2003, 2007; Westaway, 2009).
- When luminescence investigations of K-feldspar separates from Moche Borago were undertaken, the blue TL and IRSL emissions, isolated using the standard blue filter combination (BG39 + Kopp 7-59), produced the brightest measured signal. All subsequent measurements were performed using this filter combination.
- The TL signal of natural aliquots of K-feldspar displayed two distinguishable humps/peaks at ~310°C and ~480°C, and did not begin increasing above background until ~200°C. The TL glow curves for laboratory-irradiated aliquots possessed one broad TL peak, extending from ~100°C to ~400°C, centred on ~230°C. The large peak in the laboratory-irradiated TL signal was shown to have a large, thermally unstable component in the low-temperature region. The TL signal in the region of ~350°C was inferred to be roughly analogous to the optically insensitive 350°C TL peak observed for samples from Mumba.
- No discrete association could be made between the TL and IRSL signals for K-feldspars from Moche Borago, as was feasible for Mumba. Results suggest, however, that the IRSL may be associated with the lower temperature region of the TL signal.
    - Pulsed anneal experiments were inconclusive, resulting in two different possible relationships between preheat temperature and IRSL intensity. First, the IRSL signal could mostly be removed by heating up to ~300°C, indicating that the low-temperature region of the TL signal was associated with IRSL production. Second, the IRSL signal could be removed by heating over the temperature range ~220°C to 400°C. The

- In laboratory-irradiated aliquots, an IR stimulation was shown to remove the TL signal from low temperatures (<100°C) up to approximately 370°C. This suggests that the IRSL signal from Moche Borago K-feldspars is associated with a lower temperature region of the TL curve (i.e., below 370°C) than is the IRSL signal from Mumba.

- The thermally unstable, low-temperature TL component that may be associated with IRSL production was present in laboratory-irradiated aliquots but not in the natural signal. This necessitated the use of a high-temperature preheat (i.e., 260°C for 60 s) to remove the low-temperature, thermally unstable TL signal, so that accurate comparisons of the IRSL signal induced by natural and laboratory irradiations could be made.
- The IRSL signal was shown to be dependent on stimulation temperature.
  - The measured IRSL output was shown to increase as stimulation temperature was increased from 50°C to 350°C. For temperatures above 200°C, a large isothermal TL signal, which attained maximum intensity at 350°C, was shown to underlie the IRSL signal. When this signal was taken into account and subtracted, the true IRSL signal was shown to increase with stimulation temperature up to 300°C.
  - These results indicated that 200°C was the highest IR stimulation temperature that could be used for K-feldspars from Moche Borago, to avoid the inclusion of any unwanted isothermal TL in the measured IRSL signal. Therefore, all post-IR IR stimulations were performed at 200°C, instead of the often used temperature of 225°C, to avoid including the isothermal TL signal.
  - In contrast to the results from Mumba, the shape of the isothermal TL-subtracted IRSL decay curve was shown to stay relatively constant as the IR stimulation temperature was increased from 50°C to 400°C.
- Various IR stimulation conditions were tested to see if a given dose could be recovered:

- All aliquots recovered the given dose at 1σ or 2σ. However, as the stimulation temperature was increased from 50°C to 200°C (including the post-IR IR stimulation at 200°C) the measured/given dose ratio increased systematically from ~0.95 to ~0.99.
- As the IR stimulation temperature was increased from 50°C to 200°C (including the post-IR IR stimulation at 200°C), the recuperation value decreased from ~11% to ~5%.
- All aliquots, aside from one, regardless of stimulation temperature, recycled a duplicate dose within 1σ experimental error. This indicated that the SAR procedure could adequately correct for sensitivity changes and that the standard anomalous fading measurement procedure (see Section 7.6.2.1) should be applicable for K-feldspar from MB3.
- As a caveat, this experiment was performed using aliquots that had previously been annealed. Consequently, the results of this experiment may have limited applicability to natural aliquots.

- Anomalous fading was shown to affect MB3 to a far greater extent than samples from Mumba.
  - Anomalous fading was shown to affect the intensity of the TL curve up to a temperature of at least ~490°C.
  - The IRSL signal was shown to fade significantly. The fading rate of MB3 for all stimulation temperatures was approximately four times that of the IRSL signal measured at 50°C for samples from Mumba. However, the fading rate for MB3 was shown to decrease by ~43% as the IR stimulation temperature was increased from 50°C to 200°C.
- Although D_e values could be estimated for K-feldspars of MB3 using the SAR procedure, they are unlikely to be reliable indicators of the burial dose, due to the high fading rate and the differences in shape of the IRSL decay curves induced by natural and laboratory irradiations. The fading-uncorrected age calculated for MB3 should be regarded as a minimum estimate, given the caveats pertaining to the D_e and the unusually high fading rates measured for K-feldspars of MB3.

The differences in luminescence properties and behaviours of K-feldspar separates from Moche Borago and Mumba are likely to be the result of differences in the geological origin of the minerals. The volcanic origin of the sediments at Moche Borago may be the reason for their unusually high fading rates. The ambiguity of many of the observed luminescence behaviours, the abnormally high fading rates, and concerns over the reliability of D_e estimates obtained using the SAR procedure, prohibit accurate age estimation using K-feldspar from Moche Borago.

Chapter 10: Discussion: a synthesis of available archaeological and palaeoenvironmental records

Reliable OSL and IRSL chronologies were obtained for Mumba rockshelter, which is one of the few sites in East Africa that contains both MSA and LSA artefacts in its archaeological assemblage. More noteworthy than the 'MSA' or 'LSA' designations, are the characteristics and changes of the stone artefact assemblages from unit to unit. Thus, rather than being re-defined as 'LSA', the significance of the assemblage from Bed V is that it contains the first microlithic backed pieces (including geometric backed pieces), ostrich eggshell (OES) beads and ochre at Mumba. This industry replaced the point-based Kisele MSA toolkit present in Bed VIA. Differences and similarities between the toolkits of the two levels may be indicative of changes in technology and, thus, people, ideas and behaviours over time (Foley and Lahr, 2003). The luminescence chronology that has been described in this thesis can now be used to constrain the timing of technological and behavioural changes in the archaeological sequence of Mumba.

The inability to obtain reliable OSL or IRSL ages for samples from Moche Borago was unfortunate. As a result, the archaeological sequence from the site remains temporally unconstrained by luminescence methods, and the toolkits from Moche Borago cannot be compared with other, concomitant technologies. Likewise, changes in technologies and behaviours in the sequence cannot be interpreted in the context of temporally constrained palaeoclimatic and demographic reconstructions. Moche Borago will, therefore, no longer be considered for discussion in this chapter.

The first section of this chapter (Section 10.1) will be a discussion of the existing literature of the Late Pleistocene East African climate. The second section (Section 10.2) will discuss how demographic change can instigate changes in technology and behaviour. The existing genetic evidence for past population expansions and migrations will also be included. The third section (Section 10.3) will discuss the major implications of the revised chronology for Mumba for the MSA and LSA archaeological record of East Africa. Potential links between demographic and climatic change will also be discussed. Finally, these lines of evidence will be synthesised in the final section (Section 10.4) for a discussion of the timing of, and potential reasons for, changes in technology and behaviour in East Africa.

10.1 Climate of East Africa

10.1.1 Overview

The African climate can be broadly separated into zones with varying seasonal precipitation patterns (Nicholson, 2000; Gasse, 2000). The most northerly and southerly zones exhibit a Mediterranean summer-dry climate. The majority of precipitation is received during winter, as a result of the displacement of the mid-latitude westerlies towards the equator (Chase and Meadows, 2007). In southern Africa, this zone is referred to as the Winter Rainfall Zone (WRZ). In both the north and the south, the zone of winter rainfall is flanked by subtropical arid deserts: the Sahara in the north, and the Namib and Kalahari in the south (Gasse, 2000).

The tropical East African climate is complex and is influenced by multiple weather systems (Nicholson, 2000; Tierney and Russell, 2007; Trauth et al., 2009). It has traditionally been thought that the tropical African climate is mainly governed by the position of the Intertropical Convergence Zone (ITCZ), the 'meteorological Equator' (Gasse, 2000), which is effectively the ascending limb of Hadley circulation. This tropical overturning circulation is driven by solar heating of air at the Equator, causing it to rise. At the tropopause, the air turns and flows poleward until the subtropics are encountered (approximately 30°N and 30°S), where it descends and flows towards the Equator, causing the 'trade winds'. The rising air of the ITCZ results in the convective activity of thunderstorms, resulting in precipitation. The position of the ITCZ varies over the course of the year, tracking the position of most intense summer solar heating. Thus, the belts of land at the northern and southern range of the ITCZ migration have climates dominated by summer monsoonal rains and winter drought. The area between the limits of the ITCZ receives two rainfall maxima each year as the ITCZ migrates back and forth. Many studies have suggested that millennial-scale changes in the mean position of the ITCZ were one mechanism that drove climatic variability during the Late Pleistocene (Tierney and Russell, 2007; Scholz et al., 2007; Carto et al., 2009).

Additional variability in the East African climate results from Walker Circulation, such as the El Niño-Southern Oscillation (ENSO) (Gasse, 2000; Nicholson, 2000; Masline and Christensen, 2007), the position of the Congo Air Boundary (Tierney et al., 2011) and the intensity of the Indian monsoon (Tierney and Russell, 2007;

Tierney et al., 2008, 2011; Trauth et al., 2010). Tierney et al. (2008) used sediment records from Lake Tanganyika to associate periods of changing precipitation with isotopic records of changes in the Asian monsoon in China (Wang et al., 2001; Yuan et al., 2004). During the "El Niño-like" phase of ENSO, the ITCZ is shifted in a southerly direction (Koutavas et al., 2002), the Indian monsoon is influenced due to modified Walker Circulation over the Indian Ocean (Tierney and Russell, 2007), and arid conditions intensify in areas of Africa (Masline and Christensen, 2007).

Studies have also linked the position of the ITCZ and the intensity of the Indian/African monsoon to glacial/interglacial cycles (Carto et al., 2009). The LGM, for example, has been characterised throughout various East African climate archives as being cold and dry (Shanahan and Zreda, 2000; Gasse, 2000; Johnson et al., 2002; Barker et al., 2003; Zech, 2006; Felton et al., 2007; Basell, 2008; McGlue et al., 2008; Tierney et al., 2008). In addition, the Northern Hemisphere Heinrich Events appear to be synchronous with increased aridity and lake desiccation in East Africa as a result of a reduced monsoon intensity, reduced sea surface temperatures, or shifts in the position of the ITCZ (Scholz et al., 2003; Lamb et al., 2007; Tierney and Russell, 2007; Tierney et al., 2008, 2011; Carto et al., 2009; Stager et al., 2011). Heinrich Events result from abrupt reductions in Meridional Overturning Circulation ('thermohaline circulation') due to injections of freshwater into the North Atlantic.

The climate of East Africa is characterised by seasons of monsoonal rain alternating with seasons of drought. Most current research suggests that the climate of tropical East Africa is generally governed by the position of the ITCZ and the intensity of the Indian monsoon, although the dynamics of large-scale Late Pleistocene changes in precipitation are incompletely understood. Changes in East African precipitation also appear to be synchronised with MIS stages and Northern Hemisphere Heinrich Events.

10.1.2 Archives of East African palaeoclimates

Lake cores are the main archives used to reconstruct palaeoclimatic conditions in East Africa (e.g., Gasse, 2000; Barker et al., 2003; Scholz et al., 2003, 2007; Tierney et al., 2008). However, several features of lake records make them questionable as unambiguous palaeoclimate proxies. First, a recent study by Bergner et al. (2009) has demonstrated that changes in lake level and hydrochemistry do not necessarily represent

climatic changes. Instead, they may result from ongoing tectono-magmatic and geomorphic processes in the East African Rift Valley, resulting in changes in rainfall amount and distribution, catchment size and runoff routes.

Second, lake records differ widely between East African lakes over relatively short distances (Tryon et al., 2010). For example, Scholz et al. (2007) examined continuous sediment-cores from Lake Bosumtwi in Ghana, and Lakes Malawi and Tanganyika in East Africa. They identified coincident periods of drastically reduced lake-levels between ~135 and 127 ka, ~110 and 85 ka, and ~78 and 74 ka, and concluded that they were driven by regional changes in precipitation and evaporation, and not by tectonic activity or groundwater seepage. In contrast, Bergner et al. (2009) identified diatomite beds associated with volcanic tuffs dated to ~141 to ~112 ka in the Lake Nakuru, Elmenteita and Naivasha basins, suggesting episodes of lake highstands. In the Lake Naivasha basin, diatomite beds associated with ages of ~110 and ~85 ka, provide evidence for additional highstands (Trauth et al., 2003; Bergner et al., 2009). Discrepancies of this type suggest that the climates of different regions of East Africa may have responded differently to Late Pleistocene climatic changes (Clement et al., 2004; Scholz et al., 2007; Bergner et al., 2009; Tryon et al., 2010).

Third, age models used to date events in lake cores often lack robustness beyond the range of radiocarbon dating. For example, at least 15 calibrated ^{14}C ages were used to construct the Malawi Drilling Project age model used by Scholz et al. (2007) for core-sediments younger 50 ka. By contrast, the age model, which includes no estimated uncertainty, for core-sediments between 50 and 150 ka, is based on a linear regression fitted to two OSL, one inclination and six palaeointensity and ^{10}Be ages. Similarly, the age models of Barker et al. (2003), Scholz et al. (2003) and Felton et al. (2007) are based on multiple ^{14}C ages that are fitted with regressions that are extrapolated to obtain older ages (see Table 10.1).

Other archives, such as glaciations on Mt. Kenya dated by *in situ* cosmogenic ^{36}Cl measurements of boulders on moraines (Shanahan and Zreda, 2000), palaeopedological studies on Mt. Kilimanjaro (e.g., Zech, 2006) and climate modelling (e.g., Carto et al., 2009), can also be used to assess past climatic conditions. Unfortunately, no definitive link has been established between high latitude and tropical East African climatic conditions, complicating the use of high-resolution ice-core

records (e.g., NGRIP, 2004; EPICA, 2006) as East African palaeoclimatic proxies. Additionally, speleothem-derived palaeoenvironmental records from East Africa for this time period are non-existent. The closest speleothem records are from Botswana (Holmgren et al., 1995), northeast South Africa (Holzkämper et al., 2009), the Levant (e.g., Bar-Matthews et al., 2000, 2003; Almogi-Labin et al., 2009; Vaks et al., 2007, 2010) and Arabia (Fleitmann et al., 2003, 2011). Lake cores, therefore, are currently the best palaeoclimate archive available for the region. The study of sediment cores from Lake Malawi and Tanganyika by Scholz et al. (2007), despite its imprecise temporal constraints beyond 50 ka, provides one of the only continuous records of climate change between 150 and 0 ka in East Africa.

An additional source of East African palaeoclimatic information comes from the eastern Mediterranean. It has been shown that the output of the Nile River and the climate of the Levant are influenced by the position of the ITCZ and by African monsoons (Rossignol-Strick, 1983; Fleitmann et al., 2003; Revel et al., 2010; Vaks et al., 2010). The palaeoclimate of these regions can, thus, be used as a proxy for precipitation levels in East Africa. Unlike East Africa, there are many palaeoclimate archives available in the eastern Mediterranean, including high-resolution speleothems (Bar-Matthews et al., 2000, 2003; Almogi-Labin et al., 2009; Vaks et al., 2010) and marine cores (Revel et al., 2010).

10.1.3 Late Pleistocene climate reconstructions

There are few archives with continuous palaeoclimatic records that span the past 70 to 125 ka. It is, therefore, necessary to rely on a compilation of reconstructions from a variety of archives and regions. Figure 10.1 presents a compilation of palaeoclimate reconstructions that have implications for precipitation levels in East Africa during the transition from MSA to LSA toolkits at Mumba (MIS 4 and 3). Table 10.1 lists the study locations, proxies and details of the constructed age models for each reconstruction shown in Figure 10.1. The records include lake-core, marine-core, speleothem and palaeosol records from East Africa and from the eastern Mediterranean.

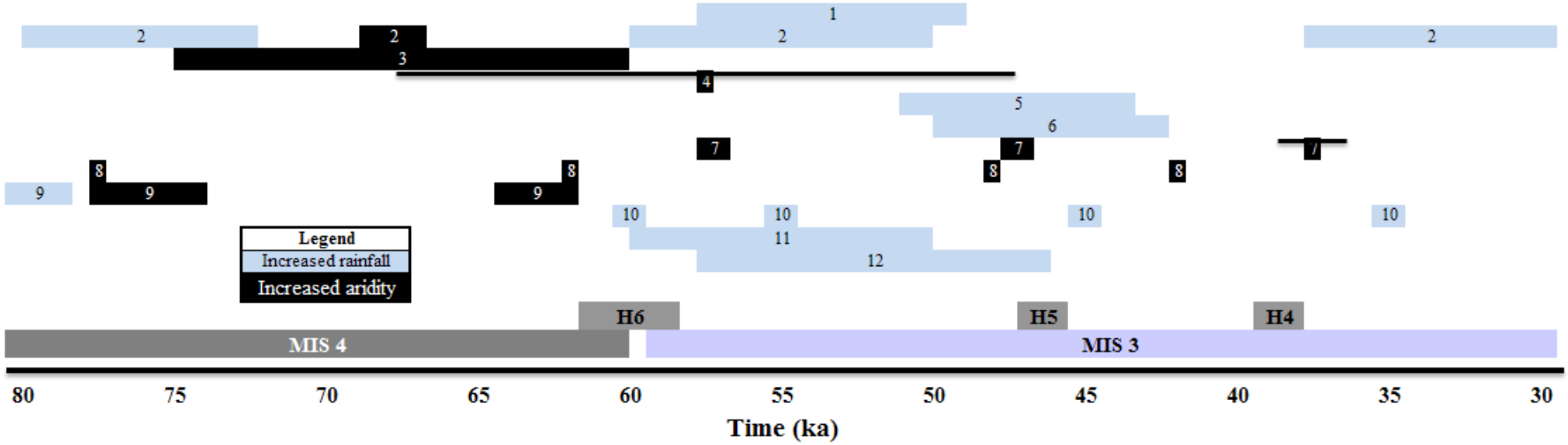

Figure 10.1: Compilation of palaeoclimate reconstructions with implications for precipitation in East Africa. Reconstructions are based on a variety of methods and proxies from eastern Africa and the eastern Mediterranean (see Table 10.1 for more information). Each number corresponds to the following studies: 1, Almogi-Labin et al. (2009); 2, Revel et al. (2010); 3, Reichart et al. (1998); 4, Zech (2006); 5, Holmgren et al. (1995); 6, Barker et al. (2003); 7, Tierney et al. (2008); 8, Scholz et al. (2003); 9, Scholz et al. (2007); 10, Tierney et al. (2010); 11, Felton et al. (2007); 12, Holzkämper et al. (2009). H6, H5 and H4 correspond to Heinrich Events 6, 5 and 4, respectively, as recorded in Hulu Cave (Wang et al., 2001). Most chronologies are based on age models and are described in Table 10.1. Error bars, where available, indicate 1σ.

Table 10.1: Study location, proxies, and description the chronology of each palaeoenvironmental study illustrated in Figure 10.1

Study	Proxy	Location	Description of age model
Holmgren et al. (1995)	Speleothem	Botswana	$^{230}Th/^{234}U$-dating of speleothem
Reichart et al. (1998)	Marine core	Arabian Sea	Correlated $\delta^{18}O$ record to $\delta^{18}O$ time series of Lourens et al. (1996). Calibrated AMS ^{14}C ages supplement the $\delta^{18}O$ record.
Barker et al. (2003)	Lake core	Lake Massoko, Tanzania	Linear regression fitted to 31 calibrated AMS ^{14}C ages up to ~35 cal ka BP (Gilbert et al., 2002).
Scholz et al. (2003)	Lake core	Lake Tanganyika	Least-squares linear regression ($R^2 = 0.9884$) fitted to 11 ^{14}C ages from 2.87 ± 0.06 cal ka BP to 45 ± 2 ka BP (only ages below 20 ka were calibrated). The model was extrapolated to a basal age of ~89 ka
Zech (2006)	Palaeosol	Mt Kilimanjaro, Tanzania	^{14}C chronology. Conventional ages younger than 17 ka BP were calibrated.
Felton et al. (2007)	Lake core	Lake Tanganyika	Linear regressions ($R^2 = 0.94$) fitted to eight and nine calibrated AMS ^{14}C ages. The linear regression for the older portion of the age model (constructed using nine ages) was extrapolated to estimate ages lower down the core.
Scholz et al. (2007)	Lake core	Lake Malawi	Below 50 ka, 15 calibrated ^{14}C ages were used to construct the age model. From 50 to 150 ka, a linear regression was fitted to two OSL, one palaeomagnetic inclination and six palaeomagnetic palaeointensity and ^{10}Be ages
Tierney et al. (2008, 2011)	Lake core	Lake Tanganyika	Regression fitted to 26 calibrated AMS ^{14}C ages from 1.45 ± 0.05 to 45 ± 0.4 cal ka BP.
Holzkämper et al. (2009)	Speleothem	northeastern South Africa	Th/U-dating of speleothem
Almogi-Labin et al. (2009)	Marine records and Speleothem	Eastern Mediterranean and Levant	Correlated $\delta^{18}O$ and $\delta^{13}C$ records from Soreq Cave speleothems with marine records. Calibrated AMS ^{14}C ages were also used to construct chronology.
Revel et al. (2010)	Lake core	Eastern Mediterranean	Constructed using 17 calibrated AMS ^{14}C ages, sapropel ages (Kallel et al., 2000) and the oxygen isotope record.

10.1.3.1 MIS 5a (85–74 ka)

Severe reductions in lake-level and concurrent increases in desertification prior to MIS 5a, have been identified from investigations of sediment records from Lake Malawi. These 'megadroughts' occurred between 135 and 127 ka (the height of the MIS 6 glacial) and between 110 and 85 ka (Scholz et al., 2007; Cohen et al., 2007). Subsequently, during MIS 5a (~85–74 ka), the level of Lake Malawi increased (Scholz et al., 2007). Higher East African lake levels during the MIS 5a interglacial are concurrent with increased sea levels, which were near or above modern-day levels (Hearty, 1998; Coyne et al., 2007; Dorale et al., 2010).

The African monsoon was also strengthened during this period. Revel (2010), investigating Nile River delta sediment records, identified a pluvial period (associated with a strengthened East African monsoon) from 98 to 72 ka. These ages are associated with sapropels, dated by correlating planktonic foraminiferal $\delta^{18}O$ records with the SPECMAP stack (Martinson et al., 1987) described by Kallel et al. (2000). Fleitmann et al. (2003), investigating speleothems from Oman dating by U-series, reported that rapid speleothem deposition occurred during MIS 5a (between 82 ± 2 and 78 ± 3 ka), indicating increased rainfall.

10.1.3.2 MIS 4 (74–60 ka)

Palaeoclimate archives from the eastern Mediterranean and Arabia indicate that MIS 4 was extremely arid (Reichart et al., 1998; Leuschner et al., 2004; Revel et al., 2010; Fleitmann et al., 2011). Revel et al. (2010) suggest that the reduction in precipitation was the result of a weakened East African monsoon. Geochemical studies of sediment cores from Lake Nkunga in Kenya (Ficken et al., 1998), and sediment cores from Lake Tanganyika (Scholz et al., 2003) and Lake Malawi (Scholz et al., 2007) indicate that lower lake levels and more arid conditions prevailed in East Africa for at least some of the period between 70 and 60 ka. Scholz et al. (2007) also reported a period of East African megadrought in early MIS 4, between 78 and 74 ka.

10.1.3.3 MIS 3 (60–24 ka)

The transition from MIS 4 to MIS 3 is clearly seen in interpretations of Nile River hydrology (and, thus, East African rainfall) from eastern Mediterranean marine

cores. Revel et al. (2010) interpreted 60 to 50 ka interval as representing a period of increased African monsoon intensity, bringing wetter conditions to East Africa and, thus, increasing the flow of the Nile River. Increased precipitation at the beginning of MIS 3 is corroborated by the East African lake-core records (e.g., Felton et al., 2007; Tierney et al., 2010) and speleothem records from northeast South Africa (Holzkämper et al., 2009).

Speleothem records from Botswana suggest that the period from 51 to 43 ka was wetter and warmer than the cooler and drier period between 27 and 21 ka (Holmgren et al., 1995). Likewise, Barker et al. (2003), investigating sediment archives from Lake Massoko, concluded that lake levels were generally high, due to wetter conditions between 50 and 42 ka. Between 42 ka and the LGM, lake levels were highly variable, with evidence for a drier climate than from 50 to 42 ka (Barker et al., 2003). They concluded that Lake Massoko was very low, and that conditions were driest, during the LGM. This agrees with many other studies that have shown that East Africa was generally cold and arid during the most recent glacial period, the LGM (e.g., Gasse, 2000; Shanahan and Zreda, 2000; Johnson et al., 2002; Zech, 2006; Felton et al., 2007; McGlue et al., 2008; Tierney et al., 2008).

10.1.3.4 Millennial-scale climatic variability

From 70 ka onwards, superimposed on to these broad climatic patterns of arid glacials and wetter interglacials, there is evidence for brief and abrupt periods of climate change. Zech (2006), working on palaeosols on Mt Kilimanjaro, identified a period of increased aridity that is associated with an uncalibrated radiocarbon age of 57 ± 9 ka BP, and likely represents a minimum estimate. He suggested that it may be related to Heinrich Event 6 (~60 ka). Likewise, Tierney et al. (2008) identified periods of abrupt and brief aridifications in sediment cores from Lake Tanganyika, the age model of which was generated using a regression constructed from 26 AMS ^{14}C ages from 1.45 ± 0.05 cal ka BP to 45 ± 0.4 cal ka BP. While two of these events are estimated to have occurred at ~57 and ~47 ka, Tierney et al. (2008) explicitly states that "our age control is not sufficient to constrain their timing." However, based on a well-constrained period of aridification identified at 37.3 ± 0.9 cal ka BP that corresponds with Heinrich Event 4, they interpreted the other periods of abrupt aridification as corresponding with

Heinrich Events 6 and 5. Evidence for brief and abrupt aridification and reduced monsoon intensity in Africa related to Heinrich Events is also provided by Holmgren et al. (1995), Scholz et al. (2003), Tierney and Russell (2007), Lamb et al. (2007), Carto et al. (2009), Stager et al. (2011) and Tierney et al. (2011).

10.1.3.5 Summary

Our current understanding of the spatial and temporal effects of climate change in Late Pleistocene East Africa is incomplete (Tryon et al., 2010). In addition, the imprecise temporal constraints beyond the range of ^{14}C dating on lake-core records and the lack of speleothem records from East Africa limit the resolution of Late Pleistocene climate reconstructions. However, by piecing together results from studies using different methods and archives, including continuous lake-core records (e.g., Barker et al., 2003; Scholz et al., 2003, 2007; Felton et al., 2007; Tierney et al., 2008, 2010), modelling studies (e.g., Carto et al., 2009), speleothem records from southern Africa (e.g., Holmgren et al., 1995; Holzkämper et al., 2009), and speleothem and marine records from the eastern Mediterranean (e.g., Almogi-Labin et al., 2007; Revel et al., 2010), a broad picture of palaeoclimatic patterns in East Africa can be developed (Figure 10.1). The picture that emerges suggests considerable variations over the Late Pleistocene, broadly coincident with glacial cycles. East Africa likely experienced a period of increased humidity during MIS 5a (Scholz et al., 2007; Revel et al., 2010). There is then evidence that suggests that more arid conditions prevailed in East Africa during MIS 4 (Ficken et al., 1998; Scholz et al., 2007; Revel et al., 2010), which gave way to more humid and favourable conditions during MIS 3 (Felton et al., 2007; Revel et al., 2010; Tierney et al., 2010). Superimposed on these broad climatic patterns, there is evidence for brief but abrupt shifts in climate during MIS 4 and 3, concurrent with Northern Hemisphere Heinrich Events (Tierney and Russell, 2007; Brown et al., 2007; Castañeda et al., 2007; Tierney et al., 2008; Carto et al., 2009). Thus, MIS 3 is characterised as a period of generally more favourable climatic conditions, with ephemeral pulses of aridity. The LGM is characterised by widespread aridification of much of sub-Saharan Africa.

10.2 Evidence for Late Pleistocene demographic change

10.2.1 Demographic change as a driver of cultural change

Much recent archaeological research and theory has focused on the role of demographic change as the stimulus for changes in technology and behaviour, especially the expression of 'modern' behaviour (e.g., Henshilwood and Marean, 2003; McBrearty, 2007; Kuhn and Stiner, 2007; Jacobs et al., 2008a; Jacobs and Roberts, 2009; Zilhão et al., 2010; Nowell, 2010). Studies by Shennan (2001) and Powell et al. (2009) have modelled the development and transmission of cultural innovation as a function of population size, density and mobility. Both studies demonstrated that, as population size increases, innovations are more likely to appear, be maintained, and proliferate. Powell et al. (2009) concluded that increased migratory activity (i.e., increased social interaction) between populations can have the same effect as increased absolute population size. In both cases, the mean skill level of the population increases.

It has also been demonstrated that decreases in population size or migratory activity can have deleterious effects on a population's technological complexity. Henrich (2004) developed a model to describe the loss of cultural complexity in Tasmania. He modelled the loss of 'cultural capital' (e.g., technological and social complexity) and reductions in population density and connectedness, concluding that complex skills are preferentially lost as these two factors decrease. This model is supported by the results of several studies (e.g., Riede, 2009; Kline and Boyd, 2010). Kline and Boyd (2010) investigated the technological complexity of island populations in Oceania around the time of European contact. They found that islands with smaller populations had less complicated marine foraging technologies than did those with larger populations. Riede (2009) used three case studies from the European UP and Mesolithic to associate decreasing population size with the loss of cultural complexity. He cited the abrupt shift from a complex, stylised microlithic toolkit to one that was more crude, less standardised, and macrolithic during the Irish Mesolithic. Environmental change was hypothesised to be the stimulus for demographic change. Riede (2009: 309) stated that "demography is the middle-range link between climatic changes and both biological and cultural evolutionary trajectories of human populations", echoing Mandryk (1993: 67) who stated that, "although ultimately environmentally driven, the operative factor resulting in cultural failure is social."

In regards to Pleistocene populations, Kuhn and Stiner (2007) convincingly discuss the proliferation of body ornaments (e.g., beads) during the later MSA and UP as a means of broadcasting social information to strangers who would be increasingly encountered when population density increases. Likewise, Nowell (2010) has suggested that climatic amelioration following MIS 4 resulted in population growth, increasing contact and exchange networks between populations. This encouraged the development of technological and social innovations and eventually led to the European UP. In southern Africa, two early examples of ornaments and other technological and behavioural innovations occur in the Still Bay and Howiesons Poort Industries. It has recently been suggested that these brief periods of technological and social ingenuity were the result of demographic changes (Jacobs et al., 2008a; Jacobs and Roberts, 2009), possibly in response to environmental factors (Chase, 2010). Zilhão et al. (2010) describe two Iberian sites associated with Neanderthals that contain pigment-coated shell beads dated to 50 ka – the same kind of artefacts cited as evidence for behavioural modernity of modern humans in northern and southern Africa (e.g., Henshilwood et al., 2004; Bouzouggar et al., 2007; d'Errico et al., 2009). They conclude that the capacity for 'modern' behaviour is not limited to humans with modern anatomy, and that these behaviours were expressed as a result of increases in population size and social complexity.

It is clear that there is ample theoretical and empirical foundation for associating changes in technology and behaviour with changes in human demography. Population expansions can be identified by investigating occupational intensification, changes in diet, and site distributions (e.g., Barut, 1994; Kuhn and Stiner, 2007; Basell, 2008). As discussed in the following section, genetic studies of modern humans from various populations can also be used to infer expansions, reductions, and divergences of past populations.

10.2.2 Genetic evidence for demographic changes.

Cann et al. (1987) were the first to show that DNA from modern human populations can be used to infer the demographic histories of ancestral populations, initiating a new field of research into human evolution. While genetic studies have been informative about past population dynamics, they are often problematic and

controversial (Mellars, 2006; Endicott et al., 2009). Endicott et al. (2009) point out that most mitochondrial DNA (mtDNA) studies rely on mutation rate estimates that use the human/chimpanzee divergence as a calibration reference. They then demonstrate that two assumptions of this calibration are not unequivocally valid: 1) that the human/chimpanzee divergence occurred ~6 Ma ago, and 2) that the molecular evolutionary process has proceeded in a homogeneous, neutral, 'clocklike' manner since the human/chimpanzee divergence. They also demonstrate that the common use of the *rho* summary statistic can lead to biased molecular age estimates. Additional ambiguities in interpreting DNA studies arise from debates regarding the mutation rates, effects of natural selection on genes, and complications of past dispersals, back migrations, and bottlenecks (Excoffier and Schneider, 1999; Mellars, 2006; Endicott et al., 2009). Excoffier and Schneider (1999) showed that more recent population bottlenecks can erase any signs of previous population expansions.

Despite these shortcomings, genetic studies still contribute greatly to the study of human evolution by providing evidence of population expansions, contractions, isolations and migrations of Pleistocene populations. Broadly speaking, most DNA evidence is in agreement with the archaeological and palaeoanthropological evidence (White et al., 2003; McDougall et al., 2005, 2008), suggesting that anatomically modern humans arose between ~200 and ~150 ka ago (Maca-Meyer et al., 2001; Gonder et al., 2007; Atkinson et al., 2008, 2009). There is evidence that modern humans were not part of a panmictic population during the Late Pleistocene, however, instead living in geographically and genetically isolated populations (Watson et al., 1997; Knight et al., 2003; Garrigan et al., 2007; Campbell and Tishkoff, 2008; Behar et al., 2008). For example, Quintana-Murci et al. (2008) has demonstrated that the pygmy hunter-gatherers of central Africa diverged from ancestral modern human populations ~70 ka ago.

Although the specific demographic changes within Africa remain unclear, modern human populations expanded and dispersed during the mid- and later-Late Pleistocene. Many studies have identified a significant expansion of the L3 superhaplogroup, although estimates of the timing of the expansion range from ~85 to ~55 ka ago (Watson et al., 1997; Maca-Meyer et al., 2001; Forester and Matsumura, 2005; Macaulay et al., 2005; Atkinson et al., 2009). Similarly, estimates of the

expansion of haplogroup M (derived from superhaplogroup L3) range from ~70 to ~50 ka ago (Quintana-Murci et al., 1999; Macaulay et al., 2005; Hudjashov et al., 2007; Atkinson et al., 2008). These age estimates for the expansion and divergence of haplogroups within the L3 superhaplogroup are especially important for discussions about dispersals of modern humans out of Africa, since L3 is the largest superhaplogroup within Africa and is the only superhaplogroup with lineages represented outside Africa. Thus, the L3 superhaplogroup most likely evolved in Africa and then dispersed from Africa after a population expansion, giving rise to the M and N haplogroups. This is supported by DNA evidence for accelerated growth of modern human populations in southern Asia (~52 ka), Australia (~48 ka) and Europe (~42 ka) (Atkinson et al., 2008), each of which carry a lineage derived from the L3 superhaplogroup.

The amalgamated picture from the literature is one of modern humans emerging ~200 ka ago, possibly in East Africa, where the oldest *Homo sapiens* fossils have been recovered (White et al., 2003; McDougall et al., 2005, 2008). People may have lived in geographically isolated populations during much of the Late Pleistocene. There is then evidence for expansions in certain populations, most notably the population that was ancestral to the modern day L3 superhaplogroup, some time between MIS 5a and 60 ka (Watson et al., 1997; Maca-Meyer et al., 2001; Forester and Matsumura, 2005; Macaulay et al., 2005; Atkinson et al., 2009).

10.3 Integrating the MSA and LSA records at Mumba into a regional context

The OSL chronology for the deposits at Mumba provides temporal constraints on the archaeological sequence. These constraints allow appropriate comparisons to be made between these assemblages and those from other sites in the region, enabling an assessment of temporal and spatial distributions of changes in technology and behaviour. In this framework, three features of the archaeological sequence at Mumba merit further discussion. First, the presence of obsidian from distant sources in the MSA and LSA deposits at Mumba is discussed, along with the associated implications for the existence of regional exchange networks. Second, the transition from a typical MSA toolkit in Bed VI to a backed piece-based toolkit in Bed V is discussed and compared to other sites that exhibit similar technological transitions. Third, the

emergence and proliferation of symbolic ornamentation at Mumba and other East African LSA sites is discussed.

10.3.1 Distant raw material transportation: evidence for regional exchange networks

The distance between a raw material source and the site of deposition of an artefact from that source has been used as an indicator of foraging range, special procurement journeys, long distance trade and extended social networks (Ambrose and Lorenz, 1990; Deacon and Wurz, 1996; Wurz, 1999, 2000; Ambrose, 2002, 2006, 2010; Marwick, 2003; Minichillo, 2006). In cases where obsidian is the raw material in question, analysis of an artefact's chemical composition can be used to identify the source outcrop from which it originated (e.g., Merrick and Brown, 1984; Merrick et al., 1994), providing a minimum distance that the lithic travelled from procurement to disposal. The obsidian artefacts found in Beds VIB, VIA, V and III at Mumba were sourced to outcrops in the Lake Naivasha region of southern Kenya, approximately 320 km NE of Mumba (Figure 10.2) (Merrick and Brown, 1984; Mehlman, 1989). These artefacts were deposited at Mumba from before 74 ± 4 ka to 37 ± 3 ka: a long period of time that spans the various climatic conditions of MIS 5, 4 and 3.

There are two plausible explanations for the presence of distant obsidian in assemblages at Mumba. First, the occupants of Mumba may have had a highly mobile, nomadic lifestyle, moving widely over the landscape and allowing them to directly procure obsidian from southern Kenya. However, ethnographic data from 70 hunter-gather cultures, compiled by Kelly (1983, 1995), indicated that the maximum, mean and modal territory radii were 140, 32 and 15 km, respectively. It should be noted, moreover, that the only cultures that approached the maximum territory distance were from Arctic regions, and some of these cultures employed horse transportation (Marwick, 2003). This estimate of a mean territorial distance is supported by Ambrose (2002, 2010), who wrote that the maximum diameter of hunter-gatherer home ranges, and, thus, a distance that may reflect direct procurement of a raw material, is approximately 40–45 km. Thus, if the territory of Mumba's MSA and LSA occupants included the southern Kenyan obsidian sources, it implies that their home ranges were five times larger than the maximum territory size observed ethnographically. While this

scenario is possible, the available evidence suggests that a source located over 300 km away would very likely lie beyond the foraging range of a hunter-gatherer group's territory (Merrick et al., 1994; Kelly, 1983, 1995).

A more likely explanation for the presence of the obsidian from distant sources at Mumba is exchange. Two lines of evidence support this explanation. First, when ethnographic data regarding raw material transport distances are examined, it is clear that a source-to-use distance of 320 km would likely result from exchange. Feblot-Augustins and Perlés (1992) reported that, while movements of 100 km may be within the range of intentional ventures of mobile foraging groups, raw materials transported over 300 km resulted from exchange between groups. Wobst (1976) reported that the maximum distance observed between groups involved in closed-system marriage networks was 300 km. Merrick et al. (1994) concluded that the transfer of raw materials over distances of more than 140 km suggests the existence of exchange networks.

The second line of evidence in support of exchange is the substantial body of evidence for large transport-distances of obsidian at other East African MSA sites (e.g., Merrick and Brown, 1984; Merrick et al., 1994). A map showing the locations of MSA and LSA archaeological sites, and the three main sources of obsidian found at these sites, is presented in Figure 10.2. Obsidian from the Kisele MSA levels at Nasera rockshelter in Tanzania were sourced from 240 km away, from Sonanchi, Eburru and Masai Gorge in Kenya (Mehlman, 1989). The MSA sites of Songhor and Muguruk contain obsidian that has been sourced from Njorowa Gorge (145 km away) and Eburru and Sonanchi (~185 km away), respectively (McBrearty and Brooks, 2000). Obsidian from the LSA Naisiusiu Beds assemblage was also traced to Sonanchi (Merrick and Brown, 1984; Mehlman, 1989). There is additional evidence for distant obsidian in the MSA and LSA assemblages at the Kenyan sites of Lukenya Hill (105–135 km transport distance), Prospect Farm (75 km transport distance), and Prolonged Drift (45–55 km transport distance), all of which are in proximity to an abundance of alternative obsidian outcrops (Merrick et al., 1994; McBrearty and Brooks, 2000). The regularity of the appearance of distantly sourced obsidian in many MSA and LSA assemblages in East Africa strengthens the hypothesis that regional exchange networks for raw materials existed in East Africa during the MSA and LSA. This conclusion is consistent with

evidence, from regional MSA site distributions (Basell, 2008) and genetic studies (Atkinson et al., 2008, 2009; Quintana-Murci et al., 2008; Behar et al., 2008), for population expansions and migrations within Africa during MIS 5.

It, thus, seems highly likely that the MSA and LSA inhabitants of Mumba who made the Sanzako, Kisele, Mumba and Nasera Industries had contact with, and/or exchanged goods and ideas with, people living in southern Kenya. This proposition is consistent with the prevalence of distant obsidian at many other MSA sites in the region. The oldest age obtained for the Kisele Industry (74 ± 4 ka), and the age of the Nasera Industry (37 ± 3 ka), provide a minimum age range for the existence of these networks at Mumba. Since no OSL samples were collected from deposits associated with the Sanzako deposits of Bed VIB, the only available age estimates for these deposits are those reported by Mehlman (1989) and discussed in Section 2.5. The available evidence suggests, therefore, that long-distance exchange networks existed across East Africa throughout at least parts of MIS 5, 4 and 3.

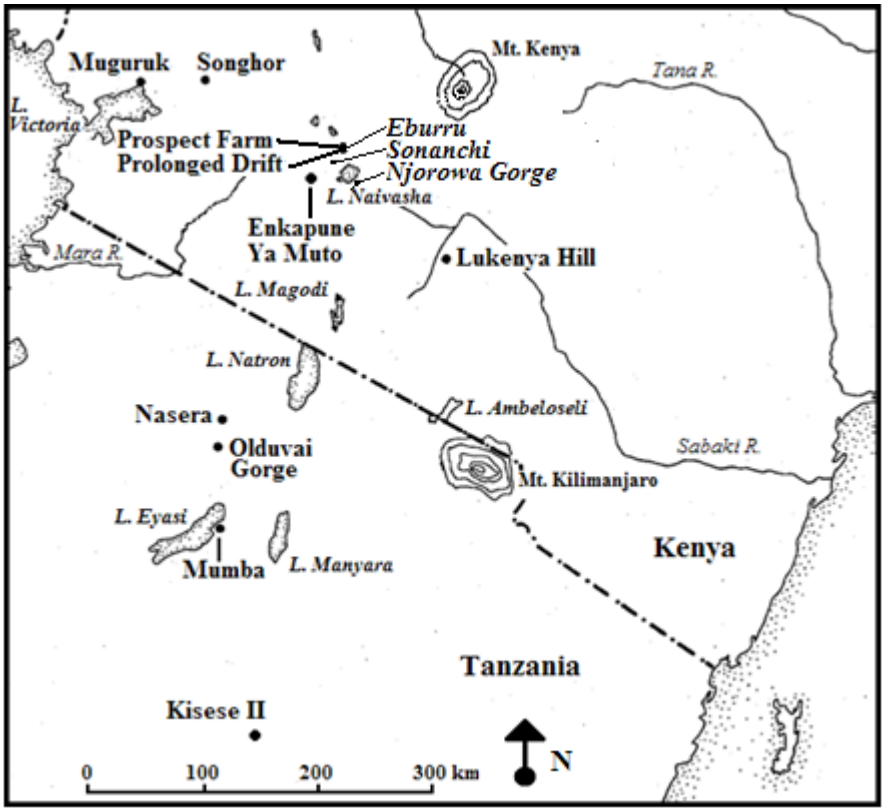

Figure 10.2: Map showing various archaeological sites that have MSA and/or LSA archaeological assemblages with obsidian from distant sources. The three main obsidian sources (Eburru, Sonanchi and Njorowa Gorge) are located around Lake Naivasha in Kenya. Map modified from Merrick and Brown (1984).

10.3.2 The MSA/LSA transition

Given the presence of typical MSA and LSA features in many 'intermediate' assemblages in East Africa, these terms may be ineffective for defining individual lithic industries in the Late Pleistocene. For the purpose of this thesis, the definition of the Mumba Industry as MSA or LSA is less consequential than the transition from the Bed VIA point-dominated Kisele Industry to the microlithic, backed piece-dominated Mumba Industry. This transition represents the MSA/LSA boundary, in the conventional parlance of the literature. Here I apply the terms MSA and LSA to Mumba in the sense defined by the most recent publication on the assemblage: Diez-Martín et al. (2009).

10.3.2.1 The emergence of backed piece-based toolkits at Mumba

The latest age obtained for deposits associated with a point-based MSA toolkit at Mumba is the upper Bed VIA age of 63 ± 6 ka. Overlying this are the 57 ± 5 ka lower Bed V deposits, which contain the earliest backed piece-based Mumba Industry assemblage. Together, these ages indicate that the inhabitants of Mumba transitioned from using a typical MSA toolkit to a more 'LSA-like' backed piece-based toolkit around 60 ka. The youngest age for the upper Bed V deposits indicate that this toolkit was still in use 49 ± 4 ka ago.

The timing of the transition from point-based to backed piece-based toolkits at Mumba is roughly synchronous with Heinrich Event 6, which also marks the transition from MIS 4 to MIS 3. This represents a major climatic transition in East Africa, from a more arid climate before 60 ka to a more humid climate afterwards (see Figure 10.1). Many authors (e.g., Henshilwood and Marean, 2003; Foley and Lahr, 2003; Mellars, 2006; McBrearty, 2007; Villa et al., 2010) have suggested that technological change is often the result of subsistence and environmental changes. Given the concurrence of technological and climatic change at ~60 ka, it is reasonable to hypothesise that favourable changes in the environment at the beginning of MIS 3 may have led to increases in human populations around Lake Eyasi, leading to increased innovations, more varied technologies and altered subsistence strategies.

10.3.2.2 Concurrent emergence of backed piece-based toolkits in East Africa

The emergence of a backed piece-based toolkit at Mumba is not an isolated occurrence. At least one assemblage in East Africa is associated with a relatively reliable chronology and may represent a potentially early occurrence of a backed piece-based toolkit, namely, the LSA assemblage of the Naisiusiu Beds at Olduvai Gorge. In addition, although it is not well temporally constrained, the Nasampolai Industry at Enkapune Ya Muto also contains a large proportion of backed pieces and has been suggested to be as old as 55 ka by Ambrose (1998). Like the Mumba Industry, these two assemblages are dominated by backed microliths (Figure 10.3), and the Nasampolai Industry directly overlies a more typical MSA assemblage.

The most recent chronologies for these sites indicate that backed piece-based toolkits first appear in the East African archaeological record at the beginning of MIS 3. The earliest backed pieces in East Africa occur synchronously in the Mumba Industry (57 ± 5 ka) and the LSA assemblage from the Naisiusiu Beds at Olduvai Gorge (60 km north of Lake Eyasi), which is associated with ESR ages, obtained from three equid teeth, of 59 ± 5 ka using an EU model and 62 ± 5 ka using a LU model (Skinner et al., 2003; Section 1.5.1). As discussed in Section 1.4.5, the EU model provides a minimum estimate of the age, and the actual age is likely to lie between estimates obtained using the EU and LU models (Grün, 2006). Likewise, while the chronology is not reliable, the Nasampolai Industry is associated with an obsidian hydration age of 46.4 ± 2.8 ka, and Ambrose (1998) suggests that it may be as old as 55 ka based on sedimentation-rate estimates (Section 1.5.3). Mehlman (1989) suggested that a Serengeti Plains counterpart to the Mumba Industry is present in Levels 8/9, 10 and 11 at Nasera rockshelter, and stated that "the Mumba Industry is almost certainly present below level XI at Kisese II rockshelter in central Tanzania (Inskeep, 1962), associated with OES beads." (Mehlman, 1989: 365).

The Mumba Industry, Naisiusiu Beds and Nasampolai Industry are the oldest backed piece-based assemblages at their respective sites and the former two represent the oldest such assemblages in East Africa associated with reliable chronologies. Several assemblages from other sites have also been attributed to the Mumba Industry, suggesting that it was relatively widespread in the East African Rift Valley. The concurrent emergence of backed piece-based toolkits at Olduvai Gorge and Mumba

rockshelter during a time of climatic amelioration ~60 ka further supports the hypothesis that the emergence of these technologies may have been the result of modern humans adapting to more favourable environmental conditions. This event may represent the spatio-temporal origin of backed piece-dominated toolkits in East Africa.

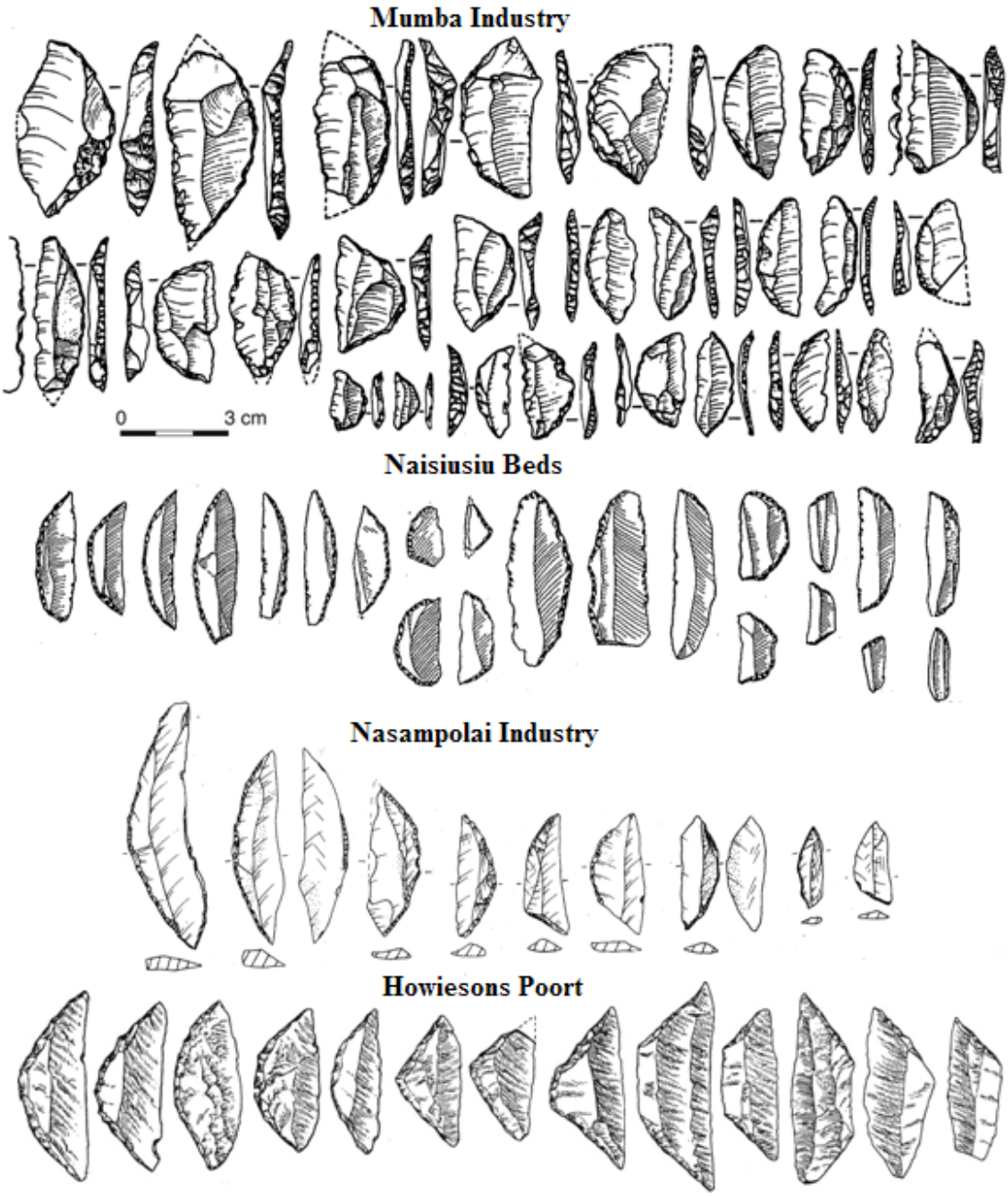

Figure 10.3: Backed pieces from the Mumba Industry at Mumba rockshelter, Tanzania (modified from Mehlman, 1989: 286), the Naisiusiu Beds at Olduvai Gorge, Tanzania (modified from Leakey et al., 1972: 338), the Nasampolai Industry at Enkapune Ya Muto, Kenya (modified from Ambrose, 1998: 386), and the Howiesons Poort Industry at Klasies River, South Africa (modified from Singer and Wymer, 1982: 96-97). Note that the scale bar is applicable to all lithics.

10.3.2.3 Mumba Industry: is there a Howiesons Poort connection?

The similarity between the backed pieces at Mumba and the Howiesons Poort Industries (Figure 10.3) has been noted previously (Deacon and Deacon, 1999; McBrearty and Brooks, 2000, but see Conard and Marks, 2006 for response). Deacon and Deacon (1999) linked this to the distribution of modern 'click' language speakers in these two regions (i.e., northern Tanzania and southern Africa) to infer the presence of long distance dispersals and exchange of ideas in the sub-Saharan Late Pleistocene. Recent genetic studies have shown that the East and southern African 'click' speakers share a common ancestor, from which they diverged as early as ~55 ka ago (Tishkoff et al., 2007). While the backed pieces of the Mumba Industry and Howiesons Poort are typologically similar, they differ technologically. The Howiesons Poort backed pieces are blade-based, with blades produced from prismatic cores (Mode 4 following Clark, 1968) (Wurz, 1999; Soriano et al., 2007). No such study of the *châine opératoire* of the Mumba Industry backed pieces has been published, however, precluding the possibility of an appropriate technological comparison of the tools from both industries. It has been noted, however, that few blade flakes or prismatic cores (i.e., blade cores: Bar-Yosef and Kuhn, 1999) have been recovered from Bed V, which suggests that blades are not a common component of the Mumba Industry (Mehlman, 1989; Diez-Martín et al., 2009). In addition, the northernmost site for which the Howiesons Poort Industry has been confidently identified (Cave of Hearths) is more than 2000 km south of Mumba rockshelter. No sites located between Mumba and the Cave of Hearths dated to MIS 4 or early MIS 3 contain a backed piece-based toolkit similar to either industry, although it is likely that this is, at least in part, due to the paucity of excavated sites in this region. Furthermore, genetic studies indicate that the San of southern Africa have been genetically isolated for most of the last 100 ka (Watson et al., 1997; Knight et al., 2003; Behar et al., 2008), suggesting that they had limited contact with the inhabitants of other regions such as East Africa, although a recent study by Henn et al. (2011) provides evidence to the contrary. Given the circumstantial nature of the evidence for a connection between the Howiesons Poort and Mumba Industries, and the lack of any technological comparison to support their similarity, any hypothesised link between the two remains speculative at best.

10.3.2.4 Symbolic ornaments associated with the Mumba Industry

Personal ornaments (e.g., OES and shell beads) are a widely accepted marker of modern symbolic behaviour (Ambrose, 1998; d'Errico et al., 2003, 2005; Henshilwood et al., 2004; Kuhn and Stiner, 2007; Bouzouggar et al., 2007). Beads have been identified in a variety of spatial and temporal contexts in the African MSA, including Morocco (~82 ka: Bouzouggar et al., 2007), South Africa (~75 ka: Henshilwood et al., 2004; d'Errico et al., 2005, 2008) and Kenya (>40 ka: Ambrose, 1998). Ambrose (1998), however, makes a case that the Kenyan age is substantially underestimated. Symbolic ornamentation, in the form of OES beads and ochre fragments, has been found in the Mumba Industry assemblages of upper Bed V, which have been dated here to 49 ± 4 ka (Chapter 6)

While the evidence discussed in Section 1.2.2 demonstrates that all modern humans are likely to have had the capacity for symbolic behaviour, the presence of OES beads and bead fragments in the upper portion of the Mumba Industry is the first unequivocal evidence for modern, symbolic behaviour at the site. The OSL age of 49 ± 4 ka makes this the earliest, reliably dated evidence for symbolic ornamentation in East Africa. This age estimate is consistent with the AAR age of ~52 ka obtained from an OES bead from Bed V, but for which no dating details or age uncertainty were provided (McBrearty and Brooks, 2000). It is curious, however, that these artefacts appear only in the upper deposits of the Mumba Industry. OES beads are found in association with the 'Second Intermediate' assemblage at Kisese II rockshelter (hypothesised to be equivalent to the Mumba Industry by Mehlman, 1989), but they are not associated with any of the other backed piece-based assemblages from the Naisiusiu Beds, the Nasampolai Industry or the Mumba Industry at Nasera. As same technologies and typologies are found in all Bed V assemblages, it is likely that the toolmakers of Bed V-lower were behaviourally very similar to, and practiced similar subsistence strategies to, the toolmakers of Bed V-upper. There are three hypotheses that can readily explain the presence of symbolic artefacts in the upper, but not the lower, deposits of Bed V.

First, the OES beads in upper Bed V may be intrusive from the overlying Bed III-lower deposits, which contain an abundance of OES beads. OSL investigations of single grains of quartz, which can identify when post-depositional mixing has occurred (Roberts et al., 1999, 2000; Feathers et al., 2006; Jacobs et al., 2006b, 2008b; Bateman

et al., 2007; David et al., 2007), do not support this hypothesis. Sediment mixing was identified in the D_e distributions of OSL samples from Bed III (MR2 and MR3) and Bed VI (MR9), but the D_e distributions of samples from Bed V (MR6, MR7 and MR8) exhibited no evidence of post-depositional mixing (Section 6.3). The spread in D_e values from Bed V samples were consistent with small-scale variations in the beta dose rate. This is consistent with Prendergast et al. (2007), who reported that sediment mixing was not observed during archaeological investigations of the geological units that are associated with the Mumba Industry (Unit C-lower, Unit E and Unit G).

Second, a case can be made that these materials were manufactured when Bed V-lower was accumulating, but that differences in sample sizes and sampling biases have rendered them archaeologically invisible. Although the Köhl-Larsens found OES beads in Bed V, they interpreted them as intrusive and did not retain any (Mehlman, 1989). In both the 1977/81 and 2005 samples, after debitáge and shatter had been removed from consideration, the assemblages of Bed V-upper were far larger and denser than those of Bed V-middle and Bed V-lower. Of the entire Bed V assemblage examined by Diez-Martín et al. (2009), upper Bed V contained 56% of the 'cores', 'flakes', and 'retouched tools'. Likewise, of the 1977/81 assemblage of Mehlman (1989), Bed V-upper/middle contained 94% of all the 'flaked tools' and 'cores' (Mehlman, 1989: 276, 283). In these uppermost Bed V assemblages, very few complete OES beads (seven and three from the 1977/81 and 2005 excavations, respectively: Mehlman, 1989; Diez-Martín et al., 2009) and ochre fragments (nine from the 2005 excavation: Diez-Martín et al., 2009) were found, suggesting that these materials were exceptionally rare at Mumba. Given the technological similarities of all Mumba Industry deposits (Diez-Martín et al., 2009), it is plausible that symbolic artefacts were present throughout Bed V. In this scenario, the reason that beads were not found in the lower and middle Bed V assemblages is because of their rarity and because of the smaller size of these assemblages relative to those from upper Bed V. If this scenario were true, then it would be an unfortunate coincidence that no symbolic artefacts were found in the lower deposits of Bed V in either of the excavations carried out subsequent to the Köhl-Larsens (i.e., in 1977/81 and 2005).

A third hypothesis (preferred by this author) for the presence of OES beads in upper Bed V is that the lower artefact densities of Bed V-middle and V-lower are the

result of smaller, less concentrated human occupations of the rockshelter. By contrast, the higher artefact density of Bed V-upper reflects a period of increased occupational intensity, due to a larger or more concentrated population. Many researchers have modelled (Shennan, 2001; Powell et al., 2009) and suggested (d'Errico et al., 2005; Kuhn and Stiner, 2007; Jacobs and Roberts, 2009; Zilhão et al., 2010) that increases in population size, density and interaction are likely stimuli for innovations, such as ornamentation and symbolic behaviour (Section 10.2.1). An increased population density during the accumulation of Bed V-upper may have resulted in increased social interaction, resulting in the first evidence for symbolic artefacts in the archaeological sequence at Mumba.

The time of deposition of Bed V-upper corresponds with a period of abrupt climatic deterioration, possibly concurrent with Heinrich Event 5 (Scholz et al., 2003; Tierney et al., 2008). Basell (2008) suggested that during periods of increased aridity, many parts of the East African Rift Valley, such as the plains, would have been less suitable for human habitation, encouraging hunter-gatherers to congregate near water sources and lake margins. If Lake Eyasi retained water through this period of climatic deterioration, Mumba rockshelter's proximity to the lake (2 to 4 km from the modern lake shore) would have made it a better shelter than the open environments of Olduvai Gorge and Nasera rockshelter. Enkapune Ya Muto's greater distance from Lake Naivasha (~15 km from the current lake shore) may also have made it less hospitable than Mumba. The climatic deterioration and associated decrease in resource availability, coupled with the increased population density around water sources, may have resulted in increased population pressure in the region. Kuhn and Stiner (2007) concluded that increases in population pressure would likely encourage the development of ornaments for social signalling. Likewise, Ambrose (1998, 2002, 2010) has posited that ornamental beads, such as those from the East African LSA, may have been involved in an institutionalised system of delayed reciprocity and gift giving, similar to the *hxaro* of the modern Kalahari !Kung San (Wiessner, 1982, 1986). These systems serve to strengthen regional social networks, enhancing survival prospects in environments of decreased resources. After the return to more favourable conditions, populations may have retained these symbolic behaviours.

10.3.3 Nasera Industry of Bed III-lower

The Nasera Industry was identified by Mehlman (1989) in the Bed III-lower deposits, dated to 37 ± 3 ka in this study. Between Bed III-lower and Bed V-upper is a culturally sterile, gravity/beach deposit, Bed IV. Thus, for some period of time after 49 ± 4 ka and ending before 37 ± 3 ka, the level of Lake Eyasi likely rose to submerge the rockshelter deposits, resulting in an occupational hiatus. This time range for a high lake level for Lake Eyasi is consistent with the results of Holmgren et al. (1995) and Barker et al. (2003) who concluded that the period between ~50 and 42 ka ago was warm and wet in East Africa (Figure 10.1). After occupation resumed, the tradition of making ornaments seemingly intensified, as bored stone balls were recovered and OES beads are abundant in Nasera Industry of Bed III-lower at Mumba. Although the lithic artefact density is smaller, the density of symbolic artefacts in Bed III-lower is substantially greater than those of Bed V-upper.

The Nasera Industry from Mumba is comprised of frequent scrapers, a low frequency of backed pieces and several classic MSA types that were not present in the Mumba Industry (see Section 2.4). The most striking feature of the assemblage is the abundance of symbolic materials. The Nasera Industry is also present in Levels 6 and 7 at Nasera rockshelter, and this assemblage is typologically similar to that from Mumba. Mehlman (1989) suggested that the Nasera Industry is also present in, or is similar to, assemblages at Kisese II rockshelter in Tanzania and Lukenya Hill in Kenya. Typological similarities also exist between the Nasera Industry and the LSA Sakutiek Industry from Enkapune Ya Muto. The latter industry is also dominated by scrapers, with several typical MSA types, but few backed pieces. Furthermore, OES beads and bead fragments are abundant in the Sakutiek Industry. Like the Nasera Industry at Mumba, it overlies a deposit containing a backed piece-dominated assemblage.

A possible link between the makers of the Nasera Industry and the makers of the Sakutiek Industry is supported by evidence at Nasera and Mumba rockshelters for the long-distance transport of obsidian. Obsidian from Levels 6 and 7 at Nasera rockshelter has been traced to sources in southern Kenya, providing further evidence that the inhabitants of northern Tanzania and southern Kenya were interacting when the Nasera Industry was being used. The source of a single piece of obsidian recovered from Mumba Bed III-lower has not been established, as no analyses have been performed.

However, given that all other obsidian found at Mumba has been traced to the Lake Naivasha region of southern Kenya, it is reasonable to hypothesise that this was also the source of the piece recovered from lower Bed III.

The chronologies associated with these toolkits are also similar. The Sakutiek Industry is associated with and age range of 43.9 ± 2.3 to 40.7 ± 1.3 cal ka BP (calibrated from reported ages of 39.9 ± 1.6 to 35.8 ± 0.6 ka BP), which precedes, but overlaps with, the OSL age associated with the Bed III-lower Nasera Industry deposits at Mumba (36.8 ± 3.4 ka). The Nasera Industry at Nasera rockshelter remains temporally unconstrained.

Palaeoclimate reconstructions suggest that the climate was variable when the Nasera and Sakutiek Industries were being used. There is evidence for increased warmth and humidity in East Africa between 50 and 42 ka (Holmgren et al., 1995; Barker et al., 2003). This period of increased water availability is corroborated by evidence for the elevated level of Lake Eyasi for some time between 49 ± 4 and 37 ± 3 ka. However, there is evidence for ephemeral episodes of aridity in East Africa at 47 ka (Scholz et al., 2003; Tierney et al., 2008), 42 ka (Scholz et al., 2003), and 37 ka (Tierney et al., 2008), suggesting that this period is characterised by abrupt changes from wetter to drier climate.

This evidence suggests that a new toolkit, associated with high frequencies of symbolic artefacts, emerged in the East African Rift Valley between ~44 and 40 cal ka BP, during a time of generally favourable, but variable climate. What instigated this change? Two related scenarios will be discussed in the following paragraphs.

First, as discussed previously in this chapter, demographic changes may be associated with changes in culture and technological innovations (Shennan, 2001; Henrich, 2004; Powell et al., 2009; Riede, 2009; Kline and Boyd, 2010). Likewise, increased size, density and interactions among populations of hominids were likely stimuli for the adoption of symbolic ornamentation (Kuhn and Stiner, 2007; Jacobs et al., 2008a; d'Errico et al., 2009; Jacobs and Roberts, 2009; Zilhão et al., 2010). Increasing population sizes and densities >40 ka ago, possibly associated with warmer, wetter conditions between 50 and 42 ka, seem to be a reasonable explanation, therefore, for the proliferation of symbolic ornaments at this time. The increased artefact densities

associated with the Sakutiek Industry and the Nasera Industry at Nasera rockshelter are consistent with this scenario.

During this time, Mumba rockshelter was submerged by Lake Eyasi, which was experiencing a highstand, possibly as a result of the warmer and wetter conditions. The Nasera Industry was deposited at Mumba ~37 ka ago and is present in the deposits that directly overlie Bed IV, which contains evidence for the submersion the rockshelter (Mehlman, 1989; Prendergast et al., 2007). The renewed occupation of Mumba during the deposition of Bed III-lower and, thus, the first evidence for the regression of Lake Eyasi, are coincident with Heinrich Event 4. It is possibly that ephemeral climatic deterioration associated with this event may have lowered the level of Lake Eyasi enough to allow occupation by people who were already making the Nasera Industry and its associated symbolic artefacts.

The second scenario involves the manufacture and use of ornamental beads as gifts to improve survival prospects during times of uncertain environments. Ornamental beads are an important part of the Kalahari !Kung San *hxaro* system of gift-giving and delayed reciprocity, which serves to strengthen regional social and economic relationships (Wiessner, 1982, 1986). Partners in the modern *hxaro* system are generally from areas with complementary resources. This system of delayed reciprocity thus maintains a regional social safety net, ensuring each partner access to vital resources in uncertain or marginal environments (Ambrose, 1998, 2002). The climatic instability between ~50 and ~35 ka may have prompted human populations in East Africa to adopt, or intensify their participation in, *hxaro*-like systems of gift-giving, to cope with unstable environments and ensure access to resources.

10.3.4 Summary

The new temporal constraints on the archaeological sequence at Mumba have enabled insights to be gained into several significant areas of Late Pleistocene human behaviour. A schematic illustration of the temporal and artefactual relationship among several of the MSA and LSA sites in East Africa is presented in Figure 10.4.

Several features are of note. First, the age of 74 ± 4 ka for the obsidian-bearing Bed VIA deposit at Mumba provides a minimum antiquity for the existence of long distance exchange networks in East Africa. Given the presence of obsidian from a dis-

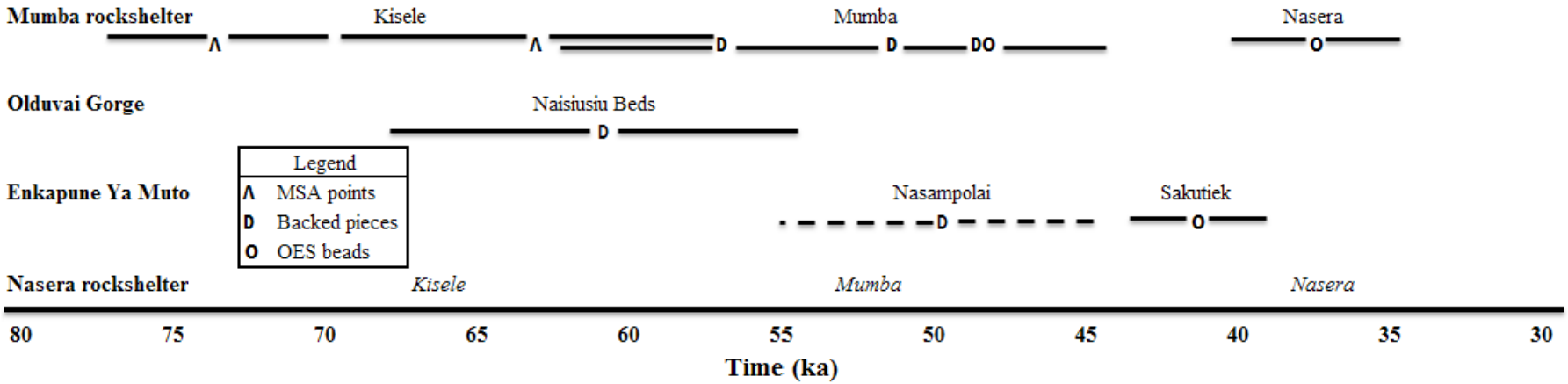

Figure 10.4: Chronologically constrained East African MSA and LSA archaeological records, showing the emergence and persistence of various artefact types (e.g., MSA points, backed pieces and OES beads) and associations between lithic industries from various sites. The unitalicised industries are associated with robust chronologies, whereas the italicised industries do not have robust age estimates and have been placed on this timeline based on age estimates of the same industries elsewhere. Symbols represent age estimates with associated 1σ uncertainties. For Mumba rockshelter, the OSL chronology described in this thesis is presented. For Olduvai Gorge, the error bars span 1σ below and above the age estimates obtained using EU and LU models, respectively. For Enkapune Ya Muto, the range shown for the Nasampolai Industry includes age estimates obtained using obsidian hydration dating and sedimentation rates. The age estimates for the Sakutiek Industry include three calibrated ^{14}C ages and their uncertainties at 1σ.

tant source in the underlying Bed VIB, these networks must have been in place earlier than ~74 ka, during MIS 5. The evidence for obsidian in Beds VIB, VIA, V and III-lower, the latter of which is here dated to 37 ± 3 ka, suggests that these networks remained in place throughout MIS 5, 4 and 3.

Second, the transition from point- to backed piece-dominated toolkits at Mumba appears to have occurred between 63 ± 6 ka and 57 ± 4 ka. The earliest backed piece-based toolkit at Mumba is contemporaneous with that of the LSA Naisiusiu Beds (~60 ka). This synchronous emergence of backed piece-dominated toolkits, corresponding to the climatic amelioration associated with the transition from MIS 4 to MIS 3 at ~60 ka, suggests that environmental change may have encouraged the development of new technologies.

Third, the presence of OES bead artefacts 49 ± 4 ka ago, in the Bed V-upper deposits of the Mumba Industry, may be related to an abrupt period of aridity associated with Heinrich Event 5. The relatively sudden and ephemeral nature of climatic deterioration may have encouraged populations to congregate near water sources and on lake margins, such as Lake Eyasi. The increased population density, pressure and interaction may have encouraged the development of symbolic ornamentation as a means of social communication.

Fourth, at 37 ± 3 ka, the Nasera Industry (which is also present at Nasera rockshelter) emerged at Mumba, slightly postdating, though overlapping with the later ages for, the typologically and compositionally similar Sakutiek Industry. Symbolic ornamentation proliferates at both of these sites. The typological and ornamental similarities, coupled with the increases in artefact density at Nasera and Enkapune Ya Muto rockshelters and the presence of obsidian from southern Kenya at Mumba and Nasera rockshelters, suggest that the proliferation of OES beads at this time may be associated with an increase in population size, density and/or social networks in the East African Rift Valley during a period of climatic and environmental instability.

10.4 Conclusions: a hypothesis

The OSL chronology obtained for the archaeological sequence at Mumba allows connections to be made between palaeoclimate reconstructions (Section 10.1), genetic evidence for demographic changes (Section 10.2) and the archaeological record

(Section 10.3) (Figure 10.5). Given the evidence that population size influences technological and behavioural innovations (Shennan, 2001; Henrich, 2004; Powell et al., 2009; Reide, 2009), and that the size of human populations varied markedly during the Late Pleistocene, demographic pressure is a likely candidate as the operative factor in changes in behaviour. The initial cause of changes in demography and resource availability may be environmental.

By 100 ka ago, modern humans were geographically dispersed from southern Africa to the Levant, and possibly as far east as the Arabian Peninsula (Armitage et al., 2011). This was not a panmictic population, however, as modern humans were likely living in geographically and genetically isolated populations (Watson et al., 1997; Knight et al., 2003; Garrigan et al., 2007; Campbell and Tishkoff, 2008; Behar et al., 2008; Quintana-Murci et al., 2008). There is a growing body of evidence for 'modern' behaviour by early modern humans (e.g., Vanhaeren et al., 2006) and non-modern hominins (e.g., Barham, 2002a,b; Zilhão et al., 2010), suggesting that humans had the cognitive capacity for modern behaviour prior to 100 ka, and that other factors (e.g., demographic pressures) were the triggers for their expression.

During MIS 5a (85–78 ka), the climates of eastern and northern Africa and the Levant became more favourable for human habitation. Sea levels were near or above modern-day levels (Hearty, 1998; Coyne et al., 2007; Dorale et al., 2010). The Arabian Peninsula was warm and humid (Reichart et al., 1998; Fleitmann et al., 2003; Leuschner et al., 2004), the African monsoon was strengthened (Revel et al., 2010) and Lake Malawi was experiencing a highstand (Scholz et al., 2007). The more favourable climates at this time may have encouraged human population expansions. Increases in North African population sizes and densities are consistent with evidence for increased symbolic expression and long distance social networks (Bouzouggar et al., 2007; d'Errico et al., 2009).

The MIS 4 glacial (78–60 ka) was a period of climatic deterioration in many parts of the Old World. There is abundant evidence for widespread aridity in Arabia (Reichart et al., 1998; Leuschner et al., 2004) and East Africa (Ficken et al., 1998). Lake Tanganyika shows two low lake-level regressions during MIS 4 (Scholz et al., 2003). The level of Lake Malawi was also substantially reduced for parts of MIS 4, suggesting megadrought conditions in East Africa between ~78 and 74 ka and increased

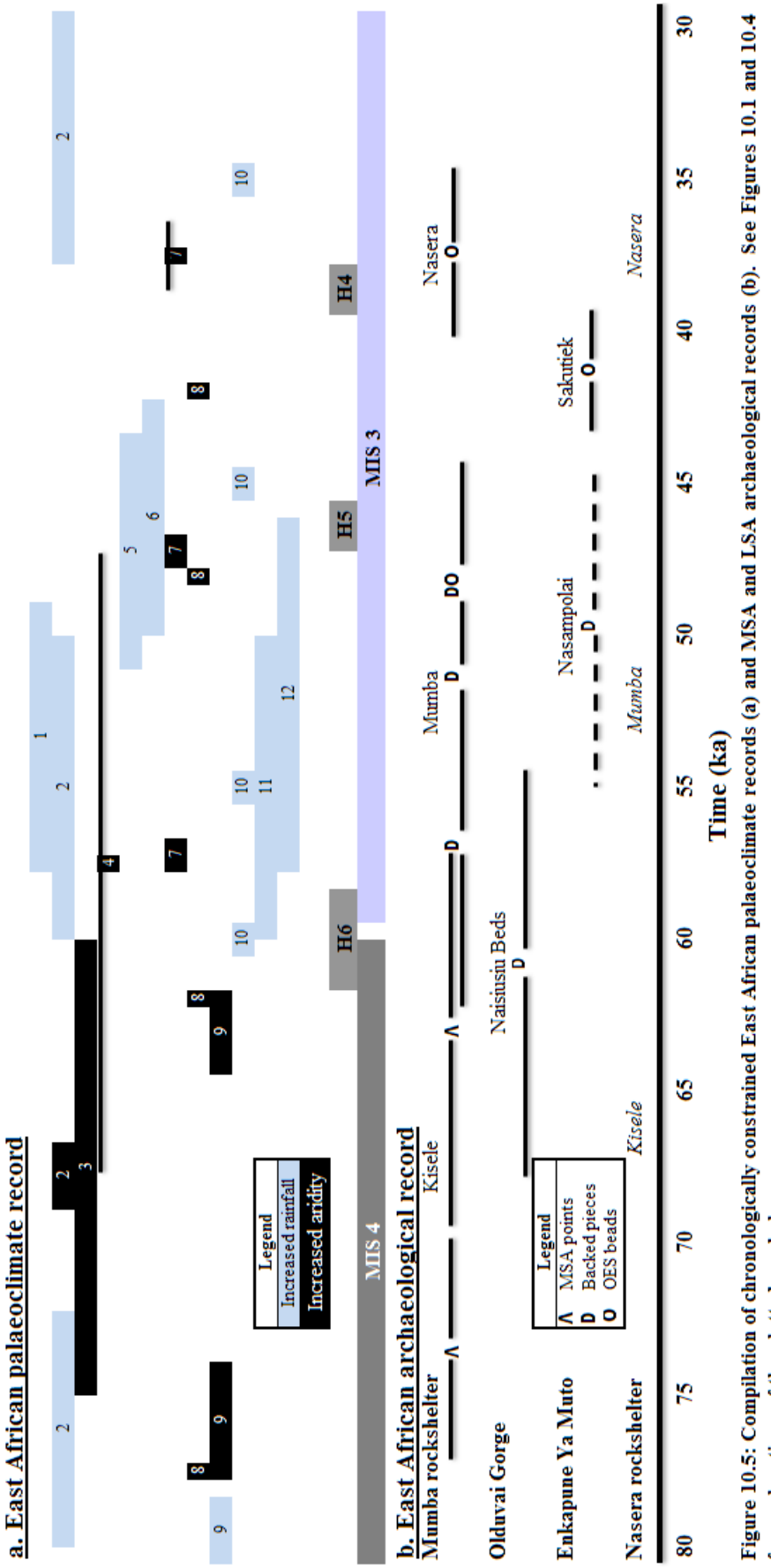

Figure 10.5: Compilation of chronologically constrained East African palaeoclimate records (a) and MSA and LSA archaeological records (b). See Figures 10.1 and 10.4 for explanations of the plotted symbols.

aridity between ~64 and 62 ka (Scholz et al., 2007). Reduced precipitation in the region is supported by evidence that the East African monsoon was weakened during MIS 4 (Revel et al., 2010). Human populations were most likely geographically distributed and isolated across parts of sub-Saharan Africa. There is evidence for the dispersal, isolation and possible extinction of groups of modern humans during this period. The ancestors of modern-day Mbuti pygmies likely diverged from other human populations during MIS 4 (Quintana-Murci et al., 2008), perhaps due to climatically forced geographic isolation. On the basis of palaeoclimatic and archaeological records, Shea (2008) contends that rapid climate change at the beginning of MIS 4 caused decreases in temperature and humidity, resulting in the extinction of modern humans in the Levant. During these periods of climatic deterioration, modern humans making MSA Kisele Industry artefacts were occupying Mumba rockshelter, and other sites in the East African Rift Valley, at low population densities.

Following Heinrich Event 6, the transition to MIS 3 at ~60 ka resulted in climatic amelioration throughout much of Africa (Felton et al., 2007; Revel et al., 2010; Tierney et al., 2010). In particular, during the period from 60 to 50 ka, humidity and rainfall increased in the Lake Tanganyika basin (Felton et al., 2007; Tierney et al., 2010) and Lake Malawi rose to near-modern levels (Scholz et al., 2007). There is additional evidence that the East African monsoon was strengthened between 60 and 50 ka (Revel et al., 2010). Nowell (2010) suggested that climatic amelioration at the start of MIS 3 may have caused increases in population size and density and associated increases in technological innovation. There is genetic evidence for population expansions and dispersals within, and out of, Africa during this period (Watson et al., 1997; Knight et al., 2003; Tishkoff et al., 2007; Atkinson et al., 2008). Thus, following climatic amelioration during early MIS 3, an expanding human population in the East African Rift Valley may have adapted to more favourable environmental conditions by developing backed tool-based technologies. This is manifested in the archaeological record as the synchronous appearance of the LSA assemblage from the Naisiusiu Beds and the Mumba Industry at the beginning of MIS 3. The latter lithic industry has been identified at Mumba and Nasera rockshelters and may also be present at Kisese II rockshelter. The LSA Nasampolai Industry at Enkapune Ya Muto may also represent an early backed piece-based toolkit.

Around 50 ka ago, abrupt and brief climatic deteriorations, potentially linked to Heinrich Event 5 (Scholz et al., 2003; Tierney et al., 2008), may have rendered parts of the East African Rift Valley less suitable for human habitation. This may have encouraged populations to congregate at shelters, such as Mumba, close to water sources and on lake margins, thus, increasing population densities and competition for limited resources. This increased population pressure may have brought groups into contact with more people more often, resulting in increased social interaction and, potentially, an increased reliance on social networks and cooperation. This may have provided the impetus for the emergence of symbolic ornamentation (e.g., OES beads) in East Africa. The establishment and maintenance of robust social networks based on increased cooperation and interaction would have allowed humans to use the available resources more effectively (Ambrose, 1998, 2002, 2003, 2010), facilitating an enlarged population to survive brief periods of climatic deterioration. This is reflected in the archaeological record of East Africa as increased artefact densities and the emergence of OES beads in the Mumba Industry of upper Bed V.

Following Heinrich Event 5, favourable climatic conditions may have returned through ~42 ka (Holmgren et al., 1995; Barker et al., 2003), resulting in a highstand for Lake Eyasi. Ephermeral periods of climatic deterioration continued, however, through 35 ka (Scholz et al., 2003; Tierney et al., 2008). During this period, population densities and social interactions may have continued to increase in the East African Rift Valley, resulting in the proliferation of symbolic ornaments (OES beads) associated with a regional system of exchange serving to ensure access to resources. The emergence of the Sakutiek Industry at Enkapune Ya Muto (~44–40 cal ka BP) and the high artefact-density of the Nasera Industry at Nasera rockshelter are consistent with this scenario. The presence of obsidian, sourced to southern Kenya, in Levels 6 and 7 at Nasera rockshelter is consistent with the hypothesised association between the Nasera Industry of northern Tanzania and the Sakutiek Industry of southern Kenya. It is also consistent with the hypothesised existence of regional exchange networks. The Nasera Industry and associated OES beads were deposited at Mumba rockshelter (37 ± 3 ka) after the end of the Lake Eyasi highstand. The first archaeological deposits after the Lake Eyasi highstand are coincident with Heinrich Event 4. This synchronicity suggests that a brief period of aridity associated with Heinrich Even 4 may have caused

a regression in Lake Eyasi, allowing modern humans living on the lake margin to occupy the newly-exposed Mumba rockshelter.

It is unclear whether occupation at Mumba continued through the LGM. The pre-LGM (Bed III-lower) and post-LGM (Bed III-middle) assemblages from the site are typologically and compositionally different (Mehlman, 1989), although there are no large stratigraphic gaps in the sequence (Prendergast et al., 2007). Furthermore, lithic and symbolic artefacts are found throughout Bed III (Prendergast et al., 2007). It is clear that humans with LSA toolkits and OES bead traditions occupied Mumba rockshelter before (37 ± 3 ka) and after the LGM (16 ± 1 ka).

The above synthesis of the revised chronology for the archaeological sequence at Mumba and existing archaeological, palaeoclimatic and demographic records for East Africa suggests that changes in human behaviour and technology are intimately linked to environmental conditions. This is highlighted by the synchronicity of major technological, behavioural and environmental changes. Backed piece-based toolkits emerged with the climatic amelioration at the start of MIS 3, and the first evidence for symbolic ornaments is synchronous with Heinrich Event 5. Similarly, technological change and the proliferation of symbolic ornaments occurred during a period of favourable climate. These temporal connections are highly suggestive of an intimate link between modern humans and their environment, although establishing a causal connection between climate and human response requires a much higher degree of resolution in the archaeological, demographic and environmental records.

Chapter 11: Conclusions

The main aim of this thesis was to provide a chronological framework for the MSA and LSA archaeological sequences of two sites in East Africa. An improved chronology would help resolve the timing of the emergence and proliferation of microlithic backed-tool technologies and symbolic behaviours in the region during the Late Pleistocene. To accomplish this, the OSL and IRSL properties of quartz and K-feldspars from deposits containing MSA and LSA assemblages were investigated to assess their suitability for obtaining robust age estimates. Recently developed analytical, procedural, optical stimulation and correction techniques were tested to overcome problems associated with the luminescence properties of the quartz and feldspar grains and the depositional and post-depositional processes that affected the D_e distributions.

11.1 General luminescence findings

1. Single-grain SAR measurements revealed substantial inter-grain variability in the OSL signal of quartz from Mumba. This variability was characterised and five major classes of grain-type were identified, based on their behaviour during a SAR procedure. The use of the pulsed-irradiation technique reduced the number of grains that produced hyperbolic dose-response curves. Standard SAR suitability tests were used to identify and reject some grain types (e.g., Class-3 type grains). Using dose recovery experiments, grains that possessed other poor qualities, such as low-dose saturation levels and malign sensitivity changes, could then be identified and rejected from the dataset. The OSL signals from the remaining grains were dominated by the fast component and could be used to recover a known dose. When multi-grain aliquots of these samples were measured using the SAR procedure, the variability in grain-types resulted in an amalgamated signal that was dominated by poorly behaving grains. This resulted in poor performances in tests of SAR suitability, an inability to recover a known dose, and large variability in the measured OSL and LM-OSL signal. These findings highlight the need for the investigation of single grains to identify variability in the OSL signal and accurately obtain dose estimates.

2. Using only the D_e values from grains that were dominated by a fast component and were suitable for using the SAR procedure, D_e distributions were obtained and analysed. Grains that were likely intrusive or that had received an attenuated beta dose rate during burial could then be identified and rejected from the dataset. The remaining D_e values were considered the most representative of the dose received during burial. The measured dose rate could then be corrected for beta microdosimetry to obtain a depositional age for most of the Mumba samples. Single-grain quartz OSL ages could not be obtained for some samples (e.g., MR10 from Bed VIA) due to the OSL signals being in saturation. These samples were then investigated using K-feldspar separates.
3. The TL and IRSL signals from K-feldspar separates of samples from Mumba were investigated with the aim of finding a luminescence signal that could be used to obtain accurate ages. The findings of this research support the donor-acceptor mode of IRSL production. Two TL peaks were identified in the natural and laboratory-irradiated samples: at 350°C and 430°C. The TL peak at 350°C was shown to be less optically sensitive than the 430°C peak. An association was made between the IRSL signal and the high-temperature TL peak at 430°C, supporting the results of Murray et al. (2009). The shape and intensity of the IRSL signal was shown to be largely dependent on stimulation temperature. The maximum IR stimulation temperature that could be used without stimulating an isothermal TL signal was 225°C.
4. The post-IR IRSL signal was characterised for K-feldspar separates from Mumba. It was shown to be bleachable in natural sunlight and suitable for using the SAR procedure to recover a known dose. Dose recovery experiments showed that other stimulation conditions (i.e., IR at 50°C and 225°C) were also suitable for recovering a known dose. A comparison of fading rates revealed that, although fading was ubiquitous, the fading rate decreased with increasing stimulation temperatures of up to 225°C. Additionally, the post-IR IRSL signal suffered the least anomalous fading out of all stimulation conditions tested (i.e., IR stimulation at 50°C, 225°C, 300°C and 350°C). D_e values and fading rates were then measured for multi-grain aliquots of K-feldspar from Mumba, and these then used to obtain fading-corrected ages. Fading-corrected IRSL ages

were consistent with single-grain OSL ages, for the three samples for which reliable OSL ages could be obtained. This provided support for the ability of the post-IR IRSL signal from K-feldspars to give reliable age estimates for samples from Mumba.

5. Quartz of volcanic origin from Moche Borago was shown to be very rare in the samples and did not contain a fast component, prompting the investigation of K-feldspars from the same samples. These K-feldspars of volcanic origin were shown to be very dim and to have very different TL and IRSL properties from the K-feldspars of metamorphic origin from Mumba. No discrete association could be made between TL peaks and the IRSL signal. The shape and intensity of the IRSL signal was shown to be largely dependent on stimulation temperature. When various IR stimulation conditions were tested in dose recovery experiments, all aliquots were able to recover a known dose. However, performance in tests of SAR suitability was improved, and the measured/given dose ratio was closer to unity, for IR stimulation at 200°C compared to lower stimulation temperatures. Anomalous fading was shown to affect K-feldspars from Moche Borago to a greater extent than at Mumba. The fading rate decreased as IR stimulation temperature was increased to 200°C, although the lowest fading rates (37 ± 4 %/decade) were still unacceptably high for fading correction using the model of Huntley and Lamothe (2001). Given the lack of quartz and feldspar grains in the Moche Borago samples, the dimness of the luminescence signals from the minerals that were present, and the high rates of anomalous fading of the K-feldspars, reliable age determination using the procedures that were investigated was not possible for Moche Borago

11.2 Implications of the OSL chronology for Mumba rockshelter on technological and behavioural evolution in East Africa

A numerical-age chronology could be obtained for the archaeological sequence from Mumba using single grains of quartz and multi-grain aliquots of K-feldspar. The ages for upper Bed V obtained using both mineral grains were consistent with each other and with independent AAR age estimates of ~52 ka and 45 to 65 ka, reported by McBrearty and Brooks (2000). The OSL and IRSL chronologies presented in this thesis

constrain the timing of transitions in technologies and behaviours at Mumba and provide insights into the possible reasons for these changes. The main findings of the new chronology are as follows:

1. Obsidian artefacts, some of which were traced to source outcrops 320 km from Mumba rockshelter in southern Kenya, were found in Beds VIB, VIA, V and III-lower. The majority of available ethnographic evidence indicates that a transport distance of 300 km or more would result from procurement via exchange networks. The frequent presence of distantly sourced obsidian at other MSA sites in East Africa is consistent with the hypothesised existence of exchange networks. Since no OSL samples were collected from Bed VIB, the age obtained for Bed VIA provides only a minimum estimate for the existence of these networks. Thus, the ages of 74 ± 4 ka and 37 ± 3 ka for Bed VIA and III-lower, respectively, provide a minimum estimate of the duration of time (~40 ka) that long-distance exchange networks were in existence among the inhabitants of East Africa. This time range spans the varied climatic conditions of MIS 5, 4 and 3.
2. The OSL chronology provides temporal constraints for the transition from MSA to LSA toolkits at Mumba. The OSL ages of 63 ± 6 ka for Bed VIA constrains the latest use of the MSA Kisele Industry. The earliest deposits containing the backed piece-based Mumba Industry (lower Bed V) are associated with an age of 57 ± 5 ka. Thus, the transition from point-dominated to backed piece-dominated toolkits at Mumba occurred between these two time periods, around 60 ka. The age for the earliest Mumba Industry is synchronous with the earliest backed piece-dominated assemblage from the Naisiusiu Beds at Olduvai Gorge. The transition in technologies at Mumba and Olduvai is synchronous with the climatic transition at approximately 60 ka, when the arid conditions of MIS 4 were replaced with more favourable conditions of MIS 3. Together, these lines of evidence suggest that a backed piece-based toolkit emerged in East Africa concomitantly with climatic amelioration at the start of MIS 3.
3. The OSL age of 49 ± 4 ka for upper Bed V temporally constrains the first evidence for symbolic materials in the archaeological sequence at Mumba. This is the earliest evidence for OES beads at Mumba rockshelter and in the region of

East Africa. The emergence of OES beads in the Mumba Industry at this time is coincident with the ephemeral climatic deterioration of Heinrich Event 5.

4. The OSL age of 37 ± 3 ka for lower Bed III provides a temporal constraint for the emergence of the Nasera Industry at Mumba. This LSA toolkit differs substantially from the underlying Mumba Industry and contains abundant symbolic materials in the form of OES beads, bored stone balls and engraved OES fragments. The Nasera Industry is also present at Nasera rockshelter and is typologically similar to the Sakutiek Industry at Enkapune Ya Muto, which is also associated with abundant OES beads. The age-range for the Sakutiek Industry suggests that it was made during a period of favourable climate, during which time Lake Eyasi was likely experiencing a highstand, which submerged Mumba rockshelter. The timing of the emergence of the Nasera Industry at Mumba is consistent with the timing of the ephemeral climatic deterioration of Heinrich Event 4, which may have caused Lake Eyasi to recede and expose Mumba rockshelter for renewed human occupation.
5. The robust OSL and IRSL chronology for Mumba rockshelter suggests that a relationship may exist between changes in technology and behaviour in East Africa and climate changes during the Late Pleistocene. The coincidence of the three major technological and/or behavioural changes at Mumba with environmental changes in East Africa supports this hypothesis, although establishing a causal relationship between the two will require a substantially higher degree of resolution in the palaeoclimatic and archaeological records.

11.3 Future research

The research described in this thesis has demonstrated that single-grain OSL and multi-grain post-IR IRSL investigations of quartz and feldspar, respectively, can be used to obtain reliable numerical ages for Late Pleistocene deposits in East Africa. Consequently, there is enormous potential for these dating techniques to constrain the timing of the MSA and LSA in this region. The lack of reliable chronologies for this period in East Africa greatly restricts the ability of researchers to appropriately interpret the archaeological, palaeoenvironmental and genetic records to understand *when*, *why* and *how* modern human technologies and behaviours changed during the Late

Pleistocene. The following areas of future research could build upon the results presented in this thesis:

1. The accuracy and precision of luminesce dating can be improved. Coupling single-grain dating with micromorphology studies of sediment can help elucidate the issue of beta dose rate heterogeneity (Jacobs and Roberts, 2007; David et al., 2007). Multiple studies, including this thesis, have demonstrated that the post-IR IRSL signal from K-feldspars can be used to recover a known dose, fade minimally, and obtain an age as accurate as single-grain quartz ages. The post-IR IRSL procedure can, thus, be used to obtain accurate ages in cases where quartz is absent, the OSL signals are dim or saturated, and post-depositional mixing is not significant. Investigations into the luminescence properties of single grains of K-feldspar may be able to identify grains with IRSL signals that do not fade, much like single-grain investigations of quartz can be used to identify grains with poor OSL behaviours. If grains whose IRSL signals fade are identified and rejected, there is no need to use the age correction procedure and its associated assumptions and limitations. In addition, single-grain K-feldspar analyses could be used to assess the various pre-depositional, depositional and post-depositional processes that may have affected the D_e distribution of each sample, enabling increased accuracy and precision on age estimates.
2. To obtain chronological controls on the entire archaeological sequence at Mumba, stratigraphically secure OSL samples could be collected from deposits associated with the Sanzako Industry. Since the quartz OSL signal will be saturated in these samples, the post-IR IRSL technique could be used to obtain ages from K-feldspar separates. Temporally constraining the Sanzako Industry would place a chronological control on the first potential evidence for long-distance exchange networks, in the form of distantly-sourced obsidian, at Mumba rockshelter.
3. More MSA and LSA sites in East Africa need to be re-dated using modern methods, sample pretreatment techniques and data analysis procedures. Sites that contain MSA and LSA assemblages associated with out-dated chronologies include Enkapune Ya Muto, Kisese II rockshelter, Nasera rockshelter, Lukenya

Hill, Prospect Farm and Prolonged Drift. Methods such as OSL dating of quartz and IRSL dating of K-feldspar could potentially be used to obtain reliable chronologies for these sites. Temporally constraining the emergence of backed piece-based toolkits, the emergence of symbolic materials and their proliferation at other sites in East Africa will be necessary to confirm or disprove the hypothesised association of these behavioural changes with contemporaneous changes in the environment and demography in the Late Pleistocene.

References

Adamiec, G., 2000. Variations in luminescence properties of single quartz grains and their consequences for equivalent dose estimation. *Radiation Measurements* 32, 427–432.

Adamiec, G., 2005. OSL decay curves – relationship between single- and multiple-grain aliquots. *Radiation Measurements* 39, 63–75.

Adamiec, G., Aitken, M.J., 1998. Dose-rate conversion factors: update. *Ancient TL* 16, 37–50.

Aitken, M.J., 1985. Thermoluminescence Dating. Academic Press, London.

Aitken, M.J., 1998. An Introduction to Optical Dating: The Dating of Quaternary Sediments by the Use of Photon-stimulated Luminescence. Oxford University Press, Oxford.

Almogi-Labin, A., Bar-Matthews, M., Shriki, D., Kolosovsky, E., Paterne, M., Schilman, B., Ayalon, A., Aizenshtat, Z., Matthews, A., 2009. Climatic variability during the last ~90 ka of the southern and northern Levantine Basin as evident from marine records and speleothems. *Quaternary Science Reviews* 28, 2882–2896.

Ambrose, S.H., 1998. Chronology of the Later Stone Age and food production in East Africa. *Journal of Archaeological Science* 25, 377–392.

Ambrose, S.H., 2001. Paleolithic technology and human evolution. *Science* 291, 1748–1753.

Ambrose, S.H., 2002. Small things remembered: origins of early microlithic industries in sub-Saharan Africa, in: Elston, R., Kuhn, S. (Eds.), Thinking small: Global perspectives on microlithic technologies. Archaeological Papers of the American Anthropological Association. No. 12, pp. 9–29.

Ambrose, S.H., 2006. Howiesons Poort lithic raw material procurement patterns and the evolution of modern human behaviour: A response to Minichillo (2006). *Journal of Human Evolution* 50, 365–369.

Ambrose, S.H., 2010. Coevolution of composite-tool technology, constructive memory, and language: implications for the evolution of modern human behavior. *Current Anthropology* 51, S135–S147.

Ambrose, S.H., Lorenz, K.G., 1990. Social and ecological models for the Middle Stone Age in Southern Africa. In: Mellars, P. (Ed.), The emergence of modern humans. Edinburgh University Press, Edinburgh, pp. 3–33.

Anderson, A., Roberts, R., Dickinson, W., Clark, G., Burley, D., de Biran, A., Hope, G., Nunn, P., 2006. Times of sand: sedimentary history and archaeology at the Sigatoka Dunes, Fiji. *Geoarchaeology: An International Journal* 21, 131–154.

Anovitz, L.M., Elam, J.M., Riciputi, L.R., Cole, D.R., 1999. The failure of obsidian hydration dating: sources, implications, and new directions. *Journal of Archaeological Science* 26, 735–752.

Anthony, B.W., 1978. The Prospect Industry: a definition. Ph.D. thesis (unpublished), Harvard University.

Armitage, S.J, Wintle, A.G., Duller, G.A.T., 2000. Quartz from southern Africa: sensitivity changes as a result of thermal treatment. *Radiation Measurements* 32, 571–577.

Armitage, S.J., Jasim, S.A., Marks, A.E., Parker, A.G., Usik, V.I., Uerpmann, H.-P., 2011. Evidence for an early expansion of modern humans into Arabia. *Science* 331, 453–456.

Arnold, L.J., Roberts, R.G., 2009. Stochastic modelling of multi-grain equivalent dose (D_e) distributions: Implications for OSL dating of sediment mixtures. *Quaternary Geochronology* 4, 204–230.

Arnold, L., Stokes, S., Bailey, R., Fattahi, M., Colls, A., Tucker, G., 2003. Optical dating of potassium feldspar using far-red (λ>665 nm) IRSL emissions: a comparative study using fluvial sediments from the Loire River, France. *Quaternary Science Reviews* 22, 1093–1098.

Arnold, L.J., Bailey, R.M., Tucker, G.E., 2007. Statistical treatment of fluvial dose distributions from southern Colorado arroyo deposits. *Quaternary Geochronology* 2, 162–167.

Arnold, L.J., Roberts, R.G., McPhee, R.D.E., Willerslev, E., Tikhonov, A.N., Brock, F., 2008. Optical dating of perennially-frozen deposits associated with preserved ancient plant and animal DNA in north-central Siberia. *Quaternary Geochronology* 3, 114–136.

Arnold, L.J., Roberts, R.G., Galbraith, R.F., DeLong, S.B., 2009. A revised burial dose estimation procedure for optical dating of young and modern-age sediments. *Quaternary Geochronology* 4, 306–325.

Atkinson Q.D., Gray R.D., Drummond A.J., 2008. mtDNA variation predicts population size in humans and reveals a major Southern Asian chapter in human prehistory. *Molecular Biology and Evolution* 25, 468–474.

Atkinson Q.D., Gray R.D., Drummond A.J., 2009. Bayesian coalescent inference of major human mitochondrial DNA haplogroup expansions in Africa. *Proceedings of the Royal Society B* 276, 367–73.

Auclair, M., Lamothe, M., Huot, S., 2003. Measurement of anomalous fading for feldspar IRSL using SAR. *Radiation Measurements* 37, 487–492.

Auclair, M., Lamothe, M., Lagroix, F., Banerjee, S.K., 2007. Luminescence investigation of loess and tephra from Halfway House section, central Alaska. *Quaternary Geochronology* 2, 34–38.

Bailey, R.M., Arnold, L.J., 2006. Statistical modelling of single grain quartz D_e distributions and an assessment of procedures for estimating burial dose. *Quaternary Science Reviews* 25, 2475–2502.

Bailey, R.M., 2001. Towards a general kinetic model for optically and thermally stimulated luminescence of quartz. *Radiation Measurements* 33, 17–45.

Bailey, R.M., 2004. Paper I–simulation of dose absorption in quartz over geological timescales and its implications for the precision and accuracy of optical dating. *Radiation Measurements* 38, 299–310.

Bailey, R.M., Smith, B.W., Rhodes, E.J., 1997. Partial bleaching and the decay form characteristics of quartz OSL. *Radiation Measurements* 27, 123–136.

Bailey, R.M., Armitage, S.J., Stokes, S., 2005. An investigation of pulsed-irradiation regeneration of quartz OSL and its implications for the precision and accuracy of optical dating (Paper II). *Radiation Measurements* 39, 347–359.

Bailiff, I.K., Poolton, N.R.J., 1989. Charge transfer in quartz and feldspar: factors affecting the dating of young sediments. In: Long and Short Range Limits in Luminescence Dating Occasional publication No. 9. Research Laboratory for Archaeology and History of Art, Oxford.

Bailiff, I.K., Poolton, N.R.J., 1991. Studies of charge transfer mechanisms in feldspars. *Nuclear Tracks and Radiation Measurements* 18, 111–118.

Bailiff, I.K., Barnett, S.M., 1994. Characteristics of infrared-stimulated luminescence from a feldspar at low temperatures. *Radiation Measurements* 23, 541–545.

Balescu, S., Lamothe, M., Lautridou., J.-P., 1997. Luminescence evidence for two middle Pleistocene interglacial events at Tourville, northwestern France. *Boreas* 26, 61–72.

Balescu, S., Lamothe, M., Mercier, N., Huot, S., Balteanu, D., Billard, A., Hus, J., 2003. Luminescence chronology of Pleistocene loess deposits from Romania: testing methods of age corrections for anomalous fading in alkali feldspars. *Quaternary Science Reviews* 22, 967–973.

Banerjee, D., Murray, A.S., Bøtter-Jensen, L., Lang, A., 2001. Equivalent dose estimation using a single aliquot of polymineral fine grains. *Radiation Measurements* 33, 73–94.

Banerjee, D., Blair, M., McKeever, S.W.S., 2002. Dose and dose-rate dependence of optically stimulated signals in quartz: theoretical simulations. *Radiation Protection Dosimetry* 101, 353–358.

Bar-Matthews, M., Ayalon, A., Kaufman, A., 2000. Timing and hydrological conditions of Sapropel events in the Eastern Mediterranean, as evident from speleothems, Soreq cave, Israel. *Chemical Geology* 169, 145–156.

Bar-Matthews, M., Ayalon, A., Gilmour, M., Matthews, A., Hawkesworth, C.J., 2003. Sea-land oxygen isotopic relationships from planktonic foraminifera and speleothems in the Eastern Mediterranean region and their implication for paleorainfall during interglacial intervals. *Geochimica et Cosmochimica Acta* 67, 3181–3199.

Bar-Yosef, O., Kuhn, S.L., 1999. The Big deal about blades: laminar technologies and human evolution. *American Anthropologist* 10, 323–338.

Bard, E., Arnold, M., Hamelin, B., Tisnerat-Laborde, N., Cabioch, G., 1998. Radiocarbon calibration by means of mass spectrometric $^{230}Th/^{234}U$ and ^{14}C ages of corals: An updated database including samples from Barbados, Mururoa and Tahiti. *Radiocarbon* 40, 1085–1092.

Barham, L.S., 1998. Possible early pigment use in south-central Africa. *Current Anthropology* 39**,** 703–710.

Barham, L.S., 2002a. Backed tools in Middle Pleistocene central Africa and their evolutionary significance. *Journal of Human Evolution* 43, 585–603.

Barham, L.S., 2002b. Systematic pigment use in the Middle Pleistocene of south-central Africa. *Current Anthropology* 43, 181–190.

Barham, L.S., Smart, P., 1996. Early date for the Middle Stone Age of central Zambia. *Journal of Human Evolution* 30, 287–290.

Baril, M.B., Huntley, D.J., 2003a. Optical excitation spectra of trapped electrons in irradiated feldspars. *Journal of Physics: Condensed Matter* 15, 8011–8027.

Baril, M.B., Huntley, D.J., 2003b. Infrared stimulated luminescence and phosphorescence spectra of irradiated feldspars. *Journal of Physics: Condensed Matter* 15, 8029–8048.

Barker, P., Williamson, D., Gasse, F., Gilbert, E., 2003. Climatic and volcanic forcing revealed in a 50,000-year diatom record from Lake Massoko, Tanzania. *Quaternary Research* 60, 368–376.

Barut, S., 1994. Middle and Later Stone Age lithic technology and land use in East African savannas. *The African Archaeological Review* 12, 43–72.

Basell, L.S., 2008. Middle Stone Age (MSA) site distributions in eastern Africa and their relationship to Quaternary environmental change, refugia and the evolution of *Homo sapiens*. *Quaternary Science Reviews* 27, 2484–2498.

Bateman, M.D., Frederick, C.D., Jaiswal, M.K., Singhvi, A.K., 2003. Investigations into the potential effects of pedoturbation on luminescence dating. *Quaternary Science Reviews* 22, 1169–1176.

Bateman, M.D., Boulter, C.H., Carr, A.S., Frederick, C.D., Peter, D., Wilder, M., 2007. Detecting post depositional sediment disturbance in sandy deposits using optical luminescence. *Quaternary Geochronology* 2, 57–64.

Bauer, F.U., 2007. The Sabiñánigo sandstone succession, Jaca Basin, Southern Pyrenees, NW-Spain – a depositional model. Ph.D. thesis (unpublished), University of Heidelberg, Germany.

Beaumont, P.B., de Villiers, K., Vogel, J.C., 1978. Modern man in sub-Saharan Africa prior to 49,000 years B. P.: a review and evaluation with particular reference to Border Cave. *South African Journal of Science* 74, 409–419.

Beck, J.W., Richards, D.A., Edwards, R.L., Silverman, B.W., Smart, P.L., Donahue, D.J., Hererra-Osterheld, S., Burr, G.S., Calsoyas, L., Jull, A.J.T., Biddulph, D., 2001. Extremely large variations of atmospheric ^{14}C concentration during the last glacial period. *Science* 292, 2453–2458.

Behar, D.M., Villems, R., Soodyall, H., Blue-Smith, J., Periera, L., Metspalu, E., Scozzari, R., Makkan, H., Tzur, S., Comas, D., Bertranpetit, J., Quintana-Murci, L., Tyler-Smith, C., Wells, R.S., Rosset, S., The Genographic Consortium, 2008. The dawn of human matrilineal diversity. *The American Journal of Human Genetics* 82, 1130–1140.

Bergner, A.G.N., Strecker, M.R., Trauth, M.H., Deino, A., Gasse, F., Blisniuk, P., Dühnforth, M., 2009. Tectonic versus climate influences on the evolution of the lakes in the Central Kenya Rift. *Quaternary Science Reviews* 28, 2804–2816.

Bird, M., Ayliffe, L., Fifield, L., Turney, C., Cresswell, R., Barrows, T., David, B., 1999. Radiocarbon dating of 'old' charcoal using a wet oxidation-stepped combustion procedure. *Radiocarbon* 41, 127–40.

Bird, M.I., Turney, C.S.M., Fifield, L.K., Smith, M.A., Miller, G.H., Roberts, R.G., Magee, J.W., 2003. Radiocarbon dating of organic- and carbonate-carbon in *Genyornis* and *Dromaius* eggshell using stepped combustion and stepped acidification. *Quaternary Science Reviews* 22, 1805–1812.

Blackwell, L., d'Errico, F., Wadley, L., 2008. Middle Stone Age bone tools from the Howiesons Poort layers, Sibudu Cave, South Africa. *Journal of Archaeological Science* 35, 1566–1580.

Blades, B.S., 1999. Aurignacian lithic economy and early modern human mobility: new perspectives from classic sites in the Vézère valley of France. *Journal of Human Evolution* 37**,** 91–120.

Blair, M.W., Yukihara, E.G., McKeever, S.W.S., 2005. Experiences with single-aliquot OSL procedures using coarse-grain feldspars. *Radiation Measurements* 39, 361–374.

Bluszcz, A., Adamiec, G., 2006. Application of differential evolution to fitting OSL decay curves. *Radiation Measurements* 41, 886–891.

Bonde, A., Murray, A., Friedrich, W.L., 2001. Santorini: Luminescence dating of a volcanic province using quartz? *Quaternary Science Reviews* 20, 789–793.

Bouzouggar, A., Barton, N., Vanhaeren, M., d'Errico, F., Collcutt, S., Higham, T., Hodge, E., Parfitt, S., Rhodes, E., Schwenninger, J.‐L., Stringer, C., Turner, E., Ward, S., Moutmir, A., Stambouli, A., 2007. 82,000‐year‐old shell beads from North Africa and implications for the origins of modern human behavior. *Proceedings of the National Academy of Sciences of the USA* 104, 9964–9969.

Bowler, J.M., Johnston, H., Olley, J.M., Prescott, J.R., Roberts, R.G., Shawcross, W., Spooner, N.A., 2003. New ages for human occupation and climate change at Lake Mungo, Australia. *Nature* 421, 837–840.

Bøtter-Jensen, L., Mejdahl, V,. 1985. Determination of potassium in feldspars by beta counting using a GM multicounter system. *Nuclear Tracks and Radiation Measurements* 10, 663–666.

Bøtter-Jensen, L., Mejdahl, V., 1988. Assessment of beta dose-rate using a GM multicounter system. *Nuclear Tracks and Radiation Measurements* 14, 187–191.

Bøtter-Jensen, L., Ditlefsen, C., Mejdahl, V., 1991. Combined OSL (infrared) and TL studies of feldspars. *Nuclear Tracks and Radiation Measurements* 18, 257–263.

Bøtter-Jensen, L., Bulur, E., Duller, G.A.T., Murray, A.S., 2000. Advances in luminescence instrument systems. *Radiation Measurements* 32, 523–528.

Bøtter-Jensen, L., Andersen, C.E., Duller, G.A.T., Murray, A.S., 2003. Developments in radiation, stimulation and observation facilities in luminescence measurements. *Radiation Measurements* 37, 535–541.

Brandt, S.A., Hildebrand, E.A., Fisher, E.C., 2007. Field Report on the 2007 Excavations at Moche Borago Rockshelter: Sodo Wolayta Archaeology Project (SWAP): Southwestern Ethiopia Archaeology Program (SWEAP). Unpublished field report.

Bräuer, G., Mehlman, M.J., 1988. Hominid molars from a Middle Stone Age level at the Mumba Rock Shelter, Tanzania. *American Journal of Physical Anthropology* 75, 69–76.

Bronk Ramsey, C., 2008. Radiocarbon dating: Revolutions in understanding. *Archaeometry* 50, 249–275.

Bronk Ramsey, C., Higham, T., Bowles, A., Hedges, R., 2004. Improvements to the pretreatment of bone at Oxford. *Radiocarb*on 46, 155–163.

Brooks, A.S., Robertshaw, P., 1990. The Glacial Maximum in tropical Africa: 22,000–12,000 BP. In Gamble, C., and Soffer, O. (eds.), *The World at 18,000 BP. Vol. 2: Low Latitudes*, Unwin Hyman, London, pp. 120–169.

Brooks, A.S., Hare, P.E., Kokis, J.E., Miller, G.H., Ernst, R.D., Wendorf, F., 1990. Dating Pleistocene archaeological sites by protein diagenesis in ostrich eggshell. *Science* 248, 60–64.

Brooks, A.S., Helgren, D.M., Cramer, J.M., Franklin, A., Hornyak, W., Keating, J.M., Klein, R.G., Rink, W.J., Schwarcz, H.P., Smith, J.N.L., Stewart, K., Todd, N.E., Verniers, J., Yellen, J.E., 1995. Dating and context of three Middle Stone Age sites with bone points in the upper Semliki Valley, Zaire. *Science* 268**,** 548–553.

Brown, K.S., Marean, C.W., Herries, A.I.R., Jacobs, Z., Tribolo, C., Braun, D., Roberts, D.L., Meyer, M.C., Bernatchez, J., 2009. Fire as an engineering tool of early modern humans. *Science* 325, 859–862.

Bulur, E., 1996. An alternative technique for optically stimulated luminescence (OSL) experiment. *Radiation Measurements* 26, 701–709.

Bulur, E., 2000. A simple transformation for converting CW-OSL to LM-OSL curves. *Radiation Measurements* 32, 141–145.

Bulur, E., Duller, G.A.T., Solongo, S., Bøtter-Jensen, L., Murray, A.S., 2002. LM-OSL from single grains of quartz: a preliminary study. *Radiation Measurements* 35, 79–85.

Buylaert, J.P., Vandenberghe, D., Murray, A.S., Huot, S., De Corte, F., Van den Haute, P., 2007. Luminescence dating of old (>70 ka) Chinese loess: a comparison of single-aliquot OSL and IRSL ages. *Quaternary Geochronology* 2, 9–14.

Buylaert, J.P., Murray, A.S., Huot, S., 2008. Optical dating of an Eemian site in Northern Russia using K-feldspar. *Radiation Measurements* 43, 715–720.

Buylaert, J.P., Murray, A.S., Thomsen, K.J., Jain, M., 2009. Testing the potential of an elevated temperature IRSL signal from K-feldspar. *Radiation Measurements* 44, 560–565.

Campbell, M.C., Tishkoff, S.A., 2008. African genetic diversity: implications for human demographic history, modern human origins, and complex disease mapping. *Annual Review of Genomics and Human Genetics* 9, 403–433.

Cann, R.L., Stoneking, M., Wilson, A.C., 1987. Mitochondrial DNA and human evolution. *Nature* 325, 31–36.

Carr, A.S., Bateman, M.D., Holmes, P.J., 2007. Developing a 150 ka luminescence chronology for the barrier dunes of the southern Cape, South Africa. *Quaternary Geochronology* 2, 110–116.

Carto, S.L., Weaver, A.J., Hetherington, R., Lam, Y., Wiebe, E.C., 2009. Out of Africa and into an ice age: on the role of global climate change in the late Pleistocene migration of early modern humans out of Africa. *Journal of Human Evolution* 56, 139–151.

Chase, B.M., 2010. South African palaeoenvironments during marine oxygen isotope stage 4: a context for the Howiesons Poort and Still Bay industries. *Journal of Archaeological Science* 37, 1359–1366.

Chase, B.M., Meadows, M.E., 2007. Late quaternary dynamics of southern Africa's winter rainfall zone. *Earth-Science Reviews* 84, 103–138.

Cheng, H., Edwards, R.L., Murrell, M.T., Benjamin, T.M., 1998. Uranium-thorium-protactinium dating systematics. *Geochimica et Cosmochimica Acta* 62, 3437–3452.

Choi, J.H., Murray, A.S., Jain, M., Cheong, C.S., Chang, H.W., 2003. Luminescence dating of well-sorted marine terrace sediments on the southeastern coast of Korea. *Quaternary Science Reviews* 22, 407–421.

Choi, J.H., Duller, G.A.T., Wintle, A.G., Cheong, C.-S., 2006a. Luminescence characteristics of quartz from the Southern Kenyan Rift Valley: Dose estimation using LM-OSL SAR. *Radiation Measurements* 41, 847–854.

Choi, J.H., Duller, G.A.T., Wintle, A.G., 2006b. Analysis of quartz LM-OSL curves. *Ancient TL* 24, 9–20.

Choi, J.H., Murray, A.S., Cheong, C.-S., Hong, S.C., 2009. The dependence of dose recovery experiments on the bleaching of natural quartz OSL using different light sources. *Radiation Measurements* 44, 600–605.

Chu, S.Y.F., Ekstorm, L.P., Firestone, R.B., 1999. WWW Table of Radioactive Isotopes, database version 1999-02-28. http://nucleardata.nuclear.lu.se/nucleardata/toi/

Clark, J.G.D., 1968. World prehistory: a new outline, 2nd ed. Cambridge: Cambridge University Press.

Clark, J.D., 1988. The Middle Stone Age of East Africa and the beginnings of regional identity. *Journal of World Prehistory* 2, 235–305.

Clark, J.D., Williamson, K.D., Michels, J.W., Marean, C.A., 1984. A Middle Stone Age occupation site at Porc Epic Cave, Dire Dawa (east-central Ethiopia. *African Archaeological Review* 2, 37–72.

Clark, J.D., Beyene, Y., WoldeGabriel, G., Hart, W.K., Renne, P.R., Gilbert, H., Defleur, A., Suwa, G., Katoh, S., Ludwig, K.R., Boisserie, J.-R., Asfaw, B., White, T.D., 2003. Stratigraphic, chronological and behavioural contexts of Pleistocene *Homo sapiens* from Middle Awash, Ethiopia. *Nature* 423, 747–752.

Clark, R.J., Sanderson, D.C.W., 1994. Photostimulated luminescence excitation spectroscopy of feldspars and micas. *Radiation Measurements* 23, 641–646.

Clarke, M.L., Rendell, H.M., 1997. Infra-red stimulated luminescence spectra of alkali feldspars. *Radiation Measurements* 27, 221–236.

Clarke, M.L., Rendell, H.M., Sanchez-Muñoz, L., Garcia-Guinea, J., 1997. A comparison of luminescence spectra and structural composition of perthitic feldspars. *Radiation Measurements* 27, 137–144.

Clarke, S.J., Murray-Wallace, C.V., 2006. Mathematical expressions used in amino acid racemisation geochronology—A review. *Quaternary Geochronology* 1, 261–278.

Clarkson, C., Petraglia, M., Korisettar, R., Haslam, M., Boivin, N., Crowther, A., Ditchfield, P., Fuller, D., Miracle, P., Harris, C., Connell, K., James, H., Koshy, J., 2009. The oldest and longest enduring microlithic sequence in India: 35 000 years of modern human occupation and change at the Jwalapuram Locality 9 rockshelter. *Antiquity* 83, 326–348.

Clement, A.C., Hall, A., Broccoli, A.J., 2004. The importance of precessional signals in tropical climate. *Climate Dynamics* 22, 327–341.

Cohen, A.S., Stone, J.R., Beuning, K.R.M., Park, L.E., Reinthal, P.N., Dettman, D., Scholz, C.A., Johnson, T.C., King, J.W., Talbot, M.R., Brown, E.T., Ivory, S.J., 2007. Ecological consequences of early Late Pleistocene megadroughts in tropical Africa. *Proceedings of the National Academy of Sciences of the USA* 104, 16422–16427.

Conard, N.J., 2005. An overview of the patterns of behavioural change in Africa and Eurasia during the Middle and Late Pleistocene. In: D'Errico, F. & Blackwell, L. (eds.), *From Tools to Symbols: From Early Hominids to Modern Humans.* Witwatersrand University Press, Johannesburg, pp. 294–332.

Conard, N.J., 2007. Cultural Evolution in Africa and Eurasia During the Middle and Late Pleistocene, in: Henke, W., Tattersall, I., (Eds.) Handbook of Paleoanthropology, Springer-Verlag, Berlin, pp 2001–2037.

Conard, N.J., Marks, A., 2006. New research on the MSA of Mumba Cave, Tanzania. Paper presented at the 71st annual meeting of the Society for American Archaeology, San Juan, PR.

Cunha, P.P., Martins, A.A., Huot, S., Murray, A., Raposo, L., 2008. Dating the Tejo river lower terraces in the Ródão area (Portugal) to assess the role of tectonics and uplift. *Geomorphology* 102, 43–54.

Cunningham, A.C., Wallinga, J., 2010. Selection of integration time intervals for quartz OSL decay curves. *Quaternary Geochronology* 5, 657–666.

d'Errico, F., Soressi, M., 2002. Systematic use of pigment by Pech de L'Azé Neandertals: Implications for the origin of behavioral modernity. Paleoanthropology Society Meeting, 19–20 March, Denver. *Journal of Human Evolution* 42, A13.

d'Errico, F., Henshilwood, C., 2007. Additional evidence for bone technology in the southern African Middle Stone Age. *Journal of Human Evolution* 52, 142–163.

d'Errico, F., Henshilwood, C., Lawson, G., Vanhaeren, M., Tillier, A.-M., Soressi, M., Bresson, F., Maureille, B., Nowell, A., Lakarra, J., Backwell, L., Julien, M., 2003. Archaeological evidence for the emergence of language, symbolism, and music – an alternative multidisciplinary perspective. *Journal of World Prehistory* 17, 1–70.

d'Errico, F., Henshilwood, C., Vanhaeren, M., van Niekerk, K., 2005. *Nassarius kraussianus* shell beads from Blombos Cave: evidence for symbolic behaviour in the Middle Stone Age. *Journal of Human Evolution* 48, 3–24.

d'Errico, F., Vanhaeren, M., Wadley, L., 2008. Possible shell beads from the Middle Stone Age layers of Sibudu Cave, South Africa. *Journal of Archaeological Science* 35, 2675–2685.

d'Errico, F., Vanhaeren, M., Barton, A., Bouzouggar, A., Mienis, H., Richter, D., Hublin, J.-J., Shannon, P., McPherron, S.P., Lozouet, P., 2009. Additional evidence on the use of personal ornaments in the Middle Paleolithic of North Africa. *Proceedings of the National Academy of Sciences of the USA* 106, 16051–16056.

David, B., Roberts, R.G., Magee, J., Mialanes, J., Turney, C., Bird, M., White, C., Fifield, K.L., Tibby, J., 2007. Sediment mixing at Nonda Rock: investigations of stratigraphic integrity at an early archaeological site in northern Australia, and implications for the human colonisation of the continent. *Journal of Quaternary Science* 22, 449–479.

Deacon, H.J., Wurz, S.G.D., 1996. Klasies River Main Site Cave 2: a Howiesons Poort occurrence. In (G. Pwiti & R. Soper, Eds) *Aspects of African Archaeology*, pp. 213–218. Harare: University of Zimbabwe Publications.

Deacon, H.J., Deacon, J., 1999. *Human Beginnings in South Africa: Uncovering the Secrets of the Stone Age*. Capetown: David Philip.

Deino, A.L., McBrearty, S., 2002. $^{40}Ar/^{39}Ar$ chronology for the Kapthurin Formation, Baringo, Kenya. *Journal of Human Evolution* 1/2 185–210.

Demuro, M., 2009. Optically stimulated luminescence dating of tephra-bearing deposits from eastern Beringia. Ph.D. thesis (unpublished), University of Wollongong.

Diez-Martín, F., Domínguez-Rodrigo, M., Sánchez, P., Mabulla, A.Z.P., Tarriño, A., Barba, R., Prendergast, M.E., Luque, L., 2009. The Middle to Later Stone Age technological transition in East Africa. New data from Mumba Rockshelter Bed V (Tanzania) and their implications for the origin of modern human behavior. *Journal of African Archaeology* 7, 147–173.

Duller, G.A.T., 1991. Equivalent dose determination using single aliquots. *Nuclear Tracks and Radiation Measurement* 18, 371–378.

Duller, G.A.T., 1994. A new method for the analysis of infrared stimulated luminescence data from potassium feldspars. *Radiation Measurements* 23, 281–285.

Duller, G.A.T., 1995. Infrared bleaching of the thermoluminescence of four feldspars. *Journal of Physics D: Applied Physics* 28, 1244–1258.

Duller, G.A.T., 1997. Behavioural studies of stimulated luminescence from Feldspars. *Radiation Measurements* 27, 663–694.

Duller, G.A.T., 2003. Distinguishing quartz and feldspar in single grain luminescence measurements. *Radiation Measurements* 37, 161–165.

Duller, G.A.T., 2004. Luminescence dating of Quaternary sediments: recent advances. *Journal of Quaternary Science* 19, 183–192.

Duller, G.A.T., 2006. Single grain optical dating of glacigenic deposits. *Quaternary Geochronology* 1, 296–304.

Duller, G.A.T., 2008. Single-grain optical dating of Quaternary sediments: why aliquot size matters in luminescence dating. *Boreas* 37, 589–612.

Duller, G.A.T., Wintle, A.G., 1991. On infrared stimulated luminescence at elevated temperatures. *Nuclear Tracks and Radiation Measurements* 18, 379–384.

Duller, G.A.T., Bøtter-Jensen, L., 1993. Luminescence from potassium feldspars stimulated by infrared and green light. *Radiation Protection Dosimetry* 47, 683–688.

Duller, G.A.T., Bøtter-Jensen, L., Murray, A.S., 2000. Optical dating of single sand-sized grains of quartz: sources of variability. *Radiation Measurements* 32, 453–457.

Ebinger, C., Poudjom, Y., Mbede, E.A., Dawson, J.B., 1997. Rifting Archaean lithosphere: the Eyasi-Manyara-Natron rifts. *Journal of the Geological Society (London)* 154, 947–960.

Endicott, P., Ho, S.Y.W., Metspalu, M., Stringer, C., 2009. Evaluating the mitochondrial timescale of human evolution. *Trends in Ecology and Evolution* 24, 515–521.

EPICA Community Members, 2006. One-to-one coupling of glacial climate variability in Greenland and Antarctica. *Nature*, 444, 195–198.

Eriksson, M.G., Olley, J.M., Payton, R.W., 2000. Soil erosion history in central Tanzania based on OSL dating of colluvial and alluvial hillslope deposits. *Geomorphology* 36, 107–128.

Eriksson, M.G., Olley, J.M., Kilham, D.R., Pietsch, T., Wasson, R.J., 2006. Aggradation and incision since the very late Pleistocene in the Naas River, south-eastern Australia. *Geomorphology* 81, 66–88.

Excoffier, L., Schneider, S., 1999. Why hunter-gatherer populations do not show signs of Pleistocene demographic expansions. *Proceedings of the National Academy of Sciences of the USA* 96, 10597–10602.

Fattahi, M., 2004. The dependence of orange-red IRSL decay curves of potassium feldspars on sample temperature. *Radiation Measurements* 38, 287–298.

Fattahi, M., Stokes, S., 2003a. Dating volcanic and related sediments by luminescence methods: a review. *Earth-Science Reviews* 62, 229–264.

Fattahi, M., Stokes, S., 2003b. Photomultiplier and filter combinations for the detection of relatively long wavelength (λ>600 nm) luminescence emissions from feldspars. *Ancient TL* 21, 25–34.

Fattahi, M., Stokes, S., 2003c. Red luminescence from potassium feldspar for dating applications: a study of some properties relevant for dating. *Radiation Measurements* 37, 647–660.

Feathers, J.K., 1996. Luminescence Dating and Modern Human Origins. *Evolutionary Anthropology* 5, 25–36.

Feathers, J.K., 2003. Single-grain OSL dating of sediments from the Southern High Plains, USA. *Quaternary Science Reviews* 22, 1035–1042.

Feathers, J.K., Migliorini, E., 2001. Luminescence dating at Katanda – a reassessment. *Quaternary Science Reviews* 20, 961–966.

Feathers, J.K., Rhodes, E.J., Huot, S., Mcavoy, J.M., 2006. Luminescence dating of sand deposits related to late Pleistocene human occupation at the Cactus Hill Site, Virginia, USA. *Quaternary Geochronology* 1, 167–187.

Feblot-Augustins, J., Perlès, C., 1992. Perspectives ethnoarchéologiques sure les échanges à longue distance, in *Ethnoarchéologie: Justification, Problémes, Limites,*

XIIe Recontres Internationales d'Archéologie et d'Histoire d'Antibes. Juan-les-Pins: APDCA, pp. 195–209.

Felton, A.A., Russell, J.M., Cohen, A.S., Baker, M.E., Chesley, J.T., Lezzar, K.E., McGlue, M.M., Pigati, J.S., Quade, J., Stager, J.S., Tiercelin, J.J., 2007. Paleolimnological evidence for the onset and termination of glacial aridity from Lake Tanganyika, tropical East Africa. *Palaeogeography, Palaeoclimatology, Palaeoecology* 252, 405–423.

Ficken, K.J., Street-Perrott, F.A., Perrott, R.A., Swain, D.L., Olago, D.O., Eglinton, G., 1998. Glacial/interglacial variations in carbon cycling revealed by molecular and isotope stratigraphy of Lake Nkunga, Mt. Kenya, East Africa. *Organic Geochemistry* 29, 1701–1719.

Fisher, E.C., Hildebrand, E.A., Brandt, S.A., Herries, A., 2009. Provisional correlations between Late Pleistocene OIS 3 millennial scale climate changes and AMS ^{14}C dated archaeological deposits at Moche Borago Rockshelter, SW Ethiopia. Paper presented at the 2nd workshop of East African Quaternary Research Association (EAQUA), Addis Ababa, Ethiopia.

Fleitmann, D., Burns, S.J., Neff, U., Mangini, A., Matter, A., 2003. Changing moisture sources over the last 330,000 years in Northern Oman from fluid-inclusion evidence in speleothems. *Quaternary Research* 60, 223–232.

Fleitmann, D., Burns, S.J., Pekala, M., Mangini, A., Al-Subbary, A., Al-Aowah, M., Kramers, J., Matter, A., 2011. Holocene and Pleistocene pluvial periods in Yemen, southern Arabia. *Quaternary Science Reviews* 30, 783–787.

Foley, R., Lahr, M.M., 2003. On stony ground: Lithic technology, human evolution, and the emergence of culture. *Evolutionary Anthropology* 12, 109–122.

Forrest, B., Rink, W.J., Bicho, N., Ferring, C.R., 2003. OSL ages and possible bioturbation signals at the Upper Paleolithic site of Lagoa do Bordoal Algarve, Portugal. *Quaternary Science Reviews* 22, 1279–1285.

Forster, P., Matsumura, S., 2005. Evolution. Did early humans go north or south? *Science* 308, 965–966.

Fullagar, R.L.K., Price, D.M., Head, L.M., 1996. Early human occupation of northern Australia: archaeology and thermoluminescence dating of Jinmium rock shelter, Northern Territory. *Antiquity* 70, 751–773.

Galbraith, R.F., 2002. A note on the variance of a background-corrected OSL count. *Ancient TL* 20, 49–51.

Galbraith, R.F., 2005. Statistics for Fission Track Analysis. Chapman & Hall, London.

Galbraith, R.F., Roberts, R.G., Laslett, G.M., Yoshida, H., Olley, J.M., 1999. Optical dating of single and multiple grains of quartz from Jinmium rock shelter, northern Australia: Part I, experimental design and statistical models. *Archaeometry* 41, 339–364.

Galbraith, R.F., Roberts, R.G., Yoshida, H., 2005. Error variation in OSL palaeodose estimates from single aliquots of quartz: a factorial experiment. *Radiation Measurements* 39, 289–307.

Gamble, C., 1993. Exchange and local hominid networks. In: Scarre, C., Healy, F. (Eds.), Trade and Exchange in Prehistoric Europe. Oxbow Monographs, 33. Oxbow Books, Oxford, pp. 35–44.

Garrigan, D., Kingan, S.B., Pilkington, M.M., Wilder, J.A., Cox, M.P., Soodyall, H., Strassmann, B., Destro-Bisol, G., de Knijff, P., Novelletto, A., Friedlaender, J., Hammer, M.F., 2007. Inferring human population sizes, divergence times and rates of gene flow from mitochondrial, X and Y chromosome resequencing data. *Genetics* 177, 2195–2207.

Gasse, F., 2000. Hydrological changes in the African tropics singe the Last Glacial Maximum. *Quaternary Science Reviews* 19, 189–211.

Gelian, G., Bin, X., Shunsheng, L., 2006. Study on feldspar thermoluminescence spectra and its luminescence dating implication. *Nuclear Instruments and Methods in Physics Research B* 251, 143–147.

Godfrey-Smith, D.I., 1994. Thermal effects in the optically stimulated luminescence of quartz and mixed feldspars for sediments. *Journal of Physics D: Applied Physics* 27, 1737–1746.

Godfrey-Smith, D.I., Cada, M., 1996. IR stimulation spectroscopy of plagioclase and potassium feldspars, and quartz. *Radiation Protection Dosimetry* 66, 379–385.

Godfrey-Smith, D.I., Huntley, D.J., Chen, W.-H., 1988. Optical dating studies of quartz and feldspar sediment extracts. *Quaternary Science Reviews* 7, 373–380.

Gonder, M.K., Mortensen, H.M., Reed, F.A., de Sousa, A., Tishkoff, S.A., 2007. Whole-mtDNA genome sequence analysis of ancient African lineages. *Molecular and Biological Evolution* 24, 757–768.

Goodwin, A.J.H., Van Riet Lowe, C., 1929. The Stone Age cultures of South Africa. *Annals of the South African Museum* 27, 1–289.

Gould, R., 1977. Puntutjarpa Rockshelter and the Australian Desert Culture. Anthropological Papers, volume 54. American Museum of Natural History, New York.

Gould, R.A., 1978. The anthropology of human residues. *American Anthropologist* 80**,** 815–835.

Gould, R.A., Saggers, S., 1985. Lithic procurement in central Australia: a closer look at Binford's idea of embeddedness in archaeology. *American Antiquity* 50, 117–136.

Green, R.E., Krause, J., Briggs, A.W., Maricic, T., Stenzel, U., Kircher, M., Patternson, N., Li, H., Shai, W., Fritz, M.H.-Y., Hansen, N.F., Durand, E.Y., Malaspinas, A.-S., Jensen, J.D., Marques-Bonet, T., Alkan, C., Prüfer, K., Meyer, M., Burbano, H.A., Good, J.M., Schultz, R., Aximu-Petri, A., Butthof, A., Höber, B., Höffner, B., Siegemund, M., Weihmann, A., Nusbaum, C., Lander, E.S., Russ, C., Novod, N., Affourtit, J., Egholm, M., Verna, C., Rudan, P., Brajkovic, D., Kucan, Z., Gušic, I., Doronichev, V.B., Golovanova, L.V., Lalueza-Fox, C., Rasilla, M., Fortea, J., Rosas, A., Schmitz, R.W., Johnson, P.L.F., Eichler, E.E., Falush, D., Birney, E., Mullikin, J.C., Slatkin, M., Nielsen, R., Kelso, J., Lachmann, M., Reich, D., Pääbo, S., 2010. A Draft Sequence of the Neandertal Genome. *Science* 328, 710–722.

Greenfield, P.M., 1991. Language, tools, and brain: the ontogeny and phylogeny of hierarchically organized sequential behaviour. *Behavioral and Brain Science* 14, 531–595.

Grün, R., 2000. An alternative for model for open system U-series/ESR age calculations: (Closed system U-series)-ESR, CSUS-ESR. *Ancient TL* 18, 1–4.

Grün, R., 2006. Direct dating of human fossils. *Yearbook of Physical Anthropology* 49, 2–48.

Grün, R., Schwarcz, H.P., Chadam, J.M., 1988. ESR dating of tooth enamel: Coupled correction for U-uptake and U-series disequilibrium. *Nuclear Tracks and Radiation Measurements* 14, 237–241.

Grün, R., Aubert, M., Hellstrom, J., Duval, M., 2010. The challenge of direct dating old human fossils. *Quaternary International* 223-224, 87–93.

Guérin, G., Valladas, G., 1980. Thermoluminescence dating of volcanic plagioclases. *Nature* 286, 697–699.

Hedges, R.E.M., van Klinken, G.J., 1992. A review of current approaches in the pretreatment of bone for radiocarbon dating by AMS. *Radiocarbon* 34, 279–291.

Henrich, J., 2004. Demography and cultural evolution: How adaptive cultural processes can produce maladaptive losses—The Tasmanian case. *American Antiquity* 69, 197–214.

Henshilwood, C.S., Sealy, J., 1997. Bone artefacts from the Middle Stone Age at Blombos Cave, southern Cape, South Africa. *Current Anthropology* 38, 890–895.

Henshilwood, C.S., Marean, C.W., 2003. The origin of modern human behavior: critique of the models and their test implications. *Current Anthropology* 44, 627–652.

Henshilwood, C., d'Errico, F., Marean, C.W., Milo, R.G., Yates, R., 2001. An early bone tool industry from the Middle Stone Age at Blombos Cave, South Africa: implications for the origins of modern human behaviour, symbolism and language. *Journal of Human Evolution* 41, 631–678.

Henshilwood, C.S., d'Errico, F., Yates, R., Jacobs, Z., Tribolo, C., Duller, G.A.T., Mercier, N., Sealy, J.C., Valladas, H., Watts, I., Wintle, A.G., 2002. Emergence of modern human behavior: Middle Stone Age engravings from South Africa. *Science* 295, 1278–1280.

Henshilwood, C., d'Errico, F., Vanhaeren, M., van Niekerk, K., Jacobs, Z., 2004. Middle Stone Age Shell Beads from South Africa. *Science* 304, 404.

Henshilwood, C.S., d'Errico, F., Watts, I., 2009. Engraved ochres from the Middle Stone Age levels at Blombos Cave, South Africa. *Journal of Human Evolution* 57, 27–47.

Higham, T.F.G., Jacobi, R.M., Bronk Ramsey, C., 2006. AMS radiocarbon dating of ancient bone using ultrafiltration. *Radiocarbon* 48, 179–195.

Holmgren, K., Karlén, W., Shaw, P.A., 1995. Paleoclimatic significance of the stable isotopic composition and petrology of a Late Pleistocene stalagmite from Botswana. *Quaternary Research* 43, 320–328.

Holzkämper, S., Holmgren, K., Lee-Thorp, J., Talma, S., Mangini, A., Partridge, T., 2009. Late Pleistocene stalagmite growth in Wolkberg Cave, South Africa. *Earth and Planetary Science Letters* 282, 212–221.

Hudjashov, G., Kivisild, T., Underhill, P.A., Endicott, P., Sanchez, J.J., Lin, A.A., Shen, P., Oefner, P., Renfrew, C., Villems, R., Forster, P., 2007. Revealing the prehistoric settlement of Australia by Y chromosome and mtDNA analysis. *Proceedings of the National Academy of Sciences of the USA* 104, 8726–8730.

Hull, K.L., 2001. Reasserting the utility of obsidian hydration dating: A temperature-dependent empirical approach to practical temporal resolution with archaeological obsidians. *Journal of Archaeological Science* 28, 1025–1040.

Huntley, D.J., 1997. A proposal for dealing with anomalous fading. *Ancient TL* 15, 28–29.

Huntley, D.J., 2006. An explanation of the power-law decay of luminescence. *Journal of Physics: Condensed Matter* 18, 1359–1365.

Huntley, D.J., Baril, M.R., 1997. The K content of the K-feldspars being measured in optical dating or in thermoluminescence dating. *Ancient TL* 15, 11–13.

Huntley, D.J., Hancock, R.G.V., 2001. The Rb contents of the K-feldspar grains being measured in optical dating. *Ancient TL* 19, 43–46.

Huntley, D.J., Lamothe, M., 2001. Ubiquity of anomalous fading in K-feldspars and the measurement and correction for it in optical dating. *Canadian Journal of Earth Sciences* 38, 1093–1106.

Huntley, D.J., Lian, O.B., 2006. Some observations on tunnelling of trapped electrons in feldspars and their implications for optical dating. *Quaternary Science Reviews* 25, 2503–2512.

Huntley, D.J., Godfrey-Smith, D.I., Thewalt, M.L.W., 1985. Optical dating of sediments. *Nature* 313, 105–107.

Huntley, D.J., Godfrey-Smith, D.I., Thewalt, M.L.W., Berger, G.W., 1988. Thermoluminescence spectra of some mineral samples relevant to thermoluminescence dating. *Journal of Luminescence* 39, 123–136.

Huntley, D.J., Hutton, J.T., Prescott, J.R., 1993. Optical dating using inclusions within quartz grains. *Geology* 21, 1087–1090.

Huntley, D.J., Short, M.A., Dunphy, K., 1996. Deep traps in quartz and their use for optical dating. *Canadian Journal of Physics* 74, 81–91.

Huntley, D.J., Baril, M.R., Haidar, S., 2007. Tunnelling in plagioclase feldspars. *Journal of Physics D: Applied Physics* 40, 900–906.

Huot, S., Lamothe, M., 2003. Variability of infrared stimulated luminescence properties from fractures feldspar grains. *Radiation Measurements* 37, 499–503.

Hütt, G., Jaek, I., 1993. Photostimulated luminescence of some minerals and its dosimetry applications. *Nuclear Tracks and Radiation Measurements* 21, 95–98.

Hütt, G., Jaek, I., Tchonka, J., 1988. Optical dating: K-feldspars optical response stimulation spectra. *Quaternary Science Reviews* 7, 381–385.

Inskeep, R., 1962. The age of the Kondoa rock painting in the light of recent excavations at Kisese II rock shelter. In (G. Mortelmans & J. Nenquin, Eds) *Actes du IVe Congrés Panafricain de Préhistoire et de l'Etude du Quaternaire (Léopoldville, 1959)*, pp. 249–256. Vol. 2. Tervuren: Musée Royale de l'Afrique Centrale. Annales Série 8, Sciences Humaines no. 40.

Jacobs, Z., 2004. Development of luminescence techniques for dating Middle Stone Age sites in South Africa. Ph.D. thesis (unpublished), University of Wales, Aberystwyth.

Jacobs, Z., Roberts, R.G., 2007. Advances in optically stimulated luminescence dating of individual grains of quartz from archeological deposits. *Evolutionary Anthropology* 16, 210–223.

Jacobs, Z., Roberts, R.G., 2009. Catalysts for Stone Age innovations: What might have triggered two short-lived bursts of technological and behavioural innovations in southern Africa during the Middle Stone Age? *Communicative and Integrative Biology* 2, 1–4.

Jacobs, Z., Wintle, A.G., Duller, G.A.T., 2003a. Optical dating of dune sand from Blombos Cave, South Africa: I – multiple grain data. *Journal of Human Evolution* 44, 599–612.

Jacobs, Z., Duller, G.A.T., Wintle, A.G., 2003b. Optical dating of dune sand from Blombos Cave, South Africa: II – single grain data. *Journal of Human Evolution* 44, 613–625.

Jacobs, Z., Wintle, A.G., Duller, G.A.T., 2006a. Evaluation of SAR procedures for D_e determination using single aliquots from two archaeological sites in South Africa. *Radiation Measurements* 41, 520–533.

Jacobs, Z., Duller, G.A.T., Wintle, A.G., 2006b. Interpretation of single grain D_e distributions and calculation of D_e. *Radiation Measurements* 41, 264–277.

Jacobs, Z., Duller, G.A.T., Wintle, A.G., Henshilwood, C.S., 2006c. Extending the chronology of deposits at Blombos Cave, South Africa, back to 140 ka using optical dating of single and multiple grains of quartz. *Journal of Human Evolution* 51, 255–273.

Jacobs, Z., Roberts, R.G., Galbraith, R.F., Deacon, H.J., Grün, R., Mackay, A., Mitchell, P., Vogelsang, R., Wadley, L., 2008a. Ages for the Middle Stone Age of southern Africa: implications for human behavior and dispersal. *Science* 322, 733–735.

Jacobs, Z., Wintle, A.G., Roberts, R.G., Duller, G.A.T., 2008b. New ages for the post-Howiesons Poort, late and final Middle Stone Age at Sibudu, South Africa. *Journal of Archaeological Science* 35, 1790–1807.

Jacobs, Z., Wintle, A.G., Roberts, R.G., Duller, G.A.T., 2008c. Equivalent dose distributions from single grains of quartz at Sibudu, South Africa: context, causes and consequences for optical dating of archaeological deposits. *Journal of Archaeological Science* 35, 1808–1820.

Jain, M., Singhvi, A.K., 2001. Limits to depletion of blue-green light stimulated luminescence in feldspars: implications for quartz dating. *Radiation Measurements* 33, 883–892.

Jain, M., Murray, A.S., Bøtter-Jensen, L., 2003. Characterisation of blue-light stimulated luminescence components in different quartz samples: implications for dose measurements. *Radiation Measurements* 37, 441–449.

Johnson, T.C., Brown, E.T., McManus, J., Barry, S., Barker, P., Gasse, F., 2002. High-resolution palaeoclimate record spanning the past 25,000 years in southern East Africa. *Science* 296, 113–132.

Jungner, H., Bøtter-Jensen, L., 1994. Study of sensitivity change of OSL signals from quartz and feldspars as a function of preheat temperature. *Radiation Measurements* 23, 621–624.

Kalchgruber, R., 2002. α-Al2O3:C als Dosimeter zur Bestimmung der Dosisleistung bei der Lumineszenzdatierung (Dose-rate assessment in luminescence dating with α-Al2O3:C dosemeters). Ph.D. thesis (unpublished), University of Heidelberg, Germany.

Kallel, N., Duplessy, J.-C., Labeyrie, L., Fontugne, M., Paterne, M., Montacer, M., 2000. Mediterranean pluvial periods and sapropel formation over the last 200,000 years. *Palaeogeography, Palaeoclimatology, Palaeoecology* 157, 45–58.

Kars, R.H., Wallinga, J., Cohen, K.M., 2008. A new approach towards anomalous fading correction for feldspar IRSL dating-tests on samples in field saturation. *Radiation Measurements* 43, 786–790.

Kelly, R.L., 1983. Hunter-gatherer mobility strategies. *Journal of Anthropological Research* 39, 277–306.

Kelly, R.L., 1995. *The Foraging Spectrum: Diversity in Hunter-Gatherer Lifeways*. Washington (DC): Smithsonian Institution Press.

Klasen, N., Fiebig, M., Preusser, F., Radtke, U., 2006. Luminescence properties of glaciofluvial sediments from the Bavarian Alpine Foreland. *Radiation Measurements* 41, 866–870.

Klasen, N., Fiebig, M., Preusser, F., Reitner, J.M., Radtke, U., 2007. Luminescence dating of proglacial sediments from the Eastern Alps. *Quaternary International* 164-165, 21–32.

Klein, R.G., 1995. Anatomy, behaviour and modern human origins. *Journal of World Prehistory* 9, 167–198.

Klein, R.G., 2001. Southern Africa and modern human origins. *Journal of Anthropological Research* 57, 1–16.

Klein, R.G., 2008. Out of Africa and the Evolution of Human Behavior. *Evolutionary Anthropology* 17, 267–281.

Kline, M.A., Boyd, R., 2010. Population size predicts technological complexity in Oceania. *Proceedings of the Royal Society B: Biological Sciences* 277, 2559–2564.

Knight, A., Underhill, P.A., Mortensen, H.M., Zhivotovsky, L.A., Lin, A.A., Henn, B.M., Louis, D., Ruhlen, M., Mountain, J.L., 2003. African Y chromosome and mtDNA

divergence provides insight into the history of click languages. *Current Biology* 13, 464–473.

Köhl-Larsen, L., 1943. *Auf den Spuren des Vormenschen.* Strecker und Schröeder Verlag, Stuttgart.

Koutavas, A., Lynch-Stieglitz, J., Marchitto, T.M., Sachs, J.P., 2002. El Niño-like pattern in ice age tropical Pacific sea surface temperature. *Science* 297, 226–230.

Krause, J., Fu, Q., Good, J.M., Viola, B., Shunkov, M.V., Derevianko, A.P., Pääbo, S., 2010. The complete mitochondrial DNA genome of an unknown hominin from southern Siberia. *Nature* 464, 894–897.

Krbetschek, M.R., Rieser, U., 1995. Luminescence spectra of alkali feldspars and plagioclases. *Radiation Measurements* 24, 473–477.

Krbetschek, M.R., Rieser, U., Stolz, W., 1996. Optical dating: some luminescence properties of natural feldspars. *Radiation Protection Dosimetry* 66, 407–412.

Krbetschek, M.R., Götze, J., Dietrich, A., Trautmann, T., 1997. Spectral information from minerals relevant for luminescence dating. *Radiation Measurements* 27, 695–748.

Krbetschek, M.R., Trautmann, T., Dietrich, A., Stolz, W., 2000. Radioluminescence dating of sediment: methodological aspects. *Radiation Measurements* 32, 493–498.

Kuhn, S.L., 1991. 'Unpacking' reduction: lithic raw material economy in the Mousterian of West-Central Italy. *Journal of Anthropological Archaeology* 10, 76–106.

Kuhn, S.L., 1992. On planning and curated technologies in the Middle Palaeolithic. *Journal of Anthropological Research* 48, 185–214.

Kuhn, S.L., 1995. Mousterian Lithic Technology: An Ecological Perspective. Princeton University Press, Princeton.

Kuhn, S.L., Stiner, M.C., 2007. Paleolithic ornaments: implications for cognition, demography and identity. *Diogenes* 214, 40–48.

Kuhn, S.L., Stiner, M.C., Reese, D., Güleç, E., 2001. Ornaments of the earliest Upper Paleolithic: new insights from the Levant. *Proceedings of the National Academy of Sciences of the USA* 98, 7641–7646.

Kusimba, S., 2001. The early Later Stone Age in East Africa: excavations and lithic assemblages from Lukenya Hill. *African Archaeological Review* 18, 77–123.

Lamb, H.F., Bates, C.R., Coombes, P.V., Marshall, M.H., Umer, M., Davies, S.J., Dejen, E., 2007. Late Pleistocene desiccation of Lake Tana, source of the Blue Nile. *Quaternary Science Reviews* 26, 287–299.

Lamothe, M., 1995. Using 600–650 nm light for IRSL sample preparation. *Ancient TL* 13, 1–4.

Lamothe, M., Auclair, M., 1997. Assessing the datability of young sediments by IRSL using an intrinsic laboratory protocol. *Radiation Measurements* 27, 107–117.

Lamothe, M., Auclair, M., 1999. A solution to anomalous fading and age shortfalls in optical dating of feldspar minerals. *Earth Planetary Science Letters* 171, 319–323.

Lamothe, M., Auclair, M., Hamzaoui, C., Huot, S., 2003. Towards a prediction of long-term anomalous fading of feldspar IRSL. *Radiation Measurements* 37, 493–498.

Lang, A., Wagner, G.A., 1997. Infrared stimulated luminescence dating of Holocene colluvial sediments using the 410 nm emission. *Quaternary Science Reviews* 16, 393–396.

Lang, A., Hatté, C., Rousseau, D.-D., Antoine, P., Fontugne, M., Zöller, L., Hambach, U., 2003. High-resolution chronologies for loess: comparing AMS ^{14}C and optical dating results. *Quaternary Science Reviews* 22, 953–959.

Larsen, R.B., Henderson, I., Ihlen, P.M., Jacamon, F., 2004. Distribution and petrogenetic behaviour of trace elements in granitic pegmatite quartz from South Norway. C*ontributions to Mineralogy and Petrology* 147, 615–628.

Leakey, M.D., Hay, R.L., Thurber, D.L., Protsch, R., Berger, R., 1972. Stratigraphy, archaeology, and age of the Ndutu and Naisiusiu Beds, Olduvai Gorge, Tanzania. *World Archaeology* 3, 328–341.

Lepper, K., Wilson, C., Gardner, J., Reneau, S., Lavine, A., 2003. Comparison of SAR techniques for luminescence dating of sediments derived from volcanic tuff. *Quaternary Science Reviews* 22, 1131–1138.

Leuschner, D.C., Sirocko, F., Schettler, G., Garbe-Schonberg, D., 2004. Geochemical implications for changing the dust supply by the Indian monsoon system for the Arabian Sea during the last glacial cycle. In: Smykatz-Kloss, S., Henningsen, F., Zoller, L. (Eds.), *Paleoecology of Quaternary Dryland*. Springer-Verlag, Stuttgart, Germany, pp. 119–135.

Li, B., 2010. The relationship between thermal activation energy, infrared stimulated luminescence and anomalous fading of K-feldspars. *Radiation Measurements* 45, 757–763.

Li, B., Li, S.-H., 2006a. Comparison of D_e estimates using the fast component and the medium component of quartz OSL. *Radiation Measurements* 41, 125–136.

Li, S.-H., 1991. Removal of the thermally unstable signal in optical dating of K-feldspar. *Ancient TL* 9, 26–29.

Li, S.-H., Li, B., 2006b. Dose measurement using the fast component of LM-OSL signals from quartz. *Radiation Measurements* 41, 534–541.

Lian, O.B., Roberts, R.G., 2006. Dating the Quaternary: progress in luminescence dating of sediments. *Quaternary Science Reviews* 25, 2449–2468.

Lomax, J., Hilgers, A., Twidale, C.R., Bourne, J.A., Radtke, U., 2007. Treatment of broad palaeodose distributions in OSL dating of dune sands from the western Murray Basin, South Australia. *Quaternary Geochronology* 2, 51–56.

Lombard, M., 2005. Evidence of hunting and hafting during the Middle Stone Age at Sibidu Cave, KwaZulu-Natal, South Africa: a multianalytical approach. *Journal of Human Evolution* 48, 279–300.

Lombard, M., 2007. The gripping nature of ochre: The association of ochre with Howiesons Poort adhesives and Later Stone Age mastics from South Africa. *Journal of Human Evolution* 53, 406–419.

Lombard, M., 2008. Finding resolution for the Howiesons Poort through the microscope: micro-residue analysis of segments from Sibudu Cave, South Africa. *Journal of Archaeological Science* 35, 26–41.

Lombard, M., Wadley, L., Jacobs, Z., Mohapi, M., Roberts, R.G., 2010. Still Bay serrated points from Umhlatuzana Rock Shelter, Kwazulu-Natal, South Africa. *Journal of Archaeological Science* 37, 1773–1784.

Lourens, L.J., Antonarakou, A., Hilgen, F.J., Van Hoof, A.A.M., Vergnaud-Grazzini, C., Zachariasse, W.J., 1996. Evaluation of the Plio-Pleistocene astronomical timescale. *Paleoceanography* 11, 391–413.

Mabulla, A.Z.P., 2007. Hunting and foraging in the Eyasi Basin, Northern Tanzania: past, present and future prospects. *African Archaeological Review* 24, 15–33.

Maca-Meyer, N., Gonzalez, A.M., Larruga, J.M., Flores, C., Cabrera, V.M., 2001. Major genomic mitochondrial lineages delineate early human expansions. *BMC Genetics* 2:13.

Macaulay, V., Hill, C., Achilli, A., Rengo, C., Clarke, D., Meehan, W., Blackburn, J., Semino, O., Scozzari, R., Cruciani, F., Taha, A., Shaari, N.K., Raja, J.M., Ismail, P., Zainuddin, Z., Goodwin, W., Bulbeck, D., Bandelt, H.-J., Oppenheimer, S., Torroni, A., Richards, M., 2005. Single, rapid coastal settlement of Asia revealed by analysis of complete mitochondrial genomes. *Science* 308, 1034–1036.

Mackay, A., Welz, A., 2008. Engraved ochre from a Middle Stone Age context at Klein Kliphuis in the Western Cape of South Africa. *Journal of Archaeological Science* 35, 1521–1532.

Mandryk, C.A.S., 1993. Hunter-gatherer social costs and the nonviability of submarginal environments. *Journal of Anthropological Research* 49, 39–71.

Manega, P.C., 1993. Geochronology, geochemistry, and isotopic study of the Plio-Pleistocene hominid sites and the Ngorongoro volcanic highland in northern Tanzania. Ph.D. thesis (unpublished), University of Colorado, Boulder.

Marean, C.W., Bar-Matthews, M., Bernatchez, J., Fisher, E., Goldeberg, P., Herries, A.I.R., Jacobs, Z., Jerardino, A., Karkanas, P., Minichillo, T., Nilssen, P.J., Thompson, E., Watts, I., Williams, H.M., 2007. Early human use of marine resources and pigment in South Africa during the Middle Pleistocene. *Nature* 449, 905–508.

Markey, B.G., Bøtter-Jensen, L., Duller, G.A.T., 1997. A new flexible system for measuring thermally and optically stimulated luminescence. *Radiation Measurements* 27, 83–89.

Martins, A.A., Cunha, P.P., Huot, S., Murray, A., Buylaert, J.P., 2009. Geomorphological correlation of the tectonically displaced Tejo river terraces (Gaviaõ-Chamusca area, Portugal) supported by luminescence dating. *Quaternary International* 199, 75–91.

Martins, A.A., Cunha, P.P., Buylaert, J.P., Huot, S., Murray, A.S., Dinis, P., Stokes, M., 2010. K-feldspar IRSL dating of a Pleistocene river terrace staircase sequence of the Lower Tejo River (Portugal, western Iberia). *Quaternary Geochronology* 5, 176–180.

Martinson, D.G., Pisias, N.G., Hays, J.D., Imbrie, J., Moore, T.C., Shackleton, N.J., 1987. Age dating and the orbital theory of the Ice Ages: Development of a high-resolution 0 to 300,000 year chronostratigraphy. *Quaternary Research* 27, 1–29.

Marwick, B., 2003. Pleistocene exchange networks as evidence for the evolution of language. *Cambridge Archaeological Journal* 13, 67–81.

Maslin, M.A., Christensen, B., 2007. Tectonics, orbital forcing, global climate change, and human evolution in Africa: introduction to the African paleoclimate special volume. *Journal of Human Evolution* 53, 443–464.

Mayya, Y.S., Morthekai, P., Murari, M.K., Singhvi, A.K., 2006. Towards quantifying beta microdosimetric effects in single-grain quartz dose distribution. *Radiation Measurements* 41, 1032–1039.

McBrearty, S., 2007. Down with the Revolution, in: Mellars, P., Boyle, K., Bar-Yosef, O., Stringer, C., (Eds.) *Rethinking the human revolution*. McDonald Institute for Archaeological Research, Cambridge. pp. 133–151.

McBrearty, S., 1981. Songhor: a Middle Stone Age site in western Kenya. *Quaternaria* 23, 171–190.

McBrearty, S., 1986. The archaeology of the Muguruk Site, western Kenya. Ph.D. thesis (unpublished), University of Illinois, Urbana.

McBrearty, S., Brooks, A.S., 2000. The revolution that wasn't: a new interpretation of the origin of modern human behavior. *Journal of Human Evolution* 39, 453–563.

McDougall, I., Brown, F.H., Fleagle, J.G., 2005. Stratigraphic placement and age of modern humans from Kibish, Ethiopia. *Nature* 433, 733–736.

McDougall, I., Brown, F.H., Fleagle, J.G., 2008. Sapropels and the age of hominins Omo I and II, Kibish, Ethiopia. *Journal of Human Evolution* 55, 409–420.

McGlue, M.M., Lezzar, K.E., Cohen, A.S., Russell, J.M., Tiercelin, J.-J., Felton, A., Mbede, E., Nkotagu, H.H., 2008. Seismic records of late Pleistocene aridity in Lake Tanganyika, tropical East Africa. *Journal of Paleolimnology* 40, 635–653.

McKeever, S.W.S., Bøtter-Jensen, L., Larsen, N.A., Duller, G.A.T., 1997. Temperature dependence on OSL decay curves: experimental and theoretical aspects. *Radiation Measurements* 27, 161–170.

Mehlman, M.J., 1979. Mumba-Höhle revisited: the relevance of a forgotten excavation to some current issues in East African prehistory. *World Archaeology* 11, 80–94.

Mehlman, M.J., 1987. Provenience, age and associations of archaic *Homo sapiens* crania from Lake Eyasi, Tanzania. *Journal of Archaeological Science* 14, 133–162.

Mehlman, M.J., 1989. Late Quaternary archaeological sequences in northern Tanzania. Ph.D. thesis (unpublished), University of Illinois, Urbana.

Mejdahl, V., 1979. Thermoluminescence dating: beta-dose attenuation in quartz grains. *Archaeometry* 21, 61–72.

Mejdahl, V., 1987. Internal radioactivity in quartz and feldspar grains. *Ancient TL* 5, 10–17.

Mejdahl, V., Bøtter-Jensen, L., 1994. Luminescence dating of archaeological materials using a new technique based on single aliquot measurements. *Quaternary Science Reviews (Quaternary Geochronolgy)* 7, 551–554.

Mejdahl, V., Bøtter-Jensen, L., 1997. Experience with the SARA OSL method. *Radiation Measurements* 27, 290–294.

Mellars, P.A., 1996. *The Neanderthal Legacy: An Archaeological Perspective From Western Europe*. Princeton: Princeton University Press.

Mellars, P., 2006. Why did modern human populations disperse from Africa ca. 60,000 years ago? A new model. *Proceedings of the National Academy of Sciences of the USA* 103, 9381–9386.

Mercader, J., Brooks, A.S., 2001. Across forests and savannas: Later Stone Age assemblages from Ituri and Semliki, Democratic Republic of Congo. *Journal of Anthropological Research* 57, 197–217.

Mercier, N., Falguéres, C., 2007. Field gamma dose-rate measurement with a NaI(Tl) detector: re-evaluation of the "threshold" technique. *Ancient TL* 25, 1–4.

Mercier, N., Valladas, H., Valladas, G., 1995. Flint thermoluminescence dates from the CFR Laboratory at Gif: contributions to the study of the chronology of the Middle Palaeolithic. *Quaternary Science Reviews (Quaternary Geochronology)* 14, 351–364.

Mercier, N., Valladas, H., Froget, L., Joron, J.-L., Reyss, J.-L., Weiner, S., Goldberg, P., Meignen, L., Bar-Yosef, O., Belfer-Cohen, A., Chech, M., Kuhn, S.L., Stiner, M.C., Tillier, A.-M., Arensburg, B., Vandermeersch, B., 2007. Hayonim Cave: a TL-based chronology for this Levantine Mousterian sequence. *Journal of Archaeological Science* 34, 1064–1077.

Merrick, H.V., Brown, F.H., 1984. Obsidian sources and patterns of source utilization in Kenya and northern Tanzania: some initial findings. *African Archaeological Review* 2**,** 129–152.

Merrick, H.V., Brown, F.H., Nash, W.P., 1994. Use and movement of obsidian in the Early and Middle Stone Ages of Kenya and northern Tanzania. In (S. T. Childs, Ed.) *Society, Culture, and Technology in Africa*, pp. 29–44. MASCA 11 (supplement).

Michels, J.W., Tsong, I.S.T., Nelson, C.M., 1983. Obsidian dating and East African archaeology. *Science* 219, 361–366.

Miller, G.H., Beaumont, P.B., Brooks, A.S., Deacon, H.J., Hare, P.E., Jull, A.J.T., 1999. Earliest modern humans in South Africa dated by isoleucine epimerization in ostrich eggshell. *Quaternary Science Reviews* 18, 1537–1548.

Minichillo, T., 2006. Raw material use and behavioral modernity: Howiesons Poort lithic foraging strategies. *Journal of Human Evolution* 50, 359–364.

Morthekai, P., Jain, M., Murray, A.S., Thomsen, K.J., Bøtter-Jensen, L., 2008. Fading characteristics of Martian analogue materials and the applicability of a correction procedure. *Radiation Measurements* 43, 672–678.

Morwood, M.J., Soejono, R.P., Roberts, R.G., Sutikna, T., Turney, C.S.M., Westaway, K.E., Rink, W.J., Zhao, J.-X., van den Bergh, G.D., Rokus Awe Due, Hobbs, D.R., Moore, M.W., Bird, M.I., Fifield, L.K., 2004. Archaeology and age of a new hominin from Flores in eastern Indonesia. *Nature* 431, 1087–1091.

Müller, A., Wiedenbeck, M., van den Kerkhof, A.M., Kronz, A., Simon, K., 2003. Trace elements in quartz – a combined electron microprobe, secondary ion mass

spectrometry, laser-ablation ICP-MS, and cathodoluminescence study. *European Journal of Mineralogy* 15, 747–763.

Murray, A.S., Roberts, R.G., 1997. Determining the burial time of single grains of quartz using optically stimulated luminescence. *Earth and Planetary Science Letters* 152, 163–180.

Murray, A.S., Roberts, R.G., 1998. Measurement of equivalent dose in quartz using a regenerative-dose single-aliquot protocol. *Radiation Measurements* 29, 503–515.

Murray, A.S., Mejdahl, V., 1999. Comparison of regenerative-dose single-aliquot and multiple-aliquot (SARA) protocols using heated quartz from archaeological sites. *Quaternary Science Reviews* 18, 223–229.

Murray, A.S., Wintle, A.G., 2000. Luminescence dating of quartz using an improved single-aliquot regenerative-dose protocol. *Radiation Measurements* 32, 57–73.

Murray, A.S., Olley, J.M., 2002. Precision and accuracy in the optically stimulated luminescence dating of sedimentary quartz: a status review. *Geochronometria* 21, 1–16.

Murray, A.S., Wintle, A.G., 2003. The single-aliquot regenerative-dose protocol: potential for improvements in reliability. *Radiation Measurements* 37, 377–381.

Murray, A.S., Roberts, R.G., Wintle, A.G., 1997. Equivalent dose measurement using a single aliquot of quartz. *Radiation Measurements* 27, 171–184.

Murray, A.S., Wintle, A.G., Wallinga, J., 2002. Dose estimation using quartz OSL in the non-linear region of the growth curve. *Radiation Protection Dosimetry* 101, 371–374.

Murray, A.S., Buylaert, J.P., Thomsen, K.J., Jain, M., 2009. The effect of preheating on the IRSL signal from feldspar. *Radiation Measurements* 44, 430–435.

Nathan, R.P., Thomas, P.J., Jain, M., Murray, A.S., Rhodes, E.J., 2003. Environmental dose rate heterogeneity of beta radiation and its implications for luminescence dating: Monte Carlo modelling and experimental validation. *Radiation Measurements* 37, 305–313.

Nicholson, S.E., 2000. The nature of rainfall variability over Africa on time scales of decades to millennia. *Global and Planetary Change* 26, 137–158.

North Greenland Ice Core Project Members, 2004. High-resolution record of Northern Hemisphere climate extending into the last interglacial period. *Nature* 431, 147–151.

Nowell, A., 2010. Defining behavioral modernity in the context of Neandertal and anatomically modern human populations. *Annual Review of Anthropology* 37, 437–452.

Olley, J.M., Murray, A.S., Roberts, R.G., 1996. The effects of disequilibria in the uranium and thorium decay chains on burial dose rates in fluvial sediments. *Quaternary Science Reviews* 15, 751–760.

Olley, J.M., Roberts, R.G., Murray, A.S., 1997. Disequilibria in the uranium decay series in sedimentary deposits at Allen's Cave, Nullarbor Plain, Australia: implications for dose rate determinations. *Radiation Measurements* 27, 433–443.

Olley, J., Caitcheon, G., Murray, A.S., 1998. The distribution of apparent dose as determined by optically stimulated luminescence in small aliquots of fluvial quartz: implications for dating young sediments. *Quaternary Science Reviews (Quaternary Geochronology)* 17, 1033–1040.

Olley, J.M., Caircheon, G.G., Roberts, R.G., 1999. The origin of dose distributions in fluvial sediments, and the prospect of dating single grains from fluvial deposits using optically stimulated luminescence. *Radiation Measurements* 30, 207–217.

Olley, J.M., Pietsch, T., Roberts, R.G., 2004a. Optical dating of Holocene sediments from a variety of geomorphic settings using single grains of quartz. *Geomorphology* 60, 337–358.

Olley, J.M., De Deckker, P., Roberts, R.G., Fifield, L.K., Yoshida, H., Hancock, G., 2004b. Optical dating of deep-sea sediments using single grains of quartz: a comparison with radiocarbon. *Sedimentary Geology* 169, 175–189.

Olley, J.M., Roberts, R.G., Yoshida, H., Bowler, J.M., 2006. Single-grain optical dating of grave-infill associated with human burials at Lake Mungo, Australia. *Quaternary Science Reviews* 25, 2469–2474.

Oppenheimer, S., 2009. The great arc of dispersal of modern humans: Africa to Australia. *Quaternary International* 202, 2–13.

Page, K., Frazier, P., Pietsch, T., Dehaan, R., 2007. Channel change following European settlement: Gilmore Creek, southeastern Australia. *Earth Surface Processes and Landforms* 32, 1398–1411.

Pawley, S.M., Toms, P., Armitage, S.J., Rose, J., 2010. Quartz luminescence dating of Anglian Stage (MIS 12) fluvial sediments: Comparison of SAR age estimates to the terrace chronology of the Middle Thames valley, UK. *Quaternary Geochronology* 5, 569–582.

Petraglia, M., Korisettar, R., Boivin, N., Clarkson, C., Ditchfield, P., Jones, S., Koshy, J., Mirazon Lahr, M., Oppenheimer, C., Pyle D., Roberts, R., Schwenninger, J.-L., Arnold, L., White, K., 2007. Middle Paleolithic assemblages from the Indian Subcontinent before and after Toba super-eruption. *Science* 317, 114–116.

Petraglia, M., Clarkson, C., Boivin, N., Haslam, M., Korisettar, R., Chaubey, G., Ditchfield, P., Fuller, D., James, H., Jones, S., Kivisild, T., Koshy, J., Lahr, M.M.,

Metspalu, M., Roberts, R., Arnold, L., 2009. Population increase and environmental deterioration correspond with microlithic innovations in South Asia ca. 35,000 years ago. *Proceedings of the National Academy of Sciences of the USA* 106, 12261–12266.

Pike, A.W.G., Hedges, R.E.M., Van Calsteren, P., 2002. U-series dating of bone using the diffusion-absorption model. *Geochemica et Cosmochimica Acta* 66, 4273–4286.

Poolton, N.R.J., Bøtter-Jensen, L., Ypma, P.J.M., Johnsen, O., 1994. Influence of crystal structure on the optically stimulated luminescence properties of feldspars. *Radiation Measurements* 23, 551–554.

Poolton, N.R.J., Bøtter-Jensen, L., Johnsen, O., 1995. Thermo-optical properties of optically stimulated luminescence in feldspars. *Radiation Measurements* 24, 531–534.

Poolton, N.R.J., Wallinga, J., Murray, A.S., Bulur, E., Bøtter-Jensen, L., 2002a. Electrons in feldspar I: on the wavefunction of electrons trapped at simple lattice defects. *Physics and Chemistry Minerals* 29, 210–216.

Poolton, N.R.J., Ozanyan, K.B., Wallinga, J., Murray, A.S., Bøtter-Jensen, L., 2002b. Electrons in feldspar II: a consideration of the influence of conduction band-tail states on luminescence processes. *Physics and Chemistry Minerals* 29, 217–225.

Poolton, N.R.J., Kars, R.H., Wallinga, J., Bos, A.J.J., 2009. Direct evidence for the participation of band-tails and excited-state tunnelling in the luminescence of irradiated feldspars. *Journal of Physics: Condensed Matter* 21, 485–505.

Powell, A., Shennan, S., Thomas, M.G., 2009. Late Pleistocene demography and the appearance of modern human behavior. *Science* 324, 1298–1301.

Prendergast, M.E., Luque, L., Domínguez-Rodrigo, Diez-Martín, F., Mabulla, A.Z.P., Barba, R., 2007. New excavations at Mumba rockshelter, Tanzania. *Journal of African Archaeology* 5, 217–243.

Prescott, J.R., Hutton, J.T., 1988. Cosmic ray and gamma ray dosimetry for TL and ESR. *Nuclear Tracks and Radiation Measurements* 14, 223–227.

Prescott, J.R., Hutton, J.T., 1994. Cosmic ray contributions to dose rates for luminescence and ESR dating: large depths and long-term time variations. *Radiation Measurements* 23, 497–500.

Prescott, J.R., Akber, R.A., Gartia, R.K., 1990. Three-dimensional thermoluminescence spectroscopy of minerals. In Coyne L.M., McKeever S.W.S. and Blake D.F. (eds) Spectral Characterisation of Minerals and Their Surfaces. ACS Series 196, pp. 180–189. American Chemical Society.

Prescott, J.R., Huntley, D.J., Hutton, J.T., 1993. Estimation of equivalent dose in thermoluminescence dating–The Australian slide method. *Ancient TL* 11, 1–5.

Prescott, J.R., Fox, P.J., Robertson, G.B., Hutton, J.T., 1994. Three-dimensional spectral studies of the bleaching of the thermoluminescence of feldspars. *Radiation Measurements* 23, 367–375.

Preusser, F., 2003. IRSL dating K-rich feldspars using the SAR protocol: comparison with independent age control. *Ancient TL* 21, 17–23.

Preusser, F., Ramseyer, K., Schlüchter, C., 2006. Characterisation of low OSL intensity quartz from the New Zealand Alps. *Radiation Measurements* 41, 871–877.

Preusser, F., Blei, A., Graf, H.F., Schlüchter, C., 2007. Luminescence dating of Würmian (Weichselian) proglacial sediments from Switzerland: methodological aspects and stratigraphical conclusions. *Boreas* 36, 130–142.

Preusser, F., Chithambo, M.L., Götte, T., Martini, M., Ramseyer, K., Sendezera, E.J., Susino, G.J., Wintle, A.G., 2009. Quartz as a natural luminescence dosimeter. *Earth Science Reviews* 97, 184–214.

Quintana-Murci, L., Semino, O., Bandelt, H.-J., Passarino, G., McElreavey, K., Santachiara-Benerecetti, A.S., 1999. Genetic evidence of an early exit of *Homo sapiens sapiens* from Africa through eastern Africa. *Nature Genetics* 23, 437–441.

Quintana‐Murci, L., Quach, H., Harmant, C., Luca, F., Massonnet, B., Patin, E., Sica, L., Mouguiama‐Daouda, P., Comas, D., Tzur, S., Balanovsky, O., Kidd, K.K., Kidd, J.R., van der Veen, L., Hombert, J.‐M., Gessain, A., Verdu, P., Froment, A., Bahuchet, S., Heyer, E., Dausset, J., Salas, A., Behar, D.M., 2008. Maternal traces of deep common ancestry and asymmetric gene flow between Pygmy hunter‐gatherers and Bantu-speaking farmers. *Proceedings of the National Academy of Sciences of the USA* 105, 1596–1601.

Readhead, M.L., 2002. Absorbed dose fraction for ^{87}RB β particles. *Ancient TL* 20, 25–28.

Readhead, M.L., Dunnell, R.C., Feathers, J.K., 1988. Recent addition of potassium: a potential source of error in calculating TL ages. *Ancient TL* 6, 1–4.

Rees-Jones, J., 1995. Optical dating of young sediments using fine-grain quartz. *Ancient TL* 13, 9–14.

Reich, D., Green, R.E., Kircher, M., Krause, J., Patterson, N., Durand, E.Y., Viola, B., Briggs, A.W., Stenzel, U., Johnson, P.L.F., Maricic, T., Good, J.M., Marques-Bonet, T., Alkan, C., Fu, Q., Mallick, S., Li, H., Meyer, M., Eichler, E.E., Stoneking, M., Richards, M., Talamo, S., Shunkov, M.V., Derevianko, A.P., Hublin, J.-J., Kelso, J., Slatkin, M., Pääbo, S., 2010. Genetic history of an archaic hominin group from Denisova Cave in Siberia. *Nature* 468, 1053–1060.

Reichart, G.J., Lourens, L.J., Zachariasse, W.J., 1998. Temporal variability in the northern Arabian Sea Oxygen Minimum Zone (OMZ) during the last 225,000 years. *Paleoceanography* 13, 607–621.

Reimer, P.J., Baillie, M.G.L., Bard, E., Bayliss, A., Beck, J.W., Bertrand, C.J.H., Blackwell, P.G., Buck, C.E., Burr, G.S., Cutler, K.B., Damon, P.E., Edwards, R.L., Fairbanks, R.G., Friedrich, M., Guilderson, T.P., Hogg, A.G., Hughen, K.A., Kromer, B., McCormac, F.G., Manning, S.W., Ramsey, C.B., Reimer, R.W., Remmele, S., Southon, J.R., Stuiver, M., Talamo, S., Taylor, F.W., van der Plicht, J., Weyhenmeyer, C.E., 2004. IntCal04 terrestrial radiocarbon age calibration, 0–26 cal kyr BP. *Radiocarbon* 46, 1029–1058.

Reimer, P.J., Baillie, M.G.L., Bard, E., Bayliss, A., Beck, J.W., Blackwell, P.G., Bronk Ramsey, C., Buck, C.E., Burr, G.S., Edwards, R.L., Friedrich, M., Grootes, P.M., Guilderson, T.P., Hajdas, I., Heaton, T.J., Hogg, A.G., Hughen, K.A., Kaiser, K.F., Kromer, B., McCormac, F.G., Manning, S.W., Reimer, R.W., Richards, D.A., Southon, J.R., Talamo, S., Turney, C.S.M., van der Plicht, J., Weyhenmeyer, C.E., 2009. IntCal09 and Marine09 radiocarbon age calibration curves, 0–50,000 years cal BP. *Radiocarbon* 51, 1111–1150.

Rendell, H.M., Clarke, M.L., 1997. Thermoluminescence, radioluminescence and cathode-luminescence spectra of alkali feldspars. *Radiation Measurements* 27, 263–272.

Revel, M., Ducassou, E., Grousset, F.E., Bernasconi, S.M., Migeon, S., Revillon, S., Mascle, J., Murat, A., Zaragosi, S., Bosch, D., 2010. 100,000 Years of African monsoon variability recorded in sediments of the Nile margin. *Quaternary Science Reviews* 29, 1342–1362.

Rhodes, E.J., 2000. Observations of thermal transfer OSL signals in glacigenic quartz. *Radiation Measurements* 32, 595–602.

Rhodes, E.J., Schwenninger, J.-L., 2007. Dose rates and radioisotope concentrations in the concrete calibration blocks at Oxford. *Ancient TL* 25, 5–8.

Richards, B.W.M., 2000. Luminescence dating of Quaternary sediments in the Himalaya and High Asia: a practical guide to its use and limitations for constraining the timing of glaciation. *Quaternary International* 65/66, 49–61.

Ridings, R., 1996. Where in the world does obsidian hydration dating work? *American Antiquity* 61, 136–148.

Riede, F., 2009. Climate and demography in early prehistory: using calibrated ^{14}C dates as population proxies. *Human Biology* 81, 309–337.

Rieser, U., Hütt, G., Krbetschek, M.R., Stolz, W., 1997. Feldspar IRSL emission spectra at high and low temperatures. *Radiation Measurements* 27, 273–278.

Roberts, H.M., Duller, G.A.T., 2004. Standardised growth curves for optical dating of sediment using multiple-grain aliquots. *Radiation Measurements* 38, 241–252.

Roberts, R.G., Jacobs, Z., 2008. Dating in Landscape Archaeology, in: David, B., Thomas, J. (Eds.), *Handbook and Landscape Archaeology*. Left Coast Press, Walnut Creek, pp. 347–364.

Roberts, R.G., Spooner, N.A., Questiaux, D.G., 1993. Cautions on the use of extended duration preheats in the optical dating of quartz. *Ancient TL* 11, 47–54.

Roberts, R.G., Spooner, N.A., Questiaux, D.G., 1994. Palaeodose underestimates caused by extended-duration preheats in the optical dating of quartz. *Radiation Measurements* 23, 647–653.

Roberts, R.G., Walsh, G., Murray, A.S., Olley, J., Jones, R., Morwood, M., Tuniz, C., Lawson, E., Macphail, M., Bowdery, D., Naumann, I., 1997. Luminescence dating of rock art and past environments using mud-wasp nests in northern Australia. *Nature* 387, 696–699.

Roberts, R.G., Bird, M., Olley, J., Galbraith, R., Lawson, E., Laslett, G., Yoshida, H., Jones, R., Fullagar, R., Jacobsen, G., Hua, Q., 1998a. Optical and radiocarbon dating at Jinmium rock shelter in northern Australia. *Nature* 393, 358–362.

Roberts, R.G., Yoshida, H., Galbraith, R., Lawson, E., Laslett, G., Jones, R., Smith, M., 1998b. Single-aliquot and single-grain optical dating confirm thermoluminescence age estimates at Malakunanja II rock shelter in Northern Australia. *Ancient TL* 16, 19–24.

Roberts, R.G., Galbraith, R.F., Olley, J.M., Yoshida, H., Laslett, G.M., 1999. Optical dating of single and multiple grains of quartz from Jinmium rock shelter, northern Australia: Part II, Results and implications. *Archaeometry* 41, 365–395.

Roberts, R.G., Galbraith, R.F., Yoshida, H., Laslett, G.M., Olley, J.M., 2000. Distinguishing dose populations in sediment mixtures: a test of single-grain optical dating procedures using mixtures of laboratory-dosed quartz. *Radiation Measurements* 32, 459–465.

Rogers, A.K., 2007. Effective hydration temperature of obsidian: a diffusion theory analysis of time-dependent hydration rates. *Journal of Archaeological Science* 34, 656–665.

Roller, O., 1954. *Die Steingeräte der Mumba-Höhle: Ein Beitrag zur Kenntnis der Vorgeschichte Ostafrikas.* Ph.D. thesis (unpublished), Universität Tübingen.

Rossignol-Strick, M., 1983. African monsoons, an immediate climate response to orbital insolation. *Nature* 304, 46–49.

Roth, B.J., 2000. Obsidian source characterization and hunter-gatherer mobility: an example from the Tucson basin. *Journal of Archaeological Science* 27, 305–314.

Scholz, C.A., King, J.W., Ellis, G.S., Swart, P.K., Stager, J.C., Colman, S.M., 2003. Paleolimnology of Lake Tanganyika, East Africa over the past 100 kyr. *Journal of Paleolimnology* 30, 139–150.

Scholz, C.A., Johnson, T.C., Cohen, A.S., King, J.W., Peck, J.A., Overpeck, J.T., Talbot, M.R., Brown, E.T., Kalindekafe, L., Amoako, P.Y.O., Lyons, R.P., Shanahan, T.M., Castaneda, I.S., Heil, C.W., Forman, S.L., McHargue, L.R., Beuning, K.R., Gomez, J., Pierson, J., 2007. East African megadroughts between 135 and 75 thousand years ago and bearing on early-modern human origins. *Proceedings of the National Academy of Sciences of the USA* 104, 16416–16421.

Schwarcz, H.P., 2002. Chronometric dating in archaeology: a review. *Accounts of Chemical Research* 35, 637–643.

Schwartz, G., 1978. Estimating the dimension of a model. *The Annals of Statistics* 5, 461–464.

Shanahan, T.M., Zreda, M., 2000. Chronology of quaternary glaciations in East Africa. *Earth and Planetary Science Letters* 177, 23–42.

Shennan, S., 2001. Demography and cultural innovation: a model and its implications for the emergence of modern human culture. *Cambridge Archaeological Journal* 11, 5–16.

Shea, J.J., 2008. Transitions or turnovers? Climatically-forced extinctions of *Homo sapiens* and Neandertals in the East Mediterranean Levant. *Quaternary Science Reviews* 27, 2253–2270.

Singarayer, J.S., 2002. Linearly modulated optically stimulated luminescence of sedimentary quartz: physical mechanisms and implications for dating. Ph.D. thesis (unpublished), University of Oxford.

Singarayer, J.S., Bailey, R.M., 2003. Further investigations of the quartz optically stimulated luminescence components using linear modulation. *Radiation Measurements* 37, 451–458.

Singarayer, J.S., Bailey, R.M., 2004. Component-resolved bleaching spectra of quartz optically stimulated luminescence: preliminary results and implications for dating. *Radiation Measurements* 38, 111–118.

Singer, R., Wymer, J., 1982. *The Middle Stone Age at Klasies River Mouth in South Africa*. Chicago: University of Chicago Press.

Skinner, A.R., Hay, R.L., Masao, F., Blackwell, B.A.B., 2003. Dating the Naisiusiu Beds, Olduvai Gorge, by electron spin resonance. *Quaternary Science Reviews* 22, 1361–1366.

Smith, B.W., Aitken, M.J., Rhodes, E.J., Robinson, P.D., Geldard, D.M., 1986. Optical dating: Methodological aspects. *Radiation Protection Dosimetry* 17, 229–233.

Smith, B.W., Rhodes, E.J., 1994. Charge movements in quartz and their relevance to optical dating. *Radiation Measurements* 23, 329–333.

Smith, F.H., Falsetti, A.B., Donnelly, S.M., 1989. Modern human origins. *Yearbook Physical Anthropology* 32, 35–68.

Smith, M.A., Prescott, J.R., Head, M.J., 1997. Comparison of ^{14}C and luminescence chronologies at the Puritjarra rock shelter, Central Australia. *Quaternary Geochronology (QSR)* 16, 299–320.

Soriano, S., Villa, P., Wadley, L., 2007. Blade technology and tool forms in the Middle Stone Age of South Africa: the Howiesons Poort and post-Howiesons Poort at Rose Cottage Cave. *Journal of Archaeological Science* 34, 681–703.

Spooner, N.A., 1994a. On the optical dating signal from quartz. *Radiation Measurements* 23, 593–600.

Spooner, N.A., 1994b. The anomalous fading of infrared-stimulated luminescence from feldspars. *Radiation Measurements* 23, 625–632.

Stafford, T.W., Hare, E., Currie, L., Jull, A.J.T., Donahue, D., 1991. Accelerator radiocarbon dating at the molecular level. *Journal of Archaeological Science* 18, 35–72.

Stager, J.C., Ryves, D.B., Chase, B.M., Pausata, F.S.R., 2011. Catastrophic drought in the Afro-Asian monsoon region during Heinrich Event 1. *Science* 331, 1299–1302.

Steffen, D., Preusser, F., Schluneggar, F., 2009. OSL quartz age underestimation due to unstable signal components. *Quaternary Geochronology* 4, 353–362.

Stoneham, D., Stokes, S., 1991. An investigation of the relationship between the 110°C TL peak and optically stimulated luminescence. *Nuclear Tracks and Radiation Measurements* 18, 119–123.

Stringer, C.B., Andrews, P., 1988. Genetic and fossil evidence for the origins of modern humans. *Science* 239, 1263–1268.

Surovell, T.A., 2000. Radiocarbon dating of bone apatite by step heating. *Geoarchaeolgy: An International Journal* 15, 591–608.

Taylor, R.E., 1987. Radiocarbon dating: An archaeological perspective. Orlando: Academic Press.

Texier, P.-J., Porraz, G., Parkington, J., Rigaud, J.-P., Poggenpoel, C., Miller, C., Tribolo, C., Cartwright, C., Coudenneau, A., Klein, R., Steele, T., Verna, C., 2010. A Howiesons Poort tradition of engraving ostrich eggshell containers dated to 60,000

years ago at Diepkloof Rock Shelter, South Africa. *Proceedings of the National Academy of Sciences of the USA* 107, 6180–6185.

Thackeray, J.F., 2009. Chronology, climate and technological innovation associated with the Howieson's Poort and Still Bay industries in South Africa. *South African Journal of Science* 105, 90.

Thomsen, K.J., Murray, A.S., Bøtter-Jensen, L., 2005. Sources of variability in OSL dose measurements using single grains of quartz. *Radiation Measurements* 39, 47–61.

Thomsen, K.J., Murray, A.S., Jain, M., Bøtter-Jensen, L., 2008. Laboratory fading rates of various luminescence signals from feldspar-rich sediment extracts. *Radiation Measurements* 43, 1474–1486.

Tierney, J.E., Russell, J.M., 2007. Abrupt climate change in southeast tropical Africa influenced by Indian monsoon variability and ITCZ migration. Geophysical Research Letters 34, doi:10.1029/2007GL029508.

Tierney, J.E., Russell, J.M., Huang, Y., Damsté, J.S.S., Hopmans, E.C., Cohen, A.S., 2008. Northern Hemisphere controls on tropical southeast African climate during the past 60,000 years. *Science* 322, 252–255.

Tierney, J.E., Russell, J.M., Huang, Y., 2010. A molecular perspective on Late Quaternary climate and vegetation change in the Lake Tanganyika basin, East Africa. *Quaternary Science Reviews* 29, 787–800.

Tierney, J.E., Russell, J.M., Damsté, J.S.S., Huang, Y., Verschuren, D., 2011. Late Quaternary behaviour of the East African monsoon and the importance of the Congo Air Boundary. *Quaternary Science Reviews* 30, 798–807.

Tishkoff, S.A., Gonder, M.K., Henn, B.M., Mortensen, H., Knight, A., Gignoux, C., Fernandopulle, N., Lema, G., Nyambo, T.B., Ramakrishnan, U., Reed, F.A., Mountain, J.L., 2007. History of click-speaking populations of Africa inferred from mtDNA and Y chromosome genetic variation. *Molecular Biology and Evolution* 24, 2180–2195.

Trauth, M.H., Deino, A.L., Bergner, A.G.N., Strecker, M.R., 2003. East African climate change and orbital forcing during the last 175 kyr BP. *Earth and Planetary Science Letters* 206, 297–313.

Trauth, M.H., Larrasoaña, J.C., Mudelsee, M., 2009. Trends, rhythms and events in Plio-Pleistocene African climate. *Quaternary Science Reviews* 28, 399–411.

Trauth, M.H., Maslin, M.A., Deino, A.L., Junginger, A., Lesoloyia, M., Odada, E.O., Olago, D.O., Olaka, L.A., Strecker, M.R., Tiedemann, R., 2010. Human evolution in a variable environment: the amplifier lakes of Eastern Africa. *Quaternary Science Reviews* 29, 2981–2988.

Trautmann, T., Krbetschek, M.R., Dietrich, A., Stolz, W., 2000. The basic principle of radioluminescence dating and a localized transition model. *Radiation Measurements* 32, 487–492.

Tryon, C.A., McBrearty, S., 2002. Tephrostratigraphy and the Acheulian to Middle Stone Age transition in the Kapthurin Formation, Kenya. *Journal of Human Evolution* 42, 211–235.

Tryon, C.A., Faith, J.T., Peppe, D.J., Fox, D.L., McNulty, K.P., Jenkins, K., Dunsworth, H., Harcourt-Smith, W., 2010. The Pleistocene archaeology and environments of the Wasiriya Beds, Rusinga Island, Kenya. *Journal of Human Evolution* 59, 657–671.

Tsukamoto, S., Duller, G.A.T., 2008. Anomalous fading of various luminescence signals from terrestrial basaltic samples as Martian analogues. *Radiation Measurements* 43, 721–725.

Tsukamoto, S., Rink, W.J., Watanuki, T., 2003. OSL of tephric loess and volcanic quartz in Japan and an alternative procedure for estimating D_e from a fast OSL component. *Radiation Measurements* 37, 459–465.

Tsukamoto, S., Murray, A.S., Huot, S., Watanuki, T., Denby, P.M., Bøtter-Jensen, L., 2007. Luminescence property of volcanic quartz and the use of red isothermal TL for dating tephras. *Radiation Measurements* 42, 190–197.

Tsukamoto, S., Duller, G.A.T., Wintle, A.G., Frechen, M., 2010. Optical dating of a Japanese marker tephra using plagioclase. *Quaternary Geochronology* 5, 274–278.

Vaks, A., Bar-Matthews, M., Ayalon, A., Matthews, A., Halicz, L., Frumkin, A., 2007. Desert speleothems reveal climatic window for African exodus of early modern humans. *Geology* 35, 831–834.

Vaks, A., Bar-Matthews, M., Matthews, A., Ayalon, A., Frumkin, A., 2010. Middle-Late Quaternary palaeoclimate of northern margins of the Saharan-Arabian Desert: reconstruction from speleothems of Negev Desert, Israel. *Quaternary Science Reviews* 29, 2647–2662.

Van der Plicht, J., 2000. The 2000 radiocarbon varve/comparison issue. *Radiocarbon* 42, 313–322.

Van Peer, P., Fullager, R., Stokes, S., Bailey, R.M., Moeyersons, J., Steenhoudt, F., Geerts, A., Vanderbeken, T., De Dapper, M., Geus, F., 2003. The Early to Middle Stone Age transition and the emergence of modern human behaviour at site 8-B-11, Sai Island, Sudan. *Journal of Human Evolution* 45, 187–193.

Vanhaeren, M., d'Errico, F., Stringer, C., James, S.L., Todd, J.A., Mienis, H.K., 2006. Middle Paleolithic shell beads in Israel and Algeria. *Science* 312, 1785–1788.

Vigilant, L., Stoneking, M., Harpending, H., Hawkes, K., Wilson, A.C., 1991. African populations and the evolution of human mitochondrial DNA. *Science* 253, 1503–1507.

Villa, P., Soriano, S., Teyssandier, N., Wurz, S., 2010. The Howiesons Poort and MSA III at Klasies River main site, Cave 1A. *Journal of Archaeological Science* 37, 630–655.

Visocekas, R., 1985. Tunnelling radiative recombination in labradorite; its association with anomalous fading of thermoluminescence. *Nuclear Tracks and Radiation Measurements* 10, 521–529.

Visocekas, R., 2002. Tunnelling in the afterglow, its coexistence and interweaving with thermally stimulated luminescence. *Radiation Protection Dosimetry* 100, 45–54.

Visocekas, R., Guérin, G., 2006. TL dating of feldspars using far-red emission to deal with anomalous fading. *Radiation Measurements* 41, 942–947.

Visocekas, R., Spooner, N.A., Zink, A., Blanc, P., 1994. Tunnel afterglow, fading and infrared emission in thermoluminescence of feldspars. *Radiation Measurements* 23, 377–385.

Visocekas, R., Tale, V., Zink, A., Tale, I., 1998. Trap spectroscopy and tunnelling luminescence in feldspars. *Radiation Measurements* 29, 427–434.

Voelker, A.H.L., Sarnthein, M., Grootes, P.M., Erlenkeuser, H., Laj, C., Mazaud, C., Nadeau, M.J., Schleicher, M., 1998. Correlation of marine ^{14}C ages form the Nordic Seas with the GISP2 isotopes record: implications for ^{14}C calibration beyond 25 ka BP. *Radiocarbon* 40, 517–534.

Wadley, L., 2005. Putting ochre to the test: replication studies of adhesives that may have been used for hafting tools in the Middle Stone Age. *Journal of Human Evolution* 49, 587–601.

Wadley, L., 2007. Announcing a Still Bay industry at Sibudu Cave, South Africa. *Journal of Human Evolution 52*, 681–689.

Wallinga, J., Murray, A., Duller, G.A.T., 2000a. Underestimation of equivalent dose in single-aliquot optical dating of feldspars caused by preheating. *Radiation Measurements* 32, 691–695.

Wallinga, J., Murray, A.S., Wintle, A.G., 2000b. The single-aliquot regenerative-dose (SAR) protocol applied to coarse-grain feldspar. *Radiation Measurements* 32, 529–533.

Wallinga, J., Murray, A.S., Wintle, A.G., Bøtter-Jensen, L., 2002. Electron-trapping probability in natural dosemeters as a function of irradiation temperature. *Radiation Protection Dosimetry* 101, 339–344.

Wang, Y.J., Cheng, H., Edwards, R.L., An, Z.S., Wu, J.Y., Shen, C.-C., Dorale, J.A., 2001. A high-resolution absolute-dated Late Pleistocene monsoon record from Hulu Cave, China. *Science* 294, 2345–2348.

Watanuki, T., Murray, A.S., Tsukamoto, S., 2005. Quartz and polymineral luminescence dating of Japanese loess over the last 0.6 Ma: comparison with an independent chronology. *Earth and Planetary Science Letters* 240, 774–789.

Watson, E., Forster, P., Richards, M., Bandelt, H.J., 1997. Mitochondrial footprints of human expansions in Africa. *American Journal of Human Genetics* 61, 691–704.

Wendorf, F., Close, A.E., Schild, R., 1994. Africa in the period of *Homo sapiens neanderthalensis* and contemporaries. In (S.J. de Laet, A.H. Dani, J.L. Lorenzo & R.B. Nunoo, Eds) *History of Humanity, Vol. 1: Prehistory and the Beginnings of Civilization* pp. 117–135. New York: Routledge & UNESCO.

Westaway, K.E., 2006. Reconstructing the Quaternary landscape evolution and climate history of western Flores: an environmental and chronological context for an archaeological site. Ph.D. thesis (unpublished). University of Wollongong.

Westaway, K.E., 2009. The red, white and blue of quartz luminescence: A comparison of D_e values derived for sediments from Australia and Indonesia using thermoluminescence and optically stimulated luminescence emissions. *Radiation Measurements* 44, 462–466.

Westaway, K.E., Roberts, R.G., 2006. A dual-aliquot regenerative-dose protocol (DAP) for thermoluminescence (TL) dating of quartz sediments using the light-sensitive and isothermally stimulated red emissions. *Quaternary Science Reviews* 25, 2513–2528.

Whallon, R., 2006. Social networks and information: non-"utilitarian" mobility among hunter-gatherers. *Journal of Anthropological Archaeology* 25, 259–270.

White, T.D., Asfaw, B., DeGusta, D., Gilbert, H., Richards, G.D., Suwa, G., Howell, F.C., 2003. Pleistocene *Homo sapiens* from Middle Awash, Ethiopia. *Nature* 423, 742–747.

Wiessner, P., 1983. Style and social information in Kalahari San projectile points. *American Antiquity* 48, 253–276.

Wiessner, P., 1986. !Kung San networks in a generational perspective. In (M. Biesele, R. Gordon and R. Lee, Eds) *The Past and Future of !Kung San Ethnography*, pp. 103–136. Hamburg: Helmut Buske Verlag Quellen zur Khoisan-Forschung, Band 4.

Wintle, A.G., 1973. Anomalous fading of thermoluminescence in mineral samples. *Nature* 245, 143–144.

Wintle, A.G., 1997. Luminescence dating: laboratory procedures and protocols. *Radiation Measurements* 27, 769–817.

Wintle, A.G., Duller, G.A.T., 1991. The effect of optical absorption on luminescence dating. *Ancient TL* 9, 37–39.

Wintle, A.G., Murray, A.S., 1999. Luminescence sensitivity changes in quartz. *Radiation Measurements* 30, 107–118.

Wintle, A.G., Murray, A.S., 2000. Quartz OSL: effects of thermal treatment and their relevance to laboratory dating procedures. *Radiation Measurements* 32, 387–400.

Wintle, A.G., Murray, A.S., 2006. A review of quartz optically stimulated luminescence characteristics and their relevance in single-aliquot regeneration dating protocols. *Radiation Measurements* 41, 369–391.

Wobst, H.M., 1976. Locational relationships in Palaeolithic society. *Journal of Human Evolutio*n 5, 49–58.

Wolpoff, M.H., 1989. Multiregional evolution: the fossil alternative to Eden. *In* "The Human Revolution: behavioural and biological perspectives on the origins of modern humans." (C. B. Stringer., P. Mellars, Ed.), pp. 62–108. Edinburgh University Press, Edinburgh.

Wright, D.K., Forman, S.L., Kusimba, C.M., Pierson, J., Gomez, J., Tattersfield, P., 2007. Stratigraphic and geochronological context of human habitation along the Galana River, Kenya. *Geoarchaeology* 22, 708–728.

Wurz, S., 1999. The Howiesons Poort backed artifacts from Klasies River: an argument for symbolic behavior. *South African Archaeological Bulletin* 54, 38–50.

Wurz, S., 2000. The Middle Stone Age at Klasies River Mouth. Ph.D. thesis (unpublished), University of Stellenbosch, Stellenbosch, South Africa.

Yellen, J.E., Brooks, A.S., Cornelissen, E., Mehlman, M.H., Stewart, K., 1995. A Middle Stone Age worked bone industry from Katanda, Upper Semliki Valley, Zaire. *Science* 268, 553–556.

Yoshida, H., Roberts, R.G., Olley, J.M., Laslett, G.M., Galbraith, R.F., 2000. Extending the age range of optical dating using single 'supergrains' of quartz. *Radiation Measurements* 32, 439–446

Yoshida, H., Roberts, R.G., Olley, J.M., 2003. Progress towards single-grain optical dating of fossil mud-wasp nests and associated rock art in northern Australia. *Quaternary Science Reviews* 22, 1273–1278.

Yuan, D., Cheng, H., Edwards, R.L., Dykoski, C.A., Kelly, M.J., Zhang, M., Qing, J., Lin, Y., Wang, Y., Wu, J., Dorale, J.A., An, Z., Cai, Y., 2004. Timing, duration, and transitions of the Last Interglacial Asian monsoon. *Science* 304, 575–578.

Zech, M., 2006, Evidence for Late Pleistocene climate changes from buried soils on the southern slopes of Mt. Kilimanjaro, Tanzania. *Palaeogeography, Palaeoclimatology, Palaeoecology* 242, 303–312.

Zhao, H., Li, S.-H., 2005. Internal dose rate to K-feldspar grains from radioactive elements other than potassium. *Radiation Measurements* 40, 84–93.

Zilhão, J., Angelucci, D.E., Badal-García, E., d'Errico, F., Daniel, F., Dayet, L., Douka, K., Higham, T.G., Martínez-Sánchez, M.J., Montes-Bernárdez, R., Murcia- Mascarós, S., Pérez-Sirvent, C., Roldán-García, C., Vanhaeren, M., Villaverde, V., Wood, R., Zapata, J., 2010. Symbolic use of marine shells and mineral pigments by Iberian Neandertals. *Proceedings of the National Academy of Sciences of the USA* 107, 1023–1028.

Zimmerman, D.W., 1971. Thermoluminescent dating using fine grains from pottery. *Archaeometry* 13, 29–52.

Zink, A.J.C., Visocekas, R., 1997. Datability of sanidine feldspars using the near-infrared TL emission. *Radiation Measurements* 27, 251–261.

Zink, A., Visocekas R., Bos, A.J.J., 1995. Comparison of 'blue' and 'infrared' emission bands in thermoluminescence of alkali feldspars. *Radiation Measurements* 24, 513–518.

Appendix 1: Approximate number of grains on multi-grain aliquots

To prepare a multi-grain aliquot of quartz and feldspar grains, a silicone oil adhesive (Silkospray) was sprayed onto a 10 mm-diameter stainless steel disc through a mask of a specified diameter. Mineral grains were then mounted onto the disc, adhering to the area covered in the oil in a monolayer. The approximate number of 180–212 µm-diameter grains that correspond to the various mask sizes used in this study are presented in Table A1.1.

Table A1.1: Approximate number of 180–212 µm grains that were mounted onto stainless steel discs using a silicone oil adhesive applied to discs using masks of the specified diameters.

Mask size (mm)	Approximate number of grains
1	10 - 20
3	100 - 200
5	300 - 500
7	500 - 1000

Appendix 2: Comparing de-convoluted LM-OSL curves

Several experiments described in Chapter 5 required the measurement, de-convolution and comparison of multiple LM-OSL curves measured after regenerative and test doses for the same aliquot over the course of an LM-OSL SAR procedure (Section 5.1.3). Several observations were made when various LM-OSL curves from the same aliquot were de-convoluted and compared. To illustrate these observed patterns, an aliquot consisting of ~500 grains of quartz from MR7 was bleached in sunlight for at least three days. It was given a dose (116 Gy), preheated to 260°C for 10 s, and then stimulated by linearly ramping the blue LEDs from 0 to 90% over 3600 s while the LM-OSL was measured (L_x). After the LM-OSL measurement, a test dose cycle was performed that consisted of a test dose of 11 Gy, a preheat of 220°C for 5 s, and a LM-OSL measurement for 3600 s (T_x). This procedure was repeated five times, serving as an extended recycling ratio test, such as that built into the SAR procedure (Section 3.3.2.2). Results, presented in Table A2.1, exhibit the following patterns:

1. When de-convoluting a LM-OSL curve, as the number of components (*N*) was increased, the PIC and *b* values of the first component increased and the size of the first component (*n*) decreased.
2. For any given aliquot, the PIC and *b* values decreased in a linear fashion with each progressive regenerative dose cycle (i.e., R_1, R_2 …R_5) for a given value of *N* (e.g., Figure A2.1).
3. When *N* was kept constant and the LM-OSL signal following a regenerative dose was compared to the LM-OSL signal following the subsequent test dose, the PIC and *b* values of the first component were always larger for the regenerative dose than for the test dose.
4. The value of *N* that best fit the data (according to the sum of the squared residuals) was not necessarily the same for the regenerative and test doses. For example, in Table A2.1, the best fit for the regenerative dose is $N = 4$, and the best fit for the test dose is $N = 5$.

Table A2.1: Results obtained by de-convoluting LM-OSL curves from a multi-grain aliquot of MR7. The aliquot was given a regenerative dose (~116 Gy), preheated (260°C), and the LM-OSL was measured. The aliquot was then given a test dose (~11 Gy), preheated (220°C), and the LM-OSL was measured. Both LM-OSL curves were then de-convoluted as described in section 3.5.2.2 for *N* = 2, 3, 4, 5, and 6. The *b* value, relative *b* values, and sum of squared residuals are shown for each de-convolution model (i.e., value of *N*).

Regenerative Dose								
Number of Components (*N*)								**Sum of squared residuals**
2	***b***	1.0	0.0006					3.E+08
	relative *b*	1	0.0006					
3	***b***	1.0	0.024	0.0005				6.E+07
	relative *b*	1	0.02	0.0005				
4	***b***	1.1	0.18	0.011	0.0005			4.E+07
	relative *b*	1	0.16	0.009	0.0004			
5	***b***	1.2	0.45	0.049	0.0066	0.0004		9.E+07
	relative *b*	1	0.37	0.04	0.005	0.0003		
6	***b***	1.3	0.59	0.101	0.020	0.0047	0.0004	5.E+07
	relative *b*	1	0.47	0.08	0.02	0.004	0.0007	

Test Dose								
Number of Components (*N*)								**Sum of squared residuals**
2	***b***	0.9	0.0006					6.52E+07
	relative *b*	1	0.0007					
3	***b***	1.0	0.020	0.0005				4.28E+07
	relative *b*	1	0.02	0.0005				
4	***b***	1.0	0.13	0.010	0.0005			2.31E+07
	relative *b*	1	0.13	0.010	0.0005			
5	***b***	1.0	0.17	0.016	0.0026	0.0005		1.05E+07
	relative *b*	1	0.16	0.02	0.002	0.0005		
6	***b***	1.1	0.36	0.084	0.012	0.0007	2.00E-04	4.20E+07
	relative *b*	1	0.33	0.08	0.01	0.0006	0.0006	

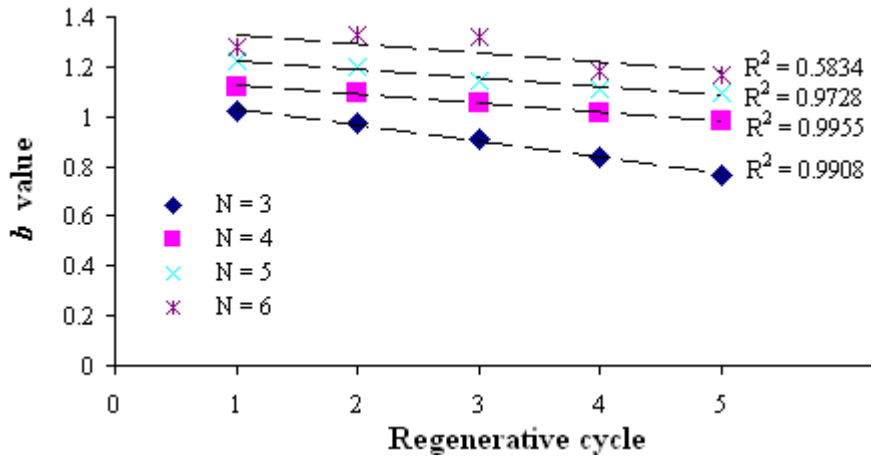

Figure A2.1: LM-OSL de-convolution results over five SAR measurement cycles for a single aliquot of MR7. The LM-OSL curve was de-convoluted as described in section 3.5.2.2.

A2.1 Determining the number of component (*N*)

Given the observations noted above, how should de-convoluted LM-OSL curves be compared to one another? Ideally, the PIC and *b* values of the components that are being compared should be identical. Li and Li (2006b) used LM-OSL signals to isolate the fast component for D_e estimation. They encountered similar problems to those faced in this study, including the inability to clearly separate and identify components in the slower part of the LM-OSL signal. They tested the effect of varying the peak position (related to the *PIC* and thus *b* value following Equation 2 in Li and Li, 2006b) of the fast component and concluded that fixing the peak position improved reproducibility and resulted in more accurate estimates of the intensity of the peak, resulting in more reliable dose-response curves.

As a means of testing the observations of Li and Li (2006b) and to establish a procedure for choosing the value of *N* to use for comparing LM-OSL curves, the results from the experiment described in this appendix were analysed using the two methods described below:

Method One:

The *N* value was chosen for each L_x using the sum of the squared residuals measure of best fit. The *N* value for each T_x was then chosen based on that which produced a *b* value closest to that for the preceding L_x.

Method two:

No measures of 'best fit' were used to choose the *N* value for either the L_x or T_x. Each LM-OSL curve was de-convoluted for *N* values of 2, 3, 4, 5 and 6, and the resulting parameters (*b* and *n*) were scrutinised. The largest value of *N* that could be fit for each T_x (always either $N = 5$ or $N = 6$ for quartz from Mumba) was chosen. This resulted in the *b* values of the fast component for all test dose LM-OSL signals being within a 0.10 s^{-1} range, for an individual aliquot. The *N* value for each L_x was then chosen based on the *N* value that resulted in a fast component with a *b* value in the range produced by test doses. In doing this, the fast components for all regenerative and test dose LM-OSL signals had *b* values within a range of 0.10 s^{-1}.

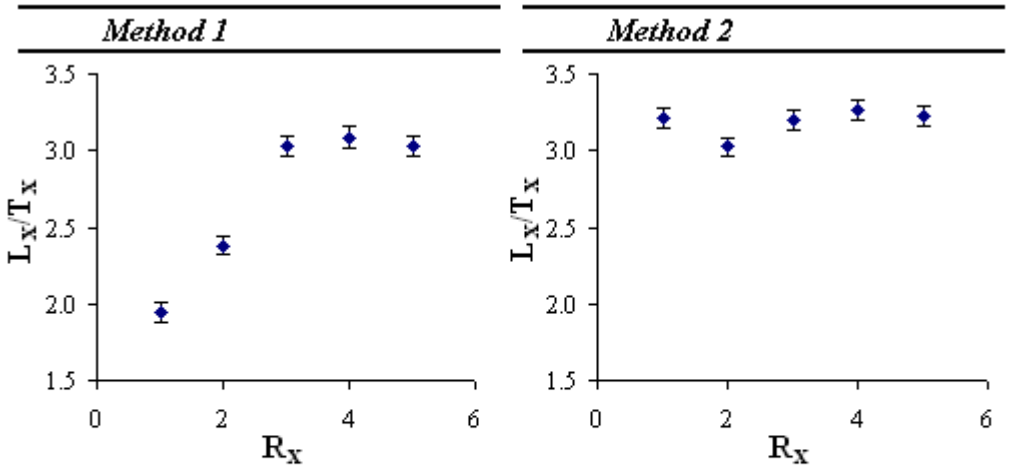

R_X		1	2	3	4	5
L_X	*N*	6	6	5	5	5
	b	1.39	1.30	1.19	1.17	1.16
T_X	*N*	6	5	6	6	6
	b	1.14	1.10	1.10	1.10	1.08

R_X		1	2	3	4	5
L_X	*N*	3	4	4	4	4
	b	1.11	1.16	1.13	1.11	1.09
T_X	*N*	6	5	6	6	6
	b	1.14	1.10	1.10	1.10	1.08

Figure A2.2: Comparison of the *Method 1* and *Method 2* for analysing LM-OSL de-convolution data for a single aliquot (see text). The error on each L_x/T_x value is displayed at 2σ. The tables display the *N* value for both L_x and T_x for each R_x. The *b* value for the fast component is also shown.

Results produced for one aliquot using both *Method 1* and *Method 2* are compared in Figure A2.2. Since all regenerative and test doses were identical, and the SAR procedure was shown to be suitable for quartz from Mumba when the fast component was used (see Chapter 5), the sensitivity corrected signal of the fast component should be the same for all SAR measurement cycles (i.e., R_1, R_2 …R_5).

Method 1 produced a large spread in the *b* values obtained for the LM-OSL curves induced by both regenerative and test doses. The *b* values varied from 1.08 to 1.39 s^{-1}, a range of 0.31 s^{-1}. The spread in *b* values was reduced considerably when *Method 2* was used. The 0.10 s^{-1} range in *b* values used for this aliquot was 1.07 to 1.17 s^{-1}. The L_x/T_x values for four out of five SAR cycles (R_x) are consistent with each other at 2σ and the fifth value is within 5% of the other four.

These results support the suggestion of Li and Li (2006b) that fixing the peak position (analogous to the *b* value) results in improved reproducibility. Consequently, in all cases when two or more LM-OSL signals are compared in this thesis, *Method 2* was used to determine the optimal de-convolution model (i.e., value of *N*) for each LM-OSL curve.